APPLIED COMPUTATIONAL ELECTROMAGNETICS SOCIETY JOURNAL

January 2019
Vol. 34 No. 1
ISSN 1054-4887

The ACES Journal is abstracted in INSPEC, in Engineering Index, DTIC, Science Citation Index Expanded, the Research Alert, and to Current Contents/Engineering, Computing & Technology.

The illustrations on the front cover have been obtained from the research groups at the Department of Electrical Engineering, The University of Mississippi.

THE APPLIED COMPUTATIONAL ELECTROMAGNETICS SOCIETY
http://aces-society.org

EDITORS-IN-CHIEF

Atef Elsherbeni
Colorado School of Mines, EE Dept.
Golden, CO 80401, USA

Sami Barmada
University of Pisa, ESE Dept.
56122 Pisa, Italy

ASSOCIATE EDITORS: REGULAR PAPERS

Mohammed Hadi
Kuwait University, EE Dept.
Safat, Kuwait

Alistair Duffy
De Montfort University
Leicester, UK

Wenxing Li
Harbin Engineering University
Harbin 150001, China

Maokun Li
Tsinghua University
Beijing 100084, China

Mauro Parise
University Campus Bio-Medico of Rome
00128 Rome, Italy

Yingsong Li
Harbin Engineering University
Harbin 150001, China

Riyadh Mansoor
Al-Muthanna University
Samawa, Al-Muthanna, Iraq

Antonio Musolino
University of Pisa
56126 Pisa, Italy

Abdul A. Arkadan
Colorado School of Mines, EE Dept.
Golden, CO 80401, USA

Salvatore Campione
Sandia National Laboratories
Albuquerque, NM 87185, USA

Wei-Chung Weng
National Chi Nan University, EE Dept.
Puli, Nantou 54561, Taiwan

Alessandro Formisano
Seconda Universita di Napoli
81031 CE, Italy

Piotr Gas
AGH University of Science and Technology
30-059 Krakow, Poland

Marco Arjona López
La Laguna Institute of Technology
Torreon, Coahuila 27266, Mexico

Paolo Mezzanotte
University of Perugia
I-06125 Perugia, Italy

Luca Di Rienzo
Politecnico di Milano
20133 Milano, Italy

Rocco Rizzo
University of Pisa
56123 Pisa, Italy

Lei Zhao
Jiangsu Normal University
Jiangsu 221116, China

Sima Noghanian
University of North Dakota
Grand Forks, ND 58202, USA

Qiang Ren
Beihang University
Beijing 100191, China

ASSOCIATE EDITORS: EXPRESS PAPERS

Lijun Jiang
University of Hong Kong, EEE Dept.
Hong, Kong

Shinichiro Ohnuki
Nihon University
Tokyo, Japan

Kubilay Sertel
The Ohio State University
Columbus, OH 43210, USA

Steve J. Weiss
US Army Research Laboratory
Adelphi Laboratory Center (RDRL-SER-M)
Adelphi, MD 20783, USA

Jiming Song
Iowa State University, ECE Dept.
Ames, IA 50011, USA

Amedeo Capozzoli
Univerita di Napoli Federico II, DIETI
I-80125 Napoli, Italy

Yu Mao Wu
Fudan University
Shanghai 200433, China

Maokun Li
Tsinghua University, EE Dept.
Beijing 100084, China

EDITORIAL ASSISTANTS

Matthew J. Inman
University of Mississippi, EE Dept.
University, MS 38677, USA

Kyle Patel
Colorado School of Mines, EE Dept.
Golden, CO 80401, USA

Madison Le
Colorado School of Mines, EE Dept.
Golden, CO 80401, USA

Shanell Lopez
Colorado School of Mines, EE Dept.
Golden, CO 80401, USA

Allison Tanner
Colorado School of Mines, EE Dept.
Golden, CO 80401, USA

EMERITUS EDITORS-IN-CHIEF

Duncan C. Baker
EE Dept. U. of Pretoria
0002 Pretoria, South Africa

Allen Glisson
University of Mississippi, EE Dept.
University, MS 38677, USA

Ahmed Kishk
Concordia University, ECS Dept.
Montreal, QC H3G 1M8, Canada

Robert M. Bevensee
Box 812
Alamo, CA 94507-0516, USA

Ozlem Kilic
Catholic University of America
Washington, DC 20064, USA

David E. Stein
USAF Scientific Advisory Board
Washington, DC 20330, USA

EMERITUS ASSOCIATE EDITORS

Yasushi Kanai
Niigata Inst. of Technology
Kashiwazaki, Japan

Mohamed Abouzahra
MIT Lincoln Laboratory
Lexington, MA, USA

Alexander Yakovlev
University of Mississippi, EE Dept.
University, MS 38677, USA

Levent Gurel
Bilkent University
Ankara, Turkey

Sami Barmada
University of Pisa, ESE Dept.
56122 Pisa, Italy

Ozlem Kilic
Catholic University of America
Washington, DC 20064, USA

Erdem Topsakal
Mississippi State University, EE Dept.
Mississippi State, MS 39762, USA

William O'Keefe Coburn
US Army Research Laboratory
Adelphi, MD 20783, USA

Fan Yang
Tsinghua University, EE Dept.
Beijing 100084, China

EMERITUS EDITORIAL ASSISTANTS

Khaled ElMaghoub
Trimble Navigation/MIT
Boston, MA 02125, USA

Christina Bonnington
University of Mississippi, EE Dept.
University, MS 38677, USA

Anne Graham
University of Mississippi, EE Dept.
University, MS 38677, USA

Mohamed Al Sharkawy
Arab Academy for Science and Technology, ECE Dept.
Alexandria, Egypt

JANUARY 2019 REVIEWERS: REGULAR PAPERS

Hany Atallah
Nikolay Atanasov
Ahmed Attiya
Herve Aubert
Emine Avsar Aydin
Zsolt Badics
Lahcene Boukelkoul
Madhav BTP
Scott Burnside
Ali Cetin
Fangyuan Chen
Dajun Cheng
Hosam El-Ocla
Grant Ellis
Gregor Ergaver
Ali Hazeri
Miroslav Joler
Fatih Kaburcuk
Robin Kalyan
Tarun Kumar
George Kyriacou
Micaela Liberti
Qun Lou
Mingyu Lu
Peng Lv
Riyadh Mansoor
Zahra Manzoor
Ricardo Matias
Ahmed Mobashsher
Arkadiusz Mystkowski
Syeda Naqvi
Guangdong Pan
Mark Panitz
Kyle Patel
Andrew Peterson
Rashid Saleem
A. Salinas
Vitawat Sittakul
Chalasani Subba Rao
Sellakkutti Suganthi
Mehmet Tabakcioglu
SureshKumar TR
Ioannis Vardiambasis
Julia Wolff
Qianyin Xiang
Qian Xu
Fan Yang
Sun Zhe

THE APPLIED COMPUTATIONAL ELECTROMAGNETICS SOCIETY JOURNAL

Vol. 34 No. 1 January 2019

TABLE OF CONTENTS – REGULAR PAPERS

Efficient TLM-Based Approach for Compact Modeling of Anisotropic Materials and Composites

Miloš D. Kostić [1], Nebojša S. Dončov [2], Zoran Ž. Stanković [2], and John D. Paul [3]

[1] Innovation Center of Advanced Technologies, Niš, 18000, Serbia
r.i.p.romeo@gmail.com

[2] Faculty of Electronic Engineering
University of Niš, Niš, 18000, Serbia
nebojsa.doncov@elfak.ni.ac.rs, zoran.stankovic@elfak.ni.ac.rs

[3] Electromagnetics scientist, Nottingham, NG1, United Kingdom
john.derek.paul@gmail.com

Abstract **─** Compact modeling approach of anisotropic media by using the Z-TLM method is proposed. Thin anisotropic multilayer material is efficiently described through connection procedure between two Z-TLM mesh cells, by using the scattering parameters to create a digital filter-based compact model. Model is incorporated into non-uniform TLM grid given here in a form fully complying with the originally proposed Z-TLM method algorithm. Accuracy and efficiency of the compact model is confirmed on a few examples through comparison with the fine mesh results.

Index Terms **─** Anisotropic materials and composites, compact model, non-uniform grid, Z-TLM method.

I. INTRODUCTION

Discrete time modeling techniques have been used by researchers for years to simulate and observe propagation and distribution of electromagnetic (EM) fields inside of different media. The two most popular modeling techniques based on time and space discretization are the Finite Difference Time Domain (FDTD) method [1] and the Transmission Line Matrix (TLM) method [2]. Generally, the FDTD method is often the favored numerical technique for solving different kinds of EM problems ranging from antenna problems, electromagnetic compatibility, microwave systems, etc. However, the TLM method, since it was established in 1970 by P. B. Johns, has proven to have certain advantages in modeling of specific complex structures and nonlinear materials.

TLM algorithm is highly localized since electric and magnetic fields are solved in the center of the TLM cell at the same time. In addition to that, the fact that any change in the state of a TLM cell affects only its immediate neighbors at the next computational step makes it more suited for modeling of anisotropic and bianisotropic media. EM fields on cell boundaries can be determined without necessity to perform temporal interpolation and field averaging, which is another important feature. An enhancement of the TLM method with Z-transform techniques (so-called Z-TLM method) [3] enables a direct mapping of dispersive EM material properties into the time-domain in order to study their time-harmonic and transient response. The Z-TLM method has already been used for simulation of linear isotropic and anisotropic media, bi-isotropic and quantum materials as well as materials with nonlinear and metamaterial properties [3-9].

In order to properly simulate behavior of geometrically small but electrically important features in an otherwise large modeling space, by using traditional approach in discrete time modeling methods, an extremely fine mesh is required. With intention to overcome this computationally and time costly requirement, and thus improve efficiency, development of compact models is required. Compact models allow for using coarser mesh, e.g. reducing all thin material cells to single boundary condition based on material panel scattering parameters [10] (sort of “black box” approach where only input and output values are observed) or by using retrieval methods for effective EM parameter extraction from the scattering parameters of thin material in order to model it and observe EM field behavior within its interior boundaries [11].

Material can be defined as anisotropic when values of one or more EM properties (such as conductivity, permittivity and permeability) depend on direction of EM propagation e.g., when EM properties are functions of the coordinate system orientation. Micro-structure of anisotropic materials consists out of different layers created and connected naturally (wood, different crystals,

Submitted On: July 14, 2018
Accepted On: December 25, 2018

minerals and rocks, etc.) or intentionally in structural/ man-made (reinforced, ribbed, perforated, layered materials etc.). General anisotropic materials, besides coefficients on main diagonal (a_{xx}, a_{yy}, a_{zz}) in EM property matrix, contain additional coefficients which describe codependency based on direction (a_{xy}, a_{xz}, a_{yx}, ...). This makes modeling of materials like carbon, graphite, glass and other composites more challenging.

In this paper, the discretization of Maxwell's equations and constitutive relations for simulation of general anisotropic and dispersive materials, using the Z-TLM method in non-linear grid, is described. The ways to describe the TLM method for modeling of dispersive and anisotropic media and/or using non-uniform meshes have been given in [12, 13] but here is given in a form that fully complies with the Z-TLM method initially proposed in [3-5]. In addition to that, an efficient approach for compact modeling of composite anisotropic materials, previously applied on a one-dimensional case [14], is here given in a generalized form and later used in a two-dimensional (2-D) problem. It uses the scattering parameters of a composite structure consisting in general of n material layers, obtained from e.g., fine Z-TLM mesh, to create a digital filter-based compact model where composite structure is efficiently described with boundary condition between two Z-TLM mesh cells. Compared to other network-based methods such as ladder type method [15], the proposed approach is more general and the created model is more easily and more memory efficiently incorporated into the TLM connection procedure. Accuracy and efficiency of the approach is confirmed on a few examples through comparison with the fine Z-TLM mesh results.

II. DISCRETIZATION OF MAXWELL'S EQUATIONS FOR NON-UNIFORM MESH

For non-uniform TLM cell, where one or more directional space steps ($\Delta x, \Delta y$, and Δz) are not equal, a compact form of Maxwell's curl equations is established through constitutive relations for electric and magnetic current and flux densities:

$$\begin{bmatrix}\nabla\times\underline{H}\\ -\nabla\times\underline{E}\end{bmatrix}-\begin{bmatrix}\underline{J_{ef}}\\ \underline{J_{mf}}\end{bmatrix}=\frac{\partial}{\partial t}\begin{bmatrix}\varepsilon_0\underline{E}\\ \mu_0\underline{H}\end{bmatrix}+\begin{bmatrix}\underline{\underline{\sigma_e}}*\underline{E}\\ \underline{\underline{\sigma_m}}*\underline{H}\end{bmatrix}+\frac{\partial}{\partial t}\begin{bmatrix}\varepsilon_0\underline{\underline{\chi_e}} & \underline{\underline{\xi_r}}/c\\ \underline{\underline{\zeta_r}}/c & \mu_0\underline{\underline{\chi_m}}\end{bmatrix}*\begin{bmatrix}\underline{E}\\ \underline{H}\end{bmatrix}, \tag{1}$$

where $*$ denotes time domain convolution, $\underline{J_{ef}}, \underline{J_{mf}}$ represent electric and magnetic current densities vectors, $\underline{\underline{\sigma_e}}, \underline{\underline{\sigma_m}}$ and $\underline{\underline{\chi_e}}, \underline{\underline{\chi_m}}$ are electric and magnetic conductivity and susceptibility matrices respectively, ε_0, μ_0 are free space permittivity and permeability, and $\underline{\underline{\xi_r}}, \underline{\underline{\zeta_r}}$ are dimensionless matrices describing magnetoelectric coupling.

By expanding curl terms of (1) in Cartesian coordinates and introducing a compact notation with defined matrices and vectors, the following expression is formed:

$$-\begin{bmatrix}\nabla\times\underline{H}\\ -\nabla\times\underline{E}\end{bmatrix}=\begin{bmatrix}\frac{1}{\eta_0}\underline{\underline{A}}^{-1} & \underline{\underline{0}}\\ \underline{\underline{0}} & \underline{\underline{A}}^{-1}\end{bmatrix}\cdot\begin{bmatrix}0 & \underline{\underline{C}}\\ -\underline{\underline{C}} & 0\end{bmatrix}\cdot\begin{bmatrix}\underline{V}\\ \underline{i}\end{bmatrix}. \tag{2}$$

In (2) η_0 is intrinsic impedance of free-space, $\underline{V}$ and $\underline{i}$ are vectors of voltages and currents defined in the center of TLM cell while the matrix of inverse cell areas and normalized curl matrix are represented as:

$$\underline{\underline{A}}^{-1}=\begin{bmatrix}(\Delta z\Delta y)^{-1} & 0 & 0\\ 0 & (\Delta z\Delta x)^{-1} & 0\\ 0 & 0 & (\Delta y\Delta x)^{-1}\end{bmatrix}, \underline{\underline{C}}=\begin{bmatrix}0 & -\partial_Z & \partial_Y\\ \partial_Z & 0 & -\partial_X\\ -\partial_Y & \partial_X & 0\end{bmatrix}, \tag{3}$$

where $\partial_X, \partial_Y, \partial_Z$ are normalized spatial derivatives in *x*, *y* and *z* direction respectively.

After applying the field circuit equivalences and defining free-current vectors, free current density terms are formed as:

$$-\begin{bmatrix}\underline{J_{ef}}\\ \underline{J_{mf}}\end{bmatrix}=\begin{bmatrix}\frac{1}{\eta_0}\underline{\underline{A}}^{-1} & \underline{\underline{0}}\\ \underline{\underline{0}} & \underline{\underline{A}}^{-1}\end{bmatrix}\cdot\begin{bmatrix}\underline{i_{ef}}\\ \underline{V_{mf}}\end{bmatrix}. \tag{4}$$

Vector matrix form of time derivative field term is established by transforming time derivative operator $\frac{\partial}{\partial t}$:

$$-\frac{\partial}{\partial t}\begin{bmatrix}\varepsilon_0\underline{E}\\ \mu_0\underline{H}\end{bmatrix}=\left(\frac{2\alpha_t}{\Delta\ell}\right)\frac{\partial}{\partial T}\begin{bmatrix}\frac{1}{\eta_0}\underline{\underline{\Delta}}^{-1} & \underline{\underline{0}}\\ \underline{\underline{0}} & \underline{\underline{\Delta}}^{-1}\end{bmatrix}\cdot\begin{bmatrix}\underline{V}\\ \underline{i}\end{bmatrix}, \tag{5}$$

by defining the matrix of inverse cell length $\underline{\underline{\Delta}}^{-1}$ as:

$$\underline{\underline{\Delta}}^{-1}=\begin{bmatrix}\Delta x^{-1} & 0 & 0\\ 0 & \Delta y^{-1} & 0\\ 0 & 0 & \Delta z^{-1}\end{bmatrix}, \tag{6}$$

and introducing parameter α_t as the time-step adjustment factor so that:

$$\frac{\partial}{\partial t}=\frac{1}{\Delta t}\frac{\partial}{\partial T}=\frac{2c\alpha_t}{\Delta\ell}\frac{\partial}{\partial T}. \tag{7}$$

Compact notation of electric and magnetic conductivity terms is defined in order to represent them as:

$$-\begin{bmatrix}\underline{\underline{\sigma_e}}*\underline{E}\\ \underline{\underline{\sigma_m}}*\underline{H}\end{bmatrix}=\begin{bmatrix}\frac{1}{\eta_0}\underline{\underline{A}}^{-1} & \underline{\underline{0}}\\ \underline{\underline{0}} & \underline{\underline{A}}^{-1}\end{bmatrix}\cdot\begin{bmatrix}\underline{\underline{g_e}}*\underline{V}\\ \underline{\underline{r_m}}*\underline{i}\end{bmatrix}. \tag{8}$$

Time derivative susceptibility term in normalized form yields:

$$\begin{aligned}&-\frac{\partial}{\partial t}\begin{bmatrix}\varepsilon_0\underline{\underline{\chi_e}} & \underline{\underline{\xi_r}}/c\\ \underline{\underline{\zeta_r}}/c & \mu_0\underline{\underline{\chi_m}}\end{bmatrix}*\begin{bmatrix}\underline{E}\\ \underline{H}\end{bmatrix}=\\ &=\left(\frac{2\alpha_t}{\Delta\ell}\right)\frac{\partial}{\partial T}\begin{bmatrix}\underline{\underline{\chi_e}}/\eta_0 & \underline{\underline{\xi_r}}/\eta_0\\ \underline{\underline{\zeta_r}} & \underline{\underline{\chi_m}}\end{bmatrix}\cdot\begin{bmatrix}\underline{\underline{\Delta}}^{-1} & \underline{\underline{0}}\\ \underline{\underline{0}} & \underline{\underline{\Delta}}^{-1}\end{bmatrix}*\begin{bmatrix}\underline{V}\\ \underline{i}\end{bmatrix}.\end{aligned} \tag{9}$$

Using expressions above along with defining background susceptibilities matrix,

$$\underline{\underline{\chi_b}} = \left(\frac{2\alpha_t}{\Delta\ell}\right)\underline{\underline{A}}\,\underline{\underline{\Delta}}^{-1} - \underline{\underline{1}}, \tag{10}$$

where $\underline{\underline{1}}$ is identity matrix, a normalized form of Maxwell's equations is assembled as:

$$\begin{aligned}&\begin{bmatrix} 0 & \underline{\underline{C}} \\ -\underline{\underline{C}} & 0 \end{bmatrix}\cdot\begin{bmatrix}\underline{V}\\ \underline{i}\end{bmatrix} - \begin{bmatrix}\underline{i_{ef}}\\ \underline{V_{mf}}\end{bmatrix} = 2\frac{\partial}{\partial T}\begin{bmatrix}\underline{V}\\ \underline{i}\end{bmatrix} + 2\frac{\partial}{\partial T}\begin{bmatrix}\underline{\underline{\chi_b}} & \underline{\underline{0}}\\ \underline{\underline{0}} & \underline{\underline{\chi_b}}\end{bmatrix}\cdot\begin{bmatrix}\underline{V}\\ \underline{i}\end{bmatrix} + \\ &+\begin{bmatrix}\underline{\underline{g_e}} * \underline{V}\\ \underline{\underline{r_m}} * \underline{i}\end{bmatrix} + \left(\frac{2\alpha_t}{\Delta\ell}\right)\frac{\partial}{\partial T}\begin{bmatrix}\underline{\underline{A}} & \underline{\underline{0}}\\ \underline{\underline{0}} & \underline{\underline{A}}\end{bmatrix}\cdot\begin{bmatrix}\underline{\underline{\chi_e}} & \underline{\underline{\xi_r}}\\ \underline{\underline{\zeta_r}} & \underline{\underline{\chi_m}}\end{bmatrix}\cdot\begin{bmatrix}\underline{\underline{\Delta}}^{-1} & \underline{\underline{0}}\\ \underline{\underline{0}} & \underline{\underline{\Delta}}^{-1}\end{bmatrix} * \begin{bmatrix}\underline{V}\\ \underline{i}\end{bmatrix}.\end{aligned} \tag{11}$$

Approximating the normalized partial derivations in the curl matrix using the finite-differences of the voltages and currents on the surface of the TLM cell and applying the transformation to the travelling wave format as explained in [3], (11) can be written as:

$$\begin{aligned}&2\begin{bmatrix} V_0^i + V_1^i + V_2^i + V_3^i \\ V_4^i + V_5^i + V_6^i + V_7^i \\ V_8^i + V_9^i + V_{10}^i + V_{11}^i \\ -\left(V_6^i - V_7^i - V_8^i - V_9^i\right) \\ -\left(V_{10}^i - V_{11}^i - V_0^i - V_1^i\right) \\ -\left(V_2^i - V_3^i - V_4^i - V_5^i\right)\end{bmatrix} - \begin{bmatrix} i_{efx} \\ i_{efy} \\ i_{efz} \\ V_{mfx} \\ V_{mfy} \\ V_{mfz}\end{bmatrix} = \\ &= 4\begin{bmatrix}\underline{V}\\ \underline{i}\end{bmatrix} + 2\frac{\partial}{\partial T}\begin{bmatrix}\underline{\underline{\chi_b}} & \underline{\underline{0}}\\ \underline{\underline{0}} & \underline{\underline{\chi_b}}\end{bmatrix}\cdot\begin{bmatrix}\underline{V}\\ \underline{i}\end{bmatrix} + \begin{bmatrix}\underline{\underline{g_e}} * \underline{V}\\ \underline{\underline{r_m}} * \underline{i}\end{bmatrix} + \\ &+\left(\frac{2\alpha_t}{\Delta\ell}\right)\frac{\partial}{\partial T}\begin{bmatrix}\underline{\underline{A}} & \underline{\underline{0}}\\ \underline{\underline{0}} & \underline{\underline{A}}\end{bmatrix}\cdot\begin{bmatrix}\underline{\underline{\chi_e}} & \underline{\underline{\xi_r}}\\ \underline{\underline{\zeta_r}} & \underline{\underline{\chi_m}}\end{bmatrix}\cdot\begin{bmatrix}\underline{\underline{\Delta}}^{-1} & \underline{\underline{0}}\\ \underline{\underline{0}} & \underline{\underline{\Delta}}^{-1}\end{bmatrix} * \begin{bmatrix}\underline{V}\\ \underline{i}\end{bmatrix}.\end{aligned} \tag{12}$$

Defining the left-side of (12) as the excitation vector and introducing an effective susceptibility matrix as:

$$\begin{bmatrix}\underline{\underline{\chi_e}}^{eff} & \underline{\underline{\xi_r}}^{eff}\\ \underline{\underline{\zeta_r}}^{eff} & \underline{\underline{\chi_m}}^{eff}\end{bmatrix} = \begin{bmatrix}\underline{\underline{\chi_b}} & \underline{\underline{0}}\\ \underline{\underline{0}} & \underline{\underline{\chi_b}}\end{bmatrix} + \left(\frac{\alpha_t}{\Delta\ell}\right)\begin{bmatrix}\underline{\underline{A}} & \underline{\underline{0}}\\ \underline{\underline{0}} & \underline{\underline{A}}\end{bmatrix}\cdot\begin{bmatrix}\underline{\underline{\chi_e}} & \underline{\underline{\xi_r}}\\ \underline{\underline{\zeta_r}} & \underline{\underline{\chi_m}}\end{bmatrix}\cdot\begin{bmatrix}\underline{\underline{\Delta}}^{-1} & \underline{\underline{0}}\\ \underline{\underline{0}} & \underline{\underline{\Delta}}^{-1}\end{bmatrix}, \tag{13}$$

the final form of discrete-time solution of Maxwell's equations can be obtained as:

$$2\begin{bmatrix}\underline{V^r}\\ \underline{\text{-}i^r}\end{bmatrix} = 4\begin{bmatrix}\underline{V}\\ \underline{i}\end{bmatrix} + \begin{bmatrix}\underline{\underline{g_e}} * \underline{V}\\ \underline{\underline{r_m}} * \underline{i}\end{bmatrix} + 2\frac{\partial}{\partial T}\begin{bmatrix}\underline{\underline{\chi_e}}^{eff} & \underline{\underline{\xi_r}}^{eff}\\ \underline{\underline{\zeta_r}}^{eff} & \underline{\underline{\chi_m}}^{eff}\end{bmatrix} * \begin{bmatrix}\underline{V}\\ \underline{i}\end{bmatrix}. \tag{14}$$

Previous expression can also be written as:

$$2\underline{F^r} = 4\underline{F} + \underline{\underline{\sigma}}(T) * \underline{F} + 2\frac{\partial}{\partial t}\left[\underline{\underline{M}}(T) * \underline{F}\right], \tag{15}$$

where $\underline{\underline{\sigma}}(T)$ is conductivity matrix and $\underline{\underline{M}}(T)$ general material matrix, which also may contain some time dependent elements indicated explicitly with (T).

$$\underline{\underline{\sigma}}(T) = \begin{bmatrix}\underline{\underline{g_e}} & \underline{\underline{0}}\\ \underline{\underline{0}} & \underline{\underline{r_m}}\end{bmatrix}, \quad \underline{\underline{M}}(T) = \begin{bmatrix}\underline{\underline{\chi_e}}^{eff} & \underline{\underline{\xi_r}}^{eff}\\ \underline{\underline{\zeta_r}}^{eff} & \underline{\underline{\chi_m}}^{eff}\end{bmatrix}. \tag{16}$$

Using e.g., the bilinear Z-transform in the form $\partial / \partial T \approx 2\left(1 - z^{-1}\right)/\left(1 + z^{-1}\right)$ (15) can be written as:

$$2\left(1 + z^{-1}\right)\cdot\underline{F^r} = \left(1 + z^{-1}\right)\left(\underline{\underline{4}}\cdot\underline{F} + \underline{\underline{\sigma}}(z)\cdot\underline{F}\right) + \left(1 - z^{-1}\right)\underline{\underline{4M}}(z)\cdot\underline{F}, \tag{17}$$

where z is a time shift operator. Additionally, matrix $\underline{\underline{4}} = 4\underline{\underline{1}}$.

In the modeling of matrices $\underline{\underline{\sigma}}(z)$ or $\underline{\underline{M}}(z)$ containing causal time-dependent elements, the overall strategy is to shift the time-dependence back to the previous time-step by taking partial fraction expansions as explained in [3,4]:

$$(1 + z^{-1})\underline{\underline{\sigma}}(z) = \underline{\underline{\sigma_0}} + z^{-1}\left[\underline{\underline{\sigma_1}} + \underline{\underline{\sigma_2}}(z)\right], \tag{18}$$

$$(1 - z^{-1})\underline{\underline{M}}(z) = \underline{\underline{M_0}} - z^{-1}\left[\underline{\underline{M_1}} + \underline{\underline{M_2}}(z)\right]. \tag{19}$$

III. COMPACT MODELING OF N-LAYER ANISOTROPIC MATERIAL

Proposed approach for a simulation of thin anisotropic multilayer material is based on acquiring the co-polarized and cross-polarized reflection and transmission coefficients in order to derivate the compact model. Hence, it is possible to eliminate the need to apply a fine mesh for modeling of material itself and replace it with interior boundary condition incorporated into a coarse mesh. When applying the compact model, the required number of cells and simulation run-time are significantly reduced in comparison with the fine mesh simulations.

The process of generating the compact model begins by numerically acquiring the co- and cross-polarized scattering parameters of thin anisotropic material by using the fine TLM mesh. Assuming that the thin anisotropic material is surrounded by air and placed in *i*-plane, the case of one-dimensional (1-D) propagation in *i* direction, with no coupling to the *i*-directed field components, has to be first considered. Two fine mesh time domain simulations have to be run with *j*- and *k*-polarized incident wave propagating in *i* direction, respectively. For each excitation, the incident field at the air-anisotropic material interface as well as the reflected and transmitted fields of appropriate polarization on both sides of this interface has to be recorded at each time-step so that the co-polarized and cross-polarized reflection and transmission coefficients of air-anisotropic material interface can be obtained using the following equations (20) and (21), respectively:

$$\begin{aligned} S_{11}^{kk} &= \frac{V_{reflected\_field}^{k}}{V_{incident\_field}^{k}}, \; S_{21}^{kk} = \frac{V_{transmitted\_field}^{k}}{V_{incident\_field}^{k}}, \\ S_{11}^{jj} &= \frac{V_{reflected\_field}^{j}}{V_{incident\_field}^{j}}, S_{21}^{jj} = \frac{V_{transmitted\_field}^{j}}{V_{incident\_field}^{j}}, \end{aligned} \tag{20}$$

$$S_{11}^{jk} = \frac{V_{reflected\_field}^{j}}{V_{incident\_field}^{k}}, S_{21}^{jk} = \frac{V_{transmitted\_field}^{j}}{V_{incident\_field}^{k}},$$
$$S_{11}^{kj} = \frac{V_{reflected\_field}^{k}}{V_{incident\_field}^{j}}, S_{21}^{kj} = \frac{V_{transmitted\_field}^{k}}{V_{incident\_field}^{j}}, \quad (21)$$

where index *k* is used to mark incident, reflected or transmitted field of *k* polarization and index *j* is used to mark incident, reflected or transmitted field of *j* polarization. The remaining co-polarized and cross-polarized reflection and transmission coefficients, S_{12} and S_{22}, can be found similarly considering *j*- and *k*-polarized incident wave propagating in -*i* direction.

After performing the Fourier transform and translating parameters from time to frequency domain, the vector fitting (VF) method [16-18] is used to calculate rational approximations of *n*-th order (NP poles) of obtained co-polarized and cross-polarized reflection and transmission coefficients as:

$$S_{ij}^{pr} = \sum_{k=0}^{NP_{ij}^{pr}-1} C_{k,ij}^{pr} / \left(s - s_{pk,ij}^{pr}\right), \quad (22)$$

where $s_{pk,ij}^{pr}$ and $C_{k,ij}^{pr}$ are complex pole frequencies and residues, respectively, NP_{ij}^{pr} is a number of poles and $(ij) \in \{(11),(12),(21),(22)\}$, $(pr) \in \{(kk),(kj),(jk),(jj)\}$. Applying the bilinear Z-transform results in discrete-time representation of (22):

$$S_{ij}^{pr} = \frac{B_{0,ij}^{pr} + \sum_{k=1}^{NP_{ij}^{pr}} B_{k,ij}^{pr} z^{-k}}{1 + \sum_{k=1}^{NP_{ij}^{pr}} A_{k,ij}^{pr} z^{-k}} \xrightarrow{PFE} B_{0,ij}^{pr} \frac{\sum_{k=1}^{NP_{ij}^{pr}} B_{k,ij}^{'pr} z^{-k}}{1 + \sum_{k=1}^{NP_{ij}^{pr}} A_{k,ij}^{pr} z^{-k}}, \quad (23)$$

where PFE stands for partial fraction expansion, $A_{k,ij}^{pr}$'s and $B_{k,ij}^{pr}$'s coefficients are real and the coefficients $B'^{pr}_{k,ij} = B_{k,ij}^{pr} - B_{0,ij}^{pr} A_{k,ij}^{pr}$.

Digital filter-based compact model is then incorporated into the connection matrix of two TLM cells at which interface the anisotropic material is modeled as internal boundary condition (Fig. 1) so that:

$$\begin{bmatrix} V_k^{inc}[\bar{i}] \\ V_k^{inc}[\bar{i}+1] \end{bmatrix} = \begin{bmatrix} S_{11}^{kk} & S_{12}^{kk} \\ S_{21}^{kk} & S_{22}^{kk} \end{bmatrix} \begin{bmatrix} V_k^{ref}[\bar{i}] \\ V_k^{ref}[\bar{i}+1] \end{bmatrix} + \begin{bmatrix} S_{11}^{kj} & S_{12}^{kj} \\ S_{21}^{kj} & S_{22}^{kj} \end{bmatrix} \begin{bmatrix} V_j^{ref}[\bar{i}] \\ V_j^{ref}[\bar{i}+1] \end{bmatrix}, (24)$$

$$\begin{bmatrix} V_j^{inc}[\bar{i}] \\ V_j^{inc}[\bar{i}+1] \end{bmatrix} = \begin{bmatrix} S_{11}^{jk} & S_{12}^{jk} \\ S_{21}^{jk} & S_{22}^{kk} \end{bmatrix} \begin{bmatrix} V_k^{ref}[\bar{i}] \\ V_k^{ref}[\bar{i}+1] \end{bmatrix} + \begin{bmatrix} S_{11}^{jj} & S_{12}^{jj} \\ S_{21}^{jj} & S_{22}^{jj} \end{bmatrix} \begin{bmatrix} V_j^{ref}[\bar{i}] \\ V_j^{ref}[\bar{i}+1] \end{bmatrix}, (25)$$

where the incident and reflected voltage pulses orientations are defined with the respect of center of the TLM cells.

Considering that wave propagation can be observed along different axes of the Cartesian coordinate system, appropriate usage of TLM cell voltage pulses in (24) and (25) for each direction accordingly is provided in Table 1.

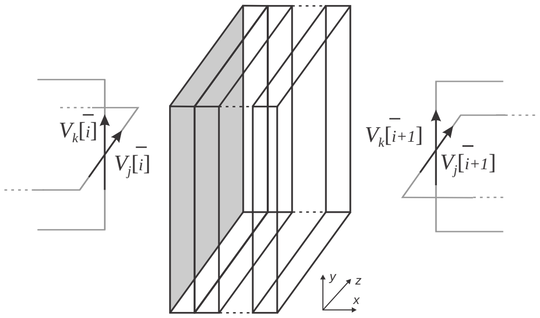

Fig. 1. Anisotropic *n*-layer material panel modeled as internal boundary condition.

Table 1: Voltage pulses notation based on wave propagation in *i* direction

i, j, k	$i \in x$	$i \in y$	$i \in z$
$V_k[\bar{i}]$	V_{12}	V_{10}	V_8
$V_k[\bar{i}+1]$	V_{11}	V_9	V_7
$V_j[\bar{i}]$	V_6	V_4	V_2
$V_j[\bar{i}+1]$	V_5	V_3	V_1

IV. MODELING RESULTS

The efficiency and accuracy of the compact modeling approach presented in section 3 is illustrated on two 2-D cases by using in-house developed TLM-Z code executed in MATLAB environment.

A. Symmetrical case

Thin single layered anisotropic material panel surrounded by air on both sides is placed in 2-D space (Fig. 2). Thickness of material is *d*=1 mm, isotropic relative permittivity has value of $\varepsilon_r = 5$ while the electric conductivity is anisotropic and described with matrix:

$$\underline{\underline{\sigma}} = \begin{bmatrix} \sigma_{xx} & \sigma_{xy} & \sigma_{xz} \\ \sigma_{yx} & \sigma_{yy} & \sigma_{yz} \\ \sigma_{zx} & \sigma_{zy} & \sigma_{zz} \end{bmatrix}, \quad (26)$$

where $\sigma_{yy} = \sigma_{yz} = \sigma_{zy} = \sigma_{zz} = 100$ while the other matrix elements are equal to zero.

In order to obtain the co-polarized and cross-polarized reflection and transmission coefficients, as explained in section 3, an initial pulse of Gaussian form polarized first in *z* and then in *y* direction while propagating along the *x* axis was considered. 1-D Z-TLM fine mesh consisting out of 210 cells in *x* direction (10 cells to accurately represent EM field inside of the material) was used. Smallest dimension in model (in this case material panel) have to be described with minimum

5 cells and it is recommended to use at least 10 cells to represent minimum wavelength. Real and imaginary parts of co-polarized and cross-polarized reflection and transmission coefficients, obtained in such way are shown in Figs. 3 and 4. Due to symmetrical case,

$$S_{11}^{yy} = S_{22}^{yy} = S_{11}^{zz} = S_{22}^{zz}\,,\; S_{11}^{yz} = S_{22}^{yz} = S_{11}^{zy} = S_{22}^{zy}\,,$$

$$S_{12}^{yy} = S_{21}^{yy} = S_{12}^{zz} = S_{21}^{zz} \text{ and } S_{12}^{yz} = S_{21}^{yz} = S_{12}^{zy} = S_{21}^{zy}\,.$$

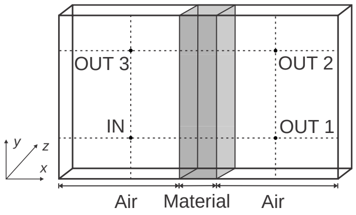

Fig. 2. Thin single layered anisotropic material placed in 2-D space.

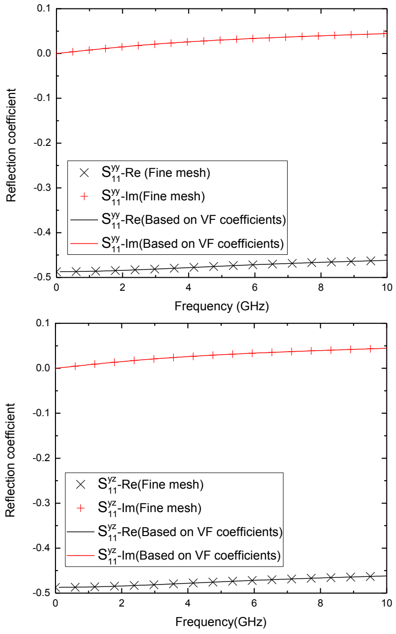

Fig. 3. Real and imaginary part of co-polarized and cross-polarized reflection coefficients (S_{11}^{yy} and S_{11}^{yz}) of thin single layered anisotropic material.

Next, coefficients A and B, obtained by the VF method in order to approximate the obtained reflection and transmission coefficients, are given in Table 2.

The rational approximations of 4-th order (number of poles NP = 4) is used to achieve needed accuracy. In [14] complex frequency dependence of reflection/ transmission curves demanded rational approximations of 24th order. This neither influenced stability of method nor reduced accuracy of results but considering that higher number of poles increases computational time it is recommended to find a proper balance. In some cases, reduction of frequency bandwidth in which the model is valid may reduce complexity of the approach and therefore can positively influence the modeling process. The approximated curves are shown also in Figs. 3 and 4.

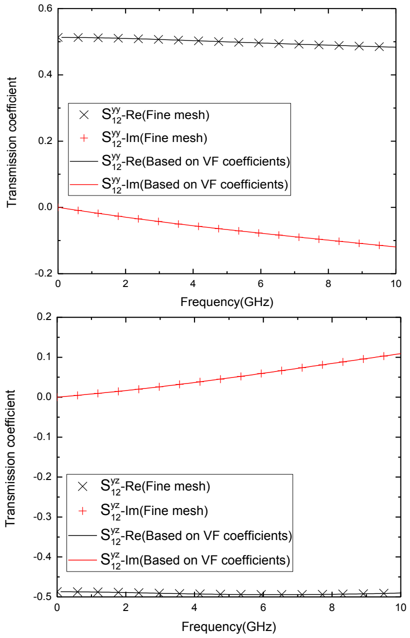

Fig. 4. Real and imaginary part of co-polarized and cross-polarized transmission coefficients (S_{12}^{yy} and S_{12}^{yz}) of thin single layered anisotropic material.

Thin single layered anisotropic material placed in 2-D space, as shown in Fig. 2, was considered in two ways:

1) Conventional approach by using the fine Z-TLM mesh to describe material (10 cells per thickness);
2) Proposed approach using coarse mesh and derived compact model placed at the position corresponding to the initial position of anisotropic material.

Fine mesh was consisted out of 882x441x1 TLM cells. The number of time steps was 6300. Material is described with 10x441 cells while the rest of the cells are defined in areas filled with air. Excitation z-polarized source is placed at point marked as IN while electric field is observed in 3 different output points (OUT1, OUT2 and OUT3). Boundaries of the mesh in *x* and *y* planes are defined as absorbing while wrapped boundary conditions are used in *z* plane.

Compact model was incorporated into the coarse mesh with 42x21x1 cells. Cell size is increased to Δl=2.1 mm in order to preserve same modeling space. In that way, the number of cells is significantly reduced from 388962 cells, used in fine mesh, to only 882 cells (almost 99.78% less required cells) and the number of time steps is reduced from 6300 to 600.

Time-domain values of the electric field components in 3 output points, obtained by using the fine mesh (dotted lines) and course mesh with incorporated compact model (solid lines) are shown in Fig. 5. A good agreement between these two results can be observed.

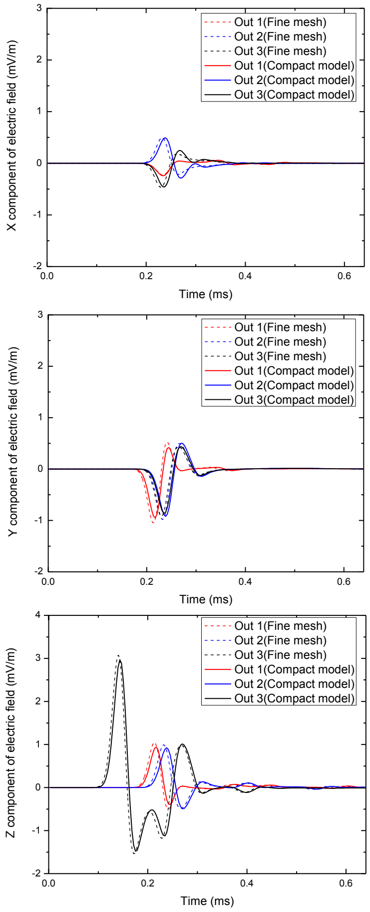

Fig. 5. Time-domain values of electric field components in 3 output points for thin single layered anisotropic material.

B. Asymmetrical case

In the second 2-D case, the composite general anisotropic material (Fig. 6) consists out of two layers of thickness d_1=d_2=1 mm, isotropic relative permittivity $\varepsilon_r = 5$, and the anisotropic electric conductivities:

$$\underline{\underline{\sigma}}_1 = \begin{bmatrix} 0 & 0 & 0 \\ 0 & 100 & 100 \\ 0 & 100 & 100 \end{bmatrix}, \quad \underline{\underline{\sigma}}_2 = \begin{bmatrix} 0 & 0 & 0 \\ 0 & 100 & 0 \\ 0 & 0 & 500 \end{bmatrix}. \tag{27}$$

Overall dimensions and cell size of 1-D fine meshes, as well as 2-D fine mesh and 2-D coarse mesh with incorporated compact model, are the same as in previously described single layered model. 10 cells per thickness are used for each layer.

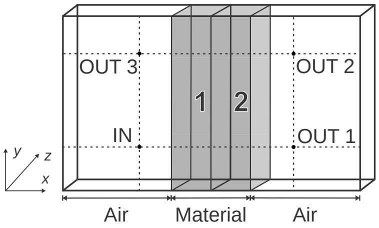

Fig. 6. Thin double layered anisotropic material placed in 2-D space.

Real and imaginary parts of some of co- and cross-polarization reflection and transmission coefficients of thin doubly layered anisotropic material are shown in Figs. 7-10.

Coefficients A and B, obtained by the VF method in order to approximate the obtained reflection and transmission coefficients, are given in Table 3. The approximated curves are shown also in Figs. 7-10.

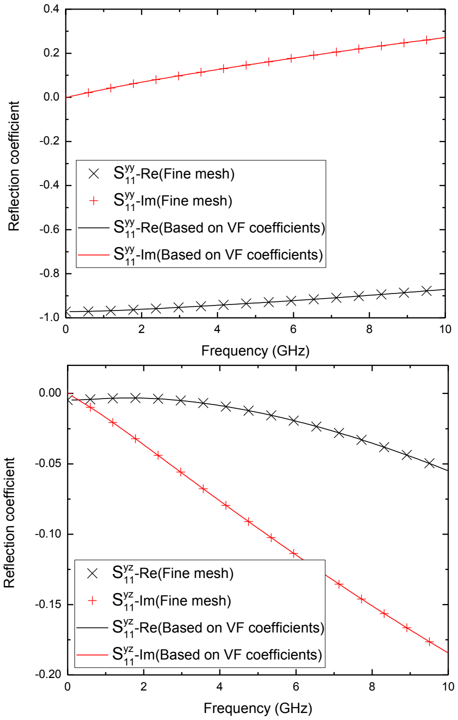

Fig. 7. Real and imaginary parts of co-polarized and cross-polarized reflection coefficients (S_{11}^{yy} and S_{11}^{yz}) of thin double layered anisotropic material.

Table 2: Coefficients used in (24) for compact representation of scattering parameters of single layered anisotropic material

Coefficient	$S_{11}^{yy}=S_{22}^{yy}=S_{11}^{zz}=S_{22}^{zz}$	$S_{11}^{yz}=S_{22}^{yz}=S_{11}^{zy}=S_{22}^{zy}$	$S_{12}^{yy}=S_{21}^{yy}=S_{12}^{zz}=S_{21}^{zz}$	$S_{12}^{yz}=S_{21}^{yz}=S_{12}^{zy}=S_{21}^{zy}$
B_0	-0.30415	-0.30415	0.063009	-0.06914
B_{prim}	-0.19535	-0.19534	0.271142	-0.24547
	0.454817	0.454811	-0.30291	0.099353
	-0.33921	-0.3392	-0.11521	0.07618
	0.079605	0.079601	0.150994	0.023792
A	1	1	1	1
	-2.02082	-2.02079	-1.94979	-1.40735
	0.942684	0.942647	1.278526	1.036736
	0.263883	0.263892	-0.48868	-0.65231
	-0.18501	-0.18501	0.168866	0.13335

Table 3: Coefficients used in (24) for compact representation of scattering parameters of double layered anisotropic material

Coefficient	S_{11}^{yy}	S_{11}^{zy}	S_{11}^{yz}	S_{11}^{yz}	S_{12}^{yy}	S_{12}^{zy}	S_{12}^{yz}	S_{12}^{zz}
B_0	-0.24811	-0.34991	-0.34991	-0.24751	-0.00064	-4.3E-05	0.000806	2.62E-05
B_{prim}	-0.36872	-0.05714	-0.05714	-0.36872	-0.00032	-5.1E-05	0.000567	3.32E-05
	0.938844	0.438528	0.438528	0.926638	0.002292	0.000184	-0.00276	-0.00011
	-0.8042	-0.68222	-0.68222	-0.77416	-0.00338	-0.00023	0.002462	0.000132
	0.232546	0.301308	0.301308	0.215514	0.001415	9.24E-05	-0.00028	-4.9E-05
A	1	1	1	1	1	1	1	1
	-3.03142	-2.0778	-2.0778	-3.00084	-3.36594	-3.5849	-2.69801	-3.51673
	3.418113	1.169718	1.169718	3.328296	4.257562	4.825226	2.615658	4.658698
	-1.69193	-0.03519	-0.03519	-1.61464	-2.40398	-2.89129	-1.06807	-2.75777
	0.30736	-0.05533	-0.05533	0.288149	0.512677	0.65106	0.152168	0.616004
Coefficient	S_{22}^{yy}	S_{22}^{zy}	S_{22}^{yz}	S_{22}^{zz}	S_{21}^{yy}	S_{21}^{zy}	S_{21}^{yz}	S_{21}^{zz}
B_0	-0.53567	9.19E-06	9.19E-06	-0.66253	-0.00064	0.000806	-4.3E-05	2.62E-05
B_{prim}	-0.40885	2.38E-05	2.38E-05	-0.39397	-0.00032	0.000567	-5.1E-05	3.32E-05
	1.018796	-5.4E-05	-5.4E-05	1.023097	0.002292	-0.00276	0.000184	-0.00011
	-0.83547	3.66E-05	3.66E-05	-0.8784	-0.00338	0.002462	-0.00023	0.000132
	0.224896	-6.4E-06	-6.4E-06	0.24896	0.001415	-0.00028	9.24E-05	-4.9E-05
A	1	1	1	1	1	1	1	1
	-2.29451	-3.62786	-3.62786	-2.21122	-3.36594	-2.69801	-3.5849	-3.51673
	1.48577	4.920007	4.920007	1.193826	4.257562	2.615658	4.825226	4.658698
	-0.02709	-2.95467	-2.95467	0.291451	-2.40398	-1.06807	-2.89129	-2.75777
	-0.16274	0.662553	0.662553	-0.2731	0.512677	0.152168	0.65106	0.616004

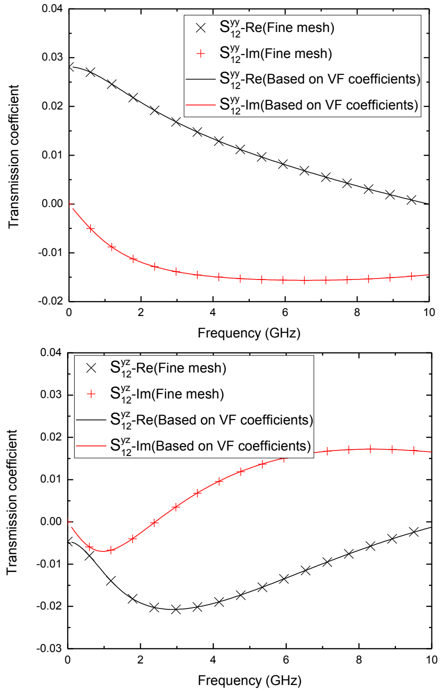

Fig. 8. Real and imaginary parts of co-polarized and cross-polarized transmission coefficients (S_{12}^{yy} and S_{12}^{yz}) of thin double layered anisotropic material.

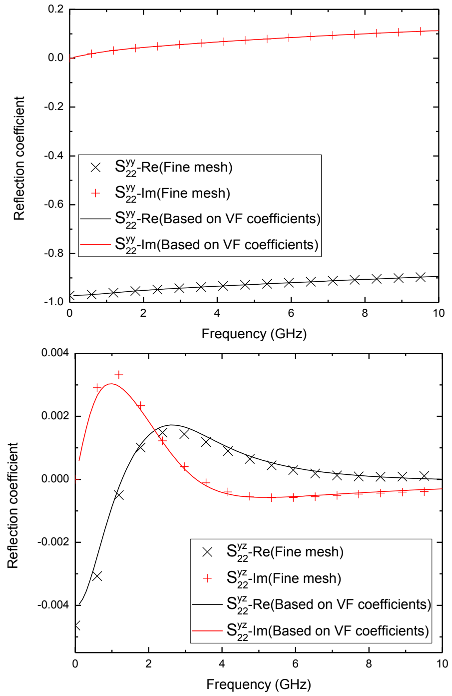

Fig. 9. Real and imaginary parts of co-polarized and cross-polarized reflection coefficients (S_{22}^{yy} and S_{22}^{yz}) of thin double layered anisotropic material.

Time-domain values of the electric field components in 3 output points, obtained by using the fine mesh (dotted lines) and course mesh with incorporated compact model (solid lines) are shown in Fig. 11. Results from point OUT3 for *z* component of electric field are shown separately for presentation purposes, because output values acquired in third point are much higher than results from first two points. A good agreement between these two results can be observed.

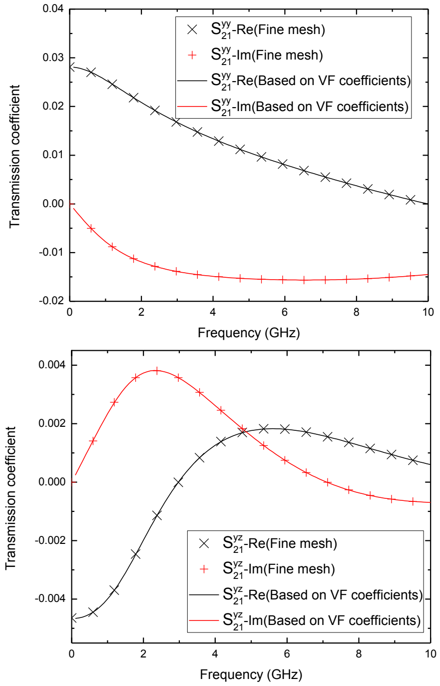

Fig. 10. Real and imaginary parts of co-polarized and cross-polarized transmission coefficients (S_{21}^{yy} and S_{21}^{yz}) of thin double layered anisotropic material.

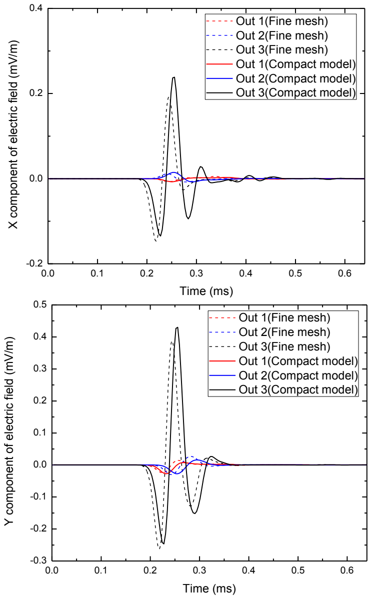

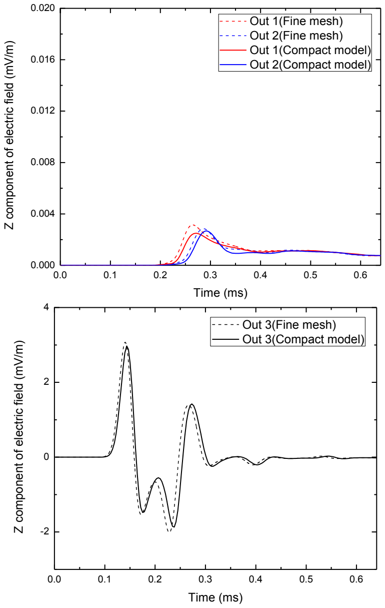

Fig. 11. Time-domain values of electric field components in 3 output points for thin double layered anisotropic material.

V. CONCLUSION

Efficient TLM based approach for compact modeling of anisotropic materials and composites is presented in this paper. Major advantage of this approach is significant reduction (over 99%) of mesh required for material modeling, which directly reduce computational costs and time. This can be very useful when modeling of thin multi-layered anisotropic material panels and structures. In future work, a proposed approach can be potentially applied for efficient modeling of anisotropic media in 3-D space.

ACKNOWLEDGMENT

This work has been supported by the Ministry of Education, Science and Technological Development of Serbia, project number TR32024.

REFERENCES

[1] K. S. Kunz and R. J. Luebbers, *The Finite Difference Time Domain Method for Electromagnetics*. CRC Press, 1993.

[2] C. Christopoulos, *The Transmission-Line Modelling (TLM) Method*. IEEE/OUP Press, 1995.

[3] J. Paul, "Modelling of general electromagnetic material properties in TLM," *Ph.D. Dissertation*, University of Nottingham, UK, 1998.

[4] J. Paul, C. Christopoulos, and D. W. P. Thomas, "Generalized material models in TLM – Part I: Materials with frequency-dependent properties," *IEEE Transactions on Antennas and Propagation*, vol. 47, no. 10, pp. 1528-1534, 1999.

[5] J. Paul, C. Christopoulos, and D. W. P. Thomas, "Generalized material models in TLM – Part II: Materials with anisotropic properties," *IEEE Transactions on Antennas and Propagation*, vol. 47, no. 10, pp. 1535-1542, 1999.

[6] J. Paul, C. Christopoulos, and D. W. P. Thomas, "Time-domain modelling of electromagnetic wave propagation in complex materials," *Electromagnetics*, vol. 19, no. 6, pp. 527-546, 1999.

[7] J. Paul, C. Christopoulos, and D. W. P. Thomas, "Generalized material models in TLM – Part III: Materials with nonlinear properties," *IEEE Transactions on Antennas and Propagation*, vol. 50, no. 7, pp. 997-1004, 2002.

[8] J. Paul, C. Christopoulos, and D. W. P. Thomas, "Time-domain simulation of electromagnetic wave propagation in two-level dielectrics," *International Journal of Numerical Modelling: Electronic Networks, Devices and Fields*, vol. 22, no. 2, pp. 129-141, 2009.

[9] T. Asenov, N. Dončov, B. Milovanović, and J. Paul, "Dispersive TLM Z-transform model of left-handed metamaterials," *International Journal of Numerical Modelling: Electronic Networks, Devices and Fields*, vol. 26, no. 5, pp. 457-463, 2013.

[10] J. Paul, V. Podlozny, D. W. P. Thomas, and C. Christopoulos, "Time-Domain simulation of thin material boundaries and thin panels using digital filters in TLM," *Turkish Journal of Electrical Engineering & Computer Sciences*, vol. 10, no. 2, pp. 185-198, 2002.

[11] F. J. Hsieh and W. C. Wang, "Full extraction methods to retrieve effective refractive index and parameters of a bianisotropic metamaterial based on material dispersion models," *Journal of Applied Physics*, vol. 112, 064907, Sept. 2012.

[12] P. Saguet, H. Louzani, and F. Ndagijimana, "The use of Z-transform in TLM with non-uniform meshes," *Proceedings of the Workshop on Computational Electromagnetics in Time-domain, CEM-TD 2005*, pp. 68-71, Atlanta, USA, 2005.

[13] A. L. Farhat, S. L. Maguer, P. Queffelec, and M. Ney, "TLM extension to electromagnetic field analysis of anisotropic and dispersive media: A unified field equation," *IEEE Transactions on Microwave Theory and Techniques*, vol. 60, no. 8, pp. 2339-2351, 2012.

[14] M. Kostić, N. Dončov, B. Stošić, and B. Milovanović, "Compact TLM model of dispersive anisotropic carbon-fibre material," *Proceedings of the 2nd International Conference on Electrical, Electronic and Computing Engineering, IcETRAN 2015*, Silver Lake, Serbia, pp. MTI1.5.1-6, June 8-11, 2015.

[15] V. Trenkic, A. P. Duffy, T. M. Benson, and C. Christopoulos, "Numerical simulation of

penetration and coupling using the TLM method," *EMC'94 Roma*, pp. 321-326, 13-16 Sept. 1994.

[16] B. Gustavsen and A. Semlyen, "Rational approx.-imation of frequency domain responses by vector fitting," *IEEE Trans. Power Delivery*, vol. 14, no. 3, pp. 1052-1061, July 1999.

[17] B. Gustavsen, "Improving the pole relocating properties of vector fitting," *IEEE Trans. Power Delivery*, vol. 21, no. 3, pp. 1587-1592, July 2006.

[18] D. Deschrijver, M. Mrozowski, T. Dhaene, and D. De Zutter, "Macromodeling of multiport systems using a fast implementation of the vector fitting method," *IEEE Microwave and Wireless Components Letters*, vol. 18, no. 6, pp. 383-385, June 2008.

Miloš Kostić received the Dipl.-Ing. degree from the Faculty of Electronic Engineering, University of Nis, Serbia, in 2013. Currently he works as Junior Researcher at Innovation Center of Advanced Technologies (ICAT), Serbia. His research interests are numerical modeling of isotropic and anisotropic materials and meta materials and their application in microwave structures.

Nebojša Dončov received the Dipl.-Ing., M.Sc., and Ph.D. degrees from the Faculty of Electronic Engineering, University of Nis, Serbia, in 1995, 1999 and 2002, respectively. Currently, he is a Full Professor at the Faculty of Electronic Engineering, Serbia. His research interests are in computational and applied electromagnetics with a particular emphasis on TLM and neural networks applications in microwaves and EMC. Dončov was the recipient of the International Union of Radio Science (URSI) Young Scientist Award in 2002.

Zoran Stanković received the Dipl.-Ing., M.Sc., and Ph.D. degrees from the Faculty of Electronic Engineering, University of Nis, Serbia, in 1994, 2002 and 2007, respectively. Currently, he is an Assistant Professor at the Department of Telecommunications, Faculty of Electronic Engineering, Serbia. His research interests include neural networks applications in the field of electromagnetics, wireless communications systems and computer communications. Stanković was the recipient of the National MTT Society Award in 2005 for the outstanding scientific results in the area of microwave techniques.

John Paul received the M.Eng. and the Ph.D. degrees in Electrical and Electronic Engineering from the University of Nottingham, U.K., in 1994 and 1999, respectively. His Ph.D. thesis involved the application of signal processing and control system techniques to the simulation of general material properties in time-domain TLM. He was employed as a Senior Research Fellow with the George Green Institute for Electromagnetics Research at the University of Nottingham, U.K. His research interests are in the application of signal processing techniques for advanced material modeling in time-domain computational electromagnetics and the simulation of complete systems for electromagnetic compatibility studies.

Spatial Partitioning Strategy for Parallelization of MLFMA with Reduced Communication

Xunwang Zhao [1], Chang Zhai [1], Zhongchao Lin [1], Yu Zhang [1], and Qifeng Liu [2]

[1] Shaanxi Key Laboratory of Large Scale Electromagnetic Computing
School of Electronic Engineering, Xidian University, Xi'an, 710071, China
xwzhao@mail.xidian.edu.cn

[2] Science and Technology on Electromagnetic Compatibility Laboratory
China Ship Development and Design Center, Wuhan 430064, China

Abstract **─** The bottleneck of the spatial partitioning for parallelizing the multilevel fast multipole algorithm (MLFMA) lies in higher levels of the tree, at which boxes are usually fewer than parallel processors, yielding a serious load imbalance. To solve the bottleneck, the higher levels of the tree are truncated to generate plenty of subtrees, which are distributed among processors to facilitate balancing the work load. At the coarsest level, the communication volume during translation between far-away processors is drastically reduced by adopting the far-field approximation. Therefore, the communication mainly occurs between nearby processors, which is favorable for modern computing clusters. In comparison with the parallel strategies that hybridize the spatial partitioning with the *k*-space partitioning, the proposed approach is more straightforward and shows good scalability.

Index Terms **─** Multilevel fast multipole algorithm (MLFMA), parallelization, reduced communication, spatial partitioning, subtrees.

I. INTRODUCTION

The multilevel fast multipole algorithm (MLFMA) is widely applied in the electromagnetic scattering analysis of electrically large objects. During last decade, high performance computing techniques have been used in order to boost its performance by designing efficient parallel strategies. Due to the use of a tree-like structure in the spatial domain and plane-wave expansions in the spectral (*k*-space) domain, the parallelization of MLFMA is much more complicated compared with other numerical methods such as the method of moments (MoM) [1] and the finite-difference time-domain (FDTD) method [2, 3]. Generally, researchers use two basic strategies when parallelizing MLFMA: the spatial partitioning (SP) and the *k*-space partitioning. When going up from the finest level to the coarsest level of the tree, the number of spatial boxes gradually decreases from $O(N)$ to $O(1)$, but the number of plane waves or *k*-space samples, by contrary, increases from $O(1)$ to $O(N)$, where N is the number of unknowns. When a large number of parallel processors are used, it is very difficult to achieve good load balance through a simple use of one of the strategies.

Therefore, to achieve high scalability, a commonly used method is to combine the aforementioned strategies in a hybrid manner [4, 5] or in a more efficient hierarchical manner [6–8]. As an efficient alternative, the MLFMA with the fast Fourier transform (FFT) was parallelized to keep up with the modern computational resources with mixed (shared/distributed) memory architectures and achieved very high parallel efficiency using MPI combined with OpenMP [9]. It takes advantage of the high scalability behavior of the fast multipole method (FMM)-FFT for the distributed-memory computations implemented at the coarsest level, while the algorithmic efficiency of the MLFMA benefits the shared-memory computations at finer levels. Internode communications are only required at the coarsest level, where all-to-all communications are carried out to accomplish the transfer between the two basic strategies. It is worth noting that all-to-all communication is one of the most demanding and the least scalable MPI collective operation, and thus the operation needs to be implemented very carefully.

Although the combination of the two basic strategies improves the scalability of the parallel MLFMA, it increases the difficulty in algorithm design and results in complex coding. Recently, a parallel discontinuous Galerkin boundary element method (DG-BEM) has been developed [10], which employs a graph partitioning library METIS to partition the entire computational domain into subdomains with nearly equal number of unknowns. The number of subdomains is kept proportional to the number of processors with the help of METIS, and thus, subdomains as well as unknowns are approximately uniformly distributed among processors.

Submitted On: November 6, 2018
Accepted On: December 24, 2018

This can be referred to as a spatial partitioning parallelization strategy. However, independent octrees created for all subdomains may have different numbers of levels and multipoles because of various diameters of subdomains, possibly resulting in unbalanced loads among processors. Besides, it is complicated to deal with radiation coupling among subdomains due to overlap or intersection of these octrees.

To develop a simpler and more efficient algorithm, we remove higher levels of the tree and move the coarsest level down to a level where the number of boxes is larger than the number of processors, and then uniformly distribute those boxes and the consequent subtrees among processors, facilitating the load balance. It is worth emphasizing that moving down the coarsest level may cause the computational complexity to increase higher than $O(N\log N)$. Meanwhile, given the fact that communication latencies are higher between far-away processes than between nearby processes in modern parallel computers, we use the far-field approximation to drastically reduce both the computational complexity and the communication volume between far-away processes during translation at the coarsest level. In other words, most of the communication volume is kept localized in a neighborhood. Note that we map nearby and far-away message passing interface (MPI) processes to nearby and far-way processors, respectively.

The proposed method bears some similarity to the parallel MLFMA-FFT and DG-BEM, where plenty of subtrees or subdomains are generated and distributed among processes. However, it differs in the following manner: (a) its communication pattern better fits with non-uniform network latencies in high performance computing clusters; and (b) its computational complexity is able to reach as low as the conventional MLFMA when the coarsest level and far-field criterion are properly chosen.

This paper is organized as follows: in Section II, the improved SP strategy and its implementation are described. Next, in Section III, the parallel efficiency is investigated, and an application including a multiscale ship model is proposed, followed by the conclusion in Section IV.

II. PARALLELIZATION

A. Spatial partitioning based on a truncated tree

In a typical MLFMA, a tree with $O(\log N)$ levels is established by recursively grouping or subdividing the N unknowns, as illustrated in Fig. 1. The one-buffer-box criterion is utilized, and the coarsest level L_c is usually set at Level 2 to make the algorithm efficient. Obviously, there are not enough boxes at higher levels to be distributed to a large number of processes, yielding an unbalanced work load among processes at these levels. A straightforward method to solve this issue is to move L_c down to a level at which the boxes become more than the processes. At this new coarsest level, the boxes are now enough to be distributed to processes, and the interactions between increasing far boxes are taken into account by using FMM. As an example, shown in Fig. 1, L_c is set at Level 4 instead of Level 2; in this case, there are ten coarsest boxes distributed to four processes as well as their descendants. It is worth noting that the operation of moving down the coarsest level is equivalent to truncating the higher levels of a MLFMA tree, which generates many subtrees below the coarsest level. Given the load balance, it is easier to distribute these shallower subtrees than distribute a single deeper tree to processes.

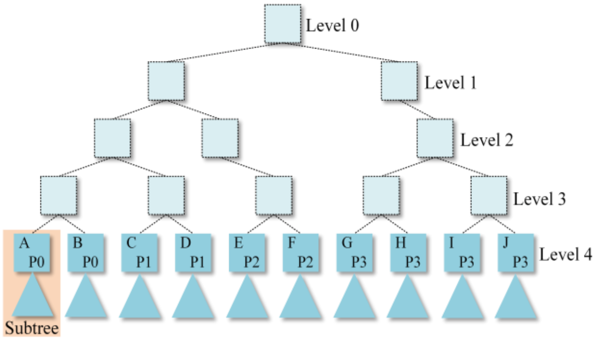

Fig. 1. Illustration of a tree in MLFMA. By moving the coarsest level down to Level 4, the boxes denoted by A–J with their descendants form plenty of subtrees, which are distributed to four processes P0–P3.

B. Reduced communication between far-away processes during translation

Nowadays, the communication between processes has become an important factor in determining the parallel performance of electromagnetic codes, especially in supercomputer environments. Even for a relatively moderate machine size, messages might travel a large number of hops on average [11]. The hop count refers to the number of intermediate devices through which data must pass between source and destination [12]. For modern mixed memory computing clusters, communications among processors belonging to the same computing node are significantly faster than those among processors located in different machines [6]. Therefore, a desirable task is to map the communicating processes using a nearby processors criterion.

Let us refer the coarsest level boxes, marked in dark blue in Fig. 1, as the observation boxes. With one-buffer-box criterion taken into account, if an observation box and its near-neighbor source boxes with their descendants are located in the same process, the communication during the aggregation and disaggregation phases can be completely avoided at the expense of some data replication [9]. However, due to the use of FMM at the coarsest level, the communication during the translation phase becomes very expensive, especially when one process communicates with its far-away neighbors to deal with the far interaction boxes.

It is noticed that, when a source box is far enough from an observation box, only one k-space direction of the translator contributes mostly to the interaction of the two boxes, whereas the other directions can be negligible. That direction points directly from the source box to the observation box, as illustrated in Fig. 2. In order to use this far-field approximation, the distance R between the two boxes should satisfy [13]:

$$R > 3\gamma\sqrt{D_x^2 + D_y^2 + D_z^2}, \quad (1)$$

where $D_{x,y,z}$ is the side lengths of the box and $\gamma \geq 1$. Consequently, the number of k-space samples for a translator is reduced from $2L^2$ to 1, where L is the number of terms in the addition theorem for FMM and proportional to the box size. Thus, if two far interaction boxes are distributed to different processes, the communication volume is also reduced from $2L^2$ to 1.

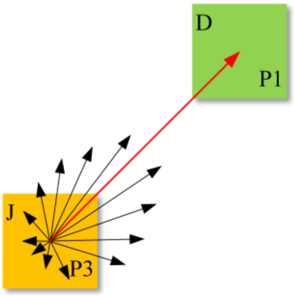

Fig. 2. Translation between two far interaction boxes J (source box) and D (observation box). The red arrow denotes the translator component along the direction from the source box to the observation box, and the black arrows denote other components.

According to the one-buffer-box criterion and Eq. (1), for an observation box at the coarsest level, its source boxes are classified into three types: near-region, resonant-region and far-field boxes, as shown in Fig. 3. The contribution from the near-region boxes is computed using MLFMA at lower levels, in the case of the resonant-region boxes, the contribution is computed using FMM, meanwhile for the last kind of boxes, the contribution is computed using the far-field approximation. When the number of boxes M is approximately $N^{0.5}$ at the coarsest level, the computational cost of the method can be as low as $0.5N\log(N)$ comparing with the conventional MLFMA, if N is very large [13]. However, as the value of γ increases at the coarsest level, more boxes are handled using FMM, resulting in increasing computational complexity and communication volume among processes. To achieve low complexity and high performance, a relatively small γ is preferred for the method. Given the above-mentioned factors, the coarsest level is commonly selected in such a way in which $M \approx N^{0.5}$, and thus the number of processes P is bounded by $O(N^{0.5})$. Assume that each process is attributed $O(N^{0.5})/P$ coarsest boxes and each box has $O(N^{0.5})$ k-space samples. At the coarsest level, the communication volume is $O(N)/P$ during full translation between two processes, whereas it is reduced to $O(N)/P^2$ by utilizing the far-field approximation. It is worth noting that the method will be more expensive than the conventional MLFMA if $M \approx N^{0.5}$, when N is small. In this case, the coarsest level is usually slightly moved down to a level at which $M < N^{0.5}$. In other words, the method might become inefficient if N is small or γ is large.

Fig. 3. Illustration of three types of source boxes for observation box D at the coarsest level (Level 4). Green boxes are near-region boxes, yellow ones are resonant-region boxes, and blue ones are far-field boxes.

C. Implementation detail

Distributing the coarsest boxes or subtrees equally among processes may fail to provide good load balance because the amount of work per box is not constant. This distribution scheme can be improved by considering the estimated amount of work per box, as was done in [9]. For convenience, more sophisticated distributions are not taken into account herein.

In a typical MLFMA with one-buffer-box criterion, the number of translators stored at each level can be reduced by exploiting the symmetries associated with translators [14]. However, as γ increases in Eq. (1), the number of translators required also increases, resulting in a larger memory footprint. Hence, translators are interpolated at the coarsest level by using Lagrange polynomial interpolation with six points and five times the required sampling rates [15], whereas at the lower levels, the translators are stored in memory with the symmetries taken into account.

For the sake of communication during translation, we build two interaction lists in each process at the coarsest level: one for resonate-region boxes and the other one for far-field boxes. The former contains box indices, and each process sends and receives full outgoing plane-wave expansions. Given a large amount of the data, we exchange them in blocks to reduce the number of communication calls. The latter contains box indices and the corresponding k-space directions, exchanging them in one block by using one communication call. Four directions are used for calculating the translator because we use four-point interpolation. To minimize latency, the MPI non-blocking communication is performed to overlap communication and computation. Note that all communications occur during translation, but aggregation and disaggregation require no communication.

During the solution procedure, we can solve the equation by using a Krylov space solver. Alternatively, we can iteratively solve the equation associated with each subtree firstly and then consider the coupling among subtrees or coarsest boxes through outer iterations. This inner-outer iterative manner has been utilized in domain decomposition methods [10]. In addition, the use of a few plane waves to compute the coupling between two far-field coarsest boxes is similar to using the ray-tracing method to take account of the coupling [16]. It is noted that the proposed method has higher numerical accuracy than that in [16] due to the rigorous computation of the coupling between near-region and resonant-region coarsest boxes.

To accelerate the iterative convergence rate, a basis-function neighbor preconditioner is employed rather than the commonly used block diagonal preconditioner. For a given basis function, its neighbor basis functions within a certain distance are collected to create the preconditioner [17]. Because the basis-function neighbor preconditioner is built independently for each basis function, it can be efficiently implemented in parallel.

III. NUMERICAL EXAMPLES

In order to investigate the strong scalability of the proposed method, the scattering analysis of a conducting sphere is carried out. Then a ship model is simulated to demonstrate the efficiency of the method in computation of bistatic radar cross section (RCS). The models are formulated by the combined field integral equation (CFIE) with a combination factor 0.5 and discretized using the RWG basis functions [18]. The parallel generalized minimal residual (GMRES) method combined with a basis-function neighbor preconditioner is selected as the iterative solver. The computational platform has 16 computing nodes, each of which is configured with four 18-core 2.3 GHz CPUs and 192 GB memory. The nodes are connected by a 100 Gb/s network.

A. Scattering from a sphere model

The scattering analysis of a conducting sphere of diameter 266.6λ is computed to test the parallel efficiency of the algorithm, where λ is the free-space wavelength. The model is discretized into 58327428 unknowns. In this case, a ten-level MLFMA is used with an edge length for the finest box of 0.25λ.

In order to demonstrate the correctness of the proposed method, a comparison of the bistatic RCS with the analytical solution (Mie series) has been carried out. The simulation parameters for the proposed method are γ equal to 3 and L_c set to 4. The residual for iterations is set to 0.001. Figure 4 shows the comparison where a very good agreement is appreciated. However, if γ were to be reduced, the results would not be so accurate since the far-field approximation might be used in some resonate-region boxes. Readers are referred to [13] for an in-depth discussion about the accuracy of the far-field approximation.

The scattering analysis of the conducting sphere has been carried out by increasing the number of processes and calculating its parallel efficiency. The computational time employed in performing one MVP for the proposed spatial partitioning (SP) technique is given in Table 1, and the memory requirement is approximately 893.04 GB. According to the definition of speedup and parallel efficiency [8], the reference number of process should be set to 1. With consideration of the MVP time and memory requirement of the algorithm, it is reasonable to set a moderately larger number of processes as in [6]. In this example, it is set to 32. As seen from Table 1, the proposed strategy is able to achieve high parallel efficiency comparable to the hybrid and hierarchical strategies in [4, 6].

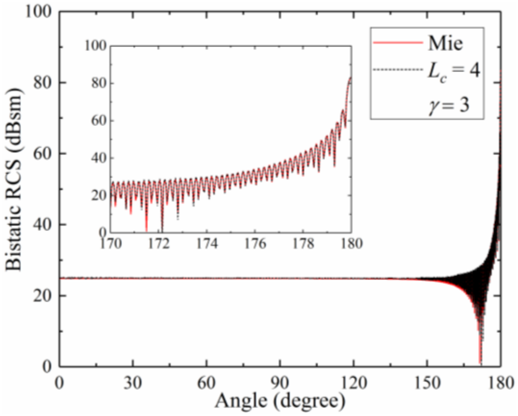

Fig. 4. Bistatic RCS comparison for a conducting sphere of diameter 266.6λ (VV polarization, for vertical transmitting and vertical receiving). A ten-level MLFMA is used, L_c is 4, and γ is chosen as 3.

Table 1: Strong scalability for one matrix-vector product in simulating the sphere when L_c is 4 and γ is 3

CPU Cores	**MVP Time (s)**	**Speedup**	**Parallel Efficiency (%)**
32	756.44	1.00	100.00
288	94.13	8.04	89.29
576	54.56	13.86	77.02
1152	32.89	23.00	63.89

It is noted that the maximum number of processes is limited by the number of boxes at the coarsest level in the proposed strategy. In this example, the maximum number of processes is 1152, which is slightly smaller than the number of boxes 1160. In order to improve the scalability of the proposed strategy, the coarsest level should be moved down to lower levels, where more coarsest boxes can be obtained. This is equivalent to transfer from coarser-grained parallelism to finer-grained parallelism, facilitating load balance and scalability. However, it is possible that moving down the coarsest level might increase the computational complexity of the algorithm. To ensure high numerical accuracy and efficiency of the method, one has to set suitable parameters L_c and γ, as discussed in Section II. B.

B. Scattering from a multiscale ship model

The second example consists of the scattering analysis of a conducting ship model. The model is 167 m long, 19 m wide and 34.7 m high, as shown in Fig. 5.

The bistatic RCS is computed at 1 GHz to verify the accuracy of the proposed SP strategy. The number of unknowns is 21772044 in this case. Figure 6 illustrates the results for this analysis where a comparison with the parallel MLFMA has been carried out [8]. Both results present a good agreement. The proposed method converges to 0.01 with 51 iterations, and it takes 920.12 s and needs 306.38 GB memory in total when $P = 1152$. The time for computing one MVP is 16.00 s and the parallel efficiency relative to 32 cores is 60.28% (the MVP time is 347.21 s when $P = 32$).

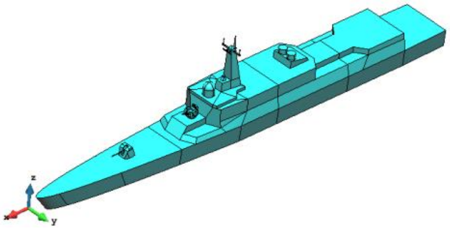

Fig. 5. Conducting ship model with dimensions of 167 m × 19 m × 34.7 m.

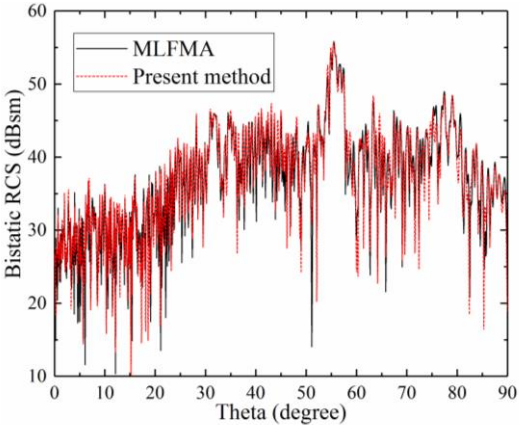

Fig. 6. Bistatic RCS comparison for the ship (VV polarization) at 1 GHz. A plane wave of frequency 1 GHz is incident at $\theta_{\text{inc}} = 55.5°$ and $\phi_{\text{inc}} = 0°$, and the observation directions are set as $0° \leq \theta_{\text{scat}} \leq 90°$ and $\phi_{\text{scat}} = 0°$. An eleven-level MLFMA is used. L_c is 7, and γ is chosen as 4.

We then consider the scattering analysis of the ship at a higher frequency 2.3 GHz. The electrical length of the ship is 1280.3λ and discretization of its model generates 115444341 unknowns, which is approximately five times the unknowns at 1 GHz. The total solution time is 4121.94 s and the memory requirement is 1495.09 GB when 1152 cores are used. The time for carrying one MVP is 72.81 s, approximately five times the MVP time at 1 GHz. In addition, the memory requirement is also about five times the memory at 1 GHz. This implies that the complexity of the present method is approximate $N\log(N)$. The bistatic RCS curve is plotted in Fig. 7.

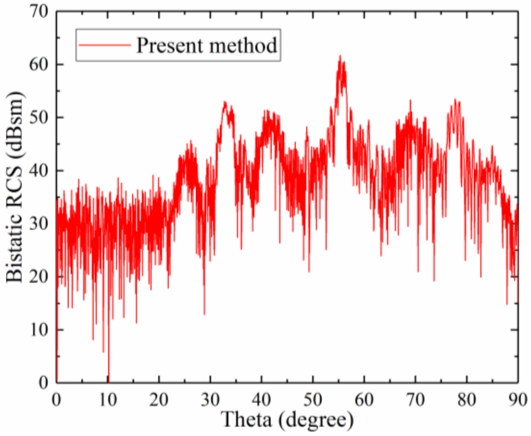

Fig. 7. Bistatic RCS comparison for the ship (VV polarization) at 2.3 GHz. The incident angle and the observation directions are the same as those in Fig. 6. A twelve-level MLFMA is used. L_c is 7, and γ is chosen as 4.

IV. CONCLUSION

The scalability of the spatial partitioning strategy for parallelizing MLFMA is improved from $O(1)$ to $O(N^{0.5})$ processes by properly setting the coarsest level. Because of the important role of communication in determining performance of parallel algorithms, the far-field approximation is employed to reduce the communication volume between far-away processes during translation at the coarsest level, and hence, most of the communication volume occurs between nearby processes that are mapped to nearby processors. The proposed algorithm can be referred to as a network topology aware algorithm. In addition, the proposed strategy can be combined with the k-space partitioning strategy to achieve better scalability.

ACKNOWLEDGMENT

This work was supported in part by the National Key Research and Development Program of China under Grant 2017YFB0202102, in part by the NSFC (61301069), in part by the China Postdoctoral Science

Foundation funded project under Grant 2017M613068, and in part by the Special Program for Applied Research on Super Computation of the NSFC-Guangdong Joint Fund (the second phase) under Grant No. U1501501.

REFERENCES

[1] X. Zhao, Y. Chen, H. Zhang, Y. Zhang, and T. K. Sarkar, “A new decomposition solver for complex electromagnetic problems [EM Programmer's Notebook],” *IEEE Antennas and Propag. Mag.*, vol. 59, no. 3, pp. 131-140, June 2017.

[2] W. Yu, X. Yang, Y. Liu, L.-C. Ma, T. Su, N.-T. Huang, R. Mittra, R. Maaskane, Y. Lu, Q. Che, R. Lu, and Z. Su, “A new direction in computational electromagnetics: solving large problems using the parallel FDTD on the BlueGene/L supercomputer providing Teraflop-level performance,” *IEEE Antennas and Propag. Mag.*, vol. 50, no. 2, pp. 26-44, Apr. 2008.

[3] S. Jiang, Y. Zhang, Z. Lin, and X. Zhao, “An optimized parallel FDTD topology for challenging electromagnetic simulations on supercomputers,” *International Journal of Antennas and Propagation*, vol. 2015, Article ID 690510, 10 pages, 2015.

[4] S. Velamparambil and W.C. Chew, “Analysis and performance of a distributed memory multilevel fast multipole algorithm,” *IEEE Trans. Antennas Propag.*, vol. 53, no. 8, pp. 2719-2727, Aug. 2005.

[5] X.-M. Pan, W.-C. Pi, M.-L. Yang, Z. Peng, and X.-Q. Sheng, “Solving problems with over one billion unknowns by the MLFMA,” *IEEE Trans. Antennas Propag.*, vol. 60, no. 5, pp. 2571-2574, May 2012.

[6] Ö. Ergül and L. Gürel, “A hierarchical partitioning strategy for an efficient parallelization of the multilevel fast multipole algorithm,” *IEEE Trans. Antennas Propag.*, vol. 57, no. 6, pp. 1740-1750, June 2009.

[7] B. Michiels, J. Fostier, I. Bogaert, and D. D. Zutter, “Weak scalability analysis of the distributed-memory parallel MLFMA,” *IEEE Trans. Antennas Propag.*, vol. 61, no. 11, pp. 5567-5574, Nov. 2013.

[8] X. Zhao, S.-W. Ting, and Y. Zhang. “Parallelization of half-space MLFMA using adaptive direction partitioning strategy,” *IEEE Antennas and Wireless Propag. Lett.*, vol. 13, pp. 1203-1206, 2014.

[9] J. M. Taboada, M. G. Araujo, F. O. Basteiro, J. L. Rodriguez, and L. Landesa, “MLFMA-FFT parallel algorithm for the solution of extremely large problems in electromagnetics,” *Proceedings of the IEEE*, vol. 101, no. 2, pp. 350-363, Feb. 2013.

[10] B. MacKie-Mason, A. Greenwood, and Z. Peng, “Adaptive and parallel surface integral equation solvers for very large-scale electromagnetic modeling and simulation (invited paper),” *Progress In Electromagnetics Research*, vol. 154, pp. 143-162, 2015.

[11] T. Agarwal, A. Sharma, A. Laxmikant, and L. V. Kale, “Topology-aware task mapping for reducing communication contention on large parallel machines,” *in Proceedings of the 20th IEEE International Parallel and Distributed Processing Symposium*, Rhodes Island, Greece, 25-29 April 2006.

[12] Hop (networking), accessed on June 25, 2017. [Online]. https://en.wikipedia.org/wiki/Hop_(networking).

[13] W. C. Chew, T. J. Cui, and J. M. Song, “A FAFFA-MLFMA algorithm for electromagnetic scattering,” *IEEE Trans. Antennas Propag.*, vol. 50, no. 11, pp. 1641-1649, Nov. 2002.

[14] S. Velamparambil, W. C. Chew, and J. Song. “10 million unknowns: is it that big?,” *IEEE Antennas and Propag. Mag.*, vol. 45, no. 2, pp. 43-58, Apr. 2003.

[15] J. Song and W. C. Chew, “Interpolation of translation matrix in MLFMA,” *Microw. Opt. Techn. Lett.*, vol. 30, no. 2, pp. 109-114, July 2001.

[16] C. Delgado and M. F. Cátedra, “Combination of ray-tracing and the method of moments for electromagnetic radiation analysis using reduced meshes,” *Journal of Computational Physics*, vol. 361, pp. 412-423, Jan. 2018.

[17] Y. Zhang, Y. J. Xie, and C. Liang, “A highly effective preconditioner for MoM analysis of large slot arrays,” *IEEE Trans. Antennas Propag.*, vol. 52, no. 5, pp. 1379-1381, May 2004.

[18] S. M. Rao, D. R. Wilton, and A. W. Glisson, “Electromagnetic scattering by surfaces of arbitrary shape,” *IEEE Trans. Antennas Propag.*, vol. 30, pp. 409-418, May 1982.

Evaluation of Temperature Elevation in Human Ocular Tissues due to Wireless Eyewear Devices

Junqing Lan and Guohong Du

College of Electronic Engineering
Chengdu University of Information Technology, Chengdu, Sichuan Province, 610225, China
ljqcuit@163.com, dghedu@hotmail.com

Abstract ─ In this paper, a numerical study is proposed to evaluate the temperature variation in the human ocular tissues during the electromagnetic radiation exposure from wireless eyewear device. The results show that the temperature in the whole eyeball increases gradually as the exposure time goes on and could reach the thermal steady state at about 30 minutes. During this process, the temperature increments in different ocular tissues are between 1.1℃ and 1.7℃. The results also show the maximal ratio of temperature increments in the initial 5 and 10 minutes to that of the whole steady state could reach to 42.9% and 69.2%, respectively. Therefore, we believe that electromagnetic radiation from wireless eyewear device might pose a threat on the health of the human eyes. People should decrease the talk time as soon as possible to protect their eyes from the possible health hazards. Finally, attention is paid to evaluate the relationship between the maximal SAR and the temperature increments. The results show the temperature increments do not increase in direct proportion to the maximal SAR, which indicates that the maximal SAR and the temperature increments should be taken into account simultaneously while evaluating the biological effect of microwave on the ocular tissues.

Index Terms ─ FDTD, ocular tissues, temperature, wireless eyewear device.

I. INTRODUCTION

With the rapid development of the mobile communication technology, increasing interest has been paid to the wireless eyewear devices (EyeTrek Insight Smart glasses, Mad Gaze X5 and so on) [1-2]. Nevertheless, continuous and longtime electromagnetic (EM) radiation from the wireless devices close to the human head might give rise to adverse physiological damage, such as headache and insomnia [3-6]. It even has been considered as the cause of cancer [7]. International organizations such as IEEE [8] and ICNIRP [9] have established the safety standards to protect human health from the EM exposures. The existing standards, however, only use the Specific Absorption Rate (SAR) which is defined as the absorption rate of EM power per unit mass to describe the extremely complex interaction between EM waves and human biological tissue. Moreover, the maximal SAR limits are not obtained by a precise quantitative process but just expert opinion which is designed to protect human body from adverse effects induced by the temperature elevation larger than the safety threshold of 1°C resulting from acute exposures. Hence, systematic quantitative research related with other parameters such as temperature, absorbed power and radiation frequency should be done [7, 10, 11]. Among them, temperature, in particular, might directly lead to physiological effects and damage. For example, brain lesions and blood chemistry change might happen when the temperature increments are between 1℃ and 5℃. Even 1℃ temperature elevation also might give rise to altered production of hormones and suppressed immune response [12]. Therefore, it is necessary to evaluate the temperature elevation due to wireless eyewear device [2].

There are many valuable researches that have evaluated the temperature rise in the human body during the EM exposure from wireless devices [13-20]. For example, Takei et al. [13] had evaluated the temperature elevation in pregnant women exposed to radiation of mobile phone. The results showed that the maximum temperature increments in fetuses were only half of those in pregnant women. Morimoto et al. [14] had studied the correlation between the peak SAR and temperature rise in the human head in the frequency range from 1 GHz to 30 GHz. Strong relationships were found between SAR and temperature rise by different algorithms. Diao et al. [15] had evaluated the influence of palpebral fissure on the variations in temperature elevation in human eyes under plane wave EM exposures. Results showed that the changes in the palpebral fissure would induce a 0.23 °C variation in the maximum temperature elevation in the human lens. Li et al. [16] had demonstrated that the elongated ocular axial length could not give rise to the significant temperature rise in human eyes. Van Rhoon et al. [17] had determined the limits of thermal dose for MR exposure by investigating the temperature elevation

Submitted On: August 21, 2018
Accepted On: December 25, 2018

in the brain. Buccella et al. [18] had evaluated the effects of different radio frequency sources on the SAR and temperature increments in the human eyes and found the maximum temperature elevation in the lens could reach to 1.6℃. Van Leeuwen et al. [19] found the maximal temperature elevation of 0.11°C in the human brain when people use the mobile phone with 0.25 W radiated power. Wang et al. [20] had evaluated the temperature rise in the human brain exposed to the mobile phone and found the temperature increments of the peak temperature is 0.06℃ and 0.02℃ under the maximal EM radiation dose of IEEE guidelines and ICNIRP standards. So far, a few studies [2, 10, 21] have also been done to evaluate the influence of EM radiation of wireless eyewear device on the human body. They, however, mainly focus on the SAR and the absorbed power in the human head.

Based on the above reasons, this paper would mainly evaluate the temperature elevation in the human head during the EM exposure from wireless eyewear device. We would mainly focus on the human ocular tissues because they are more sensitive to EM fields [4, 22]. This is because eyes, unlike other tissues with the protection of skin, fat and so on, are directly exposed to the EM radiation. Meanwhile, eyes could not dissipate the heat timely induced by the EM thermal effects due to the lower blood flow. Thirdly, once ocular tissues are damaged, they could not return to be healthy because human ocular tissues except the cornea lack the self-renewal ability. A three-dimensional anatomical CAD human head model is established in this paper, which consists of skin, fat, brain and eyeballs including eight kinds of tissues. We designed a printed coupling element (CE) antenna to act as the wireless eyewear device. It covers 0.75-0.93 with a -6dB S11. A metallic glasses model is established to support the wireless eyewear device. The calculated results, in this paper, could provide valuable data for the establishment of related safety standards and future researches in the biological effect of microwave and human eyes.

II. SIMULATION MODELS AND MATERIALS

A. Head model

To evaluate the temperature elevation in the human ocular tissues, a three-dimensional anatomical CAD human head model, in this paper, is established. This model is shown in Fig. 1 which comprises of skin, fat, brain and eyeball. Comparing with the Visible Human Project or Magnetic Resonance Imaging model, the CAD model could provide the higher resolution to precisely characterize the eyeball with complex structure. Figure 2 shows the cross-section of eyeball which is made of eight kinds of ocular tissues.

The dielectric properties at 0.915GHz and density corresponding to variety of biological tissues for the following calculation are displayed in Table 1 [22-32]. ε_r and σ represent the relative dielectric constant and conductivity, respectively. The thermal parameters of the tissues used in this study are given in Table 2, which are obtained from those in [30, 33]. C and K represent specific heat and thermal conductivity, respectively. A is the basal metabolic rate. B is associated with blood perfusion. The new blood perfusion and metabolic rate of retina are used here. From these data, it could be found choroid has the highest blood perfusion and metabolic rate among the ocular tissues due to its high vascularization. Because of the continual photoreceptor requirement for vision, retina, as well, has the relative higher metabolic rate.

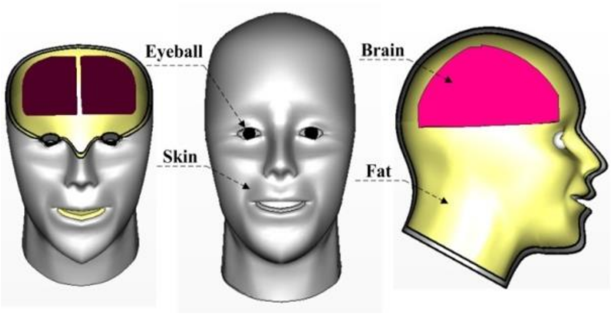

Fig. 1. Human head model.

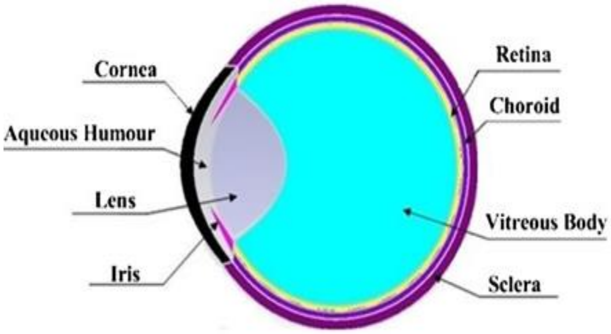

Fig. 2. Cross-section of eyeball.

Table 1. The dielectric properties and density of tissues in the human head model

Biomaterial	ε_r	σ (S/m)	ρ (kg/m^3)
Cornea	51.5	1.9	1050
Iris	55	1.18	1040
Air	1	0	0.0016
Skin	45	0.97	1100
Choroid	55	2.3	1000
Lens	44	0.8	1150
Sclera	51	1.13	1020
Aqucous Humor	74	1.97	1010
Vitreous Body	67	1.68	1030
Retina	57	1.17	1000
Fat	15	0.35	920

Table 2: Thermal properties of tissues

Biomaterial	C (J/(kg ℃))	K (W/(m ℃))	A (W/m^3)	B (W/(℃ m^3))
Cornea	4200	0.58	0	0
Iris	4178	0.58	0	0
Skin	3500	0.42	1000	9100
Choroid	3900	0.51	20000	85000
Lens	3000	0.4	0	0
Sclera	4200	0.58	0	0
Aqueous Humor	3997	0.58	0	0
Vitreous Body	4178	0.58	0	0
Retina	3700	0.56	2500	9500
Fat	2500	0.25	180	520

B. Glasses model

The wireless eyewear device is usually placed on one side of the eye by fixing on the glasses, ear and so on. Glasses is always selected as the main choice due to the reason that myopia as a typical epidemic has higher morbidity rate around the world. It is predicted that there will be 2.5 billion people with myopia by 2020 [34]. Therefore, maybe half of wireless eyewear device users would choose glasses. The glasses model, used in this paper, is shown in Fig. 3. Compared with the previous research [2] that only considers the single metallic frame, this model includes spectacle frame, spectacle lens and nose pad. The distances between two arms are 155mm. The thickness of spectacle frame is 1 mm. Polyimide (εr=3.5, σ=0.03) and Glass (εr=4.82, σ=0.0054) are selected as the materials of nose pad and spectacle lens, respectively. The spectacle frame uses the metal material rather than the plastic for the following reasons. Firstly, the metal frame has good ductility and could not lose its form with daily use comparing with the plastic frame. It is more suitable for supporting the printed circuit board (PCB) of the eyewear device. Furthermore, the former study [35] had proved the variation in conductivity posed negligible variation to the SAR in the human head, hence this paper would use the copper as the material of spectacle frame.

C. Antenna model

As is shown in Fig. 4, a printed CE antenna designed for eyewear device [1, 2] is employed in this paper. The CE is on the one side of the FR4 PCB, which is adjacent to the eyes. The ground plane is printed on the other side of the PCB. The antenna is fed by a three-elements matching network which is comprised of a shunt capacitor and two series inductors. By adjusting the matching network, the antenna could be transformed into the desired operating band. The S_{11} is displayed in Fig. 5, which covers the 0.75-0.93GHz with a -6dB S_{11}. The input power is 0.125W since a GSM terminal only transmits for one-eighth of the time.

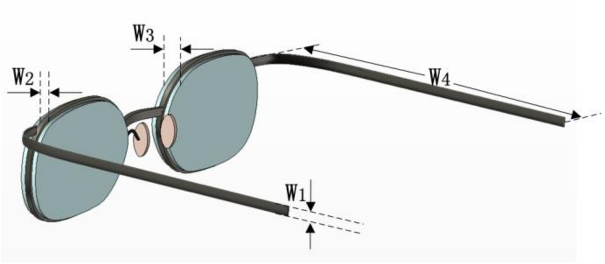

Fig. 3. Model of glasses.

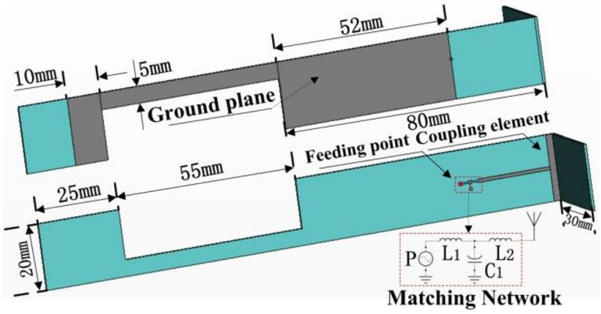

Fig. 4. Antenna model for eyewear device.

III. CALCULATION METHODS

A. EM modeling

The electromagnetic problem is calculated by solving the time-harmonic Maxwell Equations based on the FDTD method [36-38]. The computational region is divided by regular hexahedron grids. The sub-grids method is used to obtain the finer resolution by inserting the small grids into the larger one. For ease of understanding, we introduce the sub-grids method used in the two-dimensional TE propagation mode. The discretized equations are as follows:

$$H_x^{n+\frac{1}{2}}\left(i,k+\frac{1}{2}\right)=H_x^{n-\frac{1}{2}}\left(i,k+\frac{1}{2}\right)+\frac{c\Delta t}{Z_0\Delta z}\left[E_y^n(i,k+1)-E_y^n(i,k)\right], \tag{1}$$

$$H_z^{n+\frac{1}{2}}\left(i+\frac{1}{2},k\right)=H_z^{n-\frac{1}{2}}\left(i+\frac{1}{2},k\right)-\frac{c\Delta t}{Z_0\Delta z}\left[E_y^n(i+1,k)-E_y^n(i,k)\right], \tag{2}$$

$$E_y^{n+1}(i,k)=E_y^n(i,k)+\frac{Z_0c\Delta t}{\Delta z}\left[H_x^{n+\frac{1}{2}}\left(i,k+\frac{1}{2}\right)-H_x^{n+\frac{1}{2}}\left(i,k-\frac{1}{2}\right)\right]-\frac{Z_0c\Delta t}{\Delta x}\left[H_x^{n+\frac{1}{2}}\left(i+\frac{1}{2},k\right)-H_x^{n+\frac{1}{2}}\left(i-\frac{1}{2},k\right)\right], \tag{3}$$

where E and H are the electric fields strength (V/m) and magnetic fields strength (A/m). i and k refer to the Cartesian coordinates x and z, respectively. Δt is the time step. Δx and Δz are the spatial step in the x and z direction, respectively. On the basis of the sub-grids method, the fields across the interfaces between coarse grids and fine grids should be continuous. In addition, the local uniformity is vital to keep the same stability criterion. Thirdly, the grids ratio between coarse grids and fine grids should be equal to the time increment ratio.

This paper uses the 0.2mm resolution for eyeball which could represent each ocular tissue with ultra-thin millimeter-scale membrane structure separately. The resolution of 0.5mm is used for the other parts of the human head tissues. The sub-grids method helps to achieve the required computational accuracy using as little computation load as possible [39]. The uniaxial perfectly matched layer boundary with 5 cells thick is used to truncate the computational domain. The relative accuracy is 10^{-5}.

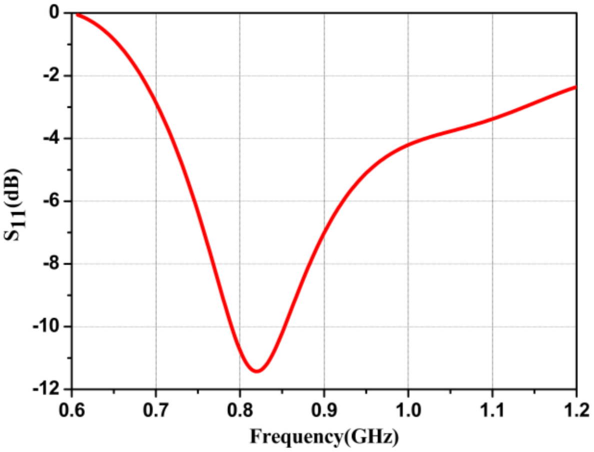

Fig. 5. S_{11} of the antenna with head model shown in Fig. 6 (L_1=9.5nH, L_2=11nH, C_1=0.95PF).

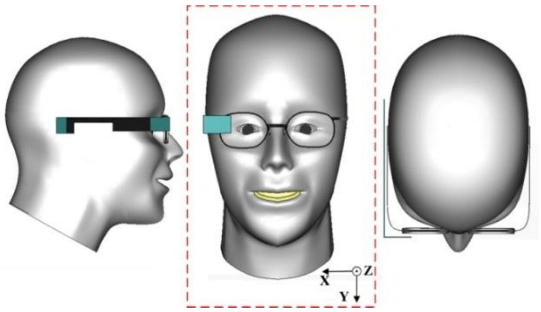

Fig. 6. Model of phone call state with glasses.

B. Thermal modeling

The temperature elevation inside the human head exposed to the EM fields from wireless eyewear device could be calculated by solving the Bioheat Equation [40]:

$$C(\vec{r})\rho(\vec{r})\frac{\partial T(\vec{r},t)}{\partial t} = \nabla\cdot\big(K(\vec{r})\nabla T(\vec{r},t)\big) + \rho(\vec{r})\cdot SAR(\vec{r}) + A(\vec{r},t) - B(\vec{r},t)\big(T(\vec{r},t) - T_b(\vec{r},t)\big). \quad (4)$$

It includes kinds of heat exchange mechanisms such as heat conduction, blood perfusion and EM heating. In Equation 4, $\rho(\vec{r})$ is the density in kg/m^3. SAR (W/kg) is obtained by:

$$\mathrm{SAR}(\vec{r}) = \frac{\sigma\left|\vec{E}(\vec{r})\right|^2}{\rho(\vec{r})}, \quad (5)$$

where $\vec{E}$ is the peak value of the electric fields strength vector. σ is the conductivity in S/m. To calculate SAR for 1 g, we add contributions of several Yee's meshes to 1 g around the cube of the maximum SAR (In this paper, all SAR refers to the SAR for 1 g.). $\vec{r}$ and t are the position vector and time, respectively. $T(\vec{r},t)$ and $T_b(\vec{r},t)$ represent the temperature of human tissues and blood, respectively. $T_b(\vec{r},t)$ is assumed to be constant of 37℃ due to the reason that the EM power absorption from eyewear device is much smaller than the metabolic heat power [41].

The boundary conditions are applied on the interfaces of skin–air and cornea–air, which could be calculated by [42-43]:

$$-K(\vec{r})\frac{\partial T(\vec{r},t)}{\partial n} = -H\big(T_s(\vec{r},t) - T_e(\vec{r},t)\big), \quad (6)$$

where $T_s(\vec{r},t)$ and $T_e(\vec{r},t)$ represent the surface temperature of the biological tissues and the temperature of air. The convection coefficient of skin–air and cornea–air are assumed to be 10.5 and 20 (W/(m^2℃)) under the condition of T_e =23℃ which takes into account the evaporation of tear film and perspiration, the convective and radiation exchange with the surrounding objects.

The forward Finite Difference scheme is adopted in solving the equation 4, as:

$$T(\vec{r},t)_{i,j,k}^{n+1} = \frac{K(\vec{r})}{C(\vec{r})\rho(\vec{r})\Delta^2}\Delta t\big[T(\vec{r},t)_{i-1,j,k}^{n} + T(\vec{r},t)_{i+1,j,k}^{n} + T(\vec{r},t)_{i,j-1,k}^{n} + T(\vec{r},t)_{i,j+1,k}^{n} + T(\vec{r},t)_{i,j,k-1}^{n} + T(\vec{r},t)_{i,j,k+1}^{n}\big] + T(\vec{r},t)_{i,j,k}^{n}\left\{1 - \left(\frac{N_i K(\vec{r})}{C(\vec{r})\rho(\vec{r})\Delta^2} + \frac{N_e H}{C(\vec{r})\rho(\vec{r})\Delta} + \frac{B(\vec{r},t)}{C(\vec{r})\rho(\vec{r})}\right)\right\}\Delta t + \frac{N_e H \Delta t T_e}{C(\vec{r})\rho(\vec{r})\Delta} + \frac{\Delta t}{C(\vec{r})\rho(\vec{r})}\big[\rho(\vec{r})\mathrm{SAR}(\vec{r})_{i,j,k} + \mathrm{A} + T_b\big]. \quad (7)$$

Here, the temperature node locates in the centre of the cell. Δ is the spatial step. N_i and N_e represent the number of internal and external cells adjacent to the studied cell identified by *i*, *j* and *k* according to the Finite Difference notation. To ensure the stability of the algorithm, the Equation 7 must be satisfied in the whole computational domain:

$$\Delta t \le \left(\frac{N_i K(\vec{r})}{C(\vec{r})\rho(\vec{r})\Delta^2} + \frac{N_e H}{C(\vec{r})\rho(\vec{r})\Delta} + \frac{N_e H}{C(\vec{r})\rho(\vec{r})\Delta}\right)^{-1}. \quad (8)$$

This would lead to a long computational time when considering the thermal steady-state condition. But, in contrast, it needed much less computational resources than the FDTD calculation.

The initial temperature of the biological tissues without any EM field exposure is used to solve the bioheat equation. It could be obtained by the steady-state equation [40, 44-45]:

$$\nabla(K\nabla T) + A - B(T - T_b) = 0. \qquad (9)$$

The Bioheat Equation is discretized by the same rectangular grids used in the FDTD calculations [46-47]. The iteration did not stop until the relative residual of the solution was less than 10^{-7}.

IV. RESULTS AND DISCUSSIONS

We firstly evaluate the temperature variation in the ocular tissues during the EM exposure from wireless eyewear device. Fig. 7 shows the temperature distribution via two orthometric cross-sections (XY plane and YZ plane shown in Fig. 6) of eyeballs. We can see that the temperature in the whole eyeball increases gradually as the time goes on and reaches the steady state at about 30 minutes. Moreover, the closer to the cornea–air boundary the location in the eyeball is, the lower the temperature is. The temperature differences increase gradually with the increasing time. This is mainly due to the reason of heat exchange on the cornea–air boundary induced by the temperature differences.

We, as well, evaluate the temperature increments in the given time intervals (5 minutes) in the ocular tissues when people use the wireless eyewear device and show the results in the Table 3. We find the temperature increments of the maximal temperature in the ocular tissues are from 1.1℃ to 1.7℃ within 30 minutes. The results also show that the maximal ratio of temperature increments in the initial 5 and 10 minutes exposure time to that of the whole steady state could reach to 42.9% and 69.2%, respectively. Based on the above results, we believe EM exposure from wireless eyewear device may pose a threat on the health of the eyes, especially for the lens which suffer from the maximal temperature increments in the whole process to reach the steady state. Wireless eyewear device users should shorten the usage time as soon as possible to protect their eyes form the possible health hazards. The calculated results could provide valuable data for the establishment of related safety standards for wireless eyewear device.

Finally, this paper evaluates the relationship between the maximal SAR [21] and the temperature increments (in 30 minutes) in the ocular tissues during the EM exposure from wireless eyewear device. The computed results are shown in Fig. 8. We find that the temperature increments do not increase in direct proportion to the maximal SAR. On the contrary, the ocular tissues such as lens with the least value of the maximal SAR have the maximal temperature increments. This is because the temperature increments are the complex process with many factors involved. Not only does it depend on the SAR, the material properties and structure parameters of the ocular tissues, but also the heat flow among the tissues. Therefore, the maximal SAR and the temperature increments should be taken into account simultaneously while evaluating the biological effect of microwave on the ocular tissues.

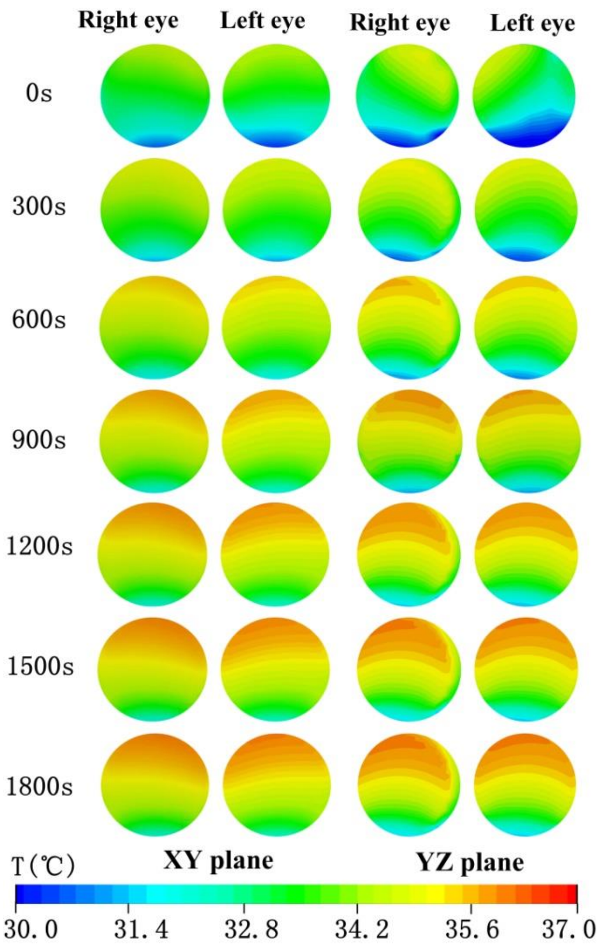

Fig. 7. Temperature distribution in the eyeballs.

Table 3. The maximal temperature Tmax (℃) at different times in the ocular tissues during the EM exposure from wireless eyewear device.

	Time (minutes)						
	0	5	10	15	20	25	30
Vitreous body	34.85	34.95	35.45	35.65	35.75	35.85	35.95
Aqueous humor	31.85	32.45	32.75	33.05	33.15	33.25	33.25
Sclera	34.85	34.95	35.45	35.65	35.85	35.85	35.95
Iris	31.55	32.05	32.45	32.65	32.75	32.75	32.85
Cornea	31.85	32.35	32.75	32.95	33.05	33.05	33.15
Lens	32.25	32.85	33.35	33.55	33.75	33.85	33.95
Choroid	34.85	35.05	35.45	35.65	35.75	35.85	35.95
Retina	34.75	34.95	35.35	35.65	35.75	35.85	35.85

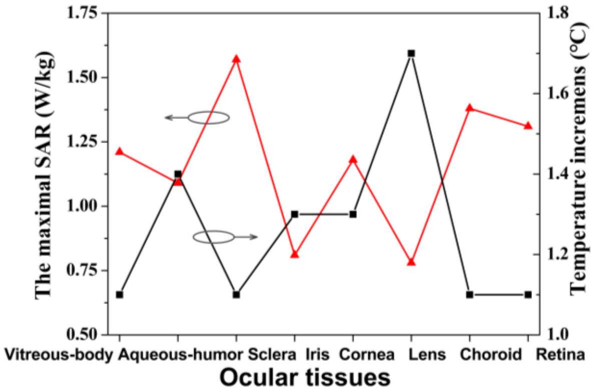

Fig. 8. The maximal SAR and the temperature increments in the ocular tissues.

V. CONCLUSION

Based on the results evaluated in this paper, we find that the temperature in the whole eyeball increases gradually and reaches the thermal steady state at about 30 minutes during the EM exposure of wireless eyewear device. The temperature increments in different ocular tissues are from 1℃ to 1.7℃. We, therefore, believe EM exposure from wireless eyewear device may pose a threat on the health of the eyes, especially for the lens which suffer from the maximal temperature increments. Meanwhile, the results also show that the maximal ratio of temperature increments in the initial 5 and 10 minutes exposure time to that of the complete thermal steady state could reach to 42.9% and 69.2%, respectively. Hence, wireless eyewear device users should shorten the usage time as soon as possible to protect their eyes from the possible health hazards. Finally, we evaluate the relationship between the maximal SAR and the temperature increments in the ocular tissues. We find that the temperature increments do not increase in direct proportion to the maximal SAR. Therefore, we believe the maximal SAR and the temperature increments should be taken into account simultaneously while evaluating the biological effect of microwave on the ocular tissues. This paper could provide valuable data for the establishment of related safety standards and future researches in the biological effect of microwave and human eyes. However, limited by the experimental condition, the experiment is not included. Therefore, conclusions presented in this paper are just indicative but not definitive.

ACKNOWLEDGMENT

This paper is supported by the key project of Education Office of Sichuan province [Grant No. 18ZA0096] and the National Natural Science Foundation of China [Grant No. 61640008].

REFERENCES

[1] A. Cihangir, W. G. Whittow, C. J. Panagamuwa, F. Ferrero, G. Jacquemod, F. Gianesello, and C. Luxey, "Feasibility study of 4G cellular antennas for eyewear communicating devices," *IEEE Antennas and Wireless Propagation Letters*, vol. 12, pp. 1704-1707, Oct. 2013.

[2] A. Cihangir, C. Luxey, G. Jacquemod, R. Pilard, F. Gianesello, W. G. Whittow, and C. J. Panagamuwa, "Investigation of the effect of metallic frames on 4G eyewear antennas," *Antennas and Propagation Conference IEEE*, pp. 60-63, Nov. 2014.

[3] "WHO research agenda for radiofrequency fields," *World Health Organization*, 2010.

[4] A. Dovrat, R. Berenson, E. Bormusov, A. Lahav, T Lustman, N. Sharon, and L. Schächter. "Localized effects of microwave radiation on the intact eye lens in culture conditions," *Bioelectromagnetics*, vol. 26, no. 5, pp. 398-405, July 2005.

[5] E. Diem, C. Schwarz, F. Adlkofer, O. Jahn, and H. Rüdiger, "Non-thermal DNA breakage by mobile-phone radiation (1800MHz) in human fibroblasts and in transformed GFSH-R17 rat granulosa cells in vitro," *Mutation Research/Genetic Toxicology and Environmental Mutagenesis*, vol. 583, no. 2, pp. 178-183, June 2005.

[6] A. B. Sharma, "A Review: Source and Effect of Mobile Communication Radiation on Human Health," *Advances in Wireless and Mobile Communications*, vol. 10, no. 3, pp. 423-435. 2017.

[7] "IARC classifies radiofrequency electromagnetic field as possibly carcinogenic to humans France," *International Agency for Research on Cancer*, Lyon, 2011.

[8] "IEEE Standard for Safety Levels with Respect to Human Exposure to Radio Frequency Electromagnetic Fields, 3 kHz to 300 GHz - Amendment 1: Specifies Ceiling Limits for Induced and Contact Current, Clarifies Distinctions between Localized Exposure and Spatial Peak Power Density," *IEEE*, 2010.

[9] ICNIRP, "Guidelines for limiting exposure to time-varying electric, magnetic and electromagnetic fields (up to 300 GHz)," *Health Phys.*, vol. 74, no. 4, pp. 494-522, 1998.

[10] J. Q. Lan, T. Hong, X. Liang, and G. H. Du, "Evaluation of Microwave Microdosimetry for Human Eyes with Glasses Exposed to Wireless Eyewear Devices at Phone Call State," *Progress In Electromagnetics Research M*, vol. 63, pp. 71-81, Jan. 2018;

[11] T. Wessapan and P. Rattanadecho, "Flow and heat transfer in biological tissue due to electromagnetic near-field exposure effects," *International Journal of Heat and Mass Transfer*, vol. 97, pp. 174-184,

June 2016.

[12] M. A. Stuchly, “Health effects of exposure to electromagnetic fields,” *Aerospace Applications Conference IEEE*, vol. 1, pp. 351-368, 1995.

[13] T. Ryota, N. Tomoaki, N. Kosuke, S. Kazuyuki, W. Soichi, and T. Masaharu, “Specific absorption rate and temperature increase in pregnant women at 13, 18, and 26 weeks of gestation due to electromagnetic wave radiation from a smartphone,” *IEICE Communications Express*, 2018XBL0026.

[14] R. Morimoto, I. Laakso, De. S. Valerio and A. Hirata, “Relationship between peak spatial-averaged specific absorption rate and peak temperature elevation in human head in frequency range of 1-30 GHz,” *Physics in Medicine & Biology*, vol. 61, no. 14, pp. 5406-5425, July 2017.

[15] Y. L. Diao, S. W. Leung, K. H. Chan, W. N. Sun, Y. M. Siu, and R. Kong, “Detailed modeling of palpebral fissure and its influence on SAR and temperature rise in human eye under GHz exposures, ” *Bioelectromagnetics*, vol. 27, no. 4, pp. 256-263, Apr. 2016.

[16] C. Li, Q, Chen, Y, Xie, and T. Wu, “Dosimetric study on eye’s exposure to wide band radio frequency electromagnetic fields: variability by the ocular axial length,” *Bioelectromagnetics*, vol. 35, no. 5, pp. 324-336, Feb. 2014.

[17] G. C. Van Rhoon, T. Samaras, P. S. Yarmolenko, M. W. Dewhirst, Esra Neufeld, and Niels Kuster, “CEM43A degrees C thermal dose thresholds: A potential guide for magnetic; resonance radio-frequency exposure levels?,” *European Radiology*, vol. 23, no. 8, pp. 2215-2227, Aug. 2013.

[18] C. Buccella, V. De Santis, and M. Feliziani, “Prediction of temperature increase in human eyes due to RF sources,” *IEEE Transactions on Electromagnetic Compatibility*, vol. 49, no. 4, pp. 825-833, Nov. 2007.

[19] G. M. Van Leeuwen, J. J. Lagendijk, B. J. Van Leersum, A. P. Zwamborn, S. N. Hornsleth, and A. N. Kotte, “Calculation of change in brain temperatures due to exposure to a mobile phone,” *Phys. Med. Biol*., vol. 44, no. 10, pp. 2367-2379, Oct. 1999.

[20] J. Wang and O. Fujiwara, “FDTD computation of temperature rise in the human head for portable telephones,” *IEEE Transactions on Microwave Theory and Techniques*, vol. 47, no. 8, pp. 1528-1534. Aug. 1999.

[21] J. Q. Lan, X. Liang, T. Hong, and G. H. Du, “On the effects of glasses on the SAR in human head resulting from wireless eyewear devices at phone call state,” *Progress in Biophysics and Molecular Biology*, vol. 136, pp. 29-36, Aug. 2018.

[22] P. J. Dimbylow and S. M. Mann, “SAR calculations in an anatomically realistic model of the head for mobile communication transceivers at 900 MHz and 1.8 GHz,” *Phys. Med. Biol*., vol. 39, pp. 1537-1553, 1994.

[23] C. Buccella, V. D. Santis, and M. Feliziani, “Numerical Prediction of SAR and Thermal Elevation in a 0.25-mm 3-D Model of the Human Eye Exposed to Handheld Transmitters,” *IEEE International Symposium on Electromagnetic Compatibility*, vol. 96, no. 4, pp. 1-6, July 2007.

[24] A. O. Rodrigues, L. Malta, J. J. Viana, L. O. C. Rodrigues, and J. A. Ramirez, “A head model for the calculation of SAR and temperature rise induced by cellular phones,” *IEEE Transactions on Magnetics*, vol. 44, no. 6. pp. 1446-1449, May 2008.

[25] O. P. Gandhi, G. Lazzi and C. M. Furse, “Electromagnetic absorption in the human head and neck for mobile telephones at 835 and 1900 MHz,” *IEEE T. Microw. Theory*, vol. 44, no. 10, pp. 1884-1897, Oct. 1996.

[26] G. M. Van Leeuwen, J. J. Lagendijk, B. J. Van Leersum, A. P Zwamborn, and S. N. Hornsleth, “Calculation of change in brain temperatures due to exposure to a mobile phone,” *Phys. Med. Biol*., vol. 44, no. 10, pp. 2367-2379. Oct. 1999;

[27] M. A. Jensen and Y. Rahmat-Samii, “EM interaction of handset antennas and a human in personal communications,” *Proceedings of the IEEE*, vol. 83, pp. 7-17, 1995.

[28] P. J. Dimbylowt and O. P. Gandhif, “Finite-difference time-domain calculations of SAR in a realistic heterogeneous model of the head for plane-wave exposure from 600 MHz to 3 GHz,” *Phys. Med. Biol*., vol. 36, no. 1. pp. 1075-1089, Jan. 1991.

[29] J. A. Scott, “The computation of temperature rises in the human eye induced by infrared radiation,” *Phys. Med. Biol*., vol. 33, no. 2, pp. 243-257, Feb. 1988.

[30] J. A. Scott, “A finite element model of heat transport in the human eye,” *Phys. Med. Biol*., vol. 33, no. 2, pp. 227-241, Feb. 1988.

[31] J. C. Lin, *Advances in Electromagnetic Fields in Living Systems*. Springer, New York, 2005.

[32] C. Gabriel, R. J. Sheppard, and E. H. Grant, “Dielectric properties of ocular tissues at 37 degrees C,” *Phys. Med. Biol*., vol. 28, no. 1, pp. 43-49, Jan. 1983.

[33] S. C. DeMarco, G. Lazzi, W. Liu, and J. D. Weiland, “Computed SAR and thermal elevation in a 0.25-mm 2-D model of the human eye and head in response to an implanted retinal stimulator-Part I: Models and methods,” *IEEE Transactions on Antennas and Propagation*, vol. 51, no. 9, pp. 2274-2285, Sep. 2003.

[34] A. H. Brien, “The myopia epidemic is there a role

for corneal refractive therapy?," *Eye Contact Lens*, vol. 30, pp. 244-246, Oct. 2004.
[35] W. G. Whittow, "Specific absorption rate perturbations in the eyes and head by metallic spectacles at personal radio communication frequencies," *PhD thesis EEE Dept.: University of Sheffield UK*, 2004.
[36] K. S. Yee, "Numerical solution of initial boundary value problems involving Maxwell's equations in isotropic media," *IEEE Trans. Antennas Propagat.*, vol. AP-14, pp. 302-307, May 1966.
[37] Z. S. Sacks, D. M. Kinsland, and J. F. Lee, "A perfectly matched anisotropic absorber for use as an absorbing boundary condition," *IEEE Trans. Antennas Propag.*, vol. 43, no. 12, pp. 1460-1463, Dec. 1995.
[38] S. D. Gedney, "An anisotropic perfectly matched layer absorbing media for the truncation of FDTD lattices," *IEEE Trans. Antennas Propag.*, vol. 44, no. 7, pp. 1630-1639, June 1996.
[39] I. S. Kim and W. J. Hoefer, "A local mesh refinement algorithm for the time domain-finite difference method using Maxwell's curl equations," *IEEE Transactions on Microwave Theory and Techniques*, vol. 38, no. 7, pp. 812-815, June 1990.
[40] H. H. Pennes, "Analysis of tissue and arterial blood temperatures in the resting human forearm," *Journal of Applied Physiology*, vol. 1, pp. 93-122, 1948.
[41] W. He, B. Xu, M. Gustafsson, Z. Ying, and S. He, "RF compliance study of temperature elevation in human head model around 28 GHz for 5G user equipment application: Simulation analysis," *IEEE Access*, vol. 6, pp. 830-838, Nov. 2018.
[42] P. Kramar, C. Harris, A. F. Emeryand, and A. W. Guy, "Acute microwave irradiation and cataract formation in rabbits and monkeys," *Journal of Microwave Power*, vol. 13, no. 3, pp. 239-249, Sep. 1978.
[43] C. Buccella, V. De Santis, and M. Feliziani, "Prediction of temperature increase in human eyes due to RF sources" *IEEE Transactions on Electromagnetic Compatibility*, vol. 49, pp. 825-833, 2007.
[44] H. C. Zhu, Y. H. Liao, W. Xiao, J. H. Ye, and K. M. Huang, "Transformation optics for computing heating process in microwave applicators with moving elements," *IEEE Trans. Microw. Theory Techn.*, vol. 65, no. 4, pp. 1434-1442, Nov. 2017.
[45] H. C. Zhu, T. Gulati, A. K. Datta, and K. M. Huang, "Microwave drying of spheres: Coupled electromagnetics-multiphase transport modeling with experimentation. Part I: Model development and experimental methodology," *Food and Bioproducts Processing*, vol. 96, pp. 314-325, Oct. 2015.
[46] W. L.Briggs, *Multigrid Tutorial*. Philadelphia: SIAM, 1987.
[47] I. Laakso, "Assessment of the computational uncertainty of temperature rise and SAR in the eyes andbrain under far-field exposure from 1 to 10 GHz," *Phys. Med. Biol.*, vol. 54, no. 11, pp. 3393-3404, May 2009

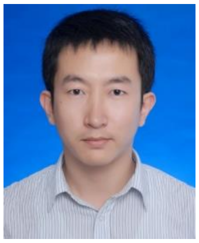

Junqing Lan was born in Shanxi, China, on October 22, 1983. He received the Ph.D. degree in Radio Physics from Sichuan University, in 2014. He joined the College of Electronic Engineering of Chengdu University of Information Technology in 2014.

Lan is mainly focused on the computational electromagnetics and antenna design.

Guohong Du was born in Hebei, China in 1977. She joined the teaching staff in 2004 and is currently a Professor with the College of Electronic Engineering of Chengdu University of Information Technology.

Her main research interests are in the fields of antenna design and numerical methods applied in electromagnetics.

An Analytical Method for Calculating Radiated Emission of Discontinuous Penetrating Cable

Bing-Xue Zhang [1], Pei Xiao [1], Dan Ren [2], and Ping-An Du [1]

[1] School of Mechanical and Electrical Engineering
University of Electronic Science and Technology of China, Chengdu 611731, China
bingxuezhang@163.com, xiaopei_uestc@sina.cn, dupingan@uestc.edu.cn

[2] Institute of Electronic Engineering
China Academy of Engineering Physics, Mianyang 621900, China
rendan_uestc@163.com

Abstract **—** Since the interconnection cable between devices is usually much longer than those inside an enclosure, it provides a main gateway for radiated interference. An analytical method for calculating the radiated field of penetrating cable including connectors is proposed based on the cascaded network. This method takes into account the effect of connectors on signal transmission in the calculation model. The discontinuous penetrating cable is regarded as two-port cascaded model which includes three parts: internal cables inside enclosure, connectors and an external cable. The terminal voltage and current of the cable are determined according to terminal conditions, and the current distribution is solved by the transmission line theory. Finally, the electromagnetic radiation of discontinuous penetrating cable is obtained by dipole approximation method. The proposed method is verified by numerical simulation.

Index Terms **—** Cable-enclosure system, cascaded network, connector, discontinuous penetrating cable, radiated emission.

I. INTRODUCTION

A cable is widely used as a connection between separate electronic devices for data or energy transmission. Due to the antenna effect, cable probably radiates considerable emission during signal transmission through it, and therefore produces significant electromagnetic interference. Thus, how to predict and control the radiated emission from cable has gained much attention, and so far, some calculation approaches have been put forward.

Meyer *et al.* proposed a calculation method of the radiated field for the interconnection cable between a power converter and a motor, which utilized the transmission line theory to obtain the current distribution along a cable, then used the electric field integral equation and the mirror theory to solve the radiated field where complex 3D modeling was avoided [1]. Xu *et al.* used several Hertzian dipoles as the equivalency of a multi-conductor transmission line and combined the current distribution of each dipole to analyze the radiated emission of cable bundle [2]. Jia *et al.* used a RF current probe to measure the amplitude of the common-mode current and obtained the phase of the current based on the phase extraction method [3], which replaced the anechoic chamber to predict the radiated emission of a cable bundle. They also used the current time-domain scanning and fast Fourier transform to determine the amplitude and phase of current to improve the accuracy of phase extraction and the quality of radiation prediction [4].

For electromagnetic radiation of a cable-enclosure system, Wang proposed a method based on asymmetrical dipole approximation and common-mode current simulation to estimate the radiation of cable connected to conductive shell [5]. However, this method can only be used for radiation estimation of simple structures, and there are still some limitations in the application. Park *et al.* presented an alternative method by measuring the common-mode current on cable to determine the equivalent source between cable and box, and computed the radiation transfer function to predict the radiated emission of box-source-cable [6]. Costa *et al.* employed an equivalent circuit model to compute the current distribution of a cable bundle and further estimate the near-field radiation [7]. However, it is rather difficult to create the exact circuit model of the device under test (EUT). Meng *et al.* considered the influence of connectors and supporting plates at both ends of the cable. Based on the dipole approximation method and the frequency domain analysis method of the transmission line, a fast calculation method was proposed for calculating the radiated emission of wire [8,9]. Jia *et al.* adopted the current scanning method and considered the radiation contribution of load structure to predict the radiation of the automotive system [10].

Submitted On: September 1, 2018
Accepted On: November 7, 2018

In practical problems, cable usually cannot be used to connect the excitation and load inside enclosures directly, but via the connectors mounted on the wall of enclosures, as shown in Fig. 1. The electrical connection function of the transmission system is realized through the mechanical engagement of pins and jacks in connector, where the contact resistance, inductance, conductance and capacitance exist and the consequent waveform distortion or even errors may occur. Thus, a cable may be divided by connectors into two parts, the external part (interconnection cable) and the internal parts (inside enclosure), so called discontinuous penetrating cable.

However, most of the present methods usually take the cable alone into account, and connectors are not included in calculation models. Since the connector impedance has considerable effect on signal transmission, which in turn affects the overall radiation of a cable-enclosure system, and thus, this paper presents a method for calculating radiated emissions of a discontinuous penetrating cable with connectors.

In the following part of the paper, Section II establishes the model of the discontinuous penetrating cable to solve the current distribution. In Section III, the radiation field approximation method is introduced and the radiated field of a cable-enclosure system is obtained. Section IV compares the method with the full-wave software CST to confirm the validation of the proposed method. And finally, some conclusions are drawn in Section V.

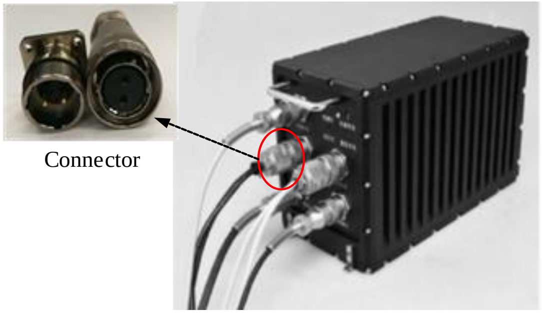

Fig. 1. A cable-enclosure system.

II. ESTABLISHMENT OF DISCONTINUOUS PENETRATING CABLE MODEL

A. Transmission parameter model of discontinuous penetrating cable

The model of a cable-enclosure system is shown in Fig. 2, which consists of an EUT and a load case with a printed circuited board (PCB), an interconnection cable connected with two internal cables through connectors between two enclosures. Within the system, radiation may be caused by the interconnection cable, internal cables and PCB. High frequency signal on the PCB may be coupled to the cable, the radiation from the cable is dominant, and thus, the radiation of PCB is often neglected.

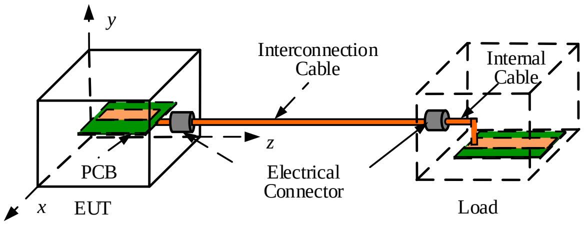

Fig. 2. The model of a cable-enclosure system.

During analysis, the radiation of cable is derived from the trace on the board. The electromagnetic radiation of PCB is mainly caused by common-mode current, while the radiation caused by differential-mode current can be neglected. Thus, a PCB with an attached cable can be modeled as an equivalent common-mode voltage source at junction between the cable and plate [11,12], as illustrated in Fig. 3. The voltage-driven principle is to couple electric field to connecting cable to generate a common-mode current. Shim [11] also presented the expression for the common-mode voltage with:

$$V_{cm} = \frac{C_{trace}}{C_{board}} V_{DM} , \tag{1}$$

where C_{trace} , C_{board} are the capacitance of trace and board, respectively, V_{DM} the signal voltage source.

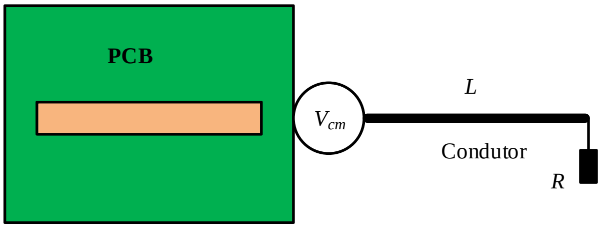

Fig. 3. Equivalent model of voltage-driven.

In the load case, the PCB terminal is connected to an impedance-matched load Z_L. Xiao [14] used a frequency-dependent lumped load Z_{eq} to replace the PCB, the equivalent load can be written as:

$$Z_{eq} = R' + Z_L . \tag{2}$$

Where R' is the resistance of trace, $R' = L_{rc}/wt\sigma$ [13].

Since the load impedance Z_L is matched with the characteristic impedance Z_m of the trace, they satisfy $Z_L = Z_m$, so Z_m can be expressed by:

$$Z_m = \begin{cases} \dfrac{60}{\sqrt{\varepsilon_{re}}}\dfrac{1}{2\pi}\ln\left(\dfrac{8h}{w}+\dfrac{w}{4h}\right) & \dfrac{w}{h}\le 1 \\ \dfrac{120\pi}{\sqrt{\varepsilon_{re}}}\left[\dfrac{w}{h}+1.393+0.667\ln\left(\dfrac{w}{h}+1.444\right)\right]^{-1} & \dfrac{w}{h}\ge 1 \end{cases}. \quad (3)$$

Where ε_{re} is the effective relative permittivity, w and h are the width and height of the trace, respectively.

Now, a discontinuous penetrating cable model, shown in Fig. 4, can be extracted from the cable-enclosure system, which includes EUT's internal cable l_0, electrical connector a and b, interconnection cable l2, load enclosure internal cable l4, equivalent voltage V_{cm}, and equivalent load Z_{eq}.

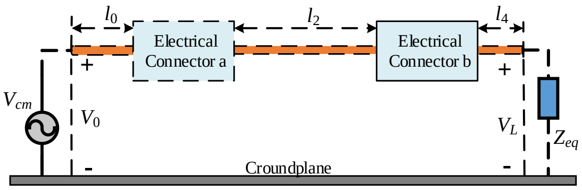

Fig. 4. A discontinuous penetrating cable model.

B. Calculation of current distribution

In general, if we are more interested in the output voltage and current of a complex circuit rather than its internal structure, the circuit can be regarded as a two-port network [13]. Thus, each part of the discontinuous penetrating cable model can be equivalent to a two-port circuit model, and a transmission matrix can be used to describe the relationship between the input and output voltage and current of each port. The expression can be expressed by:

$$\begin{pmatrix} V_i \\ I_i \end{pmatrix} = \begin{pmatrix} A_i & B_i \\ C_i & D_i \end{pmatrix}\begin{pmatrix} V_{i+1} \\ I_{i+1} \end{pmatrix}. \quad (4)$$

Where V_i and I_i (i=0, 1, 2, 3, 4) represent the voltage and current at the ports of internal cable of an EUT, connector a, interconnection cable, connector b and internal cable of load enclosure, respectively. A_i, B_i, C_i, D_i are transmission matrix parameters.

Assuming all cables are of the same type, the electrical parameters of interconnection and internal cable are consistent. Therefore, the transmission matrix of cables can be written as:

$$\begin{pmatrix} A_i & B_i \\ C_i & D_i \end{pmatrix} = \begin{pmatrix} \cosh(\gamma l_i) & Z_c \sinh(\gamma l_i) \\ \sinh(\gamma l_i)/Z_c & \cosh(\gamma l_i) \end{pmatrix} \quad i=0,2,4\,. \quad (5)$$

Where l_i is the length of each part of the cable.

To facilitate the study of a two-port cascaded network, we need to determine connector's scattering parameter first, which can be measured by a vector network analyzer (VNA) or computed by a numerical method. Then the transmission parameter matrix of connectors can be calculated by:

$$\begin{pmatrix} A_i & B_i \\ C_i & D_i \end{pmatrix} = \begin{pmatrix} \dfrac{(1+S_{11})(1-S_{22})+S_{12}S_{21}}{2S_{21}} & \dfrac{Z_{02}\left[(1+S_{11})(1+S_{22})-S_{12}S_{21}\right]}{2S_{21}} \\ \dfrac{\left[(1-S_{11})(1-S_{22})-S_{12}S_{21}\right]}{2S_{21}Z_{01}} & \dfrac{\left[(1-S_{11})(1+S_{22})+S_{12}S_{21}\right]Z_{01}}{2S_{21}Z_{02}} \end{pmatrix}$$

$$i=1,3\,. \quad (6)$$

Where Z_{01} and Z_{02} are the reference impedance of a connector port 1 and port 2, respectively.

By assembling each two-port network together, a cascade network of discontinuous penetrating cable can be formed as shown in Fig. 5, and by multiplying a series of matrix, the transmission matrix of the whole discontinuous penetrating cable system can be written as:

$$\begin{pmatrix} A & B \\ C & D \end{pmatrix} = \begin{pmatrix} A_0 & B_0 \\ C_0 & D_0 \end{pmatrix}\begin{pmatrix} A_1 & B_1 \\ C_1 & D_1 \end{pmatrix}\begin{pmatrix} A_2 & B_2 \\ C_2 & D_2 \end{pmatrix}\begin{pmatrix} A_3 & B_3 \\ C_3 & D_3 \end{pmatrix}\begin{pmatrix} A_4 & B_4 \\ C_4 & D_4 \end{pmatrix}. \quad (7)$$

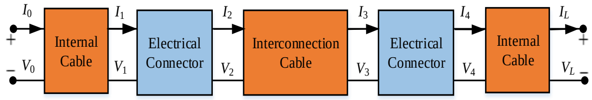

Fig. 5. A cascaded two-port network.

So, the relationship between an input and an output voltages and currents of the near and the far terminals is as follows:

$$\begin{pmatrix} V_0 \\ I_0 \end{pmatrix} = \begin{pmatrix} A & B \\ C & D \end{pmatrix}\begin{pmatrix} V_L \\ I_L \end{pmatrix}. \quad (8)$$

For a two-port network driven by the Thevenin circuit, the transmission parameters can be used to represent the load terminal voltage V_L and current I_L that can be calculated by:

$$\begin{cases} I_L = \dfrac{V_{cm}}{AZ_L + B} \\ V_L = \dfrac{Z_L V_{cm}}{AZ_L + B} \end{cases}. \quad (9)$$

The interconnection cable is the major source of radiated emission due to its relatively long length. The voltage and current of the interconnection cable l_2 are obtained by:

$$\begin{cases} V_4 = A_4 V_L + B_4 I_L = (A_4 Z_L + B_4) I_L \\ I_4 = C_4 V_L + D_4 I_L = (C_4 Z_L + D_4) I_L \end{cases}, \quad (10)$$

$$\begin{cases} V_3 = A_3 V_4 + B_3 I_4 \\ I_3 = C_3 V_4 + D_3 I_4 \end{cases}, \quad (11)$$

$$\begin{cases} V_2 = A_2 V_3 + B_2 I_3 \\ I_2 = C_2 V_3 + D_2 I_3 \end{cases}. \quad (12)$$

According to the transmission line theory, if the voltage V_2 and current I_2 at the initial end of the interconnection cable are available, the current distribution at any point can be expressed as:

$$I_2(z)=\frac{1}{2Z_c}(V_2+I_2Z_c)e^{-\gamma z}-\frac{1}{2Z_c}(V_2-I_2Z_c)e^{\gamma z}, \quad (13)$$

III. THE ANALYTICAL METHOD FOR RADIATED EMISSION OF DISCONTINUOUS PENETRATING CABLE

A. Dipole approximation method for cable radiated field

As a highly efficient transmitting antenna, a cable can propagate interference into surrounding space in the form of electromagnetic waves when the frequency of signal transmission exceeds 30MHz. Since antenna radiation is a macroscopic electromagnetic field problem, the rigorous analytical method can be used to solve Maxwell equations with different boundary conditions, but it may lead to mathematical complexity and lower efficiency. Therefore the Hertzian dipole approximation approach is often used to predict cable radiated emission.

The following set of equations defines the radiated field generated by a dipole *I*(*z*)dz at point A on a cable in Cartesian coordinate [16]:

$$\begin{cases} dE_x=e_x\left\{-j\dfrac{I(z)dz}{4\pi\omega\varepsilon}\dfrac{e^{-jkr}}{r^2}\sin\theta\cos\theta\cos\varphi[3jk-rk^2+\dfrac{3}{r}]\right\} \\ dE_y=e_y\left\{-j\dfrac{I(z)dz}{4\pi\omega\varepsilon}\dfrac{e^{-jkr}}{r^2}\sin\theta\cos\theta\sin\varphi[3jk-rk^2+\dfrac{3}{r}]\right\} \\ dE_z=e_z\left\{j\dfrac{I(z)dz}{4\pi\omega\varepsilon}\dfrac{e^{-jkr}}{r^2}[(jk-rk^2+\dfrac{1}{r})\sin^2\theta-(2jk+\dfrac{2}{r})\cos^2\theta]\right\} \end{cases},(14)$$

where $k=\omega\sqrt{\mu\varepsilon}$ is phase constant, ω angular frequency, r the distance from dipole to observation point *P*; $\varepsilon_0=8.85\times10^{-12}$ A/m and $\mu=4\pi\times10^{-7}$ A/m the permittivity and permeability for free space, respectively, θ the angle between *AP* connection and *z* axis, φ the angle between *AP* plane and *z* axis.

The electric field generated by the interconnection cable at the observation point *P* is E_{TL}, which is formed by the superposition of the electric fields by all the Hertzian dipoles on the cable, is:

$$E_{TL}=e_x\int_0^l dE_x+e_y\int_0^l dE_y+e_z\int_0^l dE_z\,. \qquad (15)$$

Similarly, the electric field E'_{TL} formed by the mirror line of interconnection cable can also be calculated. Thus, the total electric field generated by interconnection cable is expressed as:

$$E=E_{TL}+E'_{TL}\,. \qquad (16)$$

B. Analysis of the radiated field of cable-enclosure system

Because the surface current of enclosure is complex to calculate, its radiation contribution is difficult to obtain accurately. If the EUT and load enclosure are small compared to wavelength at frequency of interests and placed directly on the ground, the enclosure can be modeled as a vertical monopole antenna model [8], as shown in Fig. 6, so we have:

$$\begin{cases} I_{d1}=I'_{d1}=I_2\bullet n_y \\ I_{d2}=I'_{d2}=I_3\bullet n_y \end{cases}. \qquad (17)$$

Where I_{d1} and I'_{d1} are the real and mirror current of EUT side enclosure panel, respectively, I_{d2} and I'_{d2} are the real and mirror current of the load side enclosure panel.

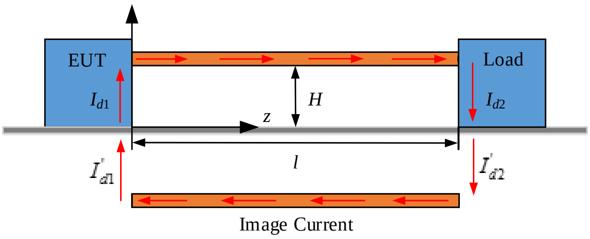

Fig. 6. A multi-dipole radiated model for cable-enclosure system.

According to the dipole antennas theory, the radiated field of all Hertzian dipole in Fig. 6 can be superimposed to obtain the radiated field E of a simple cable-enclosure system:

$$E=E_{TL}+E'_{TL}+E_{d1}+E'_{d1}+E_{d2}+E'_{d2}\,. \qquad (18)$$

Where E_{TL} and E'_{TL} are the radiated fields from the real and mirror current of an interconnection cable, respectively, and E_{d1} and E'_{d1} are the radiated fields from the real enclosure panel and the mirror image of an EUT, respectively, and E_{d2} and E'_{d2} are the radiated fields from the enclosure panel and the mirror image of a load structure.

IV. RESULTS

A. Validation of the proposed method

In order to verify the proposed method, the model shown in Fig. 2 will be calculated via the method and the results will be compared with those from the full-wave software CST. The height of the cable from ground is *H* = 50 mm, the radius of the cable is *r* = 1 mm, the length of the internal cable of EUT and load case are $l_0=l_4=0.02$ m, and the length of the interconnection cable is $l_2=2$ m.

The geometry and dimensions of the PCB consisting of a metallic trace, a substrate dielectric layer and a return path are shown in Fig. 7, where the trace is located at the middle of a PCB with dimensions of *w*×*l*×*t* and conductivity $\sigma=5.8\times10^7$ S/m. The dielectric substrate with dimensions of a×b×h has a relative permittivity of $\varepsilon_r=4.3$. The size of the internal PCB of EUT is *a* = 100 mm, *b* =40 mm, *l* = 50 mm, *w* = 1 mm, the PCB size of the load enclosure is $a = 50$ mm, b =13 mm, l = 50 mm, w = 0.5 mm, t = 0.1 mm, h = 0.3 mm.

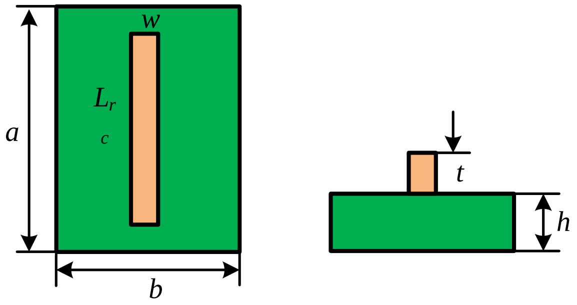

Fig. 7. The geometry and dimensions of PCB.

Figure 8 illustrates the current at the termination load calculated by the proposed method and CST simulation. The good agreement establishes the validation of the discontinuous penetrating cable model proposed in this paper. It should be noted that the result at low-frequency band of 0-500 MHz is better than that at higher frequency. The reason is that the highest frequency calculated accurately by the transmission line model is related to the height of the cable from the ground plane, which satisfies $h < \lambda / 10$ [15], and higher order modes start to propagate along the cable.

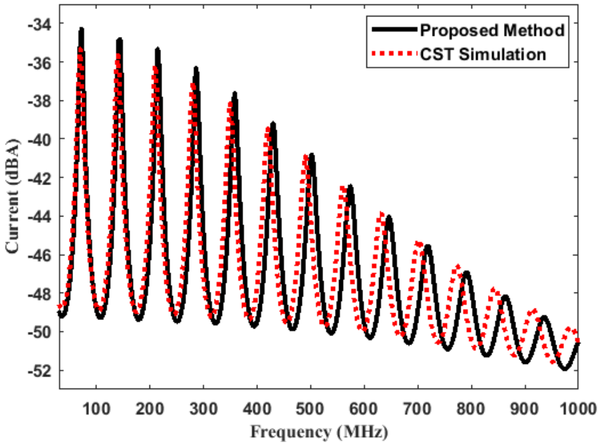

Fig. 8. Comparison of the current at the load end between the proposed method and CST simulation.

Figure 9 shows the comparison of the theoretically and numerically calculated radiated field ranging from 30 MHz to 1000 MHz at observation point P. It can be seen that the difference at most frequencies is less than 5 dB, and the calculation time for the radiated field is only 7s using the proposed method, which has an obvious speed advantage over CST simulation.

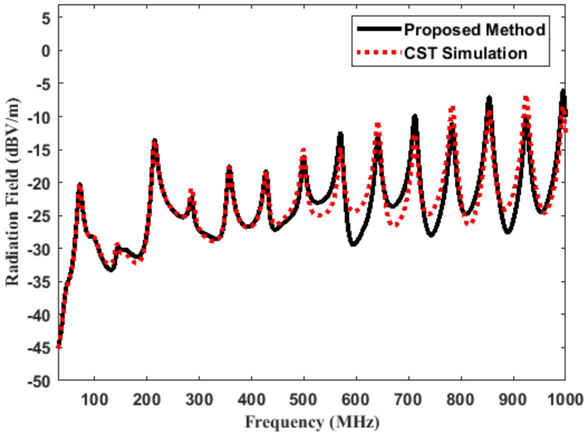

Fig. 9. Validation of radiation emission by comparing proposed method and CST simulation.

In Fig. 10, the solid line represents the current distribution at the load end in the presence of connectors, while the dotted line denotes the result of the transmission line without connectors. From the comparison, we can learn that the load end current will decay with the increase of frequency when connectors are taken into account. This can be attributed to the effect of connector’s impedance and the bonding between the cable and connector, because the resistance and conductance varied with frequency reflect the loss of electromagnetic energy. Thus, the current at load end will decreases with the increase of frequency when connectors are included in the calculation.

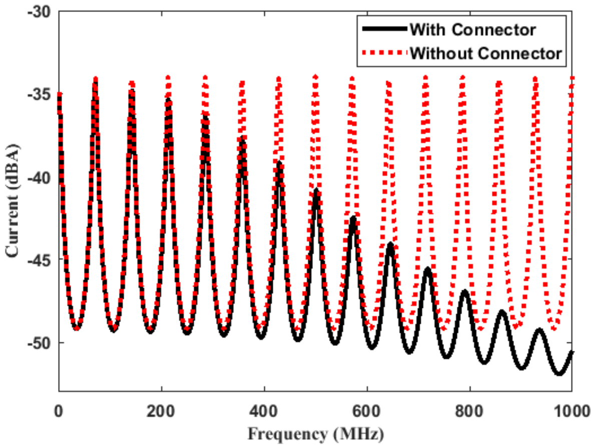

Fig. 10. A comparison of current distribution of load end with and without connectors.

B. Discussion

Because the connector can transmit signals, the transmission line theory can be used to study its distribution and transmission characteristics. As can be seen in Fig. 11, the model of connector cascades a lot of identical *RLGC* units.

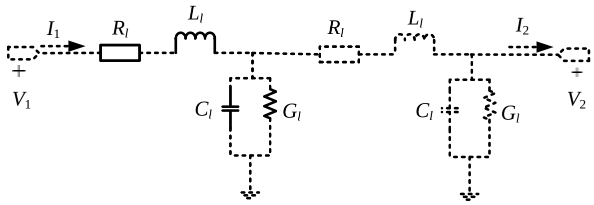

Fig. 11. The transmission line model of the connector.

In general, the characteristics of the transmission line can be represented by transmission (*ABCD*) matrix:

$$\begin{pmatrix}V_1\\ I_1\end{pmatrix}=\begin{pmatrix}A_l & B_l\\ C_l & D_l\end{pmatrix}\begin{pmatrix}V_2\\ I_2\end{pmatrix}. \tag{19}$$

The equivalent transmission line of connector has a propagation constant of γ_l and a characteristic impedance of Z_{cl}. The transmission parameter matrix is expressed as:

$$\begin{pmatrix}A_l & B_l\\ C_l & D_l\end{pmatrix}=\begin{pmatrix}\cosh(\gamma_l l_l) & Z_{cl}\sinh(\gamma_l l_l)\\ \sinh(\gamma_l l_l)/Z_{cl} & \cosh(\gamma_l l_l)\end{pmatrix}, \tag{20}$$

where l_l is the length of connector. Comparing (19) and (20), γ_l and Z_{cl} can be written as:

$$\gamma_l = ar\cosh(A_l)/l_l, \tag{21}$$

$$Z_{c_l}=\sqrt{B_l/C_l}. \tag{22}$$

The scattering matrix is transformed into a transmission matrix by the transformation in (6). According to the definitions of γ_l and Z_{cl}, we obtain:

$$\begin{cases} R_l + j\omega L_l = \gamma_l Z_{c_l} \\ G_l + j\omega C_l = \gamma_l / Z_{c_l} \end{cases}. \tag{23}$$

RLGC parameters per unit length are derived as:

$$R_l = Real\left(\gamma_l Z_{c_l}\right), \tag{24}$$

$$G_l = Real\left(\gamma_l / Z_{cl}\right), \tag{25}$$

$$C_l = \frac{\mathrm{Im}\,ag\left(\gamma_l / Z_{c_l}\right)}{\omega}, \tag{26}$$

$$L_l = \frac{\mathrm{Im}\,ag\left(\gamma_l Z_{c_l}\right)}{\omega}. \tag{27}$$

The parameters above are calculated by utilizing Matlab software and shown in Fig. 12. As shown in Fig. 12, the resistance, conductance, capacitance and inductance per unit length of connector are all strongly frequency dependent. The resistance and conductance increase with the increase of frequency, whereas the inductance and capacitance decrease with the increase of frequency. Since R_l and G_l reflect the loss of current in transmission process, the current in Fig. 10 will decrease as the frequency increases when connectors are included in the model.

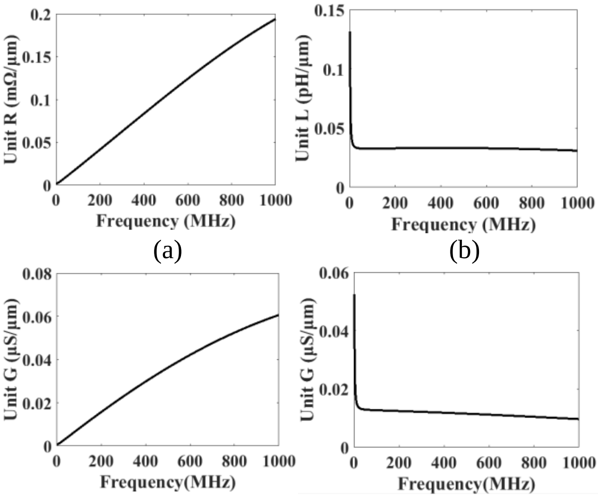

(a) (b)

(c) (d)

Fig. 12. *RLGC* parameters per unit length: (a) resistance per unit length; (b) inductance per unit length; (c) conductance per unit length; (d) capacitance per unit length.

VI. CONCLUSION

The interconnection cable between devices is usually an effective radiation antenna. In this paper, the influence of connectors on the signal transmission is considered in the calculation model. The proposed approach is verified by CST numerical analysis. The R_l and G_l of connector represent the loss during transmission, which determines the attenuation of the signal as it passes through the transmission path. The variation of connector's distribution parameters depend on the geometric design and the characteristics of the transmission material itself, which determines the voltage and current change produced by the signal when it flows through the transmission path. The results show that it is necessary to consider the influence of connector on signal current in the study of cable radiation.

ACKNOWLEDGMENT

This project is supported by the National Natural Science Foundation of China (Grant No 51675086).

REFERENCES

[1] M. Meyer and P. Asfaux, "Radiated emissions modeling of a power cable [C]," *IEEE International Symposium on Electromagnetic Compatibility-EMC*, Europe, pp. 1-5, 2008.

[2] J. Xu and Y. Lv. "Analysis of radiated emissions from multi-conductor lines [C]," *IEEE International Symposium on Antennas, Propagation and EM Theory*, pp. 1009-1012, 2008.

[3] J. Jia, D. Rinas, and S. Frei, "Prediction of radiated

fields from cable bundles based on current distribution measurements [C]," *IEEE International Symposium on Electromagnetic Compatibility (EMC EUROPE)*,pp. 1-7, 2012.

[4] J. Jia, D. Rinas, and S. Frei, "An alternative method for measurement of radiated emissions according to CISPR 25 [C]," *IEEE International Symposium on Electromagnetic Compatibility* (*EMC EUROPE)*, pp. 304-309, 2013.

[5] J. Wang, O. Fujiwara, and K. Sasabe, "A simple method for predicting common-mode radiation from a cable attached to a conducting enclosure [C]," *IEEE Asia-Pacific Microwave Conference APMC*, Taipei, pp. 1119-1122, 2001.

[6] H. H. Park, H. B. Park, and H. S. Lee, "A simple method of estimating the radiated emission from a cable attached to a mobile device [J]," *IEEE Transactions on Electromagnetic Compatibility*, 55(2), pp. 257-264, 2013.

[7] F. Costa, C. Gautier, B. Revol, et al., "Modeling of the near-field electromagnetic radiation of power cables in automotives or aeronautics [J]," *IEEE Transactions on Power Electronics*, 28(10), pp. 4580-4593, 2013.

[8] J. Meng, Y. X. Teo, D. W. P. Thomas, et al., "Fast prediction of transmission line radiated emissions using the Hertzian dipole method and line-end discontinuity models [J]," *IEEE Transactions on Electromagnetic Compatibility*, 56(6), pp. 1295-1303, 2014.

[9] J. Meng, L. Zhang, J. Tang, et al., "Computation of radiated electric fields from cables using the 1D time-domain and frequency-domain TLM methods [C]," *IEEE International Conference on Electrical Machines and Systems*, pp. 3253-3258, 2015.

[10] J. Jia, D. Rinas, and S. Frei, "Predicting the radiated emissions of automotive systems according to CISPR 25 using current scan methods [J]," *IEEE Transactions on Electromagnetic Compatibility*, 58(2), pp. 409-418, 2016.

[11] H. W. Shim and T. H. Hubing, "Model for estimating radiated emissions from a printed circuit board with attached cables due to voltage-driven sources [J]," *IEEE Transactions on Electromagnetic Compatibility*, 47(4), pp. 899-907, 2005.

[12] J. H. Goh, B. K. Chung, E. H. Lim, et al., "An improved model for estimating radiated emissions from a PCB with attached cable [J]," *Progress In Electromagnetics Research M*, 33, pp. 17-29, 2013.

[13] C. R. Paul, *Analysis of Multiconductor Transmission Lines* [M], New York: John Wiley & Sons, pp. 45-54, 1994.

[14] P. Xiao, P. A. Du, D. Ren, et al., "A hybrid method for calculating the coupling to PCB inside a nested shielding enclosure based on electromagnetic topology [J]," *IEEE Transactions on Electromagnetic Compatibility*, 58(6), pp. 1701-1709, 2016.

[15] G. Ergaver and J. Trontelj, "Prediction of radiated emissions of automotive electronics early in the design phase based on automotive component level testing [J]," *Informacije MIDEM*, 46(1), pp. 42-52, 2016.

[16] C. R. Paul, "Introduction to electromagnetic compatibility [J]," *IEE Review*, 38(7-8), pp.1-12, 1992.

Bing-Xue Zhang was born in Dezhou, Shandong province, China, in 1991. She received the B.E. fom Harbin University of Science and Technology in 2014.

She is currently a Master student of UESTC. Her research interest is numerical methods of eletromagnetic radiation from interconnecting cables.

Pei Xiao was born in Shaoyang, Hunan province, China, in 1989. He received the Bachelor of Mechanical Engineering degree from UESTC, Chengdu, China, in 2013. He is currently a Ph.D. student at UESTC.

His research interests are numerical computation, theoretical electromagnetic analysis including the EMT method, and EMC/EMI in Multiconductor transmission line (MTL).

Dan Ren was born in Huainan, Anhui Province, China, in 1986. He received the Bachelor of Industrial Engineering degree and the Ph.D. degree in Mechatronics Engineering from the University of Electronic Science and Technology of China, Chengdu, China, in 2011 and 2017, respectively.

He is also a Visiting Student in the UBC Radio Science Lab, Vancouver, BC, Canada. His research interests include numerical computation, electromagnetic measurement, electromagnetic simulation, and EMC/EMI in shielding enclosures, apertures, and cable radiation.

Ping-An Du received the M.S. and Ph.D degrees in Mechanical Engineering from Chongqing University, Chongqing, China, in 1989 and 1992, respectively.

He is currently a Full Professor of Mechanical Engineering at the University of Electronic Science and Technology of China, Chengdu, China. His research interests include numerical simulation in EMI, vibration, temperature, and so on.

Approximated Solutions on the Electromagnetic Field in Near Zone Generated by a Horizontal Electric Dipole on the Planar Surface of the Anisotropic Rock

Tingting Gu, Honglei Xu, and Kai Li

College of Information Science and Electronic Engineering
Zhejiang University, Hangzhou, 310027, China
ttgu@zju.edu.cn, hongleixu@zju.edu.cn, kaili@zju.edu.cn

Abstract **─** In this paper, the approximate formulas have been derived for ELF electromagnetic field in near zone from a horizontal electric dipole on the surface of sea water and one-dimensional anisotropic rock boundary. The computational scheme exploits the concept of quasi-static approach for ELF near-field approximations. Specifically, the integrands of Fourier-Bessel representations are approximated by adopting Maclaurin's Expansion where the ratio of wave numbers for rock and sea approaches zero. The approximated solution is in good agreement with the available experimental data.

Index Terms **─** Anisotropic rock horizontal, ELF near-field, electric dipole.

I. INTRODUCTION

The electromagnetic fields generated by a vertical electric dipole or a horizontal electric dipole near the boundary between two different media like earth and air or sea water and rock have been known in terms of analytical closed-form expressions for decades [1].

In order to evaluate these formulas, extensive studies have been made by many investigators through analytical [2-15] and numerical techniques [16-21]. Among many applied frequency bands, the ELF wave (ELF: ranges from 3 Hz to 30 Hz) has been widely used to the fields, such as deep underground exploration, submarine prospection and communication evaluation. Unfortunately, most available formulas are not used in the ELF frequencies, where the integrands have divergent terms in near zone for ELF field. Additionally, difficulties to implement in the near-field region for ELF waves arise in numerical solution because of limited resolutions near the source.

Recently, this old problem was revisited by Pan [22] in Chapter 6 of the book where the ELF near-field wave propagation is investigated in its application to marine controlled-source electromagnetics (mCSEM) method. The computational scheme is developed from the approximated formulas in the book [5] by retaining fundamental terms. As an extension of these works, the approximate formulas for ELF wave have been derived to evaluate the Sommerfeld's integrals for in near zone in the presence of half-spaces. Since it is found in some stratified rock that the conductivity is anisotropic which consists of alternating layers of dense rock and less dense rock. Specially, the conductivity transverse to the bedding surfaces is always smaller than the conductivity parallel to the surfaces [23]. This motivates us to develop the stratified prototype, where the rock layer is seen as one-dimensionally anisotropic medium.

In the present study, the approximate expressions of ELF field components due to a horizontal electric dipole is addressed near the planar surface of the anisotropic rock with analytical approximations. Specifically, the quasi-static approach is adopted for ELF waves by $\gamma_2 \approx i\lambda$ in evaluations because the permittivity of sea water can be approximated by the pure imaginary function of frequency ($\varepsilon_{\mathrm{sea}} \approx -i\sigma_{\mathrm{sea}}/\omega$) when the operating frequencies are in the range of ELF frequencies. The nature of the approximation is on basis of the asymptotic expansions of integrands of the Fourier-Bessel representations near the poles. In what follows, the near-field electromagnetic field by the conditions of $k\rho << 1$, $z/\rho << 1$, $d/\rho << 1$, the ratio of wave numbers for rock and sea $|k_2/k_1|$ (subscripts 1 and 2 represent for sea water and rock, respectively) is equivalent to an infinitesimal $|k_2^2\gamma_1|/|k_1^2\gamma_2|$. The computational evaluations of ELF field in near zone are carried out along the planar surface of anisotropic rock with the approximated formulas. The time dependence $e^{-i\omega t}$ is suppressed throughout the analysis.

II. FORMULATIONS

A. Fourier-Bessel representations for ELF near field in the sea water along the surface of one-dimensional anisotropic rock

The relevant geometry is shown in Fig. 1, where the horizontal electric dipole in the $\hat{z}$ direction is

Submitted On: March 20, 2018
Accepted On: December 25, 2018

located at (0, 0, *d*). The above half space is Region 1 (z⩾0) filled with sea water, and Region 2 is the ocean floor by the permittivity μ_0, permittivity $\varepsilon_{2x}=\varepsilon_{2y}$ and ε_{2z}, and conductivity $\sigma_{2x}=\sigma_{2y}$ and σ_{2z}. Then, the complex permittivities $\tilde{\varepsilon}_1$ and $\bar{\bar{\varepsilon}}_2$ are expressed as follows:

$$\tilde{\varepsilon}_1=\varepsilon_0(\varepsilon_{r1}-i\frac{\sigma_{sea}}{\omega\varepsilon_0}), \tag{1}$$

$$\bar{\bar{\varepsilon}}_2=\varepsilon_0\bar{\bar{\varepsilon}}_{r2}=\varepsilon_0\begin{bmatrix}\varepsilon_{rT}-i\frac{\sigma_T}{\omega\varepsilon_0} & 0 & 0\\ 0 & \varepsilon_{rT}-i\frac{\sigma_T}{\omega\varepsilon_0} & 0\\ 0 & 0 & \varepsilon_{rL}-i\frac{\sigma_L}{\omega\varepsilon_0}\end{bmatrix}. \tag{2}$$

With the time dependence $e^{-i\omega t}$, the Maxwell's equations in the two half-spaces are represented by:

$$\nabla\times\boldsymbol{E}_j=i\omega\boldsymbol{B}_j, \tag{3}$$

$$\nabla\times\boldsymbol{B}_j=\mu_0(-i\omega\hat{\varepsilon}_j\boldsymbol{E}_j+\hat{x}J_x^e), \tag{4}$$

where j = 1, 2, and,

$$J_x^e=Idl\delta(x)\delta(y)\delta(z-d), \tag{5}$$

representing for the volume current density in the dipole.

The Fourier transform is in the form of,

$$\boldsymbol{E}(x,y,z)=\frac{1}{(2\pi)^2}\int_{-\infty}^{+\infty}\mathrm{d}\xi\int_{-\infty}^{+\infty}\mathrm{d}\eta e^{i(\xi x+\eta y)}\tilde{E}(\xi,\eta,z), \tag{6}$$

and similar transform for ***B****(x, y, z)* and J_x^e are applied to Maxwell's equation. Then, we have:

$$\tilde{J}_x^e=\mathrm{Idl}\delta(z-d). \tag{7}$$

In [22], the six Fourier integrals for ELF wave components of the electromagnetic field in Region 1 in the range $0\le z\le d$ can be expressed as follows:

$$E_{1x}=\frac{Idl}{(2\pi)^2}\int_{-\infty}^{\infty}d\xi\int_{-\infty}^{\infty}d\eta e^{i(\xi x+\eta y)}\times\left(\left\{\lambda^2N_e+\xi^2\left[\gamma_1(\gamma_T\gamma_e-k_T^2)-\lambda^2\gamma_e\right]\right\}-\frac{e^{i\gamma_1 d}}{i\omega\tilde{\varepsilon}_1\gamma_1}\sin\gamma_1 z\right), \tag{8}$$

$$E_{1y}=\frac{Idl}{(2\pi)^2}\int_{-\infty}^{\infty}d\xi\int_{-\infty}^{\infty}d\eta\xi\eta e^{i(\xi x+\eta y)}\times\left[\frac{\omega\mu_0 e^{i\gamma_1(z+d)}}{\lambda^2M_TN_e}(k_T^2\gamma_1+\lambda^2\gamma_e-\gamma_1\gamma_T\gamma_e)+\frac{e^{i\gamma_1 d}}{i\omega\tilde{\varepsilon}_1\gamma_1}\sin\gamma_1 z\right], \tag{9}$$

$$E_{1z}=\frac{Idl}{(2\pi)^2}\int_{-\infty}^{\infty}d\xi\int_{-\infty}^{\infty}d\eta e^{i(\xi x+\eta y)}\xi\times\left[\frac{\omega\mu_0\gamma_e e^{i\gamma_1(z+d)}}{N_e}-\frac{e^{i\gamma_1 d}}{\omega\tilde{\varepsilon}_1}\cos\gamma_1 z\right], \tag{10}$$

$$B_{1x}=-\frac{\mu_0 Idl}{(2\pi)^2}\int_{-\infty}^{\infty}d\xi\int_{-\infty}^{\infty}d\eta e^{i(\xi x+\eta y)}\xi\eta\times\frac{e^{i\gamma_1(z+d)}}{\lambda^2M_TN_e}(k_1^2\gamma_T\gamma_e-k_T^2\gamma_1^2), \tag{11}$$

$$B_{1y}=-\frac{\mu_0 Idl}{(2\pi)^2}\int_{-\infty}^{\infty}d\xi\int_{-\infty}^{\infty}d\eta e^{i(\xi x+\eta y)}\times\left\{\frac{e^{i\gamma_1(z+d)}}{\lambda^2M_TN_e}\left[\lambda^2\gamma_1N_e+\xi^2(k_1^2\gamma_T\gamma_e-k_T^2\gamma_1^2)\right]-e^{i\gamma_1(z+d)}\cos\gamma_1 z\right\}, \tag{12}$$

$$B_{1z}=\frac{\mu_0 Idl}{(2\pi)^2}\int_{-\infty}^{\infty}d\xi\int_{-\infty}^{\infty}d\eta e^{i(\xi x+\eta y)}\eta\times\left[\frac{e^{i\gamma_1(z+d)}}{M_T}-\frac{ie^{i\gamma_1 d}}{\gamma_1}\sin\gamma_1 z\right], \tag{13}$$

where,

$$M_T=\gamma_1+\gamma_T, \tag{14}$$

$$N_e=k_T^2\gamma_1+k_1^2\gamma_e=\frac{k_T}{k_L}(k_Lk_T\gamma_1+k_1^2\gamma_L), \tag{15}$$

$$\gamma_T=\sqrt{k_T^2-\lambda^2}, \tag{16}$$

$$\gamma_e=\sqrt{k_T^2-\frac{k_T^2}{k_L^2}\lambda^2}=\frac{k_T}{k_L}\gamma_L=\frac{k_T}{k_L}\sqrt{k_L^2-\lambda^2}, \tag{17}$$

in which the square root is to be taken so that γ_n is in the first quadrant, and the upper sign "+" and the lower sign "-" correspond to $z>d$ and $0\le z\le d$ in Region 1, respectively.

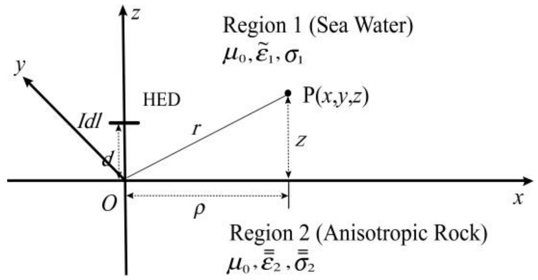

Fig. 1. The geometry for a unit horizontal electric dipole on the boundary between sea water and one-dimensional anisotropic rock.

The wave numbers of the regions are:

$$k_1=\omega\sqrt{\mu_0\varepsilon_0(\varepsilon_{r1}-i\sigma_{sea}/\omega\varepsilon_0)},$$
$$k_T=\omega\sqrt{\mu_0\varepsilon_0(\varepsilon_{rT}-i\sigma_T/\omega\varepsilon_0)},$$
$$k_L=\omega\sqrt{\mu_0\varepsilon_0(\varepsilon_{rL}-i\sigma_L/\omega\varepsilon_0)}, \tag{18}$$

respectively. With the relations,

$$x=\rho\cos\varphi,\qquad y=\rho\sin\varphi,$$
$$\xi=\lambda\cos\varphi',\qquad \eta=\lambda\sin\varphi'. \tag{19}$$

and the integral representation of the Bessel function of the first kind, viz.,

$$J_n(\lambda\rho)=\frac{i^{-n}}{2\pi}\int_0^{2\pi}e^{i\lambda\rho\cos\theta}e^{in\theta}d\theta. \tag{20}$$

Thus, the final formulas of the six components in cylindrical coordinates (ρ, φ, z) in Region 1 can be expressed as follows:

$$\begin{aligned} E_{1\rho} =& -\frac{\omega\mu_0 Idl}{4\pi k_1^2}\cos\varphi \\ &\times\left\{\int_0^\infty \left\{k_1^2 J_0(\lambda\rho) - \frac{1}{2}\lambda^2\left[J_0(\lambda\rho) - J_2(\lambda\rho)\right]\right\}\right. \\ &\times\gamma_1^{-1} e^{i\gamma_1|z-d|}\lambda d\lambda \\ &+\int_0^\infty \left\{\frac{\gamma_1(k_1^2\gamma_e - k_T^2\gamma_1)}{2(k_1^2\gamma_e + k_T^2\gamma_1)}\left[J_0(\lambda\rho) - J_2(\lambda\rho)\right]\right. \\ &\left.\left.-\frac{k_1^2(\gamma_T - \gamma_1)}{2\gamma_1(\gamma_T + \gamma_1)}\left[J_0(\lambda\rho) + J_2(\lambda\rho)\right]\right\} e^{i\gamma_1(z+d)}\lambda d\lambda\right\} \end{aligned} \quad , \quad (21)$$

$$\begin{aligned} E_{1\varphi} =& \frac{\omega\mu_0 Idl}{4\pi k_1^2}\sin\varphi \\ &\times\left\{\int_0^\infty \left\{k_1^2 J_0(\lambda\rho) - \frac{1}{2}\lambda^2\left[J_0(\lambda\rho) + J_2(\lambda\rho)\right]\right\}\right. \\ &\times\gamma_1^{-1} e^{i\gamma_1|z-d|}\lambda d\lambda \\ &+\int_0^\infty \left\{\frac{\gamma_1(k_1^2\gamma_e - k_T^2\gamma_1)}{2(k_1^2\gamma_e + k_T^2\gamma_1)}\left[J_0(\lambda\rho) + J_2(\lambda\rho)\right]\right. \\ &\left.\left.-\frac{k_1^2(\gamma_T - \gamma_1)}{2\gamma_1(\gamma_T + \gamma_1)}\left[J_0(\lambda\rho) - J_2(\lambda\rho)\right]\right\} e^{i\gamma_1(z+d)}\lambda d\lambda\right\} \end{aligned} \quad , (22)$$

$$\begin{aligned} E_{1z} =& \frac{i\omega\mu_0 Idl}{4\pi k_1^2}\cos\varphi\times\left[\int_0^\infty (\pm e^{i\gamma_1|z-d|} + \frac{k_1^2\gamma_e - k_T^2\gamma_1}{k_1^2\gamma_e + k_T^2\gamma_1} e^{i\gamma_1(z+d)})\right. \\ &\left.\times J_1(\lambda\rho)\lambda^2 d\lambda\right], \end{aligned} \quad ,(23)$$

$$\begin{aligned} B_{1\rho} =& -\frac{\mu_0 Idl}{4\pi}\sin\varphi\left\{\pm\int_0^\infty J_0(\lambda\rho) e^{i\gamma_1|z-d|}\lambda d\lambda\right. \\ &+\int_0^\infty \left\{\frac{(k_1^2\gamma_e - k_T^2\gamma_1)}{2(k_1^2\gamma_e + k_T^2\gamma_1)}\left[J_0(\lambda\rho) + J_2(\lambda\rho)\right]\right. \\ &\left.\left.-\frac{\gamma_T - \gamma_1}{2(\gamma_T + \gamma_1)}\left[J_0(\lambda\rho) - J_2(\lambda\rho)\right]\right\} e^{i\gamma_1(z+d)}\lambda d\lambda\right\} \end{aligned} \quad , \quad (24)$$

$$\begin{aligned} B_{1\varphi} =& -\frac{\mu_0 Idl}{4\pi}\cos\varphi \\ &\times\left\{\pm\int_0^\infty J_0(\lambda\rho) e^{i\gamma_1|z-d|}\lambda d\lambda\right. \\ &+\int_0^\infty \left\{\frac{(k_1^2\gamma_e - k_T^2\gamma_1)}{2(k_1^2\gamma_e + k_T^2\gamma_1)}\left[J_0(\lambda\rho) - J_2(\lambda\rho)\right]\right. \\ &\left.\left.-\frac{\gamma_T - \gamma_1}{2(\gamma_T + \gamma_1)}\left[J_0(\lambda\rho) + J_2(\lambda\rho)\right]\right\} e^{i\gamma_1(z+d)}\lambda d\lambda\right\} \end{aligned} \quad , \quad (25)$$

$$\begin{aligned} B_{1z} =& \frac{i\mu_0 Idl}{4\pi}\sin\varphi \\ &\times\left[\int_0^\infty (\pm e^{i\gamma_1|z-d|} - \frac{\gamma_T - \gamma_1}{\gamma_T + \gamma_1} e^{i\gamma_1(z+d)})\right. \\ &\left.\times\gamma_1^{-1} J_1(\lambda\rho)\lambda^2 d\lambda\right]. \end{aligned} \quad (26)$$

B. Quasi-Static field approximation

In the range of ELF frequencies, the wavelength over a hundred thousand meters and the electric propagation distance subjected to $k_j\rho << 1$ make the problem a matter of ELF near-field propagation, where the integrands from equation (21) to equation (26) have divergent terms in the conventional sense. Since the operating frequency is enough low, the "quasi-static" approach is applied in similar manner addressed in [24] in order to evaluate these integrals in the near zone, with the following approximations:

(i) Considering that $d << \rho$ and $z << \rho$ where the dipole source height d and receiving height z are much less than the radial distance ρ, and $k_j\rho << 1$, where $j = T$, L, it is assumed that:

$$\gamma_j = \sqrt{k_j^2 - \lambda^2} = \lim_{\omega\to 0}\sqrt{(\frac{\varepsilon_{rj}^{1/2}}{c}\omega)^2 - \lambda^2} \approx i\lambda \cdot \quad (27)$$

(ii) The ratio of wave numbers for rock and sea k_j/k_1 is equivalent to an infinitesimal $|k_j^2\gamma_1|/|k_1^2\gamma_j|$.

(iii) High-order terms of the infinitesimals $k_j^2\gamma_1/k_1^2\gamma_j$ are allowed to be neglected for simplification as:

$$\frac{k_1^2\gamma_e - k_T^2\gamma_e}{k_1^2\gamma_e + k_T^2\gamma_e} = \frac{k_1^2\gamma_L - k_L k_T\gamma_1}{k_1^2\gamma_L + k_L k_T\gamma_1} \approx k_1^2 k_L k_T , \quad (28)$$

with,

$$\left|\frac{k_j^2\gamma_1}{k_1^2\gamma_j}\right| \approx \frac{|k_j^2|}{|k_1^2|}\frac{\left|\sqrt{k_1^2 - \lambda^2}\right|}{|i\lambda|} \approx \left|\frac{k_j}{k_1}\right|\left|\sqrt{\left|\frac{k_j}{\lambda}\right|^2 - 1}\right| << 1. \quad (29)$$

It is seen that the integrands of F_1 to F_5 are divergent near the dipole source for what cannot be integrated directly. Consider that,

$$A(\lambda) = \frac{\gamma_T - \gamma_1}{\gamma_T + \gamma_1} = \frac{(\gamma_T - \gamma_1)^2}{(\gamma_T - \gamma_1)(\gamma_T + \gamma_1)} = \frac{(\gamma_T - \gamma_1)^2}{k_T^2 - k_1^2}. \quad (30)$$

In the near-field region,

$$\begin{aligned} |\gamma_T - \gamma_1 - k_1| d_m &\approx \left|\sqrt{k_1^2 - \lambda^2} - i\lambda - k_1\right| d_m \\ &\approx \xi|k_1 d_m| << 1 \end{aligned} \quad , \quad (31)$$

where $\xi \subseteq [-1,1]$. Equation (31) can be approximated with by,

$$i(\gamma_T - \gamma_1 - k_1)d_m \approx 1 - e^{i(\gamma_T - \gamma_1 - k_1)d_m}. \quad (32)$$

In addition, the function of $e^{i(\gamma_T - \gamma_1 - k_1)d_m}$ is approximated by Maclaurin's expansion with first two orders retained, where:

$$\begin{aligned} e^{i(\gamma_T - \gamma_1 - k_1)d_m} &\approx 1 + i(\gamma_T - \gamma_1 - k_1)d_m \\ &-\frac{((\gamma_T - \gamma_1 - k_1)d_m)^2}{2!}, \quad -\infty < x < \infty. \end{aligned} \quad (33)$$

Transpose the merger of similar items, we have:

$$\begin{aligned} (\gamma_T - \gamma_1)^2 =& \frac{2}{d_m^2} - \frac{2e^{i(\gamma_T - \gamma_1 - k_1)d_m}}{d_m^2} + \frac{2i(\gamma_T - \gamma_1 - k_1)d_m}{d_m^2} \\ &-k_1^2 + 2k_1(\gamma_T - \gamma_1). \end{aligned} \quad (34)$$

By invoking (32) and (33), it is derived that:

$$(\gamma_T - \gamma_1)^2 \approx 2ik_1\frac{1 - e^{i(\gamma_T - \gamma_1 - k_1)d_m}}{d_m} + k_1^2. \quad (35)$$

C. Approximated formulas for ELF field in near zone on the planar surface of anisotropic rock

The six components for electromagnetic field in equation (21) to equation (26) are approximated by:

$$E_{1\rho} \approx -\frac{\omega\mu_0 Idl}{4\pi k_1^2}\cos\varphi\Big[k_1^2 I_1(k_1,d_0)-\frac{1}{2}I_2(k_1,d_0) + \frac{k_1^2 k_L k_T}{2}I_9(k_1,d_1)-\frac{k_1^2}{2}F_1(d_1)\Big], \tag{36}$$

$$E_{1\varphi} \approx \frac{\omega\mu_0 Idl}{4\pi k_1^2}\sin\varphi\Big[k_1^2 I_1(k_1,d_0)-\frac{1}{2}I_2(k_1,d_0) + \frac{k_1^2 k_L k_T}{2}I_{10}(k_1,d_1)-\frac{k_1^2}{2}F_2(d_1)\Big], \tag{37}$$

$$E_{1z} \approx \frac{i\omega\mu_0 Idl}{4\pi k_1^2}\cos\varphi\Big[\pm I_4(k_1,d_0) + k_1^2 k_L k_T I_4(k_1,d_1)\Big] \quad \begin{cases} 0\le z\le d \\ z>d \end{cases}, \tag{38}$$

$$B_{1\rho} \approx -\frac{\mu_0 Idl}{4\pi}\sin\varphi\Big[\pm I_5(k_1,d_0)+\frac{k_1^2 k_L k_T}{2}I_6(k_1,d_1) - \frac{1}{2}I_{13}(d_1)\Big] \quad \begin{cases} 0\le z\le d \\ z>d \end{cases}, \tag{39}$$

$$B_{1\varphi} \approx -\frac{\mu_0 Idl}{4\pi}\cos\varphi\Big[\pm I_5(k_1,d_0)+\frac{k_1^2 k_L k_T}{2}I_7(k_1,d_1) - \frac{1}{2}F_4(d_1)\Big] \quad \begin{cases} 0\le z\le d \\ z>d \end{cases}, \tag{40}$$

$$B_{1z} \approx \frac{i\mu_0 Idl}{4\pi}\sin\varphi\big[I_8(k_1,d_0)-F_5(d_1)\big], \tag{41}$$

in which the distances d_0, d_1 and r_0, r_1 are defined by:

$$d_0 = |z-d|, \qquad d_1 = z+d,$$
$$r_0 = \sqrt{d_0^2+\rho^2}, \qquad r_1 = \sqrt{d_1^2+\rho^2}, \tag{42}$$

respectively. It is noted that the integrals I_1 to I_{10} have already been evaluated in [24]. The rest integrals F_1 to F_5 are to be evaluated, which are defined by:

$$F_1(d_1) = \int_0^\infty \{A(\lambda)[J_0(\lambda\rho)+J_2(\lambda\rho)]\}\gamma_1^{-1}e^{i\gamma_1 d_1}\lambda d\lambda, \tag{43}$$

$$F_2(d_1) = \int_0^\infty \{A(\lambda)[J_0(\lambda\rho)-J_2(\lambda\rho)]\}\gamma_1^{-1}e^{i\gamma_1 d_1}\lambda d\lambda, \tag{44}$$

$$F_3(d_1) = \int_0^\infty \{B(\lambda)[J_0(\lambda\rho)-J_2(\lambda\rho)]\}e^{i\gamma_1 d_1}\lambda d\lambda, \tag{45}$$

$$F_4(d_1) = \int_0^\infty \{B(\lambda)[J_0(\lambda\rho)+J_2(\lambda\rho)]\}e^{i\gamma_1 d_1}\lambda d\lambda, \tag{46}$$

$$F_5(d_1) = \int_0^\infty A(\lambda)J_1(\lambda\rho)e^{i\gamma_1 d_1}\gamma_1^{-1}\lambda^2 d\lambda, \tag{47}$$

where,

$$A(\lambda) = \frac{\gamma_T-\gamma_1}{\gamma_T+\gamma_1}, \quad B(\lambda) = \frac{\gamma_T-\gamma_1}{\gamma_T+\gamma_1}e^{i\gamma_1 z}. \tag{48}$$

Equation (48) is correspondingly expressed by

$$A(\lambda) = \frac{\gamma_T-\gamma_1}{\gamma_T+\gamma_1} = \frac{(\gamma_T-\gamma_1)^2}{k_T^2-k_1^2} \approx 2ik_1\frac{1-e^{i(\gamma_T-\gamma_1-k_1)d_m}}{(k_T^2-k_1^2)d_m}+\frac{k_1^2}{k_T^2-k_1^2}, \tag{49}$$

$$B(\lambda) \approx \left(2ik_1\frac{1-e^{i(\gamma_T-\gamma_1-k_1)d_m}}{(k_T^2-k_1^2)d_m}+\frac{k_1^2}{k_T^2-k_1^2}\right)e^{i\gamma_1 z}. \tag{50}$$

With the approximation by equation (49) and equation (50), F_1 to F_5 are simplified by superposition of several terms of I_1 to I_{10} so that the simplified representations for ELF electromagnetic wave near the horizontal electric dipole are readily obtained, where

$$F_1(d_m) \approx \frac{4i+2k_1 d_m}{(k_T^2-k_1^2)d_m\rho^2}\left(e^{ik_1 d_m}-e^{ik_1 r_m}\right) - \frac{4i}{(k_T^2-k_1^2)d_m\rho^2}\left(e^{ik_T d_m}-e^{ik_T r_m}\right), \tag{51}$$

$$F_2(d_m) \approx -\frac{4i+2k_1 d_m}{(k_T^2-k_1^2)d_m}\left[\frac{e^{ik_1 d_m}}{\rho^2}+\left(\frac{ik_1}{r_m}-\frac{1}{\rho^2}\right)e^{ik_1 r_m}\right] - \frac{4ik_1}{(k_T^2-k_1^2)k_T d_m}\left[\frac{e^{ik_T d_m}}{\rho^2}+\left(\frac{ik_T}{r_m}-\frac{1}{\rho^2}\right)e^{ik_T r_m}\right], \tag{52}$$

$$F_3(d_m) \approx -\frac{4ik_1+2k_1^2 d_m}{(k_T^2-k_1^2)d_m}\left[\frac{e^{ik_1 d_m}}{\rho^2}+\frac{d_m}{r_m}\left(\frac{ik_1}{r_m}-\frac{1}{r^2}-\frac{1}{\rho^2}\right)e^{ik_1 r_m}\right] + \frac{4ik_1}{(k_T^2-k_1^2)d_m}\left[\frac{e^{ik_T d_m}}{\rho^2}+\frac{d_m}{r_m}\left(\frac{ik_T}{r_m}-\frac{1}{r^2}-\frac{1}{\rho^2}\right)e^{ik_T r_m}\right], \tag{53}$$

$$F_4(d_m) \approx \frac{4ik_1+2k_1^2 d_m}{(k_T^2-k_1^2)d_m}\left(\frac{e^{ik_1 d_m}}{\rho^2}-\frac{d_m}{r_m}\frac{e^{ik_1 r_m}}{\rho^2}\right) - \frac{4ik_1}{(k_T^2-k_1^2)d_m}\left(\frac{e^{ik_T d_m}}{\rho^2}-\frac{d_m}{r_m}\frac{e^{ik_T r_m}}{\rho^2}\right), \tag{54}$$

$$F_5(d_m) \approx -\frac{(2ik_1+k_1^2 d_m)\rho k_1}{(k_T^2-k_1^2)d_m}\left(\frac{1}{r_m^2}+\frac{i}{k_1 r_m^3}\right)e^{ik_1 r_m} + \frac{2ik_1 k_T\rho}{(k_T^2-k_1^2)d_m}\left(\frac{1}{r_m^2}+\frac{i}{k_T r_m^3}\right)e^{ik_T r_m}, \tag{55}$$

III. COMPUTATIONS AND DISSCUSIONS

Based on equations (36) to (41), the evaluations are carried out by invoking of I_1 to I_{10} in appendix and F_1 to F_5 by equation (51) to equation (55), respectively. To illustrate the approximated formulas, the formulas approximated are computed correspondingly in the following for electromagnetic components of ELF waves.

In Fig. 2, the electric components $E_{2\varphi}$ and $E_{2\rho}$ in dB are computed at specific distance ρ = 10 Km with the variant of observation heights z when the horizontal electric dipole source is located at the surface of anisotropic rock, as illustrated in Fig. 3. With the operating frequency at f = 3 Hz, the parameters of sea water are taken by the relative permittivity ε_{r1} = 80 and the conductivity σ_1 = 4 S/m, and the relative permittivity of anisotropic rock are assumed to be $\varepsilon_{r2T} = \varepsilon_{r2L}$ = 10 and the conductivity (σ_x, σ_y, σ_z) of it are chosen by different directions. In Fig. 2, the blue solid and purple dot-dashed lines represent the one-dimensional anisotropic rock, in which the blue solid lines are for $\sigma_L < \sigma_T$ and the purple dot-dashed lines for the unavailable in physical but theoretical assumption $\sigma_L > \sigma_T$. The red dashed and green solid lines represent isotropic rock, respectively, and the red dashed lines are for the rock with lower conductivity and the green solid lines for the rock with high conductivity.

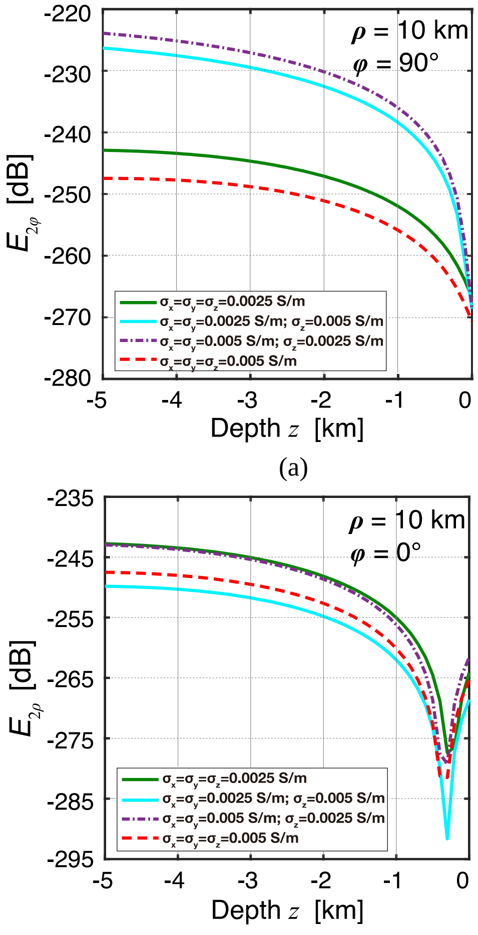

(a)

(b)

Fig. 2. Electric components of ELF field at specific distance in near zone due to a horizontal electric dipole versus the observation height on the surface of medium f = 3 Hz, ε_{r1} = 80, σ_1 = 4 S/m (Region 1 is sea), ε_{r2T} = ε_{r2L} = 10 (Region 2 is rock); d = 0 m, ρ = 10 Km, and φ = 0, π/2, respectively.

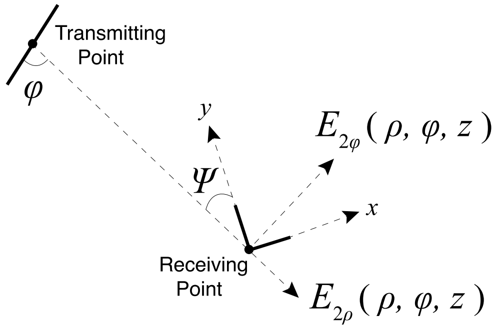

Fig. 3. The geometry and Cartesian coordinate system for a unit horizontal electric dipole excitation.

In Fig. 4, the computational results are compared with same parameters to the available experimental data addressed in [26]. The interesting experiment for detecting the subbed conductivity by the measurements of the ELF electric field on the ocean floor radiated by a horizontal antenna also on the ocean floor has been reported where the radial distance between the transmitting and receiving antennas is ρ = 18.9 Km, and the operating frequency is in the range of 0.25–2.5 Hz. The actually measured components E_X and E_Y can be expressed in the terms of the components $E_{1\rho}$ (ρ, φ, z) and $E_{1\varphi}$ (ρ, φ, z) of the field excited by the transmitter. We write:

$$E_X = E_{1\rho}(\rho,\varphi,z)\sin\psi + E_{1\varphi}(\rho,\varphi,z)\cos\psi\,, \tag{56}$$

$$E_Y = -E_{1\rho}(\rho,\varphi,z)\cos\psi + E_{1\varphi}(\rho,\varphi,z)\sin\psi\,. \tag{57}$$

In computations, we take ψ = 0° and φ = 0°, respectively.

In Fig. 4, the components E_X and E_Y vary as functions of the operating frequency. It is seen that for both the vectors E_X and E_Y only the blue solid lines are well in agreement with the measured data. For E_X, the blue solid and dot-dashed lines are nearly close together and both of them agree well with the measured data.

It is seen that E_X is not sensitive to the interchange of the two anisotropic models with $\sigma_L < \sigma_T$ and $\sigma_L > \sigma_T$. This is resulted by E_X being approximately equal to $E_{2\varphi}$ in the case of $\psi \sim 0$, and meanwhile the magnitudes of the terms including $e^{ik_L\rho}$ are approximately equal to those of the terms including $e^{ik_T\rho}$ at small radial distance (ρ = 10 km).

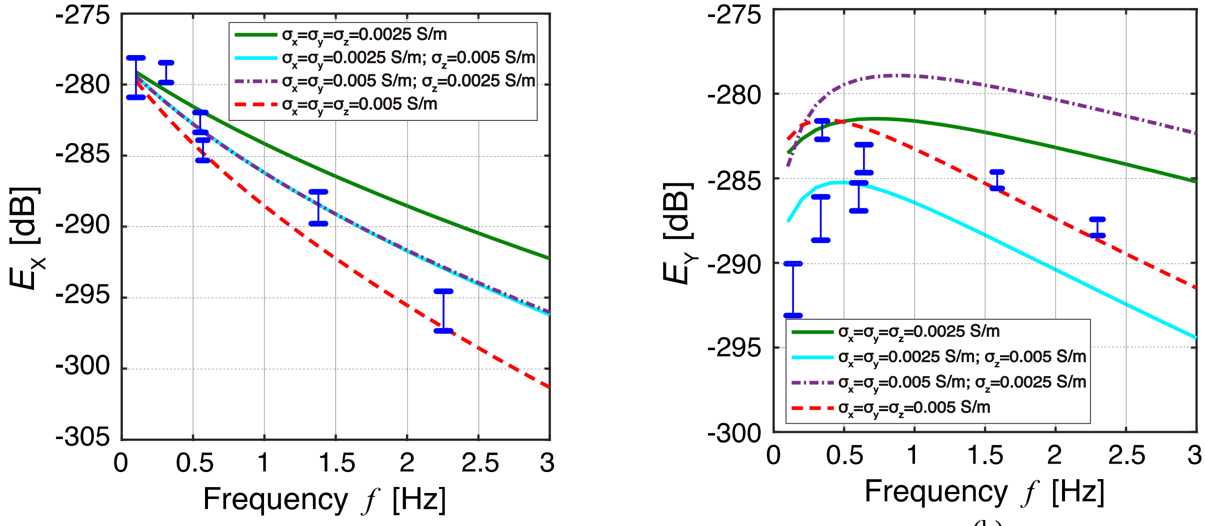

(a) (b)

Fig. 4. The comparison of the computational results by the proposed approximated formulas and ocean floor measurements by Young and Cox in 1981 [26].

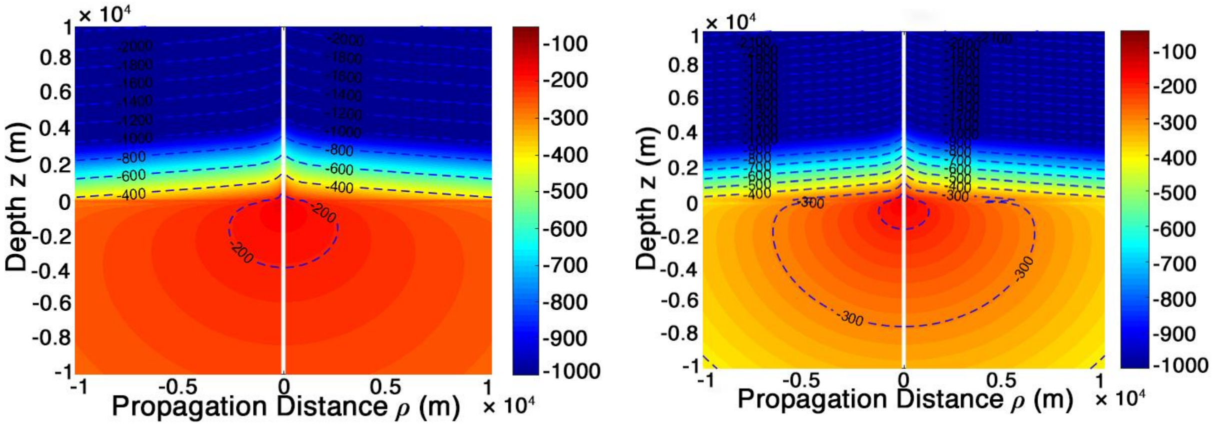

(a) with d = 0 m, σ_T = 0.0025 S/m, σ_L= 0.025 S/m (b) with d = 0 m, σ_T = 0.025 S/m, σ_L= 0.0025 S/m

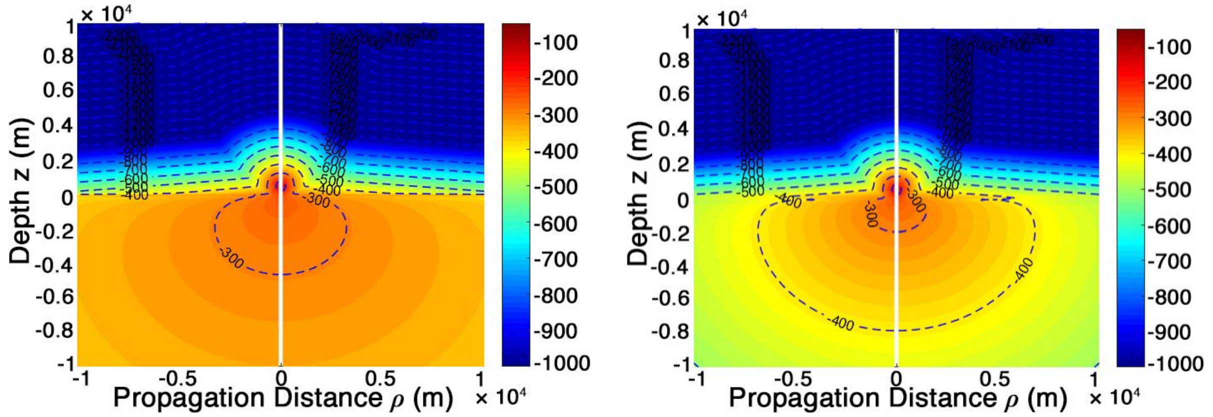

(c) with d = 500 m, σ_T= 0.0025 S/m, σ_L= 0.025 S/m (d) with d = 500 m, σ_T = 0.025 S/m, σ_L= 0.0025 S/m

Fig. 5. Projection of electric field component $|E_{2\rho}(\rho, \varphi, z)|$ with spatial distributions in $\hat{x}$ - $\hat{z}$ plane due to a horizontal electric dipole excitation in the presence of half-space regions, at f = 3 Hz, ε_{r1} = 80, σ_1 = 4 S/m (Region 1 is sea), ε_{r2T} = ε_{r2L} = 10 (Region 2 is rock); ρ = 10 Km, and φ = 0, d = 0 m, 500m, respectively.

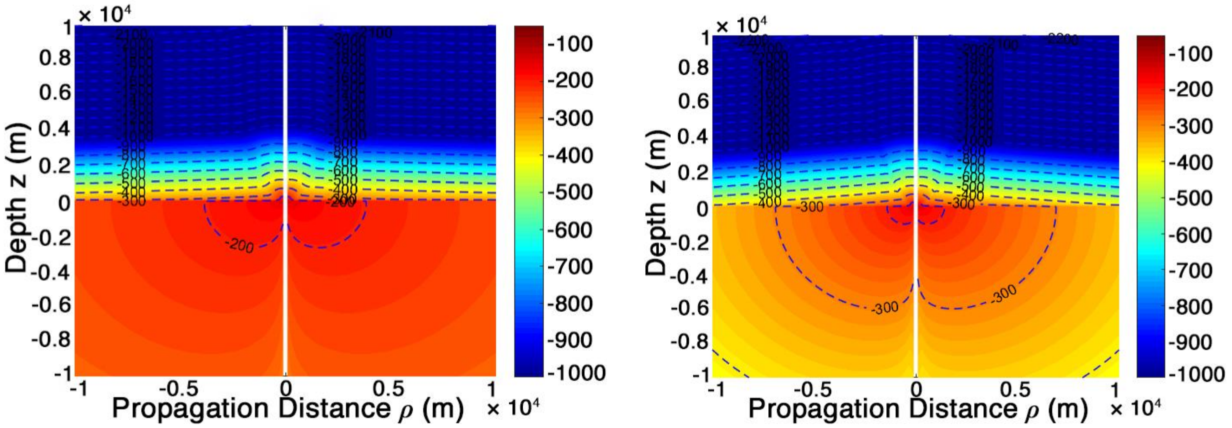

(a) with d = 0 m, σ_T = 0.0025 S/m, σ_L = 0.025 S/m (b) with d = 0 m, σ_T = 0.025 S/m, σ_L = 0.0025 S/m

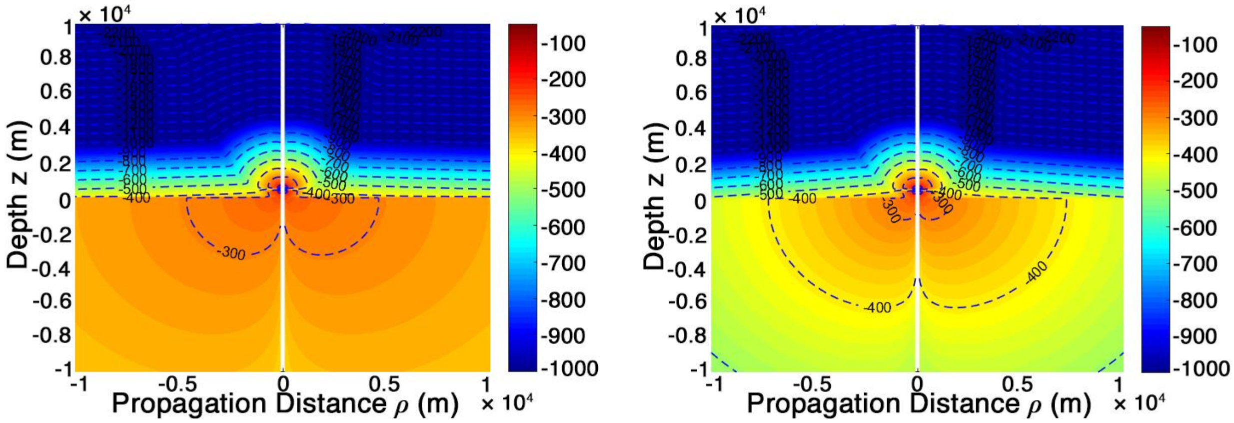

(c) with d = 500 m, σ_T = 0.0025 S/m, σ_L = 0.025 S/m (d) with d = 500 m, σ_T = 0.025 S/m, σ_L = 0.0025 S/m

Fig. 6. Projection of electric field component $|E_{2z}(\rho, \varphi, z)|$ with spatial distributions due to a horizontal electric dipole excitation in the presence of half-space regions, at f = 3 Hz, ε_{r1} = 80, σ_1 = 4 S/m (Region 1 is sea), $\varepsilon_{r2T} = \varepsilon_{r2L}$ = 10 (Region 2 is rock); ρ = 10 Km, φ = 0, and d = 0 m, 500m, respectively.

Following the above computations and analyses, it may be reasonably concluded that the measured data are well represented as the one-dimensional anisotropic model and the reasonable values are with $\sigma_L \sim$ 0.002 to 0.0025 S/m and $\sigma_T \sim$ 0.004 to 0.005 S/m.

For illustration, the observation point is chosen arbitrarily on the $\hat{x}-\hat{z}$ plane, the distributions of the six components' strength for ELF wave due to horizontal electric dipole excitation in the presence of two half-spaces are depicted in Fig. 5 and Fig. 6, where a horizontal antenna of electric dipole is buried inside in the sea water at the height of d = 0 m and d = 500 m, respectively. With the operating frequency f = 3 Hz, the conductivity and the relative dielectric constant of sea water being σ_1 = 4 S/m, ε_{r1} = 80, respectively, and the relative dielectric constant of rock being approximately $\varepsilon_{r2T} = \varepsilon_{r2L}$ = 10 and the conductivity of it (σ_x, σ_y, σ_z) are chosen by different directions, the electromagnetic components vary as a function of propagating distance ρ and the height z of source. It is seen that the electromagnetic field decays dramatically due to high loss in sea water in Region 1, while it penetrates the rock floor in Region 2.

IV. CONCLUSIONS

In summary, the approximated formulas for ELF electromagnetic field have been derived in order to evaluate the ELF near field. The computational scheme exploits the concept that ELF near-field propagation can be simplified by the quasi-static approximation with $\gamma_2 \approx i\lambda$. Accordingly, the integrands of Fourier-Bessel representations for ELF field on the surface of the anisotropic rock are approximated by adopting Maclaurin's Expansion near the poles. The approximated solution is in good agreement with the available experimental data.

APPENDIX

The integrals of I_1 to I_{10} are addressed in [22], they are rewritten as follows:

$$I_1(k_n,d_m)=\int_0^\infty \frac{e^{ir_nd_m}}{r_n}J_0(\lambda\rho)\lambda d\lambda=-\frac{ie^{ik_nr_m}}{r_m}, \tag{I1}$$

$$\begin{aligned}I_2(k_n,d_m)&=\int_0^\infty \frac{e^{ir_nd_m}}{r_n}\left[J_0(\lambda\rho)-J_2(\lambda\rho)\right]\lambda^3 d\lambda\\&=-2k_n\left[\frac{ik_n}{r_m}-\frac{2}{r_m^2}-\frac{2i}{k_nr_m^3}\right.\\&\qquad\left.-\frac{d_m^2}{r_m^2}\left(\frac{ik_n}{r_m}-\frac{2}{r_m^2}-\frac{2i}{k_nr_m^3}\right)\right]e^{ik_nr_m}\end{aligned}, \tag{I2}$$

$$\begin{aligned}I_3(k_n,d_m)&=\int_0^\infty \frac{e^{ir_nd_m}}{r_n}\left[J_0(\lambda\rho)+J_2(\lambda\rho)\right]\lambda^3 d\lambda\\&=-2k_n\left(\frac{1}{r_m^2}+\frac{i}{k_nr_m^3}\right)e^{ik_nr_m}\end{aligned}, \tag{I3}$$

$$\begin{aligned}I_4(k_n,d_m)&=\int_0^\infty e^{ir_nd_m}J_1(\lambda\rho)\lambda^2 d\lambda\\&=-\rho k_n\frac{d_m}{r_m}\left(\frac{k_n}{r_m^2}+\frac{3i}{r_m^3}-\frac{3}{k_nr_m^4}\right)e^{ik_nr_m}\end{aligned}, \tag{I4}$$

$$\begin{aligned}I_5(k_n,d_m)&=\int_0^\infty e^{ir_nd_m}J_0(\lambda\rho)\lambda d\lambda\\&=-\frac{d_m}{r_m}\left(\frac{ik_n}{r_m}-\frac{1}{r_m^2}\right)e^{ik_nr_m}\end{aligned}, \tag{I5}$$

$$\begin{aligned}I_6(k_n,d_m)&=\int_0^\infty e^{ir_nd_m}\left[J_0(\lambda\rho)+J_2(\lambda\rho)\right]\lambda d\lambda\\&=2\left(\frac{e^{ik_nd_m}}{\rho^2}-\frac{d_m}{r_m}\frac{e^{ik_nr_m}}{\rho^2}\right)\end{aligned}, \tag{I6}$$

$$\begin{aligned}I_7(k_n,d_m)&=\int_0^\infty e^{ir_nd_m}\left[J_0(\lambda\rho)+J_2(\lambda\rho)\right]\lambda d\lambda\\&=-2\left[\frac{e^{ik_nd_m}}{\rho^2}+\frac{d_m}{r_m}\left(\frac{ik_n}{r_m}-\frac{1}{r_m^2}-\frac{1}{\rho^2}\right)e^{ik_nr_m}\right]\end{aligned}, \tag{I7}$$

$$\begin{aligned}I_8(k_n,d_m)&=\int_0^\infty \frac{e^{ir_nd_m}}{r_n}J_1(\lambda\rho)\lambda^2 d\lambda\\&=-\rho k_n\left(\frac{1}{r_m^2}+\frac{i}{k_nr_m^3}\right)e^{ik_nr_m}\end{aligned}, \tag{I8}$$

$$\begin{aligned}I_9(k_n,d_m)&=\int_0^\infty r_ne^{ir_nd_m}\left[J_0(\lambda\rho)-J_2(\lambda\rho)\right]\lambda d\lambda\\&=-2k_n\left\{\frac{e^{ik_nd_m}}{\rho^2}+\left[\frac{1}{r_m^2}+\frac{i}{k_nr_m^3}\right.\right.\\&\qquad\left.\left.+\frac{d_m^2}{r_m^2}\left(\frac{ik_n}{r_m}-\frac{3}{r_m^2}-\frac{3i}{k_nr_m^3}-\frac{1}{\rho^2}\right)\right]e^{ik_nr_m}\right\}\end{aligned}, \tag{I9}$$

$$\begin{aligned}I_{10}(k_n,d_m)&=\int_0^\infty r_ne^{ir_nd_m}\left[J_0(\lambda\rho)+J_2(\lambda\rho)\right]\lambda d\lambda\\&=2k_n\left[\frac{e^{ik_nd_m}}{\rho^2}+\frac{ie^{ik_nr_m}}{k_nr_m^3}\left(1+\frac{ik_nr_md_m^2}{\rho^2}\right)\right]\end{aligned}, \tag{I10}$$

where m = 0, 1 and n = 0, 1.

ACKNOWLEDGMENT

This work was supported by the [National Natural Science Foundation of China] under Grant [number 61271086, 61571389].

REFERENCES

[1] A. N. Sommerfeld, "Propagation of waves in wireless telegraphy," *Ann. Phys.*, vol. 28, pp. 665-736, Mar. 1909.

[2] S. F. Mahmoud, "Remarks on 'The electromagnetic field of a vertical electric dipole over the earth and sea'," *IEEE Trans. Antennas Propagat.*, vol. 46, no. 12, pp. 1745-1946, Apr. 1999.

[3] W. Y. Pan, "Surface wave propagation along the boundary between sea water and one dimensionally anisotropic rock," *J. Appl. Phys.*, vol. 58, pp. 3963-3974, 1985.

[4] T. T. Wu and R. W. P. King, "Lateral electromagnetic pulses generated by a vertical dipole on the boundary between two dielectrics," *J. Appl. Phys.*, vol. 62, no. 11, pp. 4345-4355, June 1998.

[5] R. W. P. King, M. Owens, and T. T. Wu, *Lateral Electromagnetic Waves: Theory and Applications to Communications, Geophysical Exploration, and Remote Sensing*. Springer, New York, 1992.

[6] D. Margetis and T. T. Wu, "Exactly calculable field components of electric dipoles in planar boundary," *Journal of Mathematical Physics*, vol. 42, no. 2, pp. 713-745, Jan. 2001.

[7] D. Margetis, "Radiation of horizontal electric dipole on large dielectric sphere," *Journal of Mathematical Physics*, vol. 43, no. 6, pp. 3162-3201, May 2002.

[8] H. Q. Zhang, W. Y. Pan, K. Li, and K. X. Shen, "Electromagnetic field for a horizontal electric dipole buried inside a dielectric layer coated high lossy half space," *Progress in Electromagnetics Research, PIER*, vol. 50, pp. 163-186, 2005.

[9] K. Li and Y. Lu, "Electromagnetic field generated by a horizontal electric dipole near the surface of a planar perfect conductor coated with a layer," *IEEE Trans. Antennas Propagt.*, vol. 53, no. 10, pp. 3191-3200, 2005.

[10] J. P. Mei and K. Li, "Electromagnetic field from a horizontal electric dipole on the surface of a high lossy dielectric coated with a layer," *Progress in Electromagnetics Research, PIER*, vol. 73, pp. 71-91, 2007.

[11] J. L. Tang and W. Hong, "The electromagnetic field produced by a horizontal electric dipole over a dielectric coated perfect conductor," *Progress in Electromagnetics Research, PIER*, vol. 36, pp. 139-152, 2002.

[12] M. Fechner, N. A. Spaldin, and I. E. Dzyaloshinskii, "Magnetic field generated by a charge in a magnetoelectric material," *Phys. Rev. B*, vol. 89, no. 18, pp. 1719-1743, 2014.

[13] Y. L. Geng, C. W. Qiu, and N. Yuan, "Exact

solution to electromagnetic scattering by an impedance sphere coated with a anisotropic layer," *IEEE Trans. on Antennas Propagat.*, vol. 57, no. 2, pp. 572-576, 2009.

[14] M. Parise, "Second-Order formulation for the quasi-static field from a vertical electric dipole on a lossy half-space," *Progress in Electromagnetics Research*, vol. 140, no. 4, pp. 439-455, June 2013.

[15] M. Parise, "An exact series representation for the EM field from a vertical electric dipole on an imperfectly conducting half-space," *Journal of Electromagnetic Waves and Applications*, vol. 28, no. 8, pp. 932-942, Mar. 2014.

[16] J. J. Simpson and A. Taflove, "ELF radar system proposed for localized D-region ionospheric anomalies," *IEEE Geoscience and Remote Sensing Letters*, vol. 3, no. 4, pp. 500-503, Oct. 2006.

[17] J. J. Simpson, "Current and future applications of 3-D global earth-ionosphere models based on the full-vector Maxwell's equations FDTD method," *Surv. Geophys*, vol. 30, no. 2, pp. 105-130, Mar. 2009.

[18] J. J. Simpson and A. Taflove, "A novel ELF radar for major oil deposits," *IEEE Geoscience and Remote Sensing Letters*, vol. 3, no. 1, pp. 36-39, Jan. 2006.

[19] Y. Wang, H. Xia, and Q. Cao, "Analysis of ELF propagation along the earth surface using the FDTD model based on the spherical triangle meshing," *IEEE Antennas Wireless Propagat. Lett.*, vol. 8, no. 4, pp. 1017-1020, Sept. 2009.

[20] Y. Wang, H. Xia, and Q. Cao, "Analysis of ELF attenuation rate using the geodesic FDTD algorithm," *International Conference on Microwave and Millimeter Wave Technology, IEEE*, pp. 1413-1415, July 2010.

[21] Y. Wang, Q. Cao, and B. Su, "A quasi three-dimensional subgrid technique for the geodesic FDTD algorithm," *International Symposium on Antennas, Propagation & EM Theory, IEEE*, pp. 936-938, Jan. 2013.

[22] W. Y. Pan and K. Li, "ELF wave propagation along sea-rock boundary and mCSEM method," in *Propagation of SLF/ELF Electromagnetic Waves*, 1st ed. Hangzhou, CN: Zhejiang University Press; Berlin Heidelberg, GER: Springer-Verlag, ch. 6, pp. 161-219, 2014.

[23] E. I. Parkhomenko, *Electrical Properties of Rocks*. Plenum, New York, 1967.

[24] H. L. Xu, T. T. Gu, and K. Li, "Approximated solutions for ELF near-field propagation due to a horizontal electric dipole excitation near the sea-rock boundary," *IEEE Trans. on Antennas Propagat.*, vol. 66, no. 5, pp. 2471-2481, May 2018.

[25] J. R. Wait, *Electromagnetic Waves in Stratified Media*. 2nd ed., New York: Pergamon Press, 1970.

[26] P. D. Young and C. S. Cox, "Electromagnetic active source sounding near the East Pacific Rise," *Geophys. Res. Lett.*, vol. 8, no. 10, pp. 1043-1046, Oct. 1981.

Ting Ting Gu was born in Leshan, Sichuan, China, on June 18, 1988. She received the B.S. degree and M.S. degree in Electromagnetic Field and Microwave Technology from Zhejiang University of Media and Communications, and Hangzhou Dianzi University, Hangzhou, China, in 2010 and 2013, respectively.

She is currently working toward the Ph.D. degree in Electromagnetic Field and Microwave Technology with the College of Information Science and Electronic Engineering, Zhejiang University, Hangzhou, China. Her current research interests include radio wave propagation theory and its applications.

Hong Lei Xu was born in Jiangyin, Jiangsu, China, on June 7, 1990. She received the B.S. degree in Communication Engineering from Nanjing University of Posts and Telecommunications, Nanjing, China, in 2012, and the M.S. degree in Jiangsu University, Zhenjiang, China, in 2015, respectively.

She is currently working toward the Ph.D. degree in Electromagnetic Field and Microwave Technology with the College of Information Science and Electronic Engineering, Zhejiang University, Hangzhou, China. Her current research interests include radio wave propagation theory and its applications.

Kai Li was born in Xiao County, Anhui, China, on February 10, 1968. He received the B.S. degree in Physics from Fuyang Normal University, Anhui, China, in 1990, the M.S. degree in Radio Physics from Xidian University, Xi'an, Shaanxi, China, in 1994, and the Ph.D. degree in Astrophysics from Shaanxi Astronomical Observatory, the Chinese Academy of Sciences, Shaanxi, China, in 1998, respectively.

From August 1990 to December 2000, he was on the Faculty of China Research Institute Radiowave Propagation (CRIRP). From January 2001 to December 2002, he was a Postdoctoral Fellow at Information and

Communications University (ICU), Daejeon, Republic of Korea. From January 2003 to January 2005, he was a Research Fellow with the School of Electrical and Electric Engineering, Nanyang Technological University (NTU), Singapore. Since January 2005, he has been a Professor with the Department of Information Science and Electronic Engineering, Zhejiang University, Hangzhou, China. His current research interests include classic electromagnetic theory and radio wave propagation.

Li is a Senior Member of the Chinese Institute of Electronics (CIE) and a Member of the Chinese Institute of Space Science (CISS).

Attenuation in Lossy Circular Waveguides

Kim Ho Yeap [1], Eric Vun Shiung Wong [1], Humaira Nisar [1], Kazuhiro Hirasawa [2], and Takefumi Hiraguri [3]

[1] Faculty of Engineering and Green Technology
Universiti Tunku Abdul Rahman, Jln. Universiti, Bandar Barat, 31900 Kampar, Perak, Malaysia
yeapkh@utar.edu.my, ewvs1991@1utar.my, humaira@utar.edu.my

[2] University of Tsukuba, Tsukuba, Ibaraki, Japan
hirasawa@ieee.org

[3] Nippon Institute of Technology, Miyashiro-Machi, Saitama-Ken, Japan
hira@nit.ac.jp

Abstract **─** We present a simple closed-form approach to calculate the attenuation of waves in lossy circular waveguides. A set of characteristic equations is first derived by matching the tangential fields at the wall boundary with the constitutive properties of the conducting wall material. In order to represent fields' penetration into the lossy wall, a perturbation term is then introduced into the equation. We apply the Finite Difference Method to derive the closed-form expression of the perturbation terms for TE and TM modes. The propagation constant can be found by incorporating the perturbation term into the dispersion relation. Our results show good agreement with those obtained from the rigorous transcendental equations. However, unlike the transcendental approach which is usually laborious in solving, our closed-form approach leads to simpler analysis and, therefore, allows the attenuation to be easily computed.

Index Terms **─** Attenuation constant, circular waveguide, propagation constant, tangential fields, TE modes and TM modes.

I. INTRODUCTION

Analysis of loss in a circular waveguide has been widely performed using the rigorous transcendental formulation developed by Stratton [1]. Literature which implements Stratton's approach in their analysis includes those in hollow waveguides, dielectric rods, multilayered coated waveguides, as well as, lossy and superconducting waveguides [2-8]. In reality, the tangential fields in a waveguide are continuous across the boundary of the wall. In Stratton's approach, the tangential fields which describe the propagation in the waveguide are matched at the boundary with those penetrated into the lossy conducting wall. A transcendental equation is then derived by finding the determinant of the coefficients. Although the loss computed using Stratton's approach shows high accuracy, the roots of the solution can only be achieved via a root-finding algorithm. This means that an effective compiler tool, an efficient algorithm and appropriate initial guesses are necessary in order to allow the solution to converge. Hence, the process of solving numerically for the roots of a transcendental equation is usually laborious.

Unlike the transcendental equations, closed-form equations lead to much simpler analysis. The results of the closed-form solutions can easily be obtained in a straight-forward manner and they give more intuitive insights into the inherent behavior of the variable to be solved [9, 10]. However, due to the assumptions made while simplifying the equations to their closed-form expressions, the simplicity found in these equations usually comes at the expense of accuracy. Take for example, the closed-form power-loss method adopted by most textbooks to illustrate the loss in waveguides [11-13]. This method is only valid for certain modes and at a certain range of frequencies f above its cutoff f_c [14, 15]. When deriving for its mathematical expressions, the power-loss method assumes wave propagation in a lossless waveguide. Since a lossless waveguide behaves like an ideal high pass filter, it gives infinite attenuation at f below f_c. Also, the modes in a lossless waveguide are orthogonal to each other, i.e., each mode can exist separately in the waveguide. In reality, however, the modes in a practical waveguide may co-exist at the same time. Hence, the power-loss method fails to account for the loss arises from the concurrent existence of multiple modes in the waveguide. Clearly, the power-loss method may only be good enough for finding the initial approximation of loss in a waveguide. It may not, however, be appropriate when loss in the waveguide is a

Submitted On: August 31, 2018
Accepted On: November 25, 2018

critical factor and accurate prediction of it is necessary.

In [10], we have developed a novel closed-form approach to calculate the loss in both rectangular and circular waveguides with finite conducting wall. The loss in the waveguides is found by solving for the root of a quadratic equation, derived by matching the tangential fields at the boundary with the electrical properties of the wall material. Although the results were found to be accurate and that they agree very well with those obtained from the rigorous approaches (such as Stratton's formulation), the mathematical expressions are long and cumbersome. Here, we extend further the closed-form solution in [10] for the case of a circular waveguide. We will demonstrate that by removing the redundant higher-order variables in the equations, a much simpler set of equations, which give equally accurate results, can be derived.

II. FORMULATION

Figure 1 shows the geometry of a circular waveguide. At the boundary of the wall, the constitutive properties can be related to the tangential electric fields E_t and tangential magnetic fields H_t as [14, 15]:

$$\frac{E_t}{H_t} = \sqrt{\frac{\mu_w}{\varepsilon_w}}, \tag{1}$$

where μ_w and ε_w are the permeability and the permittivity of the conducting wall material, respectively. The permittivity ε_w is complex and is given by [12]:

$$\varepsilon_w = \varepsilon - j\frac{\sigma_w}{\omega}, \tag{2}$$

where ω is the angular frequency, σ_w the conductivity of the waveguide wall, and ε is the permittivity of free space. The equations obtained from (1) admit non-trivial solutions only when the determinant vanishes. This yields the following characteristic equation for a circular waveguide [14]:

$$\begin{gathered}\left[jk_r^{\,2}\sqrt{\frac{\mu_w}{\varepsilon_w}} + \omega\mu_d k_r \frac{J_n'(u)}{J_n(u)}\right]\times \\ \left[jk_r^{\,2}\sqrt{\frac{\varepsilon_w}{\mu_w}} + \omega\varepsilon_d k_r \frac{J_n'(u)}{J_n(u)}\right] = \left[\frac{nk_z}{a_r}\right]^2\end{gathered}, \tag{3}$$

where $k_r = \sqrt{k_d^{\,2} - k_z^{\,2}}$ is the dispersion relation of the circular waveguide, k_z the propagation constant, $J_n(u)$ denotes the Bessel function of the first kind, $J_n'(u)$ its derivative, n the order of the Bessel function, k_d, μ_d and ε_d are respectively the wavenumber, permeability and permittivity of the dielectric core material and a_r is the radius of the circular waveguide. The argument of the Bessel function u is given as:

$$u = \sqrt{a_r^{\,2}\left(k_d^{\,2} - k_z^{\,2}\right)}, \tag{4}$$

Since TE and TM modes in a lossless circular waveguide are determined by the roots of $J_n'(u_{nm}) = 0$ and $J_n(u_{nm}) = 0$, respectively [10], (3) can be expanded into the form of a quadratic equation, with $\frac{J_n'(u)}{J_n(u)}$ or $\frac{J_n(u)}{J_n'(u)}$ as the variables to be solved for. Here, the n and m subscripts denote the n-th order and m-th zero of $J_n(u)$, respectively. By convention, the n subscript always represents the number of half-wave field variations in the ϕ-direction; whereas, the m subscript denotes the number of half-wave field variations in the r-direction [12]. Hence, different combinations of n and m variables produce different TE and TM modes in the waveguide. By expanding (3) and substituting (4) for the lossless case (i.e., $u = u_{nm}$) into k_z (i.e., $k_z = \sqrt{k_d^{\,2} - \left(\frac{u_{nm}}{a_r}\right)^2}$) and k_r (i.e., $k_r = \frac{u_{nm}}{a_r}$), the quadratic equations for TE and TM modes can be expressed respectively as (5a) and (5b) below:

$$\begin{gathered}k_d^{\,2}\left(\frac{u_{nm}}{a_r}\right)^2\left[\frac{J_n'(u)}{J_n(u)}\right]^2 + j\omega\left(\frac{u_{nm}}{a_r}\right)^3\left(\frac{\mu_d}{Z_s} + \varepsilon_d Z_s\right)\left[\frac{J_n'(u)}{J_n(u)}\right] \\ -\left[\left(\frac{u_{nm}}{a_r}\right)^4 + \left(\frac{n}{a_r}\right)^2\left(k_d^{\,2} - \frac{u_{nm}^{\,2}}{a_r^{\,2}}\right)\right] = 0\end{gathered}, \tag{5a}$$

$$\begin{gathered}\left[\left(\frac{u_{nm}}{a_r}\right)^4 + \left(\frac{n}{a_r}\right)^2\left(k_d^{\,2} - \frac{u_{nm}^{\,2}}{a_r^{\,2}}\right)\right]\left[\frac{J_n(u)}{J_n'(u)}\right]^2 - \\ j\omega\left(\frac{u_{nm}}{a_r}\right)^3\left(\frac{\mu_d}{Z_s} + \varepsilon_d Z_s\right)\left[\frac{J_n(u)}{J_n'(u)}\right] - k_d^{\,2}\left(\frac{u_{nm}}{a_r}\right)^2 = 0\end{gathered}, \tag{5b}$$

where $Z_s = \sqrt{\frac{\mu_w}{\varepsilon_w}}$ is the surface impedance.

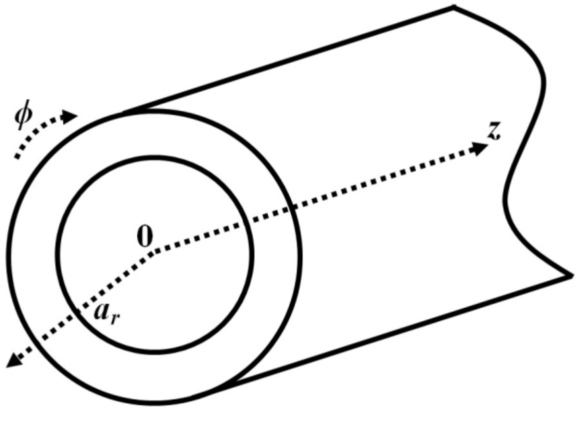

Fig. 1. A circular waveguide.

For a lossy but highly conducting waveguide, $J_n'(u)$ for TE modes and $J_n(u)$ for TM modes are close to zero. Hence, the second order of these functions can be ignored. The solutions to the quadratic equations in (5) can then be found as:

$$\frac{J_n'(u)}{J_n(u)} = \frac{\left(\frac{u_{nm}}{a_r}\right)^4 + \left(\frac{n}{a_r}\right)^2\left[k_d^{\,2} - \left(\frac{u_{nm}}{a_r}\right)^2\right]}{j\omega\left(\frac{u_{nm}}{a_r}\right)^3\left(\frac{\mu_d}{Z_s} + \varepsilon_d Z_s\right)}, \tag{6a}$$

and,

$$\frac{J_n(u)}{J_n'(u)} = \frac{jk_d^{\,2}\left(\frac{u_{nm}}{a_r}\right)^2}{\omega\left(\frac{u_{nm}}{a_r}\right)^3\left(\frac{\mu_d}{Z_s} + \varepsilon_d Z_s\right)}, \tag{6b}$$

for TE and TM modes, respectively.

The argument of the Bessel function of a lossy waveguide u is assumed to be perturbed from that of the lossless case u_{nm}, i.e.,

$$u = u_{nm} + \delta_u, \tag{7}$$

where δ_u is a perturbation term. Substituting (7) into $J_n'(u)$ for TE modes and $J_n(u)$ for TM modes, (6) can then be expressed as:

$$J_n'(u_{nm} + \delta_u) = \frac{\left\{\left(\frac{u_{nm}}{a_r}\right)^4 + \left(\frac{n}{a_r}\right)^2\left[k_d^{\,2} - \left(\frac{u_{nm}}{a_r}\right)^2\right]\right\}J_n(u)}{j\omega\left(\frac{u_{nm}}{a_r}\right)^3\left(\frac{\mu_d}{Z_s} + \varepsilon_d Z_s\right)}, \tag{8a}$$

and,

$$J_n(u_{nm} + \delta_u) = \frac{jk_d^{\,2}\left(\frac{u_{nm}}{a_r}\right)^2 J_n'(u)}{\omega\left(\frac{u_{nm}}{a_r}\right)^3\left(\frac{\mu_d}{Z_s} + \varepsilon_d Z_s\right)}. \tag{8b}$$

Using the Finite Difference Method (FDM), the first and second derivatives of the Bessel function for a lossless waveguide with argument u_{nm} can be approximated as follows:

$$J_n(u_{nm} + \delta_u) = J_n'(u_{nm})\delta_u + J_n(u_{nm}), \tag{9a}$$

and,

$$J_n'(u_{nm} + \delta_u) = J_n''(u_{nm})\delta_u + J_n'(u_{nm}). \tag{9b}$$

Substituting (9b) into (8a) and (9a) into (8b) and solving for δ_u, we obtain:

$$\delta_{uTE} = \frac{\left\{\left(\frac{u_{nm}}{a_r}\right)^4 + \left(\frac{n}{a_r}\right)^2\left[k_d^{\,2} - \left(\frac{u_{nm}}{a_r}\right)^2\right]\right\}J_n(u)}{j\omega\left(\frac{u_{nm}}{a_r}\right)^3\left(\frac{\mu_d}{Z_s} + \varepsilon_d Z_s\right)J_n''(u_{nm})}, \tag{10a}$$
$$- \frac{J_n'(u_{nm})}{J_n''(u_{nm})}$$

and,

$$\delta_{uTM} = \frac{jk_d^{\,2}\left(\frac{u_{nm}}{a_r}\right)^2 J_n'(u)}{\omega\left(\frac{u_{nm}}{a_r}\right)^3\left(\frac{\mu_d}{Z_s} + \varepsilon_d Z_s\right)J_n'(u_{nm})}, \tag{10b}$$
$$- \frac{J_n(u_{nm})}{J_n'(u_{nm})}$$

where δ_{uTE} and δ_{uTM} denote respectively the perturbation term δ_u for TE and TM modes. Since $J_n'(u_{nm}) = 0$ for TE modes, $J_n(u_{nm}) = 0$ for TM modes, and $J_n''(x) = \left[\left(\frac{n}{x}\right)^2 - 1\right]J_n(x)$ [16], by approximating $J_n(u) \approx J_n(u_{nm})$ and $J_n'(u) \approx J_n'(u_{nm})$, the perturbation terms in (10) can then be written as:

$$\delta_{uTE} = \frac{\left(\frac{u_{nm}}{a_r}\right)^4 + \left(\frac{n}{a_r}\right)^2\left[k_d^{\,2} - \left(\frac{u_{nm}}{a_r}\right)^2\right]}{j\omega\left(\frac{u_{nm}}{a_r}\right)^3\left(\frac{\mu_d}{Z_s} + \varepsilon_d Z_s\right)\left[\left(\frac{n}{u_{nm}}\right)^2 - 1\right]}, \tag{11a}$$

and,

$$\delta_{uTM} = \frac{jk_d^{\,2}\left(\frac{u_{nm}}{a_r}\right)^2}{\omega\left(\frac{u_{nm}}{a_r}\right)^3\left(\frac{\mu_d}{Z_s} + \varepsilon_d Z_s\right)}. \tag{11b}$$

The propagation constant of the lossy waveguide k_z can be computed by substituting the perturbation terms in (11) and k_z in (4) into (7), i.e.,

$$k_z = \sqrt{k_d^{\,2} - \left(\frac{u_{nm} + \delta_u}{a_r}\right)}. \tag{12}$$

The propagation constant k_z is a complex variable which consists of the phase constant β_z and attenuation constant α_z, as shown in (13) below:

$$k_z = \beta_z - j\alpha_z. \tag{13}$$

Hence, by extracting the imaginary part of the propagation constant k_z, the attenuation in the waveguide can be obtained. For the convenience of casual readers, we outline the final expressions of the attenuation constant for TE modes α_{zTE} and TM modes α_{zTM} here. It is worthwhile noting that u_{nm} for TE and TM modes can be found respectively in Tables 9.1 and 9.2 of [17]:

$$\alpha_{zTE} = \mathrm{Im}\left|\sqrt{k_d^{\,2} - \frac{1}{a_r^{\,2}}\left\{u_{nm} - \frac{j\left[\left(\frac{u_{nm}}{a_r}\right)^4 + \left(\frac{n}{a_r}\right)^2\left(k_d^{\,2} - \frac{u_{nm}^{\,2}}{a_r^{\,2}}\right)\right]}{\omega\left(\frac{u_{nm}}{a_r}\right)^3\left(\frac{\mu_d}{Z_s} + \varepsilon_d Z_s\right)\left[\left(\frac{n}{u_{nm}}\right)^2 - 1\right]}\right\}^2}\right|, \tag{14a}$$

and,

$$\alpha_{zTM} = \operatorname{Im}\left| \sqrt{ {k_d}^2 - \frac{1}{{a_r}^2}\left\{ u_{nm} + \frac{j{k_d}^2\left(\frac{u_{nm}}{a_r}\right)^2}{\omega\left(\frac{u_{nm}}{a_r}\right)^3\left(\frac{\mu_d}{Z_s}+\varepsilon_d Z_s\right)} \right\}^2 } \right| .\tag{14b}$$

III. RESULTS AND DISCUSSION

To verify our formulations, we compute and analyze the loss in a hollow circular waveguide with copper wall. The radius of the waveguide is a_r = 8.1 mm. The attenuation constants of the dominant TE11 mode below and above cutoff f_c are depicted, respectively in Figs. 2 and 3. As can be seen from the figures, the attenuations predicted by our closed-form approach agree very closely with those by Stratton's rigorous equation. Indeed, it could be observed from Fig. 3 that the attenuations below millimeter wavelengths computed using both methods are almost indistinguishable. Figures 4 and 5 show the attenuation constants of the TM11 mode. Like the case of the dominant mode, the attenuations below and above cutoff f_c of the TM11 mode, obtained from Stratton's and our methods are in very good agreement. It is worthwhile noting that, we have applied the Powell-hybrid root-finding algorithm to solve for Stratton's transcendental equation. The process has been lengthy since the initial guesses were to be constantly refined in order to ensure convergence to the appropriate solution. Unlike, Stratton's approach, however, solutions can be easily found in a straight-forward manner using our closed-form method.

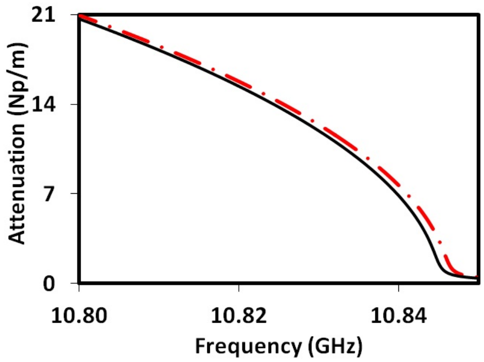

Fig. 2. Attenuation of TE11 mode below cutoff in an 8.1 mm radius, hollow waveguide with copper wall. The attenuations are computed using our method (solid line) and Stratton's (dashed-dotted line) method.

In order to show that our formulations work equally well in waveguides with different sizes, we compare the attenuation computed from both methods with the waveguide radius a_r varying from 5 mm to 55 mm. The attenuation of TE11 and TM11 modes with respect to the size of the waveguide are depicted, respectively, in Figs. 6 and 7. Since the operating frequency f = 100 GHz is above the cutoff frequencies f_c, all waves are in propagating modes. As can be observed from both figures, the attenuation constants obtained from both Stratton's and our method agree very well and are almost indistinguishable. Indeed, the maximum discrepancy found from both results is less than 1.25×10^{-4} Np/m.

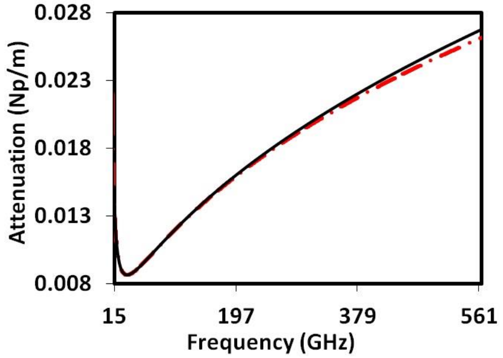

Fig. 3. Attenuation of TE11 mode above cutoff in an 8.1 mm radius, hollow waveguide with copper wall. The attenuations are computed using our method (solid line) and Stratton's (dashed-dotted line) method.

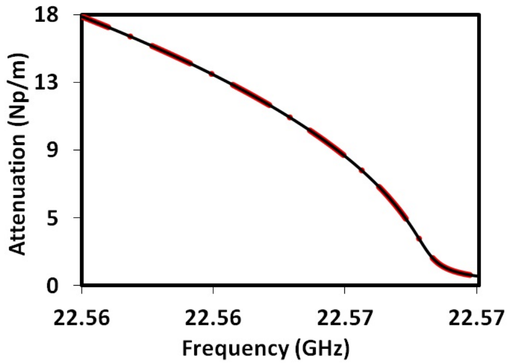

Fig. 4. Attenuation of TM11 mode below cutoff in an 8.1 mm radius, hollow waveguide with copper wall. The attenuations are computed using our method (solid line) and Stratton's (dashed-dotted line) method.

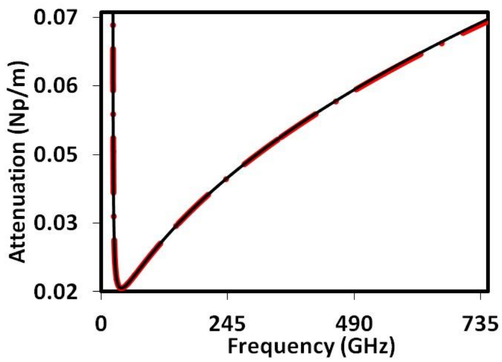

Fig. 5. Attenuation of TM11 mode above cutoff in an 8.1 mm radius, hollow waveguide with copper wall. The attenuations are computed using our method (solid line) and Stratton's (dashed-dotted line) method.

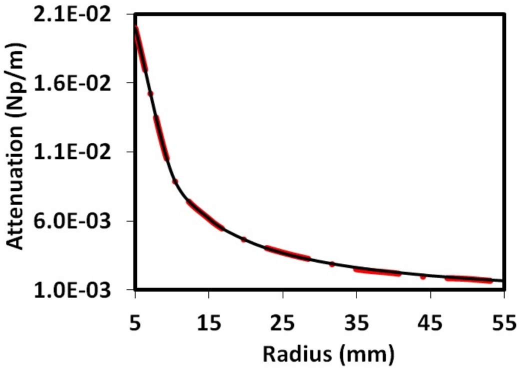

Fig. 6. Attenuation of TE11 mode when a 100 GHz wave propagates in a hollow waveguide with copper wall. The attenuations are computed using our method (solid line) and Stratton's (dashed-dotted line) method.

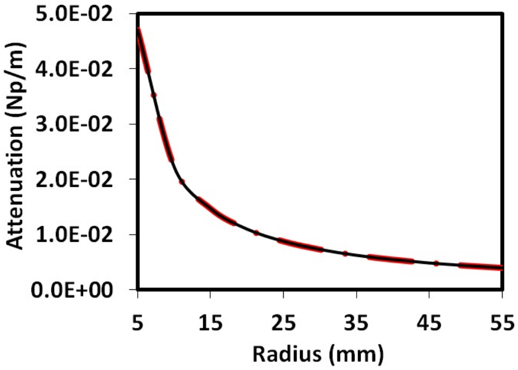

Fig. 7. Attenuation of TM11 mode when a 100 GHz wave propagates in a hollow waveguide with copper wall. The attenuations are computed using our method (solid line) and Stratton's (dashed-dotted line) method.

IV. CONCLUSION

We have developed a set of closed-form formulations for calculating the attenuation of TE and TM modes in a circular waveguide with imperfectly conducting wall. Our approach is based on matching the tangential electric and magnetic fields at the boundary with the electrical properties of the wall material. By neglecting the second-order variables, the roots of the characteristic equation can then be easily expressed in terms of the wavenumbers. Since the behavior of the lossy waveguide is assumed to be perturbed from its lossless case, a perturbation term is introduced into the Bessel function and its derivative. The attenuation constant is found by determining the perturbation terms using the Finite Difference Method and substituting them into the dispersion relation. Our closed-form equations show good agreement with those obtained using Stratton's rigorous approach. Unlike Stratton's transcendental approach, however, our approach leads to simpler and more straight-forward analysis.

ACKNOWLEDGMENT

Part of this work has been supported by the FRGS grant (Project: FRGS/2/2013/SG02/UTAR/02/1).

REFERENCES

[1] J. A. Stratton, *Electromagnetic Theory*. 1st ed., McGraw-Hill, 1941.
[2] K. H. Yeap, C. Y. Tham, G. Yassin, and K. C. Yeong, *Propagation in Lossy Rectangular Waveguides*, in Electromagnetic Waves/Book 2, 1st ed., Intech, June 2011.
[3] J. I. Glaser, "Attenuation and guidance of modes on hollow dielectric waveguides," *IEEE Transactions on Microwave Theory and Techniques (Correspondence)*, vol. 17, pp. 173-176, 1969.
[4] P. J. B. Claricoats, "Propagation along unbounded and bounded dielectric rods: Part 1. Propagation along an unbounded dielectric rod," *IEEE Monograph*, 409E, pp. 170-176, 1960.
[5] P. J. B. Claricoats, "Propagation along unbounded and bounded dielectric rods: Part 2. Propagation along a dielectric rod contained in a circular waveguide," *IEE Monograph*, 410E, pp. 177-185, 1960.
[6] R. C. Chou and S. W. Lee, "Modal attenuation in multilayered coated waveguides," *IEEE Transactions on Microwave Theory and Techniques*, vol. 36, pp. 1167-1176, 1988.
[7] K. H. Yeap, A. W. C. Tan, K. C. Lai, and H. Nisar, "A simple analytical method to calculate bending loss in dielectric rectangular waveguides," *ACES Express Journal*, vol. 33, pp. 359-361, 2018.
[8] K. H. Yeap, J. S. M. Teh, H. Nisar, K. C. Yeong, and K. Hirasawa, "Attenuation in superconducting waveguides," *Frequenz*, vol. 69, pp. 111-117, 2015.
[9] K. H. Yeap, W. Ismail and K. H. Yeap, "Analytical model for E-shaped microstrip patch antenna," *ACES Journal*, vol. 32, pp. 332-338, 2017.
[10] K. H. Yeap, E. V. S. Wong, H. Nisar, K. C. Lai, and C. A. Ng, "Attenuation in circular and rectangular waveguides," *Electromagentics*, vol. 37, pp. 171-184, 2017.
[11] R. E. Collin, *Field Theory of Guided Waves*. 2nd ed., IEEE Press, New York, 1960.
[12] D. K. Cheng, *Field and Waves Electromagnetics*. 1st ed., Addison Wesley, 1989.
[13] R. F. Harrington, *Time-Harmonic Electromagnetic Fields*. 1st ed., Mc-Graw Hill, pp. 66-73, 1961.
[14] K. H. Yeap, C. Y. Tham, K. C. Yeong, and H. J. Woo, "Wave propagation in lossy and superconducting circular waveguides," *Radioengineering Journal*, vol. 19, pp. 320-325, 2010.
[15] K. H. Yeap, C. Y. Tham, G. Yassin, and K. C. Yeong, "Attenuation in rectangular waveguides with finite conductivity walls," *Radioengineering J.*, vol. 20, pp. 472-478, 2011.
[16] T. Abe and Y. Yamaguchi, "Propagation constant

below cutoff frequency in a circular waveguide with conducting medium," *IEEE Transactions on Microwave Theory and Techniques*, vol. 29, pp. 707-712, 1981.

[17] C. A. Balanis, *Advanced Engineering Electromagnetics*. 1st ed., John Wiley and Sons, pp. 472-478, 1989.

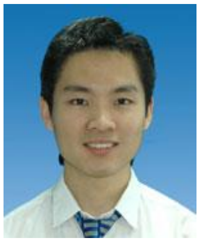

Kim Ho Yeap received his B.Eng. (Hons) from Petronas University of Technology in 2004, M.Sc. from National University of Malaysia in 2005 and Ph.D. from Universiti Tunku Abdul Rahman in 2011. He is a Senior Member of the IEEE, a Chartered Engineer registered with the UK Engineering Council and a Professional Engineer registered with the Board of Engineers Malaysia. He has published more than 100 scientific articles which include journal and conference papers, book chapters and books. He is currently an Associate Professor in Universiti Tunku Abdul Rahman. He is also the Editor-in-Chief of i-manager's Journal on Digital Signal Processing.

Eric Vun Shiung Wong graduated with a first class degree in B.Eng. (Hons) Electronics Engineering at Universiti Tunku Abdul Rahman, Malaysia. He is currently working as a Design Engineer in Motorola Solutions, Inc. He is also pursuing a part time Master degree in Universiti Sains Malaysia at the same time.

Humaira Nisar received her B.E. (Honors) in Electrical Engineering from University of Engineering and Technology, Lahore, Pakistan. She received her M.S. degree in Nuclear Engineering from Quaid-e-Azam University, Islamabad, Pakistan. She received her M.S. degree in Mechatronics and Ph.D. in Information and Mechatronics from Gwangju Institute of Science and Technology, Republic of Korea. Currently, she is an Associate Professor at the Department of Electronic Engineering, Universiti Tunku Abdul Rahman, Malaysia. She is also Senior Mmember of IEEE.

Kazuhiro Hirasawa received his Ph.D. degree in Electrical Engineering from Syracuse University, Syracuse, NY, in 1971. From 1967 to 1975, he was with the Department of Electrical and Computer Engineering, Syracuse University. From 1975 to 1977, he was a Consultant on research and development of various antennas. Since 1978, he has been with the University of Tsukuba, Ibaraki, Japan. Currently, he is an Emeritus Professor in University of Tsukuba and an International Collaborative Partner of Universiti Tunku Abdul Rahman, Malaysia. He is also an IEEE Life Fellow and IEICE Fellow.

Takefumi Hiraguri received the M.E. and Ph.D. degrees from the University of Tsukuba, Ibaraki, Japan, in 1999 and 2008, respectively. In 1999, he joined the NTT Access Network Service Systems Laboratories, Nippon Telegraph and Telephone (NTT) Corporation. He is now a Professor in Nippon Institute of Technology. He has been engaged in research and development of high speed and high communication quality wireless LANs systems. Hiraguri is a Member of IEICE.

Design of Dual-Band Miniaturized Frequency Selective Surface Using Branched Tortuous Structure

Ning Liu [1], Xianjun Sheng [2], Xiang Gao [2], Chunbo Zhang [3], and Dongming Guo [1]

[1] Department of Mechanical Engineering
Dalian University of Technology, Dalian, 116024, China
liuning@mail.dlut.edu.cn, guodm@dlut.edu.cn

[2] Department of Electrical Engineering
Dalian University of Technology, Dalian, 116024, China
568481055@qq.com, sxianjun@dlut.edu.cn

[3] Research Institute of Aerospace Special Materials and Processing Technology
Beijing, 100074, China
1628593171@qq.com

Abstract ─ A miniaturized dual-band frequency selective surface (FSS) is designed by using branched tortuous pattern of cross-dipole element backed by a wire grid of the same periodicity. By introducing the backing wire grid, the metallic line based FSS can provide two pass bands operating at 3.75GHz and 5.88GHz, respectively. The unit size of the proposed FSS is smaller than other similar FSSs and is only 0.075λ×0.075λ in size, where λ is the free-space wavelength at the first resonant frequency. Also, it shows good polarization stability and angular stability. Both simulated and measured results validate the performance.

Index Terms ─ Branched tortuous structure, dual band, frequency selective surface, periodic structure, miniaturization.

I. INTRODUCTION

Frequency selective surfaces (FSSs) are one- or two-dimensional periodic structures, which have been widely applied in the field of microwave to construct hybrid radome, antenna reflector, optical filter, electromagnetic shelter and so on [1-4]. Under some special applications, for example, multiband FSSs with independent transmission bands are required to increase the capacity of multi-frequency antenna in satellite communication system [5]. In practical applications mentioned above, FSSs are applied in limited space. To maintain the frequency selective property when applied in limited space, miniaturized FSSs are desired [6-8]. Hence, miniaturized multiband FSSs are highly demanded in practical applications.

Motivated by this requirement, different structures have been proposed to realize miniaturized dual-band or multiband FSS. Dual-band miniaturized FSS based on complementary structure is proposed in [9]. Meandered metallic pattern is used to design dual-band miniaturized FSS in [10]. A miniaturized dual-band FSS with double square slot element is proposed in [11]. Miniaturized dual-bandstop FSS based on anchor-shaped loop unit-cell structure is proposed in [12]. Miniaturized dual-band FSS based on crooked cross structure is introduced in [13, 14]. Fractal structures [15,16] are also adopted to realize miniaturized dual-band FSSs. Dual-band miniaturized FSS composed of 2-D periodic arrays of subwavelength inductive wire grids and capacitive patches separated by dielectric substrates is introduced in [17]. Nevertheless, most of the FSSs are designed to be band-stop, especially for the convoluted metallic structures, which is unsuitable to design band pass radomes. Also, unit size of the aforementioned FSSs is needed to be decreased.

To solve this problem, a miniaturized dual-band FSS composed of branched tortuous pattern of cross-dipole element backed by wire grid is proposed. By introducing the backing wire grid, the metallic line based FSS can provide two independent pass bands and has smaller unit size compared with other similar structures.

II. FSS STRUCTURE AND ITS EQUIVALENT CIRCUIT MODEL

A. Description of the FSS structure

As shown in Fig. 1 (a), the two FSS layers are separated by a thin dielectric substrate. The first FSS layer is composed of branched tortuous pattern of cross-dipole element and the second one is composed of wire grid. As discussed in [7,8], the miniaturization characteristic can be obtained by increasing the resonant

Submitted On: February 14, 2017
Accepted On: December 24, 2018

length of FSS element. Based on this idea, tortuous pattern is adopted to lengthen the resonant length. Meanwhile, branched structure is used to provide two independent resonant paths marked by a red and a blue dash line in Fig. 1 (b), respectively, which will result in two independent frequency bands.

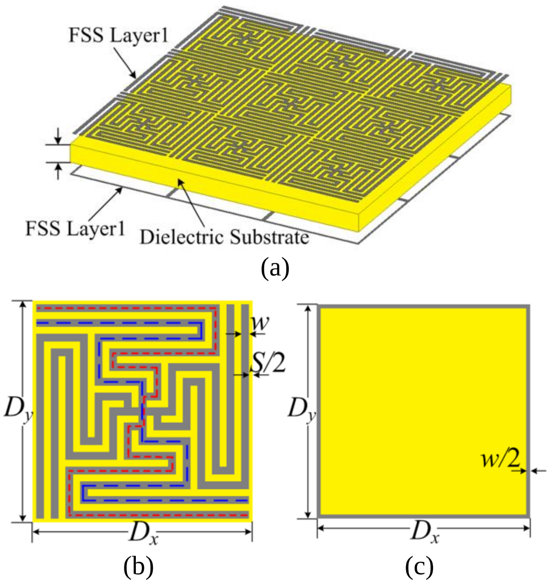

(a)

(b) (c)

Fig. 1. Structure of the proposed FSS. (a) Perspective view. (b) Top view of unit cell of FSS layer1. (c) Top view of unit cell of FSS layer2.

B. Equivalent circuit model of the proposed FSS

Based on the equivalent circuit theory, the branched tortuous pattern of cross-dipole element can be modelled by the parallel of two series *LC* resonators and the wire grid can be treated as an inductor L_0. Meanwhile, a short transmission line can be used to depict the thin dielectric substrate. Hence, the proposed FSS can be described by the equivalent circuit model shown in Fig. 2 (a). In our design, thickness of the substrate is relatively small. For simplicity, the dielectric substrate can be modelled as an inductor $L_t = \mu_0\mu_r h$, where μ_r is the relative permeability. Then the equivalent circuit model in Fig. 2 (a) can be simplified into that in Fig. 2 (b).

As indicated in Fig. 2 (b), there will be two stop bands if the two series *LC* resonators (L_1-C_1 and L_2-C_2) resonate, and the resonant frequencies of passbands can be estimated approximately by the equivalent circuit model. When the first series *LC* resonator (L_1-C_1) and the inductors (L_0 and L_t) resonate, a pass band will be produced around,

$$f_{p1} \approx 1/2\pi\sqrt{(L_1+L_0+L_t)C_1}\,. \qquad (1)$$

Assuming that the two pass bands are apart, the second pass band will be produced between the two stop bands, whose resonant frequency is around,

$$f_{p2} \approx \frac{1}{2\pi}\sqrt{(C_1+C_2)/(L_1+L_2)C_1C_2}\,. \qquad (2)$$

Based on the discussion above, it can be found that the proposed FSS can produce two pass bands separated by two transmission zeroes.

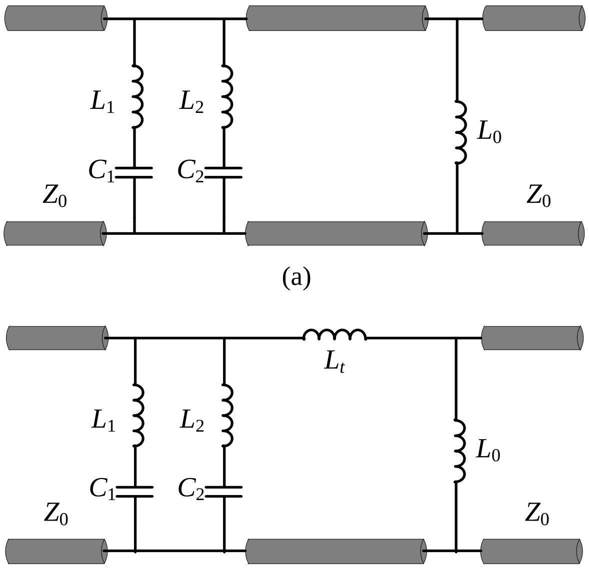

(a)

(b)

Fig. 2. Equivalent circuit model of the proposed FSS structure. (a) The transmission line model. (b) The lumped-element model.

III. SIMULATION RESULTS

To verify the performance of the proposed FSS, simulations by full-wave solver HFSS and equivalent circuit model have been carried out. As shown in Fig. 1, structure parameters of the proposed FSS are set as follows: dimension of the FSS are D_x=D_y=6mm, width of the metallic line is *w*=0.2mm, width of the slot between metallic lines is *s*=0.2mm. The two FSS layers are separated by a F4B-2 substrate. And the dielectric permittivity, tangent loss and thickness of substrate are ε_r=2.65, $tan\delta$=0.002 and *h*=0.5mm, respectively.

First, to explain the forming mechanism of the dual-band characteristic, the two metallic arrays are simulated separately and jointly. The transmission coefficients under normal incidence are shown in Fig. 3. As observed, the proposed FSS structure can provide two stopbands and two passbands. The stopbands operating at 4.54GHz and 6.52GHz are mainly formed by the top metallic array. Due to the existence of the bottom metallic array, the first passband operating at 3.75 GHz is formed. At the same time, the second passband produced by upper FSS is shifted under the influence of wire grid.

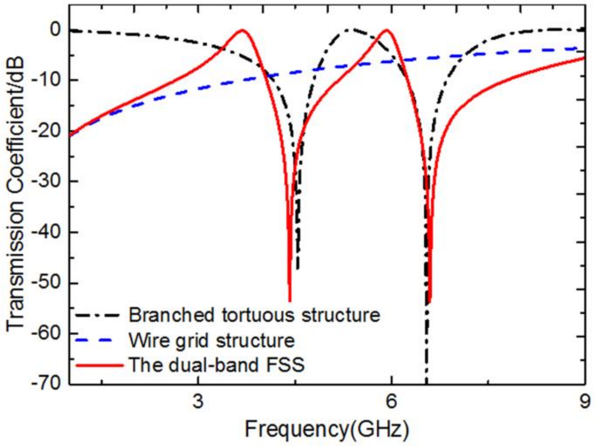

Fig. 3. Transmission coefficients of the constituting metallic arrays and the proposed FSS structure.

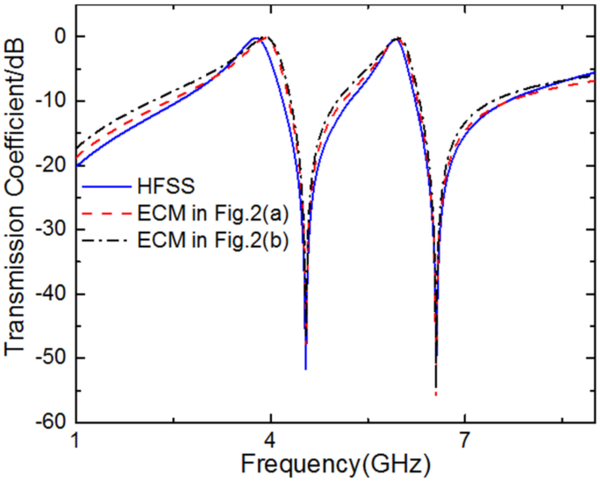

Fig. 4. Transmission coefficient of the proposed FSS at normal incidence.

After that, equivalent circuit method (ECM) is used to obtain the transmission coefficient of the proposed structure. The equivalent circuit parameters of the branched tortuous pattern of cross-dipole element (L_1, C_1, L_2 and C_2) and the wire grid (L_0) are derived from the simulated impendence Z_{FSS} using an iterative procedure proposed in [18]. To reduce the computational burden, two nulls of the impendence Z_{FSS} are used. Corresponding to such two resonances, a well-known relation $L = 1/\omega_{zero}^2 C$ can be obtained. Then, a curve fitting technique based on particle swarm optimization algorithm is applied for extracting parameters. The calculated lumped parameters are L_1=14.6nH, C_1=0.084pF, L_2=11.8nH, C_2=0.051pF, L_0=3.4nH and L_t=0.63nH, respectively.

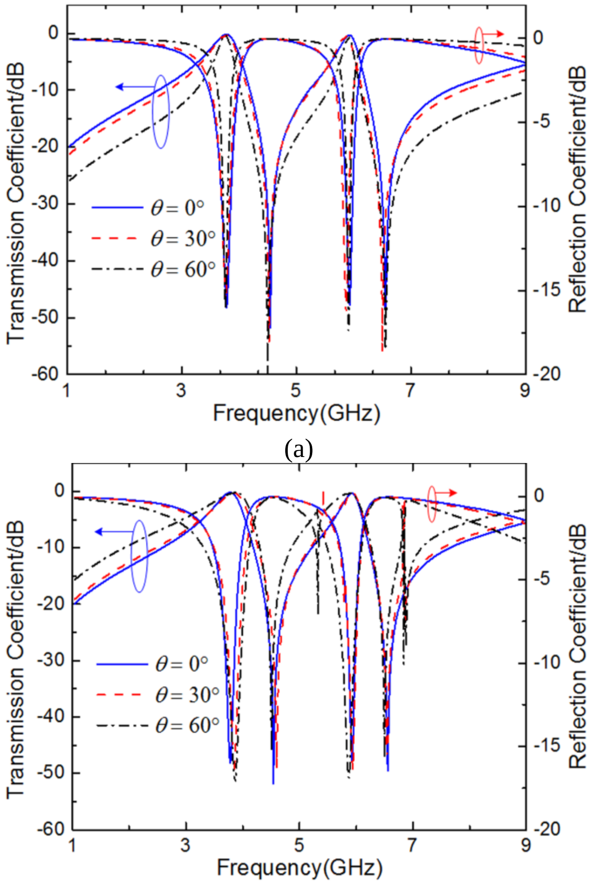

(a)

(b)

Fig. 5. Transmission coefficients of the proposed FSS under different incident. (a) TE polarization and (b) TM polarization.

The transmission coefficient under normal incidence can be calculated by equivalent circuit model in Fig. 2 using Eq. (6) in [18]. The calculated transmission coefficient is shown in Fig. 4 together with the simulated one obtained by HFSS. It can be observed that the results obtained by the two methods agree well, which verifies the validity of the equivalent circuit model in Fig. 2. The main discrepancy is the first resonant frequency shift. It is caused by the coupling effect between the two FSS layers, which is not taken into consideration by the equivalent circuit model.

Additionally, the transmission and reflection coefficients of the proposed structure under different incident angles and polarizations are obtained. The results are shown in Fig. 5. Apparently, the proposed structure shows good polarization stability and angular stability. However, as shown in Fig. 5 (b), there are some distortions and spurious resonances for TM polarization of 60° incidence. This is mainly caused by the top metallic layer. The structure composed of branched tortuous pattern connected in the center will produce the end load capacitance, which is similar with the Jerusalem Cross element. As introduced in [1], because of the existence of end load capacitance, bent mode will be produced for only TM-wave oblique incidence and then a transmission null will be formed. Owing to the branched structure design, there will be two transmission nulls. Noting that the two spurious resonances are away from the passbands, the effect of spurious resonances on frequency filter property can be ignored.

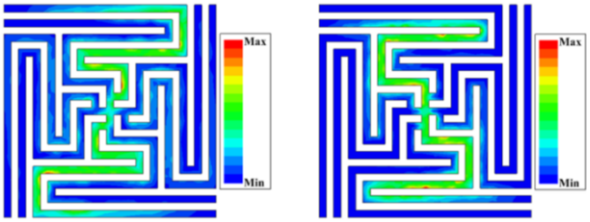

(a) (b)

Fig. 6. Surface current distribution diagram. (a) At *f*=4.54GHz and (b) at *f*=6.52GHz.

Also, the surface current distribution is given in Fig. 6. It can be observed that the proposed FSS has two stop bands operating at 4.54GHz and 6.52GHz, respectively. Based on the discussion in Section II, the two stop bands are caused by the two resonant paths provided by the branched tortuous structure. For verification, surface current distribution of the branched tortuous structure under normal incidence with TEM wave at 4.54GHz and 6.52GHz are simulated with HFSS and shown in Fig. 6. It can be observed that the branched structure can provide two independent resonant paths as predicted.

There is one point that should be emphasized: the resonant frequencies of the proposed FSS can be adjusted by changing resonant lengths. By increasing the arrangement periodicity, tortuous degree can be improved to fill the FSS unit cell, and then longer resonant lengths are obtained, which will lead to lower resonant frequencies. To further demonstrate this point, several structures with different resonant lengths are simulated under TE polarization. It should be noted that only the resonant lengths and the periodicity of the proposed structure have changed. The transmission coefficients are shown in Fig. 7. The results are tabulated in Table 1, where L_{red} and L_{blue} represent the length of two resonant paths shown in Fig. 1 (b), respectively. And the frequencies f_1 and f_2 represent the positions of the two pass bands. It can be found that the location of pass band will move toward lower frequency as the resonant lengths increase.

To further verify the performance of the proposed FSS, comparisons between previous works have been carried out. It can be observed from Table 2, unit size of the proposed FSS is smaller compared with other similar structures, which demonstrates that the proposed FSS is a better miniaturized design. Also, based on Eq. (1.5) in [1], the lowest onset frequency of grating lobe of 60° incidence is 26.8GHz, which is far from the resonant frequency.

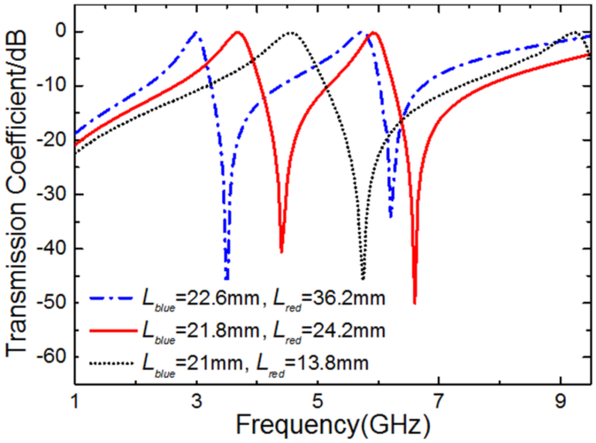

Fig. 7. Transmission coefficient of proposed structure with different resonate lengths.

Table 1: Length of two resonant paths and resonant frequencies of two pass bands

L_{blue} (mm)	L_{red} (mm)	D_x=D_y (mm)	f_1 (GHz)	f_2 (GHz)
21	13.8	2.6	4.55	9.24
21.8	24.2	3	3.75	5.88
22.6	36.2	3.4	2.99	5.68

Table 2: Comparisons with other dual-band FSSs

ε_r	FSS Structure	FSS Unit Size
2.65	FSS structure in [11]	0.1407λ×0.1407λ
	FSS structure proposed	0.075λ×0.075λ
4.4	FSS structure in [13]	0.0826λ×0.0826λ
	FSS structure in [13]	0.088λ×0.088λ
	FSS structure in [13]	0.094λ×0.094λ
	FSS structure proposed	0.0616λ×0.0616λ

IV. EXPERIMENTAL VERIFICATION

An FSS prototype has been fabricated and measured (see Fig. 8) for further verification. The prototype is consisting of 60×60 elements and the oversize is 362mm×362mm. The FSS prototype is measured with a free-space method in an anechoic chamber. The free-space measurement system is mainly composed of a transmitting antenna and a receiving antenna, which are connected to a vector network analyzer (Agilent E8363B). And the transmitting antenna and the receiving antenna are placed on each side of the prototype with a distance of 2m and 0.8m, respectively.

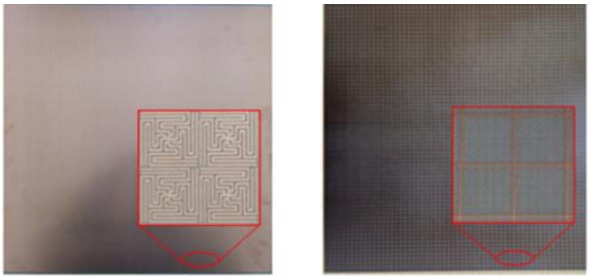
(a) (b)

Fig. 8. Photograph of the FSS prototype. (a) FSS layer1 and (b) FSS layer 2.

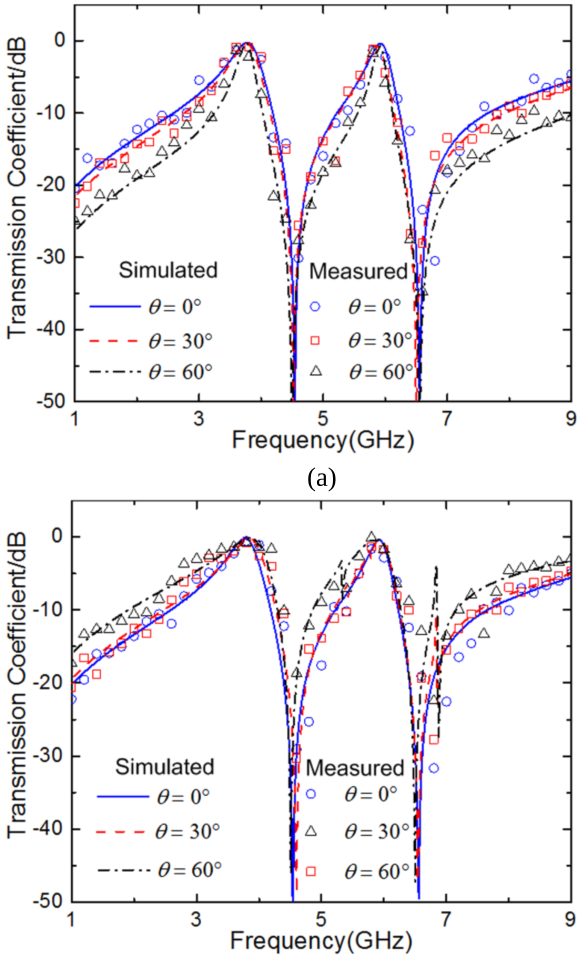

(a)

(b)

Fig. 9. Comparisons between the simulated and the measured transmission coefficients. (a) TE polarization and (b) TM polarization.

Comparisons between the measured and simulated transmission coefficients are shown in Fig. 9. Good agreements between the two methods can be observed, which demonstrates the validation of the proposed FSS structure design. And the reason causing spurious resonances has been explained above.

The passbands for simulation, ECM, and measurement under TE polarization are tabulated in Table 3. As observed, the results obtained by three methods are highly consistent. For ECM, the resonant frequency deviation respect to HFSS is slightly larger, which is 3.47% and 1.02%, respectively. This is because the coupling between upper and lower metallic layers of proposed structure is ignored. For measurement, the resonant frequency deviation is only 0.27% and 0.51%.

Table 3: The passbands obtained by three methods

Resonant Frequency	HFSS	ECM	Measurement
f_1 (GHz)	3.75	3.88	3.76
f_2 (GHz)	5.88	5.94	5.91

V. CONCLUSION

In this paper, a miniaturized dual-band band pass FSS is designed using a branched tortuous structure. The proposed FSS is analyzed, fabricated and measured. Both simulated and measured results show that the proposed FSS has smaller unit size compared with other similar structures and its unit size is only 0.075λ×0.075λ. Also, it has a better angular stability at oblique incidence and the resonant frequency deviation for the two pass bands keeps below 2% of 60° incidence under different polarizations. The proposed FSS can be applied for FSS radomes.

ACKNOWLEDGMENT

This work was supported by the National Natural Science Foundation of China under Grant 51575081.

REFERENCES

[1] B. A. Munk, *Frequency Selective Surface: Theory and Design*. John Wiley & Sons, 2005.

[2] R. Mittra, C. H. Chan, and T. Cwik, "Techniques for analyzing frequency selective surfaces-A review," *Proceedings of the IEEE*, vol. 76, no. 12, pp. 1593-1615, 1988.

[3] F. Costa and A. Monorchio, "A frequency selective radome with wideband absorbing properties," *IEEE Transactions on Antennas Propagation*, vol. 60, no. 6, pp. 2740-2747, 2012.

[4] H. Chen, X. Hou, and L. Deng, "Design of frequency selective surfaces radome for a planar slotted waveguide antenna," *IEEE Antennas and Wireless Propagation Letters*, vol. 8, pp. 1231-1233, 2009.

[5] M. Yan, J. Wang, H. Ma, *et al.*, "A tri-band, highly selective, bandpass FSS using cascaded multilayer loop arrays," *IEEE Transactions on Antennas Propagation*, vol. 64, no. 5, pp. 2046-2749, 2016.

[6] K. Sarabandi and N. Behdad, “A frequency selective surface with miniaturized elements,” *IEEE Transactions on Antennas Propagation*, vol. 55, no. 5, pp. 1239-1245, 2007.

[7] N. Liu, X. J. Sheng, and J. J. Fan, “A compact miniaturized frequency selective surface with stable resonant frequency,” *Progress In Electromagnetics Research Letters*, vol. 62, pp. 17-22, 2016.

[8] N. Liu, X. J. Sheng, J. J. Fan, and D. M. Guo, “A miniaturized FSS based on tortuous structure design,” *IEICE Electronics Express*, vol. 14, no. 2, pp. 20161129, 2017.

[9] X. D. Hu, X. L. Zhou, L. S. Wu, *et al.*, “A miniaturized dual-band frequency selective surface (FSS) with closed loop and its complementary pattern,” *IEEE Antennas and Wireless Propagation Letters*, vol. 8, pp. 1374-1377, 2009.

[10] F. C. Huang, C. N. Chiu, T. L. Wu, *et al.*, “Very closely located dual-band frequency selective surfaces via identical resonant elements,” *IEEE Antennas and Wireless Propagation Letters*, vol. 14, pp. 414-417, 2015.

[11] Y. Yang, X. H. Wang, and H. Zhou, “Dual-band frequency selective surface with miniaturized element in low frequencies,” *Progress In Electromagnetics Research Letters*, vol. 33, pp. 167-175, 2012.

[12] M. Yan, S. Qu, J. Wang, *et al.*, “A miniaturized dual-band FSS with stable resonance frequencies of 2.4 GHz/5 GHz for WLAN applications,” *IEEE Antennas and Wireless Propagation Letters*, vol. 13, pp. 895-898, 2014.

[13] C. N. Chiu and W. Y. Wang, “A dual-frequency miniaturized–element FSS with closely located resonances,” *IEEE Antennas and Wireless Propagation Letters*, vol. 12, pp. 163-165, 2013.

[14] R. Sivasamy and M. Kanagasabai, “A novel dual-band angular independent FSS with closely spaced frequency response,” *IEEE Microwave and Wireless Components Letters*, vol. 25, no. 5, pp. 298-300, 2015.

[15] T. Zhong, H. Zhang, R. Wu, *et al.*, “A single-layer dual-band miniaturized frequency selective surface with compact structure,” *IEEE Asia-Pacific International Symposium on Electromagnetic Compatibility*, pp. 122-124, 2016.

[16] Y. Y. Lv and W. L. Chen, “Dual-polarized multiband frequency selective surface with miniaturized Hilbert element,” *Microwave and Optical Technology Letters*, vol. 55, no. 6, pp. 1221-1223, 2013.

[17] M. Gao, S. M. A. M. H. Abadi, and N. Behdad, “A dual-band inductively coupled miniaturized-element frequency selective surface with higher order bandpass response,” *IEEE Transactions on Antennas Propagation*, vol. 64, no. 8, pp. 3729-3734, 2016.

[18] F. Costa, A. Monorchio, and G. Manara, “Efficient analysis of frequency-selective surfaces by a simple equivalent-circuit model,” *IEEE Transactions on Antennas Propagation*, vol. 54, no. 4, pp. 35-48, 2012.

Ning Liu received his B.S. degree in Electronic and Information Engineering from Dalian University of Technology, Dalian, China, in 2013. He is currently working towards the Ph.D. degree in Mechanical Engineering, Dalian University of Technology. His research interests include Metamaterials, Frequency selective surface design and analysis, Antenna radome, and computational electromagnetics.

Xianjun Sheng was born in Liaoning, China, in 1969. She received her M.S. and Ph.D. degrees from Dalian University of Technology, Dalian, China, in 1997 and in 2003, respectively. She works currently as a Professor in Department of Electrical Engineering, Dalian University of Technology. Her research interests include Antenna radome, Computational electromagnetics and Control theory.

Xiang Gao received his B.S. degree in Electrical Engineering, Dalian Jiaotong University China, in 2017. He is currently working towards the M.S. degree in Electrical Engineering in Dalian University of Technology. His research interest is Frequency selective surface design and analysis.

Chunbo Zhang received his M.S. degree in Electrical Engineering from Shengyang University of Technology, China, in 2004. He received his Ph.D. degree from Dalian University of Technology, Dalian, China, in 2008. He is currently working as Senior Engineer in Research Institute of Aerospace Special Materials and Processing Technology, China. His research interests include antenna radome, design and analysis of metamaterials.

Dongming Guo received his Ph.D. degree in Mechanical Engineering from Dalian University of

Technology, Dalian, China, in 1992. He is currently working as a Professor in Department of Mechanical Engineering in Dalian University of Technology. His research interests include Antenna radome, Metamaterials, special machining and precision machining technology and digital design and manufacturing.

A Varactor Loaded Tunable Dual-band Left-Handed Metamaterial

Si Li [1], Wenhua Yu [3], Atef Z. Elsherbeni [4], Wenxing Li [2], and Yunlong Mao [1]

[1] School of Electronic Information
Jiangsu University of Science and Technology, Zhenjiang, Jiangsu, 212003, China
lisi0511@just.edu.cn, maoyunlong0511@just.edu.cn

[2] College of Information and Communication
Harbin Engineering University, Harbin, Heilongjiang, 150001, China
liwenxing@hrbeu.edu.cn

[3] 2COMU, INC. Fairfax, VA 22030, USA
Wenyu@2comu.com

[4] Electrical Engineering Department
Colorado School of Mines, Golden, CO, 80401, USA
aelsherb@mines.edu

Abstract ─ In this paper, we proposed a tunable dual-band left-handed metamaterial (LHM). This dual-band LHM can be regarded as a combination of double-slits split ring resonators (DSSRRs) and rotated 'H-shape' structure loaded with varactors. The 'H-shape' structure functions like arrayed metallic wires, and is only capable of extracting negative permittivity, but with proper loaded capacitors, it can also extract negative permeability. According to the numerical analysis, such character is closely related to the mutual coupling coefficient. We analyzed both the DSSRRs and the 'H-shape' structure through equivalent circuits and simulations, respectively. Later the composed LHM loaded with varactors is also simulated. Dual-band left handed (LH) property can be observed from the retrieved effective parameters, of whom one LH band is stable and wide, approximately from 2GHz to 2.1GHz, while the other one is relatively narrow, shifting from 1.14GHz to 2.36GHz dynamically. Compared to other work where only multi-band technology or tunable method is applied, the combination of both the methods greatly extended the functioning bandwidth.

Index Terms ─ Dual-band, LHM, Tunable, Varactor-loaded.

I. INTRODUCTION

Metamaterials (MTMs) have aroused great attention since Pendry introduced periodically located metallic wires to achieve negative permittivity in 1996 [1]. Later, his team proposed spilt ring resonators (SRRs) to get negative permeability [2]. In [3,4], the authors composed SRRs and metallic wires together to get negative permittivity and permeability at the same frequency range. These kind of MTMs are also referred to as left-handed metamaterials (LHMs). However, even after so many years' development, the bandwidth limitation of MTMs remains a great challenge. There are two potential ways to cross this limitation.

Some researchers focused their studies on multi-band MTMs. The first kind of multi-band MTMs are based on well-designed metallic patterns, such as the 'S-shaped' [3], the 'H-shaped' [4] and the 'Z-shaped' [5] MTMs. An advanced well-designed metallic pattern mode is fractal shapes, such as the nested 'U-shaped' and the 'tree-shaped' [6] MTMs. Another kind of multi-band MTMs are implemented with a combination of different single-band MTM units. In [7], similar patterns are printed on different substrates, while in [8], SRRs with different opening directions are printed on 3 layers substrates.

Some researchers focused on the studies on tunable MTMs. There are multiple methods to implement tunable characteristics, such as loading varactors [9-17], applying ferrite slabs [18-21] or liquid crystal [22,23], and mechanically changing the structures [24-28]. Among these methods, varactor loaded tunability is the most applicable.

In this paper, we propose a tunable dual-band LHM to achieve a dynamical wideband. The geometry of this MTM is the same as the single-band LHM that Xin and his team published in 'Nature Communications' [29], while the loaded diode is replaced with a varactor. This single-band LHM unit can be regarded as a combination

Submitted On: May 28, 2017
Accepted On: December 24, 2018

of double-slits split ring resonators (DSSRR) and a rotated ‘H-shape’ structure. The ‘H-shape’ structure acts as arrayed metallic wires that are only capable of providing negative permittivity, however, with proper loaded capacitors, it also exhibits negative permeability. In this paper, both the basic particles of the single-band LHM are analyzed with equivalent circuits and simulations. After that, we loaded varactor diodes, the SMV-1236 from Skyworks, to the LHM. Simulations are operated with linearly increased reversed voltage from 0V to 5V, and retrieve the S parameters through the ‘S-parameter retrieval method’ published in [30] to get the effective parameters.

II. MODEL AND EQUIVALENT CIRCUIT

The geometry of the single-band LHM proposed in [29] is displayed in Fig. 1, where a=27 mm, b=54 mm, c=4 mm, d=5 mm, e=6 mm, f=0.8 mm, g=2.5 mm, r1=9 mm, r2=12 mm. The metallic pattern is printed on a 1.27 mm-thick Rogers-6006 substrate whose relative permittivity is 6.15, and the thickness of the metallic wires is t=0.017 mm.

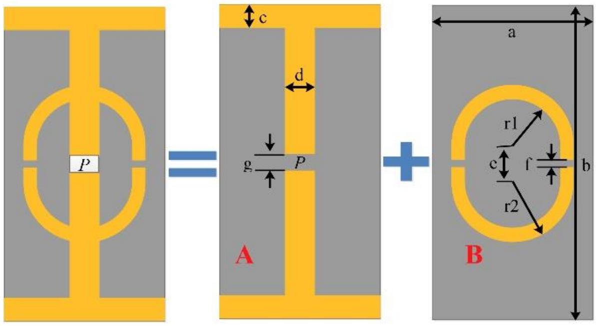

Fig. 1. Geometry illustration of the LHM proposed in [29]. It can be regarded as a combination of a rotated ‘H-shape’ (particle A) and a DSSRR (particle B).

Such structure can be regarded as a combination of rotated ‘H-shape’ metallic wires (particle A) and DSSRRs (particle B). In the discussed frequency regime [29], DSSRRs produce negative permeability while the rotated ‘H-shaped’ structure is responsible for negative permittivity.

A. Equivalent circuit analysis for particle A

In [31], the authors proposed a double-sided rotated ‘H-shape’ structure where the magnetic resonance is originated from the anti-paralleled currents in the wires with opposite signs accumulating at corresponding ends. Similarly, a proper capacitor loaded will also generate anti-paralleled currents on both ends.

According to the theoretical analysis of the split ring resonators (SRRs) proposed in [2,29], the magnetic resonance is motivated by the electromotive force around the circumference of the split rings. Considering an infinite array of such SRRs arranged in three orthogonal directions with a spatial period of d, and an incident magnetic field polarized along the y direction, that is, perpendicular to the SRRs, there would be electromotive force and induced current I along the rings, satisfying:

$$\begin{aligned}\mathrm{EMF} &= j\omega\pi r^2\mu_0 H_0 \\ &= RI + I/(-j\omega C) + (-j\omega L)I + j\omega FLI,\end{aligned} \tag{1}$$

where H_0 is the external magnetic field, R, L, and C are the parasitic resistance, the geometrical inductance, and the capacitance of each ring, respectively, and FL is the mutual inductance between different rings. With $L=\pi r^2\mu_0/d$, and $F=\pi r^2/d^2$, the current I is given as:

$$I=\frac{-j\omega\pi r^2\mu_0 H_0}{j\omega L\left[1-F\right]-R+\dfrac{1}{j\omega C}}=\frac{-dH_0}{\left(1-F-\dfrac{1}{\omega^2 LC}\right)+\dfrac{Rj}{\omega L}}. \tag{2}$$

Based on the magnetic moment per unit volume, $M=\pi r^2 I/d^3$ and $\mu_{eff}=\left(B/\mu_0\right)/(B/\mu_0-M)$, B is the corresponding external magnetic flux, then we can obtain the final effective permeability as following:

$$\mu_{eff}=1-\frac{F\left(1-\dfrac{1}{\omega^2 LC}\right)-j\dfrac{R}{\omega L}}{\left(1-\dfrac{1}{\omega^2 LC}\right)^2+\dfrac{R^2}{\left(\omega L\right)^2}}. \tag{3}$$

From the analysis above, it is obvious that the effective permeability is completely irrelevant with the shape of the magnetic resonators, but closely related to the mutual coupling and self-properties of the structure.

The equivalent circuit for the rotated ‘H-shape’ wire with an embedded capacitor C_e is displayed in Fig. 2, where L_e is the equivalent inductance.

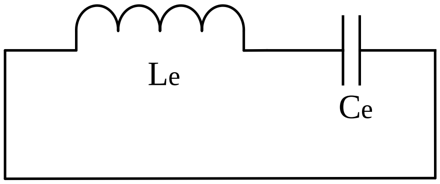

Fig. 2. Equivalent circuit of the rotated ‘H-shape’.

The self-inductance of a strip line can be calculated using [32]:

$$L=2\times10^{-4}l\left[\ln\left(\frac{l}{w+t}\right)+1.193+0.2235\frac{w+t}{l}\right], \tag{4}$$

where l is the length of the strip line, w is the width, and t is the thickness. Assume a function ‘Cal_induc(l,w,t)’ to represent (4), then for particle A, equivalent inductance L_e can be approximated as:

$$L_e = cal\_indc(b/2, d, t), \tag{5}$$

which is 0.72 nH. Hence, the magnetic resonant frequency can be calculated as:

$$f_m = \frac{1}{2\pi\sqrt{L_e C_e}}. \tag{6}$$

We listed the corresponding resonant frequencies while C_e ranging from 7 Pf to 25 Pf with a step size of 3 Pf in Table 1. The resonant frequency is linearly shifting from higher frequencies to lower frequencies with the increase of C_e.

Table 1: Resonant frequencies with C_e ranging

C_e(pF)	7	10	13	16	19
f_m(GHz)	2.25	1.88	1.65	1.49	1.37

B. Equivalent circuit analysis for particle B

The equivalent circuit for the DSSRR is displayed in Fig. 3.

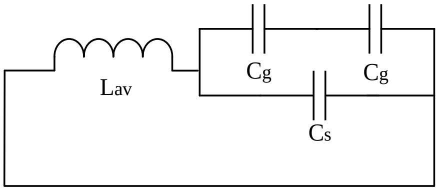

Fig. 3. Equivalent circuit for DSSRR.

The total equivalent capacitance of DSSRR is calculated as:

$$C_{total} = C_g / 2 + C_s, \tag{7}$$

where C_g is the gap capacitance, and C_s is the surface capacitance.

According to the transmission line theory [32], for the coplanar strips on a substrate as illustrated in Fig. 4, the capacitance per unit length of the paralleled strip lines are calculated using:

$$C_{pul} = \varepsilon_0 \varepsilon_e F(k), \tag{8}$$

where ε_0 is the permittivity of free space, ε_e and the first kind elliptic integral related function $F(k)$ are calculated as:

$$\varepsilon_e = 1 + (\varepsilon_r - 1) F(k) / 2F(k1), \tag{9}$$

$$F(k) = \begin{cases} \dfrac{1}{\pi} \ln\left(2\dfrac{1+\sqrt{k'}}{1-\sqrt{k'}}\right), & 0 < k \le \dfrac{1}{\sqrt{2}} \\ \pi \ln\left(2\dfrac{1+\sqrt{k}}{1-\sqrt{k}}\right)^{-1}, & \dfrac{1}{\sqrt{2}} < k \le 1 \end{cases}, \tag{10}$$

where $k=a/b$, $a=s/2$, $b=w+s/2$, $k' = \sqrt{1-k^2}$, and $k1 = \sinh(\pi a / 2h) / \sinh(\pi b / 2h)$.

In this example, with respect to the estimation method [33], $s = f$, and $w=r1 + (e-f)/2$; hence C_g can be calculated which is 0.142pf. The calculation for $C_s = C_{s1} + C_{s2}$ is approximated as [34]:

$$\begin{cases} C_{s1} = \dfrac{\varepsilon_0 (t + r2 - r1)}{\pi} \left(\log \dfrac{2(r1+r2)}{g} + e - f \right) \\ C_{s2} = \dfrac{\varepsilon_0 (\varepsilon_r - 1)(t + r2 - r1)}{2\pi} \left(\log \dfrac{2(r1+r2)}{g} + e - f \right) \end{cases}, \tag{11}$$

where C_{s1} is the surface capacitance through air, C_{s2} is the surface capacitance through the substrate, hence, $C_s = 0.192$pf. Then total capacitance Ct is 0.264pf.

The total equivalent inductance for the double slits SRR can also be approximated using (4), and it can also be approximated as:

$$L_{av} = cal\_indc(r2 - r1, \pi(r1 + r2)/2 + e - f, t), \tag{12}$$

therefore, the resonant frequency for the double slits SRR can also be calculated using a similar equation as (6), which is 1.83GHz.

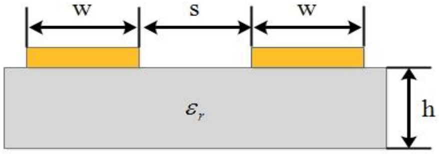

Fig. 4. Coplanar strips model.

III. SMULATIONS AND ANALYSIS

To verify the numerical analysis above, we ran simulations for particle A and B, respectively. After that, we introduced a varactor diode, SMV-1236 from Skyworks, and embedded it to the composed LHM. All the simulations are operated with HFSS software.

A. Simulation for particle A

For particle A, we ran the simulations with the embedded capacitance C_e varying from 7 pF to 19 pF linearly with a step size of 3 pF for the sake of simplify the analysis. Then we applied ‘S parameters retrieval method’ to get the effective parameters from simulated S parameters. The real part of the retrieved effective permittivity and permeability are displayed in Figs. 5 (a) and (b).

It is seen that particle A is capable of providing negative permittivity, and this property is quite similar to that of arrayed metallic wires. When C_e is 7 pF, 10 pF, and 13 pF, the effective permeability is also negative. For other values of C_e, there are also significant resonances. Compared to the resonant frequencies listed in Table 1, the simulated results match well with the numerical analysis. Hence, particle A can also be regarded as a single-band LHM with proper loaded capacitors, and it is tunable with the change of the capacitance.

B. Simulation for particle B

The simulated S parameters and the retrieved effective parameters are displayed in Figs. 6 (a) and (b).

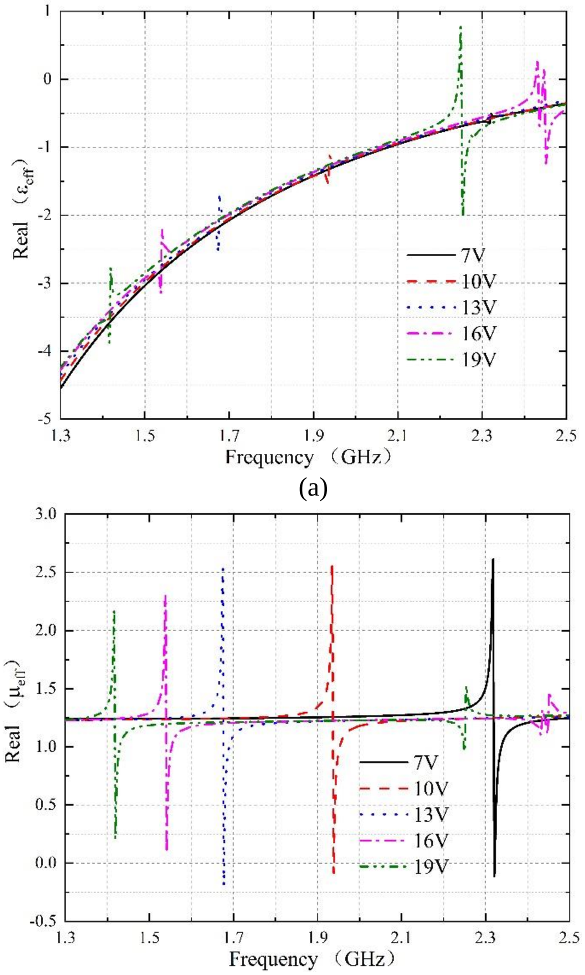

(a)

(b)

Fig. 5. Retrieved effective (a) permittivity and (b) permeability of the rotated ‘H-shape’ with the embedded capacitance varying from 7pF to 19pF.

Negative permittivity can be observed at a frequency range from 1.854GHz to 1.96GHz. The simulated results also match well with the numerical analysis.

C. Varactor-loaded LHM

In the previous sections, the tunability is discussed with a series of linearly changed capacitance for simplicity. However, in applications, tunable capacitors are usually achieved with varactor diodes. The proper varactor chosen is SMV1236 from Skyworks, and its spice model is displayed in Fig. 7 [35].

The capacitance ‘CT’ for this diode with the change of reversed voltage ‘VR’ is also listed in Table 2.

Simulations for the LHM with varactors loaded were operated and the S parameters are displayed in Fig. 8, the real part of the retrieved effective parameters are displayed in Figs. 9 (a), (b) and (c), with the reversed voltage ranging from 0V to 5V.

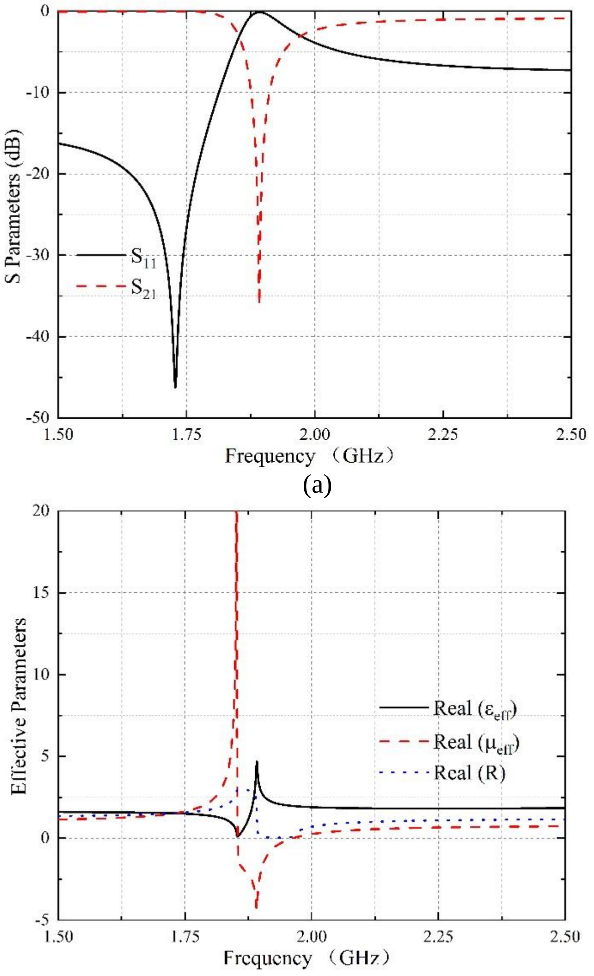

(a)

(b)

Fig. 6. (a) Simulated S parameters of DSSRR, and (b) the corresponding real part of the retrieved effective permittivity (Real(ε)), permeability (Real(μ)) and the refractive index (Real(R)).

Table 2: Total capacitance CT(pF) of the diodes varying with the reversed voltage VR(V)

VR	0	0.5	1	1.5	2	2.5
CT	26.75	20.61	17.02	14.38	12.29	10.56
VR	3	3.5	4	4.5	5	
CT	9.16	8.04	7.19	6.53	6.01	

In Fig. 8, there are 3 resonant frequencies despite the change of the reversed voltage, of whom two are only slightly shifted, while the other one is moving from lower frequencies to higher frequencies with the reversed voltage increases. Additionally, the bandwidth of the third resonance is only comparable with the stable two ones when they are close.

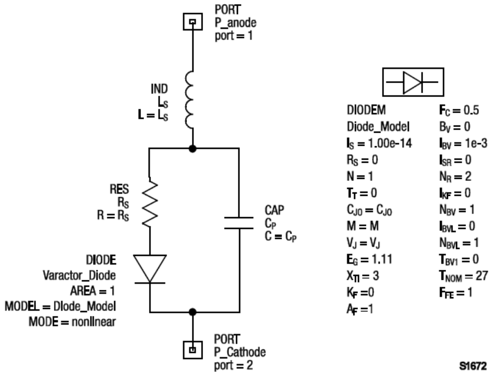

Fig. 7. The spice model of SMV1236.

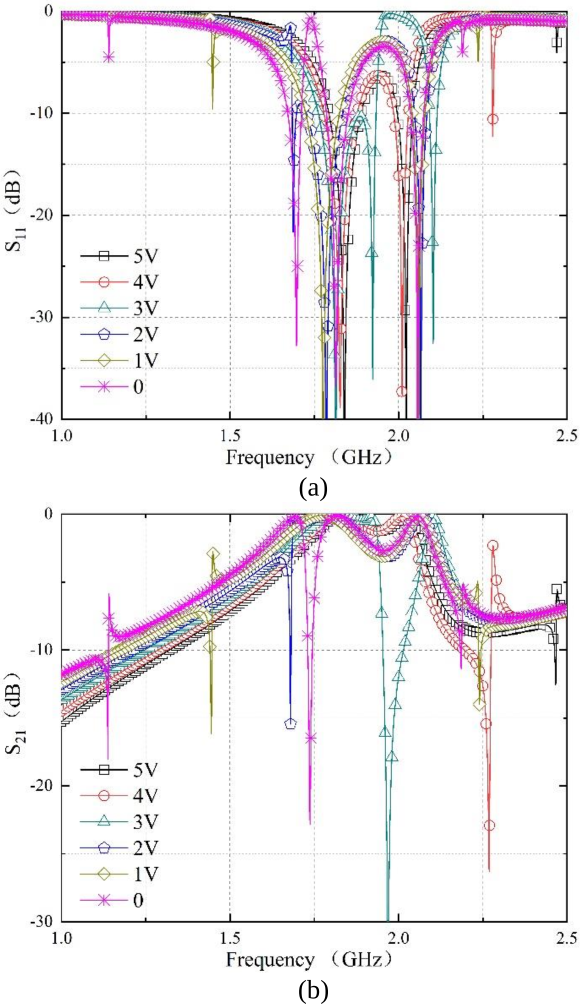

(a)

(b)

Fig. 8. Simulated (a) S_{11} and (b) S_{21} with reversed voltage ranging from 0V to 5V.

In Fig. 9 (a), permittivity is negative in the discussed frequency range only except for a narrow band approximately from 1.7GHz to 1.9GHz. In Fig. 9 (b), permeability is negative at two different frequency range, of whom one is narrow while the other one is comparable wide. Additionally, with the increase of VR, one of the negative regime is moving from lower frequencies to higher frequencies, while the other one is only slightly changed. Besides, the resonant strength of the shifting resonance gets stronger as it is moving closer to the stable resonance, such as the strong resonance when the reversed voltage is 3V. The refractive index displayed in Fig. 9 (c) show a similar property, and it remains negative despite of the change of VR.

We also listed more detailed information about the double negative band with VR changing at a step of 0.5V in Table 3, where ‘LH-1’ and ‘LH-2’ refers to the two left handed negative bands, and ‘BW’ refers to the corresponding bandwidth. They all measured with ‘GHz’. Obviously, ‘LH-1’ is stable, while ‘LH-2’ is changeable. Compared to the previous discussed particle A and B, it can be developed that ‘LH-1’ is closely related to the DSSRR, while ‘LH-2’ is closely related to the rotated ‘H-shape’ with embedded varactor.

In this table, for ‘LH-2’, when VR=2.5V, only permeability is negative, and when VR=5V, only permittivity is negative, hence, they are all marked with ‘null’ in the table. From the point of bandwidth, it is interesting to note that the bandwidth for ‘LH-2’ gets wider as the two LH bands getting closer.

From (3), the real part of permeability is closely related to the mutual coupling. Hence, when the resonant frequencies of the two particles are getting closer, the LH bandwidth originates from particle A is also getting wider.

Table 4 listed the relative bandwidth of some previous work where ‘MB’ refers to multi-band method, ‘VL’ refers to the varactor-loaded method, and ‘BW’ refers to the relative bandwidth. In our work, the 0.2GHz wide right-handed bandwidth is excluded in the calculation for relative bandwidth. Apparently, with the combination of multi-band and tunable technology, the LH bandwidth is greatly extended.

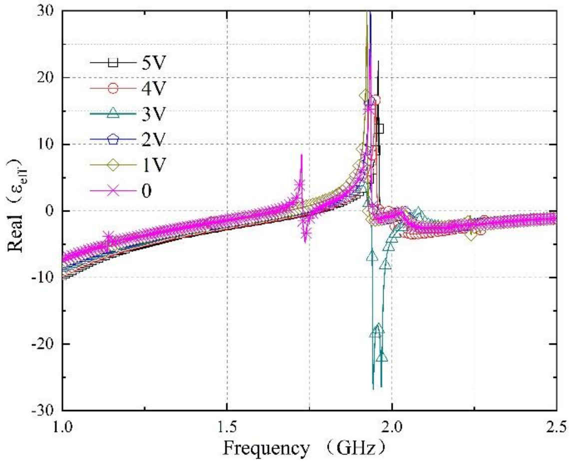

(a)

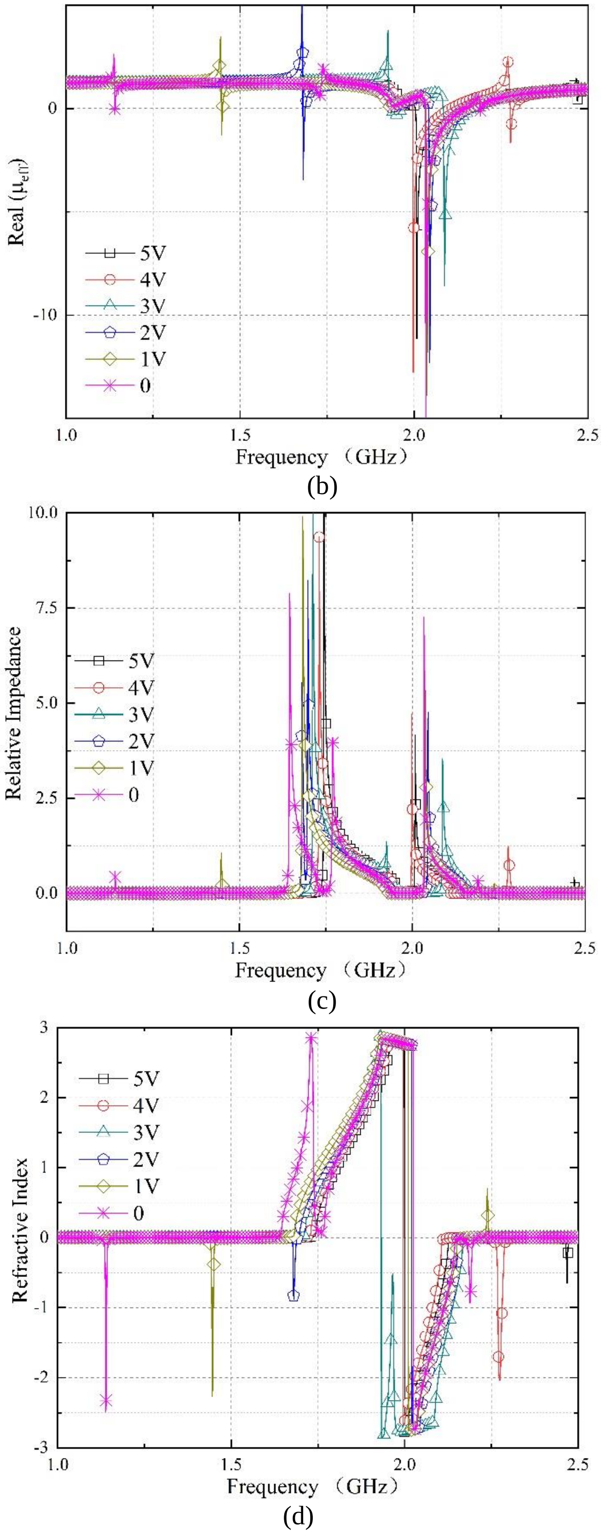

Fig. 9. The real part of the retrieved effective (a) permittivity, (b) permeability, (c) relative impedance, and (d) refractive index with the reversed voltage ranging from 0V to 5V.

Table 3: LH frequency range with VR changing

VR	LH-1	BW	LH-2	BW
0	2.032~2.144	0.112	1.142~1.14	0.002
0.5	2.034~2.15	0.116	1.311~1.313	0.002
1	2.034~2.151	0.116	1.446~1.450	0.004
1.5	2.039~2.155	0.116	1.568~1.573	0.005
2	2.041~2.156	0.115	1.680~1.688	0.008
2.5	2.054~2.161	0.107	null	null
3	2.084~2.167	0.083	1.933~1.964	0.031
3.5	1.975~2.060	0.085	2.161~2.202	0.041
4	1.995~2.107	0.112	2.275~2.287	0.012
4.5	2.003~2.123	0.12	2.363~2.368	0.005
5	2.003~2.125	0.122	null	null

Table 4: Relative bandwidth in some references using different methods

Ref	**Method**	**BW (%)**
[5]	MB	13.3
[6]	MB	25.3
[36]	MB	18.5
[9]	VL	27
[10]	VL	23
[11]	VL	38
This work	MB-VL	61.5

IV. CONCLUSION

In this paper, we proposed a varactor-loaded tunable dual-band LHM. The structure of this LHM without the varactor can be regarded as a combination of DSSRRs, that responsible for providing negative permeability, and rotated ‘H-shape’ structure that function as arrayed metallic wires providing negative permittivity. In our work, we analyzed both the basic particles with equivalent circuits and simulations and pointed out that the rotated ‘H-shape’ exhibits double negative properties with proper embedded capacitance. The loaded varactor is SMV-1236 from Skyworks. With the reversed voltage varying from 0V to 5V, there are two different frequency regimes with LHM properties, of whom one is wide and stable, approximately from 2GHz to 2.1GHz, while the other one is relatively narrow and is dynamically shifting from 1.14GHz to 2.34GHz except for frequencies between 1.7GHz to 1.9GHz. Additionally, when the two bands are close, the bandwidth of the wider one gets narrower, while the narrow one gets wider. Compared to other work where only multi-band technology or tunable method is applied, the combination of both the methods greatly extended the functioning bandwidth and can be of great use in areas such as radars and sensors.

REFERENCES

[1] J. B. Pendry, A. J. Holden, W. J. Stewart, and I. I. Youngs, "Extremely low frequency plasmons in metallic mesostructures," *Phys. Rev. Lett.*, vol. 76,

no. 25, pp. 4773-4776, June 17, 1996.

[2] J. B. Pendry, A. J. Holden, D. J. Robbins, and W. J. Stewart, "Magnetism from conductors and enhanced nonlinear phenomena," *IEEE Transactions on Microwave Theory and Techniques*, vol. 47, no. 11, pp. 2075-2084, 1999.

[3] H. Chen, et al., "Metamaterial exhibiting left-handed properties over multiple frequency bands," *Journal of Applied Physics*, vol. 96, no. 9, pp. 5338-5340, 2004.

[4] S. Islam, M. Faruque, and M. Islam, "The design and analysis of a novel split-H-shaped metamaterial for multi-band microwave applications," *Materials*, vol. 7, no. 7, pp. 4994-5011, 2014.

[5] H. Zhou, C. Wang, and H. Peng, "A novel double-incidence and multi-band left-handed metamaterials composed of double Z-shaped structure," *Journal of Materials Science: Materials in Electronics*, vol. 27, no. 3, pp. 2534-2544, 2016.

[6] H. X. Xu, et al., "Multi-band left-handed metamaterial inspired by tree-shaped fractal geometry," *Photonics and Nanostructures - Fundamentals and Applications*, vol. 11, no. 1, pp. 15-28, 2013.

[7] J. Wang, S. Qu, Y. Yang, H. Ma, X. Wu, and Z. Xu, "Multiband left-handed metamaterials," *Applied Physics Letters*, vol. 95, no. 1, pp. 014105-014105-3, 2009.

[8] X. Jia, X. Wang, Q. Meng, and Z. Zhou, "Tunable multi-band chiral metamaterials based on double-layered asymmetric split ring resonators," *Physica E: Low-dimensional Systems and Nanostructures*, vol. 81, pp. 37-43, 2016.

[9] T. Nesimoglu and C. Sabah, "A tunable metamaterial resonator using varactor diodes to facilitate the design of reconfigurable microwave circuits," *IEEE Transactions on Circuits and Systems II: Express Briefs*, vol. 63, no. 1, pp. 89-93, 2016.

[10] J. Zhao, Q. Cheng, J. Chen, M. Q. Qi, W. X. Jiang, and T. J. Cui, "A tunable metamaterial absorber using varactor diodes," *New Journal of Physics*, vol. 15, no. 4, p. 043049, 2013.

[11] W. Withayachumnankul, C. Fumeaux, and D. Abbott, "Planar array of electric-LC resonators with broadband tunability," *IEEE Antennas & Wireless Propagation Letters*, vol. 10, pp. 577-580, 2011.

[12] B. Zhu, Y. Feng, J. Zhao, C. Huang, and T. Jiang, "Switchable metamaterial reflector/absorber for different polarized electromagnetic waves," *Applied Physics Letters*, vol. 97, no. 5, pp. 051906-051906-3, 2010.

[13] E. Poutrina, "Analysis of nonlinear electromagnetic metamaterials," *New Journal of Physics*, vol. 12, no. 9, 2010.

[14] S. Larouche, A. Rose, E. Poutrina, D. Huang, and D. R. Smith, "Experimental determination of the quadratic nonlinear magnetic susceptibility of a varactor-loaded split ring resonator metamaterial," *Applied Physics Letters*, vol. 97, no. 1, pp. 011109-011109-3, 2010.

[15] D. Huang, E. Poutrina, and D. R. Smith, "Analysis of the power dependent tuning of a varactor-loaded metamaterial at microwave frequencies," *Applied Physics Letters*, vol. 96, no. 10, pp. 104104-104104-3, 2010.

[16] B. Wang, J. Zhou, T. Koschny, and C. M. Soukoulis, "Nonlinear properties of split-ring resonators," *Optics Express*, vol. 16, no. 20, pp. 16058-63, 2008.

[17] A. Velez, J. Bonache, and F. Martín, "Varactor-loaded complementary split ring resonators (VLCSRR) and their application to tunable metamaterial transmission lines," *IEEE Microwave and Wireless Components Letters*, vol. 18, no. 1, pp. 28-30, 2008.

[18] Y. Cheng, Y. Nie, X. Wang, and R. Gong, "Adjustable low frequency and broadband metamaterial absorber based on magnetic rubber plate and cross resonator," *Journal of Applied Physics*, vol. 115, no. 64902, pp. 064902-064902-5, 2014.

[19] Y. Yong-Jun, H. Yong-Jun, W. Guang-Jun, Z. Jing-Ping, S. Hai-Bin, and O. Gordon, "Tunable broadband metamaterial absorber consisting of ferrite slabs and a copper wire," *Chinese Physics B*, vol. 21, no. 3, pp. 504-508, 2012.

[20] Y. Poo, R. X. Wu, G. H. He, and P. Chen, "Experimental verification of a tunable left-handed material by bias magnetic fields," *Applied Physics Letters*, vol. 96, no. 16, pp. 161902-161902-3, 2010.

[21] T. H. Hand and S. A. Cummer, "Frequency tunable electromagnetic metamaterial using ferroelectric loaded split rings," *Journal of Applied Physics*, vol. 103, no. 6, p. 066105, 2008.

[22] D. Shrekenhamer, W.-C. Chen, and W. J. Padilla, "Liquid crystal tunable metamaterial absorber," *Physical Review Letters*, vol. 110, no. 17, p. 177403, 2013.

[23] Q. Zhao, *et al.*, "Electrically tunable negative permeability metamaterials based on nematic liquid crystals," *Applied Physics Letters*, vol. 90, no. 1, p. 011112, 2007.

[24] P. Pitchappa, *et al.*, "Micro-electro-mechanically tunable metamaterial with enhanced electro-optic performance," *Applied Physics Letters*, vol. 104, no. 15, p. 151104, 2014.

[25] C. Sabah, "Tunable metamaterial design composed of triangular split ring resonator and wire strip for

S-and C-microwave bands," *Progress In Electromagnetics Research B*, vol. 22, pp. 341-357, 2010.
[26] J. Wang, *et al.*, "A tunable left-handed metamaterial based on modified broadside-coupled split-ring resonators," *Progress in Electromagnetics Research Letter*, vol. 6, pp. 35-45, 2009.
[27] M. Lapine, D. Powell, M. Gorkunov, I. Shadrivov, R. Marqués, and Y. Kivshar, "Structural tunability in metamaterials," *Applied Physics Letters*, vol. 95, no. 8, p. 084105, 2009.
[28] J. Wang, S. Qu, Z. Xu, and H. Ma, "A controllable magnetic metamaterial: split-ring resonator with rotated inner ring," *IEEE Transactions on Antennas & Propagation*, vol. 56, no. 7, pp. 2018-2022, 2008.
[29] D. Ye, K. Chang, L. Ran, and H. Xin, "Microwave gain medium with negative refractive index," *Nat. Commun.*, vol. 5, p. 5841, 2014.
[30] X. Chen, T. M. Grzegorczyk, B. I. Wu, P. J. Jr, and J. A. Kong, "Robust method to retrieve the constitutive effective parameters of metamaterials," *Physical Review E*, vol. 70, no. 1 pt 2, pp. 811-811, 2004.
[31] J. Zhou, T. Koschny, L. Zhang, and G. Tuttle, "Experimental demonstration of negative index of refraction," *Applied Physics Letters*, vol. 88, no. 22, pp. 221103-221103-3, 2006.
[32] I. Bahl and P. Bhartia, *Microwave Solid State Circuit Design*. Wiley, 2003.
[33] S. Ghosh and A. Chakrabarty, "Estimation of capacitance of different conducting bodies by the method of rectangular subareas," *Journal of Electrostatics*, vol. 66, no. 3-4, pp. 142-146, 2008.
[34] O. Sydoruk, E. Tatartschuk, E. Shamonina, and L. Solymar, "Analytical formulation for the resonant frequency of split rings," *Journal of Applied Physics*, vol. 105, no. 1, pp. 014903-014903-4, 2009.
[35] Available: http://www.skyworksinc.com/uploads/documents/SMV123x_Series_200058W.pdf
[36] A. Sarkhel, D. Mitra, and S. R. B. Chaudhuri, "A compact metamaterial with multi-band negative-index characteristics," *Applied Physics A*, vol. 122, no. 4, pp. 1-10, 2016.

Analysis of Random Nonuniform Transmission Line Response under Plane-Wave Illumination with a Perturbation Decomposition-Polynomial Chaos Expansion Method

Jinpeng Yang, Xiaoying Sun, Yu Zhao, Jian Chen, and Hanqing Wang

College of Communication Engineering
Jilin University, Chang Chun, 130012, China
yangjp15@mails.jlu.edu.cn, sunxy@jlu.edu.cn, yzhao@jlu.edu.cn,
chenjian@jlu.edu.cn, hqwang16@mails.jlu.edu.cn

Abstract **─** A perturbation decomposition-polynomial chaos expansion method is presented to evaluate the electromagnetic effects of random nonuniform transmission line under plane-wave illumination. The nonuniformity is represented as perturbation with respect to the reference uniform transmission line. Moreover, by expanding the unknown random parameters in terms of orthogonal polynomials, the stochastic transmission line equation is projected into a set of deterministic transmission line equations. Numerical simulations are presented for several typical deterministic and random nonuniform transmission lines above an ideal ground. The results show that the proposed perturbation decomposition-polynomial chaos expansion method is accurate and computationally efficient compared with the traditional uniform cascaded section method and Monte Carlo method.

Index Terms **─** Deterministic nonuniform transmission line, parameter uncertainty, perturbation decomposition, plane-wave illumination, polynomial chaos expansion, random nonuniform transmission line.

I. INTRODUCTION

Cables and wires are usually the most sensitive parts in the electromagnetic compatibility problems of electrical and electronic systems. Owing to the mechanical manufacturing tolerances or manual installation manner errors, uncertainty [1,2] and nonuniformity [3-8] of transmission line (TL) are often encountered in practical applications, such as linearly tapered micro-strip line [3], interconnects subject to line-edge roughness [4], twisted pair [5], and undesired asymmetry differential lines [6], which may significantly affect the signal integrity and immunity. The intentional/unintentional electromagnetic interference in the free space may also aggravate the distortion effect. Therefore, it is of great significance to analyze the effect of randomness and nonuniformity on the response of TL under plane-wave illumination.

Transmission line theory [9] has been investigated for a long time. For a deterministic uniform transmission line (DUTL), the coupling mechanism is well established and has been overviewed in [10,11]. For a random uniform transmission line (RUTL), several methods have been proposed [12-16]. A direct method is the Monte Carlo (MC) method [12,13], which collects statistical information through huge samplings of random parameters to perform extensive repeated simulations of deterministic models. Although robust, MC has a large computational load. Another approach called the polynomial chaos expansion (PCE) method [14-16], which describes the statistical behavior through the orthogonal basis of a series of random variables, is fairly accurate and much faster than the MC method.

For a deterministic nonuniform transmission line (DNTL), the conventional approach is the uniform cascaded section (UCS) method [9]. UCS tackles the nonuniformity problem by subdividing the DNTL into large local uniform sections [17-21], thus leading to long computation time. Recently, a computationally efficient method called the equivalent source method [22] has been proposed to cope with DNTL. Subsequently, it has been extended to the perturbation decomposition technique (PDT) to cope with the crosstalk problem of different types of DNTL [3-8]. However, studies on the electromagnetic effect of random nonuniform transmission lines (RNTL) are scant. Moreover, the PDT is limited to DNTL, and cannot be directly applied to RNTL. So far, the PDT has only been applied to the crosstalk problems, and the ability of coping with DNTL under plane-wave illumination has not been verified.

Therefore, an N^{th}-order perturbation decomposition-M^{th}-order polynomial chaos expansion method ((N^{th}, M^{th})-order PD-PCE) is presented to analyze the RNTL response under external plane-wave illumination in this paper. The nonuniformity of TL is modeled as an equivalent distribution source for the reference uniform transmission line. Subsequently, based on the orthogonal

Submitted On: December 3, 2017
Accepted On: December 24, 2018

polynomial expansion of unknown random parameters, the stochastic transmission line equation is projected into a set of deterministic transmission line equations through a stochastic Galerkin method.

The rest of this paper is structured as follows. The derivation of the PD-PCE method is demonstrated in Section II. In Section III, the feasibility and strength of the PD-PCE method are validated by applying it to several typical simplifying RNTLs. Finally, a summary is given in Section IV.

II. PERTURBATION DECOMPOSITION-POLYNOMIAL CHAOS EXPANSION METHOD

In this section, the general solution of RNTL under plane-wave illumination is derived. Four cases of RNTL commonly observed in practical applications are considered, including vibrating RNTL, as shown in Figs. 1 (a)–(b), and floating RNTL, as shown in Figs. 1 (c)–(d). The radius of the four cases of RNTL is r_a. The left and right ends of RNTL are terminated with the impedances Z_L and Z_R, respectively. The heights of the four cases of RNTL are defined as follows:

$$\begin{aligned} h(z,\varepsilon) &= H_1 + 2\cdot(\delta_h\cdot\varepsilon)\cdot z/L && :\text{case } a,\\ h(z,\varepsilon) &= (H_2 - H_1 - \delta_h\cdot\varepsilon)\cdot(2\cdot z/L)^2 + H_1 + \delta_h\cdot\varepsilon && :\text{case } b,\\ h(z,\varepsilon) &= H_1 + \delta_h\cdot\varepsilon + 2\cdot(H_2 - H_1)\cdot z/L && :\text{case } c,\\ h(z,\varepsilon) &= (H_2 - H_1)\cdot(2\cdot z/L)^2 + H_1 + \delta_h\cdot\varepsilon && :\text{case } d, \end{aligned} \tag{1}$$

where $z\in[-L/2, L/2]$, L is the length of the RNTL in the z direction. H_1 is the height of the RNTL at $z=0$, H_2 is the height of the RNTL at $z=L/2$, ε is the normalized random variable, which is assumed to be uniformly distributed in [-1,1]. δ_h is the uncertainty coefficient.

In particular, for case *c* and case *d*, the RNTL becomes DNTL when $\delta_h = 0$ and $H_1 \neq H_2$, and the RNTL becomes RUTL when $\delta_h \neq 0$ and $H_1 = H_2$. Both DNTL and RUTL are special cases of RNTL.

There are two main steps for the construction of the proposed (N^{th}, P^{th})-order PD-PCE method for RNTL. In the first step, the perturbation solution for the RNTL under plane-wave illumination is derived; therefore, the RNTL equation is converted to an RUTL equation. In the second step, the RUTL equation is converted to a DUTL equation by applying the polynomial chaos theory.

A. Plane wave parameters

As shown in Fig. 2, considering an incident plane-wave electric field $\vec{E}^{inc}$ with amplitude E_0 described by:

$$\vec{E}^{inc} = E_0\left(e_x\vec{x} + e_y\vec{y} + e_z\vec{z}\right)e^{-j\vec{k}\cdot\vec{r}}, \tag{2}$$

where $\vec{r}$ is the observation position vector, and the scalar components e_x, e_y, and e_z in the direction of unit vectors $\hat{x}$, $\hat{y}$, and $\hat{z}$, respectively, are defined as:

$$\begin{aligned} e_x &= \cos\alpha\cos\theta\cos\varphi - \sin\alpha\sin\varphi,\\ e_y &= \cos\alpha\cos\theta\sin\varphi + \sin\alpha\cos\varphi,\\ e_z &= -\cos\alpha\sin\theta, \end{aligned} \tag{3}$$

where α is the polarization angle, θ is the elevation angle, and φ is the azimuth angle. The wave vector $\vec{k}$ with free space wave number k_0 is defined as:

$$\begin{aligned} \vec{k} &= k_x\hat{x} + k_y\hat{y} + k_z\hat{z}\\ &= k_0\sin\theta\cos\varphi\hat{x} + k_0\sin\theta\sin\varphi\hat{y} + k_0\cos\theta\hat{z}, \end{aligned} \tag{4}$$

where k_x, k_y, and k_z are the components of the wave vector along the unit vectors $\hat{x}$, $\hat{y}$, and $\hat{z}$, respectively.

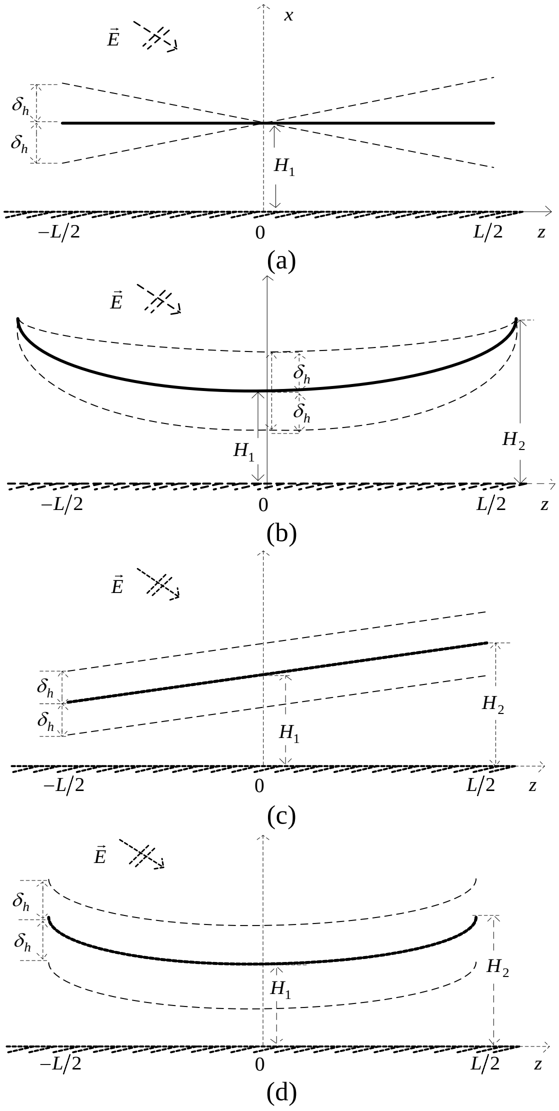

Fig. 1. (a) Case *a*: Random vibrating nonuniform straight transmission line. (b) Case *b*: Random vibrating nonuniform bending transmission line. (c) Case *c*: Random floating nonuniform straight transmission line. (d) Case *d*: Random floating nonuniform bending transmission line.

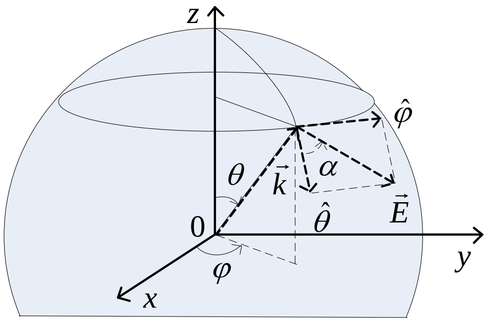

Fig. 2. Plane-wave incident direction.

Considering the reflection effect of ground, total electric field is the sum of the incident and reflection fields, and the z component $E_z^{tot}(z,\varepsilon)$ and x component $E_x^{tot}(z,\varepsilon)$ of the total electric field are given as follows:

$$\begin{aligned} E_z^{tot}(z,\varepsilon) &= -2jE_0e_z\sin\left(k_xh(z,\varepsilon)\right)e^{-j\left(k_yy+k_zz\right)}, \\ E_x^{tot}(z,\varepsilon) &= \ \ 2E_0e_x\cos\left(k_xh(z,\varepsilon)\right)e^{-j\left(k_yy+k_zz\right)}. \end{aligned} \tag{5}$$

B. Perturbation decomposition of random nonuniform transmission line equation

The Agrawal formula [11], which describes field-to-line coupling for an RNTL, is given by:

$$\begin{aligned} &\frac{d}{dz}V^s(z,\varepsilon)+j\omega L(z,\varepsilon)I(z,\varepsilon)=V_F^{'}(z,\varepsilon), \\ &\frac{d}{dz}I(z,\varepsilon)+j\omega C(z,\varepsilon)V^s(z,\varepsilon)=0, \end{aligned} \tag{6}$$

where $V^s(z,\varepsilon)$ and $I(z,\varepsilon)$ define the random scattering voltage and current of RNTL, respectively. $L(z,\varepsilon)$ and $C(z,\varepsilon)$ are the per unit length (p.u.l.) random inductance and capacitance of the RNTL, respectively. The distributed voltage source $V_F^{'}(z,\varepsilon)$ is defined as:

$$V_F^{'}(z,\varepsilon)=E_z^{tot}(z,\varepsilon)\cdot\cos\left(\eta(z,\varepsilon)\right)+E_x^{tot}(z,\varepsilon)\cdot\sin\left(\eta(z,\varepsilon)\right), \tag{7}$$

where $\eta(z,\varepsilon)$ is the position-dependent random inclination angle of the RNTL. The total voltage of the RNTL is defined as:

$$V(z,\varepsilon)=V^s(z,\varepsilon)-V^{ex}(z,\varepsilon), \tag{8}$$

where the excitation voltage $\boldsymbol{V}^{ex}(z,\varepsilon)$ is defined as:

$$V^{ex}(z,\varepsilon)=\int_0^{h(z,\varepsilon)}E_x^{tot}(z,\varepsilon)dx. \tag{9}$$

To deal with the nonuniform problem of the TL, the perturbation decomposition technique [5] is applied to the scattering voltage, current, capacitance, and inductance as follows:

$$\begin{aligned} &V^s(z,\varepsilon)\approx V_0^s(z,\varepsilon)+V_1^s(z,\varepsilon)+\ldots+V_N^s(z,\varepsilon), \\ &I(z,\varepsilon)\approx I_0(z,\varepsilon)+I_1(z,\varepsilon)+\ldots+I_N(z,\varepsilon), \\ &C(z,\varepsilon)=C_0(\varepsilon)+C_1(z,\varepsilon), \\ &L(z,\varepsilon)=L_0(\varepsilon)+L_1(z,\varepsilon), \end{aligned} \tag{10}$$

where V_0^s and I_0 are the 0th-order perturbation random scattering voltage and current, respectively. V_n^s and I_n $(n=1,2,\ldots,N)$ are the nth-order perturbation random scattering voltage and current, respectively. N is the truncated order. C_0 (C_1) and L_0 (L_1) are the 0th-order (1st-order) perturbation p.u.l. random capacitance and inductance, respectively.

Substituting equation (10) into equation (6), the RNTL equation can be decomposed to 0th-order and nth-order $(n=1,2,\ldots,N)$ RUTL equations, as follows:

$$\begin{aligned} &\frac{d}{dz}V_0^s(z,\varepsilon)+j\omega L_0(\varepsilon)I_0(z,\varepsilon)=V_F^{'}(z,\varepsilon), \\ &\frac{d}{dz}I_0(z,\varepsilon)+j\omega C_0(\varepsilon)V_0^s(z,\varepsilon)=0, \end{aligned} \tag{11}$$

$$\begin{aligned} &\frac{d}{dz}V_n^s(z,\varepsilon)+j\omega L_0(\varepsilon)I_n(z,\varepsilon)=-j\omega L_1(z,\varepsilon)I_{n-1}(z,\varepsilon), \\ &\frac{d}{dz}I_n(z,\varepsilon)+j\omega C_0(\varepsilon)V_n^s(z,\varepsilon)=-j\omega C_1(z,\varepsilon)V_{n-1}^s(z,\varepsilon). \end{aligned} \tag{12}$$

For the 0th-order perturbation equation (11), the excitation term directly originates from the incident plane-wave. For the nth-order perturbation equation (12), the excitation terms originate from the (n-1)th-order perturbation scattering voltage and current.

C. Polynomial chaos expansion

To solve the RUTL equations (11) and (12), the PCE method [14] was adopted to expand the random variable in equations (11) and (12) as follows:

$$\begin{aligned} &V_0^s(z,\varepsilon)=\sum_{p=0}^{P}V_0^{s,p}(z)\cdot\phi_p(\varepsilon),V_n^s(z,\varepsilon)=\sum_{p=0}^{P}V_n^{s,p}(z)\cdot\phi_p(\varepsilon), \\ &I_0(z,\varepsilon)=\sum_{p=0}^{P}I_0^p(z)\cdot\phi_p(\varepsilon),\ I_n(z,\varepsilon)=\sum_{p=0}^{P}I_n^p(z)\cdot\phi_p(\varepsilon), \\ &V_F^{'}(z,\varepsilon)=\sum_{p=0}^{P}V_F^{p'}(z)\cdot\phi_p(\varepsilon), \end{aligned} \tag{13a}$$

$$\begin{aligned} &C_0(\varepsilon)=\sum_{p=0}^{P}C_0^p\cdot\phi_p(\varepsilon),C_1(z,\varepsilon)=\sum_{p=0}^{P}C_1^p(z)\cdot\phi_p(\varepsilon), \\ &L_0(\varepsilon)=\sum_{p=0}^{P}L_0^p\cdot\phi_p(\varepsilon),\ L_1(z,\varepsilon)=\sum_{p=0}^{P}L_1^p(z)\cdot\phi_p(\varepsilon), \end{aligned} \tag{13b}$$

where $V_0^{s,p}$ $(V_n^{s,p})$ and I_0^p (I_n^p) represent the (0th, pth)-order ((nth, pth)-order) PD-PCE coefficients for scattering voltage and current, respectively. $V_F^{p'}$ represents the pth-order PCE coefficients for the distributed voltage source. C_0^p (C_1^p) and L_0^p (L_1^p) represent the (0th, pth)-order ((1st, pth)-order) PD-PCE coefficients for p.u.l. capacitance and inductance, respectively. $\phi_p(\varepsilon)$ is a pth-order polynomial. The random variable is assumed to be uniformly distributed; hence, the Legendre orthogonal polynomials are appropriate for this case [14], as shown in Table 1. For the random variables of number q and order m, the total number of expansion items is $(P+1)!=(p+q)!/(p!q!)$. In this study, there is only one random variable; hence, q=1.

Table 1: Legendre polynomial for one random variable

Order *p*	**p^{th}-order polynomial ϕ_p**	$\langle \phi_p, \phi_p \rangle$
0	1	1
1	ε	1/3
2	$\left(3\varepsilon^2 - 1\right)/2$	1/5
…	…	…
p	$\frac{1}{2^p\, p!}\frac{\partial}{\partial \varepsilon^p}\left(\varepsilon^2 - 1\right)^p$	$1/\left(2p+1\right)$

Substituting equation (13) into (11), the original 0^{th}-order perturbation RUTL equation is expanded as:

$$\begin{aligned}
&\frac{d}{dz}\sum_{p=0}^{P_0} V_0^{s,p}\left(z\right)\phi_p\left(\varepsilon\right) + j\omega\sum_{t=0}^{P_T} L_0^t\phi_t\left(\varepsilon\right)\sum_{p=0}^{P_0} I_0^p\left(z\right)\phi_p\left(\varepsilon\right) = \\
&\qquad\qquad \sum_{p=0}^{P_0} V_F^{p'}\left(z\right)\phi_p\left(\varepsilon\right), \qquad (14)\\
&\frac{d}{dz}\sum_{p=0}^{P_0} I_0^p\left(z\right)\phi_p\left(\varepsilon\right) + j\omega\sum_{t=0}^{P_T} C_0^t\phi_t\left(\varepsilon\right)\sum_{p=0}^{P_0} V_0^{s,p}\left(z\right)\phi_p\left(\varepsilon\right) = 0,
\end{aligned}$$

where P_0 and P_T are the expansion orders. Through a stochastic Galerkin method, equation (14) was projected to the Legendre orthogonal basis as follows:

$$\begin{aligned}
&\frac{d}{dz}\sum_{p=0}^{P_0} V_0^{s,p}\left(z\right)\left\langle\phi_p\left(\varepsilon\right),\phi_k\left(\varepsilon\right)\right\rangle + j\omega\sum_{t=0}^{P_T}\sum_{p=0}^{P_0} L_0^t I_0^p\left(z\right)\left\langle\phi_t\left(\varepsilon\right)\phi_p\left(\varepsilon\right),\phi_k\left(\varepsilon\right)\right\rangle = \\
&\qquad\qquad \sum_{p=0}^{P_1} V_F^{p'}\left(z\right)\left\langle\phi_p\left(\varepsilon\right),\phi_k\left(\varepsilon\right)\right\rangle, \qquad (15)\\
&\frac{d}{dz}\sum_{p=0}^{P_0} I_0^p\left(z\right)\left\langle\phi_p\left(\varepsilon\right),\phi_k\left(\varepsilon\right)\right\rangle + j\omega\sum_{t=0}^{P_T}\sum_{p=0}^{P_0} C_0^t V_0^{s,p}\left(z\right)\left\langle\phi_t\left(\varepsilon\right)\phi_p\left(\varepsilon\right),\phi_k\left(\varepsilon\right)\right\rangle = 0.
\end{aligned}$$

The symbol $\langle\ ,\ \rangle$ represents the inner product over the definition domain of the random variable. Solving (15), the following 0^{th}-order perturbation augmented equation in matrix form can be obtained.

$$\frac{d}{dz}\begin{bmatrix}\boldsymbol{V}_0^s\left(z\right)\\ \boldsymbol{I}_0\left(z\right)\end{bmatrix} + \begin{bmatrix}\boldsymbol{0} & j\omega\boldsymbol{L}_0\\ j\omega\boldsymbol{C}_0 & \boldsymbol{0}\end{bmatrix}\begin{bmatrix}\boldsymbol{V}_0^s\left(z\right)\\ \boldsymbol{I}_0\left(z\right)\end{bmatrix} = \begin{bmatrix}\boldsymbol{V}_F^{'}\left(z\right)\\ \boldsymbol{0}\end{bmatrix}, \qquad (16)$$

where $\boldsymbol{V}_0^s\left(z\right)$ and $\boldsymbol{I}_0\left(z\right)$ are the 0^{th}-order perturbation $\left(P_0+1\right)\times 1$ scattering voltage and current vector, respectively. $\boldsymbol{V}_F^{'}\left(z\right)$ is the 0^{th}-order $\left(P_0+1\right)\times 1$ distributed voltage source vector. $\boldsymbol{L}_0$ and $\boldsymbol{C}_0$ are the 0^{th}-order perturbation $\left(P_0+1\right)\times\left(P_0+1\right)$ inductance and capacitance matrix, respectively. The i^{th} row and j^{th} column $\left(i, j = 1, 2, ..., P_0+1\right)$ of $\boldsymbol{L}_0$ and $\boldsymbol{C}_0$ are given as follows:

$$\boldsymbol{L}_0\Big|_{ij} = \sum_{p=0}^{P_0} L_0^p\alpha_{pji}, \boldsymbol{C}_0\Big|_{ij} = \sum_{p=0}^{P_0} C_0^p\alpha_{pji}, \qquad (17)$$

where,

$$\alpha_{pji} = \left\langle\phi_p\phi_j,\phi_i\right\rangle / \left\langle\phi_i,\phi_i\right\rangle. \qquad (18)$$

Similarly, substituting equation (13) into (12), the original n^{th}-order perturbation RUTL equation becomes:

$$\begin{aligned}
&\frac{d}{dz}\sum_{p=0}^{P_n} V_n^{s,p}\left(z\right)\phi_p\left(\varepsilon\right) + j\omega\sum_{t=0}^{P_T} L_0^t\phi_t\left(\varepsilon\right)\sum_{p=0}^{P_n} I_n^p\left(z\right)\phi_p\left(\varepsilon\right) = \\
&\qquad -j\omega\sum_{t=0}^{P_T} L_1^t\left(z\right)\phi_t\left(\varepsilon\right)\sum_{p=0}^{P_{n-1}} I_{n-1}^p\left(z\right)\phi_p\left(\varepsilon\right),\\
&\frac{d}{dz}\sum_{p=0}^{P_n} I_n^p\left(z\right)\phi_p\left(\varepsilon\right) + j\omega\sum_{t=0}^{P_T} C_0^t\phi_t\left(\varepsilon\right)\sum_{p=0}^{P_n} V_n^{s,p}\left(z\right)\phi_p\left(\varepsilon\right) = \qquad (19)\\
&\qquad -j\omega\sum_{t=0}^{P_T} C_1^t\left(z\right)\phi_t\left(\varepsilon\right)\sum_{p=0}^{P_{n-1}} V_{n-1}^{s,p}\left(z\right)\phi_p\left(\varepsilon\right),
\end{aligned}$$

where $P_n = P_T + P_{n\text{-}1}$ $\left(n = 1, 2, ..., N\right)$. Projecting equation (19) to the Legendre orthogonal basis, the following equations can be obtained:

$$\begin{aligned}
&\frac{d}{dz}\sum_{p=0}^{P_n} V_n^{s,p}\left(z\right)\left\langle\phi_p\left(\varepsilon\right),\phi_k\left(\varepsilon\right)\right\rangle + j\omega\sum_{t=0}^{P_T}\sum_{p=0}^{P_n} L_0^t I_n^p\left(z\right)\left\langle\phi_t\left(\varepsilon\right)\phi_p\left(\varepsilon\right),\phi_k\left(\varepsilon\right)\right\rangle = \\
&\qquad -j\omega\sum_{t=0}^{P_T}\sum_{p=0}^{P_{n-1}} L_1^t\left(z\right) I_{n-1}^p\left(z\right)\left\langle\phi_t\left(\varepsilon\right)\phi_p\left(\varepsilon\right),\phi_k\left(\varepsilon\right)\right\rangle, \qquad (20)\\
&\frac{d}{dz}\sum_{p=0}^{P_n} I_n^p\left(z\right)\left\langle\phi_p\left(\varepsilon\right),\phi_k\left(\varepsilon\right)\right\rangle + j\omega\sum_{t=0}^{P_T}\sum_{p=0}^{P_n} C_0^t V_n^{s,p}\left(z\right)\left\langle\phi_t\left(\varepsilon\right)\phi_p\left(\varepsilon\right),\phi_k\left(\varepsilon\right)\right\rangle = \\
&\qquad -j\omega\sum_{t=0}^{P_T}\sum_{p=0}^{P_{n-1}} C_1^t\left(z\right) V_{n-1}^{s,p}\left(z\right)\left\langle\phi_t\left(\varepsilon\right)\phi_p\left(\varepsilon\right),\phi_k\left(\varepsilon\right)\right\rangle.
\end{aligned}$$

Solving (20), the n^{th}-order perturbation augmented equation in matrix form can be obtained as follows:

$$\frac{d}{dz}\begin{bmatrix}\boldsymbol{V}_n^s\left(z\right)\\ \boldsymbol{I}_n\left(z\right)\end{bmatrix} + \begin{bmatrix}\boldsymbol{0} & j\omega\boldsymbol{L}_0\\ j\omega\boldsymbol{C}_0 & \boldsymbol{0}\end{bmatrix}\begin{bmatrix}\boldsymbol{V}_n^s\left(z\right)\\ \boldsymbol{I}_n\left(z\right)\end{bmatrix} = \begin{bmatrix}\boldsymbol{V}_F^{n'}\left(z\right)\\ \boldsymbol{I}_F^{n'}\left(z\right)\end{bmatrix}, \qquad (21)$$

where the n^{th}-order distributed voltage source vector $\boldsymbol{V}_F^{n'}\left(z\right)$ and the distributed current source vector $\boldsymbol{I}_F^{n'}\left(z\right)$ are:

$$\begin{bmatrix}\boldsymbol{V}_F^{n'}\left(z\right)\\ \boldsymbol{I}_F^{n'}\left(z\right)\end{bmatrix} = -\begin{bmatrix}\boldsymbol{0} & j\omega\boldsymbol{L}_1\\ j\omega\boldsymbol{C}_1 & \boldsymbol{0}\end{bmatrix}\begin{bmatrix}\boldsymbol{V}_{n-1}^s\left(z\right)\\ \boldsymbol{I}_{n-1}\left(z\right)\end{bmatrix}, \qquad (22)$$

where $\boldsymbol{L}_1$ and $\boldsymbol{C}_1$ are the 1^{st}-order perturbation $\left(P_{n-1}+1\right)\times\left(P_{n-1}+1\right)$ inductance and capacitance matrix, respectively. The i^{th} row and j^{th} column $\left(i, j = 1, 2, ..., P_n+1\right)$ of $\boldsymbol{L}_1$ and $\boldsymbol{C}_1$ are given as follows:

$$\boldsymbol{L}_1\Big|_{ij} = \sum_{p=0}^{P_{n-1}} L_1^p\alpha_{pji}, \boldsymbol{C}_1\Big|_{ij} = \sum_{p=0}^{P_{n-1}} C_1^p\alpha_{pji}. \qquad (23)$$

D. Modal decomposition

As $\boldsymbol{L}_0$ and $\boldsymbol{C}_0$ are full matrixes, the scattering voltage and current vector in (16) are coupled. The similarity transformation method [9] is used to decouple equation (16). Through voltage (current) transformation matrix $\boldsymbol{T}_V$ ($\boldsymbol{T}_I$), the voltage vector $\boldsymbol{V}_0^s$ and current vector $\boldsymbol{I}_0$ were cast into modal voltage vector $\boldsymbol{V}_{m,0}^s$ and modal current vector $\boldsymbol{I}_{m,0}$ as follows:

$$\begin{bmatrix}\boldsymbol{V}_0^s\left(z\right)\\ \boldsymbol{I}_0\left(z\right)\end{bmatrix} = \begin{bmatrix}\boldsymbol{T}_V & \boldsymbol{0}\\ \boldsymbol{0} & \boldsymbol{T}_I\end{bmatrix}\begin{bmatrix}\boldsymbol{V}_{m,0}^s\left(z\right)\\ \boldsymbol{I}_{m,0}\left(z\right)\end{bmatrix}. \qquad (24)$$

Substituting equation (24) into equation (16), the following 0th-order perturbation decoupled modal TL equation can be obtained:

$$\frac{d}{dz}\begin{bmatrix} \boldsymbol{V}_{m,0}^{s}(z) \\ \boldsymbol{I}_{m,0}(z) \end{bmatrix} + \begin{bmatrix} \boldsymbol{0} & j\omega \boldsymbol{L}_{m,0} \\ j\omega \boldsymbol{C}_{m,0} & \boldsymbol{0} \end{bmatrix} \begin{bmatrix} \boldsymbol{V}_{m,0}^{s}(z) \\ \boldsymbol{I}_{m,0}(z) \end{bmatrix} = \begin{bmatrix} \boldsymbol{V}_{Fm}^{'}(z) \\ \boldsymbol{0} \end{bmatrix}, \tag{25}$$

where $\boldsymbol{L}_{m,0}$ and $\boldsymbol{C}_{m,0}$ can be obtained by:

$$\boldsymbol{L}_{m,0} = \boldsymbol{T}_V^{-1} \boldsymbol{L}_0 \boldsymbol{T}_I,\ \boldsymbol{C}_{m,0} = \boldsymbol{T}_I^{-1} \boldsymbol{C}_0 \boldsymbol{T}_V, \tag{26}$$

and the modal distributed voltage source $\boldsymbol{V}_{Fm}^{'}(z) = \boldsymbol{T}_V^{-1} \boldsymbol{V}_F^{'}(z)$.

Similarly, the *n*th-order perturbation equation (21) can be decoupled as follows:

$$\frac{d}{dz}\begin{bmatrix} \boldsymbol{V}_{m,n}^{s}(z) \\ \boldsymbol{I}_{m,n}(z) \end{bmatrix} + \begin{bmatrix} \boldsymbol{0} & j\omega \boldsymbol{L}_{m,0} \\ j\omega \boldsymbol{C}_{m,0} & \boldsymbol{0} \end{bmatrix} \begin{bmatrix} \boldsymbol{V}_{m,n}^{s}(z) \\ \boldsymbol{I}_{m,n}(z) \end{bmatrix} = \begin{bmatrix} \boldsymbol{V}_{Fm}^{n'}(z) \\ \boldsymbol{I}_{Fm}^{n'}(z) \end{bmatrix}, \tag{27}$$

where the *n*th-order modal scattering voltage $\boldsymbol{V}_{m,n}^{s}(z)$ and modal current $\boldsymbol{I}_{m,n}(z)$ can be obtained as follows:

$$\begin{bmatrix} \boldsymbol{V}_{m,n}^{s}(z) \\ \boldsymbol{I}_{m,n}(z) \end{bmatrix} = \begin{bmatrix} \boldsymbol{T}_V & \boldsymbol{0} \\ \boldsymbol{0} & \boldsymbol{T}_I \end{bmatrix} \begin{bmatrix} \boldsymbol{V}_{n}^{s}(z) \\ \boldsymbol{I}_{n}(z) \end{bmatrix}, \tag{28}$$

and the *n*th-order modal distributed voltage source $\boldsymbol{V}_{Fm}^{n'}(z)$ and current source $\boldsymbol{I}_{Fm}^{n'}(z)$ can be obtained as follows:

$$\begin{bmatrix} \boldsymbol{V}_{Fm}^{n'}(z) \\ \boldsymbol{I}_{Fm}^{n'}(z) \end{bmatrix} = \begin{bmatrix} \boldsymbol{T}_V^{-1} & \boldsymbol{0} \\ \boldsymbol{0} & \boldsymbol{T}_I^{-1} \end{bmatrix} \begin{bmatrix} \boldsymbol{V}_{F}^{n'}(z) \\ \boldsymbol{I}_{F}^{n'}(z) \end{bmatrix}. \tag{29}$$

E. Boundary condition

Proper boundary conditions should be imposed to obtain the solution of equations (25) and (27). Using Thevenin equivalents of line terminations, the boundary condition for equations (11) and (12) can be written as:

$$\begin{aligned} V_0^{s}(\text{-}L/2,\varepsilon) &= V^{ex}(\text{-}L/2,\varepsilon) \text{-} Z_L I_0(L/2,\varepsilon), \\ V_0^{s}(L/2,\varepsilon) &= V^{ex}(L/2,\varepsilon) + Z_R I_0(L/2,\varepsilon), \end{aligned} \tag{30a}$$

$$\begin{aligned} V_n^{s}(\text{-}L/2,\varepsilon) &= \text{-}Z_L I_n(-L/2,\varepsilon), \\ V_n^{s}(L/2,\varepsilon) &= Z_R I_n(L/2,\varepsilon). \end{aligned} \tag{30b}$$

Substituting equation (13a) into equations (30a) and (30b), and expanding the excitation voltage $\boldsymbol{V}^{ex}(z,\varepsilon)$ with the same polynomials, the 0th-order and *n*th-order perturbation random boundary condition in equations (30a) and (30b) can be expanded into equations (31a) and (31b), respectively:

$$\begin{aligned} \sum_{p=0}^{P_0} V_0^{s,p}(\text{-}L/2)\phi_p(\varepsilon) &= \sum_{p=0}^{P_0} V_p^{ex}(\text{-}L/2)\phi_p(\varepsilon) \text{-} Z_L \sum_{p=0}^{P_0} I_0^{p}(\text{-}L/2)\phi_p(\varepsilon), \\ \sum_{p=0}^{P_0} V_0^{s,p}(L/2)\phi_p(\varepsilon) &= \sum_{p=0}^{P_0} V_p^{ex}(L/2)\phi_p(\varepsilon) + Z_R \sum_{p=0}^{P_0} I_0^{p}(L/2)\phi_p(\varepsilon), \end{aligned} \tag{31a}$$

$$\begin{aligned} \sum_{p=0}^{P_n} V_n^{s,p}(\text{-}L/2)\phi_p(\varepsilon) &= \text{-}Z_L \sum_{p=0}^{P_n} I_n^{p}(\text{-}L/2)\phi_p(\varepsilon), \\ \sum_{p=0}^{P_n} V_n^{s,p}(L/2)\phi_p(\varepsilon) &= Z_R \sum_{p=0}^{P_n} I_n^{p}(L/2)\phi_p(\varepsilon). \end{aligned} \tag{31b}$$

Similarly, through a stochastic Galerkin method, projecting equations (31a) and (31b) to the Legendre orthogonal basis, the 0th-order and *n*th-order perturbation boundary conditions can be obtained as follows:

$$\begin{aligned} V_0^{s,m}(\text{-}L/2) &= V_m^{ex}(\text{-}L/2) \text{-} Z_L I_0^{m}(\text{-}L/2), \\ V_0^{s,m}(L/2) &= V_m^{ex}(L/2) + Z_R I_0^{m}(L/2), \end{aligned} \tag{32a}$$

$$\begin{aligned} V_n^{s,m}(\text{-}L/2) &= \text{-}Z_L I_n^{m}(-L/2), \\ V_n^{s,m}(L/2) &= Z_R I_n^{m}(L/2). \end{aligned} \tag{32b}$$

F. RNTL terminal solution

Given the boundary conditions, the general solution of the 0th-order and *n*th-order perturbation modal equation can be easily solved, and thus, the final terminal solution for the voltage (current) of RNTL can be obtained by substituting these modal terms into equations (24), (28), (13), (10), and (8). For brevity, the solution is omitted here.

G. DNTL terminal solution

For DNTL, namely $\delta_h = 0$ and $H_1 \neq H_2$ in case *c* and case *d*, the induced voltage can be obtained by only taking the (*N*th, 0th)-order PD-PCE solution.

H. RUTL terminal solution

For RUTL, namely $\delta_h \neq 0$ and $H_1 = H_2$ in case *c*, the terminal solution can be obtained by only taking the (0th, *P*th)-order PD-PCE solution.

III. NUMERICAL RESULTS AND APPLICATIONS

In this section, numerical simulations were performed to validate the proposed (*N*th, *P*th)-order PD-PCE method for the RNTL above an ideal ground under plane-wave illumination. For all cases, the length of the TLs is $L = 1\,\text{m}$, the radius is $r_a = 0.5$ mm, and terminal resistances are $Z_L = Z_R = 50\,\Omega$. The amplitude of the electric field is $E_0 = 100$ V / m and the frequency band ranges from 5 MHz to 4 GHz. The frequency interval was set to 5 MHz. Without loss of generality, the incident angle was set as $\theta = \pi/3$, $\varphi = \pi/6$, and $\alpha = \pi/6$.

A. Deterministic response analysis

First, the deterministic response of a nonuniform TL under plane-wave illumination was analyzed to validate the proposed method. The parameters of the TLs are shown in Table 2, where DUTL is chosen for comparison. The UCS method [9], which divides the DNTL into 600 local uniform segments to ensure sufficient accuracy, was chosen for comparison.

Table 2: Geometrical parameters of transmission lines

Analyzing Scenarios		H_1 /mm	H_2 /mm	δ_h /mm
A.1	case *c*: DNTL	12	14	0
	Comparison case *c*: DUTL	12	12	0
A.2	case *d*: DNTL	10	12	0
	Comparison case *d*: DUTL	12	12	0

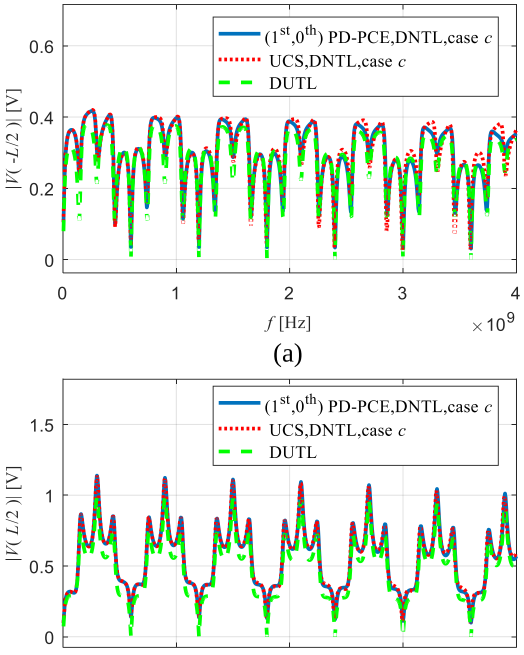

(a)

(b)

Fig. 3. Magnitude of induced voltage for DNTL of case *c* and the DUTL. (a) Induced voltage at the left end of the TL, and (b) induced voltage at the right end of TL.

A.1. DNTL of case *c*

Figures 3 (a) and (b) show the induced voltage at the left and right ends of the DNTL of case *c*, respectively. The blue curves are the results of the (1st, 0th)-order PD-PCE method. The dotted red curves are the results of the UCS method. It can be observed that at lower frequencies, the induced voltages derived from the PD-PCE method were consistent with those of UCS method at both ends of DNTL, whereas for frequencies above approximately 2 GHz, the induced voltage at the left end shows discrepancies for the two methods.

Figures 3 (a) and (b) also show the induced voltage (dashed green curves) at the left and right ends of the DUTL, respectively. For most frequencies, the induced voltage of the DNTL is larger than that of the DUTL.

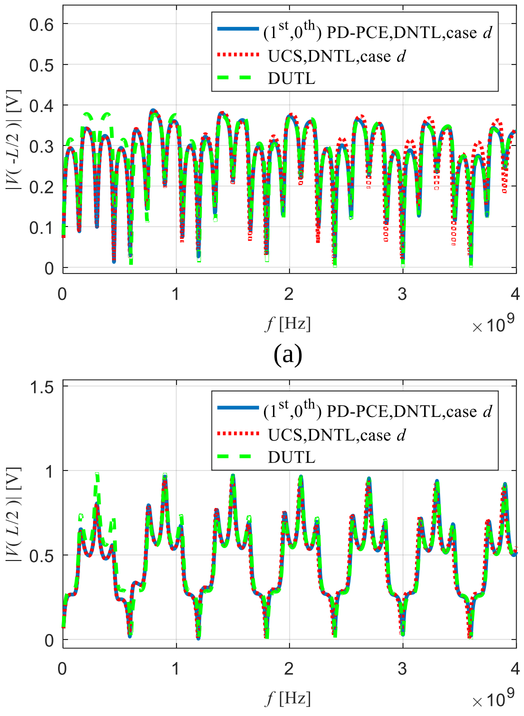

(a)

(b)

Fig. 4. Magnitude of induced voltage for the DNTL of case *d* and the DUTL. (a) Induced voltage at the left end of TL, and (b) induced voltage at the right end of TL.

A.2. DNTL of case *d*

Figures 4 (a) and (b) show the induced voltage at the left and right ends of the DNTL of case *d*, respectively. The blue curves are the results of the (1st, 0th)-order PD-PCE method for the DNTL. The dotted red curves are the results of the UCS method for the DNTL. Moreover, it can be observed that the induced voltage at the left end of the TL derived from the PD-PCE method is consistent with that derived from the UCS method at lower frequencies. However, for frequencies above approximately 2 GHz, the induced voltage at the left end shows discrepancies for the two methods. For the induced voltage at the right end of DNTL, at most frequency points, the results of the two methods are consistent with each other, which confirms the validity of the proposed method.

The induced voltage (dashed green curves) at the left and right ends of the DUTL is also shown in Figs. 4 (a) and (b), respectively. For most frequencies, the induced voltage of the DNTL is smaller than that of the DUTL, especially at lower frequencies.

Table 3 shows the comparison of computation time between the PD-PCE method and the UCS method. The simulations were performed on a workstation with an Intel Xeon CPU X5670 with clock frequency 2.93 GHz and 16 GB RAM. The (1st, 0th)-order PD-PCE method takes approximately 9.9 s for 800 frequency points, whereas the UCS method takes approximately 890.2 s for 800 frequency points. The proposed (1st, 0th)-order PD-PCE method is approximately 89.9 times faster than the UCS method while maintaining the same level of accuracy.

Table 3: CPU time of the (1st, 0th)-order PD-PCE method and UCS method

Method	**Order**	**Simulation Time /s**
UCS	--	890.2
PD-PCE	(1st, 0th)	9.9

Table 4: Parameters of the transmission line

Analyzing Scenarios		$\boldsymbol{H_1}$ **/mm**	$\boldsymbol{H_2}$ **/mm**	$\boldsymbol{\delta_h}$ **/mm**
B.1	case *a*	10	--	2
	Comparison case *a*: DUTL	10	--	0
B.2	case *b*	8	10	1
	Comparison case *b*: DUTL	10	10	0
B.3	case *c*	10	12	2
	Comparison case *c*: RUTL	10	10	2
B.4	case *d*	8	10	2
	Comparison case *d*: RUTL	10	10	2

B. Statistical response analysis of RNTL

In this section, the validity of the proposed PD-PCE method was confirmed. The MC method was chosen for comparison, which required 1000 simulations to provide sufficient samplings. The four cases of RNTL shown in Fig. 1 were analyzed. For case *a* and case *b*, DUTL was chosen for comparison. For case *c* and case *d*, RUTL was chosen for comparison. The parameters of the lines are shown in Table 4.

B.1. Random nonuniform transmission line of case *a*

Figs. 5 (a) and (b) show the probability density function (pdf) of the magnitude of the induced voltage at the right end of the RNTL for case *a* at *f* = 800 MHz and *f* = 3.5 GHz, respectively. The red curves are the results of the (1st, 5th)-order PD-PCE method, and the blue cross curves are the results of the MC method. It can be observed that the results of the two methods are consistent with each other at *f* = 800 MHz. However, there are minor discrepancies between the two methods at *f* = 3.5 GHz. This may be because the electromagnetic response of the TL is more sensitive to the variance of geometrical parameters at high frequencies.

Figures 6 (a) and (b) show the mean value and variance of the induced voltage (blue curves) at the right end of the RNTL of case *a* derived using the (1st, 5th)-order PD-PCE method, respectively. For comparison, Fig. 6 (a) shows the induced voltage at the right end of the DUTL (green dotted curves). It can be observed that the mean value of induced voltage of the RNTL equals the voltage of the DUTL, whereas the variance of RNTL exhibits periodical fluctuation.

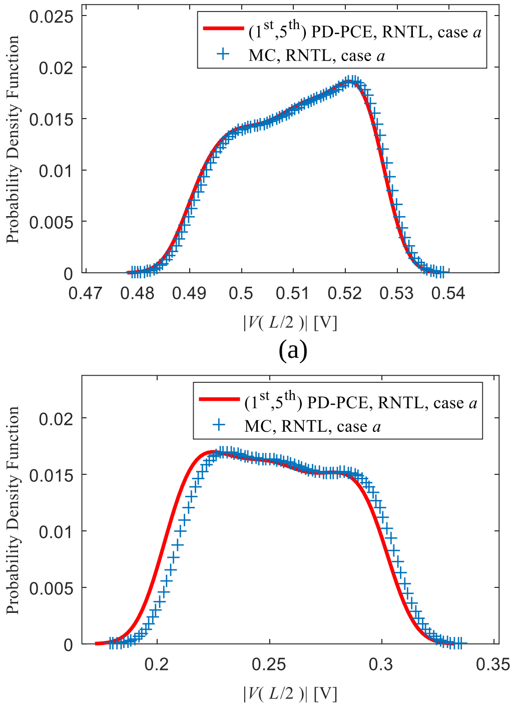

(a)

(b)

Fig. 5. Probability density function of induced voltage at the right end of the RNTL of case *a*: (a) *f* = 800 MHz, (b) *f* = 3.5 GHz.

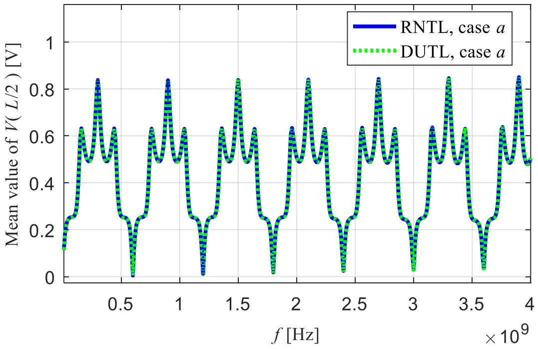

(a)

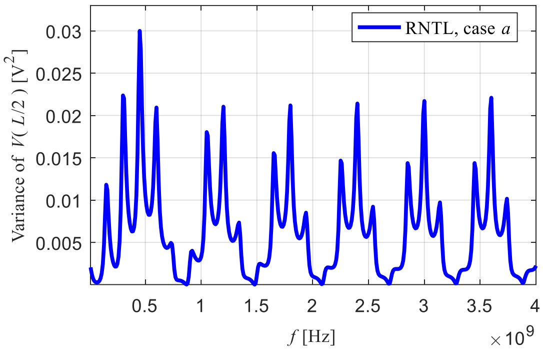

(b)

Fig. 6. (a) Induced voltage at the right end of the DUTL and mean value of induced voltage at the right end of the RNTL of case *a*. (b) Variance of the induced voltage at the right end of the RNTL of case *a*.

B.2. Random nonuniform transmission line of case b

Figures 7 (a) and (b) show the pdf of the magnitude of the induced voltage at the right end of the RNTL of case *b* at $f = 800$ MHz and $f = 3.5$ GHz, respectively. The red curves are the results of the (1^{st}, 5^{th})-order PD-PCE method, and the blue cross curves are the results of the MC method. It can be observed that the results of the two methods are consistent with each other.

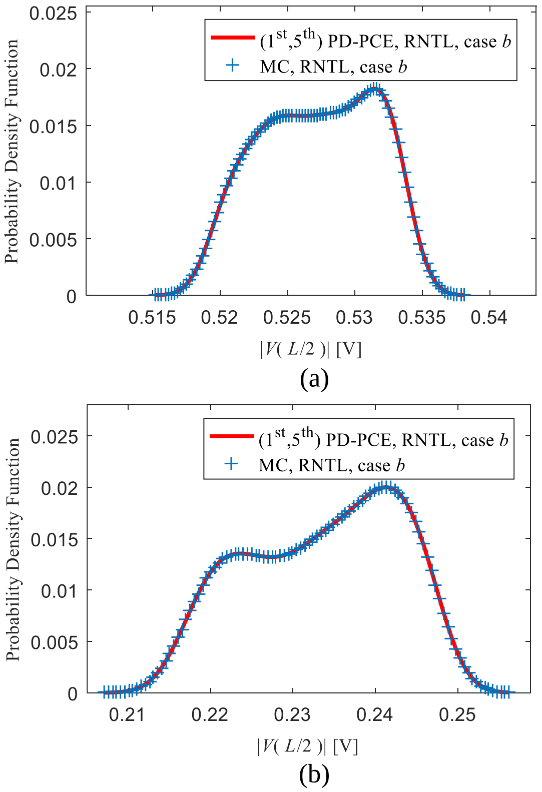

(a)

(b)

Fig. 7. Probability density function of induced voltage at the right end of the RNTL of case *b*: (a) $f = 800$ MHz, (b) $f = 3.5$ GHz.

Figures 8 (a) and (b) show the mean value and variance of induced voltage at the right end of the RNTL of case *b* obtained from the (1^{st}, 5^{th})-order PD-PCE method. Figure 8 (a) also shows the induced voltage at the right end of the DUTL. It can be observed that the mean value of voltage of the RNTL deviates from the voltage of the DUTL at lower frequencies, whereas the variance of the RNTL shows strong periodical fluctuation.

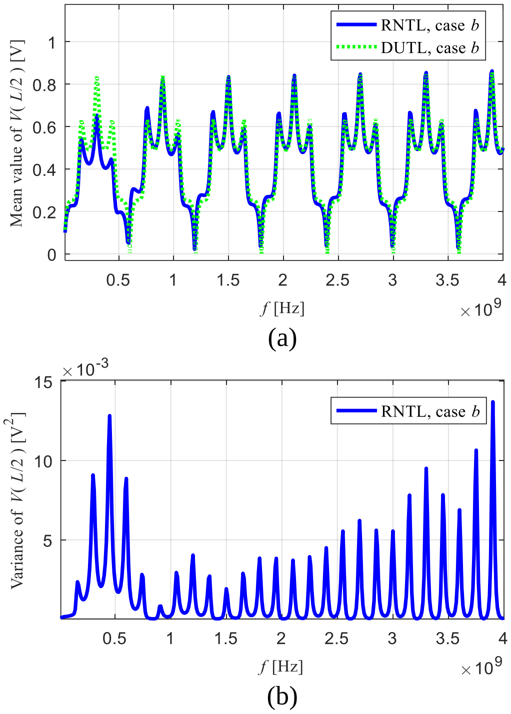

(a)

(b)

Fig. 8. (a) Induced voltage at the right end of the DUTL and the mean value of induced voltage at the right end of the RNTL of case *b*. (b) Variance of the induced voltage at the right end of the RNTL of case *b*.

B.3. Random nonuniform transmission line of case *c*

Figures 9 (a) and (b) show the pdf of induced voltage at the right end of the RNTL and RUTL of case *c* at $f = 800$ MHz and $f = 3.5$ GHz, respectively. It can be observed that, at f=800 MHz, the results of the two methods for both cases are consistent with each other, whereas at f = 3.5 GHz, there is a slight deviation between the results of the proposed PD-PCE method and the MC method. It can also be observed that the pdf of induced voltage of the RNTL is similar to that of the RUTL except with a different mean value.

Figures 10 (a) and (b) show the mean value and variance of induced voltage at the right end of the RNTL and RUTL of case *c* derived from the (1^{st}, 5^{th})-order PD-PCE method, respectively. It can be observed that the mean value of voltage of the RNTL was larger than that of the RUTL at some frequency points, whereas the variance was almost the same.

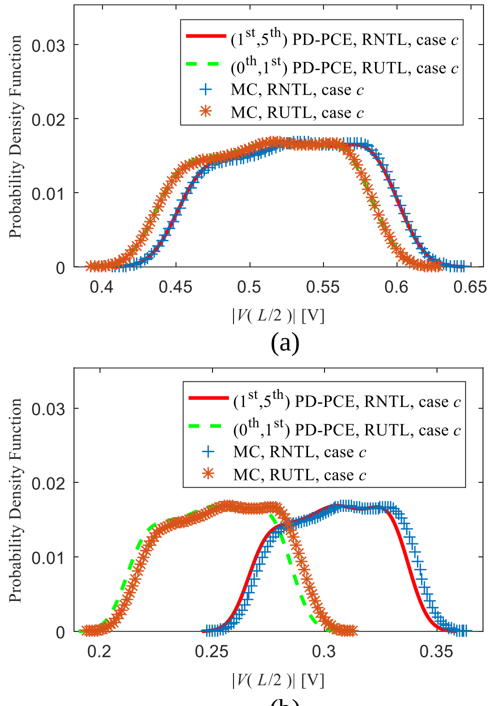

(a)

(b)

Fig. 9. Probability density function of induced voltage at the right end of RNTL and RUTL of case *c*: (a) $f = 800$ MHz, (b) $f = 3.5$ GHz.

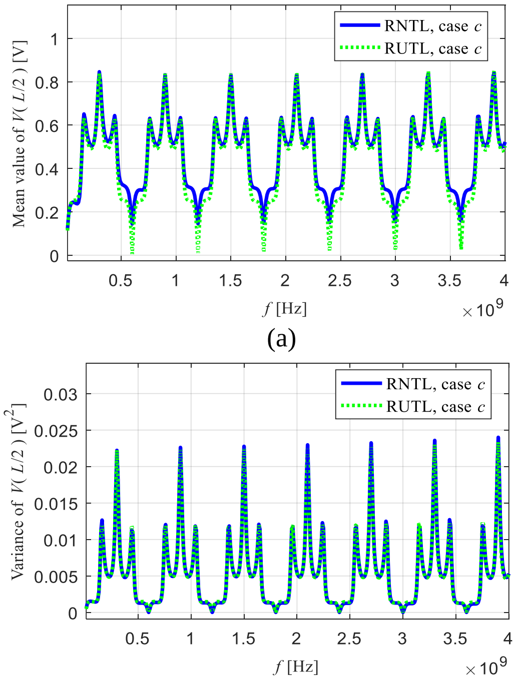

(a)

(b)

Fig. 10. (a) Mean value of induced voltage at the right end of the RNTL and RUTL of case *c*. (b) Variance of induced voltage at the right end of the RNTL and RUTL of case *c*.

B.4 Random nonuniform transmission line of case *d*

Figures 11 (*a*) and (*b*) show the pdf of induced voltage at the right end of the RNTL and RUTL of case *d* at $f = 800$ MHz and $f = 3.5$ GHz, respectively. The results derived from the proposed PD-PCE method and the MC method were consistent with each other at $f = 800$ MHz, whereas the results of the two methods show a slight deviation at $f = 3.5$ GHz. It can also be observed that the pdfs of the RNTL and RUTL were almost the same.

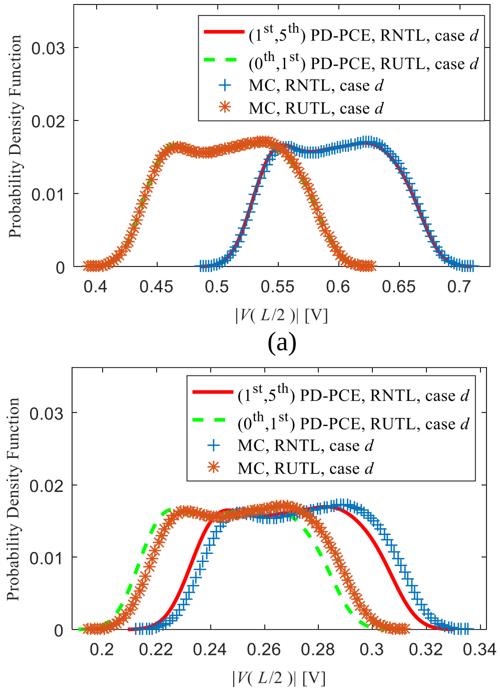

(a)

(b)

Fig. 11. Probability density function of induced voltage at the right end of the RNTL and RUTL: (a) $f = 800$ MHz, and (b) $f = 3.5$ GHz.

Figures 12 (*a*) and (*b*) show the mean value and variance of induced voltage at the right end of the RNTL and RUTL of case *d*, respectively. It can be observed that the mean value of voltage of the RNTL was slightly larger than that of the RUTL, whereas the variance was almost the same.

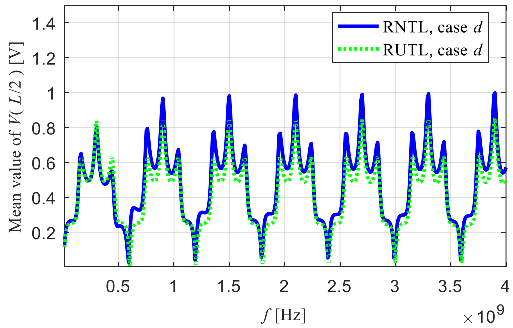

(a)

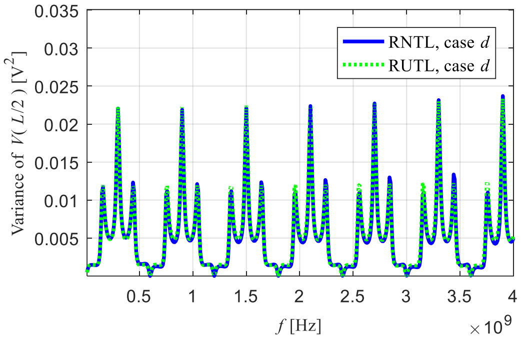

(b)

Fig. 12. (a) Mean value of induced voltage at the right end of the RNTL and RUTL of case *d*. (b) Variance of induced voltage at the right end of the RNTL and RUTL of case *d*.

Table 5 presents the computation time of the proposed (1st, 5th)-order PD-PCE method and MC method. The (1st, 5th)-order PD-PCE method takes approximately 9.8+6.8=16.6 s for 800 frequency points, whereas the MC method takes approximately 2.1*1000=2100 s for 800 frequency points. The proposed (1st, 5th)-order PD-PCE method is approximately 126.5 times faster than the MC method without losing accuracy.

Table 5: CPU time of (1st, 5th)-order PD-PCE method and MC method

Method	**PCE Projection/s**	**Total Time/s**	**Repeat Time**
MC	0	2.1*1000	1000
PD-PCE	9.8	6.8	2+6

IV. CONCLUSION

In this paper, an (Nth, Pth)-order PD-PCE method for the analysis of random nonuniform transmission line response under plane-wave illumination is presented. Simulation results show that the PD-PCE method is accurate and computationally efficient compared with the UCS and MC methods. Under the assumption of weak level of nonuniformity, small number of random variables, and lower frequency band, this method is effective and can provide quantitative guidance for evaluating the effects of the nonuniformity and uncertainty of transmission lines on the reliability of electrical systems.

REFERENCES

[1] S. Barmada, A. Musolino, and M. Raugi, “Response bounds analysis for transmission lines characterized by uncertain parameters,” *Applied Comput. Electromagn. Society J.*, vol. 20, no. 3, pp. 213-220, Jan. 2005.

[2] G. Zhang, J. J. Bai, L. X. Wang, and X. Y. Peng, “Stochastic analysis of multi-conductor cables with uncertain boundary conditions,” *Applied Comput. Electromagn. Society J.*, vol. 33, no. 8, pp. 847-853, Aug. 2018.

[3] M. Cernobryvko, D. V. Ginste, and D. D. Zutter, “A two-step perturbation technique for nonuniform single and differential lines,” *IEEE Trans. on Microw. Theory and Tech.*, vol. 61, no. 5 pp. 1758-1767, May 2013.

[4] P. Manfredi, D. V. Ginste, and D. D. Zutter, “An effective modeling framework for the analysis of interconnects subject to line-edge roughness,” *IEEE Microw. Wirel. Co.*, vol. 25, no. 8, pp. 502-504, Aug. 2015.

[5] P. Manfredi, D. D. Zutter, and D. V. Ginste, “Analysis of nonuniform transmission lines with an iterative and adaptive perturbation technique,” *IEEE Trans. on Electromagn. Compat.*, vol. 58, no. 3, pp. 859-867, Apr. 2016.

[6] F. Grassi, P. Manfredi, and X. Liu, “Effects of undesired asymmetries and nonuniformities in differential lines,” *IEEE Trans. on Electromagn. Compat.*, vol. 59, no. 5, pp. 1613-1624, Oct. 2017.

[7] I. Jacek, “Equivalent circuits for nonuniform transmission line simulation,” *Applied Comput. Electromagn. Society J.*, vol. 25, no. 9, pp. 764-779, Sep. 2010.

[8] Y. Sun and X. Wang, “Novel extraction method of inductance parameter for nonuniform transmission line in anisotropic dielectric,” *Applied Comput. Electromagn. Society J.*, vol. 32, no. 1, pp. 15-23, Jan. 2017.

[9] C. R. Paul, *Analysis of Multiconductor Transmission Lines*, New York: John Wiley and Sons, 1994.

[10] F. A. Rachidi, “A review of field-to-transmission line coupling models with special emphasis to lightning-induced voltages on overhead lines,” *IEEE Trans. on Electromagn. Compat.*, vol. 54, no. 4, pp. 898-911, Aug. 2012.

[11] C. A. Nucci, F. Rachidi, and M. Rubinstein, “An overview of field-to-transmission line interaction,” *Applied Comput. Electromagn. Society N.*, vol. 22, no. 1, pp. 9-27, Jan. 2007.

[12] C. P. Robert and G. Casella, *Introducing Monte Carlo Methods with R*, New York, Springer, 2009.

[13] Q. Zhang, J. J. Liu, J. McMacken, J. Thomson, and P. Layman, “Development of robust interconnect model based on design of experiments and multi objective optimization,” *IEEE Trans. on Electron. Devices*, vol. 48, no. 9, pp. 1885-1891, Sep. 2001.

[14] I. S. Stievano, P. Manfredi, and F. G. Canavero, “Stochastic analysis of multiconductor cables and interconnects,” *IEEE Trans. on Electromagn. Compat.*, vol. 53, no. 2, pp. 501-507, May 2011.

[15] P. Manfredi and F. G. Canavero, “Polynomial chaos for random field coupling to transmission lines,” *IEEE Trans. on Electromagn. Compat.*, vol.54, no. 3, pp. 677-680, June 2012.

[16] O. J. Alkhateeb and N. Ida, “Data-driven arbitrary polynomial chaos for uncertainty quantification in filters,” *Applied Comput. Electromagn. Society J.*, vol.33, no. 9, pp. 1048-1051, Sep. 2018.

[17] E. N. Protonotarios and O. Wing, “Analysis and intrinsic properties of the general nonuniform transmission line,” *IEEE Trans. Microw. Theory Tech.*, vol. 15, no. 3, pp. 142-150, Mar. 1967.

[18] J. F. Mao and Z. F. Li, “Analysis of the time response of nonuniform multiconductor transmission lines with a method of equivalent uniform cascaded section network chain,” *IEEE Trans. Microw. Theory Tech.*, vol. 40, no. 5, pp. 948-954, May 1992.

[19] P. Gómez, P. Moreno, and J. L. Naredo, “Frequency-domain transient analysis of nonuniform lines with incident field excitation,” *IEEE Trans. Power Del.*, vol. 20, no. 3, pp. 2273-2280, Jul. 2005.

[20] M. A. Khalaj, “Analysis of coupled or single nonuniform transmission lines using step-by-step numerical integration,” *Prog. Electromagn. Res.*, vol. 58, pp. 187-198, 2006.

[21] C. Jullien, P. Besnier, M. Dunand, and I. Junqua, “Advanced modeling of crosstalk between an unshielded twisted pair cable and an unshielded wire above a ground plane,” *IEEE Trans. Power Del.*, vol. 55, no. 1, pp. 183-194, Feb. 2013.

[22] M. A. Khalaj, “Analysis of nonuniform transmission lines using the equivalent sources,” *Prog. Electromagn. Res.*, vol. 71, pp. 95-107, 2007.

Jinpeng Yang received the B.S. degree from Jilin University in 2013. He is currently working toward the Ph.D. degree at Jilin University. His research interests include transmission line modeling and statistical electromagnetics.

Xiaoying Sun received the B.S. and M.S. degrees from Jilin University, Jilin, China, in 1991 and 1994, respectively, and the Ph.D. degree in Communication and Information System from Jilin University, where he is currently a Professor with the Laboratory of Signals Detection and Processing. He is currently Professor, Changbai Mountain scholar, Dean of the Communication Engineering College, Jilin University. His current research interests include vehicle electromagnetic compatibility, array signal processing and passive sources localization.

Yu Zhao received the B.S. degree from North-east Normal University, and M.S. degree from Jilin University, China, in 1993 and 1996, respectively, and the Ph.D. degree in Communication and Information System from Jilin University in 2005. She is currently an Associate Professor of Jilin University. Her current research interest is electromagnetic compatibility.

Jian Chen received the Ph.D. degree in Communication and Information systems from Jilin University, Changchun, China, in 2007. From February 2014 to February 2015, he was a Visiting Scholar with the School of Electric and Electrical Engineering, Leeds University, Leeds, UK. He is currently an Associate Professor with the College of Communication Engineering, Jilin University, Changchun, China. His research interests include array signal processing, electromagnetic compatibility.

Hanqing Wang received the B.S. degree in Communication Engineering from Jilin University in 2016. He is currently working toward the master’s degree in Communication and Information System. His current research interest is vehicle EMC.

Radar Target Recognition by Machine Learning of K-Nearest Neighbors Regression on Angular Diversity RCS

Kun-Chou Lee

Department of Systems and Naval Mechatronic Engineering
National Cheng-Kung University, Tainan, 701, Taiwan
kclee@mail.ncku.edu.tw

***Abstract* ─** In this paper, the radar target recognition is given by machine learning of K-NN (K-nearest neighbors) regression on angular diversity RCS (radar cross section). The bistatic RCS of a target at a fixed elevation angle and different azimuth angles are collected to constitute an angular diversity RCS vector. Such angular diversity RCS vectors are chosen as features to identify the target. Different RCS vectors are collected and processed by the K-NN regression. The machine learning belongs to the scope of artificial intelligence, which has attracted the attention of researchers all over the world. In this study, the K-NN rule is extended to achieve regression and is then applied to radar target recognition. With the use of K-NN regression, the radar target recognition is very simple, efficient, and accurate. Numerical simulation results show that our target recognition scheme is not only accurate, but also has good ability to tolerate random fluctuations.

***Index Terms* ─** Machine learning, radar cross section, radar target recognition.

I. INTRODUCTION

Radar target recognition means to identify a target from features of electromagnetic signals. It plays a very important role in both military detection and non-destructive testing. There have been many techniques of radar target recognition. The electromagnetic imaging [1-3], i.e., inverse scattering, is the most direct approach for identification. However, this is often practically difficult because the phase information of the scattered electric field is required [1-2] and is difficult in measurement. Theoretically, the electromagnetic imaging requires rigorous numerical procedures of solving integral equations which are complicated and time-consuming [3]. Note that the efficiency is very important for practical target recognition. In [4], the radar target recognition is successfully achieved by using pattern recognition techniques [5] on RCS (radar cross section) [6]. Practically, measurement of RCS is easier than that of electric field phase. Moreover, the pattern recognition computation is easier than that of inverse scattering.

Recently, machine learning [7] has attracted interest of researchers in different fields all over the world. Machine learning belongs to the scope of artificial intelligence. It teaches a computer to predict the response of a system by learning from experiences. The goal is to build an intelligent system. A machine learning technique is basically a black box, which can achieve both pattern recognition and regression. The term “black box” means that the relation between the input and output of a system is very complex. This study plans to predict the type of a target from scattered RCS. The relation between the target’s information and its RCS is complicated and strongly nonlinear. Therefore, machine learning is a good candidate for radar target recognition, e.g., [8-10].

In this paper, the radar target recognition is given by machine learning of K-NN (K-nearest neighbors) [11-14] regression [15] on angular diversity RCS. The K-NN algorithm is a fundamental machine learning algorithm. It is a non-parametric method used for both classification [11-14] and regression [15]. In both cases, the input consists of the *K* closest training examples in the feature space and the output is predicted accordingly. Similar to [4], the bistatic RCS of a target at a fixed elevation angle and different azimuth angles are collected to constitute an angular diversity RCS vector. Such angular diversity RCS vectors are chosen as features to identify the target. The target recognition procedures are divided into two stages, which are off-line (training) and on-line (predicting). In the off-line (training) stage, different RCS vectors from reference (known) targets are collected to constitute the RCS signal map. In the on-line (predicting) stage, an angular diversity RCS vector from an unknown target is detected. This on-line RCS vector is compared with the off-line RCS signal map by K-NN regression to identify the unknown target. With the use of K-NN regression, the radar target recognition is very simple and efficient. Numerical simulation results show that our target recognition scheme is not only accurate, but also has good ability to tolerate random fluctuations.

Submitted On: September 21, 2017
Accepted On: December 24, 2018

II. RCS COLLECTION

As a target is illuminated by an electric field $\overline{E}_i$, a current $\overline{J}$ will be induced and this current will then radiate a scattered electric field $\overline{E}_S$ as [16],

$$\overline{E}_S(\overline{r}) = -j\omega\mu_0 \int_{V'} \overline{\overline{G}}(\overline{r}-\overline{r}') \cdot \overline{J}(\overline{r}')dV' \cdot \qquad (1)$$

In (1), ω is the angular frequency, μ_0 is the permeability, $\overline{r}$ represents the location, and V' represents the target body. Note that the notation prime denotes the source region. The $\overline{\overline{G}}$ is the dyadic Green's function as [16],

$$\overline{\overline{G}}(\left|\overline{r}-\overline{r}'\right|) = \left(\overline{\overline{I}} + \frac{\nabla\nabla}{k_0^2}\right)\frac{e^{-jk_0\left|\overline{r}-\overline{r}'\right|}}{4\pi\left|\overline{r}-\overline{r}'\right|}, \qquad (2)$$

where k_o is the wavenumber and $\overline{\overline{I}}$ is the identity matrix. By using numerical techniques, e.g., moment methods [17], and boundary conditions on (1), the induced current $\overline{J}$ and then the scattered electric field $\overline{E}_S$ can be calculated accordingly.

Without loss of generality, this study selects the ship-shaped scatterer as the target for simplicity. Consider a ship-shaped target on the sea level (*X*-*Y* plane) located at the origin of coordinate, as shown in Fig. 1. The front end of the ship is in the $+\hat{x}$ direction and the broadside of the ship is in the $\pm\hat{y}$ directions.

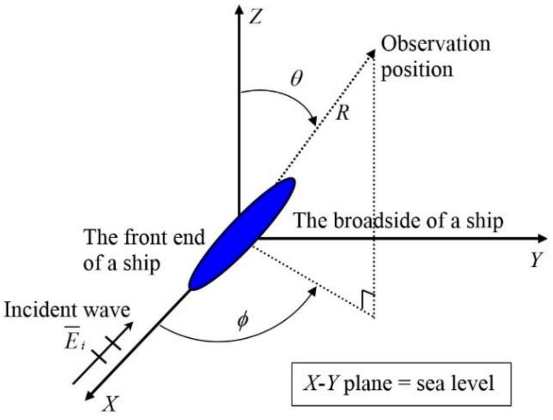

Fig. 1. Schematic diagram of a ship-shaped target illuminated by an incident plane wave.

The spherical coordinate system is defined as (R,θ,ϕ) where R is the distance from observation position to origin, θ is the elevation angle and ϕ is the azimuth angle. The target is illuminated by a $\hat{z}$-polarized plane wave $\overline{E}_i$. The bistatic RCS in the direction of (θ,ϕ) is defined as [6],

$$RCS(\theta,\phi) = \lim_{R\to\infty} 4\pi R^2 \frac{\left|\overline{E}_S(\theta,\phi)\right|^2}{\left|\overline{E}_i\right|^2}, \qquad (3)$$

where $\overline{E}_S(\theta,\phi)$ is given in equation (1). The bistatic RCS data of a ship at a fixed elevation angle θ and different azimuth angles of ϕ are collected to constitute an RCS vector. This is just the angular-diversity RCS because measurement is taken by sweeping the spatial angles. Such angular-diversity RCS vectors are chosen as features to identify the target. Different RCS vectors are collected and processed by the K-NN regression of the next section.

III. K-NN REGRESSION

The K-NN (K-nearest neighbors) rule is first proposed by Cover & Hart [11] for classification. The basic concept of K-NN rule is very simple [11-14]. Figure 2 illustrates the K-NN rule for two categories. In Fig. 2, there are many known objects, which are blue triangles (label #1) and red rectangles (label #2), from two categories. Note that the label is an integer to represent a category. The problem is to predict which category a new unknown object (green circle) belongs to. In classical K-NN rule [11-14], a new object is classified by a majority vote of its neighbors. In other words, a new object is assigned to the category which is the most common among its *K* nearest neighbors. In Fig. 2, the solid contour line represents *K*=3 because it surrounds three known objects, which are one blue triangle (label #1) and two red rectangles (label #2). Thus, we predict that the new unknown (green) object belongs to the category of red rectangles (label #2). Similarly, the dash contour line represents *K*=5 because it surrounds five known objects, which are three blue triangles (label #1) and two red rectangles (label #2). Thus, we predict that the new unknown (green) object belongs to the category of blue triangles (label #1).

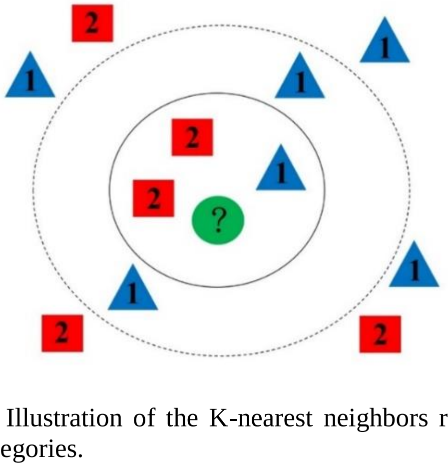

Fig. 2. Illustration of the K-nearest neighbors rule for two categories.

The above classical K-NN rule can be further extended to achieve regression [15]. In K-NN regression, the output is a continuous real number, but not an integer, to represent the property value of an object. This property value can be calculated from the weighted average on the property values of its K nearest neighbors. The procedures are divided into two stages, which are off-line (training) and on-line (predicting). For convenience, each object in Fig. 2 is viewed as a vector. In the off-line (training) stage, there are N known vectors $\bar{r}_i$ (i = 1, 2, ⋯, N) from different M categories (labeled as #1, #2, ⋯, #M). Each vector $\bar{r}_i$ (i = 1, 2, ⋯, N) has a property value $q_i \in \{1, 2, \cdots, M\}$ to represent which category $\bar{r}_i$ belongs to. Note that $\bar{r}_i$ and q_i (i = 1, 2, ⋯, N) are known off-line data. In the on-line (predicting) stage, there is a new vector $\bar{r}$. The problem is to predict the property value for this new vector $\bar{r}$. Among the N known objects, assume the K nearest neighbors (with respect to the new vector $\bar{r}$) have vectors $\bar{\alpha}_k$ and corresponding property values β_k, where k = 1, 2, ⋯, K. The property value for this new vector $\bar{r}$ is predicted as:

$$q = \sum_{k=1}^{K} w_k \beta_k , \tag{4}$$

and

$$w_k = \frac{1/d(\bar{r},\bar{\alpha}_k)}{\sum_{k=1}^{K}[1/d(\bar{r},\bar{\alpha}_k)]} , \tag{5}$$

where $d(\cdot)$ represents the Euclidean distance between two vectors. Equation (5) means that the weight (i.e., impact) of a neighbor is proportional to the reciprocal of distance. That is, near neighbors have larger impact, and vice versa. The parameter K is a user-defined parameter. The result of equation (4) is the K-NN regression.

In this study, components of a vector represent the RCS data collected at different azimuth angles under the same elevation angle, i.e., an angular diversity RCS vector. Vectors of the same category mean the RCS vectors scattered from the same type of target. Off-line training vectors are the RCS data from reference (known) targets. The property value represents the type of a target. The new vector $\bar{r}$ represents the on-line RCS data scattered from an unknown target. Note that the predicted property value q in equation (4) is a real number, but not an integer. Taking the integer that is the closest to q, the resulting integer is just the predicted label (i.e., type) of the unknown target.

IV. NUMERICAL RESULTS

In this section, numerical examples are given to illustrate the above formulations. To easily obtain the scattering RCS data, all targets are assumed to be ship-shaped models. There are three types of reference (known) targets (M=3) including type #1 (to simulate a ship of container vessel), type #2 (to simulate a naval ship) and type #3 (to simulate a fishing boat). The geometrical models for the three types of reference (known) targets are shown in Fig. 3. The ship length a is chosen as $k_o a$ = 9.4 for the reference target of type #1, $k_o a$ = 6.3 for the reference target of type #2, and $k_o a$ = 3.1 for the reference target of type #3. All targets are laid on a rough seawater surface (X-Y plane). The seawater has dielectric constant ε_r = 81 and conductivity σ = 4 S/m. The characteristic for surface roughness of the seawater is assumed to be:

$$z(x, y) = \frac{4}{75} a \cdot \sin(\frac{15\pi}{4} x) \sin(\frac{15\pi}{4} y) + \frac{8}{75} a \cdot \tag{6}$$

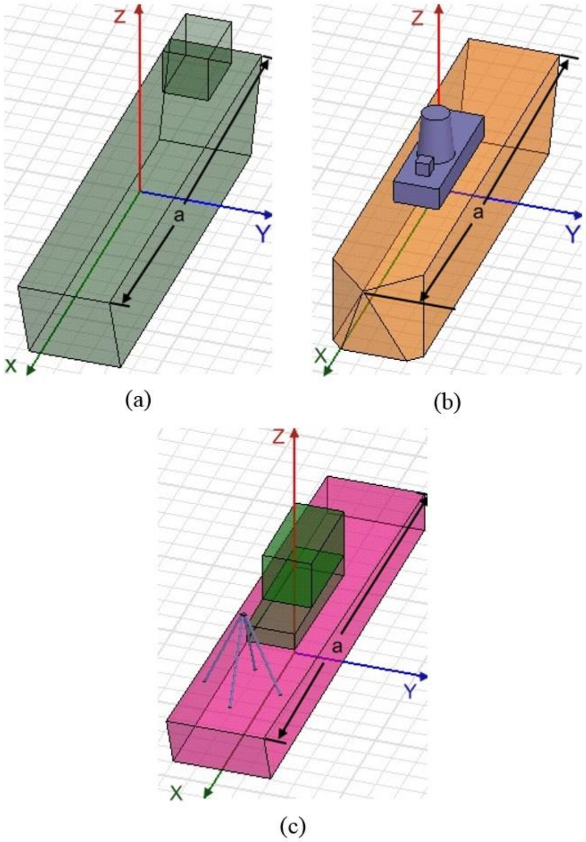

Fig. 3. Geometrical models for the three types of reference (known) targets: (a) type #1, (b) type #2, and (c) type #3.

The arrangement of RCS collection is illustrated in Fig. 1. Initially, the bistatic RCS data from the reference target of type #1 at the elevation angle θ= 61° and azimuth angles ϕ = 0°, 1°, …, 180°, are collected to constitute a 181-dimensional RCS vector, i.e., an angular diversity RCS vector. Next, the elevation angle θ is changed to be $\theta = 63^o$, 65^o, …, and 89^o, respectively. Thus, we have 15 training vectors for the reference target of type #1. Similarly, the reference targets of type #2 and type #3 both have 15 training vectors. Therefore, we have 45 (N = 15×3) training vectors in total.

The RCS is simulated by the commercial software Ansys HFSS. Initially, the operation of Ansys HFSS software is verified. The bistatic RCS from a perfectly conducting sphere centered at the coordinate origin is computed by the Ansys HFSS software. The dimension of the perfectly conducting sphere is chosen to be $k_o b$ =1.1 and $k_o b$ =7.7 (b is the sphere radius) so that the results of RCS by Ansys HFSS software can be compared with those of reference [6] under the same parameters. Our simulation results show they are consistent. Thus, we conclude that our operation of Ansys HFSS software is correct. Next, the Ansys HFSS software is utilized to compute the RCS data in this study. Figure 4 shows the distribution of trained RCS data for the three known ships. The two horizontal axes represent the azimuth (ϕ) and elevation (θ) angles, respectively. The vertical axis represents the RCS. It shows that one cannot categorize these RCS data by visual inspection directly. Therefore, our K-NN identification is meaningful.

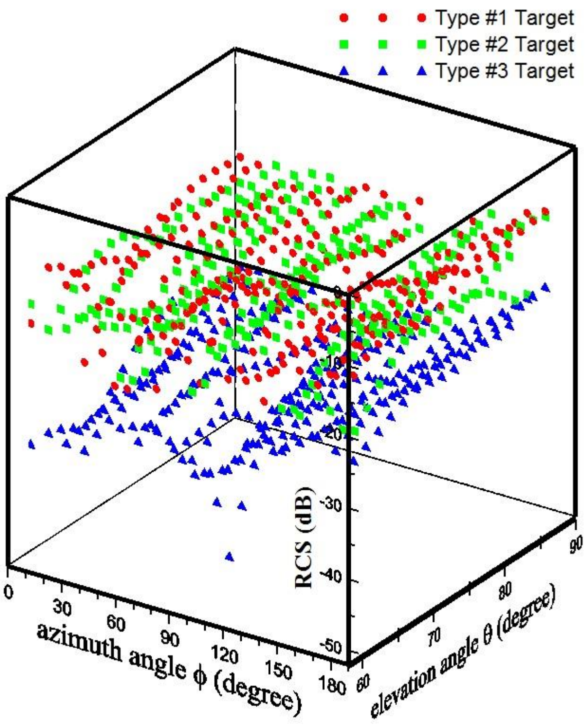

Fig. 4. Distribution of trained RCS data for the three known ships.

There are three examples to verify the above target recognition scheme. In the first example, the testing (unknown) target is the reference target of type #1. The RCS data are collected at the elevation angle $\theta = 62^o$ and azimuth angles ϕ = 0^o, 1^o, …, 180^o. Note that this elevation angle is different from any elevation angle of training RCS data. The goal is to predict the type of the testing (unknown) target by comparing on-line RCS data at $\theta = 62^o$ to training (i.e., off-line) RCS data. Following the K-NN regression rule in Section III, the predicted property value in equation (4) is q=1.048. Taking the integer that is the closest to q, the result is 1. Thus, we predict that the on-line RCS data at $\theta = 62^o$ are scattered from reference target of type #1. That is, we predict that the testing (unknown) target is just the reference target of type #1. This is consistent with the fact. Therefore, this is a correct prediction. Next, the elevation angle θ is changed to be $\theta = 64^o$, 66^o, …, and 90^o, respectively. Note that none of these elevation angles are included in elevation angles of training RCS data. Figure 5 shows the predicted property value, i.e., q of equation (4), for the 15 testing elevation angles at θ = 62^o, 64^o, …, and 90^o, respectively. Taking the integer that is the closest to q, the result is 1 for each test. Thus, we predict that the on-line RCS data at these 15 testing elevation angles are all scattered from the reference target of type #1. All predictions are correct and consistent with the fact. The successful recognition rate is 100% (=15/15).

In the second example, the testing (unknown) target is the reference target of type #2. The other conditions and procedures are the same as those of the first example. Figure 6 shows the predicted property value, i.e., q of equation (4), for the 15 testing elevation angles at θ = 62^o, 64^o, …, and 90^o, respectively. Taking the integer that is the closest to q, the result is 2 for each test. Thus we predict that the on-line RCS data at these 15 testing elevation angles are all scattered from the reference target of type #2. All predictions are correct and consistent with the fact. The successful recognition rate is 100% (=15/15).

In the third example, the testing (unknown) target is the reference target of type #3. The other conditions and procedures are the same as those of the first and second examples. The results are shown in Fig. 7. Taking the integer that is the closest to q, the result is 3 for each test. Thus, we predict that all on-line RCS data are scattered from the reference target of type #3. All predictions are correct and consistent with the fact. The successful recognition rate is 100% (=15/15).

The overall successful recognition rate is 100% (=45/45). All the above RCS data are from numerical simulation but not experiments. So, the RCS data are deterministic without random fluctuations. In practical applications, the experimental data contains random fluctuations such as interferences and noises. To investigate such effects, we add an independent random component to each RCS. This random component is with

Gaussian distribution and zero mean. The normalized standard derivation (with respect to the root mean square value of the RCS) is chosen as 0.01, 0.1, 0.2, 0.4, 1.0, 1.2, 1.4, 1.6, 1.8, and 2.0, respectively. Figure 8 shows the successful recognition rate with respect to different levels of added random components. For comparison, the results of reference [4], which utilizes PCA (principal components analysis) techniques [5], are also given. It reports that the successful recognition rate of this study is obviously better than that of reference [4] (using PCA). This study can still maintain the successful recognition rate of 75.56% even though the normalized standard derivation of the added random component is increased to 2. This result shows that the proposed target recognition scheme has good ability to tolerate random fluctuations.

In the above simulation, our ocean surface model of equation (6) is somewhat too simple. Many complex scattering mechanisms of the actual ocean, e.g., the Bragg scattering, are not included in our ocean surface model. However, this will not degrade the effectiveness of our K-NN target recognition. From Fig. 8, it reports that our recognition can still maintain the successful recognition rate of 75.56% even though the normalized standard derivation of the added random component is increased to 2. The complex scattering mechanism of the actual ocean may be viewed as one of the sources for the added random component in Fig. 8. This implies that our recognition is still available although there exists complex scattering mechanisms of the actual ocean.

The above RCS is computed by the Ansys HFSS software on a personal computer. The other processing is coded using Python-3.6 programming language in Anaconda software. The hardware is a personal computer with Intel(R) Core(TM) i7-4790 3.6 GHz CPU and 16 GB RAM.

V. CONCLUSION

This study successfully utilizes machine learning of K-NN regression to implement radar target recognition. With the use of K-NN regression, the recognition procedure is simple and accurate with good discrimination. Numerical simulation results show that the recognition scheme has good ability to tolerate random fluctuations. Unlike mathematical regression, the K-NN regression is inherently a black box. It can model a very complicated system and can be applied to many complicated and nonlinear problems of electromagnetic waves. It should be noted that our recognition has no limitation on the number of categories. As the number of categories increases, the flowchart of our target recognition is still unchanged. Like most schemes of radar target recognition, the successful rate of identification will be challenged as the RCS difference becomes smaller. Under such situations, the RCS data should be processed in advance for reducing the fluctuating components. For example, the SVD (singular value decomposition) technique [18-19] can decompose a noisy signal into clean and noisy components by mapping signals to matrix subspace. Using only the clean RCS to implement our K-NN target recognition may improve the discrimination. This will be the future work of this study.

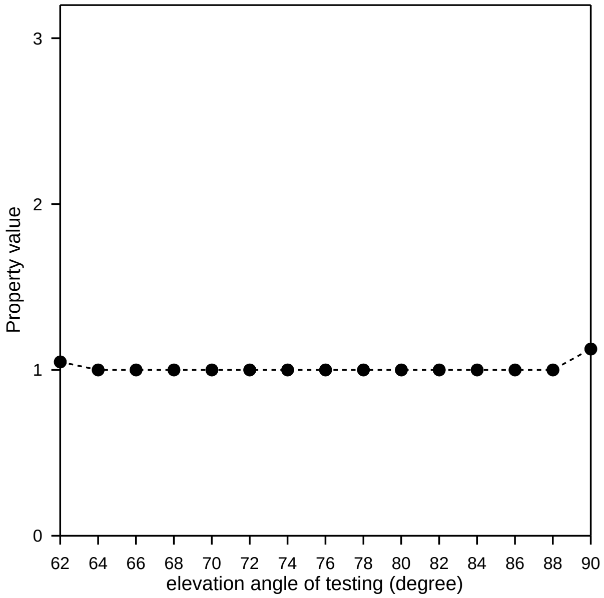

Fig. 5. Predicted property value for different elevation angles of testing as the target is the reference target of type #1.

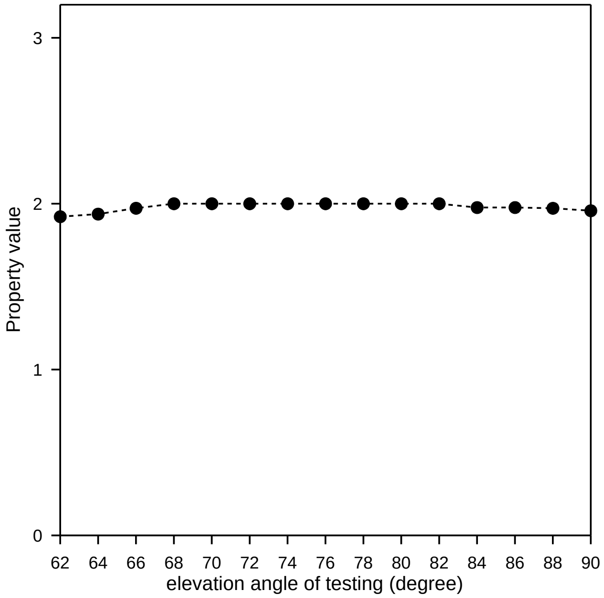

Fig. 6. Predicted property value for different elevation angles of testing as the target is the reference target of type #2.

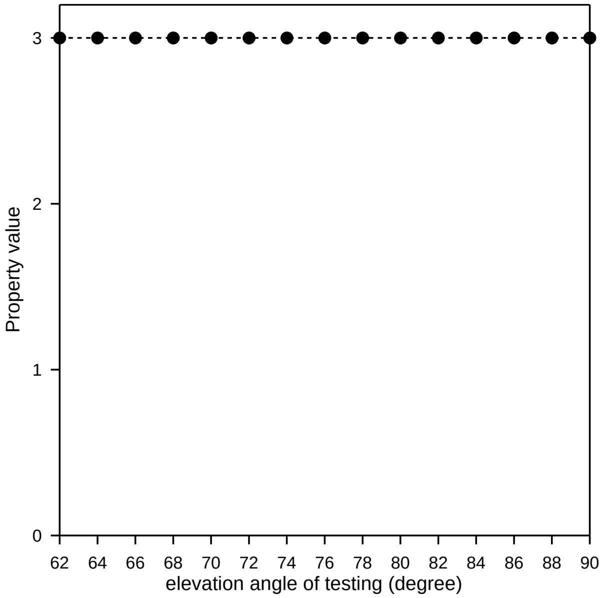

Fig. 7. Predicted property value for different elevation angles of testing as the target is the reference target of type #3.

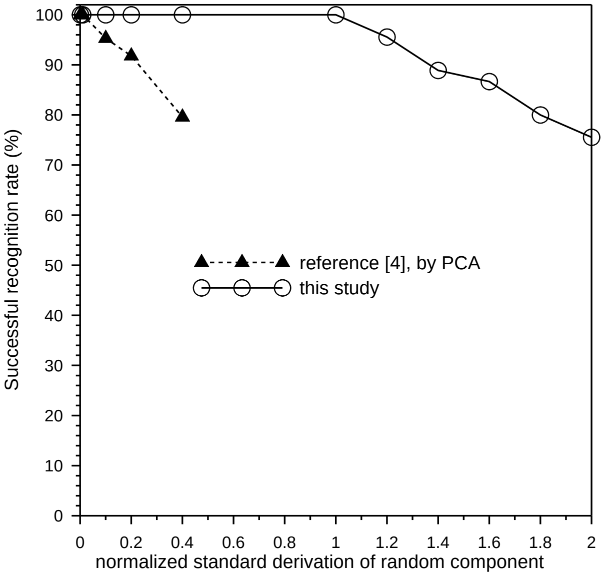

Fig. 8. Successful recognition rate with respect to different levels of added random components.

ACKNOWLEDGMENT

The authors would like to acknowledge (1) the financial support of the Ministry of Science and Technology, Taiwan, under Grant MOST 107-2221-E-006-098, (2) the National Center for High Performance Computing, Taiwan, for computer time and facilities.

REFERENCES

[1] N. H. Farhat, "Microwave diversity imaging and automated target identification based on models of neural networks," *Proc. IEEE*, vol. 77, no. 5, pp. 670-681, 1989.

[2] K. C. Lee, "Polarization Effects on Bistatic Microwave Imaging of Perfectly Conducting Cylinders," *Master Thesis*, National Taiwan University, Taipei, Taiwan, 1991.

[3] K. C. Lee, "Inverse scattering of a conducting cylinder in free space by modified fireworks algorithm," *Prog. Electromagn. Res. M*, vol. 59, pp. 135-146, 2017.

[4] K. C. Lee, J. S. Ou, and C. W. Huang, "Angular-diversity radar recognition of ships by transformation based approaches --- including noise effects," *Prog. Electromagn. Res.*, vol. 72, pp. 145-158, 2007.

[5] S. Theodoridis and K. Koutroumbas, *Pattern Recognition*. 2nd ed., Academic Press, Boston, 2003.

[6] G. T. Ruck, D. E. Barrick, W. D. Stuart, and C. K. Krichbaum, *Radar Cross Section Handbook*. vol. 1, Plenum, New York, 1970.

[7] S. Suthaharan, *Machine Learning Models and Algorithms for Big Data Classification*. Springer, New York, 2016.

[8] S. Caorsi, D. Anguita, E. Bermani, A. Boni, M. Donelli, and A. Massa, "A comparative study of NN and SVM-based electromagnetic inverse scattering approaches to on-line detection of buried objects," *Appl. Comput. Electromagn. Soc. J.*, vol. 18, no. 2, pp. 1-11, 2003.

[9] A. Kabiri, N. Sarshar, and K. Barkeshli, "Application of neural networks in the estimation of two-dimensional target orientation," *Appl. Comput. Electromagn. Soc. J.*, vol. 18, no. 2, pp. 57-63, 2003.

[10] D. Shi and Y. Gao, "Electromagnetic radiation source identification based on spatial characteristics by using support vector machines," *Appl. Comput. Electromagn. Soc. J.*, vol. 32, no. 2, pp. 120-127, 2017.

[11] T. M. Cover and P. E. Hart, "Nearest neighbor pattern classification," *IEEE Trans. Inf. Theory*, vol. IT-13, no. 1, pp. 21-27, 1967.

[12] P. E. Hart, "The condensed nearest neighbor rule," *IEEE Trans. Inf. Theory*, vol. IT-14, no. 3, pp. 515-516, 1968.

[13] P. Hall, B. U. Park, and R. J. Samworth, "Choice of neighbor order in nearest neighbor classification," *Ann. Stat.*, vol. 36, no. 5, 2135-2152, 2008.

[14] I. Mesecan and I. Bucak, "Searching the effects of

image scaling for underground object detection using K-means and K-NN," *The 8th European Modelling Symposium (EMS)*, Pisa, Italy, pp. 180-184, Oct. 2014.

[15] N. S. Altman, "An introduction to kernel and nearest-neighbor nonparametric regression," *Am. Stat.*, vol. 46, no. 3, pp. 175-185, 1992.

[16] C. T. Tai, *Dyadic Green's Functions in Electromagnetic Theory*. International Textbook Company, San Francisco, 1971.

[17] R. F. Harrington, *Field Computation by Moment Methods*. Macmillan, New York, 1968.

[18] K. C. Lee, J. S. Ou, and M. C. Fang, "Application of SVD noise-reduction technique to PCA based radar target recognition," *Prog. Electromagn. Res.*, vol. 81, pp. 447-459, 2008.

[19] T. K. Moon, and W. C. Stirling, *Mathematical Methods and Algorithms for Signal Processing*. Prentice Hall, New Jersey, 2000.

Kun-Chou Lee was born in Taiwan. He received his B.S. degree in 1989, M.S. degree in 1991, and Ph.D. degree in 1995, from the National Taiwan University, Taipei, Taiwan, all in Electrical Engineering. From 1995 to 1997, he joined the army of his country. From 1997 to 2003, he joined the Faculty of the Wu-Feng Institute of Technology, Shu-Te University, and National Kaohsiung University of Applied Sciences, respectively, all in southern Taiwan. Since 2004, he has been with the Department of Systems and Naval Mechatronic Engineering, National Cheng-Kung University, Tainan City, Taiwan, where he is currently a Professor. His research interests include electromagnetic waves, signal processing and communications. He is a Senior Member of IEEE, and a Mmember of ACES.

FMCW Chirp Diversity for Mutual Interference Mitigation in Short-range Automotive Radars under Realistic Traffic Model

Md Anowar Hossain, Ibrahim Elshafiey, and Abdulhameed Al-Sanie

Electrical Engineering Department
King Saud University, 11421, Riyadh, Saudi Arabia
ahossain@ksu.edu.sa, ishafiey@ksu.edu.sa, sanie@ksu.edu.sa

Abstract **─** With the worldwide harmonized frequency allocation for automotive radars and increasing rate of modern vehicles equipped with radar systems, mutual interference among automotive radars is becoming a key problem. This paper presents a novel approach for mutual interference mitigation based on diverse waveform design by imposing time and frequency diversity to frequency modulated continuous wave (FMCW) chirp signal considering 79 GHz short-range automotive radar. Performance of the proposed waveform in terms of auto-correlation and cross-correlation has been investigated using software-defined radio (SDR) transceiver and measurement results are provided. The system concept is validated by developing an automotive radar channel model considering a realistic 3D road traffic scenario using a ray-tracing tool. Theoretical analysis and simulation examples of different mutual interference scenarios in an automotive environment are provided to evaluate the effectiveness of the proposed method. Results show that the proposed waveform is able to detect the targets of interest successfully while mitigating the false targets in mutual interference environments.

Index Terms **─** Automotive radar, FMCW chirp, mutual interference, waveform diversity.

I. INTRODUCTION

Improving traffic efficiency and reducing road accidents are challenging tasks in most regions of the world. Traffic congestions and road accidents have been increasing, especially in urban roads and highways due to population growth as well as increasing numbers of vehicles and economic activities. Although the amount of road accidents was reduced during the last decade by introducing both traffic law enforcement and passive safety means (seatbelt, airbag), the number of accidents has remained uniform because of the increasing number of vehicles.

Recent advances in microelectronic technology provides high-performance and low-cost radar sensors suitable for automotive applications [1-3]. Thus, radar based active safety functions are being integrated into all classes of vehicles to further reduce the amount of road accidents, as they are robust against weather conditions and other environmental hazards. This will result in a high density distributed automotive radar network operating simultaneously in a close proximity, which introduces mutual interference among multiple automotive radars due to shared spectrum usage, lack of coordination among multiple radars and road traffic situation [4]. Moreover, the automotive industry and research community is currently developing vehicular communication based on IEEE 802.11p dedicated short range communication (DSRC) band at 5.9 GHz [5]. The estimated position and velocity information using automotive radar can be exchanged among the neighbor vehicles on the road to implement cooperative driving for optimizing traffic efficiency. This requires highly reliable position information of surrounding vehicles from automotive radar equipped vehicles.

II. LITERATURE REVIEW

Mutual interference in automotive radars has not been investigated much yet apart from a few efforts. Theoretical background of next generation automotive radar is analyzed in [6]. The impact of mutual interference and measurement possibilities to test and verify mitigation techniques in arbitrary RF environments with norm interferers are presented in detail. Modelling of automotive radar interference based on stochastic geometry methods is presented in [7]. The developed model has further been used to estimate the detection probability of target vehicles. Discussion of the operating range of FMCW radars in presence of interference is presented in [8]. The influence of different kinds of interference on the spectrum of a FMCW radar is shown based on measurements and simulations. However, the conventional FMCW waveform with constant slope introduces false targets due to mutual interference when multiple radars are being operated simultaneously. A modified LFMCW waveform based on the modulation

Submitted On: April 11, 2017
Accepted On: December 24, 2018

of sweep slope is proposed in [9] to mitigate the mutual interference. However, it was assumed that the pattern of sweep slope is orthogonal among multiple radars to successfully mitigate the false targets. In practice, perfect orthogonal waveforms cannot be implemented in automotive radar networks due to the lack of coordination among radars. Waveform generation for automotive radar with multiple frequency shift keying (MFSK) is presented in [10]. MFSK based automotive radars exhibit excellent speed resolution, but due to the poor range resolution, it is difficult to discriminate between two target vehicles with identical relative speed. Furthermore, target vehicles with the same speed as the radar cannot be detected at all [11]. Noise radar technology as an interference prevention method is provided in [12]. Unfortunately, this type of radar exhibits several drawbacks such as complexity in signal processing and near-far problems. Furthermore, the required computational power is very high and it is difficult to apply the noise radar signal processing in real time for high bandwidth radars. Waveform generation for automotive radar based on the spread spectrum technique for mutual interference mitigation is proposed in [13]. Spread spectrum provides a measure of immunity to multipath interference and multiple access capability, making it ideal for radar applications. However, it requires extremely fast circuitry to generate the chip sequence, because the processing gain is determined by the ratio of the chip rate to the bit rate. In addition, spread spectrum systems often require adaptive power control techniques to overcome the near-far problem.

Most of these prior research works consider the automotive radar environments as simple stochastic channel models based on the statistical properties of the surrounding environment of vehicles. Such models do not exhibit the actual evaluation of automotive radar applications because static objects such as buildings and foliage, and mutual interference from the radar of surrounding vehicles exhibit significant impact on automotive radar performance. For effective performance evaluation of an automotive radar system, realistic traffic environment and wave propagation models should be considered. That helps in evaluating system performance efficiently. Field measurement is also a possible solution, but it is expensive and provides no repeatability.

Based on this background, simulation of automotive radars under realistic environment is considered, and advanced waveform design technique is proposed in this paper to mitigate false targets due to mutual interference. To evaluate the performance of automotive radar in realistic environments, we have developed a ray-tracing model that includes every domain involved, such as advanced waveform design, transmitter and receiver frontends, and realistic 3D road traffic environment.

The remaining parts of the paper are organized as follows. Section III describes the mutual interference scenarios in automotive environments. The proposed FMCW waveform design technique is provided in Section IV. Experimental validation to evaluate the effectiveness of proposed waveform is provided in Section V. Section VI describes the developed ray-tracing simulation model considering realistic 3D road traffic environment. Section VII presents the post processing and target detection with thorough analysis of results and discussions. Final conclusions are given in Section VIII.

III. MUTUAL INTERFERENCE IN AUTOMOTIVE RADARS

Currently, only small amount of vehicles are equipped with radar sensors. Thus, in most of the cases, the scattered signals of other radars will be obstructed by further vehicles without radars in between the radar equipped vehicle (V1) and the second automotive radar (V2) as shown in Fig. 1. Usually, these unwanted indirect signals exhibit a very low energy that contributes to the noise floor. Thus, thermal noise, unwanted returns coming from the road-surface or various objects adjacent to the road (buildings and foliage) are the main source of interference in current situation.

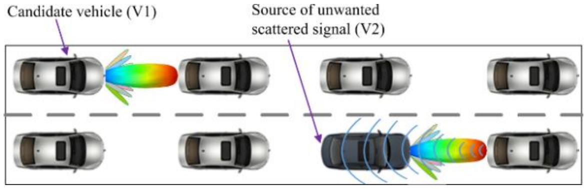

Fig. 1. Mutual interference due to scattered signals from another automotive radar.

When more vehicles will be equipped with radar sensors in near future, the indirect reflections due to the radars of neighbor vehicles will be almost the same order of magnitude as the reflected signal of the candidate vehicle's own radar. For example, indirect signals can be received by two candidate vehicles with forward looking radars moving along next to each other and a target vehicle is at some distance ahead as shown in Fig. 2.

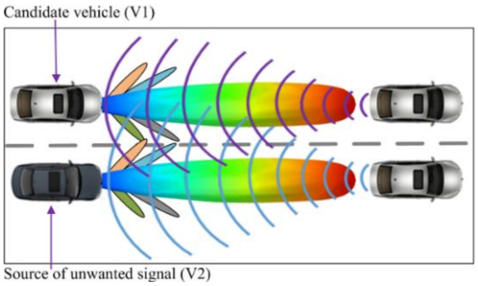

Fig. 2. Mutual interference due to indirect signals from another automotive radar.

A direct input of unwanted signal into the radar equipped vehicle can occur when the candidate vehicle is illuminated by the radar of another vehicle. For example, two vehicles V1 and V2 equipped with forward looking radars can be illuminated by each other as shown in Fig. 3. This situation can occur on the roads where adjacent lanes have traffic travelling in opposite directions. The direct reception of transmitted signal from radars of neighbor vehicles will be higher magnitude than the reflected signal of the candidate vehicle's own radar.

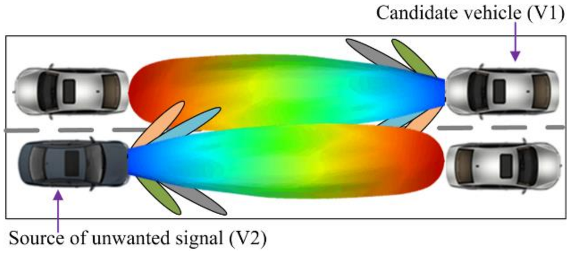

Fig. 3. Mutual interference due to direct signals between automotive radars.

For automotive radar under mutual interference, the radar equipped with the candidate vehicle will receive signals from other radars due to overlapping of main-lobes and side-lobes of antenna beams. Thus, the received signals for nth radar can be given as:

$$\Psi_{rx,n}(t) = \sum_{m=1}^{M} h_{m,n}(t)\Psi_{tx,m}\left(t-\tau_{m,n}\right) + \eta(t), \quad (1)$$

where, $m \in [1, 2, \ldots M]$ and $n \in [1, 2, \ldots N]$ are the number of transmitting and receiving radars, $\Psi_{tx,m}(t)$ is the transmitted waveform of mth radar, $h_{m,n}(t)$ is the channel coefficient associated with mth transmitting and nth receiving radar, $\tau_{m,n}$ is the signal propagation time related to mth transmitting antenna to nth receiving antenna and $\eta(t)$ is the AWGN.

If we perform matched filtering (dechirping) to extract the signal associated with candidate radar considering m=1, then equation (1) can be modified as:

$$\Psi_{MF,n}(t) = \Psi_{rx,n}(t) \otimes \Psi^{*}_{tx,1}(-t), \quad (2)$$

$$\Psi_{MF,n}(t) = h_{1,n}(t)\Psi_{tx,1}\left(t-\tau_{1,n}\right) \otimes \Psi^{*}_{tx,1}(-t) + \sum_{m=2}^{M} h_{m,n}(t)\Psi_{tx,m}\left(t-\tau_{m,n}\right) \otimes \Psi^{*}_{tx,1}(-t) + \eta(t) \otimes \Psi^{*}_{tx,1}(-t), \quad (3)$$

where, $\otimes$ denotes the convolution operator, the first term in equation (3) is the desired MF output, the second term is the mutual interference that is required to be mitigated. The third term is the system noise. The term related to mutual interference can be completely mitigated if the waveforms transmitted from multiple automotive radars are orthogonal to each other and can be given as:

$$\sum_{m=2}^{M} h_{m,n}(t)\Psi_{tx,m}\left(t-\tau_{m,n}\right) \otimes \Psi^{*}_{tx,1}(-t) = 0. \quad (4)$$

However, perfect orthogonal waveforms cannot be implemented in automotive radar network due to use of shared spectrum and the lack of coordination among radars resulting from the absence of centralized control and resource allocation unit. Thus, advanced waveform design and signal processing methods need to be incorporated to mitigate the automotive radar interference issues. If the automotive radar transmits a unique chirp at each sweep i.e. different slope at each sweep based on the advanced waveform design technique with time and frequency diversity, then matched filtering output of the candidate radar exhibits strong auto-correlation with its own transmitted signal and weaker cross-correlation properties with reflected or transmitted signals from other neighbor radars which in turns improve the detection of target vehicles and mitigate the false targets due to mutual interferences.

IV. ADVANCED WAVEFORM DESIGN

In general, automotive radar systems adopt FMCW waveform due to the possibilities of target estimation through runtime measurements. Compared to pulsed radars, FMCW radars require less power and exhibit reduced size and cost. The FMCW chirp signal can be given as:

$$\Psi_{tx}(t) = cos\left[2\pi t\left(f_0 + \frac{\beta t}{2}\right)\right], \quad (5)$$

where β denotes the sweep slope and is given as:

$$\beta = \frac{f_1 - f_0}{T} = \frac{B}{T}, \quad (6)$$

where f_0 and f_1 are the starting frequency and final frequency respectively. The terms B and T are sweep bandwidth and sweep time respectively. The sweep time T can be computed based on the time needed for the signal to travel the unambiguous maximum range and is given as:

$$T = \alpha\frac{2R_{max}}{c}, \quad (7)$$

where α denotes the slope factor, R_{max} is the unambiguous maximum range and c is the speed of light. The sweep bandwidth is related to range resolution (ΔR) and can be given as:

$$B = \frac{c}{2\Delta R}. \quad (8)$$

In general, for an FMCW radar system, the slope factor is considered as at least 5 to 6 times the round trip time. Thus, for reliable target detection in mutual interference environments, we can obtain a unique slope (β) at each sweep by modulating both sweep time and sweep bandwidth. The modulation in sweep time can be obtained considering variations in sweep factor (α) for a given maximum unambiguous range. The modulation in sweep bandwidth can be selected based on the required range resolution.

We consider FMCW chirp signal with triangular sweep that sweeps-up with a slope of (B/T) and sweeps-down with a slope of $(-B/T)$. B is the sweep bandwidth, and T is the sweep time. Figure 4 (a) shows the spectrogram representation of 16 sweeps based on the conventional triangular FMCW chirp signal with constant slope for all sweeps and Fig. 4 (b) shows the proposed FMCW chirp with random slope considering both time and frequency diversity at different triangular sweeps.

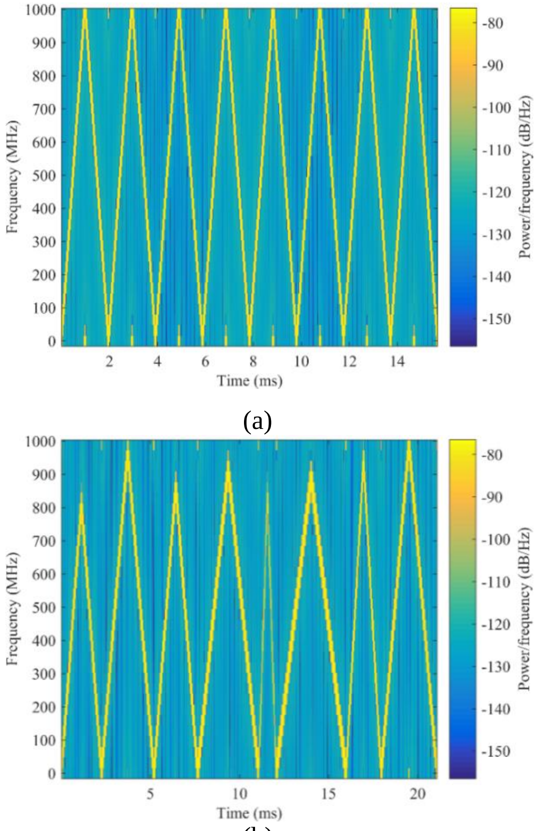

(a)

(b)

Fig. 4. Spectrogram representation of FMCW signal: (a) conventional triangular sweep, and (b) proposed triangular sweep with time and frequency diversity.

V. EXPERIMENTAL VALIDATION

It is important to ensure that the chirp signal of one radar must pose lower cross-correlation to that of another radar. Performance of the proposed waveform can be investigated by analyzing the auto-correlation and cross-correlation of the chirp signals. Hardware measurements of the proposed waveform in terms of auto-correlation and cross-correlation are conducted to assess the efficiency of the proposed waveform in mutual interference environment. Different from the 79 GHz band considered in ray-tracing simulation, an existing transceiver system from National Instrument (NI) with LabVIEW is adopted for measurements. Two NI 5791R RF transceiver adapter modules with built in FPGA are connected with NI 1085 chassis. The NI PXIe-1085 18-slot chassis features a high-bandwidth, all-hybrid backplane to meet a wide range of high-performance test and measurement application needs. The NI 5791R is an RF transceiver adapter module with 120 MHz bandwidth designed to work in conjunction with NI 7975 FlexRIO FPGA module. The NI 5791 features two channel analog-to-digital converter (ADC) and digital-to-analog converter (DAC) with 130 MS/s. It can upconvert and downconvert RF signals ranging from 200 MHz to 4.4 GHz. The hardware setup is shown in Fig. 5. We connect two transceivers at slot 6 and slot 12 of the chassis. A LabVIEW model has been developed to generate, transmit, and receive the chirp waveform. The model can also compute the correlation between transmitted and received signal. The model includes the flexibility of changing system parameters such as carrier frequency, starting and final frequency for chirp generation and output power at the transmitter. The auto-correlation and cross-correlation results have been obtained as follows:

(a) For auto-correlation, FMCW chirp has been generated and transmitted considering the carrier frequency of 4 GHz and sweep bandwidth of 100 MHz. The correlation between received signal and baseband transmitted signal was obtained.

(b) For cross-correlation, FMCW chirp has been generated and transmitted considering the carrier frequency of 3.75 GHz and sweep bandwidth of 120 MHz. The correlation between received signal and baseband transmitted signal in part (a) was obtained.

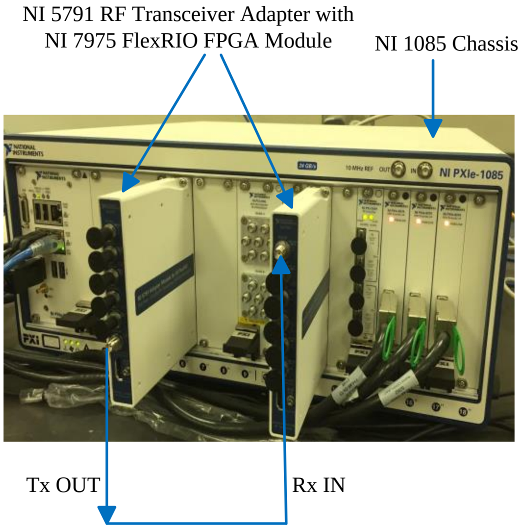

Fig. 5. NI 5791 adapter in conjunction with NI 7975 connected to NI 1085 chassis.

The auto-correlation and cross-correlation results are shown in Fig. 6 and Fig. 7 respectively. It is observed that the simulated and measured correlation results are in good agreement.

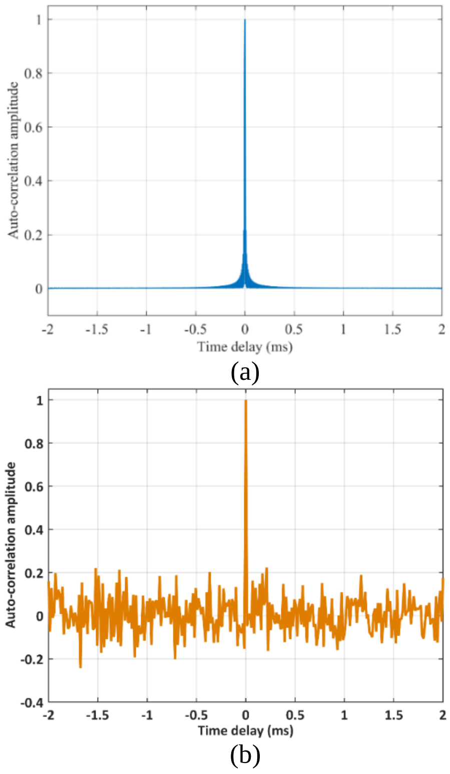

(a)

(b)

Fig. 6. Auto-correlation results of the proposed FMCW chirp. (a) Simulated and (b) measured.

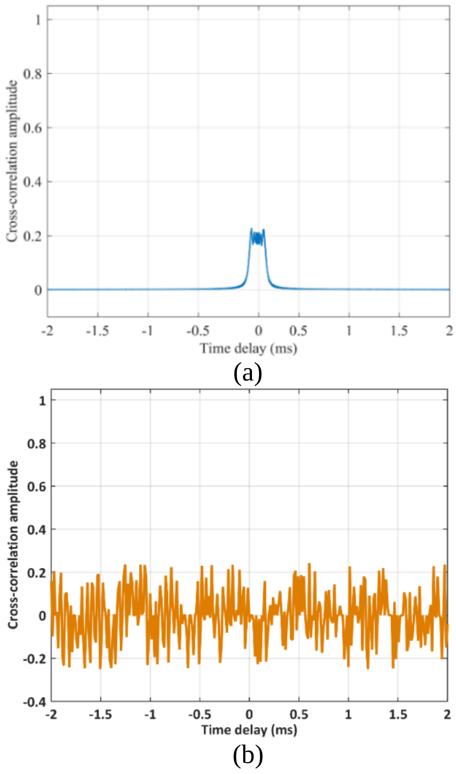

(a)

(b)

Fig. 7. Cross-correlation results of the proposed FMCW chirp. (a) Simulated and (b) measured.

For an effective comparison, the normalized auto-correlation and cross-correlation amplitude are provided with the same scale. It is observed that the proposed diverse FMCW chirp signal exhibits strong correlation characteristics, a sharp autocorrelation peak with same chirp, and lower cross-correlation with two chirp with different sweep slope considering time and frequency diversity. Thus, although the neighbor automotive radars contribute to the received signals, the received signals corresponding to transmitted chirp can be extracted efficiently in the correlation process.

VI. REALISTIC TRAFFIC SCENARIO AND WAVE PROPAGATION MODEL

Realistic and efficient modeling of the signal propagation scenario is the basis for successful evaluation of automotive radar applications. Physical characteristics of the received signal directly affect the upper layers in discriminating the range, angle and speed of the target vehicles. Realistic modeling of automotive radar channels requires the consideration of complex environments such as static objects (road terrain, buildings and foliage) and moving objects (neighbor vehicles on the road). The time-variant nature of the propagation channel for automotive radar is not only affected by the motion of the vehicles, but also by surrounding vehicles and objects adjacent to the road. Thus, to develop a realistic automotive radar channel, proper consideration of the scenario is necessary.

Figure 8 shows the automotive radar channel model that we developed using Wireless Insite ray-tracing tool [14]. To develop a realistic channel, the model randomly considers objects such as buildings of different size and shape, road terrain and tree foliage adjacent to the road. The model also includes vehicles equipped with radar unit and vehicles without radar unit as targets. These objects are designed individually and characterized with relevant material properties such as metal, glass etc. as shown in Table 1. Finally, all objects are integrated into a complete automotive radar channel model. This combination yields a virtual automotive radar environment and allows for the investigation of system performance in realistic approach.

Table 1: Considered object characterization

Object	Material
Body of vehicle	Metal
Vehicle mirrors	Glass
Wheels	Rubber
Front and rear bumpers	Plastic
Road terrain	Asphalt
Buildings	Brick
Tree foliage	Wood and leaf

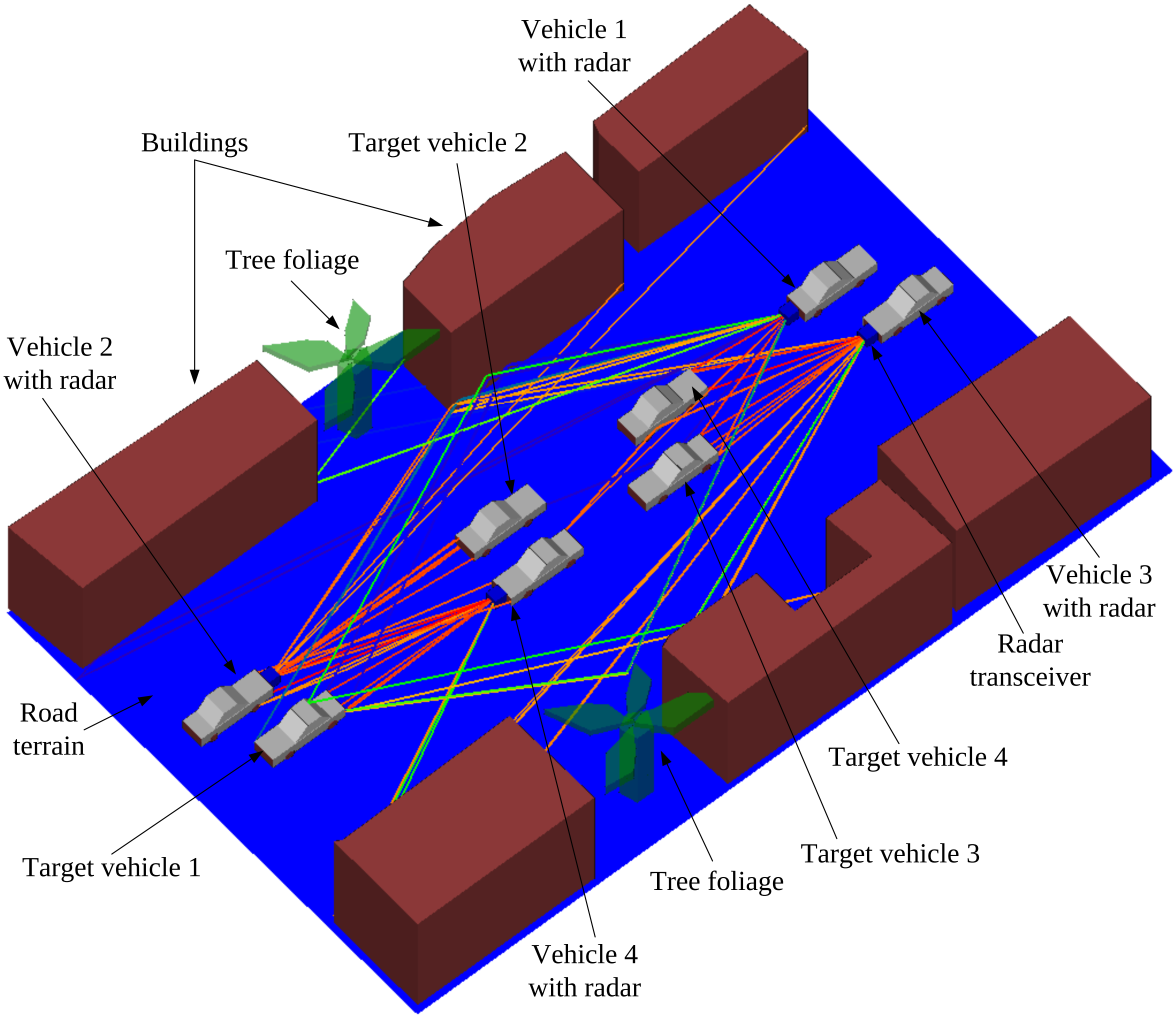

Fig. 8. Developed 3D automotive radar channel model using Wireless Insite ray-tracing tool.

Simulated data of the proposed FMCW waveform (time stamp and samples) are imported into the ray-tracing simulator as user defined waveform. The phased array and transceiver front end are parameterized in ray-tracing tool. The phased-array is configured as 4-element uniform linear array (ULA) considering directional antenna with 3-dB beamwidth of ±80° and ±10° in azimuth and elevation respectively. Table 2 shows the parameters used in signal generation and transmitter-receiver front end. The received signals are obtained by shooting rays from the transmitters and propagating them through the defined geometry of the developed channel model. These rays interact with geometrical features and make their way to receiver locations. Ray interactions include reflections from feature faces, diffractions around feature edges, and transmissions through features faces. All possible reflections of the transmit signal towards the position of the receiver are generated considering a realistic 3D traffic environment and wave propagation model developed using Wireless Insite ray-tracing tool. For every propagation path the time-domain received signal are calculated considering the related dielectric material properties of the reflecting object. Finally, post processing of the received signal has been performed to detect the range, angle and speed of the target vehicles.

Table 2: Simulation parameters

Parameter	Value
Operating frequency	79 GHz
Maximum target range	30 m
Sweep time	1-2 ms
Sweep bandwidth	800-1000 MHz
Transmit power	10 dBm
Transmit gain	36 dB
Receive gain	42 dB

VII. RESULTS AND DISCUSSION

We have considered a scenario that includes eight vehicles where four vehicles are equipped with automotive radars. We consider that radar equipped vehicle 1, 2 and target vehicle 2, 4 are in lane 1 respectively and moving toward right direction while radar equipped vehicle 3, 4 and target vehicle 1, 3 are in lane 2 and moving towards left direction as shown in Fig. 8. All possible reflections of the transmit signal towards the position of the receiver are generated using developed model in Wireless Insite ray-tracing tool. For every propagation path the time-domain received signal are calculated considering the related dielectric material properties of the reflecting object.

Dechirping is performed by mixing the output signal of the receiver front end with the reference signal. Beamforming is then applied considering a phase-shift beamformer to enhance the detection of signals by coherently summing signals across elements of arrays. The beamforming outputs are buffered for each sweep. The first step in the signal processing step is range estimation. Once the range of the targets are estimated, the data in the corresponding range bins are used to estimate the speed and angle of the same target. For range detection, the buffered signal for each sweep are converted to frequency domain. The beat frequencies of dechirped signals are converted to corresponding range and the target range is estimated. For triangular FMCW chirp, the up-sweep and down-sweep have separate beat frequencies. The difference between frequency of the transmitted and received signals during up-sweep and down-sweep frequency ramp is called the up-sweep beat frequency (f_{bu}) and down-sweep beat frequency (f_{bd}) respectively. The range estimation can be given as [15]:

$$R = \frac{cT}{4B} \cdot \frac{(f_{bu}+f_{bd})}{2}, \tag{9}$$

where B and T are the sweep bandwidth and sweep time respectively. For speed estimation, the Range-Doppler response is computed by converting dechirp data into frequency domain. The Doppler domain data is then converted to speed to determine the relative speed between radar and the target vehicles. The relative velocity of the target can be given as:

$$V_r = \frac{\lambda}{2} \cdot \frac{(f_{bd}-f_{bu})}{2}. \tag{10}$$

Where λ denotes the wavelength. The terms f_{bu} and f_{bd} are the up-sweep and down-sweep beat frequencies respectively. The angle estimation of target vehicles can be performed by converting dechirp output in frequency domain and applying root MUSIC algorithm [16].

From the ray-tracing output, we obtain the received signal for all Tx-Rx combinations. Based on the ray-analysis as shown in Fig. 8, it is observed that each radar receives the reflected signals associated with its own transmission as well as the reflected or direct signal from other radars. Let us investigate the target detection performance of automotive radar based on the conventional FMCW waveform and the proposed waveform with time and frequency diversity under different scenarios as follows.

A. Ideal scenario without mutual interference

Let us assume an ideal scenario, i.e., without any mutual interference. We consider the conventional FMCW waveform with the same slope as transmitted signals from radar equipped vehicle 1 and 2 as shown in Fig. 8. The reflected signal associated only with the transmitted signal from the candidate radar are considered in the dechirping process. Figure 9 (a) shows that radar equipped on rear bumper of vehicle 1 estimates the range of target vehicles 3 and 4 accurately at about 9.15 and 6.5 meters respectively. Figure 9 (b) shows the radar equipped vehicle 2 estimates the range of target vehicle 2 and radar equipped vehicle 4 accurately at about 12.6 and 13.65 meters respectively. Thus, it is observed that the range of target vehicles is estimated accurately with negligible ambiguities or unwanted peaks with lower values from roadside buildings and road terrain.

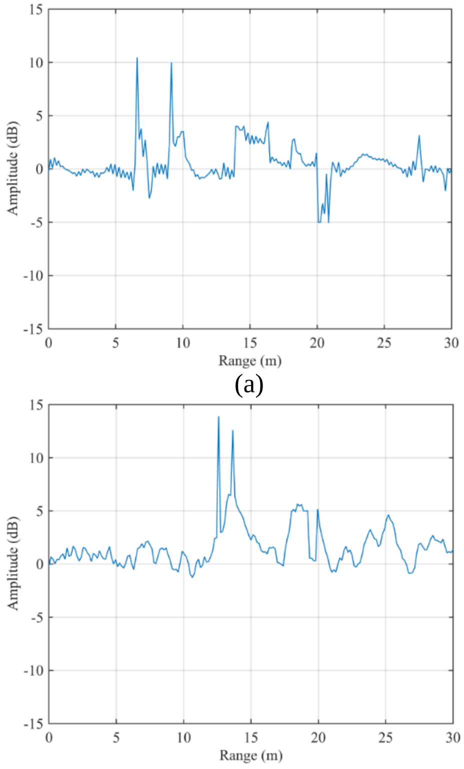

(a)

(b)

Fig. 9. Estimated range of target vehicles (a) target vehicles 3 and 4 are detected at radar equipped vehicle 1 and (b) target vehicle 2 and radar equipped vehicle 4 are detected at radar equipped vehicle 2.

B. Mutual interference due to indirect signal

Let us consider the mutual interference of indirect reflected signals due to the transmitted signal from other radars as shown in Fig. 2. In this scenario, radar equipped vehicles 1 and 3 are transmitting conventional FMCW waveform with constant slope in same directions to the target vehicles simultaneously as shown in Fig. 8. Thus, both radars will receive the reflected signal from the target vehicles due to the transmission of other radar. Let us consider the target detection in radar equipped vehicle 1 including the indirect interference from radar equipped vehicle 3. Figure 10 (a) shows the range estimation results of radar equipped vehicle 1. It is observed that four targets are detected where two false targets are introduced due to indirect mutual interference from radar equipped vehicle 3.

Let us investigate the same scenario by transmitting two different FMCW waveforms from radar equipped vehicles 1 and 3 with time and frequency diversity at each sweep considering the proposed waveform design technique. The dechirping operations for this case can be given as:

$$\Psi_{MF,n}(t) = \Psi_{rx,n}(t)\otimes\Psi^{*}_{tx,n}(-t), \qquad (11)$$

where $\Psi_{rx,n}(t)$ and $\Psi_{tx,n}(t)$ are the received signal and transmitted signal associated with nth radar respectively. Figure 10 (b) shows the range estimation results of radar equipped vehicle 1 based on the proposed FMCW waveform. It is observed that the two target vehicles are detected successfully and false targets due to indirect interference from radar equipped vehicle 3 are mitigated.

C. Mutual interference due to direct signal

Let us consider the mutual interference due to the direct signal transmitted from other radars as shown in Fig. 3. In this scenario, radar equipped vehicles 2 and 4 as shown in Fig. 8 are in opposite directions and transmitting conventional FMCW waveforms with same slope simultaneously. Thus, both radars will receive the delayed version of the transmitted signal directly from other radar. Let us consider the target detection in radar equipped vehicle 2 including the direct interference from radar equipped vehicle 4.

Figure 11 (a) shows the range estimation results of radar equipped vehicle 2. It is observed that three targets are detected where one false target is introduced at about 6.6 meters due to the direct reception of delayed version of the transmitted signal from radar equipped vehicle 4. It is also observed that the amplitude of the false target is higher than the actual target because of the direct reception of the transmitted signal.

Let us investigate the same scenario by transmitting two different FMCW waveform in radar equipped vehicles 2 and 4 with time and frequency diversity at each sweep considering the proposed waveform design technique. Figure 11 (b) shows the range estimation results of radar equipped vehicle 2 based on the proposed FMCW waveform. It is observed that the two vehicles (target vehicle 2 and radar equipped vehicle 4) are detected successfully at 12.6 meters and 13.65 meters respectively and false target at 6.6 meters is mitigated.

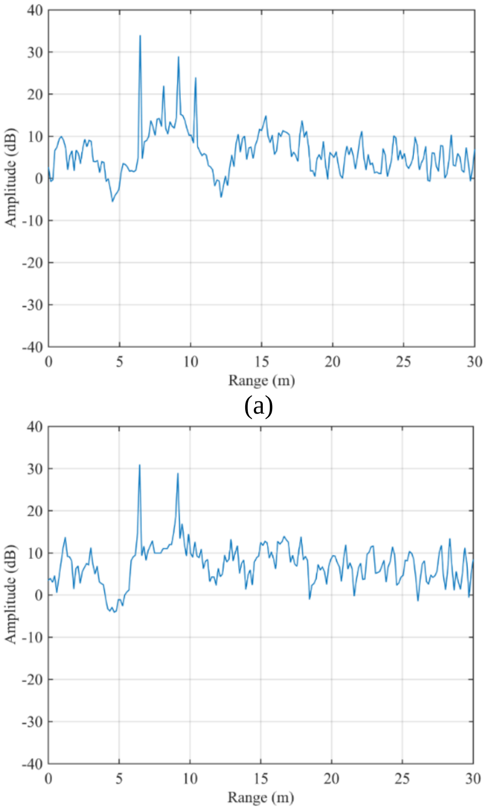

(a)

(b)

Fig. 10. Estimated range of target vehicles at radar equipped vehicle 1: (a) four target vehicles are detected including two false targets due to indirect mutual interference from radar equipped vehicle 3, and (b) two target vehicles are detected without false targets.

To evaluate the effectiveness of the proposed waveform in multi-target scenarios, the ray-tracing model is modified for varying number of target vehicles at different locations of the road terrain. The received signals for each scenario are processed to estimate the range, angle and speed of the target vehicles. For target detection, we consider adaptive decision threshold based on the mean of the matched filtering output, which is given as:

$$\delta = \mathrm{E}\{\Psi_{MF,n}(t)\}, \qquad (12)$$

where E{.} denotes the average of the dechirping output. For an effective analysis, the probability of target detection as well as root mean-squared errors (RMSE) between actual and estimated range, angle and speed of the target vehicles are obtained as:

$$RMSE = \sqrt{\frac{1}{N}\sum_{n=1}^{N}\left[\phi-\hat{\phi}\right]^{2}}, \tag{13}$$

where ϕ and $\hat{\phi}$ are the actual and estimated values of range, angle and speed of the target vehicles.

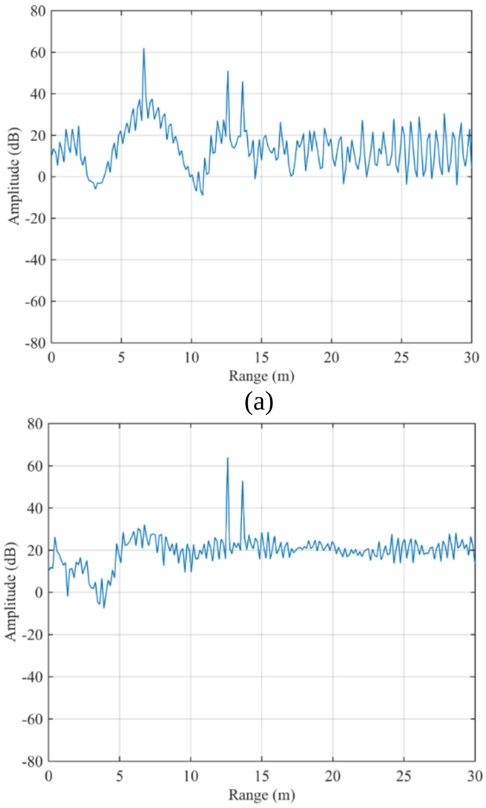

(a)

(b)

Fig. 11. Estimated range of target vehicles at radar equipped vehicle 2: (a) three target vehicles are detected including one false target due to direct mutual interference from radar equipped vehicle 4, and (b) two target vehicles are detected without false target.

The probability of detection for varying numbers of target vehicles is shown in Fig. 12, where the probability of detection can be defined as the ratio of the number of detected real targets to the number of total real targets. It is observed that the proposed waveform outperforms the conventional FMCW waveform and exhibits higher probability of target detection. Figure 13 shows the RMSE of range, angle and speed for varying number of target vehicles. It is observed that RMSE increases with the number of target vehicles increases. The proposed waveform exhibits multi-target detection with range accuracy of about 0.13 m, angle and speed accuracy of about 0.12° and 0.1 km/h considering 10 target vehicles.

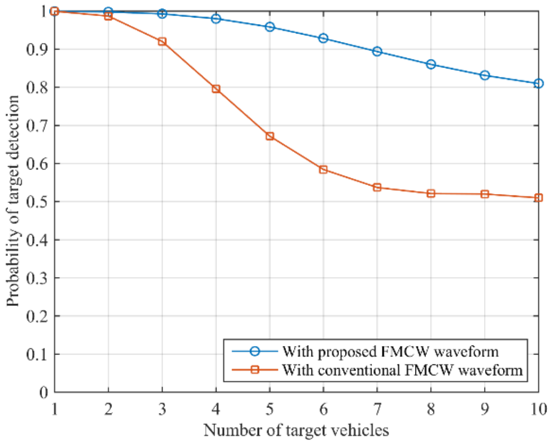

Fig. 12. Detection probability for varying number of target vehicles.

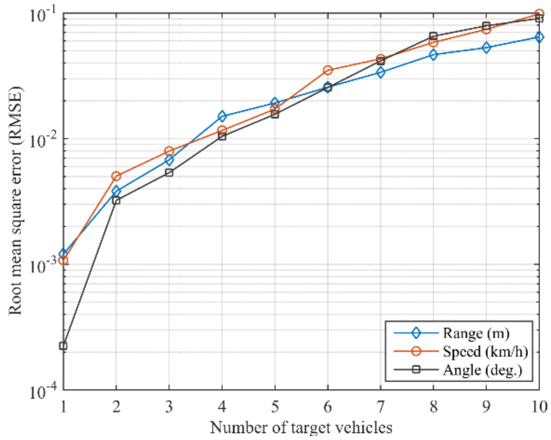

Fig. 13. Root mean squared error (RMSE) for varying number of target vehicles.

VIII. CONCLUSION

Advanced waveform design technique is proposed for multi-target detection and mutual interference mitigation in short-range automotive radars. Ray-tracing model is developed that allows for investigating the entire signal flow considering the wave propagation in a realistic road traffic scenario. Performance of the proposed waveform in different mutual interference scenarios has been presented. The thorough analysis of the proposed system concept has been investigated in terms of detection accuracy and probability of detection. However, there are many additional aspects that can be investigated with the developed model, e.g., the performance investigation of different beamforming techniques and influence of various array configurations can be assessed under realistic conditions. Hence, the developed realistic model can be regarded a comprehensive solution for the virtual performance evaluation of automotive radar concepts.

ACKNOWLEDGMENT

This work is supported by the Deanship of Scientific Research and Research Center at the College of Engineering, King Saud University, Riyadh, Saudi Arabia.

REFERENCES

[1] B. H. Ku, P. Schmalenberg, O. Inac, O. D. Gurbuz, J. S. Lee, K. Shiozaki, and G. M. Rebeiz, “A 77-81 GHz 16-element phased-array receiver with ±50° beam scanning for advanced automotive radars,” *IEEE Trans. on Microwave Theory and Techniques*, vol. 62, pp. 2823-2832, 2014.

[2] N. Sönmez, F. Tokan, and N. Türker Tokan, “Double lens antennas in millimeter-wave automotive radar sensors,” *Applied Computational Electromagnetics Society (ACES)*, vol. 32, no. 10, pp. 901-907, 2017.

[3] V. Jain, F. Tzeng, L. Zhou, and P. Heydari, “A single-chip dual-band 77-81 GHz BiCMOS transceiver for automotive radars,” *IEEE Journal of Solid-State Circuits*, vol. 44, pp. 3469-3485, 2009.

[4] G. Brooker, “Mutual interference of millimeter-wave radar systems,” *IEEE Trans. on Electromagnetic Compatibility*, vol. 49, pp. 170-181, 2007.

[5] Y. Han, E. Ekici, H. Kremo, and O. Altintas, “Automotive radar and communications sharing of the 79-GHz band,” *ACM Int. Workshop on Smart, Autonomous, and Connected Vehicular Systems and Services*, pp. 6-13, 2016.

[6] S. Heuel, “Automotive radar sensors must address interference issues,” *Microwave Journal*, vol. 59, pp. 22-36, 2016.

[7] A. Al-Hourani, R. J. Evans, S. Kandeepan, B. Moran, and H. Eltom, “Stochastic geometry methods for modeling automotive radar interference,” *IEEE Trans. on Intelligent Transportation Systems*, vol. 19, no. 2, pp. 333-344, 2018.

[8] T. Schipper, M. Harter, T. Mahler, O. Kern, and T. Zwick, “Discussion of the operating range of frequency modulated radars in the presence of interference,” *Int. Journal of Microwave and Wireless Technologies*, vol. 6, pp. 371-378, 2014.

[9] Y. Kim, “Identification of FMCW radar in mutual interference environments using frequency ramp modulation,” *European Conf. on Antennas and Propagation (EuCAP)*, pp. 1-3, 2016.

[10] Q. Nguyen, M. Park, Y. Kim, and F. Bien, “77 GHz waveform generator with multiple frequency shift keying modulation for multi-target detection automotive radar applications,” *Electronics Letters*, vol. 51, pp. 595-596, 2015.

[11] C. Kärnfelt, A. Péden, A. Bazzi, G. E. H. Shhadé, M. Abbas, and T. Chonavel, “77 GHz ACC radar simulation platform,” *Int. Conf. on Intelligent Transport Systems Telecommunications (ITST)*, pp. 209-214, 2009.

[12] G. Galati and G. Pavan, “Noise radar technology as an interference prevention method,” *Journal of Electrical and Computer Engineering*, vol. 2013, p. 4, 2013.

[13] B. Kim and J. Lee, “Mutual interference-resilient vehicular spread spectrum radar using ZCZ code,” *IEMEK Journal of Embedded Systems and Applications*, vol. 11, pp. 29-37, 2016.

[14] Remcom. Wireless InSite. Available at: http://www.remcom.com/wireless-insite

[15] S. Kim, I. Paek, and M. Ka, “Simulation and test results of triangular fast ramp FMCW waveform,” *IEEE Radar Conf.*, pp. 1-4, 2013.

[16] H. L. Van Trees, “Optimum array processing, part IV of detection, estimation, and modulation theory,” EISBN: 0-471-09390-4, pp. 362-382, 2002.

Md Anowar Hossain received his B.S. degree in Computer and Communication Engineering from International Islamic University Chittagong. He obtained his M.S. and Ph.D. degrees in Electrical Engineering from King Saud University. He is currently working as a Researcher in the Electrical Engineering Department, King Saud University. His research interests include radar signal processing, automotive radar, intelligent transportation system (ITS), cooperative driving, vehicular communication, and software-defined radio (SDR) systems.

Ibrahim Elshafiey received his B.S. degree in Communications and Electronics Engineering from Cairo University in 1985. He obtained his M.S. and Ph.D. degrees from Iowa State University in 1992 and 1994, respectively. He is currently working as a Professor in the Electrical Engineering Department, King Saud University. His research interests include computational electromagnetics and biomedical imaging.

Abdulhameed Al-Sanie received his Ph.D. degree from Syracuse University, New York, in 1992. He has been with the Department of Electrical Engineering at King Saud University since 1983, where he is currently working as Department Chair. His research interests include MIMO communication systems and space time codes, Coded Modulations, and ARQ Systems.

Time-Domain Spectral Inversion Method for Characterization of Subsurface Layers in Ground-Penetrating-Radar (GPR) Applications

Zohre Motevalli and Bijan Zakeri

Department of Electrical and Computer Engineering
Babol Noshirvani University of Technology, Babol, Iran
zohre.dmt@gmail.com, zakeri@nit.ac.ir

Abstract **─** Ground-Penetrating-Radar (GPR) data analysis has been widely utilized in subsurface and geophysics applications. One of the applications turning into great importance is multilayer subsurface hydraulic parameter identification and soil water content estimations. The classic GPR techniques have shown limitations in detecting deeper soil layers and unsatisfactory accuracy in estimating the electrical properties of the layers. Spectral inversion methods have been recently identified and developed to be an effective tool to tackle these problems. In this work, the spectral inversion method is extended in time-domain and a comprehensive formulation of the algorithm along with an improved well-defined cost function is presented. The Time-Domain Spectral Inversion (TDSI) method is then applied to environmentally-relevant multilayer soil geometries and the corresponding estimated electrical properties are drawn. The results show the TDSI method considerably ameliorates the performance of the inversion in terms of simplicity, accuracy, and applicability.

Index Terms **─** Ground-Penetrating-Radar (GPR), microwave imaging, multilayer subsurface characterization, noise, soil moisture, Time-Domain Spectral Inversion (TDSI).

I. INTRODUCTION

There are numerous methods to extract electrical properties of a material [1-4]. Among all existing methods, microwave imaging techniques including Synthetic Aperture Radar (SAR) [5], Time-Reversal (TR) [6, 7], and Ground-Penetrating-Radar (GPR) [8, 9] have become promising tools due to their non-destructive capabilities. These techniques rely on comparing the transmitted signals with the received ones. Moreover, choosing the best technique is primarily governed by the corresponding application. For instance SAR is prevalent for remote sensing applications [10] whereas GPR is employed for near-field subsurface characterizations [11]. Soil-based GPR constitutes countless activities in the fields of civil and construction [12], water resources [13], underground aquifers [14], and soil water content measurements [15]. GPR method is a function of soil's electrical parameters (electric permittivity, magnetic permeability, and conductivity), number of soil layers, and the performed survey method (e.g. Common Offset or Common Midpoint modes) [16]. More information regarding the principles and history of the GPR technique is covered by Jol [17].

Most of GPR techniques in the last decade for subsurface characterizations can be classified into four common categories: 1) Reflected Wave Velocity technique [18] identifies the dielectric constants by employing the wave velocity information and the corresponding propagation times reflected from the layers. 2) In Ground Wave technique [19], direct ground waves travel from the transmitting antenna to the receiving antenna just below the soil surface. The velocity of the direct ground wave is used to estimate the dielectric properties and the soil water content at shallow depths. 3) In Borehole Direct Wave Velocity technique [20], a transmitting and a receiving antenna are each separately placed in a nonmetallic tube. The tubes are then vertically deployed in the soil. Assuming the electromagnetic wave sent from the transmitter travels along a direct path through the soil to reach the receiver, and by knowing the line-of-sight distance between the transmitting and receiving antennas, the wave velocity is calculated. By knowing the wave velocity within the soil, the dielectric constant and the water content are derived. 4) Last not least, in Reflection Coefficient technique [21] two reflected waveforms from a flat soil surface and from a reference metallic layer are compared which eventually results in calculating the dielectric constant of the top surface layer. Ground Wave and Reflection Coefficient techniques yield the estimation of the top and shallow layers and are not capable of providing information for deeper layers [22]. The Borehole technique is also destructive and, in many cases, would not be feasible to excavate the soil. Furthermore, the main limitation of the aforementioned techniques arises from the fact that they almost employ partial information of the available data, either the propagation times or the reflection amplitudes. These techniques also suffer from

Submitted On: January 12, 2017
Accepted On: December 24, 2018

geometrical simplifications, such as ignoring the transceiver couplings and the distance from the soil's surface. The multiple reflections in soil layers are also not considered. To tackle the innate lack of data interpreting, a need for a new technique which considers the possible electromagnetic interactions seems desirable. Recently spectral inversion-based methods [22, 23] have shown promising results that would enable the utilization of the whole information of the data. The spectral inversion methods have also shown strong adaptability for thin layers [24]. Frequency-domain spectral inversion methods have been lately developed in terms of near-field wave modeling effects [25].

Even though the spectral inversion methods have been improved in recent years, most improvements have been achieved by defining the cost function in the frequency domain [26, 27]. Nonetheless, it is possible to have further improvements in the formulation, accuracy, and applicability of the method. With this goal, this paper presents formulations of Time-Domain Spectral Inversion (TDSI) method in presence of noise and exploits a well-defined cost function to ameliorate the performance of the method for multi-layer subsurface soil problems.

The remainder of the paper is organized as follows: In Section II the necessary formulations and theories behind a multilayer soil problem along with the details of TDSI method are introduced. In Section III, the specifications of the computational setup for synthetically-generated GPR data are explained. The results pertaining to the performance of TDSI method on environmentally-relevant soil geometries and in presence of noise are presented in Section IV and Section V, respectively. Finally, a summary of the present work and future contributions are drawn in Section VI.

II. PROBLEM FORMULATION

In this section the necessary formulations and theories behind a multilayer soil problem are presented. The final formulation lays a foundation upon an improved TDSI method which will be performed for estimating the electrical properties of a three-layer soil problem.

A. Generalized reflection coefficient

Figure 1 illustrates a semi-infinite two-dimensional N-layer model of multilayer soil geometry, where ε_i is the relative permittivity, μ_i is the relative permeability, σ_i is the conductivity, and $d_i = z_{i+1} - z_i$ is the thickness of each layer. The most fundamental modeling of such geometry is carried out by considering a homogeneous, linear, and isotropic medium. Moreover, the layers' interfaces are assumed to be non-rough. In the case the propagating wave with frequency f is plane and incident perpendicularly on the surface, the reflection Γ and the transmission T coefficients corresponding to each interface are formulated as (1) and (2), respectively [28],

$$\Gamma_{i,i+1} = \frac{\eta_{i+1} - \eta_i}{\eta_{i+1} + \eta_i} \ , \tag{1}$$

$$\mathrm{T}_{i,i+1} = \frac{2\eta_{i+1}}{\eta_{i+1} + \eta_i} \ , \tag{2}$$

where η_i is the characteristic impedance of each layer, and is written as (3),

$$\eta_i = \sqrt{\frac{j2\pi f \mu_0 \mu_i}{\sigma_i + j2\pi f \varepsilon_0 \varepsilon_i}} \ , \tag{3}$$

where ε_0=8.85×10^{-12} (F/m) and μ_0=1.26×10^{-6} (H/m) are the vacuum permittivity and permeability, respectively. By solving the Maxwell's equations and applying the proper boundary conditions, the generalized reflection coefficient R looking from the top surface is formulated as (4)-(5) [28],

$$R = \frac{\Gamma_{12} + \tilde{\Gamma}_{23} e^{-2\gamma_2 d_1}}{1 + \Gamma_{12}\tilde{\Gamma}_{23} e^{-2\gamma_2 d_1}} \ , \tag{4}$$

$$\begin{aligned} \tilde{\Gamma}_{23} &= \frac{\Gamma_{23} + \tilde{\Gamma}_{34} e^{-2\gamma_3 d_2}}{1 + \Gamma_{23}\tilde{\Gamma}_{34} e^{-2\gamma_3 d_2}} \ , \\ &\vdots \\ \tilde{\Gamma}_{i,i+1} &= \frac{\Gamma_{i,i+1} + \tilde{\Gamma}_{i+1,i+2} e^{-2\gamma_{i+1} d_i}}{1 + \Gamma_{i,i+1}\tilde{\Gamma}_{i+1,i+2} e^{-2\gamma_{i+1} d_i}} \ , \end{aligned} \tag{5}$$

where γ_i is the propagation constant of the i-th layer as formulated in (6),

$$\gamma_i = 2\pi f \sqrt{\mu_0 \mu_i \varepsilon_0 \varepsilon_i} \sqrt{1 - j\frac{\sigma_i}{2\pi f \varepsilon_0 \varepsilon_i}} \ . \tag{6}$$

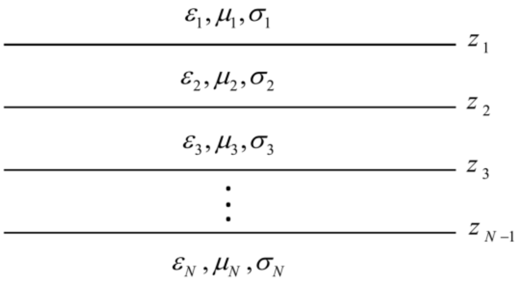

Fig. 1. Semi-infinite N-layer model of multilayer soil geometry.

For a three-layer model which will be conducted throughout this work the generalized reflection coefficient R can be obtained from (4)-(5) as (7),

$$R = \frac{\Gamma_{12} + \Gamma_{23} e^{-2\gamma_2 d}}{1 + \Gamma_{12}\Gamma_{23} e^{-2\gamma_2 d}} \ , \tag{7}$$

where d is the thickness of the middle soil layer. In practical GPR applications, there is a close distance between the antenna transceivers and the top soil surface. The generalized reflection coefficient looking at the soil from the location of transceivers, therefore, needs to be corrected. If h is the distance from the top soil layer and the transceivers, the corrected general reflection coefficient R_c can be written as (8),

$$R_c = Re^{-2\gamma_1 h} = \frac{\Gamma_{12}+\Gamma_{23}e^{-2\gamma_2 d}}{1+\Gamma_{12}\Gamma_{23}e^{-2\gamma_2 d}}\, e^{-2\gamma_1 h} . \tag{8}$$

Based on the corrected general reflection coefficient $R_c(f)$ and the incident waveform $F_x(f)$, the reflected waveform $F_y(f)$ back from the multilayer medium is calculated as (9),

$$F_y(f) = F_x(f) R_c(f) G(f) , \tag{9}$$

where $G(f)$ is the gain of the antenna. Assuming an isotropic radiation pattern with $G(f)=1$, (9) is simplified to (10),

$$F_y(f) = F_x(f) R_c(f) . \tag{10}$$

The next step to initiate the Time-Domain Spectral Inversion (TDSI) method is to convert the frequency-domain signal waveform (10) into a time-domain signal waveform. This can be performed by means of Inverse Fast Fourier Transform (IFFT). After modifying $R_c(f)$ and $F_x(f)$ to their proper conjugate double-side banded frequency-domain versions, the time-domain reflected waveform $f_y(t)$ can be represented as (11),

$$f_y(t) = \int_{-\infty}^{+\infty} F_x(f) \left[\frac{\Gamma_{12}+\Gamma_{23}e^{-2\gamma_2 d}}{1+\Gamma_{12}\Gamma_{23}e^{-2\gamma_2 d}}\; e^{-2\gamma_1 h} \right] e^{j2\pi ft} df , \tag{11}$$

where $F_x(f)$ can be calculated by taking the Fast Fourier Transform (FFT) of the incident time-domain waveform $f_x(t)$ as in (12),

$$F_x(f) = \int_{-\infty}^{+\infty} f_x(t) e^{-j2\pi ft}\, dt . \tag{12}$$

B. Time-Domain Spectral Inversion (TDSI) method

The main concept behind TDSI method is to minimize a well-defined cost function $O[f_y(t), g_y(t)]$ to achieve the best estimate (closeness) of the actual reflected waveform $g_y(t)$ by using the modeled reflected waveform $f_y(t)$. The actual waveform $g_y(t)$ can be either calculated synthetically (by computational methods) or measured practically. It is worth mentioning that the minimization problem is within ill-posed and non-unique classes of inverse scattering problem. This means the modeled waveform could become very similar to the actual waveform, but providing an inaccurate estimate of the modeled parameters. Converging to an answer yielding the correct estimate of the parameters and minimizing the cost function simultaneously is challenging [27].

Before treating the cost function, rectangular time windows are executed on $g_y(t)$ to remove the leakage of the transmitted signal into the received waveform. The next step is to identify the propagation times corresponding to each layer interface. We have taken advantage of the Short-Time Fourier Transform (STFT) algorithm and applied it on $g_y(t)$ to obtain the time-frequency spectrum $\bar{g}_y(f,\tau)$ as:

$$\bar{g}_y(f,\tau) = \mathrm{STFT}\left[g_y(t)\right] = \int_{-\infty}^{+\infty} g_y(t)\, w(t-\tau)\, e^{-j2\pi ft}\, dt , \tag{13}$$

where $w(t-\tau)$ is a window function and generally chosen as Hann or Gaussian window. At each time cell τ, the maximum magnitude of the entire frequencies is calculated and plotted against τ. The propagation time of each layer interface is then identified as an extrema point in this plot (demonstrated in Section IV). In three-layer model, there are two interfaces which correspond to the first M_1 and second M_2 extrema points in the time-frequency spectrum, respectively, as (14)-(15),

$$\left\{t_{M_1}, t_{M_2}\right\} = t\left\{\max_{1,2}\left|\mathrm{STFT}\left[g_y(t)\right]\right|\right\} , \tag{14}$$

$$\left\{t'_{M_1}, t'_{M_2}\right\} = t'\left\{\max_{1,2}\left|\mathrm{STFT}\left[f_y(t)\right]\right|\right\} . \tag{15}$$

The improved cost function of this work is formulated to prevent solutions from trapping in ill-posed answers. The cost function has been gradually modified through a variety of test cases to yield a robust and case-independent performance. Taking into account (11)-(15), the cost function is then expressed as (16),

$$O\left[f_y(t), g_y(t)\right] = \left(\sum_{i=1}^{N} L_3(t_i)\right)^2 L_4 L_5 , \tag{16}$$

where L_1, L_2, L_3, L_4, and L_5 are the functions calculated through (17)-(21). $L_1^{\max}$ and $L_2^{\max}$ are the maxima of L_1 and L_2 calculated within t_1 to t_N. L_1, L_2, and L_3 are formulated to evaluate the similarity between the modeled and actual waveforms. L_4 and L_5 also force the amplitude and corresponding time of the extrema points meet each other,

$$L_1(t_i) = f_y(t_i) - g_y(t_i) , \tag{17}$$

$$L_2(t_i) = \left|f_y(t_i)\right| - \left|g_y(t_i)\right| , \tag{18}$$

$$L_3(t_i) = \left[\frac{L_1(t_i)}{L_1^{\max}} + \frac{L_2(t_i)}{L_2^{\max}}\right] + \frac{L_1(t_i) L_2(t_i)}{L_1^{\max} L_2^{\max}} , \tag{19}$$

$$L_4 = f_y\left(t'_{M_1}\right) - g_y\left(t_{M_1}\right) + f_y\left(t'_{M_2}\right) - g_y\left(t_{M_2}\right) , \tag{20}$$

$$L_5 = \left(t_{M_1} - t'_{M_1}\right)^2 + \left(t_{M_2} - t'_{M_2}\right)^2 . \tag{21}$$

In the following sections the TDSI method will be applied on synthetically generated GPR data for a three-layer subsurface soil problem and the corresponding results and discussion will be presented.

III. COMPUTATIONAL SETUP

The computational geometry of a three-layer soil problem is shown in Fig. 2. The common offset (CO) GPR data have been synthesized using 2D GPRMax [29] free-commercial software, which simulates the electromagnetic fields based on finite-difference-time-domain (FDTD) method [30]. The 2D computational domain is gridded into dimensions X×Y=200×200 cm^2, with a uniform spatial discretization of $\Delta x=\Delta y=\Delta=5$ mm. The value of Δ is so assigned to create at least 10 nodes per λ_{m}, where λ_{m} denotes the wavelength (proportion to layers permittivity) corresponding to the maximum frequency content of the excitation signal. The maximum runtime is set sufficiently enough for the incident wave to travel from the source to the bottom end of the domain in a round trip. The boundary condition is also a perfectly matched layer (PML) to provide reflectionless truncation of the computation domain. The PML thickness is set to 10Δ at all four sides of the boundaries. A z-directed infinitesimal electric dipole plays as a transceiver and moves along the x-axis in 18 cm (36Δ) steps and linearly surveys the soil layers. The perpendicular distance h from the transceivers to the top surface layer is 75 cm (150Δ).

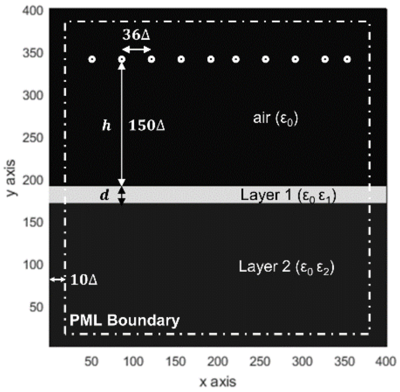

Fig. 2. Computational geometry (200×200 cm^2) of multilayer soil problem.

In this study twelve cases, six for each sandy and loamy soil cases with different volumetric water contents (VWC) [31] have been defined and evaluated by TDSI method, as shown in Table 1. The conductivity σ, however, is assumed constant and equal to 0.01 S/m for all cases.

The excitation signal is generally determined with respect to various constraints and specifications including particular electrical characteristics of the media, signal penetration through the soil layers, and portability of the setup [6]. To provide sufficient resolution for separating the layer responses in GPR data, a time-domain Ricker function (22) with proper adjusting parameters is considered as the excitation signal,

$$J\left(t\right)=-2\zeta\sqrt{e^{\frac{1}{2\zeta}}}\,e^{-\zeta\left(t-\chi\right)^{2}}\left(t-\chi\right)\,, \tag{22}$$

where $\zeta=2\pi^2 f^2$, $\chi=1/f$, and f is the central frequency chosen as 2 GHz.

Minimization of the cost function O[$f_y(t)$,$g_y(t)$] in (16) was performed by means of Trust-Region-Reflective algorithm in Matlab ™ where the function takes the vector arguments $V_n=[\varepsilon_1,\varepsilon_2,\ d\,]^n$ in every iteration and returns a scalar value. The *finite-differential-relative-step* parameter of the algorithm also needs to be correctly adjusted to prevent the solutions from trapping in local optima.

Table 1: Sandy and loamy soil parameters. The conductivity $\sigma=0.01$ S/m is constant for all cases

	Sandy			Loamy		
VWC (cm^3/cm^3)	ε_1	ε_2	d (cm)	ε_1	ε_2	d (cm)
0.05	1.6	4.5	10	1.6	4.5	12.5
0.1	2.9	6.2	10	2.9	6	12.5
0.15	4.7	8.8	10	4.7	7.6	12.5
0.2	7.2	12	10	7.2	9.8	12.5
0.25	10.3	15.6	10	10.3	12.6	12.5
0.3	13.6	19.1	10	13.6	16.5	12.5

IV. RESULTS

In this section the TDSI method is performed on the scenarios mentioned in the previous section. Fig. 3 represents a B-scan image of the loamy soil with VWC=0.15 cm^3/cm^3. The B-scan image is formed by collecting 10 A-scan traces of the linearly-surveyed GPR data. Each layer interface reflects a notable portion of the incident wave back to the transceiver. The interfaces are detectable as a bold line in the B-scan image. There are, however, a weaker trail of lines which may incorrectly be considered as additional interfaces. These trails are generally the consequence of near-field cylindrical wave propagation and multiple-reflections within the layers. The aforementioned problem can be tackled by exploiting STFT algorithm and the time-frequency spectrum as demonstrated in Fig. 4. The maximum magnitude of all frequencies at each time cell is plotted and shown in Fig. 4 (c). The extrema points (usually a threshold value is chosen) represent the time locations of the first and second actual interfaces, i.e., t_{M_1} and t_{M_2}.

Following the formulations and methods described in Section II, the comparison between the synthetically-generated sample A-scan signal gy(t) (the fifth trace) and the estimated one fy(t) based on TDSI method is depicted in Fig. 5.

The estimated parameters, i.e., ε_1, ε_2, and d, by TDSI method for sandy soil and loamy soil along with the actual parameters for all VWC cases listed in Table 1 are illustrated in Fig. 6. As can be seen qualitatively the estimated values are within close agreement with the actual values for both the sandy and loamy soil types. The results prove that the TDSI algorithm developed in this work is robust and its performance is case-independent. For the sandy soil, the average relative error between the estimated and actual values are calculated 3.70% for d, 9.01% for layer 1 relative permittivity ε_1, and 10.20% for layer 2 relative permittivity ε_2. For the loamy soil, the error values are calculated likewise as 5.43% for d, 12.94% for ε_1, and 13.88% for ε_2. The error values are ameliorated with respect to previous literature results [26, 27]. The GPR-based TDSI method also outperforms time-domain methods such as TR as it will not need the laborious data collection of time reversed array.

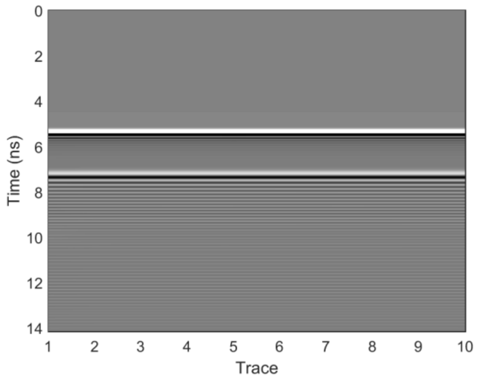

Fig. 3. B-scan image of 10 traces of linearly-surveyed GPR data for multilayer loamy soil with VWC=0.15 cm^3/cm^3. Each interface is displayed as a bold line in the B-scan image.

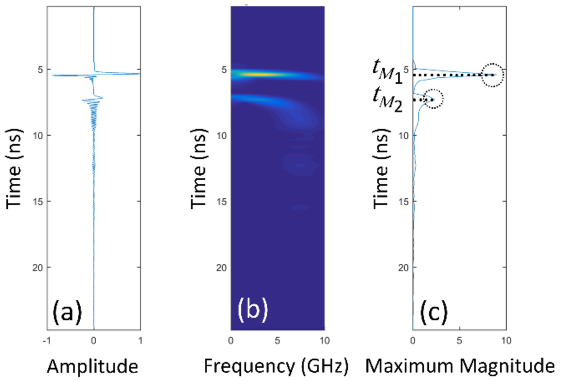

Fig. 4. Short-Time Fourier Transform (STFT) algorithm performed on a sample A-scan signal (the fifth trace) for the loamy soil with VWC=0.15 cm^3/cm^3. (a) A-scan signal, (b) time-frequency spectrum, and (c) magnitude-time plot. The extrema points and corresponding t_{M_1} and t_{M_2} are also shown.

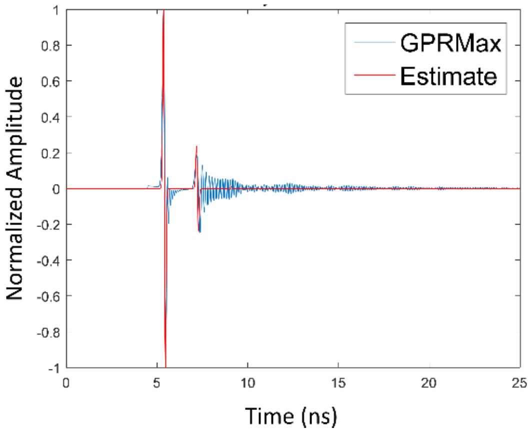

Fig. 5. Comparison of synthetically generated sample A-scan signal (the fifth trace) by GPRMax (blue) and the estimated one (red) using TDSI method for loamy soil with VWC=0.15 cm^3/cm^3.

V. PRESENCE OF NOISE

In this section sandy soil with VWC=0.1 cm^3/cm^3 and loamy soil with VWC=0.25 cm^3/cm^3 have been chosen to evaluate the efficiency of TDSI method in presence of a random Gaussian noise with SNR=10 dB superimposed on the received signals. Figure 7 demonstrates the actual and estimated parameter values for the aforementioned soil types. According to Fig. 7 the relative permittivity values of the soil with higher VWC are overestimated. As VWC increases there is less contrast between the permittivity of layers (Table 1), therefore, the amplitude of the reflected waveform gets smaller and drowns below the noise level. This phenomenon influences the TDSI method as it yields overestimation of relative permittivity values.

VI. CONCLUSION

In this work, a completed formulation of Time-Domain Spectral Inversion (TDSI) method was represented. The corresponding differential cost function was developed to a new well-defined function which was capable of minimizing the cost function and converging to a non-ill-posed answer representing a correct estimate of the parameters. The proposed TDSI method was then applied to twelve cases of environmentally-relevant three-layer sandy and loamy soil problems with different volumetric water contents. The results showed the estimated parameters were within a good agreement with the actual values and the calculated relative errors were substantially degraded and stood within appreciable tolerance compared to previous literature results.

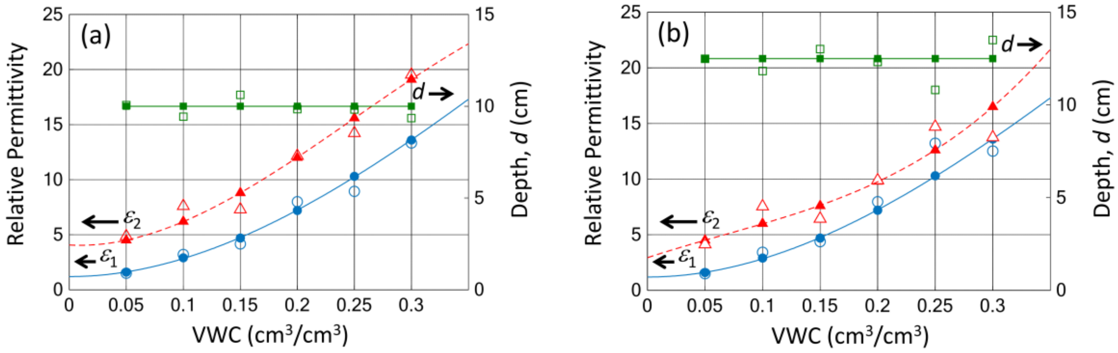

Fig. 6. Estimated (hollow symbols) and actual (filled symbols) parameter values of three-layer: (a) sandy and (b) loamy soil based on TDSI method. Solid lines are cubic fitted polynomial.

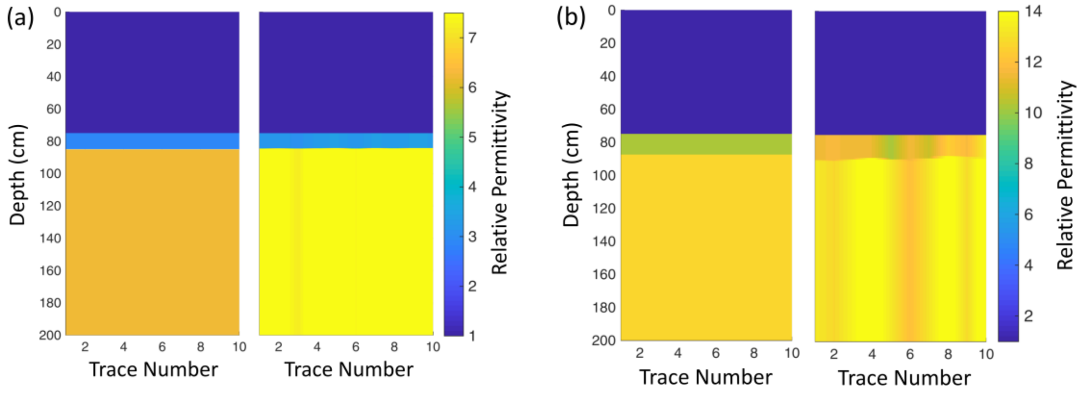

Fig. 7. Comparison of actual parameter values (left) and estimated values (right) based on TDSI method in presence of a 10 dB Gaussian noise for: (a) sandy soil with VWC=0.10 cm^3/cm^3, and (b) loamy soil with VWC=0.25 cm^3/cm^3.

ACKNOWLEDGMENT

The authors would like to thank the reviewers for their valuable comments. The authors gratefully acknowledge Amin Gorji from Iowa State University, USA, for his support and knowledge in this project.

REFERENCES

[1] M. Ozturk, U. K. Sevim, O. Akgol, E. Unal, and M. Karaaslan, "Determination of physical properties of concrete by using microwave nondestructive techniques," *Applied Computational Electromagnetics Society Journal*, vol. 33, 2018.

[2] A. Gorji and N. Bowler, "Dielectric measurement of low-concentration aqueous solutions: assessment of uncertainty and ion-specific responses," *Measurement Science and Technology*, 2018.

[3] J.-S. Lee, W.-T. Hong, K. Park, S. Hong, S.-H. Lee, and Y.-H. Byun, "Evaluation of water content in an active layer using penetration-type time domain reflectometry," *Applied Sciences*, vol. 8, p. 935, 2018.

[4] A. Elboushi, A. R. Sebak, and T. Denidni, "Through wall gap detection using monostatic radar," *Applied Computational Electromagnetics Society Journal*, vol. 28, 2013.

[5] C. Thajudeen, W. Zhang, and A. Hoorfar, "Efficient forward modeling of large scale buildings and through-the-wall radar imaging scenarios," *28th Annual Review of Progress in Applied Computational Electromagnetics (ACES)*, pp. 122-126, 2012.

[6] A. B. Gorji and B. Zakeri, "Time-reversal through-wall microwave imaging in rich scattering environment based on target initial reflection method," *Applied Computational Electromagnetics Society Journal*, vol. 30, 2015.

[7] S. Sadeghi and R. Faraji-Dana, "A practical UBE microwave imaging system using time-domain DORT for tumor detection," *Applied Computational Electromagnetics Society Journal*, vol. 31, 2016.

[8] K. Prokopidis and T. Tsiboukis, "Modeling of ground-penetrating radar for detecting buried objects in dispersive soils," *Applied Computational Electromagnetics Society Journal*, vol. 22, p. 287, 2007.

[9] S. MakalYucedag and A. Kizilay, "Time domain

analysis of ultra-wide band signals from buried objects under flat and slightly rough surfaces," in *ACES*, p. 646, 2013.

[10] B. K. Hornbuckle, J. C. Patton, A. VanLoocke, A. E. Suyker, M. C. Roby, V. A. Walker, *et al.*, "SMOS optical thickness changes in response to the growth and development of crops, crop management, and weather," *Remote Sensing of Environment*, vol. 180, pp. 320-333, 2016.

[11] D. Comite, A. Galli, I. Catapano, and F. Soldovieri, "Advanced imaging for down-looking contactless GPR systems," in *Applied Computational Electromagnetics Society Symposium-Italy (ACES) International*, 2017, pp. 1-2, 2017.

[12] Z. W. Wang, M. Zhou, G. G. Slabaugh, J. Zhai, and T. Fang, "Automatic detection of bridge deck condition from ground penetrating radar images," *IEEE Transactions on Automation Science and Engineering*, vol. 8, pp. 633-640, 2011.

[13] H. Liu, K. Takahashi, and M. Sato, "Measurement of dielectric permittivity and thickness of snow and ice on a brackish Lagoon using GPR," *IEEE Journal of Selected Topics in Applied Earth Observations and Remote Sensing*, vol. 7, pp. 820-827, 2014.

[14] H. Liu, X. Xie, J. Cui, K. Takahashi, and M. Sato, "Groundwater level monitoring for hydraulic characterization of an unconfined aquifer by common mid-point measurements using GPR," *Journal of Environmental and Engineering Geophysics*, vol. 19, pp. 259-268, 2014.

[15] L. Weihermüller, J. Huisman, S. Lambot, M. Herbst, and H. Vereecken, "Mapping the spatial variation of soil water content at the field scale with different ground penetrating radar techniques," *Journal of Hydrology*, vol. 340, pp. 205-216, 2007.

[16] R. W. Jacob and T. Urban, "Ground-penetrating radar velocity determination and precision estimates using common-midpoint (CMP) collection with hand-picking, semblance analysis and cross-correlation analysis: A case study and tutorial for archaeologists," *Archaeometry*, vol. 58, pp. 987-1002, 2016.

[17] H. M. Jol, *Ground Penetrating Radar Theory and Applications*. Elsevier, 2008.

[18] Y. Nakashima, H. Zhou, and M. Sato, "Estimation of groundwater level by GPR in an area with multiple ambiguous reflections," *Journal of Applied Geophysics*, vol. 47, pp. 241-249, 2001.

[19] L. Galagedara, G. Parkin, J. Redman, P. Von Bertoldi, and A. Endres, "Field studies of the GPR ground wave method for estimating soil water content during irrigation and drainage," *Journal of Hydrology*, vol. 301, pp. 182-197, 2005.

[20] D. F. Rucker and T. Ferré, "Near-surface water content estimation with borehole ground penetrating radar using critically refracted waves," *Vadose Zone Journal*, vol. 2, pp. 247-252, 2003.

[21] G. Serbin and D. Or, "Ground-penetrating radar measurement of soil water content dynamics using a suspended horn antenna," *IEEE Transactions on Geoscience and Remote Sensing*, vol. 42, pp. 1695-1705, 2004.

[22] S. Lambot, E. C. Slob, I. van den Bosch, B. Stockbroeckx, and M. Vanclooster, "Modeling of ground-penetrating radar for accurate characterization of subsurface electric properties," *IEEE Transactions on Geoscience and Remote Sensing*, vol. 42, pp. 2555-2568, 2004.

[23] C. I. Puryear and J. P. Castagna, "Layer-thickness determination and stratigraphic interpretation using spectral inversion: Theory and application," *Geophysics*, vol. 73, pp. R37-R48, 2008.

[24] J. Minet, S. Lambot, E. C. Slob, and M. Vanclooster, "Soil surface water content estimation by full-waveform GPR signal inversion in the presence of thin layers," *IEEE Transactions on Geoscience and Remote Sensing*, vol. 48, pp. 1138-1150, 2010.

[25] A. P. Tran, F. Andre, and S. Lambot, "Validation of near-field ground-penetrating radar modeling using full-wave inversion for soil moisture estimation," *IEEE Transactions on Geoscience and Remote Sensing*, vol. 52, pp. 5483-5497, 2014.

[26] Y. Huang, J. Zhang, and J. Chen, "Application of time-frequency domain spectral decomposition based on least-square matching pursuit to improve subsurface imaging," in *29th Annual Review of Progress in Applied Computational Electromagnetics*, Monterey, CA, USA, 2013.

[27] Z.-l. Huang and J. Zhang, "Determination of parameters of subsurface layers using GPR spectral inversion method," *IEEE Transactions on Geoscience and Remote Sensing*, vol. 52, pp. 7527-7533, 2014.

[28] W. C. Chew, *Waves and Fields in Inhomogeneous Media*. vol. 522: IEEE Press New York, 1995.

[29] A. Giannopoulos, "Modelling ground penetrating radar by GPRMax," *Construction and Building Materials*, vol. 19, pp. 755-762, 2005.

[30] A. Taflove and S. Hagness, *Computational Electrodynamics: The Finite-Difference Time Domain Method*. 3rd ed., Artech House Boston, 2005.

[31] J. Cihlar and F. T. Ulaby, "Dielectric properties of soils as a function of moisture content," 1974.

Mutual Coupling Reduction Between Patch Antenna and Microstrip Transmission Line by Using Defected Isolation Wall

Yuting Zhao [1], Yingsong Li [1,2,*], Wanlu Shi [1], and Wenhua Yu [3]

[1] College of Information and Communication Engineering
Harbin Engineering University, Harbin, Heilongjiang 150001, China

[2] National Space Science Center
Chinese Academy Science, Beijing 100190, China
*liyingsong@ieee.org

[3] School of Mathematics and Statistics
Jiangsu Normal University, Xuzhou 221116, China

Abstract **─** A mutual coupling reduction method for closely installed patch antenna (PA) and microstrip transmission line (MTL) is proposed by means of defected isolation wall structure (DIWS) which is comprised of a metal patch with periodically G-shaped structure and two dielectric substrate sheets set on both sides of the metal patch. The DIWS model, design procedure and investigation on its stop filtering characteristics are presented. Also, the dominant parameters of DIWS are discussed in order to flexibly adjust the stop band to meet the frequency band that we are interested in. Finally, the optimized DIWS is installed on the closely set PA and MTL with a distance of 2 mm to suppress the mutual coupling. The proposed structure is fabricated and measured to verify the simulation results which demonstrated that a high isolation of 27 dB and 37 dB between the antenna and MTL are achieved, respectively.

Index Terms **─** Antenna and microstrip transmission line, band stop filtering, coupling reduction, DIWS.

I. INTRODUCTION

With the proliferation of mobile electronic products and ongoing push for great functionality in a small area, miniaturization has become a key technique for many wireless communication devices. Inevitably, the density of internal elements increases, which easily cause the coupling and interference between elements. For well transmitting and receiving radio wave, antenna is almost omnipresent in most wireless communication products. Moreover, with the development of the miniaturization for wireless communication device, internal printed antenna (PA) gradually has been widely chosen instead of the external antenna [1-2]. Thus, closely spaced PA and microstrip transmission line (MTL) can be found in many microwave systems, leading to inevitable mutual coupling which probably causes performance degradation of the system.

In fact, mutual coupling problem has attached much attention in the field of signal processing [3-5], MIMO antenna arrays and electromagnetic capability [6]. In MIMO antenna array, the presence of mutual coupling will affect its radiation patterns and input characteristic, which probably degrades the performance of the antenna array [6]. In the field of electromagnetic compatibility (EMC), the undesired coupling between MTLs is one of the main issues for signal integrity. Electromagnetic coupling between tightly spaced lines will degrade the performance of the circuit or give interference to close lines, which has become an important issue that draws lots of attention in high-speed circuit design. Consequently, a large amount of coupling reduction methods have been proposed and investigated in literatures. Techniques concerning on reducing the mutual coupling between antenna array mainly based on: (i) field cancellation method which introduces an indirect coupling field to cancel out the original direct coupling field to reduce the mutual coupling, such as neutralization line [7-10], and U-shaped microstrip line in [11]. (ii) band-stop filtering method, such as electromagnetic band gap structure (EBG) [12-16], metamaterial structure [17-18], defected ground structure (DGS) [19-20], planar soft surfaces [21-22] and so on. Although these band-stop resonate structures are effective for coupling suppression, most of them have a complex structure and need a large space, which makes it difficult to implement practically. (iii) decoupling network [23-26], which is similar to field cancellation method, but its indirect coupling field is introduced by antenna feeding network rather than independent structure. For crosstalk reduction between adjacent MTLs, various methods

Submitted On: September 18, 2018
Accepted On: November 24, 2018

have also been introduced and investigated in [27-30], such as increasing the distance between adjacent lines, reducing parallel lines, and defected microstrip structure (DMS). Some of these methods are hard to accomplish, and the complex structure will increase the overall size of the system. Moreover, unlike the existing decoupling techniques applied in antenna array and coupled MTL, decoupling technique used in adjacent antenna and microstrip transmission line is much more challenging. In order to suppress the mutual coupling, it is necessary to make a tradeoff between the antenna performance and MTL signal integrity to make the isolation better than -20 dB or more.

In this article, a simple and effective method based on band-stop filtering technique is proposed and investigated to reduce the mutual coupling between the antenna and the transmission line which might happened in the system integration like the compact terminals and the portable devices because there are antennas and the microstrip lines. The proposed defected isolation wall structure (DIWS) is comprised of a vertical metal wall with periodical G-shaped structure and thin dielectric slabs on each side. Simulation results depict that the proposed DIWS can provide a band-stop filtering characteristic with an adjustable operating frequency band, which attributes to the fact that the transmission of energy is rejected. By installing the DIWS vertically between the closely spaced PA and MTL, the mutual coupling is effectively suppressed in the operating frequency band of the antenna, and a maximum reduction of 25 dB is obtained without sacrificing the performance of the PA and MTL.

II. MODEL AND PERFORMANCE OF THE DESIGNED DIWS

The designed DIWS is presented for mutual coupling reduction between closely spaced PA and MTL. The design DIWS model and its analysis are presented in detail. The configuration of the presented G-shaped DIWS is shown in Fig. 1. The proposed DIWS comprises of a thin metal with three periodical G-shaped structure and two Polyflon NorCLAD dielectric substrates loading on both sides of the metal. The two dielectric substrates have a same thickness of 0.2 mm and permittivity of 2.55. In addition, the metal and two dielectric substrates have a same dimension of w × l = 18 × 4.7 mm^2.

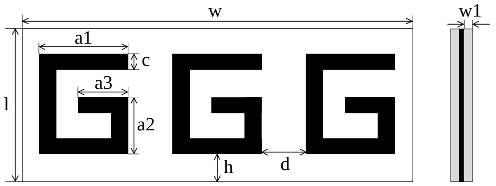

Fig. 1. The configuration of the proposed DIWS: front view and side view.

To study the electromagnetic characteristic of the proposed DIWS, a MTL printed on a FR-4 dielectric substrate is designed and modeled, where the DIWS is installed in the middle of it, and the configuration is shown in Fig. 2. The MTL is a typical 50 Ohm microstrip line printed on a FR-4 dielectric substrate whose dielectric substrate is 1.6 mm. Modeling and simulation analysis of this structure is implemented by utilizing high frequency structure simulator (HFSS). The energy is injected from port 1, and the port 2 is output. In Fig. 3, the S parameters shows a band-stop response between 4.8 GHz and 5.6 GHz. By installing the proposed DIWS in the 50 Ohm microstrip line, there is a band stop characteristic happened, which is given in Fig. 3. To understand the mechanism of decoupling intuitively, the current distribution at 5.2 GHz is given in Fig. 4. From the current distribution, we can see that the current is mainly distributed on the input port of the microstrip line.

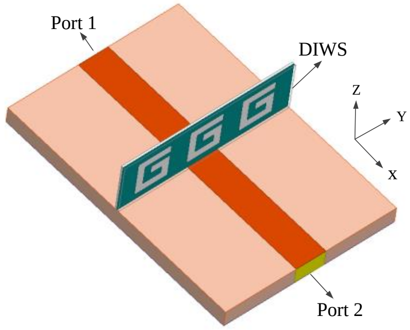

Fig. 2. The MTL loaded DIWS.

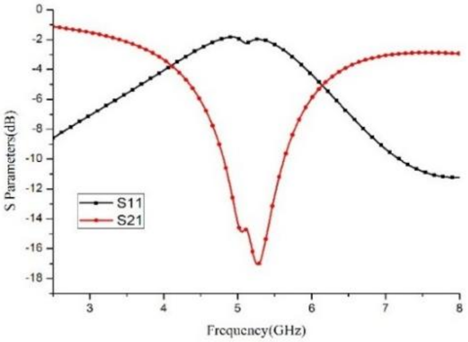

Fig. 3. S parameters of the microstrip transmission line loaded DIWS.

After the DIWS, there is almost no current because the current at the operating frequency is effectively rejected by the DIWS loaded in the middle of the transmission line. Thus, the DIWS can block the electromagnetic wave from the PA to the MTL. The band stop characteristic created by the periodical G-shaped DIWS can be used to reduce the mutual coupling between the PA and MTL. The band stop characteristic is realized by means of the DIWS, which is mainly introduced by the metal plate with G-shaped slots. Since the slots and strips act as capacitor and inductor, respectively, the current at the resonance frequency will be block by this filter, which can help to isolate the propagation between the antenna and the MTL, and the resonant frequency can be adjusted by changing the dimensions of G-shaped elements (GSEs) and distance between GSEs.

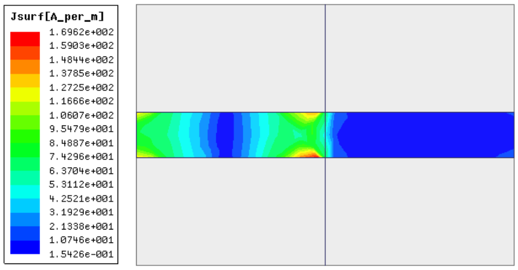

Fig. 4. Current distribution (at 5.2GHz) of the microstrip transmission line loaded with DIWS.

In order to flexibly adjust the stop band of DIWS to meet the frequency band we are interested in, its key design parameters are studied herein. The distance *d* between the GSEs and the distance *h* between the GSEs and the bottom edge of DIWS are selected to discuss the effects. From Fig. 5 (a), we can see that the resonance frequency decreases as the capacitance decreases, resulting in that the center frequency of the stop band moves to higher frequency as the length of GSE *a1* decreases. As shown in Fig. 5 (b), when the distance *d* between GSEs is increased, the equivalent inductance decreases, which renders that the center frequency shifts toward higher frequency. Meanwhile, the in-band attenuation decreases. Similarly, when the distance *h* is decreased given in Fig. 5 (c), the center frequency of the DIWS moves to the high frequency.

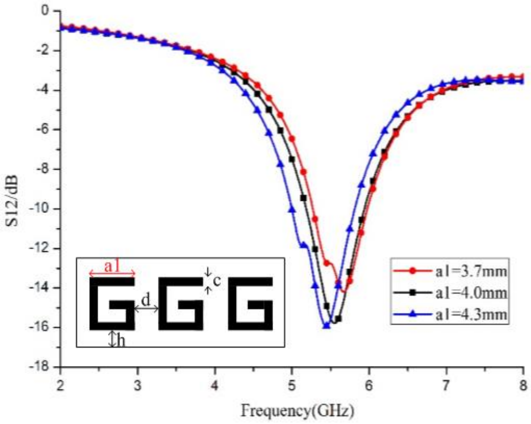

(a) Effects of parameter a1

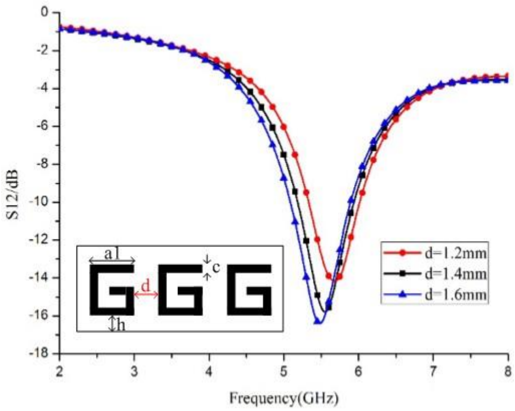

(b) Effects of parameter d

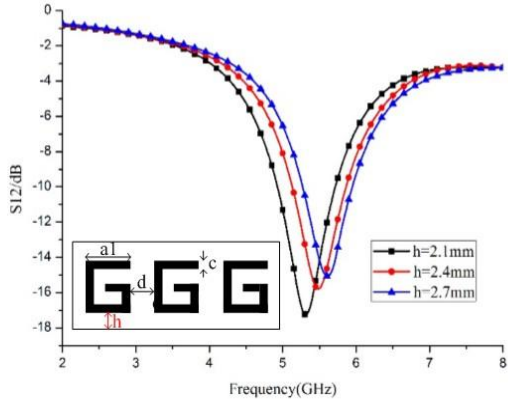

(c) Effects of parameter h

Fig. 5. Effects on the band stop characteristic of DIWS.

From the responses and results analysis, we can draw a conclusion that the center frequency of stop band for DIWS is mainly determined by *a1*, *d* and *h*. Thus, we can adjust the resonance frequency of the proposed DIWS to meet the coupling reduce between PA and MTL.

III. PERFORMANCE OF THE PROPOSED STRUCTURE

The proposed DIWS is eventually used to reduce the mutual coupling between the closely spaced PA and MTL, which is shown in Fig. 6. Herein, the PA is designed to operate in a WLAN sub-band (5.725-5.825 GHz). The original dimension of PA is given by the following equations:

$$L2 = \frac{c}{2f_0}\frac{1}{\sqrt{\varepsilon_e}} - 2\Delta L \, , \; W2 = \frac{c}{2f_0}\left(\frac{\varepsilon_r+1}{2}\right)^{-1/2} . \tag{1}$$

The feed point is also calculated based on empirical formulas. The final dimensions of the PA are 15 × 11.65 mm^2. Meanwhile, the MTL is a typical 50 Ohm microstrip line which can be regularly seen in many microwave circuits. The distance between the PA and MTL is 2 mm. Due to this small distance, the radiation from the antenna and surface current will inevitably cause strong mutual coupling to the MTL. Therefore, the proposed DIWS is considered as a coupling reduction structure to suppress the mutual coupling because it can provide a band stop characteristic that reject electromagnetic energy in a specific frequency band.

As a result, the proposed DIWS equivalently behaves to be a band stop filter which is installed on the coupling path between the PA and MTL. Since the resonance frequency of the proposed DIWS can be adjusted by properly selecting its dimensions, we adjust the dimensions of DIWS to provide a band stop characteristic at the frequency band of the PA. The optimized dimensions obtained from the sweep analysis of the HFSS are given as: w = 18 mm, l = 4.7 mm, w1 = 0.2 mm, a1 = 3.4 mm, a2 = 2.3 mm, a3 = 2 mm, h = 2.1 mm, d = 2.5 mm.

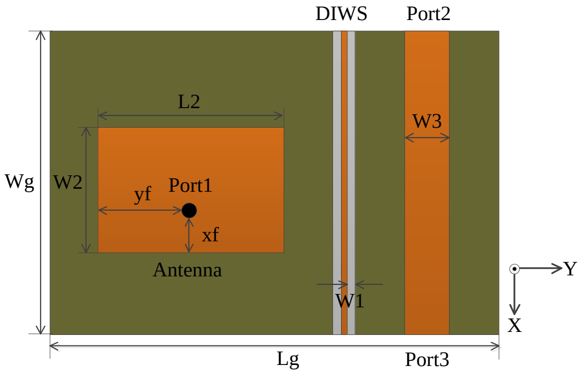

(a) Top view of the PA and MTL

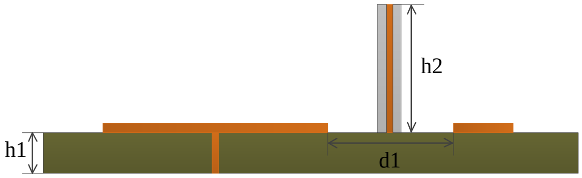

(b) Side view of the PA and MTL

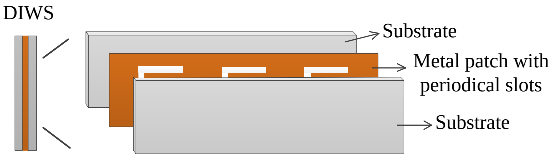

(c) View of the DIWS

Fig. 6. PA and MTL with the proposed DIWS.

The S-parameters with/without the proposed DIWS are given in Figs. 7 and 8. Here, mutual coupling between the PA and MTL are measured by S21 and S31, respectively. In fact, the isolations are better than -20dB, which is helpful for practical engineering applications.

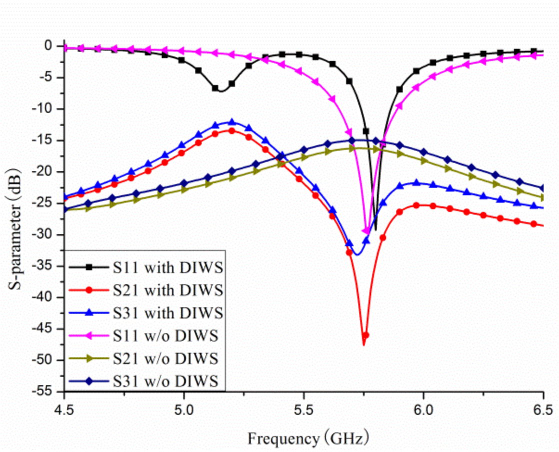

Fig. 7. S-parameter with/without DIWS.

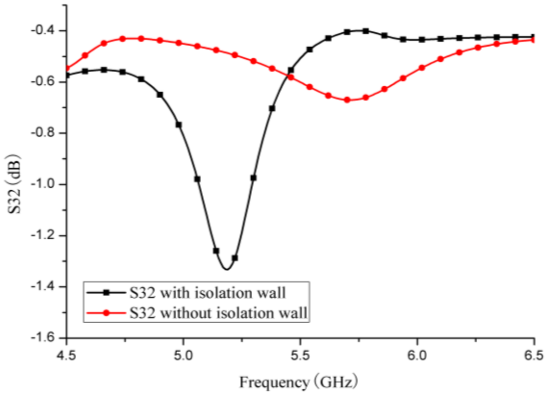

Fig. 8. S32 with/without DIWS.

It can be seen that S21 is reduced by 33dB and S31 is reduced by 18dB at operating frequency band by loading the proposed DIWS, and the center frequency of the PA is slightly shifted towards higher frequency. It is verified that the proposed DIWS can efficiently reduce the mutual coupling. Moreover, from the S32 (transmission coefficient of the MTL) shown in Fig.8, we can see that there is a decrease at low frequency band by loading the proposed DIWS. However, S32 is still less than -3 dB at the operating band, which means that almost all the energy is transmitted from the input port to the output port. It is noted that the proposed DIWS has a little effect on the transmission characteristic of the MTL. Moreover, the comparison of input impedance of PA is given in Fig.9. It is found that there is a resonance in low frequency with DIWS, which is produced by the effects of the DIWS. This is because the mutual capacitance and mutual inductance generated by the strong coupling between PA and DIWS.

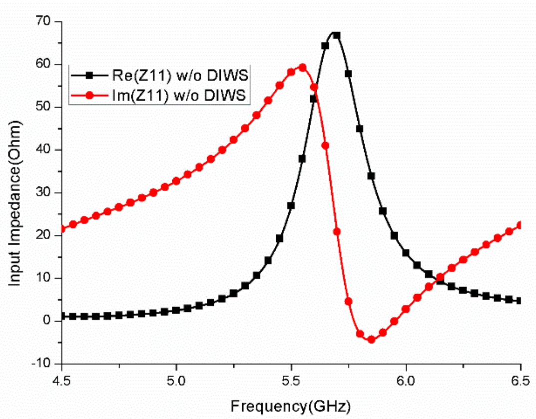

(a) Input impedance of PA without DIWS

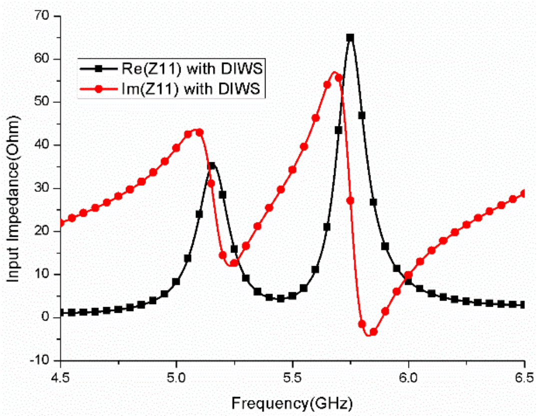

(b) Input impedance of PA with DIWS

Fig. 9. Comparison of the input impedance (Z11) of PA with/without DIWS.

IV. EXPERMENTAL RESULTS

In this section, the measurement results are presented and compared with the simulation results. Figure 10 shows the fabricated structure of proposed PA and MTL with DIWS loading. The dimension of patch antenna is 15 × 11.65 mm^2. The width of signal line (designed for 50 Ω) is $w2$ = 3.13 mm and the length is l = 18 mm. The PA and MTL are printed on a FR4 substrate with relative permittivity of 4.4 and thickness of 1.6 mm. The distance between coupled PA and MTL is $d1$ = 2 mm. In this design, the optimum dimensions of DIWS are the same as that given in section 3. The measurement results are obtained using network analyzer (Agilent N9923A).

Experimental results are given for the proposed closely coupled PA and MTL with/without DIWS from 4.5 GHz to 6.5 GHz. The measured and simulated results are compared in Fig. 11. It is found that the coupling is reduced, where the measurements agree well with the simulations. The isolation improvements between input port of PA and two ports of MTL are 27 dB and 37 dB, respectively. It is also worth noting that the measured center frequency shifts to lower frequency, which might be caused by the fabricated bias. The comparisons of radiation patterns with and without DIWS are given in Fig. 12. We can see the measured results agree well with the simulation results overall. Although there are some discrepancies, the PA still has a good direction radiating in the operating band.

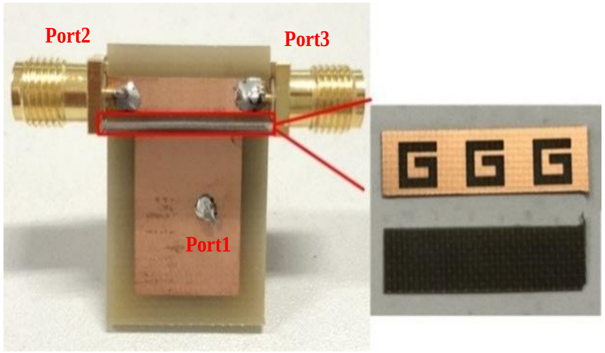

Fig. 10. Fabricated closely PA and MTL with DIWS.

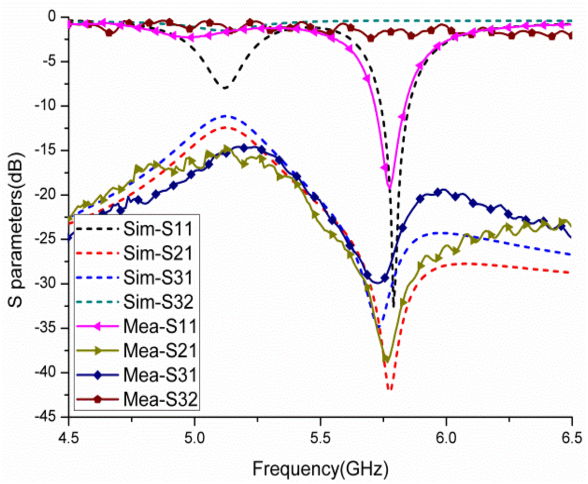

Fig. 11. Simulation and measured S parameters of closely PA and MTL with DIWS.

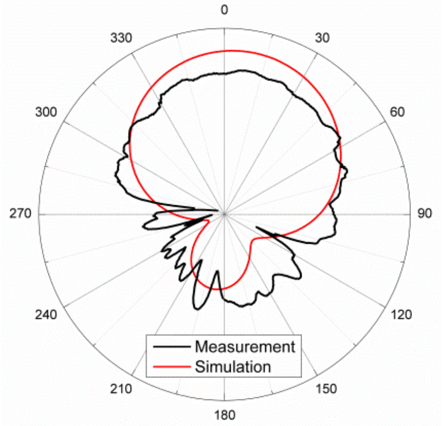

(a) XOZ plane without DIWS

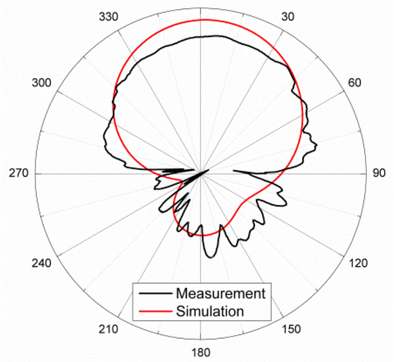

(b) YOZ plane without DIWS

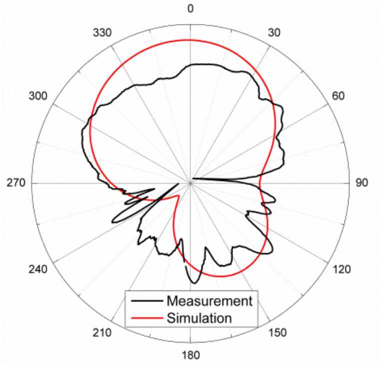

(c) XOZ plane with DIWS

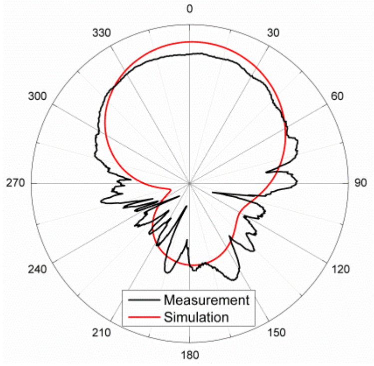

(d) YOZ plane with DIWS

Fig. 12. Comparison between simulation results and measured results of radiation patterns of antenna with and without DIWS.

V. CONCLUSIONS

A DIWS has been devised for mutual coupling reduction between PA and MTL. The design procedure of the DIWS has been presented in detail by adjusting the key parameters. Then, the coupling reduction of the DIWS is investigated and verified when it is used in a closely set PA and MTL. The experimental results have been obtained and compared with the HFSS simulation results. The results showed that the isolations between PA and MTL are improved by 27 dB and 37 dB, respectively.

ACKNOWLEDGMENT

This work was partially supported by the National Key Research and Development Program of China (2016YFE0111100), Key Research and Development Program of Heilongjiang (GX17A016), the Science and Technology innovative Talents Foundation of Harbin (2016RAXXJ044), Fundamental Research Funds for the Central Universities (HEUCFM180806) and China Postdoctoral Science Foundation (2017M620918).

REFERENCES

[1] Y. Li, W. Li, and W. Yu, "A switchable UWB slot antenna using SIS-HSIR and SIS-SIR for multi-mode wireless communications applications," *Applied Computational Electromagnetics Society Journal*, vol. 27, no. 4, pp. 340-351, 2012.

[2] Y. Li, W. Li, and W. Yu, "A multi-band/UWB MIMO/diversity antenna with an enhance isolation using radial stub loaded resonator," *Applied Computational Electromagnetics Society Journal*, vol. 28, no. 1, pp. 8-20, 2013.

[3] Y. Li, Y. Wang, and T. Jiang, "Norm-adaption penalized least mean square/fourth algorithm for sparse channel estimation," *Signal processing*, vol. 128, pp. 243-251, 2016.

[4] Y. Li, Y. Wang, and T. Jiang, "Sparse-aware set-membership NLMS algorithms and their application for sparse channel estimation and echo cancelation," *AEÜ - International Journal of Electronics and Communications*, vol. 70, no. 7, pp. 895-902, 2016.

[5] Y. Li, Z. Jiang, O. M. Omer-Osman, X. Han, and J. Yin, "Mixed norm constrained sparse APA algorithm for satellite and network channel estimation," *IEEE Access*, DOI: 10.1109/ACCESS.2018.2878310, Oct. 2018.

[6] C. A. Balanis, *Antenna Theory Analysis and Design*. 3rd ed., New York: Wiley Interscience, 2012.

[7] Y. Wang and Z. Du, "A wideband printed dual-antenna with three neutralization lines for mobile terminals," *IEEE Trans. Antenna and Propagation*, vol. 62, no. 3, pp. 1495-1500, 2014.

[8] Y. Kim, J. Itoh, and H. Morishita, "Decoupling method between L-shaped folded monople antennas for bandsets using a bridge line," *IET Microwaves. Antenna & Propagation*, vol. 4, no. 7, pp. 863-870, 2010.

[9] S. W. Su, C. T. Lee, and F. S. Chang, "Printed MIMO-antenna system using neutralization-line technique for wireless USB-dongle applications," *IEEE Trans. Antenna and Propagation*, vol. 60, no. 2, pp. 456-463, 2012.

[10] S. Zhang and G. F. Pedwesen, "Mutual coupling reduction for UWB MIMO antennas with a wideband neutralization line," *IEEE Antenna and*

Propagation Letters, vol. 15, pp. 166-169, 2016.

[11] S. Farsi, H. Aliakbarian, and D. Schreurs, "Mutual coupling reduction between planar antennas by using a simple microstrip U-section," *IEEE Antenna and Wireless Propagation Letters*, vol. 11, pp. 1501-1503, 2012.

[12] T. Jiang, T. Jiao, and Y. Li. "Array mutual coupling reduction using L-loading E-shaped electromagnetic band gap structures," *International Journal of Antennas and Propagation*, vol. 2016, pp. 1-8, 2016.

[13] A. Yu and X. Zhang, "A novel method to improve the performance of microstrip antenna arrays using a dumbbell EBG structure," *IEEE Antennas and Wireless Propagation Letters*, vol. 2, no. 1, pp. 170-172, 2003.

[14] S. Ebadi and A. Semnani, "Mutual coupling reduction in waveguide-slot-array antennas using electromagnetic bandgap (EBG) structure," *IEEE Antennas and Propagation Magazine*, vol. 56, no. 3, pp. 68-69, 2014.

[15] L. Yang, M. Fan, F. Chen, and J. She, "A novel compact electromagnetic-bandgap (EBG) structure and its application for microwave circuits," *IEEE Trans, Microwave Theoty and Techniques*, vol. 53, no. 1, pp. 183-190, 2005.

[16] E. Rajo-Iglesia, O. Quevedo-Teruel, and L. Inclan-Sanchez, "Study of mutual coupling reduction in single and stacked mutilayer patch antennas by using planar EBG structures," *IEEE International Symposium on Antenna and Propagation* (APS), pp. 393-396, 2007.

[17] K. Yu, Y. Li, and X. Liu, "Mutual coupling reduction of a MIMO antenna array using 3-D novel meta-material structures," *Applied Computational Electromagnetics Society Journal*, vol. 33, no. 7, pp. 758-763, 2018.

[18] M. Tang, Z. Chen, H Wang, et al., "Mutual coupling reduction using meta-structures for wideband, dual-polarized, and high-density patch arrays," *IEEE Transactions on Antennas and Propagation*, vol. 65, no. 8, pp. 3986-3998, 2017.

[19] T. Jiao, T. Jiang, and Y. Li, "A low mutual coupling antenna array using alternating direction S-shaped defected ground structures," *IEEE 5th Asia-Pacific Conference on Antennas and Propagation* (APCAP), 2016

[20] Y. Li, W. Li, and Q. Ye, "A reconfigurable triple notch band antenna integrated with defected microstrip structure band-stop filter for ultra-wideband cognitive radio applications," *International Journal of Antennas and Propagation*, vol. 2013, Article ID: 472645, pp. 1-13, 2013.

[21] G. Dadashzadeh, A. Dadgarpour, and F. Jolani, "Mutual coupling suppression in closely spaced antennas," *IET Microwave Antenna and Propagation*, vol. 5, no. 1, pp. 113-125, 2011.

[22] T. J. Cho, J. K. Kim, and H. M. Lee, "Mutual coupling reduction between two microstrip patch antennas using isolated soft surface structures," *IEEE International Symposium on Antenna and Propagation* (APS), pp. 1-4, 2009.

[23] R. L. Xia, S. W. Qu, and P. F. Li, "An efficient feeding network for microstrip antenna array," *IEEE Antenna and Wireless Propagation Letters*, vol. 14, pp. 871-874, 2015.

[24] A. Nisson, P. Bodlund, and A. Stjemman, "Compensation network for optimizing antenna system for MIMO application," *European Conference on Antennas and Propagation* (EUCAP), pp. 1-5, 2007.

[25] S. Cui, S. X. Gong, and Y. Liu, "Compact and low coupled monopole antennas for MIMO system applications," *IEEE Trans. Antennas and Propagation*, vol. 56, no. 12, pp. 3650-3658, 2008.

[26] Y. Liu, W. Jiang, and S. Gong, "Novel miniaturized and high-isolated MIMO antenna," *Microwave and Optical Technology Letters*, vol. 54, pp. 511-515, 2012.

[27] R. Mallahzadeh, A. H. Ghasemi, S. Akhlaghi, B. Rahmati, and R. Bayderkhani, "Crosstalk reduction using step shaped transmission line," *Progress In Electromagnetic Research*, vol. 12, pp. 139-148, 2010.

[28] A. Mehdipour and M. Kamarei, "Optimization of the crosstalk of crossing microstrips in multilayered media using lumped circuit model," *11th International Conference on Mathematical Methods in Electromagnetic Theory*, pp. 279-281, 2006.

[29] M. Kazerooni, M. A. Salari, and A. Cheldavi, "A novel method for crosstalk reduction in coupled pair microstrip lines," *International Journal of RF and Microwave Computer-Aided Engineering*, vol. 22, pp. 167-174, 2012.

[30] F. D. Mbairi, W. P. Siebert, and H. Hesselbom, "High-frequency transmission lines crosstalk reduction using spacing rules," *IEEE Trans. Components and Packaging Technologies*, vol. 31, no. 3, pp. 601-610, 2008.

A Novel Beam-Steerable Antenna Using HIS-SWG Reconfigurable Artificial Ground Structure

You-Feng Cheng [1], Xiao Ding [2], Wei Shao [2], and Cheng Liao [1]

[1] Institute of Electromagnetics
Southwest Jiaotong University, Chengdu 610031, China
juvencheng1377@gmail.com, c.liao@swjtu.edu.cn

[2] Institute of Applied Physics
University of Electronic Science and Technology of China, Chengdu, 610054, China
xding@uestc.edu.cn, weishao@uestc.edu.cn

Abstract ─ An artificial ground structure (AGS) which can be switched between the high-impedance surface (HIS), the surface-waveguide (SWG) and the HIS-SWG hybrid structure is proposed for the design of a beam-steerable antenna. The AGS is reconfigured with PIN diodes inserted on the bottom ground. The antenna radiates a broadside far-field pattern when the AGS is reconfigured into an HIS, and it steers its main beam to the endfire direction when the AGS exhibits as an HIS-SWG hybrid structure. The reconfigured HIS and SWG are analyzed using the Brillouin dispersion theory and the eigenvalue analysis, respectively. A prototype of the proposed beam-steerable antenna is fabricated and measured. The measured results including the reflection coefficients and radiation patterns validate the antenna performance.

Index Terms ─ Artificial ground structure (AGS), beam-steerable antenna, eigenvalue analysis, high-impedance surface (HIS), surface-wave guide (SWG).

I. INTRODUCTION

The rapid development of modern communication systems has shown the increasing demand of multi-functional antennas which are capable of achieving more than one operational status by electronic or mechanical implementation. Reconfigurable antennas are attractive and effective solutions [1-3]. As one versatile type of reconfigurable antennas, the beam-steerable antenna can dynamically switch its radiation pattern with other antenna characteristics unchanged. Generally, for many practical applications, it is required that the beam-steerable antenna should have a good gain flatness between the radiation patterns of different modes, a wide combined main-beam coverage and a powerful reconfigurable ability. These rigorous but essential requirements have brought great challenges to the designs of beam-steerable antennas.

The beam-steerable antenna can be realized by various solutions, such as reconfiguring its parasitic structures [4-8], reconfiguring its feeding networks [9-11], and reconfiguring its radiator loads [12]. In [8], a beam-steerable antenna based on a dual-reconfiguration technique was proposed. The reconfigured strips on the lower layer realize a preliminary beam control, and the parasitic pixel structure is exploited to further increase the beam-steerable ability. Recently, many efforts have been devoted to the design of beam-steerable antennas based on meta-materials [13-15]. In [14], a high-impedance surface (HIS) was designed to propagate the TE Floquet mode in the given frequency band, and a surface-wave assistant antenna based on the HIS was proposed to achieve reconfigurable radiation patterns.

In this paper, a novel beam-steerable antenna based on the artificial ground structure (AGS) is presented. Firstly, the proposed AGS is designed and analyzed to have the capability of being switched between the HIS, the surface-wave-guide (SWG) and the HIS-SWG hybrid structure. Then, a dipole is placed upon the AGS and it can steer its far-filed pattern from a broadside radiation with an HIS to an end-fire radiation with an HIS-SWG hybrid structure. At last, a prototype of the proposed antenna is fabricated and measured, and the measured results show good gain flatness and wide combined-beam coverage.

II. AGS DESIGN AND ANALYSIS

In order to realize the HIS-SWG reconfiguration at a selected operation frequency, the AGS is required to meet two conditions simultaneously. On one hand, the reconfigured HIS should form a forbidden frequency band-gap which contains the operation frequency, and on the other hand, the reconfigured SWG is able to support the propagation of required surface waves at the same frequency.

The geometries of the HIS and SWG reconfigured

Submitted On: February 25, 2018
Accepted On: December 25, 2018

from the AGS are shown in Fig. 1. The mushroom-shaped HIS [16] consists of 5 × 5 square units, which have a size of $D_H \times D_H$. The square patches with a length of L_c are periodically printed on the top of a substrate. Vertical metal vias with a diameter of D_c connect the upper square patches to the ground plane. The substrate has a relative permittivity of 2.95 and a height of H_2. The structure of the proposed SWG is the same as the HIS except for the ground plane, which are also pixelated as 5 × 5 square patches. Thus, the upper and lower surfaces of the SWG are the same.

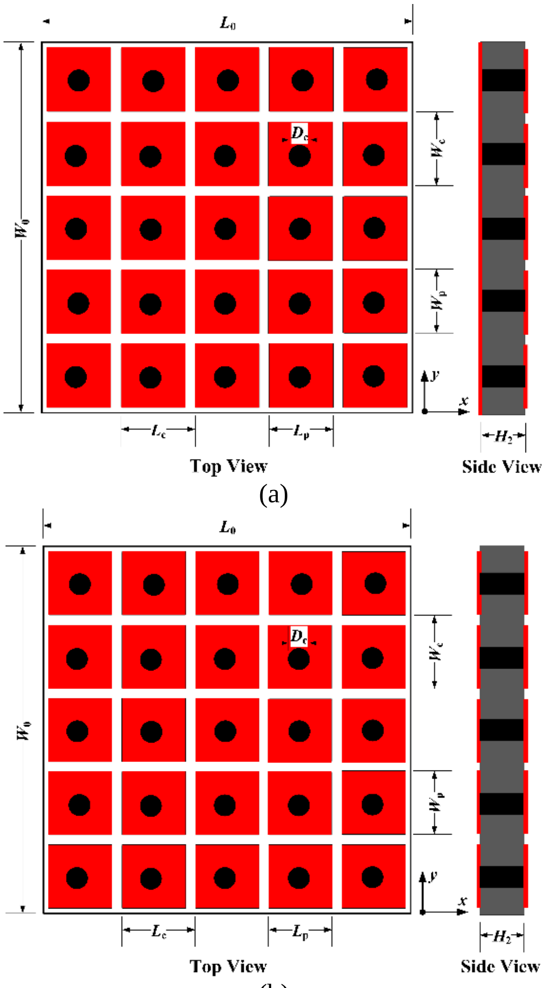

(a)

(b)

Fig. 1. Structures of the reconfigured HIS and SWG. (a) Mushroom-shaped HIS, and (b) designed SWG.

The HIS unit cell can be equivalent as a series LC circuit in which the major contribution to the overall capacity (C_g) comes from the gap discontinuity at both ends of the patch, and the overall inductance (L_c) comes from the current loop through the vias and the ground plane. Thus, there exists a resonance according to the LC circuit, and the equivalent sheet impedance at the resonant frequency can be calculated by:

$$Z = \frac{j\omega L_c}{1-\omega^2 L_c C_g}, \quad (1)$$

where ω is the angular frequency, and the resonant frequency is:

$$\omega_0 = \frac{1}{\sqrt{L_c C_g}}. \quad (2)$$

It can be seen from (1) and (2) that the surface impedance is very high near the resonant frequency. Thus, a forbidden frequency band-gap is formed. The simulated dispersion diagrams of the proposed HIS are shown in Fig. 2. It can be observed that there exists a complete band-gap between the first and second modes which is centered at 4.5 GHz and spans from 3.43 to 5.42 GHz.

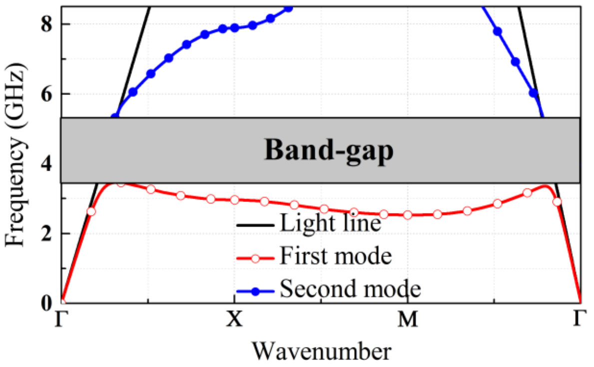

Fig. 2. Dispersion diagram of the reconfigured HIS.

The band-gap would disappear when the ground plane is also pixelated as square patches. In terms of the reconfigured SWG, the Snell's law, effective surface impedance and eigenvalue analysis are used to illustrate that it can support the propagation of TE_0- and TM_0-mode surface waves.

Firstly, the propagation of the surface wave in the proposed SWG can be explained with the Snell's law:

$$n_1 \cdot \sin\theta_1 = n_2 \cdot \sin\theta_2. \quad (3)$$

Equation (3) means that the refraction angle θ_2 would get larger with the increase of the refractive index of the SWG as shown in Fig. 3. Thus, the total reflection may be realized when the refractive index is large enough. The real part of the refractive index of the SWG can be calculated from the simulated S-parameters, and the transform can be given as [17]:

$$n_{\text{eff}} = \frac{1}{k_0 L_c}\cos^{-1}\left[\frac{1}{2S_{21}}(1 - S_{11}^2 + S_{21}^2)\right], \quad (4)$$

where k_0 is the wavenumber of the incident wave in free space. The calculated refractive index is shown in Fig. 4 (a). It can be observed that the SWG has a significant portion of the calculated real part of n_{eff} at a selected frequency (3.6 GHz). Therefore, the surface wave can propagate in the proposed SWG.

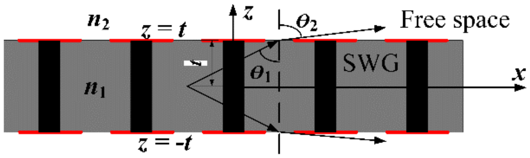

Fig. 3. Sketch map of electromagnetic wave transmission.

Secondly, the relative surface impedance Z_s of the SWG can also be calculated from the simulated S-parameters [18], and the transform is given as:

$$Z_s = \pm\sqrt{\frac{(1+S_{11})^2 - S_{21}^2}{(1-S_{11})^2 - S_{21}^2}}\,. \tag{5}$$

Since the SWG is a passive medium, the sign in (5) should satisfy the requirement that the real part of the relative impedance should be positive. The calculated relative surface impedance is also plotted in Fig. 4 (a). It can be seen that, at 3.6 GHz, the imaginary part of the surface impedance is zero and the real part is close to the free-space wave impedance, which indicates that the proposed SWG is matched to the free space. According to [19], the dielectric SWG can support both the TE- and TM-mode surface waves.

At last, the solution of eigenvalues is utilized to explain that the selection of the SWG height makes it only guide surface waves of TE$_0$ and TM$_0$ modes. According to [19], the eigenvalue equations are:

$$\begin{cases} \varepsilon_r pt = ht\tan ht & \text{TM even modes} \\ \varepsilon_r pt = \text{-}ht\cot ht & \text{TM odd modes} \\ pt = ht\tan ht & \text{TE even modes} \\ pt = \text{-}ht\cot ht & \text{TE odd modes} \end{cases}, \tag{6}$$

where ε_r is the relative dielectric constant which can be calculated by the refractive index in (4), ht and pt are two eigenvalues from the geometry and boundary condition, $t = H_2/2$. h and p are the cutoff wavenumber of the air and the SWG, respectively, and they satisfy:

$$\begin{cases} (pt)^2 + (ht)^2 = (\varepsilon_r - 1)(k_0 t)^2 \\ \beta^2 = k_0^2 + p^2 = \varepsilon_r k_0^2 - h^2 \end{cases}. \tag{7}$$

According to (6) and (7), the solution of eigenvalues of the SWG can be illustrated in Fig. 4 (b). It can be deduced that only the TE$_0$ and TM$_0$ modes are guaranteed to propagate and other higher-order modes are rapidly attenuated since there is almost no intersection between the quarter-circle with a radius of $R = (\varepsilon_r - 1)^{1/2} k_0 t = 0.52$ and the eigen-functions of higher order modes.

Based on the above analysis, it can be indicated that the proposed AGS can forbidden the propagation of TE$_0$- and TM$_0$-mode surface waves when it is reconfigured into an HIS, and it can guide these surface waves to a selected direction when it is partly switched into an HIS and partly into an SWG.

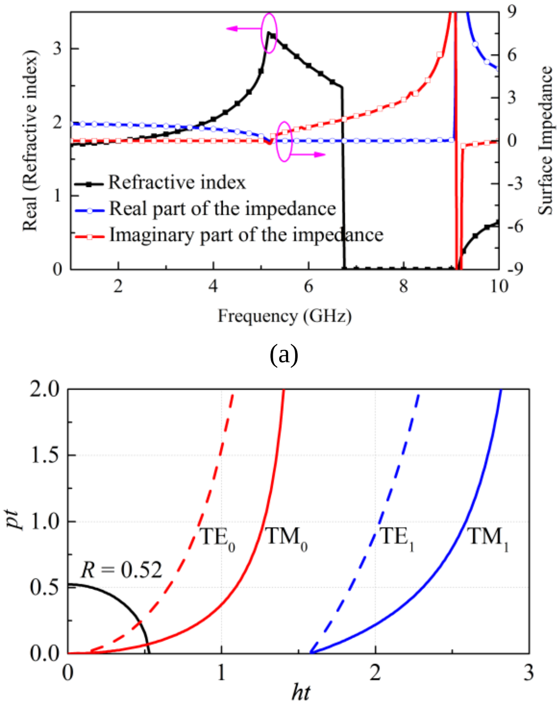

(a)

(b)

Fig. 4. Calculated real part of the refractive index, relative surface impedance and solution of eigenvalues. (a) Real part of the refractive index and relative surface impedance, and (b) solution of eigenvalues.

Infineon's BAR64-02V PIN diodes are used to reconfigure the AGS. As shown in Fig. 5, the square patches on the bottom of the substrate are divided into three groups, namely Groups 1, 2 and 3. When the AGS operates at Mode 1, the square patches of Group 2 are all connected. In this situation, the AGS exhibits as an HIS-SWG hybrid structure, and the surface waves can only propagate to the negative x direction. Similarly, when the AGS operates at Mode 2, the square patches of Group 3 are all connected. The AGS is also an HIS-SWG hybrid structure in this situation and the surface waves can only propagate to the positive x direction. When the square patches of Groups2 and 3 are all connected, the surface works as an HIS, and this case is denoted as Mode 3. Herein no surface waves can be supported in this case. The bias circuits are also shown in Fig. 5. Note that the bias circuits have small effects on the AGS performance since they are placed on the back side of the substrate.

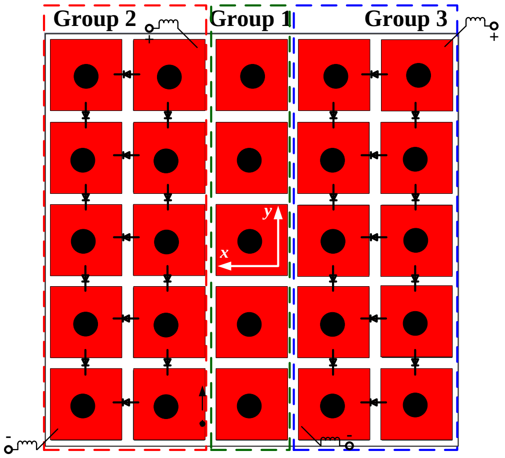

Fig. 5. Back side of the AGS and its bias circuits.

III. BEAM-STEERABLE ANTENNA DESIGN AND EXPRIMENT VALIDATION

A beam-steerable antenna is designed based on the proposed AGS as plotted in Fig. 6. A symmetric dipole is printed on the upper substrate which is placed on the AGS. The substrate has a thickness of H_1 and a relative permittivity of 2.2. To provide the excitation of the antenna, a coaxial probe penetrates the lower and upper substrates and connects to one side of the dipole. The other side of the dipole is shorted to the back side of the artificial surface with a shorting pin, which has a same radius with that of the coaxial inner conductor. In addition, two slots with a radius of 2.3 times of the radius of the coaxial inner conductor are etched on the artificial surface. The antenna is designed to operate at 3.6 GHz. The optimized parameters are: $L_0 = W_0 = 45$ mm, $L_c = W_c = 9$ mm, $L_p = W_p = 7.8$ mm, $L_d = 19.2$ mm, $W_d = 1.5$ mm, $D_f = 3.2$ mm, $D_s = 1.2$ mm, $D_v = 0.2$ mm, $H_1 = 0.508$ mm and $H_2 = 3$ mm.

The simulated E- and H-field distributions of the antenna are depicted in Fig. 7. Since TE_0-mode surface waves only exist the E_y component while TM_0-mode surface waves exist the E_x and E_z components, it can be indicated from Fig. 7 that the excited surface waves are of TE_0 mode.

The explanations of the beam-steering principles are given as follows. When the AGS operates at Mode 1, the propagation of the surface wave toward the positive x-direction is forbidden and that toward the negative x-direction is supported. Thus, an endfire radiation tilted to the negative x-direction is generated. When the AGS operates at Mode 2, the situation is exactly opposite to Mode 1, and an endfire pattern tilted to the positive x-direction is radiated. When the AGS operates at Mode 3, an HIS-based antenna is obtained, and it generates a broadside radiation. Therefore, the antenna is able to steer its far-filed pattern from a broadside radiation with an HIS ground to an end-fire radiation with an HIS-SWG hybrid ground.

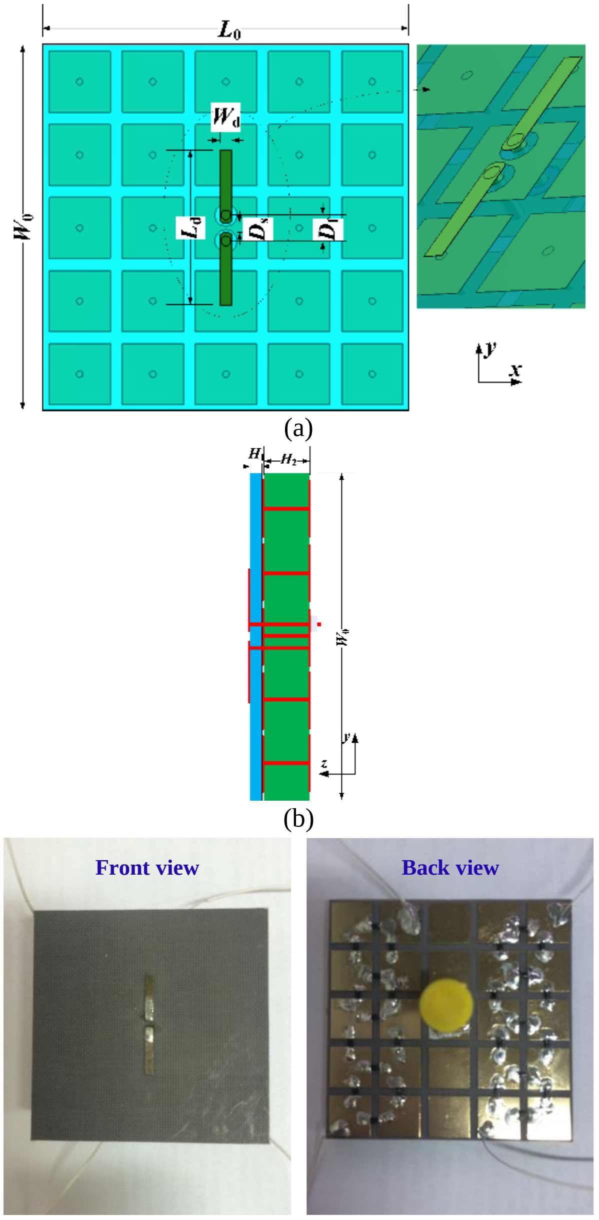

(a)

(b)

(c)

Fig. 6. Antenna geometry and its fabricated prototype sample. (a) Front view, (b) side view, and (c) prototype.

The antenna is fabricated and measured, and the fabricated prototype is shown in Fig. 6 (c). Figure 8 plots the simulated and measured input performance in terms of S_{11}. From the curves of the reflection coefficients, the two modes have a common bandwidth of 3.53 – 3.78 GHz with S_{11} below -10 dB. It should be noted that the results of Mode 2 are omitted due to the geometry symmetry between Modes 2 and 3.

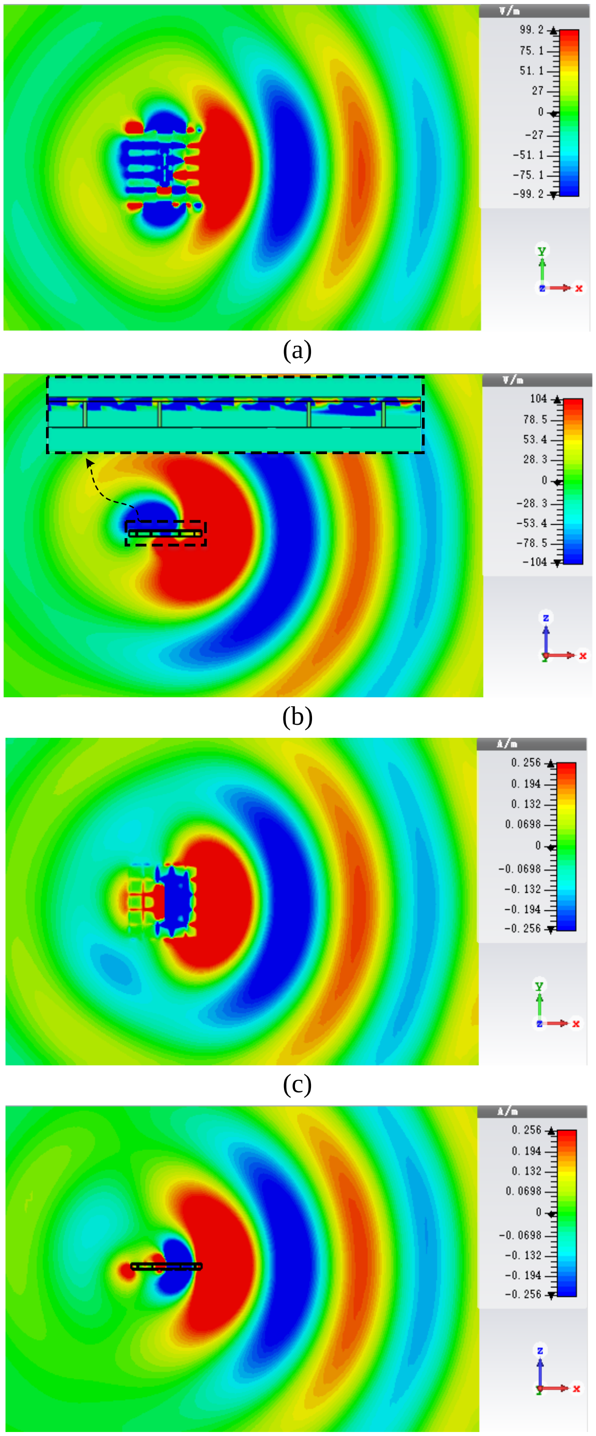

Fig. 7. Simulated E_y and H_z distributions: (a)-(b) E_y distribution on the vertical observation plane $z = 3.6$ mm and the horizontal observation plane $y = 0$ mm. (c)-(d) H_z distribution on the vertical observation plane $z = 3.6$ mm and the horizontal observation plane $y = 0$ mm.

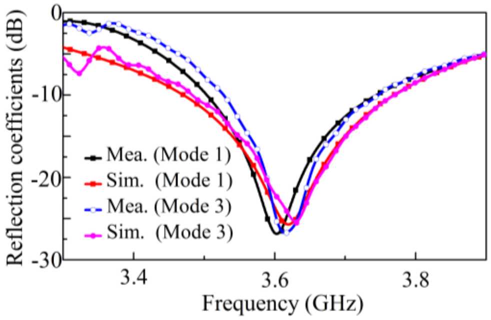

Fig. 8. Measured and simulated return losses of the beam-steerable antenna.

The antenna resonance is determined by the AGS and the length of the above dipole. When the beam-steerable antenna radiates an endfire pattern, the radiation aperture is one edge of the SWG. In this situation, the SWG size determines the resonant frequency and the dipole determines should excite surface waves at the frequency. When the antenna generates a broadside radiation, the dipole becomes the radiation source. In this case, the dipole length determines the antenna resonance. In order to validate the above description, here some comparisons and parametric studies are carried out. Firstly, when the AGS is reconfigured into an HIS, the antenna reflection performance with different dipole lengths is studied. As shown in Fig. 9 (a), with the increase of the dipole length, the antenna resonance is shifted downwards to the lower frequency band. Besides, the antenna resonant performance has no deterioration with the change of the dipole length. Secondly, when the AGS is switched into an HIS-SWG hybrid structure, the influence of the SWG size on the reflection coefficients is investigated and shown in Fig. 9 (b). It can be found that the resonant frequency decreases when the SWG cells increases form 3×3 to 7×7. In addition, the resonant performance deteriorates when the SWG size is changed. The reason is there is a discrepancy between the resonant frequency of surface waves excited by the dipole and the resonance radiated by the SWG edge.

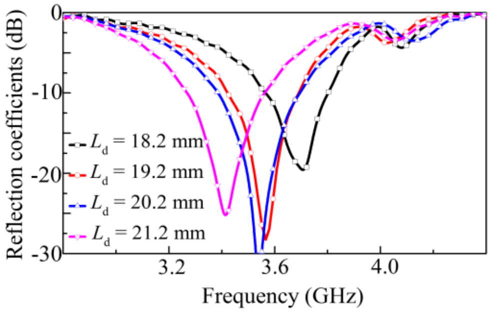

(a)

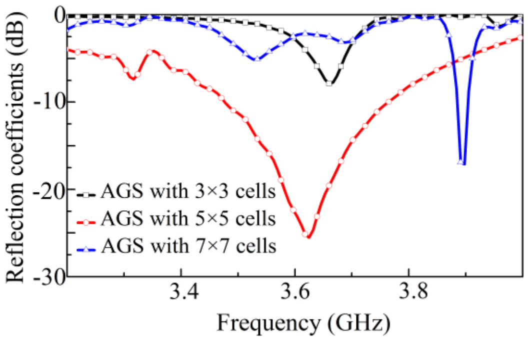

(b)

Fig. 9 Simulated |S11| curves with different dipole lengths and SWG sizes. (a) With different dipole lengths when the AGS works as an HIS, and (b) with different SWG sizes when the AGS works as an HIS-SWG hybrid structure.

The reconfigured patterns at these three modes are listed in Fig. 10. The far-field patterns are measured in an anechoic chamber with a SATIMO Antenna Measurement System. Figure 11 illustrates the measured and simulated radiation patterns and polarization information of the proposed antenna in the *xoz* plane. In Fig. 11 (a), when the antenna operates at Mode 1, it radiates a broadside beam with a measured gain of 5.2 dBi. When the antenna operates at Mode 3, it has an end-fire radiation beam pointing to θ_{max}= -90° direction as shown in Fig. 11 (b). The measured gain at Mode 3 is 4.9 dBi, which is a little lower than that at Mode 1. The half-power beamwidths at Modes 1 and 3 are 96° and 118°, respectively. Based on the symmetry of the Modes 2 and 3, it can be indicated that the proposed reconfigurable antenna is able to switch its main beam to cover the above half space.

Figure 12 shows the measured efficiencies at Modes 1 and 3, which are the total efficiencies defined as the ratio of the radiated power from the antenna to the input power to the antenna. It can be observed that the measured efficiencies of the both modes are about 90% at the resonant frequency. The reason why the measured efficiencies are quite high can be addressed from two aspects. Firstly, Infineon's BAR64-02V PIN diodes are adopted to the antenna design. According to its datasheet, the insertion loss of this diode is about 0.05 dB, which means the inserted PIN diodes bring only a small amount of loss. Secondly, all these PIN diodes are placed on the lower layer of the AGS. When the AGS works as an HIS, the PIN diodes are placed on the ground plane and they lead low loss into the design, which has been described in [20]. When the AGS works as an HIS-SWG hybrid structure, high-frequency surface waves are bounded into the SWG and the current doesn't flow through the PIN diodes. In addition, all the PIN diodes are switched off when the AGS works as an SWG.

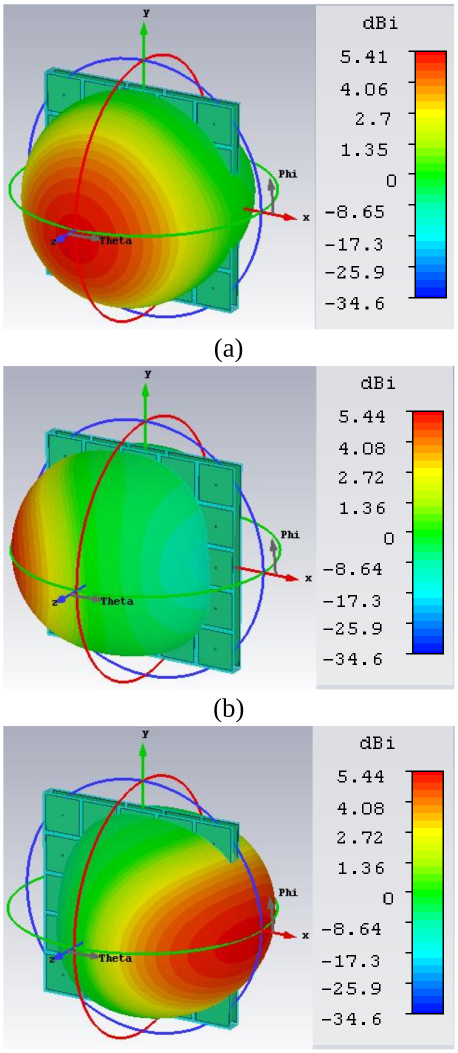

(a)

(b)

(c)

Fig. 10. Simulated 3-D reconfigurable patterns of the antenna. (a) Broadside pattern, and (b)-(c) endfire patterns.

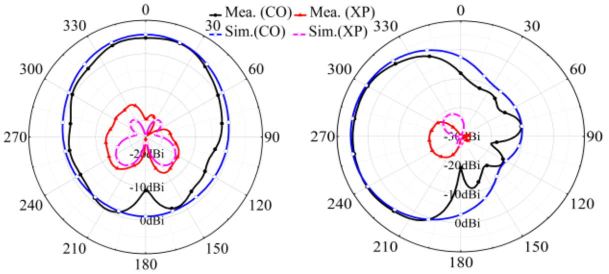

(a) (b)

Fig. 11. Measured and simulated radiation patterns of the beam-steerable antenna. (a) Mode 1 and (b) Mode 3.

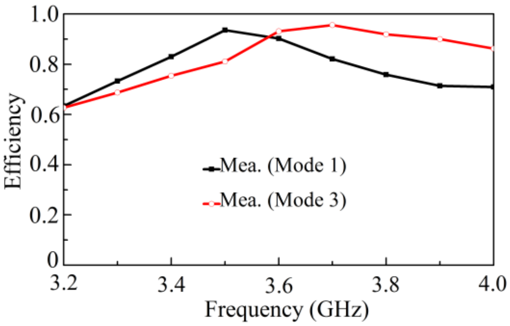

Fig. 12. Measured efficiencies of the proposed antenna when it works at Modes 1 and 3.

IV. CONCLUSION

In this work, a beam-steerable antenna based on the HIS-SWG AGS is presented. Firstly, an AGS which can be switched between the HIS, SWG and HIS-SWG hybrid surface is designed. The switching is realized by PIN diodes. Then, a dipole is located above the AGS for beam steering. When the AGS works as an HIS, a broadside radiation is obtained. An end-fire main beam can be generated when the AGS works as an HIS-SWG hybrid structure. At last, a prototype is fabricated and measured, and the measured results agree well with the simulated ones. The measured results also validate the beam-steering performance of the antenna.

ACKNOWLEDGMENT

This work was supported by the National Natural Science Foundation of China (Grants No. 61731005, No. 61771407 and No. 61801405) and Aeronautical Science Foundation of China (ASFC-20162080008).

REFERENCES

[1] J. Bernhard, E. Bonek, C. G. Christodoulou, D. Kunkee, and K. L. Melde, “Guest editorial for the special section on antenna systems and propagation for cognitive radio,” *IEEE Trans. Antennas Propagat.*, vol. 62, no. 3, pp. 1015-1018, Mar. 2014.

[2] C. G. Christodoulou, Y. Tawk, S. A. Lane, and S. R. Erwin, “Reconfigurable antennas for wireless and space applications,” *Proc. IEEE*, vol. 100, no. 7, pp. 2250-2261, July 2012.

[3] N. Ojaroudi, Y. Ojaroudi, S. Ojaroudi, Y. Ebazadeh, and M. Shirgir, “Small reconfigurable monopole antenna integrated with PIN diodes for multimode wireless communications,” *Applied Computational Electromagnetics Society Journal*, vol. 29, no. 7, pp. 541-546, July 2014.

[4] S. Zhang, G. H. Huff, J. Feng, and J. T. Bernhard, “A pattern reconfigurable microstrip parasitic array,” *IEEE Trans. Antennas Propagat*., vol. 52, pp. 2773-2776, Oct. 2004.

[5] J. Zhang, X. S. Yang, J. L. Li, and B. Z. Wang, “Triangular patch Yagi antenna with reconfigure-able pattern characteristics,” *Applied Computational Electromagnetics Society Journal*, vol. 27, no. 11, pp. 541-546, Nov. 2012.

[6] D. Rodrigo and L. Jofre “Frequency and radiation pattern reconfigurability of a multi-size pixel antenna,” *IEEE Trans. Antennas Propagat.*, vol. 60, no. 5, pp.2219-2225, 2012.

[7] D. Rodrigo, B. A. Cetiner, and L. Jofre, “Frequency, radiation pattern and polarization reconfigurable antenna using a parasitic pixel layer,” *IEEE Trans. Antennas Propagat.*, vol. 62, no. 6, pp. 3422-3427, June 2014.

[8] Y. F. Cheng, W. Shao, X. Ding, and et.al., “A novel beam steerable antenna based ondual-reconfiguration technique,” *J. Electromagn Waves Appl.*, vol. 31, no. 7, pp. 740-751, Apr. 2017.

[9] X. Ding and B.-Z. Wang, “A millimeter-wave pattern-reconfigurable antenna with a reconfigurable feeding network,” *J. Electromagn. Waves Applicat.*, vol. 27, no. 5, pp. 649-658, Jan. 2013.

[10] X. Jiang, Z. Zhang, Y. Li, and Z. Feng, “A novel null scanning antenna using even and odd modes of a shorted patch,” *IEEE Trans. Antennas Propag.*, vol. 62, no. 4, pp. 1903-1909, Apr. 2014.

[11] Y. F. Cheng, X. Ding, B. Z. Wang, and W. Shao, “An azimuth-pattern-reconfigurable antenna with enhanced gain and front-to-back ratio,” *IEEE Antennas Wireless Propag. Lett.*, vol. 16, pp. 2303-2306, Aug. 2017.

[12] W. H. Chen and Z. H. Feng, “Planar reconfigurable pattern antenna by reactive-load switching,” *Microw. Opt. Technol. Lett.*, vol. 47, no. 5, pp. 506-507, Dec. 2005.

[13] P. Deo, A. Mehta, D. Mirshekar-Syahkal, and H. Nakano, “An HIS based spiral antenna for pattern reconfigurable applications,” *IEEE Antennas Wireless Propag. Lett.*, vol. 8, pp. 196–199, 2009.

[14] J. Ren, X. Yang, J. Yin, and Y. Yin, “A novel antenna with reconfigurable patterns using H-shaped structures,” *IEEE Antennas Wireless Propag. Lett.*, vol. 14, pp. 915-918, 2015.

[15] M. Li, S. Q. Xiao, Z. Wang, and B. Z. Wang, “Compact surface-wave assisted beam-steerable antenna based on HIS,” *IEEE Trans. Antennas Propag.*, vol. 62, no. 7, pp. 3511-3519, July 2014.

[16] D. Sievenpiper, L. J. Zhang, Romulo, F. J. Broas, N. G. Alexopolaus, and E. Yablonovitch, “High-impedance electromagnetic surfaces with a forbidden frequency band,” *IEEE Microwave Theory Tech.*, vol. 47, no. 11, pp. 2059-2074, Nov. 1999.

[17] D. R. Smith, D. C. Vier, T. Koschny, and C. M. Soukoulis, “Electromagnetic parameter retrieval from inhomogeneous metamaterials,” *Phys. Rev. E*, vol. 71, p. 036617, Mar. 2005.

[18] X. D. Chen, T. M. Grzegorczyk, B. I. Wu, J. Pacheco, and J. A. Kong, "Robust method to retrieve the constitutive effective parameters of metamaterials," *Phys. Rev. E*, vol. 70, p. 016608, July 2004.
[19] R. E. Collin, *Field Theory of Guided Waves*. 2nd edition, New York: IEEE Press, 1991.
[20] B. Majumda and K. P. Esselle, "Fixed frequency broadside–endfire beam steerable antennas," *Electro. Lett.*, vol. 52, no. 15, pp. 1282-1284, July 2016.

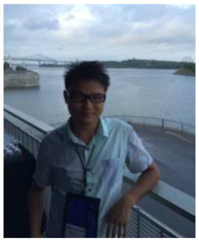

You-Feng Cheng was born in Anhui, China, in 1989. He received the Ph.D. degree in Radio Physics from the University of Electronic Science and Technology of China (UESTC), Chengdu, China, in 2018. In 2017, he was a Visiting Scholar with the Mechanical Engineering Department, University of Houston, Houston, TX, USA. He joined Southwest Jiaotong University (SWJTU), Chengdu, China, in 2018. His research interests include phased arrays, reconfigurable antennas, and evolutionary algorithms.

Xiao Ding received the B.S. and M.S. degrees in Electronic Engineering, from Guilin University of Electronic Science and Technology (GUET), Guilin, China, and the Ph.D. degree in Radio Physics from University of Electronic Science and Technology of China (UESTC), Chengdu, China, in 2014. He joined the UESTC in 2014, where he is currently an Associate Professor. In 2013, he was a Visiting Scholar at the South Dakota School of Mines and Technology, SD, USA. From June 2016 to June 2017, he was a Visiting Scholar at the University of Houston, TX, USA. His research interests include reconfigurable antennas and its' applications and phased arrays.

Wei Shao received the M.Sc. and Ph.D. degrees in Radio Physics from UESTC, Chengdu, China, in 2004 and 2006, respectively. He joined the UESTC and is now a Professor. He has been a Visiting Scholar in the Electromagnetic Communication (CEM) Laboratory, Pennsylvania State University in 2010. His research interests include computational electromagnetics and antenna design.

Cheng Liao was born in Chongqing, China, in 1964. He received the Ph.D. degree in Electromagnetic Fields and Microwave Techniques from the University of Electronic Science and Technology of China (UESTC), Chengdu, China, in 1995. From 1997 to 1998, he was a Visiting Scholar at the City University of Hong Kong, Kowloon Tong, Hong Kong. He became a Professor at Southwest Jiaotong University, Chengdu, China, in 1998. His research interests include computational electromagnetic, electromagnetic compatibility, and antenna theory and design.

A Metallic Patch Antenna Using a Simple Short Probe for Improving Impedance Match Bandwidth

Ziyang Wang [1,2], Zhao Yang [1], and Yingzeng Yin [1]

[1] National Key Laboratory of Antennas and Microwave Technology
Xidian University, Xi'an, Shaanxi 710071, People's Republic of China
yangzhaoxd@sina.com, yyzeng@mail.xidian.edu.cn

[2] State Key Laboratory on Microwave and Digital Communications
Tsinghua National Laboratory for Information Science and Technology
Department of Electronic Engineering, Tsinghua University, Beijing, 100084, China
wangziyang1@126.com, fan_yang@tsinghua.edu.cn

Abstract **─** A metallic patch antenna using double-tuned impedance matching is presented in this paper. The antenna mainly consists of a rectangular ground plane, a radiation patch with U-slot and two short metal cylinders, with a size of 200mm×200mm×25.5mm. The two metal cylinders are used to connect the patch and the ground. With the common effects of the U-slot and the two metal cylinders, the impedance match has become better than before. Moreover, high harmonics and cross polarization are suppressed after loading two short pins. Measured results show that the antenna has a wide impedance bandwidth from 830 MHz to 970 MHz (16%) for voltage standing wave ratio (VSWR) less than 1.5, and a high gain level about 9.3dBi in a wide band. A good agreement is achieved between simulated and measured results. Therefore, the proposed metal antenna is a good choice for UHF RFID applications.

Index Terms **─** Cross polarization, high harmonics, short probe, UHF RFID applications, wideband.

I. INTRODUCTION

Broadband antenna with a small size is a hot topic for antenna designers and it is a pair of contradictory unity of opposites. As we all know, a traditional antenna has a narrow band since only one resonance has been used [1]. An effective approach to add a new resonance point has been adopted to improve the bandwidth. Firstly, a ring slot has been reported in paper [2], while the radiation pattern is not very good. Another capacitive coupled technology is presented to enhance the bandwidth in paper [3], but the gains are not satisfactory results. U-slot and other capacitive gaps have been used to enhance the bandwidth in papers [4-5]. A parasitic element is also used to increase the bandwidth in [6-7], while there are a few reports about improving the impedance match. Other broadband antennas [11-12] are also presented.

In this paper, a U-slot has been used to improve the bandwidth. After that, two metal cylinders are placed on the ends of the feeder symmetrically to improve the impedance match. Furthermore, the cross polarization and high order modes are also improved. The proposed antenna has a perfect impedance match bandwidth covering from 830MHz to 970MHz with desirable gains. It can be used for UHF RFID applications. Detailed design processes and test results are presented in the following chapters.

II. ANTENNA DESIGN AND ANALYSIS

Geometry for the proposed antenna and detailed design process will be presented in this section.

A. Geometry of the proposed antenna

Figure 1 shows the geometry and dimensions for the proposed antenna. The all-metal antenna is made of aluminum material. Air substrate is used to separate the ground with the radiation patch, which can improve the bandwidth. A single-probe is adopted as feeding structure installed at the center of radiation patch. Then, the bandwidth has improved by using a U-slot. Moreover, a good impedance match performance in a wide operating bandwidth is achieved by two metal cylinders. The antenna can be fixed by four dielectric cylinders. A prototype of the antenna is illustrated in Fig. 1, and the optimized parameters are as follows: W=200mm, L=200mm, W1=9mm, W2=8mm, W3=36mm, Wr=70mm, L1=126mm, L2=77mm, Lr=8mm, H=25mm, h1=1.5mm, h2=2mm.

B. Theoretical analysis

In this paper, multistage matching technology is used for broadening the bandwidth of antenna. In equation (1), the impedance matching equation is presented for guiding the design of broadband antenna

Submitted On: August 26, 2017
Accepted On: December 25, 2018

where n is the tuned stage, and B_n is the optimal impedance bandwidth at the corresponding state. As we know, a single radiation patch antenna can be considered as a first-order resonant circuit as shown in Fig. 2 (a). Corresponding to the impedance equation, the value of n is equal to 1. The optimal bandwidth about B_1 is presented in equation (2). Furthermore, an optimal first-order resonant mode can be obtained by tuning the parameter of the antenna. In addition, the bandwidth for mid-band and edge-band are demonstrated in equations (4) and (5):

$$B_n(\tau) = \frac{1}{Q}\frac{1}{b_N \sinh(\frac{1}{a_n}\ln(\frac{1}{\tau})) + \frac{1-b_n}{a_n}\ln(\frac{1}{\tau})}. \tag{1}$$

While $n=1$, $a_n=1$, $b_n=1$, the bandwidth is shown as following:

$$B_1 = \frac{1}{Q}\frac{\pi}{\ln(\frac{1}{\tau})} = \frac{1}{Q}\frac{\pi}{\ln(\frac{VSWR+1}{VSWR-1})}, \tag{2}$$

$$Q = \frac{\omega_0 L}{R}, \tag{3}$$

$$B_{1MB} = \frac{1}{Q}\frac{2\tau^2}{\sqrt{1-\tau^2}} = \frac{1}{Q}\frac{VSWR-1}{\sqrt{VSWR}}, \tag{4}$$

$$B_{1EB} = \frac{1}{Q}\frac{2\tau}{1-\tau^2} = \frac{1}{Q}\frac{VSWR^2-1}{2*VSWR}. \tag{5}$$

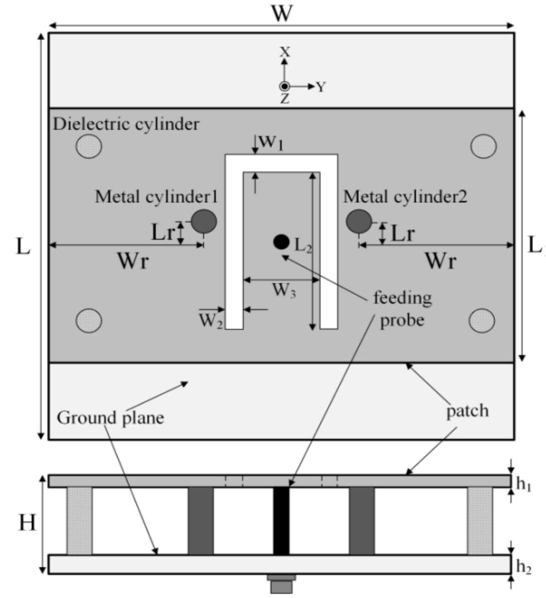

Fig. 1. Geometry of the proposed antenna.

The relationship about reflection coefficients, phase and bandwidth about the double-tuned matching are shown in the following equations (6), (7), (8):

$$B = \frac{1}{Q}\tan(\varphi_{EB}), \tag{6}$$

$$\tau_1 = \tan(\tfrac{\varphi_{EB}}{2}), \tag{7}$$

$$\tau_2 = \tau_1^2, \tag{8}$$

φ_{EB} is the phase at the case of edge-band, τ_1 is the reflection coefficient of single tuning, τ_2 is the value of double tuning. The blue curve represents the mid-band and the red curve represents the case of edge-band. The equivalent circuit for double tuned match is presented in Fig. 2 (b). Firstly, the patch is acted as a series RLC circuits [11], then the gap of U type is etched on the patch, it can be replaced by a capacitor, approximately. After that, a pair of short pins are connected between the patch and the ground to further improve matching.

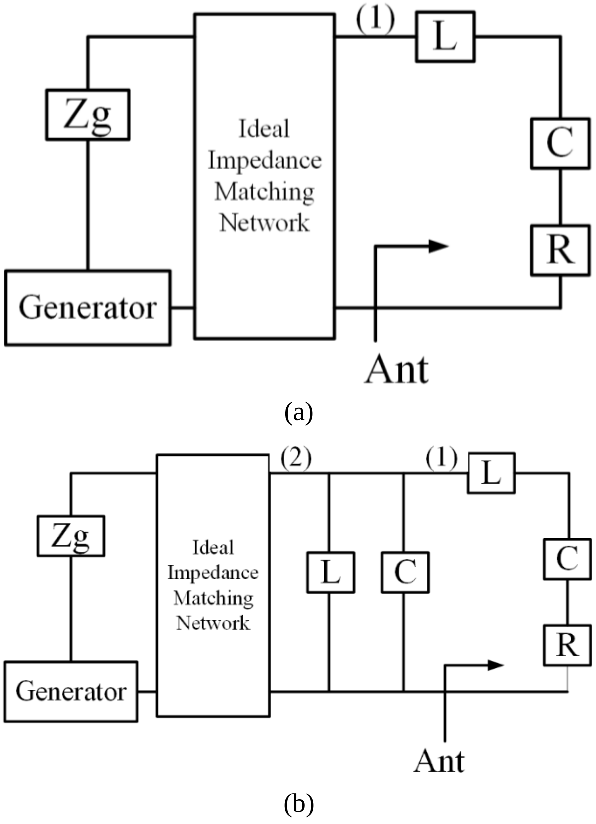

(a)

(b)

Fig. 2. (a) Equivalent circuit of the single tuning match, and (b) equivalent circuit of the proposed patch antenna.

In the end, the processes of the double tuning match are presented in the smith chart as shown in Fig. 3. Fractional bandwidth can be calculated by the following equations (9) and (10). The value of B1 and B2 are about 6% (40 MHz) and 16.8% (140 MHz), respectively, with VSWR less than 1.5:

$$B_n = (f_H - f_L) / f_0, \tag{9}$$

$$f_0 = \sqrt{f_H f_L}\,. \tag{10}$$

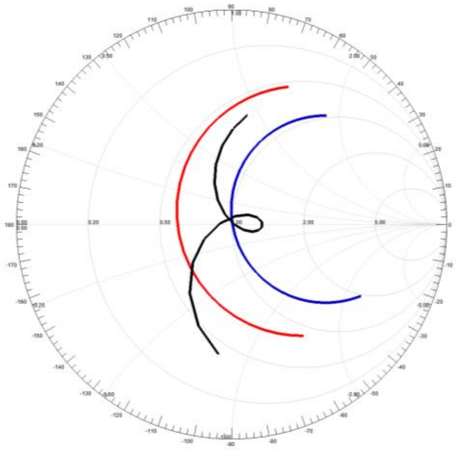

Fig. 3. Smith chart of double tuning match.

III. RESULTS AND DISCUSSION

The prototype of the antenna is fabricated which is shown in Fig. 4. The Key-sight E5080A vector network analyzer is used to measure the scattering performance. Simulated and measured S parameters are illustrated in Fig. 4. It is seen that the S11 is less than 15dB ranging from 830 MHz to 970MHz. A good agreement is obtained between the simulated and measured results. Figure 5 shows S parameters of the antennas with and without two metal cylinders, and the high harmonics have been suppressed with and without metal cylinders. Moreover, it can be observed that a good impedance matching is obtained by using a pair of short pins. The short probes can act as LC resonance elements, and a double-tuned impedance matching has been got, therefore the bandwidth of the proposed antenna has improved.

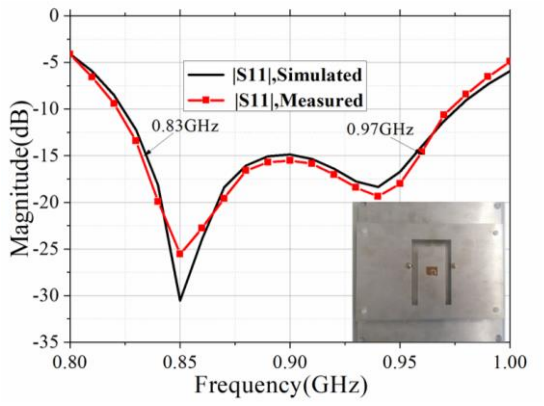

Fig. 4. The value of simulated and measured S11.

In order to further investigate the performance of suppressing cross polarization by using the metal cylinder, the main polarization and cross polarization in XOZ plane and YOZ plane are shown in Fig. 6. The cross polarizations with metal cylinder decrease 10dB and 5dB, in XOZ and YOZ plane, respectively. Therefore, the cross polarization has been suppressed with two metal cylinders obviously.

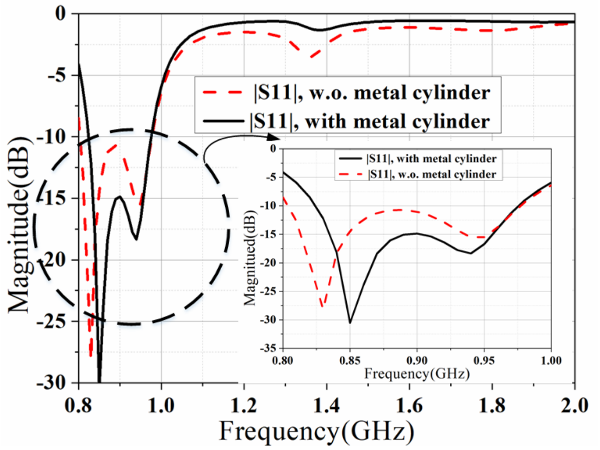

Fig. 5. S parameter of the antennas with and without metal cylinders.

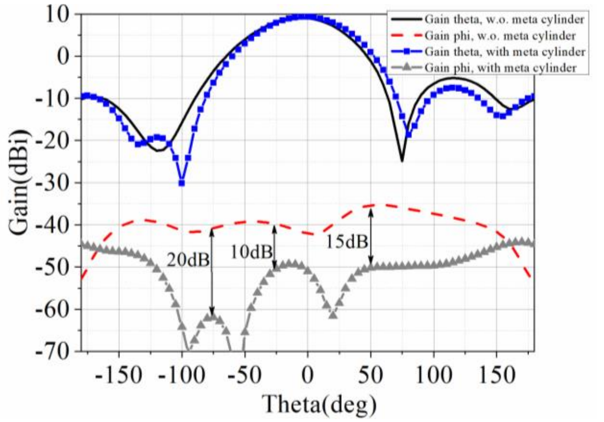

XOZ-plane

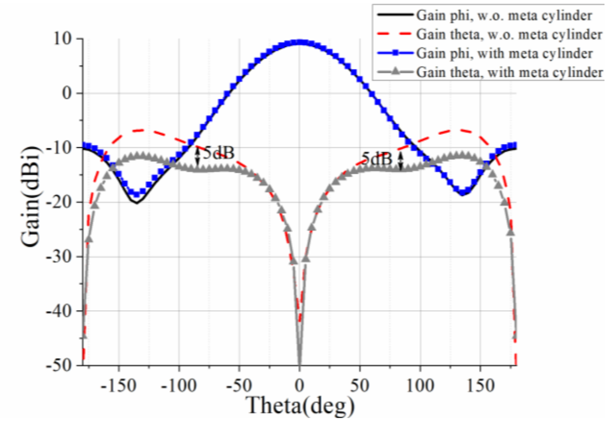

YOZ-plane

Fig. 6. Main polarization and cross polarization in XOZ and YOZ plane.

Parameter analysis has been shown to describe the design mechanism of the wideband RFID antenna. In Figs. 7-9, the S parameter for the proposed antenna with different values of W3, h, Wr are shown, respectively. Figure 7 illustrates the effects of the size of the U slot. It is found that the low frequency changes fiercely with high frequency invariance. In Fig. 8, the impedance match performance has improved with the distance of the two short pins changing, while the dual resonant frequencies are almost unchanged. In Fig. 9, as the value of h changes from 21mm to 31mm, both of the dual resonator frequencies shift down to the low frequency, while the bandwidth of the antenna changes slightly.

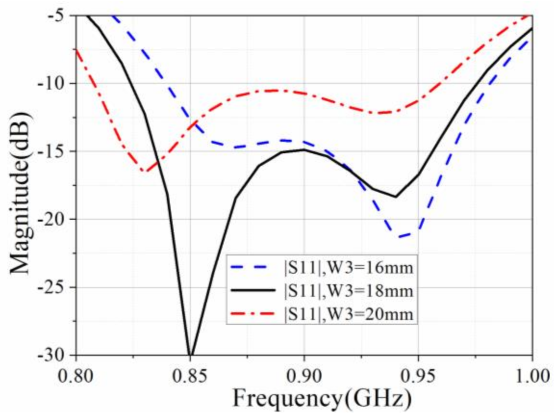

Fig. 7. Influence of U slot on the value of S11.

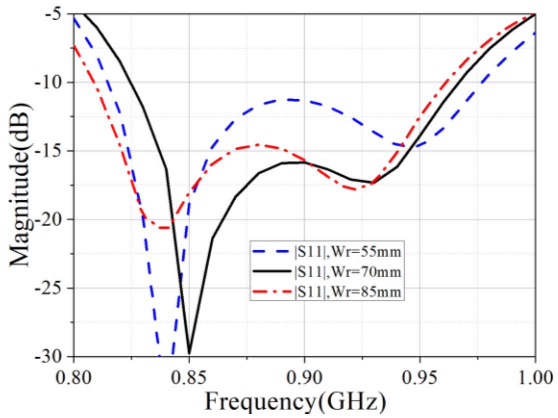

Fig. 8. Influence of two short pins on the value of S11.

The radiation patterns, gains and efficiencies are tested by using a SATIMO system. Figures 10-12 show the measured and simulated far field radiation patterns for XOZ-plane and YOZ-plane at 840MHz, 900MHz, and 950MHz in the desired band. It is clear that stable radiation patterns are obtained, and 3 dB beam width are both 65◦ for XOZ and YOZ plane.

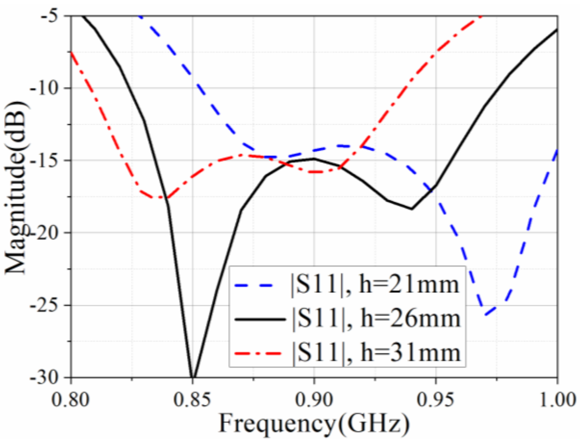

Fig. 9. Influence of height on the value of S11.

The simulated and measured gains and efficiencies of the proposed antenna are shown in Fig. 13 and Fig. 14. It is found that the gains of the proposed antenna are more than 9dBi in the desire band. Meanwhile, the simulated and measured efficiencies of the proposed antenna are more than 80%. Therefore, it can satisfy the traditional requirement in the whole UHF band.

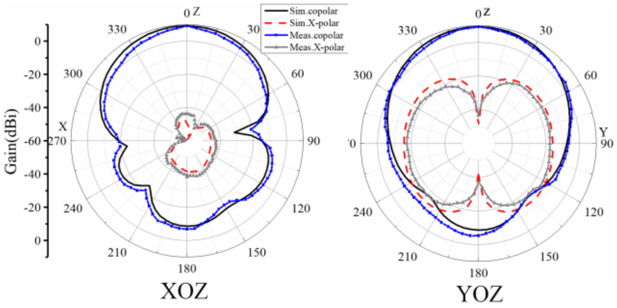

Fig. 10 Simulated and measured radiation patterns for XOZ plane and YOZ plane at 840MHz.

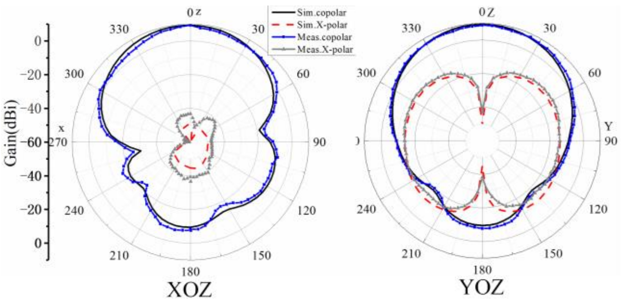

Fig. 11. Simulated and measured radiation patterns for XOZ plane and YOZ plane at 900MHz.

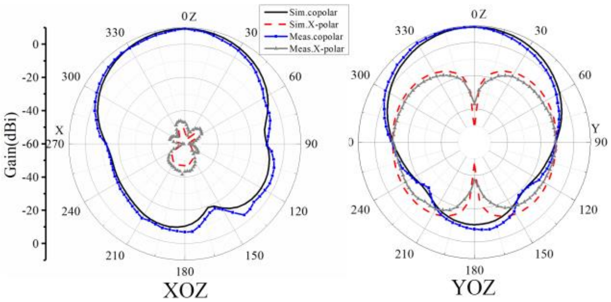

Fig. 12. Simulated and measured radiation patterns for XOZ plane and YOZ plane at 960MHz.

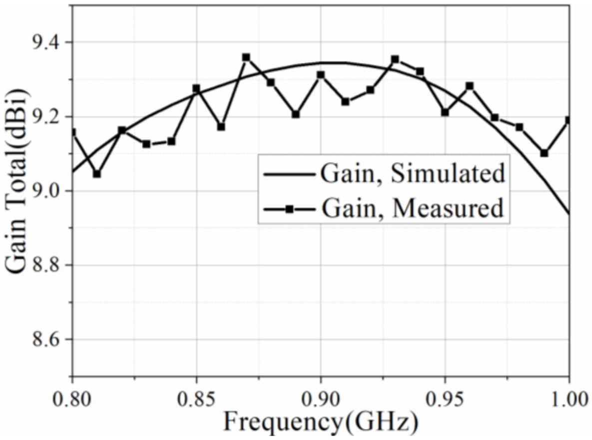

Fig. 13. Simulated and measured gains for the proposed antenna.

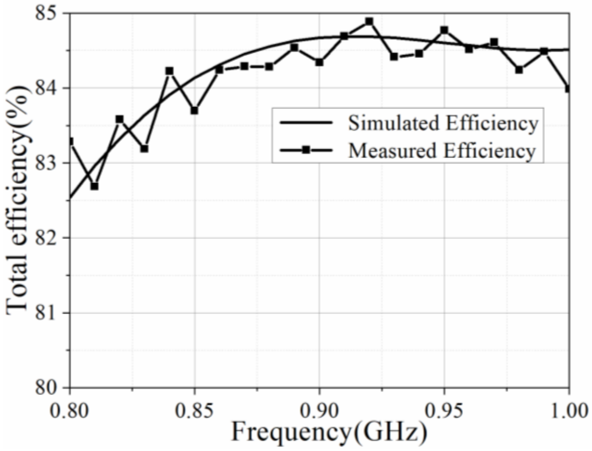

Fig. 14. Simulated and measured efficiencies for the proposed antenna.

The sizes, gain performance, and the bandwidth of the proposed RFID antenna have been compared with several other antennas in Table 1. By observing these data, all the performances of the designed antenna are superior to those of other reference antenna. Accurate comparative data are as follows.

Table 1: Performance of several other antennas

ANT	BW(VSWR<1.5) (MHz)	Gain (dBi)	Height
Ref. [8]	1620-1800 (10.53%)	7	0.125λ
Ref. [9]	2170-2580 (17.2%)	7.3	0.08λ
Ref. [10]	818-964 (16.3%)	3.5	0.125λ
Ref. [6]	4200-5400 (25%)	7	0.14λ
Prop.	830-970 (16.8%)	9.2	0.06λ

IV. COPYRIGHT AND RELEASE INFORMATION

No conflict of interest exits in the submission of this manuscript. All authors have seen the manuscript and approved to submit to your journal.

V. CONCLUSION

A wideband metal patch antenna basing on double-tuned impedance match is proposed. Owing to the common effect of the short probes and the U slot, the impedance matching bandwidth is improved ranging from 830MHz to 970 MHz (S11<-15). Moreover, high harmonics and cross polarization have been suppressed with the effect of metal cylinders. A good radiation performance has been obtained for the proposed antenna. Gains is more than 9dBi in the desired band, and the efficiencies are about 80%. Moreover, the radiation patterns are satisfying in a wide band, and 3-dB beam width are both 65◦ in XOZ and YOZ plane. Therefore, stable gain, low cost, compact structure, and easy manufacturing make the proposed antenna become a good candidate for UHF RFID applications.

REFERENCES

[1] Z. Xing, Z. Zhang, and K. Wei, "One terminal improving method of open-circuit near-field antenna of UHF RFID system," *Journal of Electromagnetic Waves & Applications*, vol. 28, no. 3, pp. 306-315, 2014.

[2] A. A. Deshmukh and K. P. Ray, "Broadband proximity-fed modified rectangular microstrip antennas," *IEEE Antennas Propag., Mag*, vol. 53, no. 5, pp. 41-56, Oct. 2011.

[3] V. G. Kasabegoudar and K. J. Vinoy, "Coplanar capacitively coupled probe fed microstrip antennas for wideband applications," *IEEE Trans. Antennas Propag.*, vol. 58, no. 10, pp. 3131-3138, Oct. 2010.

[4] S. Liu, S. S. Qi, W. Wu, and D. G. Fang, "Single-feed dual-band single/dual-beam U-slot antenna for wireless communication application," *IEEE Trans. Antennas Propag.*, vol. 63, no. 8, pp. 3759-

3764, Aug. 2015.

[5] K. F. Tong and T. P. Wong, "Circularly polarized U-slot antenna," *IEEE Trans. Antennas Propag.*, vol. 55, no. 8, pp. 2382-2385, Aug. 2007.

[6] E. Nishiyama and M. Aikawa, "Wide-band and high-gain microstrip antenna with thick parasitic patch substrate," in *Proc. IEEE Antennas Propag. Soc. Int. Symp. (APSURSI)*, pp. 273-276, June 2004.

[7] M. Arrawatia, M. S. Baghini, and G. Kumar, "Differential microstrip antenna for RF energy harvesting," *IEEE Trans. Antennas Propag.*, vol. 63, no. 4, pp. 1581-1588, Apr. 2015.

[8] X. H. Tang, K. L. Lau, Q. Xue, and Y. L. Long, "Miniature circularly polarised patch antenna," *Electron. Lett.*, vol. 46, no. 6, pp. 391-392, Mar. 2010.

[9] A. Khidre, K. F. Lee, F. Yang, and A. Elsherbeni, "Wideband circularly polarized E-shaped patch antenna for wireless applications," *IEEE Antennas Propag. Mag.*, vol. 52, no. 5, pp. 219-229, Oct. 2010.

[10] Nasimuddin, Z. N. Chen, and X. M. Qing, "Dual-band circularly polarized S-shaped slotted patch antenna with a small frequency-ratio," *IEEE Trans. Antennas Propag.*, vol. 58, no. 6, pp. 2112-2115, June 2010.

[11] F Yang, X. X. Zhang, X. N. Ye, and R. S. Yahya, "Wide-band E-shaped patch antennas for wireless communication," *IEEE Transactions on Antennas and Propagation*, vol. 49, no. 7, pp. 1094-1100, June 2010.

[12] K. Yu, Y. S. Li, and W. H. Yu. "Wide-band E-shaped patch antennas for wireless communication," *IEEE Transactions on Antennas and Propagation*, vol. 32, no. 5, pp. 424-429, May 2017.

Zi-Yang Wang was born in Henan Province, China, in 1991. He received the Ph.D. degree in Electromagnetic Wave and Microwave Technology from Xidian University, Xi'an, P. R. China, in 2018. He is currently doing postdoctoral research at National Laboratory for Information Science and Technology, Department of Electronic Engineering, in Tsinghua University. His research interests include the design of metamaterial and meta-surface, array decoupling, MIMO, RFID antennas, wideband antenna.

Zhao Yang was born in Shanxi Province, China, in 1992. He received the B.S. degree from Xidian University, Xi'an, China, in 2014. He is currently pursuing the M.S. degree in Electromagnetic Field and Microwave Technology from the Key Laboratory of Science and Technology on Antennas and Microwaves, Xidian University, Xi'an, China.

Ying-Zeng Yin received the B.S. degree and the M.S. degree and Ph.D. degree in Electromagnetic Wave and Microwave Technology from Xidian University, Xi'an, China, in 1987, 1990, and 2002, respectively. From 1990 to 1992, he was a Research Assistant and an Instructor at the Institute of Antennas and Electromagnetic Scattering, Xidian University. From 1992 to 1996, he was an Associate Professor in the Department of Electromagnetic Engineering, Xidian University. Since 2004, he has been a Professor at Xidian University.

His research interests include design of microstrip antennas, artificial magnetic conductors, phased array antennas, and computer aided design for antennas.

Design of Reconfigurable Ultrawide Band Antenna with Switchable Single/Dual/Triple Band Notch Functions

Jian Dong, Shan Wang, and Guoqiang Hu

School of Information Science and Engineering
Central South University, Changsha, 410083, China
dongjian@csu.edu.cn

Abstract **─** A reconfigurable ultrawide band (UWB) antenna with switchable single, dual, and triple band notch functions is presented in this study. In the proposed structure, by etching slots on the radiating patch, the ground plane, and the feedline, triple band-notched characteristics at the WLAN, WiMAX and X-band frequencies are obtained. Then, by introducing switch modes on the slots, the antenna offers eight working modes and can realize an interconversion between one UWB mode, three single band-notched modes, three dual band-notched modes, and one triple band-notched mode. Simulated and measured results show that the proposed antenna can provide good band-notched functions on the stopbands and has nearly omnidirectional radiation patterns on the passbands.

Index Terms **─** Band-notched, reconfigurable antenna, slots, switch, ultrawide band (UWB) antenna.

I. INTRODUCTION

Ultrawide band (UWB) technology was used in military initially and has drawn more and more attention since the Federal Communications Commission (FCC)'s allocation of the frequency band 3.1-10.6 GHz for commercial use [1]. Compared to a narrow band system, UWB technology would be more attractive because of its wide transmission bandwidth, low transmission power, and high data transmission rates and so on. However, UWB systems have encountered a hostile radio environment which may cause potential interferences to the UWB band. For instance, IEEE 802.16 WiMAX system operates at 3.3–3.7 GHz; IEEE 802.11a WLAN system operates at 5.15–5.825 GHz and X-band satellite downlink signal operates at 7.25-7.75GHz, uplink signal operates at 7.9~8.4GHz. To solve this problem, it is desirable to design UWB antennas with intrinsic band-notched characteristic to suppress the interference from these narrow band systems [2].

Various methods for designing band-notched UWB antennas have been presented and reported. Designs of using parasitic stubs as resonators to achieve band-notched function were presented in [4-[7]. In these designs, the antenna structures cannot be compact enough due to the use of parasitic stubs. In order to make the structure of band-notched antenna more compact, etching slots such as L-shaped, C-shaped, E-shaped, H-shaped, and other slots on the radiating patch or on the ground plane was used to achieve band-notched function [8]-[18]. In [8], by etching a pair of inverted-L-shaped slots around the microstrip line on the ground, a frequency-notched function centered at 5.2 GHz is obtained. In [9], a rejected frequency band of 5-6 GHz is obtained by etching an H-shaped slot from the back patch of a conventional UWB antenna. In [10], the proposed antenna can obtain a UWB property with a 5.1–5.9 GHz notch by embedding an elliptic slot into a convex-shaped patch.

In order to avoid the interference from services working at different frequency bands, dual band-notched UWB antennas were presented [11]-[15]. In [11], by cutting an elliptical slot on the modified circular patch and an inverted G-shaped slot on the ground plane, a 3.5/5.5 GHz dual band-notched UWB antenna was presented. In [12], by cutting two L-shaped slits and an E-shaped slot with variable dimensions on the radiating patch, dual band-notch characteristics are generated. In [13], the proposed antenna generated dual band-notched function by using four rectangular-shaped slots. In [14], the proposed antenna can obtain a UWB property with dual notched band by using two U-shaped slots on the radiating patch. In these designs, the desired notched band frequencies are achieved by usually adjusting the total lengths of the etching slots, which makes the switch of the center frequency limited. Hence, in order to improve the performance of the UWB system, antennas with reconfigurable structures which exhibit switchable band notch performances are desirable. In [15], by etching two symmetrical notches on the feed-line and cutting two slots on the radiating patch and embedding two positive-intrinsic-negative (PIN) diodes along these slots, a reconfigurable ultra-wideband slot antenna with switchable single/dual band notch functions was proposed. In this structure, the change of the bias states of the PIN diodes makes the antenna capable of

Submitted On: October 30, 2016
Accepted On: December 21, 2018

exhibiting four different performances of UWB spectrum coverage. However, most reported UWB antennas were designed with no more than two notched bands, which reveals that potential interference from other narrow bands may still exist with such antennas. In [16], a wideband circular slot antenna with tri-band rejection characteristics at 2.45, 5.45, and 8 GHz was proposed by using a split ring and an inverted L-shaped slot on the circular patch. In [17], the triple band-notched characteristics, rejecting the 3.4–3.6 GHz, 5.5–6.05 GHz and 7.8–8.3 GHz frequency bands, are obtained by etching a complementary split-ring resonator (CSRR) inside the radiate patch of printed elliptical monopole antenna (PEMA) and inserting a U-Shaped slot in the ground plane respectively. Although three notched bands are obtained, it is difficult to control the bandwidth of the desired notched-bands because of strong couplings between the band-notched characteristic designs. For instance, the notched band for WiMAX (3.3-3.7 GHz) is missing and the notched band for WLAN (5.15–5.825 GHz) is not complete in [16]. The notched bands for both WiMAX (3.3-3.7 GHz) and WLAN (5.15–5.825 GHz) are not complete in [17].

In this paper, a reconfigurable UWB antenna with switchable single/dual/triple band notch functions is proposed by etching slots on the radiating patch, the ground plane, and the feedline. The proposed antenna can operate within an ultrawide band from 3.53 GHz to above 9.56 GHz. Meanwhile, the antenna can reject the frequency bands of 3.30~4.68 GHz, 5.15~6.48 GHz, and 7.25~8.54 GHz and hence avoid the interference from WiMAX, WLAN, and X-band satellite systems. Furthermore, it is observed that the notch frequencies of the antenna could be varied independently by switching PIN diode switches. The switches being either shorted or open will allow the antenna to operate at eight modes and can realize an interconversion between one UWB mode, three single band-notched modes, three dual band-notched modes, and one triple band-notched mode. Details of antenna design, the simulated and measured results are presented and discussed in the following sections.

II. ANTENNA DESIGN

The schematic configuration of the proposed microstrip-fed planar monopole antenna for triple band-notched operation is shown in Fig. 1. The slot antenna is printed on an FR-4 substrate with a relative permittivity of 4.4 and a thickness of 1.6mm and loss tangent 0.02. The antenna consists of a planar circular disc monopole with an arc H-shaped slot and is fed by a 50 ohm microstrip line. Compared to the straight-shaped H-shaped slot [18], the arc H-shaped slot can provide more degrees of freedom (such as α, R_1, L_1) for tuning the center frequency of the desired rejectband. An inverted L-shaped slot is etched on the microstrip feedline. The ground plane is reshaped as a T-shaped defected ground structure with two narrow L-shaped slots. The top corners and rectangular panes are removed to improve the impedance bandwidth and reduce the return loss. Note that, each end of arc H-shape slot is short circuit and then the arc H-shape slot can be equivalent to a half-wavelength resonator. The length of the arc H-shaped slot, l_1, can be calculated by:

$$l_1 = \frac{\lambda_g}{2} = \frac{c}{2f_{notch}\sqrt{\varepsilon_e}}, \tag{1}$$

$$\varepsilon_e = \frac{(\varepsilon_r+1)}{2}. \tag{2}$$

The narrow L-shaped slots and the inverted L-shaped slot short at one end, open at the other. They can be equivalent to quarter-wavelength resonator and the length of the slots l, can be approximately calculated by:

$$l = \frac{\lambda_g}{4} = \frac{c}{4f_{notch}\sqrt{\varepsilon_e}}, \tag{3}$$

where f_{notch} is the center frequency of the stopband, c is the speed of light, λ_g is the guide wavelength, ε_e is the effective permittivity, ε_r is the relative permittivity. Assume the center frequency of the WiMAX working frequency band is 3.6 GHz and the length of the arc H-shaped slot is about 25mm. Similarly, assume the center frequency of WLAN is 5.6 GHz and X-band satellite systems is 8.1 GHz, the length of narrow L slot is about 8mm and the inverted L-shaped slot is about 5mm. The length of the arc H-shaped slot, l_1, for 3.6 GHz resonant frequency can be derived by:

$$l_1 = 2(\alpha R_1 + R_1 - W_2). \tag{4}$$

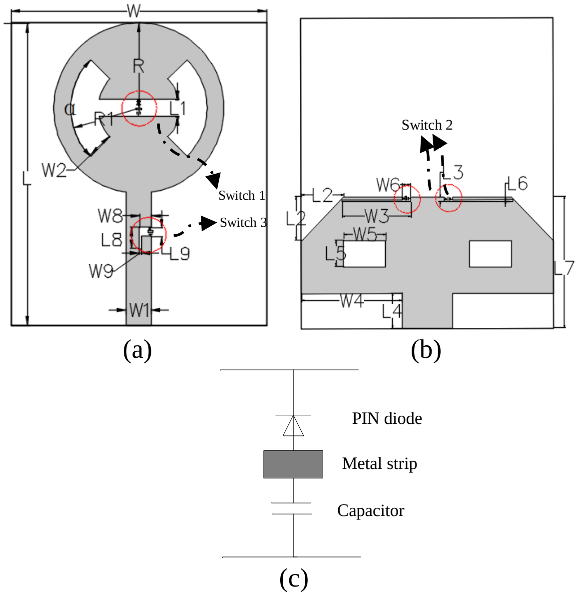

(a) (b)

(c)

Fig. 1. Schematic configuration of the proposed UWB antenna: (a) front view, (b) back view, and (c) switch structure.

Similarly, the length of the narrow L slot, l_2, for 5.6 GHz resonant frequency and the length of the inverted L slot, l_3, for 8.1 GHz can be derived by:

$$l_2 = L_3 + W_3, \tag{5}$$

$$l_3 = L_8 + W_8. \tag{6}$$

The final triple band-notched UWB antenna design is achieved by tuning the length, width, and the slot dimensions of the radiating patch, the microstrip line, and the defected ground structure. The optimized parameter values of the proposed band-notched UWB antenna are summarized in Table 1.

Table 1: Design parameters of the proposed UWB antenna (unit: mm)

Parameter	**Value**	**Parameter**	**Value**
W	30	W_3	7.3
L	35.5	L_3	0.5
α	π/3	W_4	12
R	10	L_4	4
R_1	8	W_5	5
W_1	3	L_5	3
L_1	2	W_6	1
W_2	3.2	L_6	0.2
L_2	5	L_7	15
W_8	1.5	L_8	2.5
W_9	0.3	L_9	1

By etching an arc H-shaped slot on the circular radiating patch, the antenna can avoid the interference from IEEE 802.16 WiMAX system operating at 3.3–3.7 GHz. By etching two narrow L-shaped slots on the defected ground plane, a second band notch function, which can prevent the influence from IEEE 802.11a WLAN system operating at 5.15–5.825 GHz, can be achieved. Further, in order to avoid the interference from X-band satellite signals operating at 7.25-7.75 GHz and 7.9-8.4 GHz, a third stopband is implemented by etching an inverted L-shaped slot on the microstrip feedline.

Furthermore, the proposed antenna can realize the switchable band notch characteristics by introducing PIN diode switches. Since each slot acts as a resonator and the resonant frequency mainly depends on its length, PIN diode switches are used in the slots to change their effective electrical length. In order to apply DC voltage to PIN diodes, metal strips are used inside the slots. Moreover, a 100-pF blocking capacitor is placed in each slot to create RF connection of PIN diode and isolate the RF signal from DC. Therefore, the band-notched function can be flexibly controlled by the status of the switches, which will be discussed in detail in the next section.

III. BAND-NOTCHED FUNCTION ANALYSIS

A. Triple band-notched function

Figure 2 illustrates the return loss of the proposed antenna structure. It is clearly evident from this figure (curve (i)) that by cutting an arc H-shaped slot on the radiating patch, one stopband at the low frequency is excited. Curve (ii) illustrates that two stopbands (one at the same low frequency and the other at the medium frequency) are excited by cutting the arc H-shaped slot on the radiating patch and two narrow L-shaped slots on the ground plane. Furthermore, curve (iii) illustrates that a third stopband at the high frequency is excited by etching an inverted L-shaped slot on the microstrip feedline. Therefore, by cutting an arc H-shaped slot on the radiating patch, narrow L-shaped slots on the ground plane, and an inverted L-shaped slot on the microstrip feedline, three stopband rejections will be formed with a center frequency of each stopband at 3.6 GHz, 5.6 GHz, and 8.1 GHz, respectively.

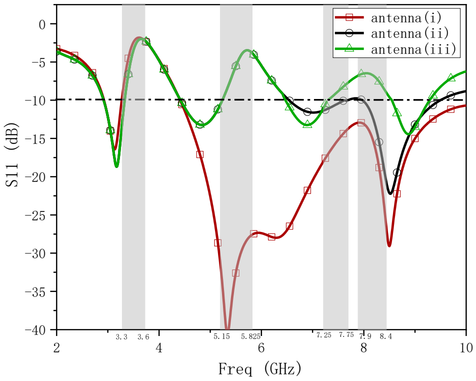

Fig. 2. Simulated return loss against frequency for the various configurations. (i) single band-notched antenna by cutting an arc H-shaped slot on the radiating patch; (ii) dual band-notched antenna by cutting an arc H-shaped slot on the radiating patch and two narrow L-shaped slots on the ground plane; (iii) triple band-notched antenna by cutting an arc H-shaped slot on the radiating patch, two narrow L-shaped slots on the ground plane, and an inverted L-shaped slot on the microstrip feedline.

To clarify the phenomenon behind the excitation of stopbands, Fig. 3 presents the input impedance of the proposed antenna with triple band-notched functions. In this figure, the input resistance and the input reactance keep the normal value except for the notch bands. When the working frequency is set at 3.6 GHz, 5.6 GHz and 8.1 GHz which are the center frequencies of the stopband, the proposed antenna would be at a state of parallel resonance. The input resistance is maximum and the input reactance vanishes when the antenna works at the state of parallel resonance. The equivalent circuit of the proposed antenna with triple band-notched function is presented in Fig. 4. As shown in Fig. 4, the proposed antenna could be equivalent to a combination of three parallel resonant circuits. When the working frequency is set at 3.6 GHz, the first parallel resonant circuit sets up a resonance. Thus, a total impedance mismatch occurs between the feed line and radiating patch, and the first band-notched characteristic is generated. Similarly, the second parallel resonant circuit resonates at 5.6 GHz and the third at 8.1 GHz.

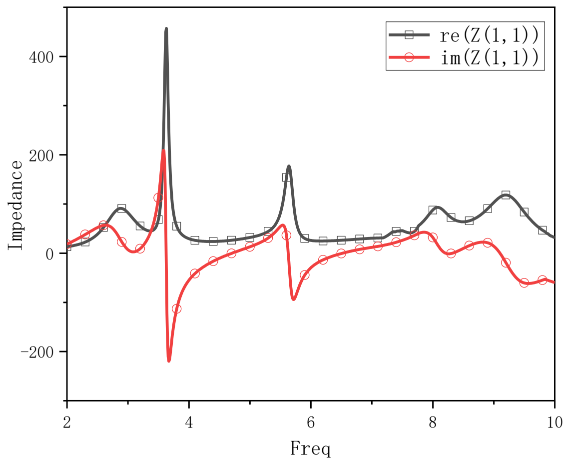

Fig. 3. Impedance of the proposed antenna with triple band-notched function.

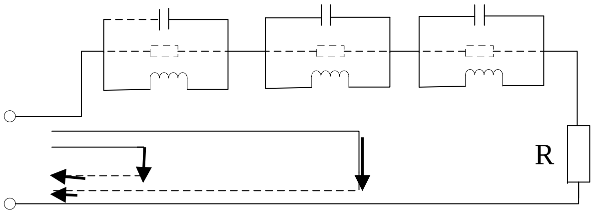

Fig. 4. Equivalent circuit of the proposed antenna with triple band-notched function.

In order to further explain the triple band-notched function resulting from slotted structure, the simulated surface current distribution for the proposed antenna at the resonant frequencies of 3.6, 5.6, and 8.1 GHz are shown in Fig. 4. It can be observed from the figure that the current distributions are different at the three notched bands. In particular, when the antenna operates at 3.6 GHz, as shown in Fig. 5 (a), most of the currents are concentrated near the arc H-shaped slot on the radiating patch; As shown in Fig. 5 (b), the currents are mainly distributed around two L-shaped slots on the ground plane when the antenna works at 5.6 GHz; when the antenna works at 8.1 GHz, as shown in Fig. 5 (c), the currents are mainly concentrated around the inverted L-shaped slot. Therefore, the antenna resonates at these frequencies due to the band-notched functions of these slotted structures.

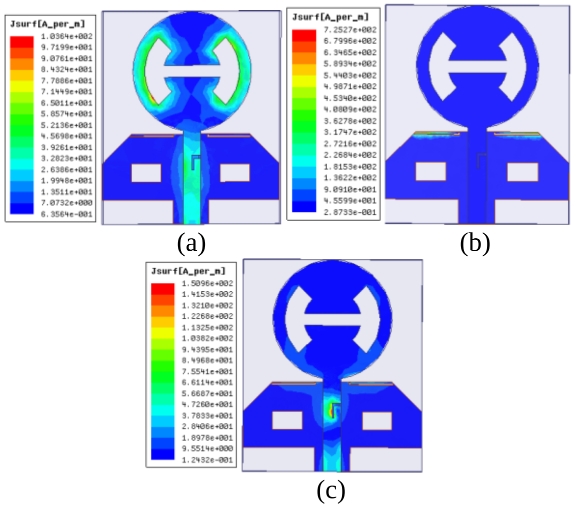

Fig. 5. Simulated surface current distributions on the radiation patch for the proposed antenna at: (a) 3.6 GHz, (b) 5.6 GHz, and (c) 8.1 GHz.

B. Switchable single/dual/triple band-notched function

As shown in Fig. 1, the controllability of band-notched functions is realized by adding one PIN diode in each slot. Since each slot act as a resonator and the resonant frequency mainly depends on its length, PIN diode switches are used in the slots to change their effective electrical length. Thus, each stopband being existing or not can be controlled by biasing PIN diode in the slot, respectively.

The PIN diode in the arc H-shaped slot which excites one stopband at the low frequency is called switch 1 and the switch 1 being shorted or open controls whether the stopband at the low frequency exists or not. Since two narrow L-shaped slots work together to excite one stopband at the medium frequency, the two PIN diodes in the two slots are called switch 2 and the switch 2 being shorted or open controls whether the stopband at the medium frequency exists or not. The PIN diode in the inverted L-shaped slot on the feedline which excites one stopband at the high frequency is called switch 3 and the switch 3 being shorted or open controls whether the stopband at the high frequency exists or not. When all three switches are open, the slots can excite three stopbands normally and the proposed antenna works at the triple-band-notched mode. When none of three switches is open, the three slots in the antenna cannot work properly and the proposed antenna works at the UWB mode. When one of three switches is open, the antenna works at single band-notched mode. The antenna works at the dual-band-notched mode when two of three switches are open. For the proposed antenna, eight operating modes are investigated, and their corresponding diode states are shown in Table 2.

Table 2: The switch states and stopbands when the proposed antenna work at different modes

Mode	Switch 1	Switch 2	Switch 3	Stopbands
1	0	0	0	none
2	1	0	0	3.28~4.41 GHz
3	0	1	0	5.46~6.55 GHz
4	0	0	1	7.76~8.25 GHz
5	1	1	0	3.30~4.42 GHz, 5.15~6.54 GHz
6	1	0	1	3.30~4.65 GHz 7.7~8.34 GHz
7	0	1	1	5.4~6.61 GHz, 7.25~8.46 GHz
8	1	1	1	3.30~4.68 GHz, 5.15~6.48 GHz, 7.25~8.54 GHz

1: Open, 0: Shorted.

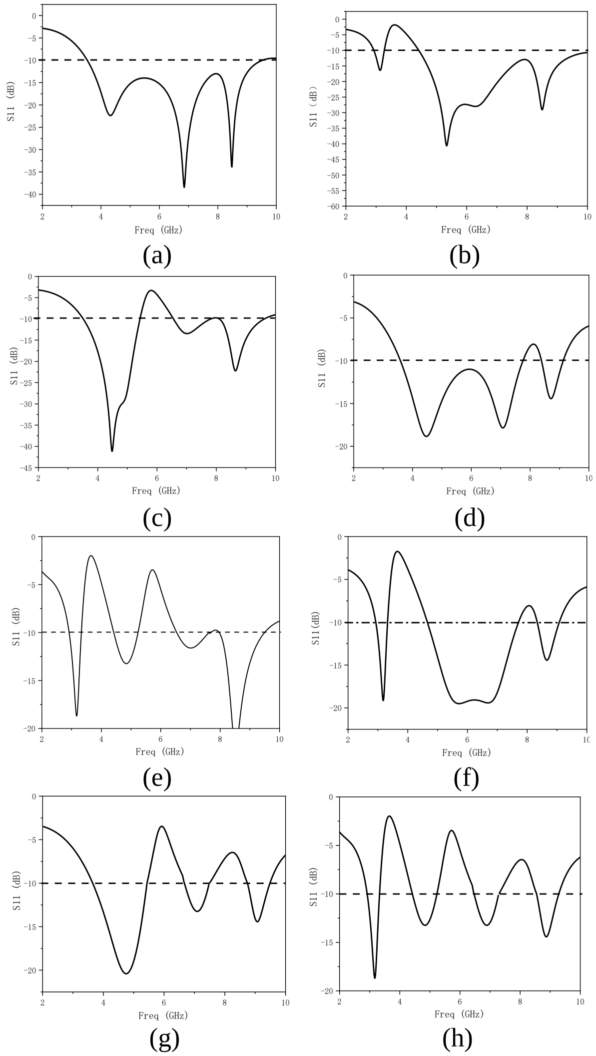

(a) (b) (c) (d) (e) (f) (g) (h)

Fig. 6. Simulated return loss of the proposed antenna: (a) Mode 1, (b) Mode 2, (c) Mode 3, (d) Mode 4, (e) Mode 5, (f) Mode 6, (g) Mode 7, and (h) Mode 8.

Figure 6 presents the return loss of the antenna in each mode.

IV. EXPERIMENTAL RESULTS AND DISCUSSIONS

To verify the proposed design, the antenna is practically fabricated on FR-4 substrate with the dimensions of 35.5mm×30mm×1.6mm, and the photograph of the fabricated antenna is shown in Fig. 7. The measured results are obtained by using an Agilent N5230A vector network analyzer and an anechoic chamber. For brevity, Fig. 8 only presents the measured return loss curves of three typical modes among the eight modes, showing a good agreement with the simulated return loss in Fig. 2. The slight deviation may be due to fabrication errors, feed wires, and imperfections of components. It is found that proposed design can reject the frequency band of 3.08~4.22 GHz and avoid the interference from WiMAX when the switch 1 is open, switch 2 and switch 3 are shorted. The proposed antenna can reject frequency bands of 3.1~4.23 GHz and 5.17~6.12 GHz and avoid the interferences from WiMAX and WLAN when switch 1 and switch 2 are open, switch 3 is shorted.

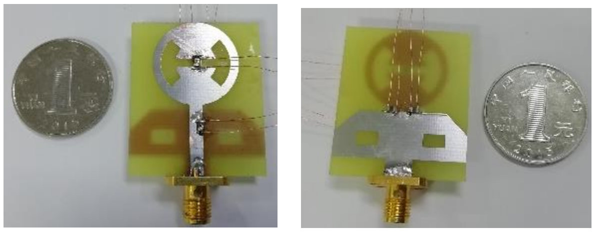

(a) (b)

Fig. 7. Photo of fabricated switchable band-notched UWB antenna: (a) front view and (b) back view.

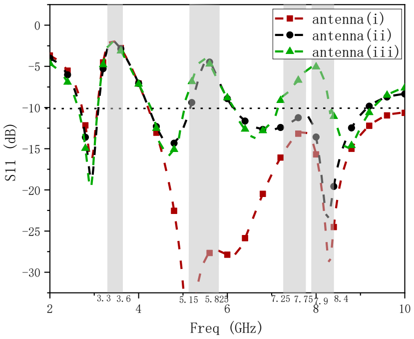

Fig. 8. Measured return loss against frequency for the various configurations. (i) single band-notched antenna by opening switch 1, shorting switch 2 and switch 3; (ii) dual band-notched antenna by opening switch 1 and switch 2, shorting switch 3; (iii) triple band-notched antenna by opening switch 1, switch 2, and switch 3.

The proposed antenna can reject frequency bands of 3.08~4.29 GHz, 5.03~6.15 GHz and 7.15~8.3 GHz and avoid the interferences from WiMAX, WLAN, and X-band satellite systems when switch 1, switch 2, and switch 3 are open.

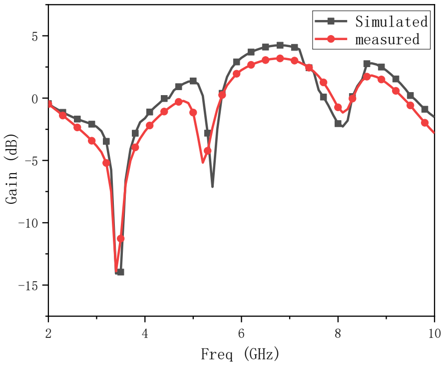

Fig. 9. Gain of the proposed antenna with triple band-notched function.

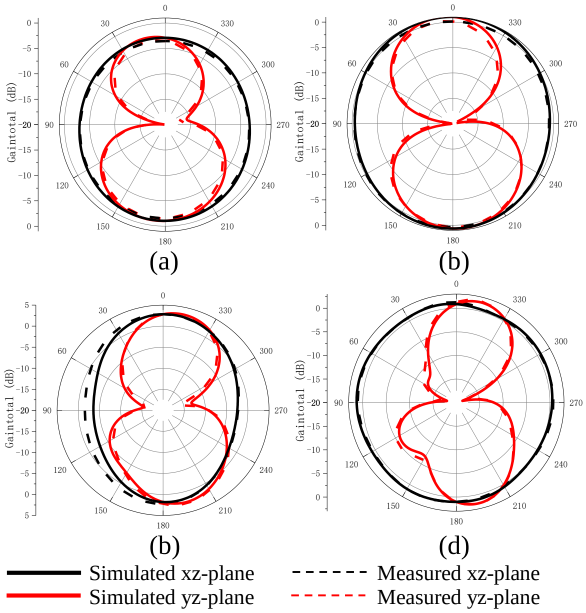

(a) (b)

(b) (d)

Fig. 10. Simulated and measured radiation patterns at: (a) 2.8 GHz, (b) 4.9 GHz, (c) 6.8 GHz, and (d) 8.7 GHz frequencies for the proposed antenna with triple band-notched function.

Figure 9 shows the measured and simulated gain variations with the frequency for the proposed triple band-notched antenna. Three sharp decreases of gain values are observed in the notched bands at 3.5, 5.5, and 8 GHz, respectively. Figures 10 (a-d) show the 2-D far-field radiation patterns in the E- plane (yz-plane) and H-plane (xz-plane) at sampling frequencies of 2.8 GHz, 4.9 GHz, 6.8 GHz, and 8.7 GHz respectively. In these figures, good omnidirectional radiation characteristics are observed. The results show that the proposed antenna performs well in four different passbands and meets the requirements of UWB communications.

V. CONCLUSION

A reconfigurable ultrawide band (UWB) antenna with switchable single, dual, and triple band notch functions is presented in this paper. The low frequency band-notched function is formed by an arc H-shaped slot on the radiating patch; the medium frequency band-notched function is formed by two narrow L-shaped slots on the ground plane; and the high frequency band-notched function is formed by an inverted L-shaped slots on the microstrip feedline. The proposed antenna can avoid the interference from WiMAX, WLAN, and X-band satellite systems. Further, by introducing switch modes on the slots, the antenna offers eight working modes and can realize an interconversion between one UWB mode, three single band-notched modes, three dual band-notched modes, and one triple band-notched mode. The results of the return loss and the input impedance show that the designed bandwidth with good band rejection is presented. Nearly omnidirectional radiation patterns and desirable gain are also presented to verify the satisfactory performance of the proposed antenna.

ACKNOWLEDGMENT

This work was supported in part by the National Natural Science Foundation of China under Grant No. 61801521, in part by the Natural Science Foundation of Hunan Province under Grant No. 2018JJ2533, and in part by the Fundamental Research Funds for the Central Universities under Grant No. 2018gczd014.

REFERENCES

[1] Federal Communications Commission. First report and order in the matter of revision of part 1-5 of the commission rules regarding ultra-wideband transmission systems. USA: FCC, 2002.

[2] A. Kerkhoff and H. Ling, “Design of a planar monopole antenna for use with ultra-wideband (UWB) having a band-notched characteristic,” *Proc. IEEE AP/S Int. Symp. Dig.*, Columbus, OH, vol. 1, pp. 830-833, June 2003.

[3] H. Schantz, G. Wolenec, and E. Myszka, “Frequency notched UWB antenna,” *Proc. IEEE Conf. Ultra Wideband Syst. Technol.*, pp. 214-218, Nov. 2003.

[4] D.-Z. Kim, W.-I. Son, W.-G. Lim, H.-L. Lee, and J.-W. Yu, “Integrated planar monopole antenna with microstrip resonators having band-notched characteristics,” *IEEE Transactions on Antennas and Propagation*, vol. 58, pp. 2837-2842, 2010.

[5] S. Ghosh, “Band-notched modified circular ring

monopole antenna for ultrawideband applications," *IEEE Antennas and Wireless Propagation Letters*, vol. 9, pp. 276-279, 2010.

[6] S.-J. Wu, C.-H. Kang, K.-H. Chen, and J.-H. Tang, "Study of an ultrawideband monopole antenna with a band-notched open-looped resonator," *IEEE Transactions on Antennas and Propagation*, vol. 58, pp. 1890-1897, 2010.

[7] A. Ghobadi, C. Ghobadi, and J. Nourinia, "A novel band-notched planar monopole antenna for ultra-wideband applications," *IEEE Antennas and Wireless Propagation Letters*, vol. 9, pp. 608-611, 2009.

[8] J. B. Jiang, Y. Song, Z. H. Yan, X. Zhang, and W.Wu, "Band-notched UWB printed antenna with an inverted-L-slotted ground," *Microw. Opt. Technol. Lett.*, vol. 51, no. 1, pp. 260-263, Jan. 2009.

[9] K. Ruchandani and M. Kumar, "A novel CPW fed octagonal aperture antenna with back patch for UWB applications," *International Conference on Nascent Technologies in the Engineering Field (ICNTE) - Navi Mumbai*, India, 2015.

[10] Z.-J. Tang, X.-F. Wu, and J. Zhan, "Novel compact band-notched UWB antenna using convex-shaped slot patch," *Microw. Opt. Technol. Lett.*, vol. 57, no. 1, pp. 201-203, Jan. 2015.

[11] G. Srivastava and A. Mohan, "A planar UWB monopole antenna with dual band notched function," *Microw. Opt. Technol. Lett.*, vol. 57, no. 1, pp. 99-104, Jan. 2015.

[12] M. Mehranpour, J. Nourinia, C. Ghobadi, and M. Ojaroudi, "Dual band-notched square monopole antenna for ultrawideband applications," *IEEE Antennas and Wireless Propagation Letters*, vol. 11, pp. 172-175, 2012.

[13] Z. Esmati and M. Moosazadeh, "Dual band-notched small monopole antenna with bandwidth enhancement by means of defected ground structure (DGS) for UWB application," *Applied Computational Electromagnetics Society Journal (ACES)*, vol. 30, no. 6, pp. 619-625, 2015.

[14] A. Sharma and M. M. Sharma, "An UWB antenna design with dual band notched characteristic using U-shaped slots," *International Conference on Signal Processing & Communication*, *IEEE*, 2017.

[15] B. Badamchi, J. Nourinia, C. Ghobadi, and A. Shahmirzadi, "Design of compact reconfigurable ultra-wideband slot antenna with switchable single/dual band notch functions," *IET Microwaves, Antennas & Propagation*, vol. 8, no. 8, pp. 541-548, 2014.

[16] J. Yeo, "Wideband circular slot antenna with tri-band rejection characteristics at 2.45/5.45/8 GHz," *Microwave and Optical Tech. Lett.*, vol. 50, pp. 1910-1914, 2008.

[17] J.-Y. Deng, Y.-Z. Yin, S.-G. Zhou, and Q.-Z. Liu, "A novel triple band-notched monopole antenna," *Journal of Electromagnetic Waves and Application*, vol. 23, pp. 139-147, 2009.

[18] X. L. Bao and M. J. Ammann, "Printed UWB antenna with coupled slotted element for notch-frequency function," *International Journal of Antennas and Propagation*, 2008.

Jian Dong received the B.S. degree in Electrical Engineering from Hunan University, Changsha, China, in 2004, and the Ph.D. degree in Electrical Engineering from Huazhong University of Science and Technology, Wuhan, China, in 2010. He is now an Associated Professor and the Vice Director of Communications and Networks Research Center at the Central South University (CSU), Changsha, China. He has been a Visiting Scholar at the ELEDIA Research Center of the University of Trento, Italy, from March 2016 to March 2017. His research work is mainly focused on antenna array synthesis, ultrawide band/multi-band antennas, and numerical optimization techniques. He holds about 30 innovation patents and has published six books and over 100 peer reviewed papers on international journals and conferences.

Shan Wang received the B.S. degree in Communication Engineering from Center South University, Changsha, China, in 2018. She is now pursuing her M.S. degree at Center South University, Changsha, China. Her current research interests focus on reconfigurable antennas, ultrawide band/multi-band antennas. She has published two journal/conference papers.

Guoqiang Hu received the B.S. degree in Electrical Engineering from Anhui Normal University, Wuhu, China, in 2014, and the M.S. degree in Electrical Engineering from Center South University, Changsha, China, in 2017. He is now a Senior Antenna Engineer at Transsion Holdings Limited Inc., Shanghai, China. His current research interests focus on wideband/multiband antenna designs. He has published three journal papers and holds two innovation patents.

Design and Optimization of Slotted Micro-Machined Patch Antenna Using Composite Substrate

Ashish Kumar and Amar Partap Singh

Department of Electronics and Communication Engineering
Sant Longowal Institute of Engineering and Technology, Longowal, Sangrur, Punjab, 148016, India
ashish@sliet.ac.in

Abstract **─** A slotted L-shaped micro-machined patch antenna on composite substrate has been proposed in this article. The slotted patch has been designed on the composite substrate with overall height of 1.675 mm and effective dielectric constant of 3.23. The desired frequency and bandwidth has been achieved by the parametric optimization using Ant Lion optimization technique. The design resonates at 8.1 GHz and 13.5 GHz with the gain of 6 dBi. The simulated and measured results are quite promising. The obtained resonating characteristics of the proposed design are used in the earth exploration satellite services defined by ITU.

Index Terms **─** Ant Lion optimization, bandwidth, gain, micro-machining, satellite communications.

I. INTRODUCTION

As the requirement of the low power and small size wireless communication systems, it is desired to fabricate the complete module including oscillators, phase shifters, patch antenna and other circuitry on the single chip using monolithic microwave integrated circuit (MMIC) with improved performance parameters. This can only be achieved when patch antenna will be implemented on the high index substrate. To achieve high gain and bandwidth of the patch antenna designed on high index material, micromachining concept has been developed [1]. Performance characteristics of the patch antenna are highly influenced by the choice of the substrate. Although low refractive index substrate like roger and RT duroid shows the better performance than the high index materials like silicon and GaAs, this is due to the fact of low surface waves generation in case of low index materials rather than the high index materials. However, high index materials have their own advantages in terms of reduction in dimensions of the patch because the dimensions of the patch antenna are inversely proportional to the dielectric constant of the substrate. Moreover, the antennas designed on high index substrate are suitable for the MMIC designs. So, there is contrast between the performance parameters of the antennas implemented on the low and high dielectric constant substrate [2-3]. One solution is to use one substrate for the patch antenna, and another is for the other circuitry, but this would increase the overall cost of the system. So, from the above discussion it can be deduced that to design the patch on high index substrate for the integration on the single chip with superior performance characteristics, high index material is removed underneath the patch creating a low index environment under the patch and remain high index environment on all other section. The process of removal of the substrate underneath the patch is called bulk micromachining [4-5]. Micro-machining offers an alternative solution that satisfies all the requirements for both antenna and circuit. Further, to achieve the multiband characteristics current distribution plays a vital role which can be achieved by cutting the slot in the patch [6-9]. Previous work [10-15] reported the application of micromachining in various patch antennas for Ka band and Ku band. The 8.025-8.4 GHz band is used for earth exploration satellite services, the service is used in military operations, space agencies, commercial and many other organizations [16].

Bandwidth is the major drawback of the patch antenna, there are number of ways to improve the bandwidth represented in the literature [17-19]. One of the concepts is to increase the overall thickness of the substrate. So, the concept of composite substrate has been used in this paper. Further, to achieve the desired operating frequency and bandwidth of the patch antenna, Ant Lion optimization has been applied on the two-dimensional parameters of the antenna with composite substrate. First length of the micro-machined patch has been optimized to achieve the required operating frequency and then height of the composite substrate has been optimized to achieve the required bandwidth of operation.

II. MICRO-MACHINED PATCH ANTENNA

The idea of micro-machining has been driven from drilling the holes in conventional substrates like FR4

Submitted On: July 16, 2018
Accepted On: November 4, 2018

or Duroid to improve the antenna performance characteristics [20]. There will be a reduction in effective dielectric constant with these holes near the patch; the same approach has been extended for the high index substrate. The shape of the micro-machined structure determined by the available etching processes, which include etching method, etching duration and crystal orientation of the substrate. In the process of Micro-machining, a portion of high index substrate has been removed underneath the patch to create the low index environment underneath the patch. This creates a cavity underneath the patch which consists of a mixed region of air and high dielectric substrate. In this work T = 655 μm of silicon substrate is removed of the total 675 μm thickness underneath the patch. Slanting positions of the walls of the cavity due to the anisotropic nature of the etching and the angle of slanting wall position is 54.7° as shown in Fig. 1.

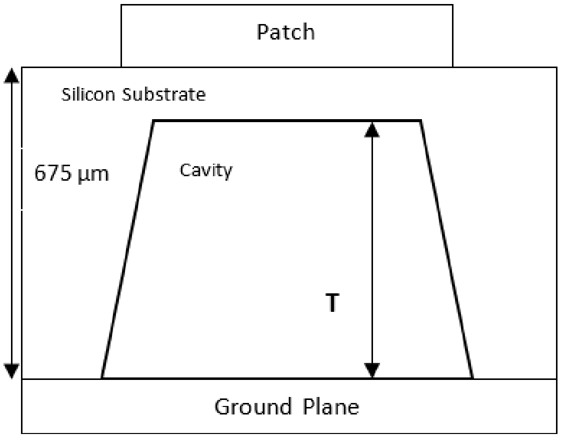

Fig. 1. Micro-machined patch antenna.

As shown in Fig. 1, there is a region of mixed air-silicon. The effective dielectric constant can be calculated by using cavity model. The capacitance of the patch in mixed region is given by [1,4]:

$$C = \frac{\varepsilon_{eff}\, A}{d}, \tag{1}$$

where C is the capacitance, A is the area of patch and d is the substrate thickness $\varepsilon_{eff} = \varepsilon_{reff}\varepsilon_o$. In this context, walls of the cavity assumed to be straight and ε_{reff} is estimated from following equations:

$$\varepsilon_{cavity} = \frac{\varepsilon_{air}\varepsilon_{sub}}{\varepsilon_{air}+(\varepsilon_{sub}-\varepsilon_{air})X_{air}}, \tag{2}$$

$$\frac{\varepsilon_{fringe}}{\varepsilon_{cavity}} = \frac{\varepsilon_{air}+(\varepsilon_{sub}-\varepsilon_{air})X_{air}}{\varepsilon_{air}+(\varepsilon_{sub}-\varepsilon_{air})X_{fringe}}, \tag{3}$$

$$\varepsilon_{reff} = \varepsilon_{\text{cavity}}\left(\frac{\text{L}+2\Delta\text{L}\frac{\varepsilon_{\text{fringe}}}{\varepsilon_{\text{Cavity}}}}{\text{L}+2\Delta\text{L}}\right). \tag{4}$$

In the above formula ε_{sub} is dielectric constant of substrate. ε_{air} is dielectric constant of air X_{air} the ratio of the air to full substrate thickness in the mixed field region and X_{fringe} the ratio of the air to full substrate thickness in the fringing field regions.

III. EFFECT OF COMPOSITE SUBSTRATE

Micro-strip patch antenna has several disadvantages like narrow bandwidth, low gain etc. Choice of the substrate material and height of the substrate have great impact on the performance characteristics of the patch antenna. Low permittivity substrates can increase the bandwidth at the cost of large dimensions and higher permittivity substrate will improve the quality factor hence the bandwidth reduces. The bandwidth is improved by micro-machining process in the high index substrates as explained in the above sections. Further improvement in the bandwidth of patch antenna can be achieved by using the concept of composite substrate [21]. The concept of composite substrate illustrates the insertion of the commonly available microwave substrate into the micro-machined designs, so the overall height of the substrate increases and bandwidth will improve. Also with the use of composite substrate resonant frequency of the microstrip patch can be shifted upward or downward without changing the actual patch dimensions. The choice of the substrate is based on the fact that low dielectric substrate lies below the patch and dielectric constant increases as we move towards the ground as shown in Fig. 2.

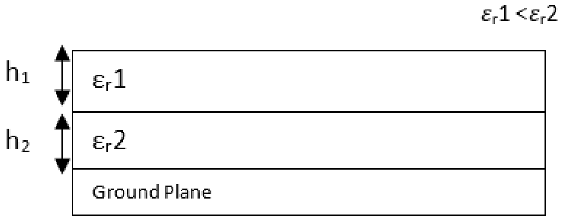

Fig. 2. Patch antenna on composite substrate.

The effective dielectric constant of both the layers has been recalculated by using equation (5) taking height of each substrate into consideration. The effective dielectric constant is calculated from equation (5) [21]:

$$\varepsilon_{rc} = \frac{h_1 + h_2}{\frac{h_1}{\varepsilon_r 1} + \frac{h_2}{\varepsilon_r 2}}, \tag{5}$$

where, ε_r1 is the dielectric constant and h_1 is the height of the low index substrate and ε_r2 is the dielectric constant and h_2 is the height of high index substrate.

IV. PROPOSED ANTENNA DESIGN

An L-shaped slotted patch antenna is designed on the composite substrate to achieve the multiband and wideband characteristics in X-band and Ku-band. Conventional rectangular patch antenna is designed on silicon substrate having dielectric constant of 11.8 of thickness 0.675 mm and loss tangent of 0.001. Due to the large surface wave generations in high index substrate micro-machined patch antenna has been designed with calculated effective dielectric constant from equation (4). Further to achieve the multiband characteristics, L-shape slot of effective length of 8mm and width of 1 mm has been cut from the patch and overall design has been implemented on the composite substrate, one is micro-machined silicon and other is glass substrate. The top view and side view of the proposed design has been shown in the Fig. 3 and Fig. 4 respectively.

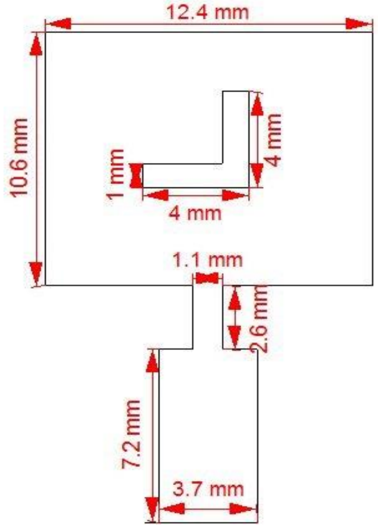

Fig. 3. Front view of L-shaped slotted patch antenna on composite substrate.

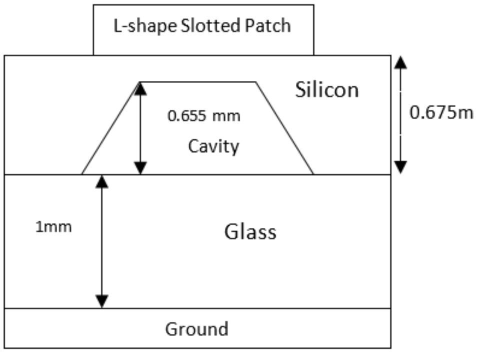

Fig. 4. Side view of slotted antenna on composite substrate.

The overall height of the substrate has been taken as 1.675 mm from which 0.675mm is for the micro-machined silicon substrate and 1mm for the glass substrate. The effective dielectric constant has been calculated from the equation (5). The calculated dimensions of the design have been shown in the Table 1.

Table 1: Dimensions of proposed design

	Conventional Rectangular Patch on Silicon Substrate	**Rectangular Patch on Micro-Machined Silicon Substrate**	**L-shaped Slotted Patch on Composite Substrate of Micro-Machined and Glass**
Effective dielectric constant	11.8	2.01	3.23
Overall height (mm)	0.675	0.655 mm cavity from 0.675 mm	1.675
L (mm)	4.94	12.76	10.6141
W (mm)	7.23	14.64	12.418
W_{qw} (mm)	0.023	0.11	1.14
L_{qw} (mm)	2.62	2.62	2.66
W_f (mm)	0.588	0.588	3.7
L_f (mm)	3.88	3.88	7.23

V. IMPLEMENTATION OF ANT LION OPTIMIZATION

Ant Lion optimization has been implemented to find the certain optimized dimensional parameter to achieve the required performance parameters.

A. Concept of Ant Lion optimization

Ant Lion optimization (ALO) is executed to achieve optimized rectangular patch. In its execution, an antlion builds a sharp edged cone structure under the soil and waits for the prey. When the respective prey (ant) slips into the hole, the prey tries to come out of the hole and antlion throws sand on to the prey. This process is repeated until the respective prey gets exhausted in its action. Ultimately, antlion consumes the body of the exhausted prey. After that antlion builds another hole and the process repeats again and again [22-23]. It is supposed that fitness of the Ant should be more than the fitness of the corresponding Ant Lion, then and only then Ant Lion consumes body of the ant. An Ant Lion updates its position to catch other ant. This process is imitated using the equation (6) proposed in the work at [24]:

$$Antlion_k^i = Ant_k^i$$

If

$$Fitness(Ant_k^i) > fitness(Antlion_k^i). \qquad (6)$$

Where, $Antlion_k^i$ is the position of k-th antlion in i-th iteration and Ant_k^i shows the position of k-th ant at i-th iteration. In all the iterations fittest antlion produced is called elite. Due to this elite, the movement of all the ants have been altered during each iteration. Therefore, every ant updates their position according to the equation (7) reported in the work at [24]:

$$Ant = (Roulette\ wheel\ selection$$
$$random\ walk\ selection)/2. \qquad (7)$$

Ant-Lion optimization is better than particle swarm optimization, Genetic algorithm and other algorithms in terms of average value and the standard deviation of the fitness function [24]. The purpose of the algorithm is to find the minimum value of the fitness function to find the user defined frequency and bandwidth.

B. Optimization of patch length to find the required resonant frequency

From the calculated parameters as shown in Table 1. the length of the patch is 9.2 mm with total thickness of substrate is 1.675mm. Based on these calculations, the resonant frequency has been found to be 9 GHz. But required band is 8.025 to 8.4 GHz. So to obtain this operating band the length of the patch has to be optimized by using Ant Lion optimization. The polynomial equation has been formed from the curve fitting method:

$$Frequency = -0.8835 \times L^5 + 43.685 \times L^4 - 863.41L^3 + 8526.7L^2 - 42075L + 83001.6, \quad (8)$$

$$FitnessFunction = \left(8.3 - f\right)^2. \quad (9)$$

The above fitness function has been optimized using Ant Lion optimization and the optimized value of the length of the patch is 10.6142 mm at which the resonance frequency is 8.3 GHz as shown in Fig. 5.

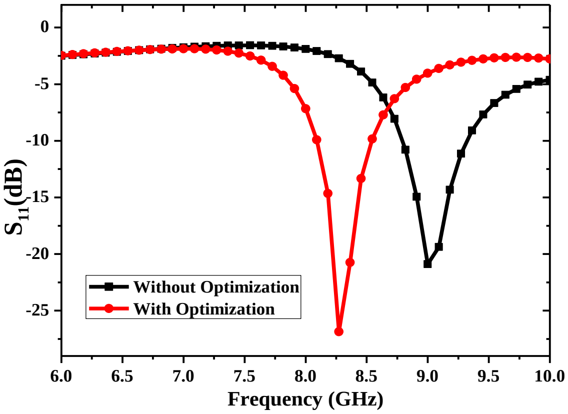

Fig. 5. Resonant frequency v/s Reflection Coefficient variation with and without optimization.

C. Optimization of the height of glass substrate to find the required operating band

For the Earth Exploration Satellite Service, the minimum required bandwidth of the patch antenna is 375 MHz (8.025-8.4 GHz). Bandwidth of the patch antenna depends upon the height of the substrate. So, in this section, required operating band can be achieved with the variation of the height of the glass substrate. The polynomial equation has been formed between the height of the glass substrate and bandwidth:

$$BW = 1960H_g^3 - 4906H_g^2 + 4253H_g - 859. \quad (10)$$

$$FitneesFunction = (375 - H_g)^2. \quad (11)$$

As the height of the substrate goes on increasing, the reflection coefficient and bandwidth improves. So the glass material with height 1 mm has been chosen due to large bandwidth and improved reflection coefficient. Fig. 6 shows the comparison between the micro-machined patch antenna and with sandwiching composite substrate underneath the micro-machined patch antenna, which illustrates the significant improvement in the bandwidth in case of micro-machined with composite substrate design over conventional micro-machined patch antenna design.

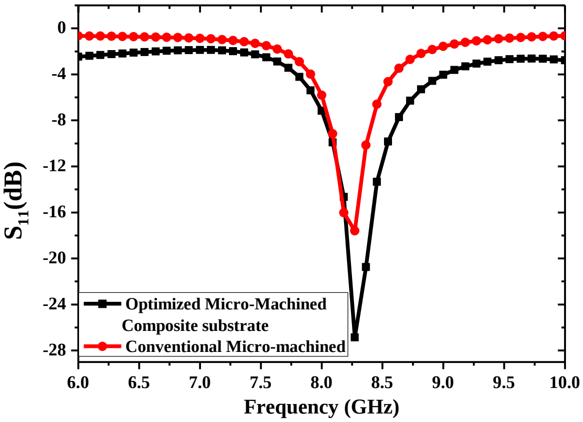

Fig. 6. Bandwidth variation of conventional micro-machined and optimized composite substrate structure.

VI. RESULTS AND DISCUSSIONS

The proposed antenna has been simulated using High Frequency Structure Simulator (HFSS 14.0) and measured results have been validated with Anritsu VNA master and Anritsu MS2719B spectrum analyzer. The fabricated prototype and the measurement setup have been shown in the Fig. 7 & Fig. 8 respectively. The simulated and measured resonant characteristics of the L-shaped slotted micro-machined patch antenna on composite substrates has been shown in Fig. 9. It has been seen that antenna resonates in X-band and Ku-band. In X-band it resonates at 8.1 GHz with a 5.3% impedance bandwidth and in Ku-band it resonates at 13.5 GHz with wideband characteristics of 30.3 % bandwidth. Further, radiation patterns have been measured in the anechoic chamber and simulated and measured radiation pattern for both frequencies have been shown in the Fig. 10 & Fig. 11. Figure 12 shows the gain v/s frequency graph which shows gain of 6.2 dBi at 8.1 GHz and 6.3 dBi at 13.5 GHz.

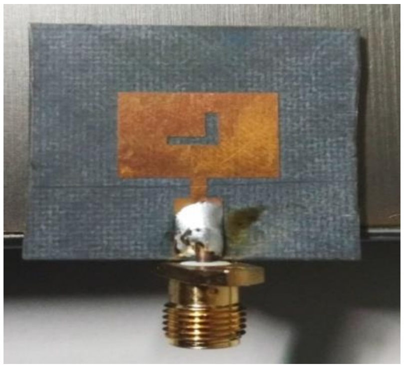

Fig. 7. Fabricated prototype of slotted micro-machined patch antenna.

Fig. 8. Antenna mounted in anechoic chamber.

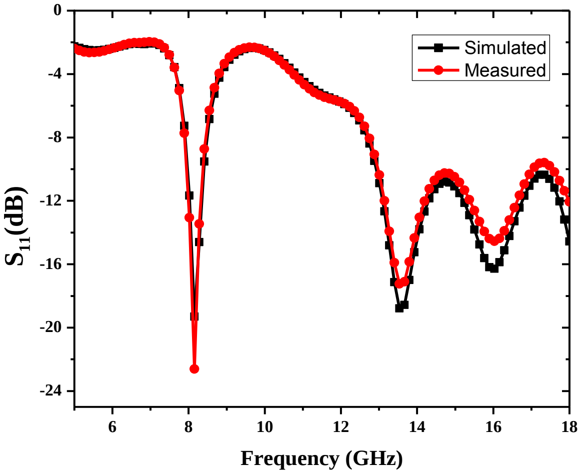

Fig. 9. Reflection coefficient v/s frequency curve of slotted micro-machined patch antenna.

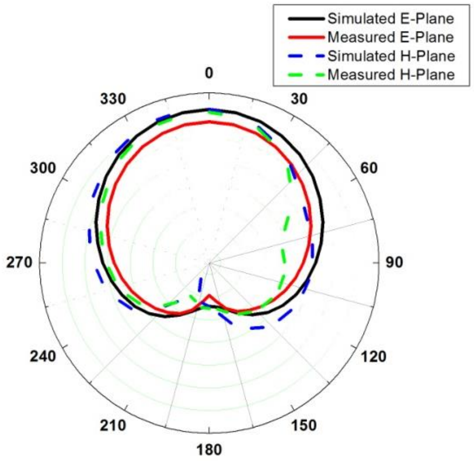

Fig. 10. Radiation pattern of slotted micro-machined patch antenna at 8.15 GHz.

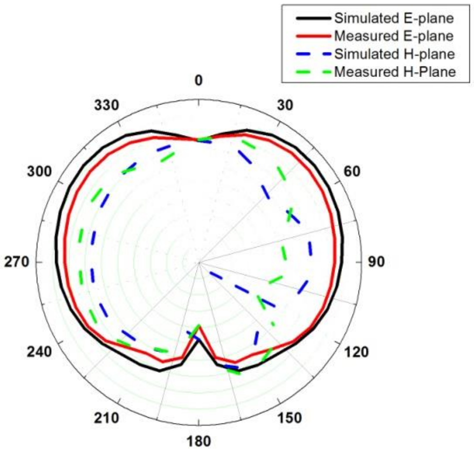

Fig. 11. Radiation pattern of slotted micro-machined patch antenna at 13.5 GHz.

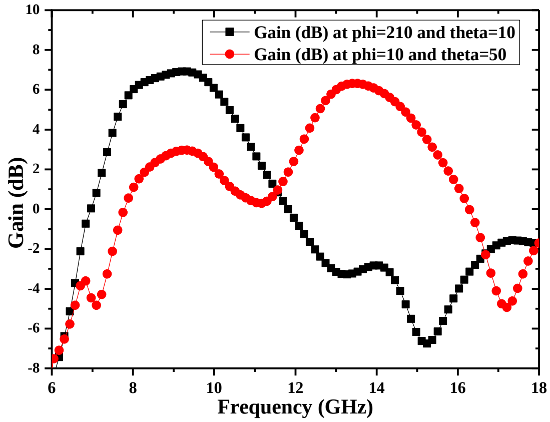

Fig. 12. Gain v/s frequency of slotted micro-machined patch antenna.

Table 2: Performance parameters

	Conventional Rectangular Silicon Substrate	**Rectangular Micro-Machined Silicon Substrate**	**L-shaped Slotted Patch on Composite Substrate of Micro-Machined and Glass**	
Resonant freq. (GHz)	8.3	8.3	8.15	13.5
Reflection coefficient (dB)	-15.5	-17.6	-22.6	-17
Bandwidth (MHz)	197	266	434	4.1 GHz
Fractional bandwdith	2.3%	3.2%	5.3%	30.3%
Gain (dBi)	0.8 at θ=12° and Φ = 230°	6.6 at θ=0° and Φ = 270°	6.2 at θ=10° and Φ = 270°	6.3 at θ=50° and Φ = 10°

VII. CONCLUSION

L-shaped slotted patch antenna is designed on the composite substrate. The patch antenna design has been implemented on the micro-machined substrate combined with the glass substrate to increase the overall height of the substrate. The proposed design resonates at 8.1 GHz and 13.5 GHz with a 6 dBi gain. There is an improvement of 38% in the bandwidth over the conventional rectangular micro-machined patch antenna design, which can be used in various X-band and Ku-band applications like earth exploration satellite services.

ACKNOWLEDGMENT

The authors are grateful to the department of ECE, SLIET, Longowal, Semi Conductor Laboratory, Mohali and Indian Institute of Delhi (IIT-D) for extending admirable technical support by the way of making lab facilities.

REFERENCES

[1] I. Papapolymerou, R. F. Dryton, and L. P. B. Katehi, "Micro machined patch antenna," *IEEE Transactions on Antennas and Wave Propagation*, vol. 46, no. 2, pp. 275-283, 1998.

[2] C. A. Balanis, *Antenna Theory*. John Wiley & Sons, Inc., 1997.

[3] R. Garg, I. J. Balh, P. Bhartia, and A. Ittipiboon, *Microstrip Antennas Design Handbook*. Artech House, Norwood, M.A., 2001.

[4] M. Zheng, Q. Chen, P. S. Hall, and V. F. Fusco, "Broadband microstrip patch antenna on micro machined silicon substrate," *Electronic Letters*, vol. 34, no. 1, pp. 3-4, 1998.

[5] J. G. Yook and L. P. B Katehi, "Micro machined microstrip patch antenna with controlled mutual coupling and surface waves," *IEEE Transactions on Antennas and Wave Propagation*, vol. 49, no. 2, pp. 1282-1289, 2001.

[6] Y. N. Phua, E. H. Lim, and B. K Chung, "Broad range microstrip patch refflect array element loaded with multiple L-shaped slots," *International Journal of Electronics and Communications* (AEU), vol.84, pp. 123-130, 2018.

[7] T. Ali, A. W. M. Sadh, R. C. Biradar, J. Anguera, and A. Andujar, "A miniaturized metamaterial slot antenna for wireless applications," *International Journal of Electronics and Communications (AEU)*, vol. 82, pp. 368-382, 2018.

[8] K. ElMahgoub, "Slotted triangular monopole antenna for UHF RFID readers," *Applied Computational Electromagnetic Society Express Journal*, vol. 1, no. 1, 2016.

[9] M. H. B. Ucar and Y. E. Erdemli, "Triple band microstripline-fed printed wide slot antenna for WiMAX/WLAN Operations," *Applied Computational Electromagnetic Society Journal*, vol. 29, no. 10, 2014.

[10] H. Kratz and L. Stenmark, "Micro machined S-band patch antenna with reduced dielectric constant," *International Conference on Solid-State Sensors, Actuators and Microsystems, IEEE*, 2005.

[11] E. Y. Tsai, A. M. Bacon, M. Tentzeris, and I. Papapolymerou, "Design and development of novel micro machined patch antennas for wireless applications," *Proceedings of APMC*, 2002.

[12] V. K. Singh, "Ka-Band micro-machined microstrip patch antenna," *IET Microwaves, Antenna & Propagation*, vol. 4, no. 3, pp. 316-323, 2009.

[13] M. V. Lukic and D. S. Filipovic, "Surface micromachined dual Ka-band cavity backed patch antenna," *IEEE Transactions on Antennas and Wave Propagation*, vol. 55, no. 7,pp. 2107-2110, 2007.

[14] B. Pan, Y. K. Yoon, G. E. Ponchak, M. G. Allen, and I. Papapolymerou, "Analysis of characterization of a high-performance Ka-band surface micro machined elevated patch antenna," *IEEE Transactions on Antennas and Wave Propagation*, vol. 5, pp. 511-514, 2006.

[15] R. Saha, C. T. Bhunia, and S. Maity, "Design of micromachining based patch antenna to enhance performances of RFID tag applications," *International Journal of Future Generation Communication and Networking*, vol. 8, no.1, pp. 261-268, 2015.

[16] P. E. Gawthrop, "Use of the frequency band 8025-8400 MHz by EESS," *Electronic Communications Committee Report*, 1997.

[17] D. Sarmah, N. S. Bhattacharyya, and S. Bhattacharyya, "Study of graded composite (LDPE/TIO$_2$) materials as substrate for microstrip patch antenna in X-band," *IEEE Transactions on Dielectrics & Electrical Insulation*, vol. 20, no. 5, pp. 1845-1850, 2013.

[18] W. K. W. Ali and S. H. AI-Charchafchi, "Using equivalent dielectric constant to simplify the analysis of patch microstrip antenna with multilayer substrates," *IEEE Antenna & Propagation Society International Symposium*, vol. 2, pp. 676-679, 1998.

[19] K. R. Jha and G. Singh, "Analysis and design of rectangular microstrip antenna on two-layer substrate materials at terahertz frequency," *Journal of Computational Electronics* vol. 9, pp. 68-78, 2010.

[20] N. Tyagi, S. Singh, and N. Sinha, "Enhancement of bandwidth in microstrip patch antenna using EBG," *International Journal of Computer Applications*, vol. 92, no.15, 2014.

[21] R. P. Rao, B. Sarinu, and C. D. Raj, "Design and analysis of multi substrate microstrip patch antenna," *Microelectronics, Electromagnetics & Telecommunications, Proceedings of ICMEET*, vol. 372, pp. 733-739, 2015.

[22] I. Scharf, A. Subach, and O. Ovadia, "Foraging

behavior and habitat selection in pit-building antlion larvae in constant light or dark conditions," *Animal Behavior*, vol. 76, no. 6, pp. 2049-2057, 2008.

[23] D. Griffiths, "Pit construction by ant-lion larvae: A cost benefit analysis," *Journal of Animal Ecology*, vol. 55, no. 1, pp. 39-57, 1986.

[24] S. Mirjalili, "The ant lion optimizer," *Advances in Engineering Software*, vol. 83, pp. 80-98, 2015.

Ashish Kumar has received his B.Tech. in 2008 and M.Tech. in 2012 from Punjabi University, Patiala, Punjab, India. At present, he is pursuing his Ph.D. degree since July, 2015 in the field of Microstrip Patch Antennas from Sant Longowal Institute of Engineering and Technology, Longowal, Sangrur. He has a teaching experience of more than 5 years in various engineering colleges. He has published about 10 research papers in various national and international journals/conferences. His research includes reconfigurable patch antennas, fractal antennas, MEMS Design.

A. P. Singh was born in Sangrur, Punjab in 1967 and received his B.Tech. degree in ECE from GNDU, Amritsar in 1990. He received his M.Tech. degree from REC, Kurukshetra in 1994 and Ph.D. degree in 2005. Presently, he is a Professor in ECE at SLIET, Longowal. Singh is credited with a professional experience of more than 24 years. He has guided seven Ph.D. theses and six more students are pursuing their Ph.D. degrees under his supervision. He has published more than 165 research papers in various national and international journals/conferences and received various awards including IETE Students Journal Award-2006 by IETE, New Delhi, Certificate of Merit in 2006, KF Anita Award in 2009, Sir Thomas Ward for the year 2010, and again KF Anita Award in 2014 by the Institution of Engineers (India).

Compact Dual-band Hybrid-Fractal MIMO System for UMTS and LTE Mobile Applications

P. Prabhu and S. Malarvizhi

Department of Electronics and Communication Engineering
SRM Institute of Science and Technology, Katankulathur, Chennai, India
prabhu.beece66@gmail.com, malarvizhi.g@ktr.srmuniv.ac.in

Abstract **─** This article presents a bandwidth enriched, dual-band, compact, multiple-input-multiple-output (MIMO) antenna with high isolation for UMTS and LTE applications. The proposed coplanar waveguide (CPW)-fed, hybrid fractal MIMO antenna was created by integrating Koch fractal and Sierpinski fractal on a rectangular patch radiator. The MIMO antenna uses a rectangular shaped partial ground plane with a T-shaped stub on the ground plane to improve the isolation between radiators. The iterative technique, using the Koch curve and the Sierpinski square slot fractal was used on the rectangular patch to reduce the size of the MIMO antenna and retain the electrical performance. By using an amalgamated fractal configuration and a CPW feed, a large impedance bandwidth was achieved: 80% wide bandwidth over the operating frequency of 1.81–3.17 GHz with a compact size of 25×35 mm^2. The prototype of the optimized MIMO configuration was fabricated using the FR4 substrate, and its characteristics were measured. The proposed antenna resonates at 2.1 and 2.6 GHz. The antenna parameters, including the reflection coefficient (S11, S12, S21, and S22), surface current distributions, realized gain and radiation patterns were simulated and measured. Additionally, the diversity performances of the MIMO antenna were analyzed in terms of diversity gain (DG) and envelope correlation coefficient (ECC). The proposed antenna retains high isolation of less than -20 dB from 1.81–3.17 GHz band; the DG and the ECC are greater than 9.5 dB and less than 0.08, respectively. The peak gains of the proposed antenna are 5.8 dBi and 6.9 dBi at 2.1 GHz and 2.6 GHz, respectively. Hence, the proposed hybrid fractal MIMO antenna is a good candidate for both UMTS and LTE applications.

Index Terms **─** CPW-MIMO, Hybrid Fractal, LTE, MIMO antenna, Mobile applications, UMTS.

I. INTRODUCTION

As multiple-input-multiple-output (MIMO) antenna have improved tremendously in recent years, MIMO antenna technology is playing a vital role in modern wireless communications systems, such as in UMTS, LTE, and WLAN. The future generation of communication systems requires a heterogeneous network with an improved channel capacity and reliability for modern mobile communications standards, such as GSM, UMTS, and LTE. Therefore, multiband and broadband MIMO antenna systems are significant to current mobile handsets. MIMO antenna systems can notably improve the reliability and data rate by using the same spectrum and power level. However, in practical situations electromagnetic mutual coupling will occur among the radiators due to a limited amount of space. Hence, isolation or a new decoupling structure is essential to compact a MIMO antenna. Fractal antennas provide multi-band, broadband, and compact antenna designs for various mobile standards. The self-filling and self-affine characteristics of the fractal reduce the size of the antenna and resonate multiple frequencies with broad bandwidth. An iterative structure can be obtained by reducing the initial dimension of the fractal structure [1-5]. In addition, a Koch fractal can be used to miniaturize the antenna size and increase the electrical length [6]. The planar monopole MIMO antenna can be implemented using the hybrid fractal shape by combining the Minkowski island curve and the Koch curve fractal, operating at 1.65 GHz to 1.9 GHz [7]. Isolation and impedance of the antenna can be improved by the T-shaped strip and etching at the top of the ground plane, respectively. Two elements of a meander-line MIMO antenna proposed that operates at 699–798 MHz and 1920–2170 MHz for PCS and LTE, respectively [8]. The polarization diversity method can be utilized to decouple the two antenna elements. By stimulating orthogonal polarization between the two antenna elements, polarization diversity can be achieved [9, 10]. In [11, 12], high isolation can be obtained by attaching parasitic elements to the ground plane. Isolation between the two elements can be enhanced and achieved through the use of a metal strip and two bent slits [13]. To enhance the port to-port isolation, a protruded ground may be utilized [14]. Dual orthogonal polarization and parasitic elements may be employed for cavity-backed bow tie MIMO

Submitted On: July 25, 2017
Accepted On: December 24, 2018

antenna [15]. The MIMO antenna can be implemented through the use of circular and annular slots, and a varactor diode may be used inside its annular slot to make it re-configurable [16-18]. Although many MIMO antennas have been implemented in the past decade, there is a need for high isolation with a high degree of miniaturization [18]. Fractal configuration, having space-filling and self-affine properties, can create a significant electrical length in a small space. Hence, this article proposes the CPW-fed composite fractal MIMO system with high isolation for modern mobile applications. This hybrid fractal antenna was created through the amalgamation of the Koch fractal and Sierpinski fractal with a miniaturized size of 25×35 mm^2. The antenna consists of two square-shaped hybrid fractal radiators and a T-shaped stub, which is connected to the ground to enhance isolation between the ports. Comparison of existing MIMO antenna parameter with proposed hybrid fractal MIMO antenna is shown in Table 1.

Table 1: Comparison of existing MIMO antenna parameter with proposed hybrid fractal MIMO antenna

Ref.	**Size (mm)**	**Operating Bands (GHz)**	**Isolation (dB)**	**Peak Gain (dBi)**
[7]	100×50	1.65-6.25	-15	2.5-7.8
[8]	80 X 67	0.699-2.17	-22	5
[9]	50 X 26	2.45	-30	-
[10]	120 X 140	2.4 & 2.6	-15	5.5-6.4
[12]	50 X 100	1.79-3.77	-20	2-6
[13]	78 X 40	2.4-6.55	-18	-
[16]	60 X 120	1.8-2.45	-15	2.43
Pro	25 X 35	2.1 & 2.6	< -20	7

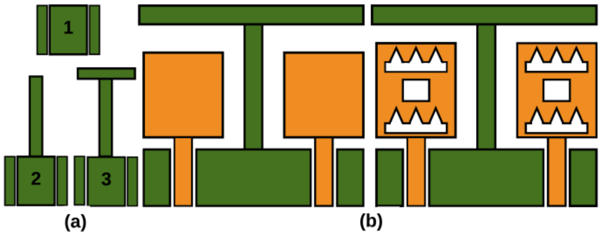

Fig. 1. (a) Development of decoupling structure, and (b) 0th and 1st iteration structure of proposed hybrid fractal MIMO system.

II. ANTENNA DESIGN PROCEDURE

A. Fractal Iterative Function System (IFS)

The Iterative Function System (IFS) is a very convenient technique for correctly generating various fractal configurations. The utilization of the affine transform sequence (v) is an essential character of IFS [3]. The regeneration (v) is expressed as:

$$\begin{pmatrix} x \\ y \end{pmatrix} = \begin{pmatrix} p & q \\ r & s \end{pmatrix} \begin{pmatrix} v \\ w \end{pmatrix} + \begin{pmatrix} t \\ u \end{pmatrix}, \tag{1}$$

$$v(x,y) = (px+qy+s, rx+dy+u). \tag{2}$$

Where, p, q, r, s, t and u are real coefficients.

On the other hand, the movement of fractal elements in the space based on these elements is a scaling factor, are rotation factors, by θ$_1$, θ$_2$ and linear rendering it can be represented as $p = \delta_1 \cos\varphi_1, s = \delta_2 \cos\varphi_2$. Consider v$_1$, v$_2$...,v$_N$ as a collection of successive transmutations, and the fundamental structure is B. By using the collection of transformations to the primary structure geometry, a new configuration is formed. In addition to that, accumulating the results from v$_1$(B), v$_2$(B),...,v$_N$(B), it can be exposed as $q = \delta_1 \sin\varphi_1, r = \delta_2 \sin\varphi_{2x}$ and $V_1(B) = \bigcup_{n=1}^{N} v_n(B)$ where 'V' is the Hutchinson vector. The fractal configuration is achieved by reusing the previous configuration. Using a fractal calculation, a Sierpinski carpet and Koch fractals were obtained.

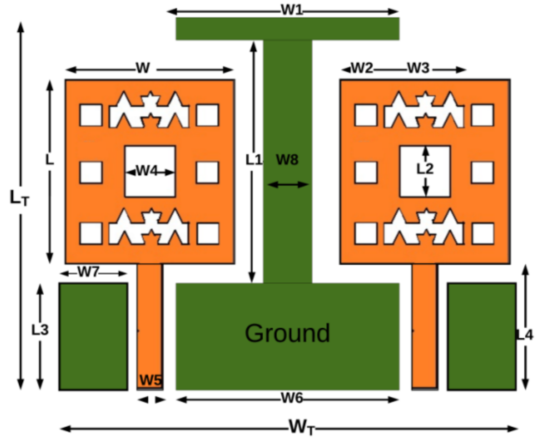

Fig. 2. Geometry of proposed second iteration hybrid fractal MIMO system.

B. Koch and Sierpinski fractal formation

The Koch fractal configuration is determined by applying the formulas [3, 4]. The IFS of Sierpinski fractal and Koch fractal are as shown below,

$$W_q \begin{pmatrix} x \\ y \end{pmatrix} = \begin{pmatrix} \delta_{q1} \cos\theta_{q1} & -\delta_{q_2} \sin\theta_{q2} \\ \delta_{q1} \sin\theta_{q1} & \delta_{q_2} \cos\theta_{q2} \end{pmatrix} \begin{pmatrix} x \\ y \end{pmatrix} + \begin{pmatrix} t_{q1} \\ t_{q2} \end{pmatrix}. \tag{3}$$

The Scaling operator of Koch fractal is shown below, θ$_q$- the angle of slope between the two-part of the initiators. θ$_{qi}$=60^{0}and t$_{q1}$ are the movements of the parts on the correlative surface.

Sierpinski fractal geometry can also be obtained using fractal IFS. The calculation method is shown below,

$$v_1(x,y)=\left[\frac{1}{3}x;\frac{1}{3}y\right],v_2(x,y)=\left[\frac{1}{3}x;\frac{1}{3}y+\frac{1}{3}\right], \quad (4)$$

$$v_3(x,y)=\left[\frac{1}{3}x;\frac{1}{3}y+\frac{2}{3}\right],\ v_4(x,y)=\left[\frac{1}{3}x+\frac{1}{3}y;\frac{1}{3}y\right], \quad (5)$$

$$v_5(x,y)=\left[\frac{1}{3}x+\frac{1}{3};\frac{1}{3}y+\frac{2}{3}\right],v_6(x,y)=\left[\frac{1}{3}x+\frac{1}{3};\frac{1}{3}y\right], \quad (6)$$

$$v_7(x,y)=\left[\frac{1}{3}x+\frac{2}{3};\frac{1}{3}y+\frac{1}{3}\right],v_8(x,y)=\left[\frac{1}{3}x+\frac{2}{3};\frac{1}{3}y+\frac{1}{3}\right]. \quad (7)$$

Table 2: Iteration computation of fractal (for 2 iterations)

Level	Length (In Terms of Fraction)	Boundary	Area (mm^2)
Initial square	1	(4). (1) = 4	$(1)^2 = 1$
1st iteration	1/2	(4).(1/2) = (4/2) = 2	$(1/2)^2 = 1/4$
2nd iteration	1/4	(4). (1/4)=1	$(1/4)^2 = /16$

III. ANTENNA STRUCTURE

Figure 1 (a) development of decoupling structure, zeroth and Fig.1 (b) illustrates the first iteration structure of the proposed antenna, whereas Fig. 2 depicts the configuration of the proposed hybrid fractal MIMO antenna. The suggested MIMO system is printed on a FR4 mater substrate with a thickness of 1.6 mm and dielectric constant of 4.4. The objective of using a hybrid fractal configuration is the development of the characteristic of space-filling, in which the structure converts into the reduced dimension of the antenna with multi-band features. The proposed rectangular patch configuration consists of a pair of fractals, such as a Sierpinski carpet and a Koch fractal. Furthermore, the rectangular patch antenna results in improved performance [5].

The iteration techniques were used in the rectangle shaped antenna to achieve the three repetitions for the Koch and Sierpinski fractals. The 0-th iteration is the fundamental configuration of the suggested antenna, consisting of a rectangular patch radiator with two rectangular ground planes, a CPW feed, and a small current flowing in the middle of the rectangular patch. The first iteration of the Sierpinski fractal configuration was created through the insertion of square slots in the center of a rectangular radiator. Since there is negligible current in the center, this does not change the performance characteristics of the antenna. Subsequently, by contracting the rectangular slot of the first iteration at a ratio of 0.33, a second iteration pattern was achieved and cut out, comprising the central square shaped slot of the first repetition structure. Similarly, the three iterations of the Koch curve fractal were achieved using the IFS method. The 0-th iteration consists of a rectangular-shaped radiator with rectangular slots at its upper and lower part. The first iteration was obtained by splitting a small rectangular slot into three parts. The length of the triangular slot formed in the center had a slope of 60° between the two parts. The second iteration of the Koch fractal was achieved by reproducing the same method as the first iteration. The numerical calculation of fractal iterations up to 2 iterations are shown in Table 2. Since fractals have various patterns such as squares and triangles, the surface current of the radiator increased. Consequently, multiple frequencies resonate without altering the dimension of the antenna. The antenna was triggered by CPW feed with partial rectangular ground plane. CPW feed technology was utilized because of its advantages, including its wide bandwidth, easy fabrication, and other beneficial properties, such as the absence of loss. The antenna consists of two rectangular-shaped partial ground planes which produce a capacitive effect by canceling the inductive effect of a square radiator and provide purely resistive impedance to antenna configuration. Multiple resonance frequencies and enhanced bandwidth coverage can be achieved through the successive optimization strategies: increasing the number of fractal repetitions, regulating the width of the rectangular-shaped patch and the height of the two grounds surface. The optimized geometry of the proposed MIMO system is presented in Table 3.

Table 3: Geometry of proposed hybrid fractal MIMO antenna dimensions (all dimensions are in mm)

W_T	W	W_1	W_2	W_3	W_4	W_5	W_6	W_7	W_8
35	13	10	1	6	3	3	20	6	4
L_T	L	L_1	L_2	L_3	L_4				
25	11	19	3	4.5	4.5				

Using a decoupling structure reduces mutual coupling, but the problem with this approach is that a MIMO structure occupies considerable space. The design put forward in this work features a T-shaped stub decoupling structure, which effectively reduces the mutual coupling of radiators. Figure 1 (a) shows the development of the decoupling structure. MIMO antenna 1 is a compact device at 4.5 × 35 mm^2 and represents a combination of two hybrid fractals that share the same ground plane. Because of the diminutive size of the antenna, the partial ground plane acts as a radiating element and radiates energy normal to the radiating element. Due to the current distribution on the ground plane, there is influential coupling between the two MIMO system elements. Therefore, the isolation of MIMO antenna 1 is poor, as shown in Fig. 4 (a).

In MIMO antenna 2, the attachment of a rectangular-shaped stub to the ground plane changes the surface current on the partial ground, thereby improving isolation. That is, S12 / S21 is < - 15 dB at 2 to 10 GHz.

As shown in Fig. 4 (a), however, isolation is needed for improvement at resonating frequencies. The size of the T-shaped stub was optimized to improve isolation. The results are shown in Fig. 4 (a). In MIMO antenna 3, a rectangular stub is connected horizontally with a vertical stub that is attached to the ground plane, thus enhancing isolation in the operating frequencies. That is, S12 / S21 less than < - 20 dB at 1 to 10 GHz. In order to demonstrate the performance of the suggested isolation configuration, the surface current of the antenna at different frequencies is shown in Figs. 5 (a)-(d).

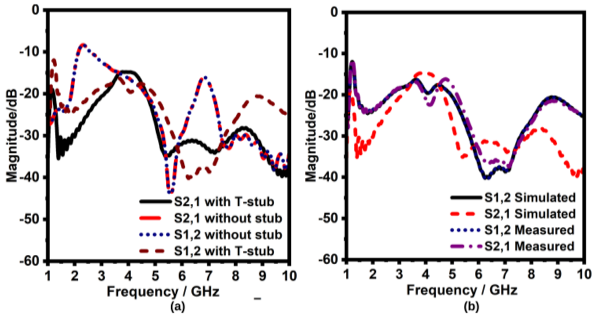

Fig. 4. (a) Simulated S12/S21 -parameters for the various decoupling structures. (b) Simulated and measured S12/ S21-parameters of proposed MIMO antenna with T-Stub decoupling structures.

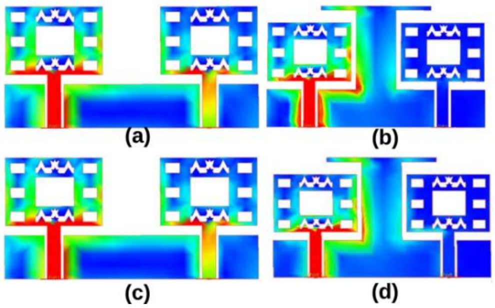

Fig. 5. Surface current of the hybrid fractal MIMO system with and without an isolation structure with port 1 (energized) (a) 2.1 GHz, (b) 2.6 GHz, (c) and (d).

The surface current distributions of two resonant frequencies were obtained. Without the stub isolation structure, energizing port 1 causes a strong current to be coupled at port 2. With the T-stub isolation structure, energizing port 1 causes no coupling current at port 2, and energizing port 2 causes no coupling current at port1. Therefore, the coupling current from ports 1 to 2 and vice versa is suppressed by the T-shaped stub decoupling structure proposed in the partial ground plane. In order to verify the effectiveness of the proposed MIMO system, a simulation was carried out using Microwave Studio and Advanced Design System (ADS).

IV. RESULTS AND DISCUSSIONS

The proposed MIMO antenna was printed on the FR4 substrate, after which the prototype was measured using Keysight N9926A vector network analyzer to verify the simulation results. Figure 8 shows the fabricated antenna with a CPW feed. Three hybrid fractal iterations were designed for the proposed MIMO antenna, and because the second iteration has fractals of various shapes, performance improves over that observed under all other iterations. Also, the current distribution occurs maximum at the corners of the fractals. The simulated S-parameter for the different iterations (e.g., zeroth, first, second iterations) is depicted in Fig. 6. It can be perceived from Fig. 6, that the second iteration has better performance compared to other iterations. The correlation of the simulated results for various partial ground sizes is presented in Fig. 7. Resonance is achieved at 2.1 and 2.6 GHz. Besides, the second iteration of a composite fractal configuration with a partial ground plane having the size of 35×4.5 mm^2 was fabricated on FR4 substrate presents the optimal design. The simulated and measured reflection coefficient (S11) of the proposed hybrid fractal MIMO system for optimized dimensions are shown in Fig. 8. The simulation and measured bandwidth of the proposed MIMO antenna is 2 GHz (1.9–3 GHz). MIMO antennas that resonate at 2.1 GHz (UMTS) and 2.62 GHz (LTE) have reflection of –48 and –47 dB, respectively. This is according to the results mentioned in [7].

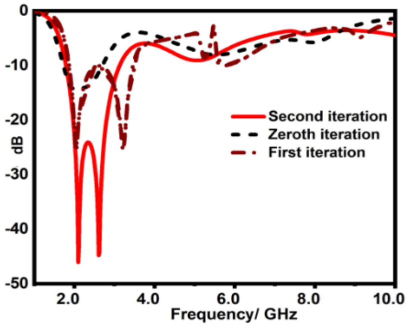

Fig. 6. Simulated Return Loss of Hybrid Fractal for Zeroth Iteration, First Iteration, and Second Iteration.

The comparison of simulated and measured S12/ S21 parameters of the proposed MIMO antenna with T-stub isolation configuration is shown in Fig. 4 (b). From the figure, it can be observed that the isolation between two radiators in the proposed MIMO system is less than –20 dB over the operating frequency band. It can be inferred from these results that the simulated and measured insertion loss are approximately the same, implying the fact that it is suitable for MIMO systems. The radiation aspects of the proposed composite fractal MIMO antenna system were also investigated. The composite structure of Koch's and Sierpinski fractal increases surface current distribution uniformly throughout the rectangular patch and creates a radiation pattern. Besides, CPW feed employed with two partial ground planes that contributed to obtain better radiation characteristics.

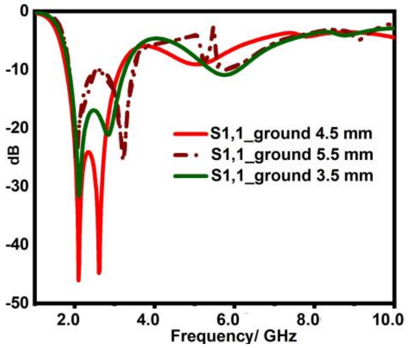

Fig. 7. Simulated reflection coefficient of hybrid fractal MIMO antenna with different ground size.

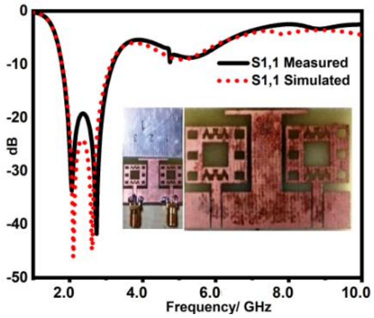

Fig. 8. Simulation and Measured S11 for the Proposed Hybrid Fractal MIMO System.

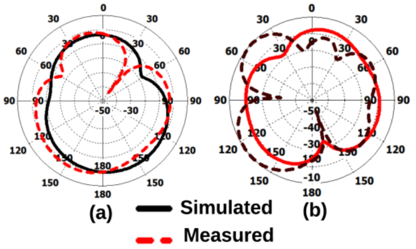

Fig. 9. Simulated and Measured Radiation Pattern of the proposed MIMO System at 2.1 and 2.6 GHz

The simulated and measured radiation patterns for the proposed antenna in the x-y plane at 2.1and 2.6 GHz are illustrated in Figs. 9 (a) and (b). From Figs. 9 (a) and (b), it can be perceived that the radiation pattern is approximately constant at the operating frequency band and the composite fractal MIMO antenna radiates uniformly in all directions. The peak gain of the MIMO antenna is 5.8 and 6.9 dBi at 2.1 and 2.6 GHz, respectively. The antenna's efficiency levels were 85% and 90% at 2.1 and 2.6 GHz, respectively. Therefore, the proposed MIMO structure is better in terms of size, peak gain, isolation, ECC and DG when compared to existing MIMO antennas mentioned Table 1. Hence, it is well suited for UMTS and LTE applications.

V. MIMO PERFORMANCE

The MIMO characteristics of the proposed antenna are assessed by diversity gain (DG) and envelope correlation coefficient (ECC). Isolation between radiating components can be investigated from the perspective of ECC. ECC can be determined using either the scattering parameter method or the fair field radiation pattern. The scattering parameters based ECC calculation is preferred because 3D far field measurement is difficult. The ECC of the MIMO antenna system is calculated by the following equation [4],

$$ECC = \frac{\left|S_{11}^{*}S_{12} + S_{21}^{*}S_{22}\right|^{2}}{\left(1-\left|S_{11}\right|^{2}-\left|S_{21}\right|^{2}\right)\left(1-\left|S_{22}\right|^{2}-\left|S_{12}\right|^{2}\right)}. \tag{8}$$

The diversity gain of the MIMO antenna system is evaluated using following equation $DG = 10\sqrt{1\text{-}ECC^{2}}$. Although the ECC ideally must be zero, the practical limit of ECC is less than 0.5 for an isolated MIMO diversity antenna. The ECC of the recommended composite fractal MIMO antenna is estimated using both S-parameter and radiation pattern method that is less than 0.08. It is perceived from Fig. 10. The DG of the proposed hybrid fractal MIMO antenna system can be observed in Fig. 10 that shows the simulated and measured DG that is greater than 9.5 dB.

VI. CONCLUSION

We have proposed a bandwidth-enriched, dual-band, compact MIMO antenna with high isolation for UMTS and LTE applications. By using an amalgamated fractal configuration and CPW feed, a broad impedance bandwidth of 80% is obtained at 1.81 to 3.17 GHz with a miniature size of 25×35mm^{2} . The proposed hybrid fractal MIMO antenna provides good impedance matching over the 1.81 to 3.17 GHz frequency band. With the help of the T-shaped stub isolation configuration, isolation between ports is enhanced; that is, less than −20 dB is attained throughout the operating frequency band. The proposed hybrid fractal MIMO system is also a right candidate for MIMO multi-polarized performance as the DG, and the ECC is greater than 9.5 dB and less than 0.08, respectively, throughout the operating band. The obtained peak gains of the proposed antenna are 5.8 and 6.9 dBi at 2.1GHz and 2.6 GHz, respectively. The composite fractal MIMO antenna has omnidirectional radiation pattern at 2.1 and 2.6 GHz. The simulation and measurement results show that the proposed MIMO structure is better in terms of size, peak gain, isolation, ECC and DG when compared to existing MIMO antennas. Hence, the suggested hybrid fractal MIMO antenna system is well suited for UMTS and LTE applications.

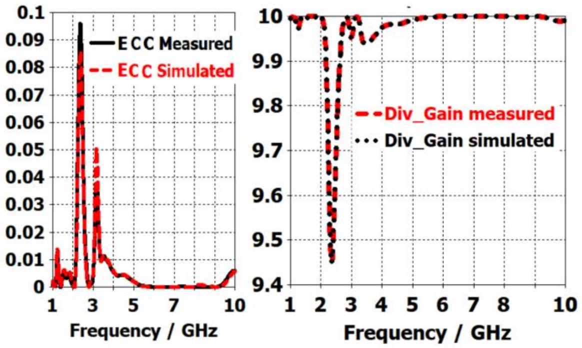

Fig. 10. Simulated and measured ECC and DG for proposed MIMO antenna.

REFERENCES

[1] B. B. Mandelbrot, “The fractal geometry of nature,” *American Journal of Physics*, vol. 51, no. 3, p. 286, 1983.

[2] D. H. Werner and R. Mittra, *Frontiers in Electromagnetics*. New York: Wiley, 1999.

[3] K. Falconer, *Fractal Geometry: Mathematical Foundation and Application*. New York, NY, USA: Wiley, 1990.

[4] H. Peitgen, H. Jurgens, and D. Saupe, *Chaos and Fractals: New Frontiers of Science*. Berlin, Germany: Springer-Verlag, 1992.

[5] D. H. Werner and S. Ganguly, “An overview of fractal antenna engineering research,” *IEEE Antennas Propag. Mag.*, vol. 45, no. 1, pp. 38-57, 2003.

[6] C. P. Baliarda, J. Romeu, and A. Cardama, “The Koch monopole: A small fractal antenna,” *IEEE Trans. Antennas Propag.*, vol. 48, pp. 1773-1781, 2000.

[7] Y. K. Choukiker, S. K. Sharma, and S. K. Behera, “Hybrid fractal shape planar monopole antenna covering multiband wireless communications with MIMO implementation for handheld mobile devices,” *IEEE Transactions on Antennas and Propagation*, vol. 62, no. 1, pp. 12-13,2014.

[8] M. M. Morsy and A. M. Morsy, “Dual-band meander-line MIMO antenna with high diversity for LTE/UMTS router,” *IET Microwaves, Antennas Propagation*, vol. 12, no. 3, pp. 395-399, 2018.

[9] M. M. Morsy, “2.45GHz dual polarized aperture-coupled antennas with high isolation performance,” in *Proceedings of the 2012 IEEE International Symposium on Antennas and Propagation*, pp. 1-2, July 2012.

[10] A. MoradiKordalivand, T. A. Rahman, and M. Khalily, “Common elements wideband MIMO antenna system for WiFi/LTE access-point Applications,” *IEEE Antennas Wireless Propag. Lett.*, vol. 2014, pp. 13-1601, 2014.

[11] Y. Wang and Z. Du, “A printed dual-antenna system operating in the 2.4-GHz WLAN bands for mobile terminals,” *IEEE Antennas and Wireless Propagation Letters*, vol. 13, pp. 233-236, 2014.

[12] A. Toktas and A. Akdagli, “Wideband MIMO antenna with enhanced isolation for LTE, WiMAX and WLAN mobile handsets,” *Electronics Letters*, vol. 50, no. 10, pp. 723-724, May 2014.

[13] J.-F. Li, Q.-X. Chu, and T.-G. Huang, “A compact wideband MIMO antenna with two novel bent slits,” *IEEE Transactions on Antennas and Propagation*, vol. 60, no. 2, pp. 482-489, Feb 2012.

[14] J.-F. Li, Q.-X. Chu, Z.-H. Li, and X.-X. Xia, “Compact dual band-notched UWB MIMO antenna with high isolation,” *IEEE Transactions on Antennas and Propagation*, vol. 61, no. 9, pp. 4759-4766, Sept. 2013.

[15] H.-T. Hu, F.-C. Chen, and Q.-X. Chu, “A wideband U-shaped slot antenna and its application in MIMO terminals,” *IEEE Antennas and Wireless Propagation Letters*, vol. 15, pp. 508-511, 2016.

[16] R. Hussain, G. Asim, and M. S. Sharawi, “Annular slot-based miniaturized frequency-agile MIMO antenna system,” *IEEE Antennas and Wireless Propagation Letters*, vol. 16, pp. 2489-2492, 2017.

[17] T. Shabbir, R. Saleem, M. F. Shafique, and A. Akram, “UWB-MIMO qauadruple with FSS inspired decoupling structures and defected grounds,” *The Applied Computational Electromagnetic Society*, vol. 30, no. 2, pp. 184-190, 2015.

[18] J. Mazloum and N. Ojaroudi, “Utilization of protruded strip resonators to design a compact UWB antenna with WiMAX and WLAN notch bands,” *The Applied Computational Electromagnetic Society*, vol. 31, no. 2, pp. 12-13, 2016.

Compact Wideband Filtering Power Dividers Based on Short-Circuited Stubs

Gaoya Dong, Bo Zhang, Weimin Wang, and Yuanan Liup

Beijing Key Laboratory of Work Safety Intelligent Monitoring
Beijing University of Posts and Telecommunications, Beijing 100876, China
gaoyadong@bupt.edu.cn, zhangbo2008beiyou@bupt.edu.cn, wangwm@bupt.edu.cn, yuliu@bupt.edu.cn

Abstract **─** A novel circuit is proposed to design filtering power dividers (FPDs) with bandpass filtering responses and out-of-band rejection performances. The presented circuit is constructed of two transmission line sections, four short-circuited sections and one resistor. Based on the introduced novel circuit, FPD1 is designed by selecting transmission line sections and short-circuited sections as quarter-wave transmission lines. The FPD2 is proposed to realize more compact size, enhanced bandpass selectivity and improved out-of-band rejection performance by replacing the quarter-wave transmission lines in FPD1 with dual transmission lines. The corresponding equations are derived to calculate the initial parameter values of FPD1 and FPD2 by adopting even-odd mode method. For verification, two FPDs centered at 2.0 GHz are designed and fabricated. The measured 3-dB fractional bandwidths of FPD1 and FPD2 achieve up to 63.2% and 52.3%, while the measured rejections with the level better than 20 dB extend to $2.4f_0$ and $4.0f_0$, respectively.

Index Terms **─** Filtering response, high selectivity, out-of-band rejection, power divider.

I. INTRODUCTION

Power dividers and bandpass filters play important roles in modern microwave systems. By integrating two functions of power division and filtering response in only one component, the passband insertion loss and construction size can be reduced effectively. Recently, many efforts have been done to realize dual functions in only one component, i.e., filtering PDs [1-8]. Various stub-loaded resonators are utilized in [1-5] to design FPDs. In [6], Wilkinson PD integrated with bandpass filter is presented to design FPD. Source-loading coupling is adopted in [7] to generate transmission zeros, ensuring high bandpass selectivity. Moreover, FPD is proposed in [8] based on right-/left-handed transmission line resonators, which can not only split the microwave signals, but also provide filtering performance.

In modern communication system, out-of-band rejection performance is greatly demanded to suppress the interferences, i.e., intermodulation signals from nonlinear components. Thus, many studies [9-14] have been done to design PDs integrated with harmonic suppression performances. Open-circuited stubs are employed in [9-10] to build PDs with enhanced spurious suppressions. In addition, coupled lines and non-uniform transmission lines are introduced in [11] and [12] to obtain harmonic suppression performances. In [13-14], low-pass filter and front coupled tapered compact microstrip resonant cell (FCTCMRC) are inserted into quarter-wave transmission lines of conventional Wilkinson PDs to realize good out-of-band rejections.

From the discussion above, PDs integrated with filtering responses and out-of-band rejections are popular and desirable. Some efforts [15-19] have been made to design FPDs with out-of-band rejections, which could suppress the unwanted high-frequency signals. The structure proposed in [15] is embedded with dual-mode resonators to obtain out-of-band rejection, and the filtering response is obtained by combining the filter with the power divider together. In [16-19], stub-loaded resonators are introduced to create transmission zeros (TZs) in stopband, resulting in good out-of-band rejections. The structure presented in [17] achieves the best out-of-band rejection performance among the five structures introduced in [15-19], where the upper stopband extends to $2.7f_0$ with the level better than 23 dB. Thus, simple design method for FPDs with better out-of-band rejections is demanded.

In this work, FPD1 and FPD2 are proposed based on the designed basic FPD circuit. The upper stopband of FPD1 (FPD2) extends to $2.4f_0$ ($4.0f_0$) with the level better than 20 dB. Even-odd mode method is adopted to analyze the operating mechanisms of FPD1 and FPD2, and the corresponding equations are derived to calculate the initial parameter values of FPDs. Based on the mentioned above, two FPDs with good out-of-band rejections are designed based on simple design methods.

II. STRUCTURE AND THEORY

A. Analysis of basic FPD circuit

The schematic of the proposed basic FPD circuit is shown in Fig. 1. Even-odd mode method is adopted to explain the operating mechanisms of basic FPD circuit.

Submitted On: May 25, 2017
Accepted On: December 24, 2018

Under even-mode excitation, the power input from port 1 will be totally transmitted to port 2 and port 3 with no current flowing through insolation resistor R. Thus, the even-mode equivalent circuit of basic FPD circuit is exhibited in Fig. 1 (b). The symmetrical plane can be seen as virtual ground under odd-mode excitation, and the odd-mode equivalent circuit of basic FPD circuit is described in Fig. 1 (c).

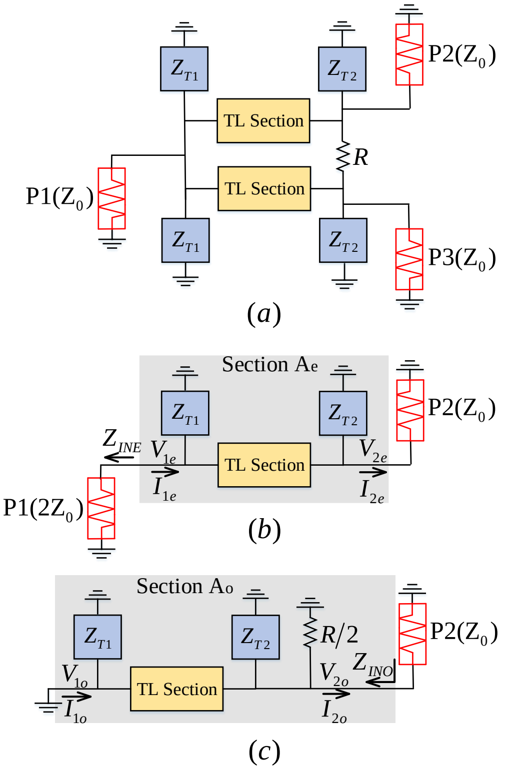

Fig. 1. Proposed basic FPD circuit: (a) the schematic of basic FPD circuit, (b) even-mode equivalent circuit of basic FPD circuit, and (c) odd-mode equivalent circuit of FPD circuit.

Define $Z_{T1} = 1/jX_{T1}$ and $Z_{T2} = 1/jX_{T2}$. From the even-mode equivalent circuit shown in Fig. 1 (b), the $A_eB_eC_eD_e$ matrix can be deduced as equation (1). Based on transmission line theory and equivalent even-mode circuit displayed in Fig. 1 (b), the input impedance in port 1 (Z_{INE}) can be derived as equation (2). Thus, S_{11} and S_{21} can be expressed as equation (3):

$$\begin{bmatrix} A_e & B_e \\ C_e & D_e \end{bmatrix} = \begin{bmatrix} 1 & 0 \\ \dfrac{1}{jX_{T1}} & 1 \end{bmatrix} \begin{bmatrix} A_{TL} & B_{TL} \\ C_{TL} & D_{TL} \end{bmatrix} \begin{bmatrix} 1 & 0 \\ \dfrac{1}{jX_{T2}} & 1 \end{bmatrix}, \tag{1}$$

$$Z_{INE} = \frac{X_{T1}(X_{T2}F - jB_{TL}Z_0)}{X_{T1}X_{T2}E - jX_{T2}F - (jX_{T1}D_{TL} + B_{TL})Z_0}, \tag{2}$$

where $E = C_{TL}Z_L + D_{TL}$,

$F = A_{TL}Z_L + B_{TL}$,

$$S_{11} = \left| \frac{Z_{INE} - 2Z_0}{Z_{INE} + 2Z_0} \right|, \tag{3a}$$

$$S_{21} = \sqrt{1 - \left(\frac{Z_{INE} - 2Z_0}{Z_{INE} + 2Z_0} \right)^2} . \tag{3b}$$

The expression $A_oB_oC_oD_o$ matrix can be derived as equation (4) based on odd-mode equivalent circuit depicted in Fig. 1 (c). According to equations (4) and transmission line theory, the input impedance in port 2 (Z_{INO}) can be calculated as equation (5). Thus, S_{22} can be expressed as equation (6):

$$\begin{bmatrix} A_o & B_o \\ C_o & D_o \end{bmatrix} = \begin{bmatrix} A_{TL} & B_{TL} \\ C_{TL} & D_{TL} \end{bmatrix} \begin{bmatrix} 1 & 0 \\ \dfrac{1}{jX_{T2}} & 1 \end{bmatrix} \begin{bmatrix} 1 & 0 \\ \dfrac{2}{R} & 1 \end{bmatrix}, \tag{4}$$

$$Z_{INO} = \frac{B_{TL}X_{T2}R}{X_{T2}(A_{TL}R + 2B_{TL}) - jB_{TL}R}, \tag{5}$$

$$S_{22} = \left| \frac{Z_{INO} - Z_0}{Z_{INO} + Z_0} \right| . \tag{6}$$

B. Analysis of FPD1

Based on basic FPD circuit, FPD1 is presented by selecting TL section, Z_{T1} and Z_{T2} as quarter-wave transmission lines. The schematic of FPD1 is shown in Table 1, which consists of two quarter-wave transmission lines (Z_1, θ), four short-circuited transmission lines (Z_2, θ) and one isolation resistor (R_1), and all electrical lengths (θ) of transmission lines are selected as π/2 at the center frequency (f_0). According to the schematic of FPD1, $A_{TL}B_{TL}C_{TL}D_{TL}$ matrix, X_{T1} and X_{T2} can be expressed as equation (7). The expressions of Z_{INE} and Z_{INO} can be derived as equation (8) by submitting equation (7) into equations (2) and (5). In a specific case, Z_{INE} and Z_{INO} in FPD1 can be simplified as Z_1^2/Z_0 and $R_1/2$ at f_0, respectively. Thus, the initial value of Z_1 should be chosen as $\sqrt{2}Z_0$ to realize good impedance matching in port 1 under even-mode excitation, and the initial value of R_1 should be selected as $2Z_0$ to obtain good impedance matching in port 2 under odd-mode excitation. Thus, the initial values of Z_1 and R_1 are calculated as 70.7 Ω and 100 Ω when Z_0 is adopted as 50 Ω:

Table 1: Summary of proposed FPD1 and FPD2

	Schematic	Layout	Normalized Frequency Response
FPD1	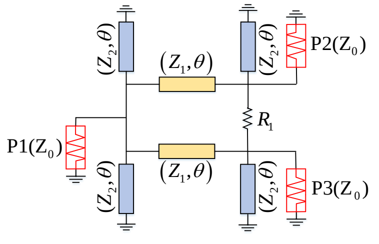	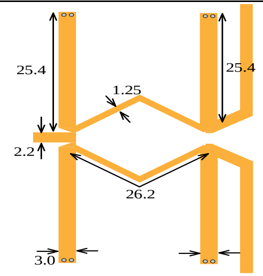	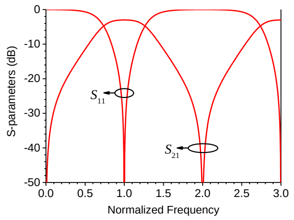
FPD2	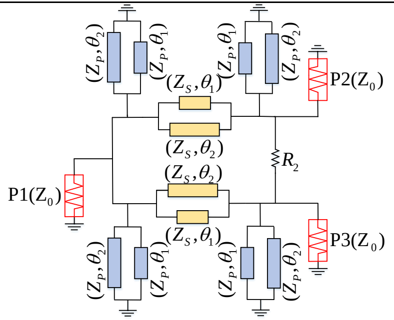	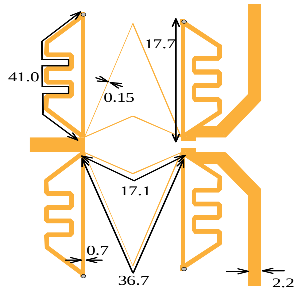	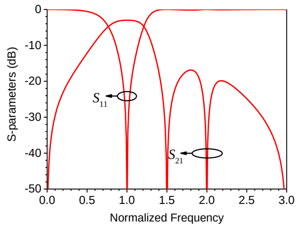

$$\begin{bmatrix} A_{TL} & B_{TL} \\ C_{TL} & D_{TL} \end{bmatrix} = \begin{bmatrix} \cos\theta & jZ_1\cos\theta \\ jY_1\sin\theta & \cos\theta \end{bmatrix}, \tag{7a}$$

$$X_{T1} = Z_2\tan\theta, \tag{7b}$$

$$X_{T2} = Z_2\tan\theta, \tag{7c}$$

$$Z_{INE} = \frac{Z_0 Z_1 Z_2 \cos\theta(Z_1+Z_2) + j(Z_1 Z_2\sin\theta)^2}{2(Z_1 Z_2\sin\theta\cos\theta(Z_1+Z_2) + jZ_0((Z_2)^2 - (\cos\theta)^2(Z_1+Z_2)^2))}, \tag{8a}$$

$$Z_{INO} = \frac{jRZ_1Z_2\sin\theta}{R\cos\theta(Z_1+Z_2) + 2jZ_1Z_2\sin\theta}. \tag{8b}$$

Transmission zeros could be obtained when $S_{21} = 0$. According to the equations (3) and (7), the frequencies of TZs in FPD1 can be summarized as equation (9):

$$f_{TZn} = \left\{ 2nf_0 \mid n \in N, f > 0 \mid \tan\left(\frac{f\theta}{f_0}\right) = 0 \right\}, \tag{9a}$$

$$f_{TZn} = \left\{ 2nf_0 \mid n \in N, f > 0 \mid \right\}, \tag{9b}$$

To further explain the operating mechanisms of FPD1, the normalized frequency responses with various values of Z_1 and Z_2 are shown in Fig. 2. As observed in Fig. 2 (a), the return loss of FPD1 can be optimized by choosing proper value of Z_1, which has a good agreement with equations (8a). According to Fig. 2 (b), the 3-dB fractional bandwidth (FBW) can be adjusted by tuning the value of Z_2, which agrees with equations (8a).

C. Analysis of FPD2

In order to further improve the upper stopband rejection and miniaturization performances, FPD2 is presented by replacing the quarter-wave transmission line (Fig. 3 (a)) in FPD1 with the harmonic suppression dual transmission lines (Fig. 3 (b)), and dual transmission lines have been analysed in our previous work [20]. The schematic of FPD2 is depicted in Table 1, where six pairs of dual transmission lines ((Z_S,θ_1; Z_S,θ_2), (Z_P,θ_1; Z_P,θ_2)) are employed, and the electrical lengths of dual transmission lines are chosen as $\theta_1 = \pi/3$ and $\theta_2 = 2\pi/3$. Based on the equations (1-7) exhibited in paper [21], the $A_{TL}B_{TL}C_{TL}D_{TL}$ matrix of dual transmission lines can be deduced as equation (10a), and X_{T1}, X_{T2} can be expressed as (10b), (10c) respectively:

$$\begin{bmatrix} \dfrac{\cos\theta_1\sin\theta_2 + \cos\theta_2\sin\theta_1}{\sin\theta_1 + \sin\theta_2} & \dfrac{jZ_S\sin\theta_1\sin\theta_2}{\sin\theta_1+\sin\theta_2} \\ j\dfrac{(\cos\theta_1 - \cos\theta_2)^2 + (\sin\theta_1 + \sin\theta_2)^2}{Z_S(\sin\theta_1+\sin\theta_2)} & \dfrac{\cos\theta_1\sin\theta_2 + \cos\theta_2\sin\theta_1}{\sin\theta_1+\sin\theta_2} \end{bmatrix}, \tag{10a}$$

$$X_{T1} = Z_P\frac{\tan\theta_1\cdot\tan\theta_2}{\tan\theta_1 + \tan\theta_2}, \tag{10b}$$

$$X_{T2} = Z_P\frac{\tan\theta_1\cdot\tan\theta_2}{\tan\theta_1 + \tan\theta_2}, \tag{10c}$$

$$Z_{INO} = \frac{jZ_S R\sin\theta_1\cdot\sin\theta_2}{2R(\cos\theta_1\sin\theta_2 + \sin\theta_1\cos\theta_2) + 2jZ_S\sin\theta_1\sin\theta_2}. \tag{11}$$

In FPD2, the detailed expressions of Z_{INE} and Z_{INO} can be obtained by substituting equation (10) into equations (2) and (5), and the specific expression of Z_{INO} is shown in equation (11). In a particular case, Z_{INE} and Z_{INO} can be simplified as $3Z_S^2/16Z_0$ and $R_2/2$ at f_0. The initial value of Z_S should be selected as $4\sqrt{2/3}\,Z_0$ to obtain good impedance matching in port 1 under even-mode excitation, and the initial value of R_2 should be chosen as $2Z_0$ to realize good impedance matching in port 2 under odd-mode excitation. Thus, the initial values of Z_S and R_2 are calculated as 163.3 Ω and 100 Ω when

Z_0 is adopted as 50 Ω.

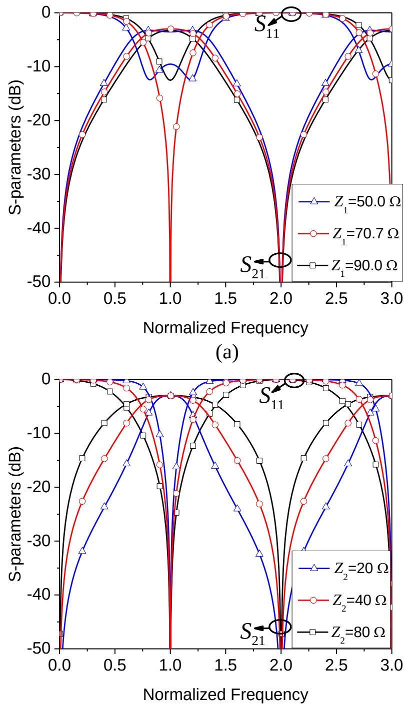

(a)

(b)

Fig. 2. Normalized frequency responses of FPD2 with various: (a) Z_1 and (b) Z_2.

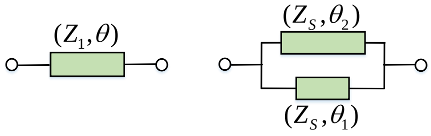

(*a*) (*b*)

Fig. 3. Schematic of: (a) conventional quarter-wave transmission lines, and (b) dual transmission lines.

Transmission zeros could be obtained when $S_{21}=0$. The frequencies of TZs in FPD2 can be summarized as equation (12) based on the equations (3) and (10):

$$f_{TZn}^{S}=\left\{2nf_0 \mid n\in N, f>0 \mid \tan(\frac{f\theta_1}{f_0})=-\tan(\frac{f(\pi-\theta_1)}{f_0})\right\}, \quad (12a)$$

$$f_{TZn}^{P}=\left\{\frac{n\pi f_0}{\theta_1},\frac{n\pi f_0}{(\pi-\theta_1)}, n\in N\right\}. \quad (12b)$$

To further explain the operating mechanisms of FPD2, the normalized frequency responses with various values of Z_S and Z_P are displayed in Fig. 4. As observed in Fig. 4 (a), the return loss in FPD2 can be optimized by choosing a proper value of Z_S, which has a good agreement with equations (2-3) and (10). It can be seen from Fig. 4 (b) that 3-dB FBW can be adjusted by tuning the value of Z_P, which agrees with equations (2-3) and (10).

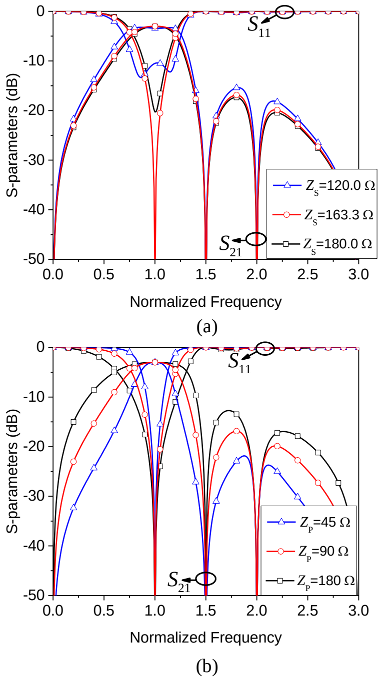

(a)

(b)

Fig. 4. Normalized frequency responses of FPD2 with various: (a) Z_S and (b) Z_P.

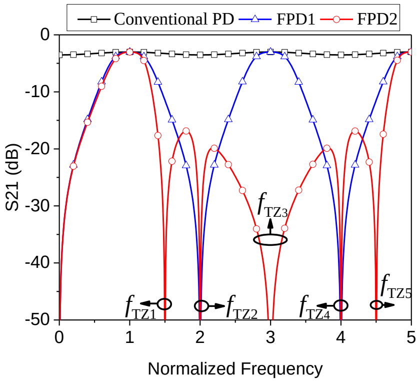

Fig. 5. Normalized frequency responses of different PD structures.

The normalized frequency responses of the conventional Wilkinson PD, FPD1 and FPD2 are plotted in Fig. 5. By comparing with conventional Wilkinson PD, good bandpass filtering response can be obtained in FPD1 and FPD2. Three additional TZs (f_{TZ1}, f_{TZ3} and f_{TZ5}) in the upper stopband are introduced in FPD2 by comparing with FPD1, which can greatly enhance the passband selectivity and improve out-of-band rejection performance. Transmission zeros depicted in Fig. 5 agree well with equations (9) and (12).

Based on the analysis above, the design procedures of the proposed FPD1 is described as following:

1) Given specific center frequency (f_0), FBW and out-of-band rejection performances of FPD1.
2) Calculate the initial values of Z_1 and R_1 based on equation (8).
3) Adjust the value of Z_2 to obtain required FBW.
4) Tune the value of R_1 to realize a good isolation between port 2 and port 3.
5) Optimize return loss in port 1 by changing the value of Z_1.
6) Return to step (3) until designed FPD1 meets the requirement required in step (1).

The detailed design procedures of FPD2 is summarized as following:

1) Given specific center frequency (f_0), FBW and out-of-band rejection performances of FPD2.
2) The initial values Z_S and R_2 are adopted as $4\sqrt{2/3}\,Z_0$ and $2Z_0$, respectively
3) Adjust the value of Z_P to realize required FBW.
4) The good isolation between port 2 and port 3 can be obtained by tuning the value of R_2.
5) Optimize return loss in port 1 by tuning the value of Z_S.
6) Return to step (3) until designed FPD2 satisfies the requirement given in step (1).

III. SIMULATION AND MEASUREMENT RESULTS

Based on design procedures listed above, FPD1 and FPD2 are fabricated at a center frequency (f_0) of 2.0 GHz. The substrate used herein has a dielectric constant of 2.55 and a thickness of 31 mil. The layouts and specific dimensions of FPD1 and FPD2 are exhibited in Table 1. Figure 6 shows the photographs of fabricated FPD1 and FPD2, where size miniaturization can be observed in FPD2 compared with FPD1.

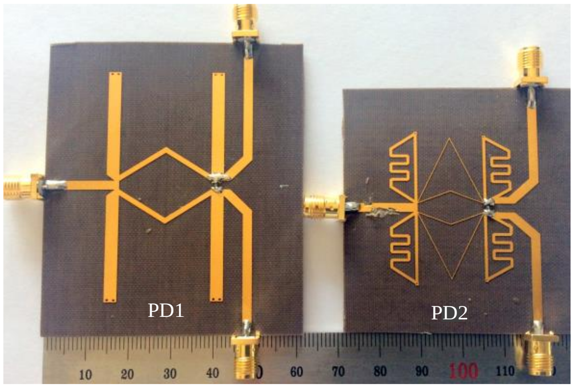

Fig. 6. Photographs of proposed FPD1 and FPD2.

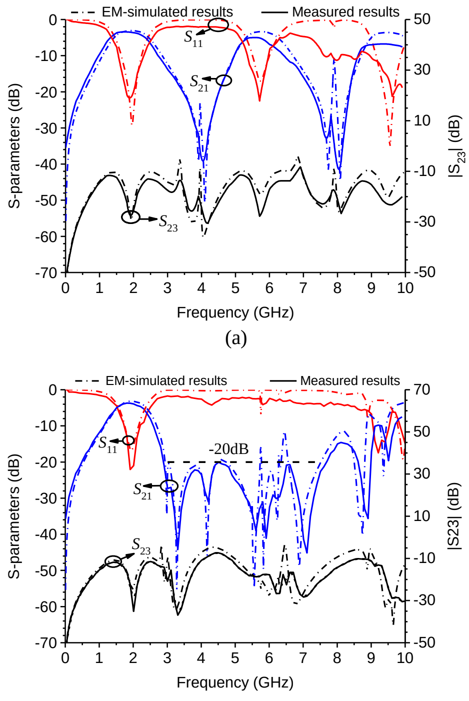

(a)

(b)

Fig. 7. EM-simulated and measured results: (a) FPD1 and (b) FPD2.

Table 2: Performance comparisons between proposed FPDs and the published works

References	FBW	Insertion Loss (dB)	Out-of-band Rejection Performance (dB)
[15]	7.2%	4.2	>20 dB (2.9 f_0)
[16]	70%	3.3	>13 dB (2.7 f_0)
[17]	8.3%	3.9	>20 dB (2.7 f_0)
[18]	5.8%	4.6	>20 dB (1.5 f_0)
[19]	6.5%	3.99	>35 dB (2.5 f_0)
FPD1	**63.2%**	**3.4**	**>20 dB (2.4 f_0)**
FPD2	**52.3%**	**3.7**	**>20 dB (4.0 f_0)**

The EM-simulated and measured results of FPD1 and FPD2 are demonstrated in Fig. 7. As shown in Fig. 7 (a), the measured FPD1 operates at the center frequency of 1.9 GHz with the 3-dB FBW of 63.2%. The measured passband return loss is better than 22 dB and the minimum insertion loss is 3.4 dB, including 3 dB power splitting loss. The measured isolation in FPD1 is better than 12 dB ranging from DC to 10 GHz which can be observed in Fig. 7 (a). The upper stopband extends up to 4.8 GHz ($2.4f_0$) with the rejection level of better than 20 dB. As demonstrated in Fig. 7 (b), the measured minimum insertion loss in FPD2 is 3.7 dB, including 3 dB power splitting loss. The measured passband in FPD2 is centered at 1.97 GHz with the 3-dB FBW of 52.3%, while the return loss is better than 20 dB. The upper stopband in FPD2 extends up to 8 GHz ($4.0f_0$) with the rejection level of better than 20 dB. The isolation in FPD2 is better than 12 dB ranging from DC to 10 GHz.

For comparison, Table 2 lists some major performances of the published and proposed FPDs. It can be seen from Table 2 that the presented FPDs demonstrate low insertion losses, deep out-of-band rejections and wide upper stopband suppression bandwidths.

IV. CONCLUSIONS

In this paper, a novel basic FPD circuit is introduced to design FPDs. To achieve more compact size, enhanced passband selectivity and improved out-of-band rejection performance, FPD2 is presented by replacing the quarter-wave transmission lines in FPD1 with harmonic suppression dual transmission lines. The designed FPDs have the advantages of good filtering responses, wide upper stopband rejections and simple design procedures, which are suitable for practical FPD design.

ACKNOWLEDGMENT

This work was supported in part by National Natural Science Foundations of China (No. 61701041 and No. 61327806).

REFERENCES

[1] S. K. Chao and W.-C. Lin, "Filtering power divider with good isolation performance," *Electronics Letters*, vol. 50, no. 11, pp. 815-817, June 2014.

[2] H. Zhu, A. Abbosh, and L. Guo, "Wideband four-way filtering power divider with sharp selectivity and wide stopband using looped coupled-line structures," *IEEE Microwave and Wireless Components Letters*, vol. 26, no. 6, pp. 413-415, June 2016.

[3] K. Song, Y. Mo, and Y. Fan, "Wideband four-way filtering-response power divider with improved output isolation based on coupled lines," *IEEE Microwave and Wireless Components Letters*, vol. 24, no. 10, pp. 674-676, July 2014.

[4] S. W. Wong and L. Zhu, "Ultra-wideband power dividers with good isolation and sharp roll-off skirt," *Microwave Conference, 2008. APMC 2008, Asia-Pacific. IEEE*, pp. 1-4, May 2008.

[5] X. Wang, J. Wang, and G. Zhang, "Design of wideband filtering power divider with high selectivity and good isolation," *Electronics Letters*, vol. 52, no. 16, pp. 1389-1391, July 2016.

[6] L. Gao and X.-Y. Zhang, "Novel 2:1 Wilkinson power divider integrated with bandpass filter," *Microwave and Optical Technology Letters*, vol. 55, pp. 646-648, Jan. 2013.

[7] X.-L. Zhao, L. Gao, J.-X. Xu, and J. Xiang, "High-selectivity dual band filtering power divider using stub-loaded quarter-wavelength resonator," *Journal of Electromagnetic Waves and Application*, vol. 29, no. 16, pp. 2216-2223, Oct. 2015.

[8] X. Ren, K.-J. Song, B.-K. Hu and Q.-K. Chen, "Compact filtering power divider with good frequency selectivity and wide stopband based on composite right-left-handed transmission lines," *Microwave and Optical Technology Letters*, vol. 56, pp. 2122-2125, June 2014.

[9] M. Hayati and S. Roshani, "A novel Wilkinson power divider using open stubs for the suppression of harmonics," *Applied Computational Electromagnetics Society (ACES) Journal*, vol. 28, no. 6, pp.501-506, June 2013.

[10] J. Li, Y. Liu, S. Li, et al., "A novel multi-way power divider design with enhanced spurious suppression," *Applied Computational Electromagnetics Society (ACES) Journal*, vol. 29, no. 9, pp. 692-700, Sep. 2014.

[11] X. Xu and X. Tang, "Design of an ultra-wideband power divider with harmonics suppression," *International Journal of RF and Microwave Computer-Aided Engineering*, vol. 25, no. 4, pp. 299-304, Oct. 2015.

[12] K.-A. Shamaileh, A. Qaroot, N. Dib, et al., "Design of miniaturized unequal spilt Wilkinson power divider with harmonics suppression using non-uniform transmission lines," *Applied Computational Electromagnetics Society (ACES) Journal*, vol. 26, no.6, pp. 530-538, June 2011.

[13] M. Hayati, S. Roshani, S. Roshani, et al., "A novel miniaturized Wilkinson power divider with n-th harmonic suppression," *Journal of Electromagnetic Waves and Applications*, vol. 27, no. 6, pp. 726-735, Dec. 2013.

[14] M. Hayati, S. Roshani, and S. Roshani, "Miniaturized Wilkinson power divider with nth harmonic suppression using front coupled tapered CMRC," *Applied Computational Electromagnetic Society (ACES) Journal*, vol. 28, no.3, pp. 221-227, Mar. 2013.

[15] K. J. Song, "Compact filtering power divider with high frequency selectivity and wide stopband using embedded dual-mode resonator," *Electronics Letters*, vol. 56, no. 6, pp. 495-497, May 2015.

[16] B. Zhang and Y. Liu, "Wideband filtering power divider with high selectivity," *Electronics Letters*, vol. 51, pp. 1950-1952, Nov. 2015.

[17] B. Zhang, C.-P. Yu, and Y. Liu, "Compact power divider with bandpass response and improved out-of-band rejection," *Journal of Electromagnetic Waves and Application*, vol. 30, no. 9, pp. 1124-

1132, May. 2016.

[18] K. J. Song, S. Y. Hu, and C. L. Zhong, “Novel bandpass response power divider with high frequency selectivity using centrally stub-loaded resonators,” *Microwave and Optical Technology Letters*, vol. 55, no.7, pp. 1560-1562, Apr. 2013.

[19] X.-Y. Zhang, K.-X. Wang, and B.-J. Hu, “Compact filtering power divider with enhanced second-harmonic suppression,” *IEEE Microwave Wireless and Wireless Components Letters*, vol. 23, no. 9, pp. 483-485, Aug. 2013.

[20] B. Zhang, Y. Wu, C. Yu, and Y. Liu, “Miniaturized wideband bandpass filter based on harmonic suppressed dual transmission lines,” *Electronics Letters*, vol. 52, pp. 734-736, Apr. 2016.

[21] C. W. Tang, M. G. Chen, and C. H. Tsai, “Miniaturization of microstrip branch-line coupler with dual transmission lines,” *IEEE Microwave and Wireless Components Letters*, vol. 18, no. 3, pp. 185-187, Mar. 2008.

Gaoya Dong was born in Shanxi, China, in 1993. She received the B.S. degree in Applied Physics from Xidian University, Xi ’an, China, in 2015. She is currently pursuing the Ph.D. degree of Electrical Engineering in Beijing University of Posts and Telecommunications, Beijing, China.

Her current research interests include planar microwave power dividers, and antennas.

Bo Zhang was born in Shanxi, China, in 1991. He received the B.S. and M.S. degrees in Electronic and Information Engineering from the Beijing University of Posts and Telecommunications, Beijing, China, in 2012 and 2015, respectively, where he is currently working towards Ph.D. degree in Electrical Engineering.

His current research interests include planar microwave filters, power dividers, and antennas and power amplifiers.

Weimin Wang was born in Shandong, China, in 1977. She received the B.Eng. degree in Telecommunication Engineering, M.Sc. degree in Electromagnetics and Microwave Technology and the Ph.D. degree in Electronic and Information Engineering from the Beijing University of Posts and Telecommunications, Beijing, China, in 1999, 2004 and 2014, respectively.

In 2014, She joined the BUPT. She is currently a Lecturer with the School of Electronic Engineering, BUPT. Her research interests include microwave components and MIMO OTA.

Yuan Liu received the B.E., M.Eng., and Ph.D. degrees in Electrical Engineering from the University of Electronic Science and Technology of China, Chengdu, China, in 1984, 1989, and 1992, respectively.

In 1984, he joined the 26th institute of the Electronic Ministry of China to develop the inertia navigating system. In 1992, he held his first post-doctoral position with the EMC Laboratory at the Beijing University of Posts and Telecommunications (BUPT), Beijing, China. In 1995, he held his second post-doctoral position with the Broadband Mobile Laboratory at the Department of System and Computer Engineering, Carleton University, Ottawa, ON, Canada. Since 1997, he has been a Professor with the Wireless Communication Center at the College of Telecommunication Engineering, BUPT, where he is involved in the development of next-generation cellular systems, wireless LAN, Bluetooth application for data transmission, electromagnetic compatibility design strategies for high-speed digital systems, and electromagnetic interference and expected value of mean square measuring sites with low cost and high performance.

Spatial Domain Generation of Random Surface Using Savitzky-Golay Filter for Simulation of Electromagnetic Polarimetric Systems

Shimaa A. M. Soliman [1], Asmaa E. Farahat [1], Khalid F. A. Hussein [1], and Abd-El-Hadi A. Ammar [2]

[1] Microwave Engineering Department
Electronics Research Institute, Cairo, 12622, Egypt
megahed.shaimaa@yahoo.com, asmaa@eri.sci.eg, khalid_elgabaly@yahoo.com

[2] Electronics and Electrical Communications Department
Faculty of Engineering, El-Azhar University, Cairo, Egypt
hady42amar@gmail.com

Abstract ─ A spatial-domain algorithm is introduced for generating both isotropic and anisotropic natural rough surface models with predetermined statistical properties using Savitzky-Golay filter. Unlike the spectral-domain methods, the proposed method does not require the calculation of two-dimensional inverse Fourier transforms which constitute a computational burden for generating large ensembles of high-resolution surfaces. A comparative analysis between the proposed spatial-domain method and one of the conventional spectral-domain methods is presented. The comparison shows that the proposed spatial-domain method results in substantially improved computational performance. The fitness of the generated rough surface to the predetermined statistical properties is verified by calculating a variogram for numerical measurement of the variance and the correlation lengths. To demonstrate the importance of generating such a rough surface for simulation of electromagnetic polarimetric systems, a rough surface with anisotropic statistical properties is placed in the near field region of two antennas of orthogonal polarizations. It is shown that the self and mutual electromagnetic coupling coefficients of the two antennas can be used for measuring the orientation of the rough surface.

Index Terms ─ Polarimetric SAR, rough surface generation, Savitzky-Golay filter.

I. INTRODUCTION

Many applications make use of electromagnetic (EM) scattering from natural surfaces such as earth remote sensing via imaging synthetic aperture radar (SAR) [1-16]. In such applications it is usually required to numerically generate randomly rough surface (RRS) models with a predetermined set of statistical properties to simulate EM scattering from natural ground surfaces [17-21]. One often desires to generate a random surface with a particular probability distribution (may be Gaussian with a given mean and variance) and with a specific spatial correlation length. In such simulations it may be an objective to find the relation between the polarization of the backscattered field and the geometrical and electrical properties of the imaged ground surface. The presented work is concerned with the generation of rough surface that is realistic in simulating natural ground surface and to assess the backscattered field due to incident EM waves. The purpose of such a study is to find the relation between the polarization properties of the EM scattering from such surfaces and the geometrical characteristics of the rough surface itself. The main goal is to arrive at numerical results that may be useful for understanding the land images taken by fully polarimetric SAR systems.

The conventional techniques used for generating rough surface models depend on the surface generation in the spectral domain and then the application of the inverse discrete Fourier transformation (IDFT) to get the rough surface heights in the spatial domain [22-24]. However, in some other methods [18], the random surfaces are generated numerically with an arbitrary predetermined distribution function and correlation function of surface roughness. This leads to discretize the surface into a large number of segments, which can be considered uncorrelated roughness (white noise). The resulting profile is then smoothed to get the final model of the rough surface. All these methods arrive at a model for the required random rough surface with good accuracy of the resulting statistical parameters but, however, a great numerical effort is required and the assessment of the agreement with the required statistical properties should be explicitly done in subsequent operations.

Submitted On: July 11, 2018
Accepted On: October 19, 2018

The present work introduces a spatial-domain technique for generating anisotropic spatially-correlated random rough surface with predetermined statistical properties (mean height, root-mean-square height and correlation length). This technique applies the Savitzky-Golay filter (SGF) to realize the required correlation lengths between the adjacent heights in two perpendicular directions (x and y). It depends on the generation of a two-dimensional array of uncorrelated Gaussian random numbers that represent surface heights, which are further refined by linear interpolation to get higher resolution of the rough surface points. The SGF is then applied with appropriate smoothing factor and window size to get the surface heights correlated with the desired correlation lengths in both x and y directions. Due to the application of SGF the mean value and the variance of the resulting spatially correlated array of random numbers may be different from those predetermined values. For this purpose, the mean value of the resulting array is set to the required value by adding a constant value to the array elements. Also, the array elements are rescaled to get the desired root-mean-squared height.

The method proposed in the present work to generate a random rough surface directly in the spatial domain does not need the heavy mathematical procedures including two-dimensional inverse Fourier transform for high resolution surface models or convolutional integrals required in the other techniques. Moreover, it is simple and capable of generating both isotropic and anisotropic rough surfaces with the predetermined statistical parameters. Furthermore, it insures the fitness of the resulting spatially correlated rough surface to the desired Gaussian distribution and the required statistical properties within a predetermined acceptable error by achieving histogram and variogram measurements.

The present work demonstrates the importance of generating such rough surfaces for EM simulation of the fully polarimetric land imaging synthetic aperture radar systems, and its dependence on the polarization properties of the EM field backscattered from natural rough surfaces.

In the following sections of this paper the statistical properties of the natural rough surfaces, including ergodicity, isotropy and anisotropy, are discussed. The computational procedure of applying the proposed spatial-domain SGF correlation method is described in detail. Also, one of the conventional spectral-domain methods that are commonly used to generate Gaussian rough surface models is described in Appendix A. The numerical results are presented and discussion where a variety of random rough surfaces with various statistical properties are generated. The polarization of the near field backscattered by a rough surface is studied. The dependence of the co-polarized and cross-polarized components of the backscattered field on the geometrical and statistical parameters of the surface is investigated and discussed. To demonstrate the improved computational performance achieved by the proposed method, a comparative analysis with the conventional spectral-domain technique is presented. The rate of convergence of ensemble averaged coefficients of EM scattering from the generated RSS with the ensemble is investigated and discussed.

II. STATISTICAL PROPERTIES OF NATURAL RANDOM ROUGH SURFACES

The statistical distribution of the heights of the points on a natural rough surface is most commonly described by a Gaussian probability distribution function with zero mean, which is expressed as:

$$g(z) = \frac{1}{\sigma\sqrt{2\pi}} \exp\left(-\frac{z^2}{2\sigma^2}\right), \tag{1}$$

where z represents the height of a point on the surface, σ is the standard deviation

The root-mean-squared height, h_{rms}, of such a rough surface is equal to σ and is often used to give an indication of the “degree of roughness”.

Another important parameter that describes the spatial distribution of the surface heights is the spatial correlation function between adjacent points on the surface. For two points at horizontal locations $\mathbf{r}$ and $\acute{\mathbf{r}}$, respectively, the height-height correlation function is defined as,

$$C_{zz}(\mathbf{r}, \acute{\mathbf{r}}) = \langle z(\mathbf{r}) z'(\acute{\mathbf{r}}) \rangle = \int_{-\infty}^{\infty}\int_{-\infty}^{\infty} z\, z'\, p(\mathbf{r}, z, \acute{\mathbf{r}}, \acute{z})\, dz\, d\acute{z}, \tag{2}$$

where,

$$\mathbf{r} = x\,\hat{\mathbf{a}}_{\mathbf{x}} + y\,\hat{\mathbf{a}}_{\mathbf{y}}, \tag{3}$$

where x and y are the horizontal coordinates of the point on the rough surface.

A. Ergodicity, isotropy and anisotropy of the rough surface and the spatial correlation function

In statistics, the term "ergodic" describes a random process for which the global average of one sequence of events is the same as the ensemble average. If the ensemble average is dependent on the ensemble chosen, (i.e. the mean varies from ensemble to ensemble), then the random process is not ergodic. It happens frequently that each realization of the ensemble carries the same statistical information about the homogeneous random process as every other realization. The spatial averages calculated for any realization are then all equal and coincide with the ensemble average. The homogeneous random process is then said to be an ergodic process.

A rough surface is called homogeneous if the characteristics of the surface height distribution over the horizontal dimensions do not change with the horizontal location on the surface. Consequently, the height-height correlation between two points on the surface will depend only on the vector difference, $\mathbf{r} - \acute{\mathbf{r}}$, between the horizontal locations, $\mathbf{r}$ and $\acute{\mathbf{r}}$, of the two points. The rough surface is called isotropic if it has the same characteristics along any direction. For a homogeneous isotropic rough surface, the random process will be "isotropically ergodic" in all the directions. However, some homogenous rough surfaces have their height-height correlation function dependent on the horizontal direction; such a rough surface is “directionally homogeneous” and, consequently, the random process for the surface heights is “directionally ergodic”.

For isotropic homogeneous rough surface, the height-height correlation function depends only on the scalar horizontal distance between the two points. For directionally homogenous anisotropic rough surface the height-height correlation function depends on the vector distance between the two points and the expression (2) for the correlation function can be written as:

$$C_{zz}(\mathbf{r},\mathbf{r}') = C_{zz}(d_x, d_y) = \int_{-\infty}^{\infty}\int_{-\infty}^{\infty} z\, z'\, p(z, z', d_x, d_y)\; dz\, dz', \qquad (4)$$

where,

$$d_x = |x - \acute{x}|,\; d_y = |y - \acute{y}|. \qquad (5)$$

B. Two-point height-height probability distribution function

The common types of natural rough surfaces have a Gaussian two-point joint probability distribution function for the heights of any two points on the surface of horizontal separations (d_x, d_y).

The correlation length can be qualitatively defined as the maximum length over which two points are correlated. For directionally homogenous anisotropic rough surface, the Gaussian height-height probability density function can be expressed as follows:

$$p(z, z', d_x, d_y) = \frac{1}{2\pi\sqrt{\sigma^4 - C_{zz}^2(d_x, d_y)}} \exp\left(-\frac{\sigma^2(z^2 + z'^2) - 2zz'C_{zz}(d_x, d_y)}{2\sigma^4 - 2C_{zz}^2(d_x, d_y)}\right), \qquad (6)$$

where $C_{zz}(d_x, d_y)$ is the correlation function whose definition is given by (4). The power exponential, or Gaussian, correlation function can be expressed as:

$$C_{zz}(d) = \sigma^2 \exp\left(-\left(\frac{d_x^2}{l_{cx}^2} + \frac{d_y^2}{l_{cy}^2}\right)\right), \qquad (7)$$

where l_{cx} and l_{cy} are the correlation lengths in the x and y directions, respectively.

III. SPATIAL CORRELATION OF UNCORRELATED RANDOM NUMBERS USING SGF

As the most important and critical process for creating a natural model of rough surface is to correlate the heights of the adjacent points of a two-dimensional array with the required correlation length, this section is dedicated for the description of the application of SGF [25] on a one-dimension of set of uncorrelated random numbers. The generalization of the method to correlate a two-dimensional set is then described.

The concept of smoothing can be thought of as removing the effect of noise (spatially uncorrelated random values) from a set of measured values. This can simply be achieved by replacing each data point by the average of the surrounding points, because nearby points measure values almost close to each other, so averaging will reduce the effect of the noise.

SGF belongs to the category of digital filters. It is a well-adapted low pass filter used for smoothing data. SGF is used to smooth data in the domain of the data generation, it doesn’t require to Fourier transform the data to another domain to remove undesired components and transform back.

For correlating a set of random numbers that represent the values of a random function $z(x)$ at equally spaced distances along x-direction, a digital filter is applied to the data values $z_i \equiv z(x_i)$, where $x_i \equiv x_o + i\Delta$ and Δ is a constant spacing between points, $i = \cdots - 2, -1, 0, 1, 2, \cdots$. The simplest type of digital filter is the one that replaces each z_i by a linear combination Z_{i} of itself and the neighboring points, that is,

$$Z_i = \sum_{n=-n_L}^{n_R} c_n z_{i+n}\, , \qquad (8)$$

where n_L is the number of the random values on the left of z_i, the desired value to be replace, and n_R is the number of data points to the right of it; $\mathrm{c_n}$ is the weights of averaging. Here it is assumed that we have a moving window of length $n_L + n_R + 1$ to sequentially scan the values of the vector z. In each step it replaces the value of the function $z(x) = z_i$ at the center point of the window by the weighted average of itself and the neighbouring points.

To understand the SGF, let’s start by considering the simplest case where all the points have the same weight in equation (8), i.e., $c_n = 1/\ (n_L + n_R + 1)$. If the function $z\,(x)$ representing these set of points $(-n_L\ to\ n_R)$ is constant or is changing linearly with its argument x (increasing or decreasing), then no bias is introduced in the resulting z after applying the averaging filter. Under this condition, the moving average technique will preserve the zero-order and the first order harmonic of z. However, if the function z has significant second or higher order components, these harmonics will be significantly affected or almost removed by applying a moving average filter. In case these higher order harmonics are of physical interest, then the application of such a moving averaging window filter will result in significant loss of information which may be unacceptable. The idea of SGF is to find coefficients c_n that preserve higher moments. Equivalently, the idea is to approximate the underlying function within the moving window not by a constant (whose estimate is the average), but by a polynomial of higher order, typically quadratic, cubic or quartic. For each point Z_i a polynomial is least-squares fitted to all $n_L + n_R + 1$ points in the moving window, and then Z_i is set to be the value of that polynomial at position i. Simply, the quadratic polynomial will preserve the second order harmonic and the cubic will preserve the third order one and so forth. The smoothing polynomial is found using least square fitting which minimizes the sum of squared differences between an observed value, and the fitted value provided by the filter model.

For a two-dimensional RRS extending in x- and y-directions, the height $z(x, y)$ at each point represents the height function in the z-direction. The height z is the function to be smoothed by the SGF. In this case the above procedure is applied on each row of the surface points and then applied on each column consecutively. Applying SGF to the generated Gaussian random heights constituting a rough surface will create a correlation between the heights of the neighbouring points for the surface. The aim is to correlate the surface points with a desired correlation length and preserve the Gaussian probability density function of the surface heights.

IV. PROCEDURE OF GENERATION OF SPATIALLY CORRELATED GAUSSIAN ROUGH SURFACE

The main idea behind the method presented here for generating a spatially correlated Gaussian rough surface is to spatially correlate the adjacent elements of two-dimensional array of uncorrelated Gaussian numbers so as to satisfy the required statistical parameters of a natural rough surface as described in Section II. The properties of the resulting array after correlation shall satisfy the following requirements:

- Gaussian distribution of the surface heights, $g(z)$,
- zero mean, $\mu = 0$,
- The standard deviation is equal to the required root-mean-squared height, $\sigma = h_{rms}$,
- The required spatial correlation lengths (l_{cx} and l_{cy} in x and y directions, respectively),
- The required height-height correlations function, $C_{zz}\left(d_x, d_y\right)$, and, finally,
- The required two-point joint probability distribution function for the surface heights $p\left(z, z', d_x, d_y\right)$.

The procedure for the process of generating spatially correlated Gaussian rough surface is described in some detail in the following subsections.

A. Generation of two-dimensional uncorrelated Gaussian random data

Two-dimensional arrays of spatially uncorrelated random numbers can be generated to satisfy a set of predetermined statistical parameters such as a specific probability distribution, mean value and variance. Various generation methods are available in literature [26-28] and can be used to generate such two-dimensional arrays. To generate a realistic model for a natural ground surface, the first step of the procedure is to generate two-dimensional $(M \times N)$ array of Gaussian random numbers so as to fit the desired Gaussian probability density function. Let this two-dimensional array of uncorrelated random numbers be $G(M, N)$:

$$G(M, N) = GaussianRndGen(\mu = 0, \sigma = h_{rms}, M, N). \tag{9}$$

B. Refinement of the uncorrelated Gaussian random data

To get improved resolution of the uncorrelated random number array and to get it more suitable for subsequent application of the SGF, the generated array is refined by linear interpolation to insert an element between each two successive elements of the random number array. This refinement is carried out in both rows (x) and columns (y) directions. The dimensions of the refined array for the heights of the rough surface are $(2M \times 2N)$. Let the output array of this stage, or the refined version of $G(M, N)$ be $G(2M, 2N)$; this can be expressed as:

$$G(2M, 2N) = Refine\{G(M, N)\}. \tag{10}$$

C. Application of SGF

For correlating the heights of the adjacent points of G the SGF, described in Section III, is applied as a smoothing window of length W points moving sequentially on the array elements to scan the rows and then to scan the columns, thereby correlating all the sequential points lying within the window on both rows and columns. Thus, the SGF acts as a correlator for each group of W neighbouring array elements. This process can be described by the following equation:

$$G(2M, 2N) = SGF\{G(2M, 2N, W, W)\}. \tag{11}$$

It is clear that the output of the SGF, $G(2M, 2N)$, is a two-dimensional array of correlated random numbers with correlation length of W points in both the row (x) and column (y) directions. In this manner, the resulting rough surface has $(W - 1)$ segments per correlation length in both x and y directions. The entire surface has resolution of $(2M - 1)$ and $(2N - 1)$ segments along the x and y directions, respectively. It is convenient to set $(2M - 1)$ as well as $(2N - 1)$ to be integer multiples of $(W - 1)$.

If one sets the horizontal separations between the successive surface rows and columns to Δx and Δy, respectively, the resulting correlation lengths will be $l_{cx} = (W - 1)\Delta x$ and $l_{cy} = (W - 1)\Delta y$. It should be noted that Δx and Δy can be arbitrarily set to get the predetermined values of l_{cx} and l_{cy}. In this way, the width and length of the entire rough surface are $L_x = (2M-1)\Delta x$ and $L_y = (2N-1)\,\Delta y$.

For accurate results of EM scattering, the number of segments per correlation length should be large enough, i.e., $W-1 \gg 1$. In the same time, the electrical length of one segment should be small enough, i.e., $\Delta x \ll \lambda$ and $\Delta y \ll \lambda$, where λ is the free space wavelength.

D. Preserving the required mean and standard deviation of resultant rough surface

Due to the refinement and the application of SGF processes to the uncorrelated two-dimensional Gaussian numbers as described in Sections IV.B and IV.C, both the mean value and the standard deviation of the resulting may become different from the target values required for the final heights of the rough surface.

Let the mean value and the variance of G be:

$$\mu_S = Mean(G), \tag{12}$$

$$\sigma_S^2 = Variance(G)\,. \tag{13}$$

To preserve zero mean of the finally generated rough surface, the mean value μ_S is subtracted from each element of the array G. The resulting array is then scaled by a factor h_{rms}/σ_S to get the final value of the standard deviation equal to the target value, h_{rms}. This process can be described as follows:

$$z(2M,2N) = \frac{h_{rms}}{\sigma_S}\,(G-\mu_S). \tag{14}$$

E. Variogram for measuring the statistical properties of the final rough surface

To check the fitness of the resulting spatially correlated rough surface to the predetermined statistical properties, a variogarm is calculated for numerical measurement of the variance h_{rms}^2 and the correlation lengths l_{cx} and l_{cy} in x and y directions, respectively. The variogram is an indication for of how the spatial data are related with distance, therefore it's a measure of the correlation length l_c in a specific direction. The variogram for lag vector $\mathbf{h}$ is defined as the average squared difference of values separated approximately by $\mathbf{h}$ and is expressed as follows:

$$\gamma(\mathbf{h}) = \frac{1}{N(\mathbf{h})}\sum_{\propto=1}^{N(\mathbf{h})}[z(\mathbf{r}_\propto+\mathbf{h}) - z(\mathbf{r}_\propto)]^2\,, \tag{15}$$

where, $\mathbf{h} = h_x\,\hat{\mathbf{a}}_x + h_y\,\hat{\mathbf{a}}_y$ is the lag vector representing the vector separation between two spatial locations, $\mathbf{r} = x\,\hat{\mathbf{a}}_x + y\,\hat{\mathbf{a}}_y$ is the horizontal vector of spatial coordinates, $z(\mathbf{r}_\propto)$ is the (height) variable under consideration as a function of the spatial location $\mathbf{r}_\propto$, $z(\mathbf{r}_\propto+\mathbf{h})$ is lagged version of variable under consideration, $N(\mathbf{h})$ is the count of all pairs of points having vector separation $\mathbf{h}$.

Figure 1 shows a model plot of the variogram against the lag distance h. After a long enough lag distance the plotted curve becomes constant and equal to the variance and the random data are no more correlated. The correlation length l_c (in the direction of $\mathbf{h}$) is the lag distance at which the variogram reaches about 63% of the variance whereas the range ($3l_c$) is the lag distance at which the variogram reaches about 95% of the variance.

By setting $\mathbf{h} = h_x\,\hat{\mathbf{a}}_x$, the variogram can be plotted and fitted to the following exponential function from which one can deduce the correlation length in the x direction:

$$\gamma(h_x) = h_{rms}^2\left(1-e^{-h_x/l_{cx}}\right). \tag{16}$$

Similarly, by setting $h = h_y\,\hat{\mathbf{a}}_y$, the variogram can be plotted and fitted to the following exponential function from which one can deduce the correlation length in the y direction:

$$\gamma(h_y) = h_{rms}^2\left(1-e^{-h_y/l_{cy}}\right). \tag{17}$$

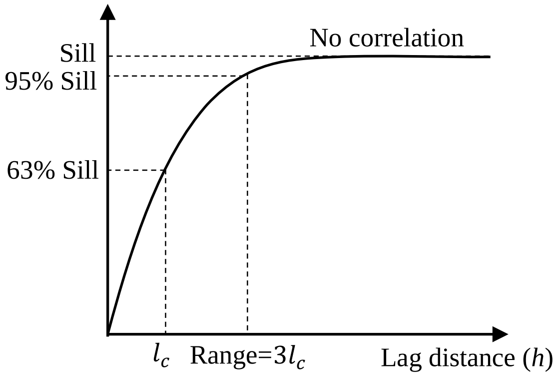

Fig. 1. Variogram of the rough surface model.

V. POLARIZATION CHARACTERISTICS OF THE SCATTERED NEAR FIELD

To demonstrate the importance of generating a random rough surface for the simulation of electromagnetic polarimetric systems, an anisotropic rough surface with predetermined statistical properties is placed in the near field region of two coplanar linearly polarized antennas of orthogonal polarizations.

The antenna arrangement is shown in Fig. 2. To account for the vertical and horizontal polarizations of the backscattered field, two orthogonal dipoles (crossed dipoles) are used as transmitter/receiver. One of the two dipoles is vertically oriented whereas the other one is horizontally oriented.

The crossed dipole antennas are designed to get a perfect impedance matching for negligible reflection coefficient. The generated rough surface has a perfectly electric conducting material. It is shown that the self and mutual electromagnetic coupling coefficients of the two antennas can be used for measuring the orientation of the rough surface.

Let E_{vt} and E_{vr} be the transmitted and received electric fields, respectively, at the port of the vertical dipole and let E_{ht} and E_{hr} be the transmitted and received electric fields, respectively, at the port of the horizontal dipole.

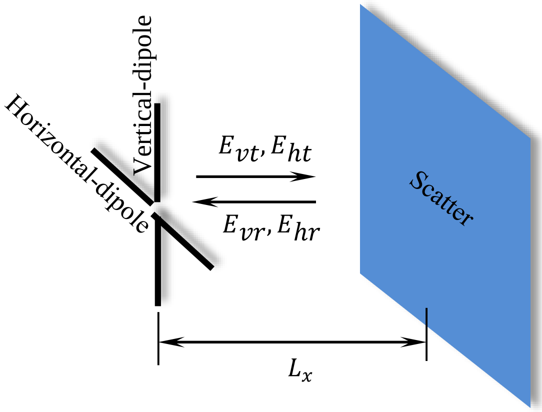

Fig. 2. The configuration of the antenna system used to study the polarization characteristics of the near field scattered from the rough surface.

The edges bounding the rough surface due to the geometrical truncation are not found in the real (natural) surfaces. For an incident plane wave the entire rough surface including its truncation edges will be illuminated; in this case, the edges would significantly contribute to the EM scattering. Therefore, a Gaussian beam may be a solution to avoid the surface edge contribution. However, in the present work another solution is employed to avoid such unwanted effect. The dipoles used to calculate the (near zone) scattering parameters are very short relative to the rough surface dimensions. Moreover, they are placed near the center of the truncated rough surface (i.e., far from the edges) which causes the interaction between the dipoles and the rough surface edges to be very weak and of insignificant contribution to the scattering parameters calculated at the antenna ports.

Let the port of the vertical dipole be denoted as (1) and the horizontal one as (2). To calculate the co-polarized component of the field backscattered from the arbitrary surface we consider the following parameters,

$$S_{vv} \equiv S_{11} = \left.\frac{E_{vr(1)}}{E_{vt}}\right|_{E_{ht}=0}, \tag{18}$$

where $E_{vr(1)}$ is the electric field received by the vertical dipole when the same dipole is acting as a transmitter:

$$S_{hh} \equiv S_{22} = \left.\frac{E_{hr(2)}}{E_{ht}}\right|_{E_{vt}=0}, \tag{19}$$

where $E_{hr(2)}$ is the electric field received by the horizontal dipole when the same dipole is acting as a transmitter. Also, to calculate the cross-polarized component of the backscattered field we consider the following parameters:

$$S_{hv} \equiv S_{21} = \left.\frac{E_{hr(1)}}{E_{vt}}\right|_{E_{ht}=0}, \tag{20}$$

where $E_{hr(1)}$ is the electric field received by the horizontal dipole when the vertical dipole is acting as a transmitter.

$$S_{vh} \equiv S_{12} = \left.\frac{E_{vr(2)}}{E_{ht}}\right|_{E_{vt}=0}, \tag{21}$$

where $E_{vr(2)}$ is the electric field received by the vertical dipole when the horizontal dipole is acting as a transmitter.

VI. RESULTS AND DISCUSSION

The presentation of the numerical results in this section aim to investigate the theoretical and procedural issues discussed in the previous sections. The capability of the algorithm developed for applying SGF to generate a random rough surface which maintains the target statistical parameters as required is numerically investigated. The numerical results concerned with the generation of a variety of both isotropic and anisotropic rough surfaces with various statistical parameters such the correlation lengths in x and y directions are presented. Other results are presented to verify that the generated rough surface realizes the target statistical parameters such as the overall Gaussian distribution of the surface heights, the correlation lengths in the different directions, the root-mean-squared height, the two-point height-height joint probability density function and the correlation function. Finally, the numerical results concerned with the polarization properties of the scattered field from rough surface are demonstrated for the purpose of relating the properties of the backscattered field to the statistical properties of the RRS itself.

A. Application of SGF to spatially correlate two-dimensional random data

As described in Section 4.1, the first step of generating a spatially correlated random rough surface with the desired statistical properties is to generate a $M \times N$ array of uncorrelated Gaussian random numbers with zero mean and unity variance. These random numbers can be considered as the heights of a spatially uncorrelated rough surface. The Matlab “normrnd()” function is used to generate 100×100 array of uncorrelated random numbers. A three-dimensional plot of such an array with $M = N = 100$ is shown in Fig. 3. These random numbers are $10{,}000$ data samples of spatially uncorrelated heights, which are to be subjected to the procedure described in Section IV.C to generate the spatially correlated rough surface with the desired statistical properties.

As described in Section IV.B, the resolution of the uncorrelated two-dimensional array presented in Fig. 3 is doubled by inserting an extra point between each two successive points of the original array by linear interpolation to obtain a two-dimensional array of 200×200 elements. To get a spatially correlated rough surface of size 200×200 points with 18 points correlation length, the SGF with a smoothing window of 18-point length is applied to correlate the random numbers on each row and column as described in Section IV.C.

Figure 4 shows the resulting spatially correlated Gaussian random rough surface with $\mu = 0$, $h_{rms} = 1.0$, and $l_{cx} = l_{cy} = 18$ points. Figure 5 presents a comparison between the spatially correlated rough surface (after the application of SGF correlation method) and the uncorrelated random numbers for 100 points lying on the central row of the two-dimensional array.

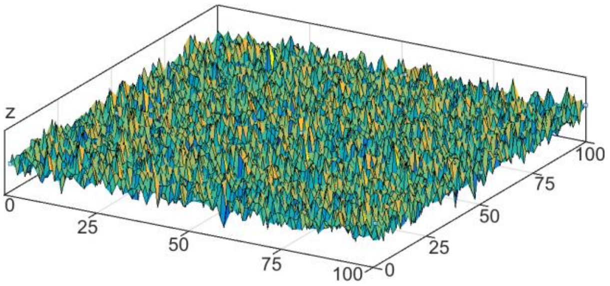

Fig. 3. Plot of two-dimensional array of 100×100 uncorrelated Gaussian random numbers with zero mean and unity standard deviation.

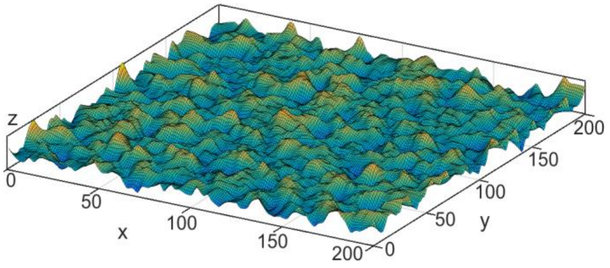

Fig. 4. Plot of the spatially correlated rough surface generated by applying the procedure described in Section IV to the uncorrelated Gaussian array presented in Fig. 3.

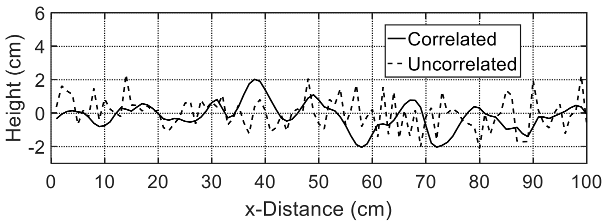

Fig. 5. Comparison between the spatially correlated rough surface and the uncorrelated random numbers for 100 points lying on the central row of the two-dimensional array.

The correlation length can be numerically measured using the variogram as described in Section IV.E. The measured variogram of the generated RRS is plotted as shown in Fig. 6. The fitted curve for the variogram gives a correlation length of 18 points, which is exactly as desired. This indicates the accuracy and efficiency of the proposed method for generating a rough surface with predetermined statistical properties.

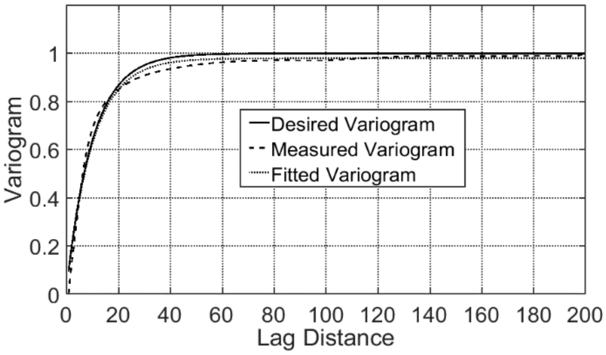

Fig. 6. Variogram of the spatially correlated rough surface generated by the SGF correlation method.

B. Comparative analysis between the spectral and spatial domain techniques of rough surface generation

Numerical comparisons between the proposed spatial-domain method and the conventional spectral-domain methods of generating RRS are presented. The following comparisons are concerned with accuracy of the statistical parameters of the generated RRS and some computational performance metrics such as the computational time and memory space requirements.

B.1 Fitness of the generated rough surface to the predetermined statistical model

One-dimensional 100-point resolution rough surfaces generated by the proposed spatial-domain method and the conventional spectral-domain method are presented in Fig. 7 (a) and Fig. 7 (b), respectively.

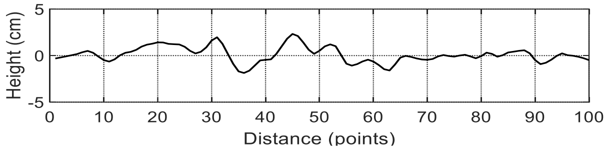

(a) Spatial-domain technique

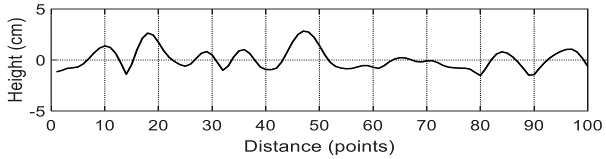

(b) Spectral-domain technique

Fig. 7. One-dimensional rough surfaces generated by the spatial-domain and the spectral-domain methods.

Three-dimensional plots of 20×20 cm rough surfaces generated using both the spatial and spectral domain techniques are presented in Fig. 8 (a) and Fig. 8 (b), respectively. Both surfaces are isotropic with $l_{cx} = l_{cy} = 2$ cm. Figure 9 presents anisotropic rough surfaces generated using both techniques with $l_{cx} = 0.2 l_{cy} = 2$ cm. The corresponding variograms of the two rough surfaces are plotted in Fig. 10. Comparing the variograms of the two surfaces shows that both the spatial-domain and spectral-domain methods are successful in generating rough surfaces that accurately satisfy the predetermined statistical properties.

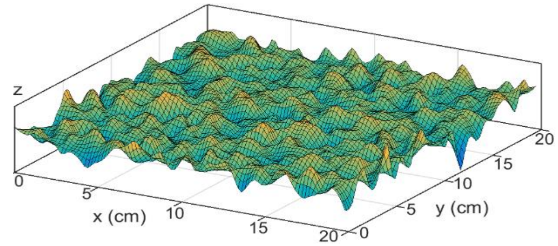

(a) Spatial-domain technique

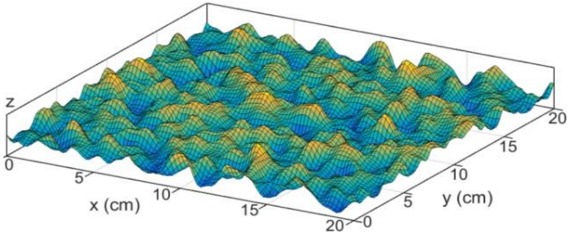

(b) Spectral-domain technique

Fig. 8. Rough surfaces of dimensions 20×20 cm generated using the spatial and spectral methods, $l_{cx} = l_{cy} = 2$ cm.

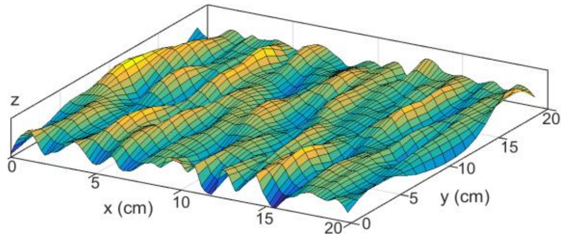

(a) Spatial-domain technique

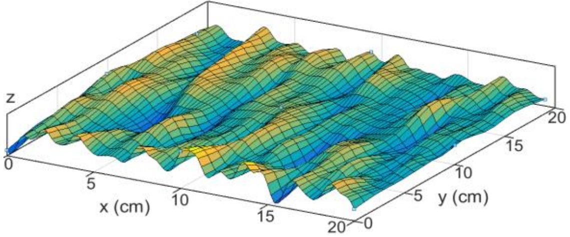

(b) Spectral-domain technique

Fig. 9. Rough surfaces of dimensions 20×20 cm generated using the spatial and spectral methods, $l_{cx} = 0.2 l_{cy} = 2$ cm

B.2. Computational performance

To generate a surface of $N \times N$ discrete points using the spectral domain method described in Appendix A, one has to compute a two-dimensional $(N \times N)$ IDFT. For large values of N, this takes a substantially larger computational time than that taken by the proposed spatial-domain method to generate the same surface.

For the sake of comparing the computational performance of the proposed spatial domain technique to that of the conventional spectral domain one, a $10 \times 10\ cm$ rough surface with statistical parameters: $l_{cx} = l_{cy} = 1$ cm, $\sigma = 1$ cm and $\mu = 0$, has been generated using both of them. The surface dimensions are $N \times N$ points; a higher value of N produces a surface of higher resolution.

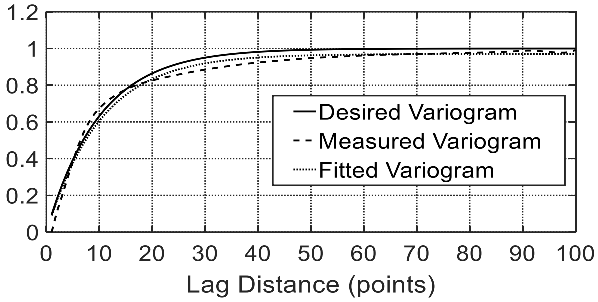

(a) Spatial-domain technique

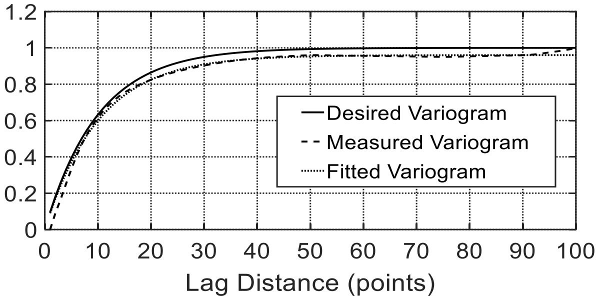

(b) Spectral-domain technique

Fig. 10. Variograms of the spatially correlated rough surfaces generated by the proposed SGF correlation method and the spectral-domain method.

B.2.1. Improved computational time

The computational time required to generate a square random surface of $N \times N$ points (using a specific computer) is plotted against N as shown in Fig. 11 for both the spectral-domain and the spatial-domain methods. It is clear that the spatial-domain method takes substantially less time than that taken by the spectral domain method.

Figure 12 shows a plot of the percentage of the computational time taken by the proposed spatial-domain method relative to that taken by the spectral-domain method. It is clear that the computational time is reduced by about 20%-35% when compared to the time taken by the spectral domain method depending on the surface resolution.

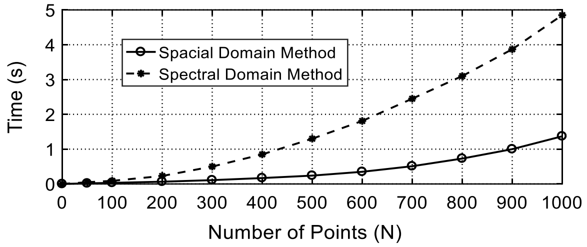

Fig. 11. Computational time required for generating square rough surface of dimensions $N \times N$ points.

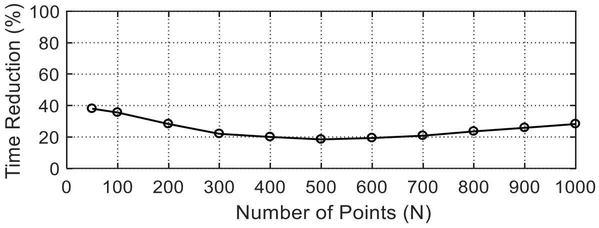

Fig. 12. Percentage of computational time taken by the proposed spatial domain method relative to that taken by the spectral domain method.

B.2. Improved memory space

According to the algorithm of the spectral-domain method as described in Appendix A, the two-dimensional complex arrays $F(k_p, k_q)$ and its inverse Fourier transform $f(x_m, y_n)$ require a storage capacity of $2 \times (N \times N) \times 16$ bytes. According to the algorithm of the spatial-domain method as described in Section VI, the two-dimensional array G requires a storage capacity of $(N \times N) \times 8$ bytes. This means that the percentage of the memory space reduction due to the application of the spatial domain method instead of the spectral domain method can be expressed as:

$$Memory\ Space\ Redution\ (\%) = \frac{(N \times N) \times 8}{2 \times (N \times N) \times 16} \times 100\ \% = 25\ \%. \quad (22)$$

C. Polarization characteristics of the near field scattered from finite rough surfaces

The aim of this section is to find the relation between the polarization characteristics of the near field scattered from a rough surface and the geometrical and statistical properties of the surface. For this purpose, and before going into a deep study of the rough surface response to EM waves, we study the polarization characteristics of the near field scattered from a square conducting sheet whose heights are given as sinusoidal variation in one direction (x) and constant with the other direction (y). For polarimetry, a crossed-dipole antenna arrangement is used for transmission and reception. For accurate polarimetry, both of the crossed dipoles should be designed to have perfectly matched impedance.

C.1. Crossed-dipole antenna characteristics

This section is concerned with the design of the crossed-dipole antenna arrangement to get perfect impedance matching for accurate estimation of the EM polarization properties of the field scattered from the surface under consideration. This antenna arrangement consists of co-planar vertical and horizontal dipoles as shown in Fig. 13. Each dipole has a length l, diameter d and excitation gap width g. The main goal is to get the optimum values of l, d and g for minimum return loss at the dipole antenna ports.

The dipole parameters are set to $l = 2.7\ cm$, $d = l/20$ and $g = l/18$. The numerical results for the variation of the input impedance of this dipole with the frequency are presented in Fig. 14. It is shown that the imaginary part of the input impedance is zero at a frequency of 4343 MHz where the real part is about 44 Ω. To obtain perfect matching of the dipole antenna the operation should be achieved at this frequency with Z_0 set to 44 Ω in the numerical simulation. Figure 14 shows a plot of the reflection coefficient, S_{11}, against the frequency. It is shown that S_{11} has a minimum value of −47 dB at a frequency of 4343 MHz.

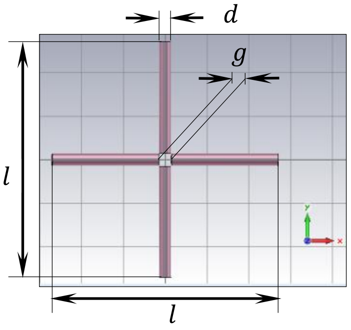

Fig. 13. The crossed-dipole antenna arrangement.

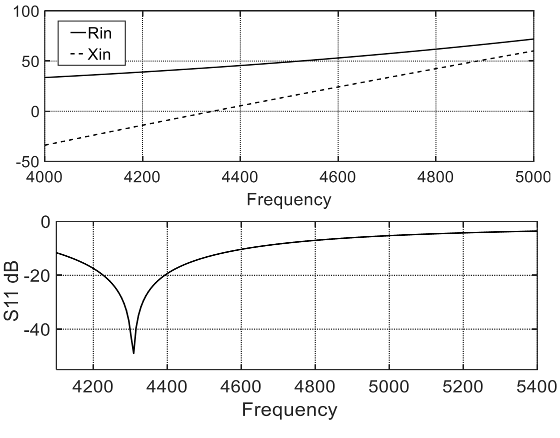

Fig. 14. Variation of the dipole input impedance and the reflection coefficient S_{11} with the frequency; $l =$ 2.7 cm, $d = l/20$ and $g = l/18$.

C.2. Mutual coupling between sinusoidal surface and a nearby antenna

A surface taking the shape of sinusoidal wave is generated with a wave length of λ_s and is placed in the xy plane. The heights of the points of this surface are described by the equation,

$$z(x) = A \sin\left(\frac{2\pi x}{\lambda_s}\right), \tag{22}$$

where A is the amplitude of the sinusoidal height variations. The surface dimensions are set to 20×20 cm, $A = 0.8$ cm and $\lambda_s = 1.7$ cm.

As shown in Fig. 15, the crossed dipole antennas described in section V are located at a distance $L_x = 1.72$ cm from the sinusoidal sheet. The plane of the crossed dipoles is parallel to the sheet. The scattering parameters required to study the polarization characteristics of the near field are calculated as described in section V. For convenience, the y-oriented dipole will be referred-to as the vertical dipole whereas the x-oriented dipole will be referred-to as the horizontal one. For demonstrating the dependence of the backscattered field on the orientation of the sinusoidal sheet the scattering parameters are calculated while the surface rotates from 0° to 90° about the z-axis.

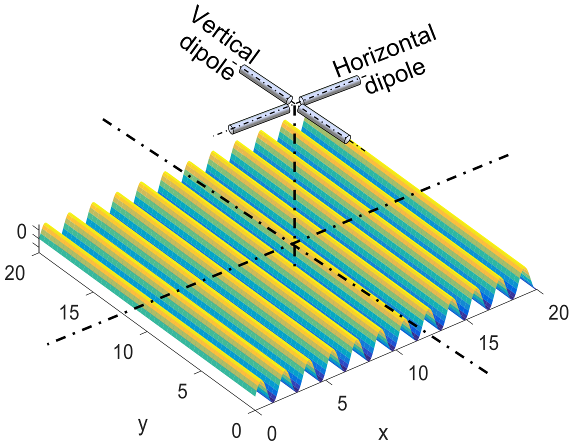

Fig. 15. The crossed dipole antennas are placed facing the center of the sinusoidal sheet.

The co-polarized scattering parameters S_{11} and S_{22} and the cross-polarized scattering parameters S_{12} and S_{21} are plotted with the angle of rotation (θ) of the sinusoidal sheet. As shown in Fig. 16, the scattering parameter of the vertical dipole S_{11} has a value of -7.4 dB at $\theta = 0°$ where the vertical dipole is parallel to the straight lines of the sinusoidal sheet. With increasing the angle of rotation, the scattering parameter S_{11} decreases reaching a minimum value of -11 dB at $\theta = 90°$ where this dipole is perpendicular to the straight lines of the sinusoidal sheet. Similarly, the scattering parameter S_{22} reaches a maximum value of -7.2 dB at $\theta = 90°$ and a minimum value of -11 dB at $\theta = 0°$.

As shown in Fig. 16, the cross-polarized parameters S_{12} and S_{21} have their minimum values (-69.8 dB) at $\theta = 0°$ and $\theta = 90°$, i.e., when one of the dipoles is parallel to the straight lines of the sinusoidal sheet. They reach their maximum values (-15 dB) at $\theta = 45°$, i.e., when the straight lines of the sinusoidal sheet make an angle of 45° with each dipole.

In conclusion, the orientation of the sinusoidal sheet around the z-axis can be indicated by the scattering parameters S_{11}, S_{22}, S_{21} and S_{12}, and hence these scattering parameters can be used as polarimetric parameters for scatterers having geometrical shape similar to the sinusoidal sheet.

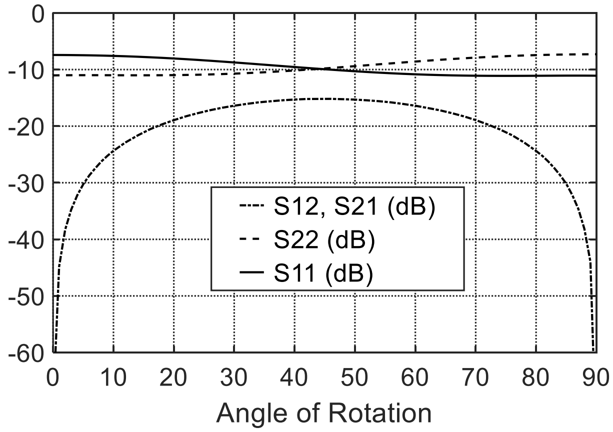

Fig. 16. Variation of the scattering parameters (S_{11}, S_{22}, S_{21} and S_{12}) with the rotational angle of the sinusoidal surface around z-axis.

C.3. Ensemble size for converging backscattering coefficients

The purpose of the following discussion is to investigate the rate of convergence of the coefficients of backscattering from rough surfaces generated using both the spectral-domain and the spatial-domain methods with increasing the ensemble size (number of sample rough surfaces over which the results are averaged). More precisely, it is required to get the minimum size of the ensemble to get converging results.

For this purpose, a crossed-dipole antenna with same parameters as described in Section VI.C.1 is placed at a distance $\boldsymbol{L = 1.72}$ **cm** from a $\boldsymbol{20 \times 20}$ cm rough surface of the statistical parameters: $\boldsymbol{l_{cx} = l_{cy} = 1.8}$ **cm**, $\boldsymbol{h_{rms} = 0.5}$ **cm**. The scattering parameters $\boldsymbol{S_{11}}$ and $\boldsymbol{S_{22}}$ representing copolarized bacscattered EM field are investigated at $\boldsymbol{f = 4343}$ **MHz**.

The results for the variation of the averaged S_{11} and S_{22} with the ensemble size using the spectral and spatial domain methods are presented in Fig. 17 and Fig. 18, respectively. It is clear that both methods are fast convergent and a minimum ensemble size of 5 is fairly acceptable for both of them.

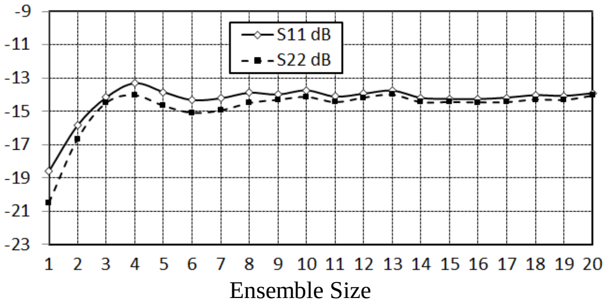

Fig. 17. Convergence of S_{11} and S_{22} with increasing the ensemble size of rough surfaces generated using the spectral domain method.

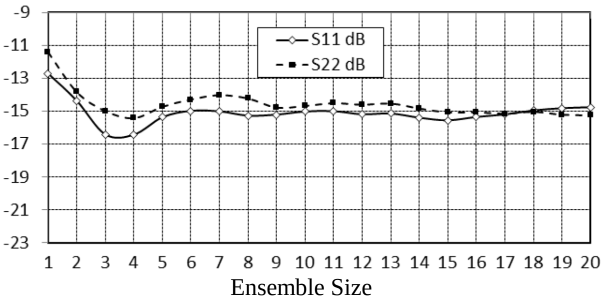

Fig. 18. Convergence of S_{11} and S_{22} with increasing the ensemble size of rough surfaces generated using the spatial domain method.

C.4. Polarization characteristics of the mutual coupling between rough surfaces and nearby antennas

In this section we study the EM scattering from various anisotropic rough surfaces; each with a correlation length in one direction relatively larger than that in the perpendicular direction, for example, $l_{cy} > l_{cx}$. It is expected that the larger the ratio l_{cy}/l_{cx}, the closer the polarization characteristics of the near field scattered from the rough surface to that of the sinusoidal sheet studied in Section VI.C.2.

For this purpose, we demonstrate anisotropic rough surfaces with various ratios of the correlation lengths: $l_{cy}/l_{cx} = 20, 10, 5, 1$; each with dimensions 20×20 cm. The geometrical models of these rough surfaces are presented in Fig. 19. The scattering parameters concerning the co-polarization and cross polarization of the backscattered field are compared to those obtained for the sinusoidal surface, which are presented in Section VI.C.2.

Figure 20 shows the variation of the co-polarized and cross-polarized scattering parameters with the rotational angle θ, from $\theta = 0°$ to $\theta = 90°$ for each of the rough surfaces described above.

In Fig. 20 (a) it is clear that, for the rough surface with $l_{cy}/l_{cx} = 20$, the variations of both the co-polarized and cross-polarized scattering parameters with the rotational angle θ are closer to the behavior of those parameters for the sinusoidal sheet presented in Fig. 16. The maximum difference between S_{11} and S_{22} occurs at $\theta = 0°$ and $\theta = 90°$ where it is equal to about ± 2.5 dB.

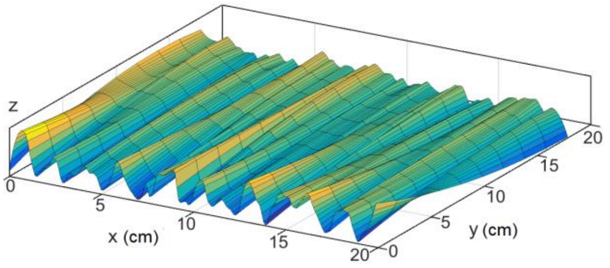

(a) Rough surface with $l_{cy} = 20\, l_{cx}$

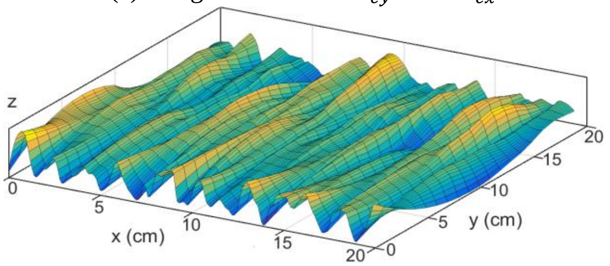

(b) Rough surface with $l_{cy} = 10\, l_{cx}$

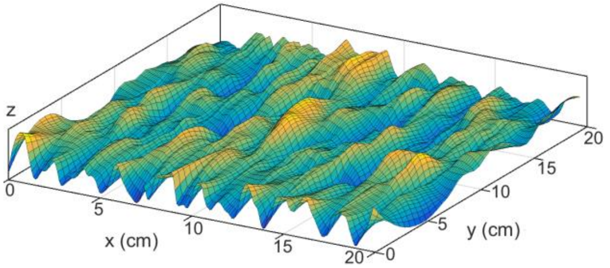

(c) Rough surface with $l_{cy} = 5\, l_{cx}$

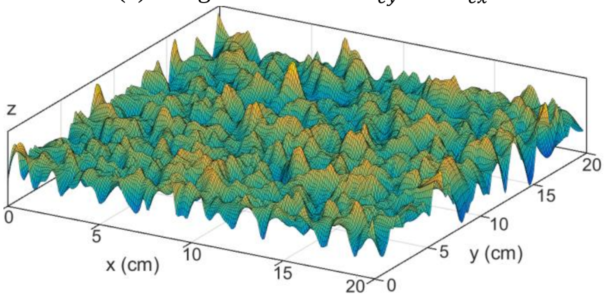

(d) Rough surface with $l_{cy} = l_{cx}$

Fig. 19. The generated rough surfaces with different correlation lengths.

For such a rough surface, the cross-polarized scattering parameters S_{12} and S_{21} have their minimum values (about -40 dB) near $\theta = 0°$ and $\theta = 90°$, i.e., when one of the dipoles is approximately parallel to the direction of the larger correlation length. They reach their maximum values (about -23 dB) near $\theta = 45°$, i.e., when each dipole makes an angle of about 45° with the direction of larger correlation length. This makes analogy with the same results concerning the sinusoidal sheet, presented in Fig. 16.

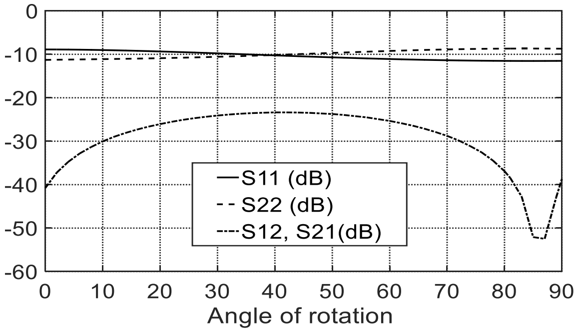

(a) $l_{cy}/l_{cx}=20$

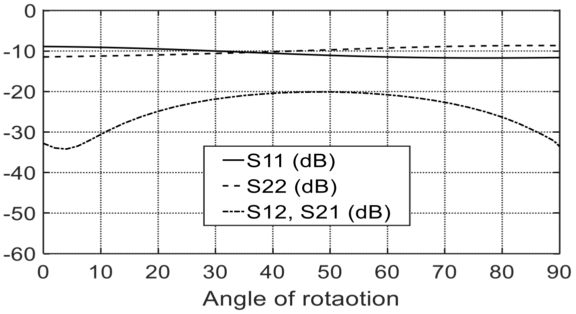

(b) $l_{cy}/l_{cx}=10$

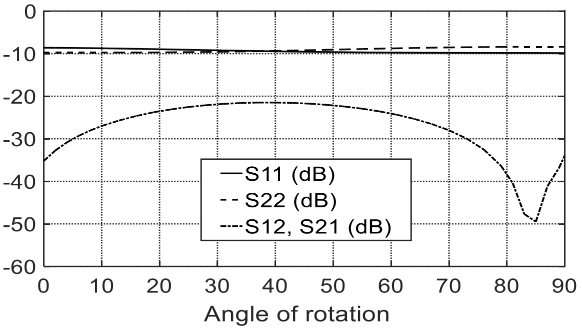

(c) $l_{cy}/l_{cx}=5$

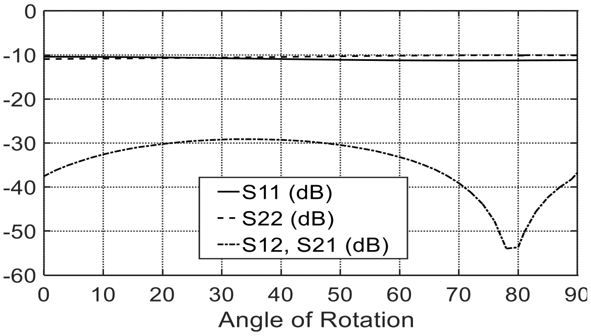

(d) $l_{cy}/l_{cx}=1$

Fig. 20. Variation of the scattering parameters with the rotational angle of the rough surface around $\boldsymbol{z}$ considering the backscattered field from a $\mathbf{20}\times\mathbf{20}$ cm rough surface of $\mathbf{l_{cx}=0.85\ cm}$, $\mathbf{h_{rms}=\ 0.4\ cm}$.

For the rough surfaces with lower ratios (l_{cy}/l_{cx}), the behaviour of both the co-polarized and cross-polarized scattering parameters with varying the rotational angle θ are significantly different from those of the sinusoidal sheet. For isotropic rough surface ($l_{cy}=l_{cx}$), as shown in Fig. 20 (d), the parameters S_{11} and S_{22} are very close to each other indicating very weak polarization discrimination of the EM backscattering from such a surface.

VII. SUMMARY AND CONCLUSION

A computationally efficient and inexpensive spatial-domain technique for generating spatially-correlated random rough surface with predetermined statistical properties using the SGF is described and examined by generating a variety of random rough surfaces with various statistical properties. It is shown that the generated rough surfaces fit the required Gaussian distribution and the other statistical properties including the mean value, the root-mean-squared height and the correlation lengths in the different directions with accuracy not less than 97%.

The importance of generating such rough surfaces for simulating the fully polarimetric land imaging systems are demonstrated by investigating the polarization properties of the near field scattered by various isotropic and anisotropic rough surfaces.

It is shown that the cross-polarized component of the near field scattered from anisotropic rough surfaces is significantly increased especially when the correlation length in one direction along the rough surface is much larger than that in the perpendicular direction.

For a rough surface with $l_{cy}\gg l_{cx}$, the cross-polarized component of the backscattered field has its minimum value near $\theta=0°$ and $\theta=90°$, i.e., when one of the dipoles is approximately parallel to the direction of the larger correlation length. They reach their maximum values near $\theta=45°$, i.e., when each dipole makes an angle of about 45° with the direction of larger correlation length.

APPENDIX A. SPECTRAL-DOMAIN METHOD OF ROUGH SURFACE GENERATION

To generate a random rough surface of dimensions $L\times L$ with resolution $N\times N$ discrete segments, the spectral-domain-method obtains the surface heights $z_{mn}=f(x_m,y_n)$ by calculating the following IDFT for each point (x_m,y_n); $m,n=1,2,..,N$ of a uniform horizontal two-dimensional grid [22]:

$$f(x_m,y_n)=\frac{1}{L^2}\sum_{p=-\frac{N}{2}}^{\frac{N}{2}-1}\sum_{q=-\frac{N}{2}}^{\frac{N}{2}-1}F(k_p,k_q)\,e^{j(k_px+k_qy)},\tag{A.1}$$

where,

$$F(k_p,k_q) = 2\pi L\sqrt{W(k_p,k_q)}$$
$$\begin{cases} \dfrac{N(0,1)+jN(0,1)}{\sqrt{2}}, & p,q \neq 0,\dfrac{N}{2} \\ N(0,1), & p,q = 0,\dfrac{N}{2} \end{cases} L, \tag{A.2}$$

where k_p and k_q are the discrete set of spatial frequencies and are expressed as:

$$k_p = \frac{2\pi p}{L}, \qquad k_q = \frac{2\pi q}{L}, \tag{A.3}$$

$W(k_p,k_q)$ is the power spectral density function of the surface and is expressed as:

$$W(k_p,k_q) = \frac{l_{cx}\, l_{cy}\, h_{rms}}{4\pi}\ \mathrm{e}^{\frac{1}{4}\left(-k_p^2 l_{cx}^2 - k_q^2 l_{cy}^2\right)}. \tag{A.4}$$

For $f(x,y)$ to be real the following condition should be satisfied:

$$F(k_p,k_q) = F^*(-k_p,-k_q). \tag{A.5}$$

REFERENCES

[1] M. Sugimoto, K. Ouchi, and Y. Nakamura, “Four-component scattering power decomposition algorithm with rotation of covariance matrix using ALOS-PALSAR polarimetric data,” *Remote Sensing*, vol. 4, no. 8, pp. 2199-2209, July 2012.

[2] A. Nascimento, A. Frery, and R. Cintra, “Detecting changes in fully polarimetric SAR imagery with statistical information theory,” *IEEE Transactions on Geoscience and Remote Sensing*, vol. 4, Sep. 2018.

[3] W. Wang, et al., “A fully polarimetric SAR imagery classification scheme for mud and sand Flats in intertidal zones,” *IEEE Transactions on Geoscience and Remote Sensing*, vol. 55, no. 3, pp. 1734-1742, Mar. 2017.

[4] Y. Zhang, Yu Li, X. San Liang, and J. Tsou “Comparison of oil spill classifications using fully and compact polarimetric SAR images,” *Applied Sciences*, vol 7, no. 2, pp. 193-214, Feb. 2017.

[5] S. Uhlmann and S. Kiranyaz “Integrating color features in polarimetric SAR Image classification,” *IEEE Transactions on Geoscience and Remote Sensing*, vol. 52, no. 4, pp. 2197-2216, Apr. 2014.

[6] L. Zhang, L. Sun, B. Zou, and W. Moon, “Fully polarimetric SAR image classification via sparse representation and polarimetric features,” *IEEE Journal of Selected Topics in Applied Earth Observations and Remote Sensing*, vol. 8, no. 8, pp. 3923-3932, Aug. 2015.

[7] B. Zhang, W. Perrie, Paris W. Vachon, X. Li, W. Pichel, J. Guo, and Y. He, “Ocean vector winds retrieval from C-band fully polarimetric SAR measurements,” *IEEE Transactions on Geoscience and Remote Sensing*, vol. 50, no. 11, pp. 4252-4261, Nov. 2012.

[8] C. Hsieh, “Energy transition for depolarized backscatter from rough surfaces,” *Journal of Microwave Power and Electromagnetic Energy*, vol. 44, no. 3, pp. 132-138, Jan. 2010.

[9] N. Sajjad, A. Khenchaf, and A. Coatanhay, “Depolarization of electromagnetic waves from sea surface,” *In OCOSS. European Conf.*, June 2010.

[10] A. Sentenac, H. Giovannini, and M. Saillard, “Scattering from rough inhomogeneous media: Splitting of surface and volume scattering,” *JOSA A*, vol. 19, no. 4, pp. 727-736, Apr. 2002.

[11] K. O’Donnell and E. Mendez, “Experimental study of scattering from characterized random surfaces,” *JOSA A*, vol. 4, no. 7, pp. 1194-1205, July 1987.

[12] M. Zubair, Z. Haider, S. Khan, and J. Nasir, “Atmospheric influences on satellite communications,” *Przeglad Elektrotechniczny*, vol. 87, no. 5, pp. 261-264, Jan. 2011.

[13] G. Wolosinski, V. Fusco, and P. Rulikowski, “Broadband dual-polarized antenna with high port isolation and polarization purity,” *In Antennas and Propagation (APSURSI), IEEE International Symposium on*, pp. 1581-1582, June 2016.

[14] C. Holler, A. Taylor, M. Jones, O. King, S. Muchovej, M. Stevenson, R. Wylde, et al., “A circularly symmetric antenna design with high polarization purity and low spillover,” *IEEE Transactions on Antennas and Propagation*, vol. 61, no. 1, pp. 117-124, Jan. 2013.

[15] J. M. Ralston and E. L. Ayers, “Antenna effects on polarimetric imagery in ultrawide synthetic aperture radar,” *Institute for Defense Analyses*, No. IDA-D-2735, Alexandria, Virginia Sep. 2002.

[16] Y. Cocheri and R. Vauzelle, “A new ray-tracing based wave propagation model including rough surfaces scattering,” *Progress In Electromagnetics Research*, vol. 75, pp. 357-381, 2007.

[17] S. Coons, “Surfaces for computer aided design of space forms,” *Massachusetts Inst. of Tech. Cambridge Project Mac*, no. MAC-TR-41, June 1967.

[18] M. Escobar and A. Meyerovich, “Applications and identification of surface correlations,” *arXiv Preprint arXiv:1404.1291*, vol. 2, Apr. 2014.

[19] C. Mack, “Generating random rough edges, surfaces and volumes,” *Applied Optics*, vol. 52, no. 7, pp.1472-1480, 1 Mar. 2013.

[20] A. Francisco and N. Brunetière, “A hybrid method for fast and efficient rough surface generation,” *Proceedings of the Institution of Mechanical Engineers*, vol. 230, no. 7, pp. 747-768, July 2016.

[21] K. Uchida, J. Honda, and K. Y. Yoon, “An algorithm for rough surface generation with inhomogeneous parameters,” *Journal of Algorithms & Computational Technology*, vol. 5, no. 2, pp.

259-271, June 2011.

[22] Y. Kuga and P. Phu, "Experimental studies of millimeter - wave scattering in discrete random media and from rough surfaces," *Progress In Electromagnetics Research*, vol. 14, no. 7, pp. 37-88, 1996.

[23] K. Uchida, M. Takematsu, and J. Honda, "A discretization criterion for generating random rough surface based on convolution method," *Complex, Intelligent and Software Intensive Systems (CISIS), Eighth International Conference, IEEE*, pp. 307-312, July 2014.

[24] T. Jacobs, et al., "Quantitative characterization of surface topography using spectral analysis," *Surface Topography: Metrology and Properties*, Vol. 5, no. 1 p. 013001, Jan. 2017.

[25] S. Abraham and M. Golay, "Smoothing and differentiation of data by simplified least squares procedures," *Analytical Chemistry*, vol. 36 no. 8, pp. 1627-1639, July 1964.

[26] R. Torala and A. Chakrabarti, "Generation of Gaussian distributed random numbers by using a numerical inversion method," *Computer Physics Communications*, vol. 74, no. 3, pp. 327-334, Mar. 1993.

[27] D. Thomas, W. Luk, P. Leong, and J. Villasenor, "Gaussian random number generators," *ACM Computing Surveys*, vol. 39, no. 4, p. 11, Nov. 2007.

[28] R. Ritabrata, "Comparison of Different Techniques to Generate Normal Random Variables," *Stochastic Signals and Systems (ECE 330: 541)*, Rutgers, The State University of New Jersey, Nov. 2002.

FEMC Performance of Pyramidal Microwave Absorber using Sugarcane Baggasse and Rubber Tire Dust at 1 GHz to 18 GHz Frequencies

Liyana Zahid [1], Muzammil Jusoh [2*], R.Badlishah Ahmad [3], Thennarasan Sabapathy [2], Mohd Fareq Malek [4], Muhammad Ramlee Kamarudin [5], Mohd Najib Yasin [6], and Mohamed Nasrun Osman [2]

[1] Department of Electronic, Faculty of Engineering Technology, Universiti Malaysia Perlis (UniMAP)
Kampus UniCITI Alam, Sg Chuchuh, Padang Besar, 02100 Perlis
liyanazahid@unimap.edu.my

[2,6] Bioelectromagnetics Research Group (BioEM)
[2] School of Computer and Communication Engineering, [6] School of Microelectronic Engineering
Universiti Malaysia Perlis (UniMAP), Kampus Pauh Putra, Perlis, Malaysia
muzammil@unimap.edu.my*, thennarasan@unimap.edu.my, najibyasin@unimap.edu.my

[3] Faculty of Informatics and Computing
Universiti Sultan Zainal Abidin, 22200 Besut, Terengganu, Malaysia
badli@unisza.edu.my

[4] Faculty of Engineering and Information Sciences, University of Wollongong in Dubai, Blocks 5, 14 & 15
Dubai Knowledge Park - Dubai - United Arab Emirates
MohamedFareqMalek@uowdubai.ac.ae

[5] Centre for Electronic Warfare, Information and Cyber (EWIC), Cranfield Defense and Security
Cranfield University, College Rd, Cranfield MK43 0AL, UK
Ramlee.Kamarudin@cranfield.ac.uk

Abstract ─ The solid, geometrically tapered microwave absorbers are preferred due to their better performance. The goal of this study is to design absorbers that can reduce the electromagnetic reflections to less than −10 dB. Two waste materials of sugarcane bagasse and rubber tire dust in the powder form were used to fabricate independent samples in the pyramidal form. This paper presents the complex permittivity measurements of sugarcane bagasse and rubber tire dust materials. These two materials are found to be potential absorbing materials in microwave frequency to allow absorption of microwave EMI energy. The materials were combined and fabricated in the composite structure. A measurement system using open- ended coaxial probe method was used for characterizing the dielectric properties of the materials in the range of 1 to 18 GHz microwave frequencies. The dielectric property was used to compare the propagation constants of the material. Comparison of the results proved that these two materials have industrial potential to be fabricated as solid absorbers.

Index Terms ─ Microwave absorber, open-ended coaxial probe, permittivity.

Submitted On: January 25, 2018
Accepted On: December 25, 2018

I. INTRODUCTION

In line with the rapid growth of microwave device fabrication technology, communication systems can now operate at higher and broader frequencies. The requirement of the electromagnetic compatibility (EMC) applications such as microwave absorbing material within the microwave signal’s frequency range of kilohertz (kHz) to gigahertz (GHz) have incredibly extended the applications in GHz range for mobile phones and local area network and radar systems, among others [1], [2]. Electromagnetic interference is the degradation which occurs in the performance of a device, equipment, or a system caused by an electromagnetic disturbance. Electromagnetic disturbance can be caused by an electromagnetic noise, or an unwanted signal, or a change in the propagation medium itself [3]. The effects of EMI include malfunction, or even the permanent damage to the electronic devices which may lead to permanent failure [4]–[11]. Therefore, absorbers are used in a wide range of applications to eliminate stray or unwanted radiation that could interfere with a system’s operation. Previous research showcased several materials which exhibited the potential applications in the design and development of the microwave absorber. Carbon loaded plaster, carbon black, iron powder, aluminum flakes and copper are some of such materials [12]. However, the principle element in the dielectric absorber is the carbon itself. The carbon is used as the dielectric loss adder in lossless polymer matrix materials. This process is also known as carbon consumption and it is used in the microwave industry, especially in the production of foam based absorbers. In humid surroundings, the carbon is chosen due to its resistance to corrosion [13]. Besides, carbon has less density as compared metal; hence, it is preferred in the fabrication of the absorbers [14]–[16].This project is focused on microwave absorber using sugarcane bagasse and rubber tire dust (SCBRTD) as the main composite materials to design and develop the absorber. The adding of filler, namely the rubber tire dust increases the performance of the microwave absorber. These absorbers were designed based on wave attenuation and depth of penetration data. Additionally, their EMC performance was evaluated in terms of bi-static reflectivity performance. The different concentrations of the fillers were measured, and the reflectivity was found to be better than -20 dB when the amount of rubber tire dust was increased.

II. MICROWAVE ABSORBER PROPERTIES

In this work, sugarcane (*Saccarhum officinarum*) bagasse was used as the main material to design the microwave absorber. Sugarcane bagasse is a residue produced in large quantities by sugar industries. In general, 1 ton of sugarcane generates 280 kg of bagasse, the remaining fibrous by-product of sugarcane after sugar extraction [17]. Sugarcane bagasse is also a potential material for the pyramidal microwave absorbers used in anechoic chamber to eliminate signal reflections [18]. The large percentage of carbon that is produced naturally in sugarcane bagasse can provide good reflectivity performance [19]. The first stage of this study involved the preparation of samples for the dielectric measurement.

In this work, the fillers are the agricultural waste which is sugarcane bagasse (SCB) and rubber tire dust (RTD) from tire wear whereas the polymer matrix is unsaturated Polyester Resin RP9509 (UPR) which is a rigid, flexible and electromagnetically transparent polymer. UPR is one type of the thermosetting polymers and it is needed to be added with a binder to start the cross linking process. Methyl ethyl ketone peroxide (MEKPO) which is in liquid state was being used as the binder with UPR. In the composites with more filler, the composites seem to be more compact and have less air space.

Dielectric properties of the materials in a broad frequency range of 1.0 GHz to 18 GHz were investigated. The samples were fabricated in composite form. There are two methods of measuring the dielectric properties: the coaxial probe technique and transmission line method. Figure 1 shows the fabricated pyramidal absorbers using mold.

(a) (b)

Fig. 1. Fabricated pyramidal parts of the absorbers: (a) Sugarcane Bagasse pyramidal Microwave Absorber without the square base part with height of 13 cm, and (b) Rubber Tire Dust pyramidal Microwave Absorber without a square base part with height of 13 cm.

A. Frequency spectrum, dielectric properties and wave propagation properties of the material

In this work, the results of dielectric characterization, along with the wave propagation characteristics of the composite samples composed of lossy sugarcane bagasse and lossy rubber tire dust are presented. Sugarcane bagasse and rubber tire dust are dielectric materials with $\mu_r = 1+0j$; therefore, only relative complex permittivity was measured, and the results are presented in this section. In dielectric materials, the dielectric constant and the dissipation factor of energy are the main properties that enable them to be applicable for microwave absorbers. In designing the absorber materials, equation (1) can be used to determine their absorption capability, which relies on the conductivity, dielectric loss, or magnetic loss of the absorber materials [20]. The dielectric properties are essential to determine the materials' performance in the context of microwave absorption. Permittivity is a function of frequency that could vary significantly over a small range [21]:

$$A = \frac{1}{2}\,\sigma E^2 + \frac{1}{2}\omega\varepsilon_0\varepsilon_R\,E^2 + \frac{1}{2}\omega\mu_0\mu_R H^2, \qquad (1)$$

where A (W/m3) is the electromagnetic energy absorbed per unit volume, E (V/m) is the electric field strength of the electromagnetic signal, H (A/m) is the magnetic field strength of the electromagnetic signal, σ (S/m) is the conductivity of the material, ω (sec-1) is the angular speed of the electromagnetic wave, ε_0 is the dielectric permittivity of vacuum, ε_R is the complex permittivity of the material, μ_0 is magnetic permeability of the vacuum and μ_R is the complex permeability of the material.

Open-ended coaxial probe has been used for measurements on a number of agricultural products such as rice husk and grain [22],[23]. Calibration is required before the measurements are carried out by connecting the coaxial probe with open and broadband load as referred in Fig. 4 [24], [25]. This method consists of a network analyzer and a coaxial probe. It includes a mechanical load for short circuit calibration, air for open calibration and water (at room temperature) as a broadband load. Instead of using water as a broadband load, any solid dielectric material with known dielectric properties can also be used as the broadband load. However, the dielectric properties of the known materials in broad frequency ranges are unavailable. Many researchers have used this calibration technique due to the unavoidable air gap at the probe-sample interface to determine the dielectric properties of the solid samples [26]–[28].

At first, the samples were fabricated in three categories, namely, pure sugarcane bagasse, pure rubber tire dust and composite of lossy filler of sugarcane bagasse and rubber tire dust. The permittivity and permeability of the samples were determined by using the transmission line rectangular waveguide technique. Full 2-port calibration or transmission-reflection-load (TRL) calibration is essential for accurate phase measurements [29]. It is imperative that a sample fit inside the coax or waveguide since a poorly fit sample will not yield good results. As frequencies extend into millimeter waves, calibration and sample fit become even more critical due to the short wavelength. Magnetic constant and magnetic loss factor of the sugarcane bagasse (SCB), rubber tire dust (RTD) and sugarcane bagasse rubber tire dust (SCBRTD) composite samples were measured by using this technique. The results showed that relative magnetic properties of the tested materials were nearly equal to free space, $\mu_r = 1 - j0$. Therefore, these materials are non-magnetic materials. Figures 2 and 3 show the magnetic constant and magnetic loss factor of the material.

Since the materials used in this work are dielectric materials, the loss mechanism is purely dielectric. The loss can arise from a variety of sources within the dielectric. The commercial dielectric absorbers are usually made with low cost foam but can also be used with elastomers. Absorbers are characterized by their electric permittivity and magnetic permeability. Permittivity is a measure of the material's effect on the electric field in the electromagnetic wave. It arises from the dielectric polarization of the material.

The quantity $\varepsilon^{'}$ is sometimes called the dielectric constant, which is something of a misnomer when applied to absorbers as $\varepsilon^{'}$ can vary significantly with frequency. The quantity $\varepsilon^{"}$ is a measure of the attenuation of the electric field caused by the material. So, the dielectric constant of SCB, RTD and composite samples composed of SCB and lossy RTD need to be defined first to identify the material performance. Figure 4. shows the schematics of the experimental setup, indicating the field infringement at the open end of the probe due to the abrupt change in impedance.

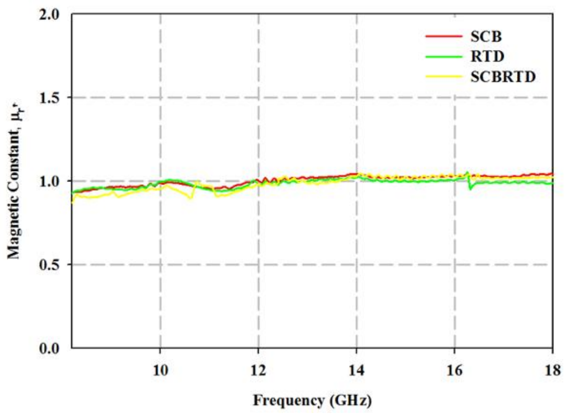

Fig. 2. Magnetic constant of the material.

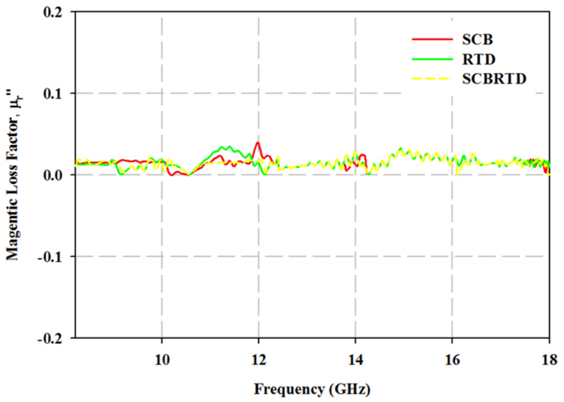

Fig. 3. Magnetic loss factor of the material.

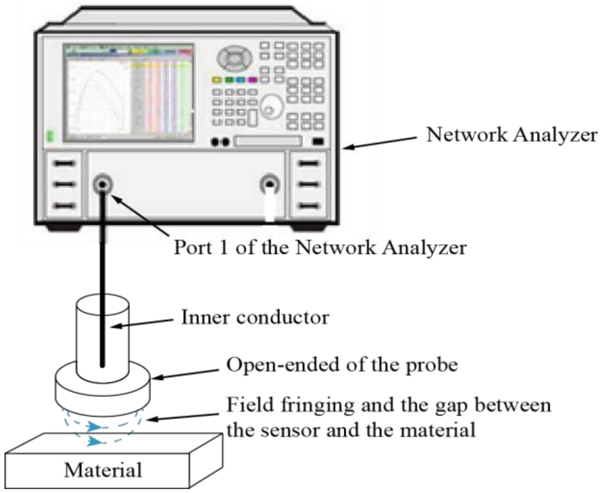

Fig. 4. Diagram of the experimental setup, showing field infringement at the open end of the probe due to abrupt change in impedance.

The complex dielectric properties of a medium can impact the propagation parameters of an electromagnetic

(EM) plane wave in defining the wave behavior in that medium. Absorbers are usually composed of materials that are affected by dissipation of loss. Hence, they attenuate the propagating wave inside the material. The impedance of electromagnetic wave propagating in free space is:

$$\eta_o = \sqrt{\frac{\mu_o}{\varepsilon_o}}, \quad (2)$$

where

μo =4π×10-7 Henry/m,
ε0 =8.854 ×10-12 Farad/m.

III. GEOMETRIC TAPERING OF LOSSY MATERIAL

A. Solid pyramidal microwave absorber

Impedance at each interface can be found by using the propagation constant and the characteristic impedance of each layer, according to the following transmission line theory:

$$Z_i = \eta_i \frac{\eta_{i+1} + \eta_i tanh(\gamma_i d_i)}{\eta_i + \eta_{i+1} tanh(\gamma_i d_i)}. \quad (3)$$

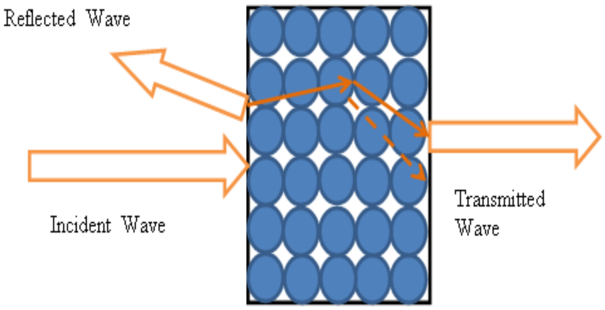

Fig. 5. Wave transmission into the absorber material.

Figure 5 shows the wave transmission into the absorber material. If the same wave interacts with a lossy dielectric medium such as SCB and RTD, the characteristic impedance of the medium can be expressed as:

$$\eta_m = \frac{\eta_o}{\sqrt{\varepsilon'_r - j\varepsilon''_r}}. \quad (4)$$

The impedance lies in the discontinuity at the interface of the air-dielectric (η0 ≠ ηm); so, the wave energy is reflected on the source medium. The remaining propagated energy within the lossy material can be expressed with a complex wave propagation constant, as follows:

$$\gamma = \left(\frac{2\pi}{\lambda}\right)\sqrt{\varepsilon'_r - j\varepsilon''_r}. \quad (5)$$

α is the real and β is the imaginary part of the propagation constant, which resembles the phase shift per unit length in the medium and the speed at which the signal was propagated. Hence, α and β express the dielectric properties of the material, as follows:

$$\alpha = \frac{2\pi}{\lambda}\sqrt{\frac{\varepsilon'_r}{2}(\sqrt{1 + tan^2\delta}} - 1, \quad (6)$$

$$\beta = \frac{2\pi}{\lambda}\sqrt{\frac{\varepsilon'_r}{2}(\sqrt{1 + tan^2\delta}} + 1. \quad (7)$$

The function of an absorbing material is to attenuate the EM electromagnetic wave and prevent the EM wave from being reflected or transmitted pass through the material. The characteristic impedance is important in determining the performance of the absorbing material. Reflection can happen at the air-absorber interface due to the impedance mismatch between free space and characteristic impedance of the material. The reduction of the reflected wave from the front layer or surface can occur when the impedance of the material matches the impedance of free space (377Ω). The impedance of a material is given by the following relation:

$$Z = 120\pi\sqrt{\mu_r/\varepsilon_r}. \quad (8)$$

From this equation, it can be clearly inferred that the basic parameters for the absorption characteristics depend on permittivity and permeability of material. At microwave frequencies, when a dielectric material is exposed to a time varying electromagnetic field, the electric field component of the wave polarizes the molecules [30].

B. Wave propagation properties and dielectric properties of SCBRTD

The characteristic impedance, depth of penetration and phase constant of the materials are calculated to determine the wave propagation properties of the materials. The fraction of the incident wave energy (R) reflected off the interface of the dielectric material depends upon the characteristic impedance of the material. It should be noted that greater values of α are desired for absorbers, but these values are important only for the attenuation of the wave fraction that enters the material. Therefore, the characteristic impedance of the target medium is a very important parameter in the selection of the appropriate filler loading.

Five composite samples were fabricated in different compositions of SCB and RTD. Figure 6 below shows the dielectric constant of five samples with different percentages of fillers (sugarcane bagasse and rubber tire dust (SCBRTD)).

The complex permittivity increased when there is an increment in percentage of fillers in the composite samples. The addition of sugarcane bagasse and rubber tire dust increased the number of dipoles as they are lossy dielectric fillers. The electrostatic dipole energy and capacitance of the medium is increased when the energy from the incident wave is stored in these dipoles. Therefore, the dielectric constant increased with the increasing filler loading. From this result, the attenuation constant can be determined to examine the wave propagation into the material. Figure 7 shows the attenuation constant of the material for different filler loadings.

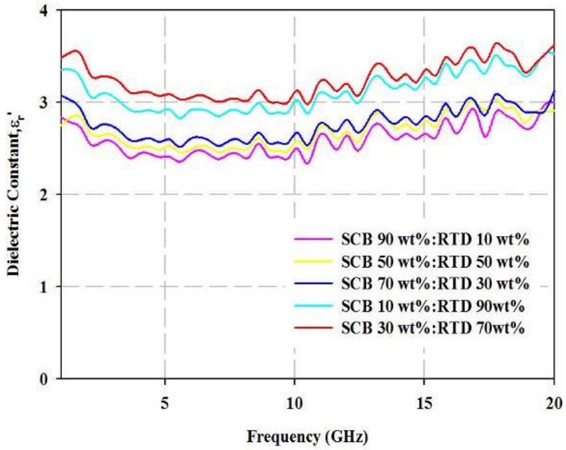

Fig. 6. Dielectric constant of different percentage of fillers (sugarcane bagasse mixed with rubber tire dust).

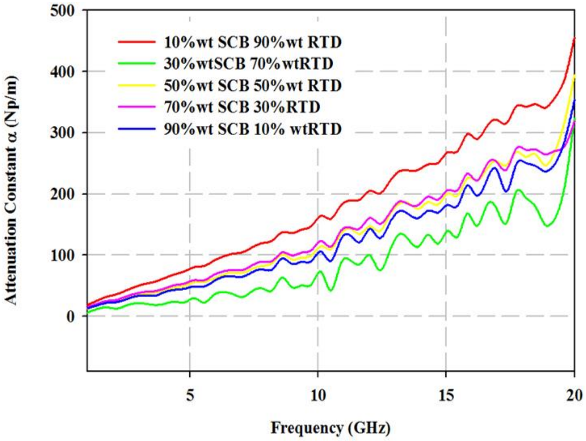

Fig. 7. Attenuation constant of the material for different filler loading.

Attenuation constant is inversely proportional to the frequency. The penetration depths were lower at high frequencies and become higher at lower frequencies. At high frequencies, the wavelength was shorter; so, the wave cannot penetrate deep into the medium due to the large attenuation offered by the medium as the reason. Figure 8 shows the penetration depth of the material. The values are calculated using the following formula:

$$D_p = \frac{1}{2\alpha}. \tag{9}$$

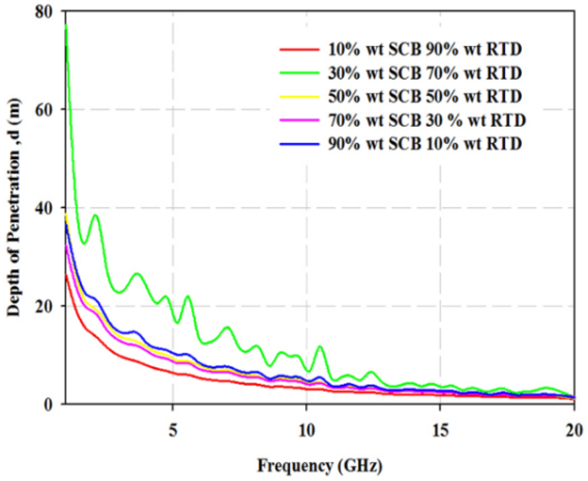

Fig. 8. Depth of material penetration.

Table 1 shows the measured relative values of the complex permittivity and magnitude of normalized characteristic impedance |Za| for different SCB and RTD filler compositions.

Table 1: Values of complex permittivity and magnitude of normalized impedance of the composite of sugarcane bagasse and rubber tire dust

Samples		Properties	Average
SCB (wt %)	RTD (wt %)		
10	90	εr’	3.12
		εr”	0.24
		tan δ	0.005
		| Z |	207 Ω
30	70	εr’	3.25
		εr”	0.12
		tan δ	0.003
		| Z |	250 Ω
50	50	εr’	2.69
		εr”	0.22
		tan δ	0.007
		| Z |	230 Ω
70	30	εr’	2.76
		εr”	0.18
		tan δ	0.005
		| Z |	227 Ω
90	10	εr’	2.60
		εr”	0.15
		tan δ	0.004
		| Z |	234 Ω

Impedance discontinuity ($\Delta Z = 377 - Za$) is the least for 30 wt% of SCB loading; however, in this case, the value of the tangent loss is also minimum. This shows the maximum transmission of the signal with less attenuation and it is not preferred in the case of absorbers. An absorber must have a lossy medium with minimum impedance discontinuities at the interfaces. The best value of tangent loss is (0.007) when 50 wt% of SCB and RTD filler are used at the impedance of 230.

IV. MEASUREMENT OF ANECHOIC PROPERTIES OF PYRAMIDAL MICROWAVE ABSORBER

A. Method for reflectivity measurement

Commercially, the geometrically tapered (GT) absorbers can be found in a wedge or pyramidal shapes in truncated or non-truncated geometries with different heights. They are designed to transform the high impedance (377 Ω) of the incident wave to a very low impedance of the metal. The pyramidal absorbers have the most preferred shape for the anechoic chambers due to their enhanced ability to transform the impedance in wide bands of frequencies smoothly. This pyramidal shape was developed so that there is a gradual transition in impedance from air to the tip of the absorber and to the base of the pyramidal. In this work, the samples were fabricated in pyramidal microwave absorber (PMA) shape using the lossy filler of RTD and the SCBRTD PMA. In the case of the pyramidal absorbers, the broadband performance was achieved by the wave trapping. In other words, there are multiple reflections of the high frequency waves in-between the adjacent pyramids and the wave attenuation (or absorption) of the low and high frequency waves within the pyramidal lossy material [31]. The energy of the wave is lost in both the processes and a very weak signal is returned to the incident medium. Figure 9 shows the schematics setup for the measurement of reflectivity of the absorber using the S_{21} parameter.

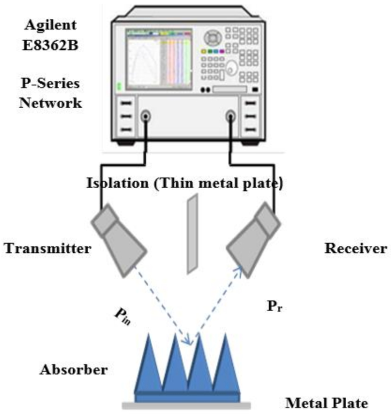

Fig. 9. Diagram of test setup for the reflectivity measurement of the absorber by using the S21 parameter.

B. Rubber Tire Dust (RTD) Pyramidal Microwave Absorber

The addition of RTD filler in SCB composite can increase the dielectric constant of the composite because of its high dielectric value. Based on the numerical study in X band and Ku Band frequency, the addition of rubber tire dust increased the reflectivity performance of the absorber to less than -10 dB (90% of absorption). Therefore, in this section, the frequency spectrum of the free-space, bi-static, reflectivity measurements for the pure rubber tire dust in an array of 4×4 pyramids are presented to investigate the performance of rubber tire dust in solid pyramidal form. Figure 10 shows the bi-static, normal reflectivity performance of a RTD PMA with reference to a metal plate in frequency range of 1 GHz to 18 GHz. The investigation was performed with the presence and absence of the base part.

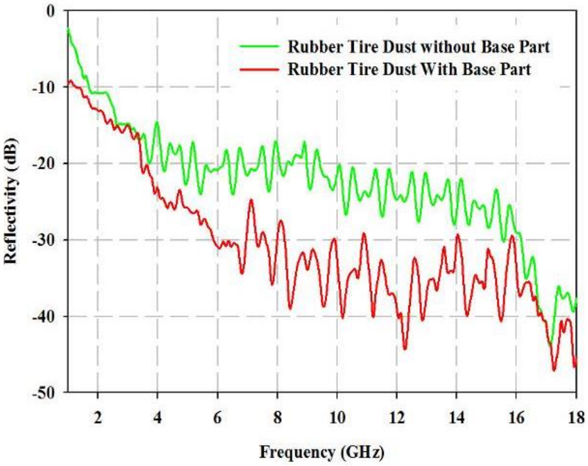

Fig. 10. Bi-static, normal reflectivity performance of a RTD PMA with reference to a metal plate in a frequency range of 1 to 18 GHz.

All the reflectivity measurements were done with reference to a metal plate that was used as a perfect reflector. It is observed that the values of the reflectivity was not below - 10 dB in the frequency range of 1 GHz to 2 GHz; however, in higher frequency (2 GHz to 18 GHz), the reflectivity can be achieved up to -45 dB (99.999% of absorption). The pyramidal part plays its role along with the base part and the reflectivity values were found to be lower than -20 dB from 4 GHz to 18 GHz. The best reflectivity performance of -30 dB to -45 dB is observed in the frequency range of 8 GHz-18 GHz of the X-band and Ku-Band. From the result, it is obvious that when the pyramidal part is placed along with the base part, there is improvement in the performance of the reflectivity of PMA. All the values of reflectivity were better than -10 dB for 1 GHz to 18 GHz frequency range.

In order to identify the use of those composite materials in microwave applications, their electromagnetic properties need to be defined first. In dielectric absorbers, there is no magnetic loss component involved. Therefore, the absorption of the dielectric absorber depends on dielectric properties of the absorber. The characteristic impedance (η_m) of a dielectric material will match with the free space impedance (η_0) only when $\mu_r = 1 + jo$, $\varepsilon'_r = 1$ and $\varepsilon''_r = 0$. Under these conditions, no partial reflection of the wave exists at the air-dielectric interface and the entire wave will be transmitted in the dielectric medium. As the SCB and RTD-based absorbers are composed of non-magnetic lossy materials with $\varepsilon'_r > 1$ and $\varepsilon''_r > 0$, their characteristic impedances will never match the free space impedance. However, the input impedance, Z_{in} that will be experienced by the incoming wave at the interface can be matched to the free space wave impedance.

Input impedance is a function of absorber's geometry, dielectric properties as well as the frequency of the incident wave. Therefore, the impedance will be matched only at certain frequencies and the resonance behavior will be observed at those (resonant) frequencies.

The different fillers' loadings can affect the performance of a microwave absorber. In Section 3.2, the dielectric properties and the wave propagation of the different weight percentage of sugarcane bagasse and rubber tire dust are discussed. There are five different weight percentages for each filler (SCB and RTD). Figure 11 shows the bi-static, normal reflectivity performance of a different filler loading of RTD and SCB PMA with reference to a metal plate in the frequency range of 1 GHz to 18 GHz. The large attenuation value occurred when 30 wt% SCB and 70 wt% RTD were used. The reflectivity of less than -25 dB to -40 dB (99.99% of absorption) was achieved for the frequency range of 1 GHz to 12 GHz. At 18 GHz, the reflectivity was approximately -42 dB.

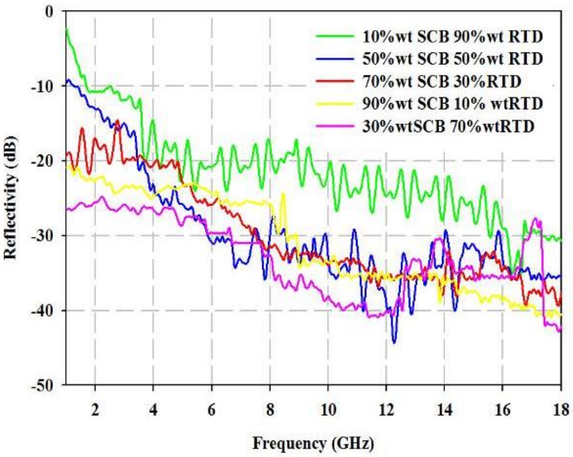

Fig. 11. Bi-static, normal reflectivity performance of a different filler loading of RTD and SCB PMA with reference to a metal plate in frequency range of 1 GHz to 18 GHz.

When 50 wt% for SCB and RTD was being used respectively, the result indicated better reflectivity of -10 dB for the range of 2 GHz to 4 GHz frequencies. However, at X band and Ku Band frequencies (8.2 GHz to 18 GHz), the reflectivity was much better, from - 30 dB to -40 dB. Poor performance was exhibited at the frequency range of 1 GHz to 2 GHz when 10 wt% SCB and 90 wt% RTD were measured. However, the rest of the frequency showed good reflectivity, with better than -10 dB and from the frequency range of 4 GHz to 18 GHz, the reflectivity was better than -20 dB to -30 dB. The composition of 90 wt% SCB and 10 wt% of RTD showed a better reflectivity of -20dB at low frequency. In the frequency range of 8.0 GHz to 18 GHz, the reflectivity was in the range between -30 to -40 dB. Different concentrations of filler loadings affected the performance of the microwave absorber. In this case, 30:70 SCBRTD demonstrated better reflectivity at 1 GHz to 12 GHz frequency range.

V. CONCLUSION

In this paper, we have described the experimental investigation to fabricate a microwave absorber for future EMC solutions. In addition, we have included the experimental measurement of dielectric properties and the performance of the proposed materials to be used as absorber. The experimental results show that these materials can be used to fabricate the microwave absorber to provide an anechoic surrounding (non-reflective) isolated from the waves entering from the surroundings and is able to absorb completely the reflections of electromagnetic waves. The design that has been investigated in this work was pyramidal solid shape and the results show that their performance was better than -10 dB, which indicates almost 90% of the incident microwave energy absorption. Based on the permittivity result, SCB and RTD materials can be considered as dielectric and lossy materials. The real part of permittivity has been found to be strongly dependent on frequencies. When the frequencies are increased, the permittivity values decrease. The imaginary part of the permittivity also showed variation with frequency, although not parallel to the real permittivity. From the permittivity, the propagation constant including attenuation constant and the depth of penetration were investigated. From the calculated wave impedance of the material result, the composition of 50 wt% of SCB and 50 wt% of RTD revealed to have the highest lost tangent and less impedance discontinuities, indicating its potential to be a good absorbent material. The reflectivity of the materials was analyzed for varying thickness values of the samples. When the RTD filler was added to the SCB composite, the reflectivity of the absorber achieved was better than -10 dB. The usage of agricultural waste materials such as SCB could be a potential solution in developing a microwave absorber that helps to reduce agricultural wastes that are usually burned off, which in turn leads to the emission of CO2 gas in the atmosphere and causes harm to the ecology. The cost of the pyramidal microwave absorber can be reduced by using SCB as the main material. An effort was made to adopt simple and low cost methods for the fabrication and evaluation that can easily be repeated and arranged on laboratory scale. This alternate use of sugarcane waste, or bagasse, reduce the amount of agricultural waste that contaminating the environment, so here in Perlis, Malaysia the sugarcane bagasse is available for free. The methods that were used in this study, to fabricate and measure the dielectric properties and performance of the pyramidal impedance graded absorber shape (15 cm height) samples were fabricated manually by using the open-mold. This SCB-based material is an eco-friendly raw material in the microwave absorber fabrication industry. The pyramidal microwave absorber made with waste materials (SCB and RTD) achieves 20dB of reflectivity which corresponds to the absorption of ~99.99 % of the waves.

ACKNOWLEDGEMENTS

This work is partly supported by the Research Management and Innovation Centre of Universiti Malaysia Perlis, under short research grant scheme (STG 9001-00569).

REFERENCES

[1] M. S. Kim, E. H. Min, and J. G. Koh, “Comparison of the effects of particle shape on thin FeSiCr electromagnetic wave absorber,” *J. Magn. Magn. Mater.*, vol. 321, no. 6, pp. 581-585, Mar. 2009.

[2] C. Y. Feng, Y. B. Qiu, and T. Shen, “Absorbing properties and structural design of microwave absorbers based on carbonyl iron and barium ferrite,” *J. Magn. Magn. Mater.*, vol. 318, pp. 8-13, 2007.

[3] W. P. Kodali, *Engineering Electromagnetic Compatibility: Principles, Measurements, Technologies, and Computer Models*. 2nd Edition. 2001.

[4] F. Al-Ghamdi and A. El-Tantawy, “New electromagnetic wave shielding effectiveness at microwave frequency of polyvinyl chloride reinforced graphite/copper nanoparticles,” *Compos. Part A*, vol. 41, pp. 1693-1701, 2010.

[5] J. K. Gooch and J. W. Daher, *Electromagnetic Shielding and Corrosion Protection for Aerospace Vehicles*. New York : Springer, 2007.

[6] D. Morgan, *A Handbook for EMC Testing and Measurement*. (L. P. Peregrinus., Ed.), 1994.

[7] R. Schmitt, *Electromagnetics Explained: A Handbook for Wireless/RF, EMC, and High-Speed Electronics*. Elsevier Science. USA, 2002.

[8] X. C. Tong, “Advanced materials and design for electromagnetic interference shielding advanced materials and design for electromagnetic interference shielding,” 2009.

[9] I. A. Zhang, W. Xu, Y. Yuan, L. Ca, and J. Zhang, “Microwave absorption and shielding property of composite with FeSiAl and carbonous materials as filler,” *J. Mater. Sci. Technol.*, vol. 28, no. 10, pp. 913-919, 2012.

[10] T. Williams, *EMC for Product Designers*. 3rd ed., 2001.

[11] P. D. Ch and T. E. Ch, “Technical notes theory and application of RF/microwave absorbers.”

[12] W. H. Emerson, “Electromagnetic wave absorbers and anechoic chambers through the years,” *IEEE Trans. Antennas Propag.*, vol. AP-21, no. 4, pp. 484-490, 1973.

[13] M. Sharon, D. Pradhan, R. Zacharia, and V. Puri, “Application of carbon nanomaterial as a microwave absorber,” *J. Nanosci. Nanotechnol.*, vol. 5, no. 12, pp. 2117-2120, Dec. 2005.

[14] J. Kim, S. Lee, and C. Kim, “Comparison study on the effect of carbon nano materials for single-layer microwave absorbers in X-band,” *Compos. Sci. Technol.*, vol. 68, no. 14, pp. 2909-2916, Nov. 2008.

[15] B. K. Chung and H. T. Chuah, “Design and construction of a multipurpose wideband anechoic chamber,” *IEEE Antennas and Propagation Magazine*, pp. 41-47, 2003.

[16] R. C. M.N. Iqbal, F. Malek, S. H. Ronald, M. Shafiq, and K. M. Juni, “A study of the EMC performance of a graded-impedance, microwave, rice-husk absorber,” *Prog. Electromagn. Res.*, vol. 131, pp. 19-44, July 2012.

[17] A. Hasnain, B. M. Hafiz, M. I. Imran, A. A. Takiyuddin, A. Rusnani, and O. M. Khusairi, “Development of an economic and effective microwave absorber,” in *Asia-Pacific Conference on Applied Electromagnetics Proceedings*, no. 1, pp. 1-5, 2007.

[18] Z. Liyana, F. Malek, H. Nornikman, N. A. M. Affendi, L. Mohamed, N. Saudin, and A. A. Ali, “Investigation of sugar cane bagasse as alternative material for pyramidal microwave absorber design,” pp. 66-70, 2012.

[19] L. Huang and H. Chen, “Multi-band and polarization insensitive metamaterial absorber,” *Prog. Electromagn. Res.*, vol. 113, pp. 103-110, 2011.

[20] “Sony’s Electromagnetic Wave Absorber Reduces EMC and SAR Problems.”

[21] A. Sharma and M. N. Afsar, “Accurate permittivity and permeability measurement of composite broadband absorbers at microwave frequencies,” no. 1, 2011.

[22] H. N. F. Malek, E. M. Cheng, O. Nadiah, P. J. S. M. Ahmed, M. Z. A. Abd Aziz, A. R. Osman, M. N. T. A. A. H. Azremi, and A. Hasnain, “Rubber tire dust-rice husk pyramidal microwave absorber,” *Prog. Electromagn. Res.*, vol. 117, pp. 449-477,

Mar.2011.

[23] S. O. Nelson, “Fundamentals of dielectric properties measurements and agricultural applications,” vol. 44, no. 2, pp. 98-113, 2010.

[24] A. Note, “Agilent basics of measuring the dielectric properties of materials.”

[25] I. Agilent Technologies, “Agilent basics of measuring the dielectric properties of materials,” 2006.

[26] S. O. Nelson, W. Guo, S. Trabelsi, and S. J. Kays, “Dielectric spectroscopy of watermelons for quality sensing,” *Meas. Sci. Technol.*, vol. 18, no. 7, pp. 1887-1892, July 2007.

[27] P. Savi, M. Miscuglio, M. Giorcelli, and A. Tagliaferro, “Analysis of microwave absorbing properties of epoxy MWCNT composites,” vol. 44, pp. 63-69, Oct. 2014.

[28] S. J. K. W.-C. Guo, S. O. Nelson, and S. Trabelsib, “10–1800-MHz dielectric properties of fresh apples during storage,” *J. Food Eng.*, vol. 83, no. 4, pp. 562-569, Dec. 2007.

[29] T. E. Ch, “Tech Theory and Application of RF/Microwave Absorbers.”

[30] M. Hotta, M. Hayashi, M. T. Lanagan, and D. K. Agrawal, “Complex permittivity of graphite, carbon black and coal powders in the ranges of X-band frequencies (8. 2 to 12.4 GHz) and between 1 and 10 GHz,” vol. 51, no. 11, pp. 1766-1772, 2011.

[31] K. Malaric, *Emi Protection for Communication Systems*. Norwood, MA, USA : Artech House, 2009.

Liyana Binti Zahid received the B.Eng. (Hons.) and Ph.D. degrees in Communication Engineering from University Malaysia Perlis (UniMAP), in 2012 and 2017 respectively. She has been a Senior Lecturer with the Faculty of Engineering Technology (Electronic Department), UniMAP, Malaysia since 2017. Her current research interests include RF and microwave technologies.

Muzammil Jusoh is currently working with Universiti Malaysia Perlis (UniMAP) as an Associates Professor and BioEM Principal Researcher based in School of Computer and Communication Engineering (SCCE). Experienced as an RF and Microwave Engineer for Telekom Malaysia Berhad (TM) Company from 2006-2009 which used to be Engineer (team leader) of Specialized Network Services (SNS) Department based in TM Senai Johor. He has received Ph.D. in Communication Engineering from UniMAP in 2013. While received Ms.C. (2010) in Electronic Telecommunication Engineering and Bachelor Degree (2006) in Electrical-Electronic and Telecommunication Engineering from Universiti Teknologi Malaysia (UTM). He holds an H-Index of 13 (SCOPUS) and has published over 132 technical papers in journals and proceedings including the IEEE Access, IEEE Antenna and Wireless Propagation Letter (AWPL), Microwave and Optical Technology Letter (MOTL), International Journal on Antenna and Propagation (IJAP), Progress in Electromagnetics Research (PIER) and Radio Engineering Journal and more than 50 conference papers. His research interests include antenna design, reconfigurable beam steering antenna, wearable antenna, MIMO, UWB, wireless on-body communications, in-body communications (implantable antenna), wireless power transfer, RF and microwave communication system. Currently, supervising a number of Ph.D. and Ms.C. students and also managing few grants under Ministry of Higher Education Malaysia. Moreover, Muzammil is an IEEE Member (MIEEE), a Member of IET (MIET), a Member of Antenna and Propagation (AP/MTT/EMC), Malaysia Chapter, and has received his Chartered Engineering on July 2017.

Ir. R. Badlishah Ahmad obtained B.E. in Electrical and Electronic Engineering from Glasgow University in 1994. He obtained his M.Sc. and Ph.D. in 1995 and 2000 respectively from University of Strathclyde, UK. His research interests are on computer and telecommunication network modeling using discrete event simulators, optical networking and coding, and embedded system based on GNU/Linux for vision. He has five (5) years teaching experience in University Sains Malaysia. Since 2004 until 15 March 2017, he was working with University Malaysia Perlis (UniMAP) as Dean at School of Computer and Communication Engineering. Currently as the Deputy Vice Chancellor (Research and Innovation), Universiti Sultan Zainal Abidin (UniSZA).

Thennarasan Sabapathy received his B.Eng. degree in Electrical-Telecommunication Engineering from the Universiti Teknologi Malaysia, in 2007 and M.Sc.Eng. degree in Multimedia University, Malaysia in 2011. He pursued his Ph.D. in Communication Engineering from University Malaysia Perlis in 2014. In 2007, he served as Test Development Engineer in Flextronics, working on the hardware and software test solutions for the mobile phone manufacturing. Then he joined Multimedia

University as Research Officer from 2008 to 2010 while pursuing his M.Eng.Sc. From 2012 to 2014, he was a research fellow in University Malaysia Perlis during his Ph.D. He is currently a Senior Lecturer at the School of Computer and Communication Engineering (SCCE), Universiti Malaysia Perlis. His current research interests include antenna and propagation, millimeter-wave wireless communications and fuzzy logic for wireless communications.

Mohd Fareq Abd Malek is an Associate Professor in the Faculty of Engineering and Information Sciences at UOWD. Before he joined UOWD, Mohd Fareq worked for Universiti Malaysia Perlis. Prior to this, he held industry positions for five years with Alcatel Malaysia and Siemens Malaysia. At Alcatel, he worked in the Asia Pacific Regional Centre of Competence, specialising in mobile radio network design. At Siemens, he worked in the Information and Communication Mobile division, where he developed the mobile strategy for the Malaysia market. Mohd Fareq maintains a broad range of research interests that covers a wide range of applied engineering, including applied electromagnetic, telecommunication engineering, antenna, microwave absorbers from agricultural wastes (rice husks, sugar cane bagasse, banana leaves), microwave drying, effects of RF on health, RF energy harvesting, and wireless communication. He believes in hybrid, multi-disciplinary teamwork and collaboration with researchers from other disciplines.

Muhammad Ramlee Kamarudin received Bachelor from Universiti Teknologi Malaysia (UTM), Johor Bahru, Malaysia, with honors, majoring in Electrical and Telecommunication Engineering and graduating in 2003. He received the M.S. degree in Communication Engineering in 2004 from the University of Birmingham, Birmingham, UK, and later he obtained his Ph.D. degree in 2007 from the same University under the supervision of Professor Peter Hall. Kamarudin is currently working as a Senior Lecturer at Centre for Electronic Warfare, Information and Cyber (EWIC), Cranfield Defence and Security, Cranfield University, UK. He is an author of a book chapter of a book entitled *Antennas and Propagation for Body-Centric Wireless Communications* and has published more than 200 technical papers in journals and proceedings including IEEE Transaction on Antenna and Propagation (TAP), IEEE Antennas and Wireless Propagation Letter (AWPL), IEEE Antenna Magazine, IEEE Access, International Journal of Antennas and Propagation (IJAP), Progress in Electromagnetics Research (PIER), Microwave and Optical Technology Letters (MOTL), and Electronics Letters. His research interests include antenna design for 5G, wireless on-body communications, in-body communications (implantable antenna), RF and microwave communication systems, and antenna diversity.

Mohd Najib Mohd Yasin received the M.Eng. degree in Electronic Engineering from the University of Sheffield, United Kingdom, and the Ph.D. degree from the University of Sheffield, Sheffield, U.K., in 2007 and 2013, respectively. Since 2013, he has been a Lecturer in the School of Microelectronics, Universiti Malaysia Perlis, Malaysia. His research interests include computational electromagnetics, conformal antennas, mutual coupling, wireless power transfer, array design and dielectric resonator antennas.

Mohamed Nasrun Osman was born in November 1987. He received his Electrical Engineering degree major Telecommunication from Universiti Teknologi Malaysia in 2010. From 2010 to 2012, he was an Assistant Director at Malaysian Communication and Multimedia Commission, responsible on implementation and monitoring of communication and technology project specifically in rural area. He obtained his Ph.D. degree in Electrical Engineering at the Universiti Teknologi Malaysia. He is currently worked at Universiti Malaysia Perlis as Senior Lecturer. His research interests include reconfigurable antenna design, wearable antenna, RF design and wireless MIMO system.

Role of Surface Geometric Patterns and Parameters in the Dispersion Relations of Spoof Surface Plasmon Polaritons at Microwave Frequency

Rana Sadaf Anwar, Lingfeng Mao, and Huansheng Ning*

School of Computer and Communication Engineering
University of Science and Technology Beijing, Beijing, 100083, China
engr_rs@126.com, lingfengmao@ustb.edu.cn, *ninghuansheng@ustb.edu.cn

Abstract **─** Spoof surface plasmon polaritons (SSPPs) can be excited using geometric shapes on conducting surfaces in microwave (MW) regime. They are eminent as compared to the conventional microstrip (MS) transmission lines, due to their better efficiency and compactness in high density and high-speed circuitry. In this work, we compare normalized dispersion curves (DCs) of different groove shapes engineered on the planar metallic strip with the variation of geometric parameters of the structure, which are obtained by Eigen-mode solver of ANSYS's HFSS. It is found the dispersion characteristics are determined by the shape and the asymptotic frequency can finely be tuned through the geometric parameters. All DCs deviate further from the light line indicating slow propagation of SSPPS. The performance of rectangular grooves is clearly outstanding; however, the circular grooves behave comparably better than Vee-groove. Further, a low pass plasmonic filter has been proposed with semi-circular gradient subwavelength grooves designed on a planar metallic strip with transition sections to match both the impedance and momentum of MS line and the plasmonic waveguide. Results of S-parameters and magnitude of electric field distributions show excellent transmission efficiency from fast guided wave to slow SSPPs. It is also observed that the confinement of such surface waves is dependent on the geometric parameters which can be useful in plasmonic structure engineering and fine-tuning the cutoff frequencies, hence posing a new prospect for advanced plasmonic integrated devices and circuits.

Index Terms **─** Microwave, plasmonics, surface plasmon polaritons, sub-wavelength, surface geometry.

I. INTRODUCTION

Manipulating the electromagnetic waves through subwavelength apertures has invoked the interest of many researchers and formed the basis of extensive investigation in the field of plasmonics, after the discovery of extraordinary transmission through nanohole arrays in the metallic film by Ebbesen et al. [1]. Applications of plasmonics are focused in diverse fields such as Surface-Enhanced Raman Scattering [2], surface plasmon resonance sensors [3], and surface plasmon spectroscopy systems [4]. Numerous areas have been flourished by plasmonics, ranging from chemistry, biology, physics, and material science [5-7].

Surface plasmon polaritons **(**SPPs) are the self-sustaining and propagating electromagnetic (EM) waves, which are provoked on the metal-dielectric interface in the optical regime where the incident energy is highly accumulated across the edges of the periodic corrugations in metal film and so it can easily cross through [1, 8]. SPPs have much smaller wavelength as compared to the light of incidence. Once SPPs are excited, they travel in a direction parallel to the metal-dielectric interface. They are evanescent by nature, and so they decay exponentially along the perpendicular direction of the metal-dielectric interface. The propagation of SPPs can be manipulated through couplers and waveguides. However, there is a mismatch in momentum between SPPs and free space photon of light, due to bound nature of SPPs, which is evident by k-vector differences on dispersion diagrams. This mismatch depends on the surface nature of the structure. Momentum matching can be achieved by scattering of EM waves through the use of methods such as using high index prism, evanescent field coupling and grating coupling [9, 10].

Free carriers have a major contribution to the dielectric function which is of significant importance in metals and semiconductors. A classical conductivity model based on standard equations for electron motion in an electric field is referred to as the Drude model and presents the straightforward theory for the optical parameters. The dielectric constant of conducting metal film is related to plasma frequency and is given by Drude's model as:

$$\varepsilon_M(\omega) = 1 - \frac{\omega_P^2}{\omega^2 - i\Gamma\omega}, \tag{1}$$

$$\omega_P = \sqrt{ne^2 / m\varepsilon_0}. \tag{2}$$

Here, ω_P defines the plasma frequency of the metal, ω is the angular frequency of the incident electromagnetic wave, ε_0 is the permittivity of free space, Γ is the

Submitted On: June 29, 2018
Accepted On: December 25, 2018

scattering rate of electron motion, while n is the free carrier density, e and m are the charge and the mass of an electron, respectively. Usually, metals have a higher density of free electrons; therefore, their ω_P is higher. The dispersion relation for light in a metal bounded to a dielectric layer is derived by solving Maxwell's equations by substituting dielectric constant relation (1):

$$k_x = k_0\sqrt{\frac{\varepsilon_I \varepsilon_M}{(\varepsilon_I + \varepsilon_M)}}\ , \qquad (3)$$

The in-plane wavevector k_x, named as the momentum of SPPs (also represented by β), is a function of angular frequency [10] and is the wavevector in the plane of the un-textured surface along which it propagates. k_0 is the free-space wavevector. ε_I and ε_M are the frequency dependent complex dielectric functions (relative permittivity) of adjacent dielectric film and metal, respectively. It has been noticed at $\omega<\omega_P$, the condition $k_x>k_0$ is satisfied. Therefore, SPP's field decays exponentially with the distance from the surface, along with the perpendicular direction of the metal-dielectric interface. The occurrence of this field is temporary by nature, and so it is limited to the surface of the metal. The field confinement of SPPs is tighter for higher values of wavevector.

In contrast to the optical regime, the metal behaves as a perfect electric conductor (PEC) at lower frequencies. To overcome this problem, properties similar to the SPPs have been achieved by using plasmonic metamaterials proposed by many researchers by use of subwavelength textured structures after the proposal by Pendry et al. [11]. Different shapes of metallic subwavelength aperture arrays, grooves or single slit structures are being explored, working at the microwave to terahertz regime. Such textured surfaces support the propagation of surfaces waves also called as spoof SPPs (SSPPs) [12]. A lower working frequency of SPPs to gigahertz can be achieved through surface decorations, such as holes [13], metallic apertures [14, 15], rectangular gratings [16, 17], triangular corrugations [18], T-grooves [19] and elliptical grooves [20]. A review of recent progress on exciting SPPs in microwave (MW) and terahertz (THz) regimes by incorporating various subwavelength corrugated shapes on conductive or metal surfaces has been presented in [21].

It has been known that propagating EM waves on the surface of a structure have a propagation constant given as $\gamma=\alpha+j\beta$, where α represents the attenuation constant and β is the phase constant. It is known that the confinement of SSPPs mainly depends on the β (wavenumber along the direction of propagation k_x) which is related to k_0 by a related parameter of the decay constant (along tangential direction) and is given by [22]:

$$\alpha_t = \sqrt{k_x^2 - k_0^2}\ , \qquad (4)$$

Here, $k_0=2\pi/\lambda$. It can be observed from (4) that the level of field confinement is positively related to the wavenumber in the direction of propagation.

The analysis presented in this paper gives a comparison of the dispersion curves by engineering different type of surface textures as the phenomenon of exciting SSPPs has been proved in earlier investigations on the planar conducting layer with surface decorations. We consider three geometric structure shapes to excite the SSPPs and analyze their effects on DCs (ω–β relations) in detail by performing comparisons of their dispersion and confinement capacities. It is proved that basic unit cell geometry can play a prominent role in SSPPs excitation. For example, we find that they are highly bound to the surface with rectangular corrugations and have a lower asymptotic frequency as compared to surfaces with circular/V-groove patterns. Due to the lower value of momentum mismatch for circular and V-groove structures, they are closer to the wave vector of free space (k_0). Therefore, surface texture engineering can cause prominent influence in applications of planar plasmonic metamaterials and nanophotonics.

II. DISPERSION RELATIONS AND ANALYSIS

We investigate the dispersion characteristics of SSPPs for planar metallic structures having different etched geometries by the Eigen mode solver of the commercial software package, ANSYS's High Frequency Structure Simulator (HFSS) which uses Finite element method (FEM). The TM-polarized waves are propagating in the x-direction which is along the corrugated metal plate structures as depicted in Fig. 1. The properties of SSPPs modes are primarily controlled by the geometric parameters of the structure. To perform a comparison; the structure is composed of a thin metallic strip (parameter 't' for thickness) on top of a dielectric substrate with a thickness of 2.65mm, the relative dielectric constant of 2.2 and loss tangent of 0.0009. We denote the width and depth of grooves by 'w' and 'h' respectively while the period of the structure is 'P' and height of the metallic strip is 'H' for all grooved structures as shown in Fig. 1. Firstly, to study the dispersion behavior, we start with circular groove and vary the height 'h' from 5mm to 7.5mm while 'P', 'w' and 'H' are kept constant at 20mm, 7.5mm, and 8mm respectively. The dispersion curves so obtained for the fundamental propagating mode are plotted in Fig. 2. The continuous black curve is the light line (LL), and the black dashed curve shows the DC of microstrip (un-textured) structure.

It is clear from Fig. 2 that all the dispersion curves deviate from the light line and reach a constant asymptotic frequency at the edge of the Brillouin zone which is the region in k-space which can be occupied by low "k" electrons without being affected by diffraction phenomenon. The DCs for SSPPs show that the asymptotic frequency is dominantly related to the depth of the grooves. As the depth of the grooves increases, the asymptotic frequency gets lower (higher β), which implies the stronger confinement of surface waves in the circular groove strip. As the depth of grooves is decreased, the in-plane wave vector gradually approaches k_0. Therefore, the SSPPs are strongly bounded for higher in-plane wavevector and vice versa. At low frequency limit, the SSPPs dispersion curves are closer to the light line. The metal acts as a perfect electric conductor (PEC) in this regime (comprises of microwave frequency region). The dispersion relation for this limit is reduced to $k_x=k_0$ and corresponds to EM wave propagating parallel to the interface in a dielectric layer. That is the reason, at low frequency, the SSPPs behave like light.

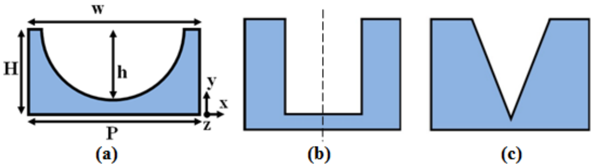

Fig. 1. Unit cell of a SSPPs structure with geometric parameters characterizing the groove geometry for: (a) Circular (Cir) groove, (b) Rectangular (Rec) groove, and (c) V (Vee) groove.

At high frequency range, as it approaches surface plasmon frequency, the propagation constant of SSPPs is greater than that of vacuum, which implies that they are more strongly confined. For example, in Fig. 2, when h=5mm, the asymptotic frequency reaches 4.3GHz, the dispersion approaches SSPP modes which propagate more gradually and localize more tightly on the surface of the semi-circular grooved metal plate.

To make a comparison among SSPPs structures with differently patterned grooves, we consider the unit cells as shown in Figs. 1 (a-c), to perform simulations. All the grooved patterns have the same geometric parametric values as for Fig. 2 along with h=7.5mm, and the dispersion relations are shown in Fig. 3. It is prominent that geometric shape and their parameters play a major role in determining the dispersion properties. All the dispersion curves deviate from the light line and increasingly become steady until they reach their asymptotic frequencies. Although all of them pose a similar trend, these curves exhibit different frequency band behavior for different grooves patterns. Noticeably, the asymptotic frequency of the rectangular groove structure is lower than other types, confirming that it has strongest field confinement of SSPPs on the surface. Circular groove dispersion behavior is better than Vee groove as it has a comparatively lower asymptotic frequency.

Single sided rectangular grooves structure on a dielectric substrate can be assumed as similar to an array of coplanar strip aligned vertically, and the dispersion relation of such a corrugated MS can be found by (5) as given in [23] where k_0 is replaced by $\sqrt{\varepsilon_{eff}}k_0$ to estimate the asymptotic frequency:

$$\sqrt{k_x^2-\varepsilon_{eff}k_0^2}=\sqrt{\varepsilon_{eff}}\,k_0\left(\frac{w}{P}\right)\tan\left(\sqrt{\varepsilon_{eff}}\,k_0 h\right), \qquad (5)$$

ε_{eff} is the effective permittivity where the SSPPs propagate and can be estimated by (6):

$$\varepsilon_{eff}=1+\left(\frac{\varepsilon_I-1}{2}\right)\frac{K(k')K(k_1)}{K(k)K(k_1')}, \qquad (6)$$

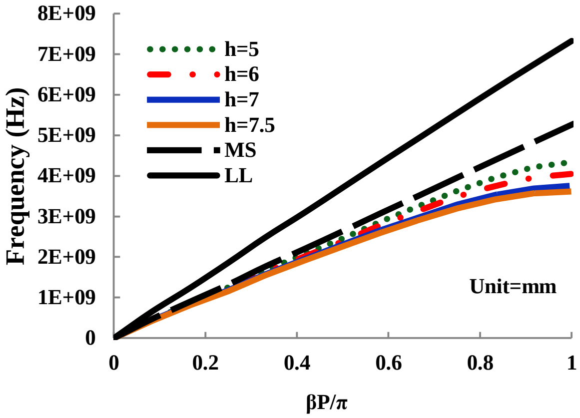

Fig. 2. Dispersion relations of SSPPs for the fundamental mode with varying circular groove depths.

Here, K represents the whole elliptic integral of the first type, $k=w/P$, $k'=\sqrt{1-k^2}$, $k_1'=\sqrt{1-k_1^2}$, and

$$k_1=\frac{\sinh\left(\pi w/4t\right)}{\sinh\left(\pi P/4t\right)}.$$

Explicit effect of structure parameters on the dispersion characteristics can be understood through an analysis, by changing the parametric values. The corrugation size significantly impacts on the SSPPs characteristics. Higher is the value of groove width ‘w’ and height ‘h’, lower is the asymptotic frequency and therefore stronger is the field confinement [24].

Figure 4 depicts the effect of groove width ‘w’ on the dispersion curves of different SSPPs structures. Width ‘w’ of all three types of structures is reduced to 1mm comparatively as used in the previous analysis (7.5mm) shown in Fig. 3. A comparison of DCs for circular and rectangular grooved structures respectively is given in Fig. 5, in which groove width is reduced from 7.5mm to 1mm. It is seen that the asymptotic frequency depends prominently on the groove width and decreases when ‘w’ increases, indicating that this geometric parameter notably affects the confinement ability of the surface waves.

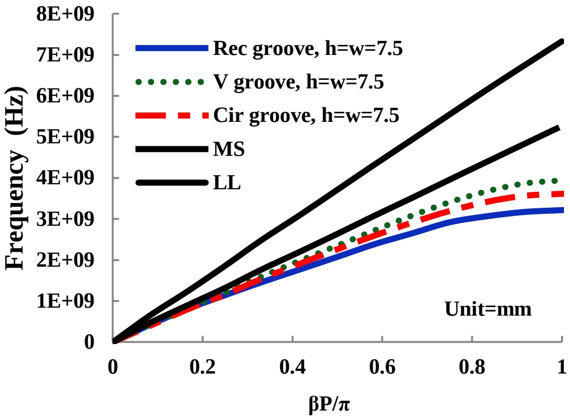

Fig. 3. Dispersion relations of SSPPs for the fundamental mode of different structures at w=h.

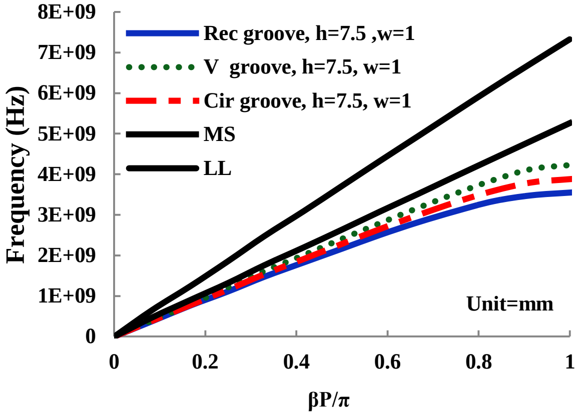

Fig. 4. Dispersion relations of SSPPs for the fundamental mode of different structures with w<<h.

Similarly, the structure size parameters, height 'H' and period 'P' of the unit cell have a prominent influence on the frequency range, but the trend of the dispersion curves remains less effective. The frequency domain is reduced with the bigger size of the structure. To estimate the impact of period 'P' on structure performance, we evaluate the dispersion relations of a unit cell having a circular groove with different 'P' values as shown in Fig. 6. The period is varied from 16mm to 24mm with a step size of 4mm with remaining parameters set equal as in Fig. 3. It is illustrated that the DCs are very sensitive to the change in period 'P' for the complete frequency range, and it is prominent that the asymptotic frequency decreases remarkably as 'P' increases. Furthermore, at a constant frequency in the SSPPs mode, the propagation constant increases as the period is increased, for example, in Fig. 6, it is demonstrated that at the asymptotic frequency of 2 GHz, $\beta3>\beta2>\beta1$. Therefore, the length of the period can improve the field confinement ability of the grooved structures.

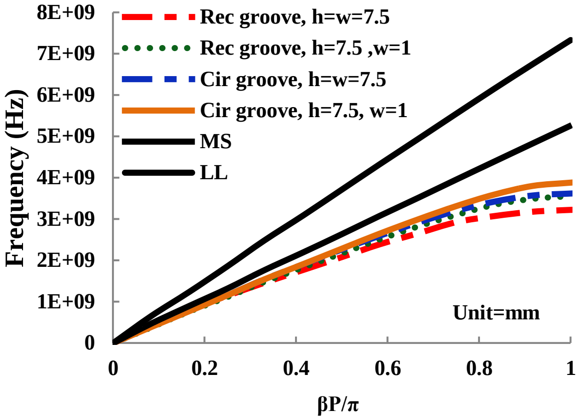

Fig. 5. Dispersion relations of SSPPs for the fundamental mode of rectangular and circular groove structure with varying groove width.

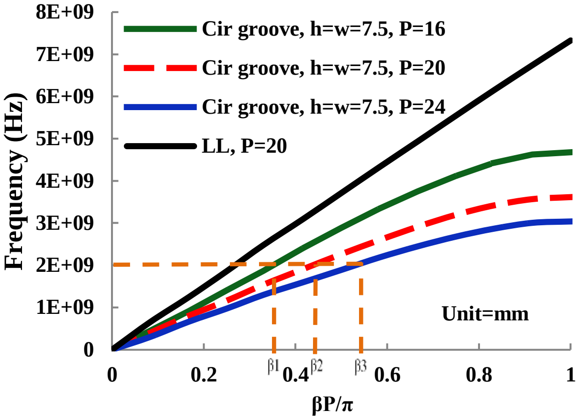

Fig. 6. Dispersion curves of SSPPs for the fundamental mode of the circular grooved with varying period length.

A. Field confinement analysis

To get a direct insight of the modal characteristics of the SSPPs on different groove structures, the magnitude electric field distributions are plotted at the cross section of unit cells (location shown by dotted line in Fig. 1 (b) and field confinement capacities are compared in Figs. 7 (a-c). The parameters are set equal as for dispersion analysis in Fig. 3. It has been clearly observed that the rectangular groove has the strongest confinement of SSPPs whereas the V-groove exhibits the weakest localization of field, therefore explicitly confirming the findings in dispersion curves of Fig. 3.

Furthermore, Figs. 8 (a-c) gives a demonstration of magnitude electric field distributions with varying groove depth, width and period for the circular groove. When the groove depth is kept constant as in the previous analysis of Fig. 7 (b) while the width is reduced to 1mm, relatively the field is not confined anymore as shown in Fig. 8 (a) and spreads into the substrate. The same effect is ratified in the dispersion relation of Fig. 5 by a rise in asymptotic frequency.

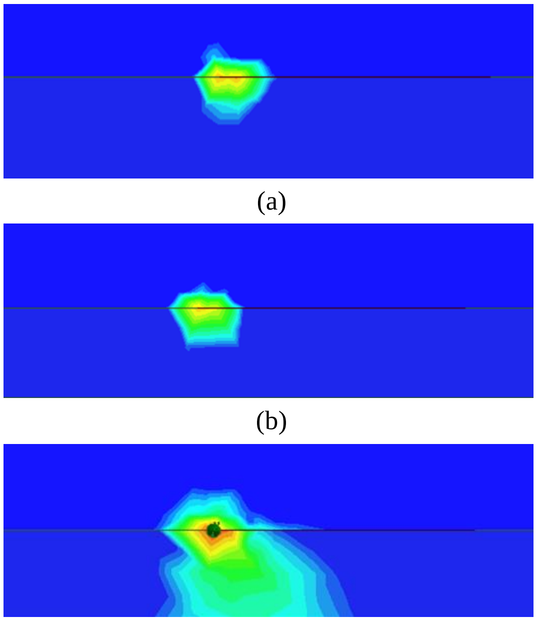
(a)
(b)
(c)

Fig. 7. Simulated magnitude electric field distribution at the cross section of the structure with h=w=7.5: (a) Rectangular groove, (b) Circular grooven, and (c) Vee groove.

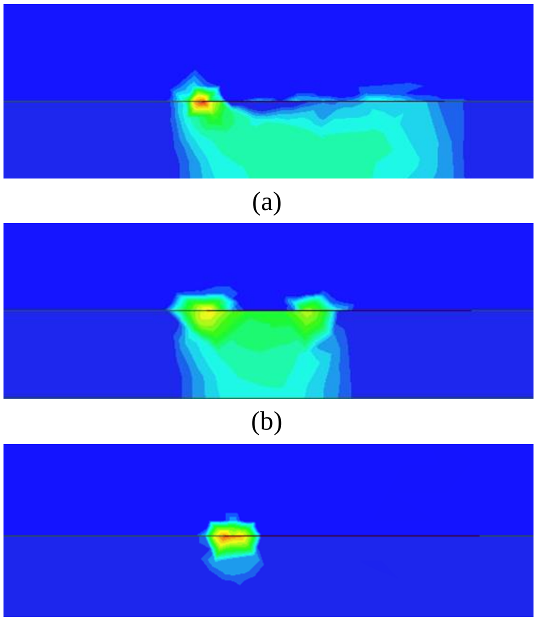
(a)
(b)
(c)

Fig. 8. Simulated magnitude electric field distribution at the cross section of the structure: (a) Circular groove with h=7.5, w=1mm, (b) Circular groove with h=w=5, and (c) Circular groove with h=w=7.5 and P=24mm.

Therefore, to maintain the frequency back to the lower value, the only solution is to increase the groove's height; however, it will cause the structure dimensions to augment [25]. Figure 8 (b) depicts the delocalization of electric field when both the depth and width of groove is decreased to 5mm. However, in contrast, when the period is raised to 24mm with the maximum groove depth of 7.5mm, an enhanced field confinement ability is observed, fortifying the results in Fig. 6 by a reduction in asymptotic frequency.

As demonstrated previously, the ability to confine surface waves is highly responsive to the period length of the structure as well as to the corrugation depth and width. When the frequency of the incident wave reaches near the asymptotic frequency, it couples deeper into the grooves, and so electromagnetic field is confined on the surface because of the higher mismatch of wavevector between SSPPs and free space photon of light. While, at a lower frequency, propagation of EM waves exhibits weaker confinement on the surface, consequently the dispersion characteristics are close to the light line. Hence, the design of subwavelength SSPPs structures in microwave regime is facilitated by controlling the asymptotic frequency with the variation of groove shape, its depth, width and period length on the surface of the structure.

III. STRUCTURE DESIGN OF LOW-PASS PLASMONIC FILTER

From dispersion relations, it has been noticed that the wavevector of SSPPs are highly mismatched to that of light line especially when the asymptotic frequency is reached. This will result in extremely less transmission performance. Therefore, to efficiently feed in and extract out the maximum power, a plasmonic filter with transition structure is designed. In contrast to planar defected MS filter proposed in [26-28] and earlier investigated plasmonic filters based on rectangular gratings [17], triangular corrugations [18], and T-grooves [19], here we investigate SSPPs based on semi-circular gratings etched on planar metallic strip which is highly unexplored textured surface until now to the best of our knowledge. It consists of a microstrip line with gradient subwavelength semi-circular grooves with depth h varying from 7mm to 3mm with a step of 1mm designed on a dielectric substrate as investigated in Section II as shown in Fig. 9. Two transition links at both ends provide a gradient momentum and impedance matching; therefore, conversion of guided waves to spoof SPPs is achieved. The dimensions are given here: L_1=2.5mm, L_2=60mm, L_3=105mm, H=7.5mm, P=15mm. A is the traditional microstrip section, B is the mode transition section and C is the SSPPs section with h=7mm and w=14mm. To evaluate the performance of this filter structure, the S-parameters are obtained by simulation software ANSYS's HFSS and shown in Fig. 10. The cutoff frequency (f_c) of the filter is 4.91GHz which is mainly anticipated by the asymptotic frequency of SSPPs mode support by the waveguide region C. An efficient passband is achieved with S11 less than -10dB from 0.45 to 4.91GHz. The upper stopband covers a frequency range from 5.11 to 10GHz with rejection less than -18dB (even < -25dB from 5.15 to 8.11GHz) which points to an outstanding realization of impedance matching between the MS and the SSPPs.

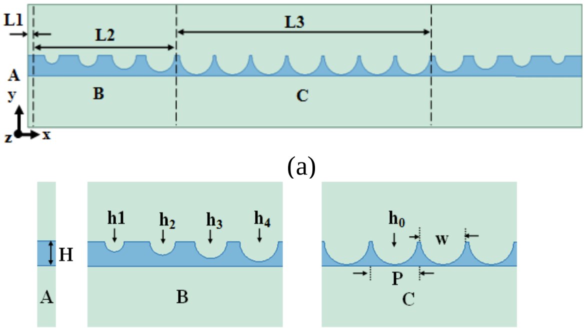

(a)

(b)

Fig. 9. (a) The configuration of the proposed plasmonic filter showing the top view of SSPPs structure with three sections. (b) Detailed view of Region A, B, and C.

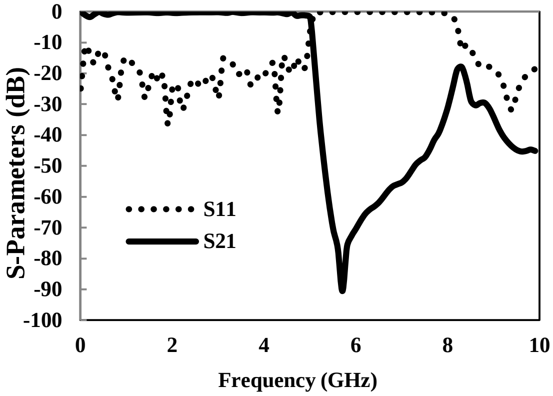

Fig. 10. The simulated S-parameters of the proposed plasmonic filter.

Moreover, we compare the scattering parameters by changing the dielectric constant of substrate material (from 2.2 to 10) as shown in Fig. 11. It can be noticed that increasing the dielectric constant results in lowering the cutoff frequency. Especially, it is pointed that with dielectric constant of 10, the cutoff frequency is reduced to 2.61GHz and a clear stop band is obtained from 2.61 to 4.11GHz with higher rejection level up to -116 dB at 3.31GHz.

Additionally, we observe the magnitude distribution of electric field by numerical simulations on a xy plane 1mm above the structure as shown in Fig. 12, at an in-band (top) and out of band (bottom) frequency of 2.5 and 5.6 GHz, respectively. It can be noticed that at the in-band frequency, the surface waves transmit effectively from one end to the far end of the filter with an underlying lossless substrate material. Evidently, the SSPPs confine more strongly inside the semi-circular grooves.

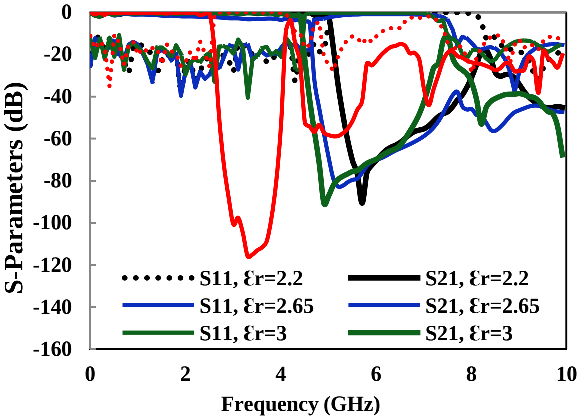

Fig. 11. The effect of varying dielectric constant on S-parameters of the proposed plasmonic filter.

It can be observed that the magnitude of electric field at both ends is approximately the same, demonstrating a negligible transmission loss in the passband. On the other hand, at out-band frequency of 5.6 GHz, the SSPPs unambiguously stop propagating right from the beginning of the Region C, therefore confirming the envisaged response in the stopband region. Figure 13 presents the magnitude distribution of magnetic field at an in-band frequency of 2.5 GHz and demonstrates that H-field profoundly confines in the depth of the groove.

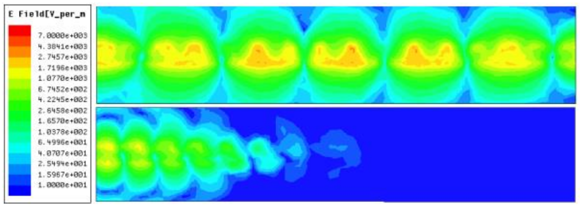

Fig. 12. The simulated magnitude electric field distribution showing confinement and propagation at (top) 2.5 GHz (bottom) 5.6 GHz.

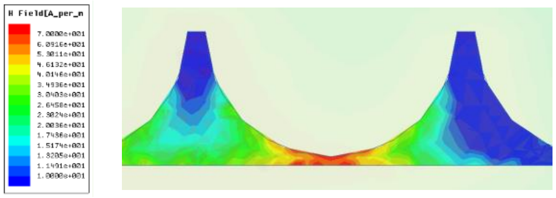

Fig. 13. The simulated magnitude magnetic field, showing the confinement inside the grooves at 2.5 GHz (A portion of SSPPs filter).

Table 1: Comparison of the proposed plasmonic filter with earlier works

Ref.	**f_c (GHz)**	**Return Loss (dB)**	**Upper band Rejection Range**	**Filter Type**	**Length L**	**Compare L**	**Width W**	**Compare W**
This Work	4.91	< -12.5	5.1 GHz	Low-Pass	230	---	45	---
[22]	12.4	< -7.5	7.6 GHz	Low-Pass	412	79%	65.2	45%
[20]	11.4	< -11	18.6 GHz	Low-Pass	200	-13%	50	12%
[25]	7.9	< -12	2.1 GHz	Low-Pass	130	-43%	20	-55%
[29]	13	< -10	2 GHz	NA	97	-57%	50	12%
[30]	12.3	< -9	1.7 GHz	Low-Pass	320	40%	70.8	58%

A comparison of the proposed plasmonic filter with previously published researches is presented in Table 1. Although the dimensions of the structure are slightly larger than some of the listed filters, comparatively, it comes up with the lowest cutoff frequency which has not been reported yet. Besides, it has good return loss in the passband with a superior stopband frequency range. Keeping in view all above demonstrations, it is proposed that such kind of SSPPs structure can find prospective use in numerous plasmonic circuits and systems.

IV. CONCLUSION

In this work, we investigate the dispersion relations of spoof SPPs for planar metallic structures having different shaped geometries. It is shown that the surface textures and groove shapes play a substantial role in defining the confinement of SSPPs in subwavelength frequency regime. Firstly, the comparison is illustrated for normalized DCs by varying depth of circular grooves structure. Afterward, DCs relations are assessed among rectangular, circular and Vee-grooves engineered on the metallic strip by varying width, and period of the structure. It has been clearly found that dispersion characteristics can be determined and asymptotic frequency can be tuned by engineering the surface's geometric parameters at will. Although the rectangular grooves performance is explicitly preeminent, the circular groove efficiency is comparable to rectangular groove structure, while it is much superior to Vee-groove structure and MS line. Likewise, the confinement of these surface waves is dependent on the period length of the structure as well as on the corrugation width and depth. A low-pass plasmonic filter has been designed based on the semi-circular grooves on planar metallic strip with two conversion sections at both ends to match the impedance and momentum of MS and the plasmonic waveguide. S-parameters and magnitude E-field distribution results show excellent transmission performance from MS to a plasmonic waveguide. The confinement of such SSPPs depends on the geometric parameters that may be useful to fine-tune the cutoff frequencies and in developing advanced plasmonic filters to be applied in integrated circuits at the microwave frequency.

ACKNOWLEDGMENT

This work was supported in part by the National Natural Science Foundation of China (Grant No. 61774014) and the Fundamental Research Funds for the Central Universities (Grant No. FRF-BD-18-016A).

REFERENCES

[1] T. W. Ebbesen, H. J. Lezec, H. Ghaemi, T. Thio, and P. Wolff, "Extraordinary optical transmission through sub-wavelength hole arrays," *Nature*, vol. 391, no. 6668, p. 667, 1998.

[2] X. Qian, X. Peng, D. Anasari. Q. Yin-Goen, G. Chen, D. Shin, L. Yang, A. Young, M. Wang, and S. Nie, "In vivo tumor targeting and spectroscopic detection with surface-enhanced Raman nano-particle tags," *Nature Biotechnology*, vol. 26, no. 1, p. 83, 2008.

[3] J. Homola, S. S. Yee, and G. Gauglitz, "Surface plasmon resonance sensors," *Sensors and Actuators B: Chemical*, vol. 54, no. 1, pp. 3-15, 1999.

[4] K. A. Willets and R. P. Van Duyne, "Localized surface plasmon resonance spectroscopy and sensing," *Annu. Rev. Phys. Chem.*, vol. 58, pp. 267-297, 2007.

[5] E. Ozbay, "Plasmonics: Merging photonics and electronics at nanoscale dimensions," *Science*, vol. 311, no. 5758, pp. 189-193, 2006.

[6] L. Feng, K. A. Tetz, B. Slutsky, V. Lomakin, and Y. Fainman, "Fourier plasmonics: Diffractive focusing of in-plane surface plasmon polariton waves," *Applied Physics Letters*, vol. 91, no. 8, p. 081101, 2007.

[7] J. R. Lakowicz, "Plasmonics in biology and plasmon-controlled fluorescence," *Plasmonics*, vol. 1, no. 1, pp. 5-33, 2006.

[8] W. L. Barnes, W. A. Murray, J. Dintinger, E. Devaux, and T. Ebbesen, "Surface plasmon polaritons and their role in the enhanced trans-mission of light through periodic arrays of sub-wavelength holes in a metal film," *Physical Review Letters*, vol. 92, no. 10, p. 107401, 2004.

[9] J. F. O'Hara, R. D. Averitt, and A. J. Taylor, "Prism coupling to terahertz surface plasmon polaritons," *Optics Express*, vol. 13, no. 16, pp. 6117-6126,

2005.

[10] H. Raether, "Surface plasmons on smooth surfaces," in *Surface Plasmons on Smooth and Rough Surfaces and on Gratings*: *Springer*, pp. 4-39, 1988.

[11] J. Pendry, L. Martin-Moreno, and F. Garcia-Vidal, "Mimicking surface plasmons with structured surfaces," *Science*, vol. 305, no. 5685, pp. 847-848, 2004.

[12] A. P. Hibbins, B. R. Evans, and J. R. Sambles, "Experimental verification of designer surface plasmons," *Science*, vol. 308, no. 5722, pp. 670-672, 2005.

[13] L. Martin-Moreno and F. Garcia-Vidal, "Optical transmission through circular hole arrays in optically thick metal films," *Optics Express*, vol. 12, no. 16, pp. 3619-3628, 2004.

[14] F. J. Garcia-Vidal, L. Martin-Moreno, T. Ebbesen, and L. Kuipers, "Light passing through subwavelength apertures," *Reviews of Modern Physics*, vol. 82, no. 1, p. 729, 2010.

[15] X. Shou, A. Agrawal, and A. Nahata, "Role of metal film thickness on the enhanced transmission properties of a periodic array of subwavelength apertures," *Optics Express*, vol. 13, no. 24, pp. 9834-9840, 2005.

[16] X. Wan and T. J. Cui, "Guiding spoof surface plasmon polaritons by infinitely thin grooved metal strip," *Aip Advances*, vol. 4, no. 4, p. 047137, 2014.

[17] X. Gao, L. Zhou, Z. Liao, H. F. Ma, and T. J. Cui, "An ultra-wideband surface plasmonic filter in microwave frequency," *Applied Physics Letters*, vol. 104, no. 19, p. 191603, 2014.

[18] T. Søndergaard and S. I. Bozhevolnyi, "Surface-plasmon polariton resonances in triangular-groove metal gratings," *Physical Review B*, vol. 80, no. 19, p. 195407, 2009.

[19] C. Chen, "A new kind of spoof surface plasmon polaritons structure with periodic loading of T-shape grooves," *AIP Advances*, vol. 6, no. 10, p. 105003, 2016.

[20] R. S. Anwar, Y. Wei, L. Mao, X. Li, and H. Ning, "Novel spoof surface plasmon polaritons on a planar metallic strip with periodic semi-elliptical grooves at microwave frequency," *Journal of Electromagnetic Waves and Applications*, pp. 1-13, 2018.

[21] R. S. Anwar, H. Ning, L. Mao, and "Recent advancements in surface plasmon polaritons-plasmonics in subwavelength structures at microwave and terahertz regimes," *Digital Communications and Networks*, 2017.

[22] H. C. Zhang, Q. Zhang, J. F. Liu, W. Tang, Y. Fan, and T. J. Cui, "Smaller-loss planar SPP transmission line than conventional microstrip in microwave frequencies," *Scientific Reports*, vol. 6, 2016.

[23] X. Liu, Y. Feng, B. Zhu, J. Zhao, and T. Jiang, "High-order modes of spoof surface plasmonic wave transmission on thin metal film structure," *Optics Express*, vol. 21, no. 25, pp. 31155-31165, 2013.

[24] X. Shen, T. J. Cui, D. Martin-Cano, and F. J. Garcia-Vidal, "Conformal surface plasmons propagating on ultrathin and flexible films," *Proceedings of the National Academy of Sciences*, vol. 110, no. 1, pp. 40-45, 2013.

[25] J. Xu, Z. Li, L. Liu. C. Chen, B. Xu, P. Ning, and C. Gu., "Low-pass plasmonic filter and its miniaturization based on spoof surface plasmon polaritons," *Optics Communications*, vol. 372, pp. 155-159, 2016.

[26] J. Wang, H. Ning, Q. Xiong, and L. Mao, "A compact narrow-band bandstop filter using spiral-shaped defected microstrip structure," *Radioengineering*, vol. 23, no. 1, 2014.

[27] H. Ning, J. Wang, Q. Xiong, and L. Mao, "Design of planar dual and triple narrow-band bandstop filters with independently controlled stopbands and improved spurious response," *Progress In Electromagnetics Research*, vol. 131, pp. 259-274, 2012.

[28] H. Ning, J. Wang, Q. Xiong, H. Liu, and L. Mao, "A compact quad-band bandstop filter using dual-plane defected structures and open-loop resonators," *IEICE Electronics Express*, vol. 9, no. 21, pp. 1630-1636, 2012.

[29] S. Zhou, *et al.*, "Spoof surface plasmon polaritons power Divider with large Isolation," *Scientific Reports*, vol. 8, no. 1, p. 5947, 2018.

[30] H. F. Ma, X. Shen, Q. Cheng, W. X. Jiang, and T. J. Cui, "Broadband and high-efficiency conversion from guided waves to spoof surface plasmon polaritons," *Laser & Photonics Reviews*, vol. 8, no. 1, pp. 146-151, 2014.

LCP Plane Wave Scattering by a Chiral Elliptic Cylinder Embedded in Infinite Chiral Medium

A.-K. Hamid

Department of Electrical Engineering
University of Sharjah, Sharjah, UAE
akhamid@sharjah.ac.ae

Abstract **—** An analytic solution is presented to the scattering of a left circularly polarized (LCP) plane wave from a chiral elliptic cylinder placed in another infinite chiral medium, using the method of separation of variables. The incident, scattered, as well as the transmitted electromagnetic fields are expressed using appropriate angular and radial Mathieu functions and expansion coefficients. The unknown scattered and transmitted field expansion coefficients are subsequently determined by imposing proper boundary conditions at the surface of the elliptic cylinder. Numerical results are presented graphically as normalized scattering widths for elliptic cylinders of different sizes and chiral materials, to show the effects of these on the scattering widths.

Index Terms **—** Chiral-chiral material, elliptic cylinder, LCP and RCP, Mathieu functions, scattering cross section.

I. INTRODUCTION

It is well known that a reciprocal and isotropic chiral medium is characterized by different phase velocities for right- and left-circularly polarized (RCP and LCP) waves. In a lossless isotropic chiral medium, a linearly polarized wave undergoes a rotation of its polarization while it propagates. Numerous developments linked to chiral media overall are described in [1-3], and some analytical and numerical solutions to scattering from various types of chiral objects are given in [4-11].

The elliptic cylinder is a geometry that has been extensively analyzed in literature due to its ability to create cylindrical cross sections of different shapes by changing the axial ratio of the ellipse. Furthermore, since the elliptic cylindrical coordinate system is one of the coordinate systems in which the wave equation is separable, solutions to problems involving elliptic cylinders can be obtained in exact form. The solution of chiral cylinder immersed in unbounded chiral media will be the first step in providing an analytic solution to the complex problem of chiral elliptic cylinder coated with another layer of chiral media. Also, the analytic solution may be used as a benchmark for validating solutions to similar scattering problems using approximate or numerical methods.

In this paper, we present a solution to the problem of the scattering of a left-circularly polarized (LCP) plane wave from a chiral elliptic cylinder of arbitrary axial ratio placed in a distinct infinite chiral medium, while in [11] the chiral cylinder was embedded in free space. The solution of the chiral cylinder immersed in unbounded free space involves co and cross polarized fields with free space wave numbers where in the case of unbounded chiral media the solution involves both co and cross polarized fields with left and right circularly polarized wave numbers regardless if the incident field is left or right circularly polarized field. It is required to compute Mathieu functions with left and right circulation wave numbers inside and outside the elliptic cylinder. Both chiral media in this problem are isotropic. The obtained solution will therefore provide more parameters to control the normalized bistatic scattering width when compared to that in reference [11].

II. FORMULATION

Consider a LCP plane wave that is propagating in an infinite isotropic chiral medium, being incident on an infinitely long elliptic cylinder at an angle φ_i with respect to the minus x-axis of a Cartesian coordinate system located at the center of a cross section of the cylinder with its z-axis along the axis of the cylinder, which is made up of a different chiral material and of major axis length $2a$ and minor axis length $2b$, as shown in Fig. 1.

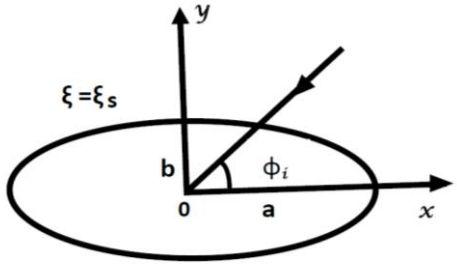

Fig. 1. Geometry of the scattering problem.

Submitted On: July 2, 2018
Accepted On: August 11, 2018

The incident electric field for LCP can be expanded in terms of elliptical vector wave functions as:

$$\mathbf{E}^{\mathrm{i}} = \sum_{m=0,1}^{\infty} A_{\substack{em\\om}}[\mathbf{N}^{(1)}_{\substack{em\\om}}(c_{L1},\mathbf{r}) - \mathbf{M}^{(1)}_{\substack{em\\om}}(c_{L1},\mathbf{r})], \tag{1}$$

in which,

$$A_{\substack{em\\om}} = E_0 j^m \frac{\sqrt{8\pi}}{N_{\substack{em\\om}}(c_{L1})} S_{\substack{em\\om}}(c_{L1},\cos\phi_i), \tag{2}$$

where,

$$N_{\substack{em\\om}}(c_{L1}) = \int_0^{2\pi} [S_{\substack{em\\om}}(c_{L1},\cos v)]^2 dv, \tag{3}$$

with $c_{L1} = k_{L1}F$, $S_{qn}(c_\alpha,\cos v)$ for *q*=*e*,*o* being the angular Mathieu function of order *n* and arguments c_α and $\cos v$, and *F* being the semi-focal length of the cylinder. $\Xi^{(i)}_{qm}(c_\alpha,\mathbf{r})$ for *q*=*e*,*o*, and $\boldsymbol{\Xi} = \mathbf{M},\mathbf{N}$ are defined in [13-14] in terms of angular and radial Mathieu functions, with **r** designating the elliptic coordinate dyad (ξ,η). The summation over *m* in (1) starts from 0 for even (*e*) functions and from 1 for odd (*o*) functions, and is the same for the other field expansions given below too. The wavenumber of the left circularly polarized wave is given by [12],

$$k_{L1} = \frac{k_0\sqrt{\mu_{r1}\varepsilon_{r1}}}{1 + k_0\gamma_1\sqrt{\mu_{r1}\varepsilon_{r1}}}, \tag{4}$$

where k_0 is the wavenumber in free space, γ_1 is the chirality parameter of the external chiral medium, and μ_{r1} and ε_{r1} are the relative permeability and relative permittivity of the external chiral medium.

The incident magnetic field may be expressed in terms of elliptical vector wave functions as:

$$\mathbf{H}^{\mathrm{i}} = \frac{j}{Z_1}\sum_{m=0,1}^{\infty} A_{\substack{em\\om}}[\mathbf{M}^{(1)}_{\substack{em\\om}}(c_{L1},\mathbf{r}) - \mathbf{N}^{(1)}_{\substack{em\\om}}(c_{L1},\mathbf{r})], \tag{5}$$

where $Z_1 = Z_0\sqrt{\mu_{r1}/\varepsilon_{r1}}$, with Z_0 denoting the free space wave impedance.

As the elliptic cylinder consists of an isotropic chiral material and is surrounded by another infinite isotropic chiral medium, the scattered and transmitted electromagnetic fields will have both co-polar and cross-polar components. The scattered fields can be written as:

$$\mathbf{E}^{\mathrm{s}}_{\mathbf{cp}} = \sum_{m=0,1}^{\infty} B_{\substack{em\\om}}[\mathbf{N}^{(4)}_{\substack{em\\om}}(c_{L1},\mathbf{r}) - \mathbf{M}^{(4)}_{\substack{em\\om}}(c_{L1},\mathbf{r})], \tag{6}$$

$$\mathbf{E}^{\mathrm{s}}_{\mathbf{xp}} = \sum_{m=0,1}^{\infty} C_{\substack{em\\om}}[\mathbf{N}^{(4)}_{\substack{em\\om}}(c_{R1},\mathbf{r}) + \mathbf{M}^{(4)}_{\substack{em\\om}}(c_{R1},\mathbf{r})], \tag{7}$$

$$\mathbf{H}^{\mathrm{s}}_{\mathbf{cp}} = \frac{j}{Z_1}\sum_{m=0,1}^{\infty} B_{\substack{em\\om}}[\mathbf{M}^{(4)}_{\substack{em\\om}}(c_{L1},\mathbf{r}) - \mathbf{N}^{(4)}_{\substack{em\\om}}(c_{L1},\mathbf{r})], \tag{8}$$

$$\mathbf{H}^{\mathrm{s}}_{\mathbf{xp}} = \frac{j}{Z_1}\sum_{m=0,1}^{\infty} C_{\substack{em\\om}}[\mathbf{N}^{(4)}_{\substack{em\\om}}(c_{R1},\mathbf{r}) + \mathbf{M}^{(4)}_{\substack{em\\om}}(c_{R1},\mathbf{r})], \tag{9}$$

where B_{qm} and C_{qm} for *q*=*e*,*o* are the unknown field expansion coefficients, $c_{R1} = k_{R1}F$, with the wave-number k_{R1} for the RCP wave given by [12],

$$k_{R1} = \frac{k_0\sqrt{\mu_{r1}\varepsilon_{r1}}}{1 - k_0\gamma_1\sqrt{\mu_{r1}\varepsilon_{r1}}}. \tag{10}$$

The fields transmitted into the chiral elliptic cylinder may also be expressed as:

$$\mathbf{E}^{t}_{\mathbf{cp}} = \sum_{m=0,1}^{\infty} D_{\substack{em\\om}}[\mathbf{N}^{(1)}_{\substack{em\\om}}(c_{L2},\mathbf{r}) - \mathbf{M}^{(1)}_{\substack{em\\om}}(c_{L2},\mathbf{r})], \tag{11}$$

$$\mathbf{E}^{t}_{\mathbf{xp}} = \sum_{m=0,1}^{\infty} G_{\substack{em\\om}}[\mathbf{N}^{(1)}_{\substack{em\\om}}(c_{R2},\mathbf{r}) + \mathbf{M}^{(1)}_{\substack{em\\om}}(c_{R2},\mathbf{r})], \tag{12}$$

$$\mathbf{H}^{t}_{\mathbf{cp}} = \frac{j}{Z_2}\sum_{m=0,1}^{\infty} D_{\substack{em\\om}}[\mathbf{M}^{(1)}_{\substack{em\\om}}(c_{L2},\mathbf{r}) - \mathbf{N}^{(1)}_{\substack{em\\om}}(c_{L2},\mathbf{r})], \tag{13}$$

$$\mathbf{H}^{t}_{\mathbf{xp}} = \frac{j}{Z_2}\sum_{m=0,1}^{\infty} G_{\substack{em\\om}}[\mathbf{N}^{(1)}_{\substack{em\\om}}(c_{R2},\mathbf{r}) + \mathbf{M}^{(1)}_{\substack{em\\om}}(c_{R2},\mathbf{r})], \tag{14}$$

where D_{qm} and G_{qm} for *q*=*e*,*o* are the unknown field expansion coefficients, $c_{R2} = k_{R2}F$ and $c_{L2} = k_{L2}F$, with expressions for k_{R2} and k_{L2} obtained from (4) and (10), respectively, by changing the subscript 1 in these equations to 2.

The unknown expansion coefficients can be obtained by imposing the boundary conditions corresponding to the continuity of the tangential field components at the surface $\xi = \xi_s$ of the chiral elliptic cylinder [15], which may be expressed mathematically as:

$$(\mathbf{E}^{\mathrm{i}} + \mathbf{E}^{\mathrm{s}})\times\hat{\xi}\big|_{\xi=\xi_s} = \mathbf{E}^{t}\times\hat{\xi}\big|_{\xi=\xi_s}, \tag{15}$$

$$(\mathbf{H}^{\mathrm{i}} + \mathbf{H}^{\mathrm{s}})\times\hat{\xi}\big|_{\xi=\xi_s} = \mathbf{H}^{t}\times\hat{\xi}\big|_{\xi=\xi_s}, \tag{16}$$

where $\hat{\boldsymbol{\xi}}$ is the outward unit normal to the surface of the elliptic cylinder.

Substituting the above developed expressions into the fields of (15) and (16), and applying the orthogonal property of the angular Mathieu functions, yield:

$$\begin{aligned}
&[A_{qn}R^{(1)}_{qn}(c_{L1},\xi_s) + B_{qn}R^{(4)}_{qn}(c_{L1},\xi_s)]N_{qn}(c_{L1})\\
&+\sum_m C_{qm}R^{(4)}_{qm}(c_{R1},\xi_s)M_{qmn}(c_{L1},c_{R1})\\
&=\sum_m D_{qm}R^{(1)}_{qm}(c_{R2},\xi_s)M_{qmn}(c_{R2},c_{L1})\\
&+\sum_m G_{qm}R^{(1)}_{qm}(c_{L2},\xi_s)M_{qmn}(c_{L2},c_{L1})
\end{aligned}, \tag{17}$$

$$\begin{aligned}
&[A_{qn}R^{(1)'}_{qn}(c_{L1},\xi_s) + B_{qn}R^{(4)'}_{qn}(c_{L1},\xi_s)]N_{qn}(c_{L1})\\
&-\frac{k_{L1}}{k_{R1}}\sum_m C_{qm}R^{(4)'}_{qm}(c_{R1},\xi_s)M_{qmn}(c_{L1},c_{R1})\\
&=\frac{k_{L1}}{k_{R2}}\sum_m D_{qm}R^{(1)'}_{qm}(c_{R2},\xi_s)M_{qmn}(c_{R2},c_{L1})\\
&-\frac{k_{L1}}{k_{L2}}\sum_m G_{qm}R^{(1)'}_{qm}(c_{L2},\xi_s)M_{qmn}(c_{L2},c_{L1})
\end{aligned}, \tag{18}$$

$$\begin{aligned}&[A_{qn}R_{qn}^{(1)}(c_{L1},\xi_s)+B_{qn}R_{qn}^{(4)}(c_{L1},\xi_s)]N_{qn}(c_{L1})\\&-\sum_m C_{qm}R_{qm}^{(4)}(c_{R1},\xi_s)M_{qmn}(c_{L1},c_{R1})\\&=\frac{Z_1}{Z_2}\sum_m D_{qm}R_{qm}^{(1)}(c_{R2},\xi_s)M_{qmn}(c_{R2},c_{L1})\\&-\frac{Z_1}{Z_2}\sum_m G_{qm}R_{qm}^{(1)}(c_{L2},\xi_s)M_{qmn}(c_{L2},c_{L1})\end{aligned}\quad , \qquad (19)$$

$$\begin{aligned}&[A_{qn}R_{qn}^{(1)'}(c_{L1},\xi_s)+B_{qn}R_{qn}^{(4)'}(c_{L1},\xi_s)]N_{qn}(c_{L1})\\&+\frac{k_{L1}}{k_{R1}}\sum_m C_{qm}R_{qm}^{(4)'}(c_{R1},\xi_s)M_{qmn}(c_{L1},c_{R1})\\&=\frac{k_{L1}Z_1}{k_{R2}Z_2}\sum_m D_{qm}R_{qm}^{(1)'}(c_{R2},\xi_s)M_{qmn}(c_{R2},c_{L1})\\&+\frac{k_{L1}Z_1}{k_{L2}Z_2}\sum_m G_{qm}R_{qm}^{(1)'}(c_{L2},\xi_s)M_{qmn}(c_{L2},c_{L1})\end{aligned}\quad , \qquad (20)$$

for *q=e,o* where $R_{qn}^{(i)}(c_\alpha,\xi_s)$ is the radial Mathieu function of order *n* and kind (*i*) of arguments c_α and ξ_s, and $M_{qmn}(c_\alpha,c_\sigma)$ is given by:

$$M_{qmn}(c_\alpha,c_\sigma)=\int_0^{2\pi} S_{qm}(c_\alpha,\cos v)S_{qn}(c_\sigma,\cos v)dv. \qquad (21)$$

The system of equations (17) to (20) may be written in matrix form as:

$$\begin{bmatrix} Q_{11} & Q_{12} & Q_{13} & Q_{14}\\ Q_{21} & Q_{22} & Q_{23} & Q_{24}\\ Q_{31} & Q_{32} & Q_{33} & Q_{34}\\ Q_{41} & Q_{42} & Q_{43} & Q_{44}\end{bmatrix}\begin{bmatrix} B_q\\ C_q\\ D_q\\ G_q\end{bmatrix}=\begin{bmatrix} V_1\\ V_2\\ V_3\\ V_4\end{bmatrix}, \qquad (22)$$

where the elements of the submatrices are defined in Appendix A. We solve for unknown expansion coefficients B_q, C_q, D_q, G_q from equation (22) by using matrix inversion technique.

Using asymptotic expressions of the radial Mathieu functions of the fourth kind and their first derivatives, we can write expressions for the normalized bistatic echo width of the right- and left-polarized waves can then be written as:

$$\frac{\sigma_L}{\lambda_L}=\left|\Omega_{cp}(\phi)\right|^2,\ \frac{\sigma_R}{\lambda_R}=\left|\Omega_{xp}(\phi)\right|^2, \qquad (23)$$

where,

$$\Omega_{cp}(\phi)=\sum_{q=e,o}\sum_{m=0,1}^{\infty} j^m B_{qm}S_{qm}(c_{L1},\cos\phi), \qquad (24)$$

$$\Omega_{xp}(\phi)=\sum_{q=e,o}\sum_{m=0,1}^{\infty} j^m C_{qm}S_{qm}(c_{R1},\cos\phi), \qquad (25)$$

where B_{qm}, C_{qm} can be obtained by invoking equation (22).

III. NUMERICAL RESULTS

Since the summations are infinite in extent, to obtain numerical results these summations have to be truncated to include only the first N terms, where N is an integer proportional to the electrical size and the constitutive parameters of the composite object. The results given in this paper have been checked for convergence, and obtained by considering only the first 10 terms (i.e., N = 10) of the infinite series associated with each even and odd function.

Numerical results are presented as normalized echo pattern widths for isotropic chiral elliptic cylinders of different axial ratios, embedded in another infinite isotropic chiral medium of different relative permittivities and chirality parameters. First, we select the parameters $\varepsilon_{r1}=1.0$, $\mu_{r1}=1.0$, $k_0\gamma_1=0.0$ for the exterior region while $k_0a=0.16\pi$, $\varepsilon_{r2}=4.0$, $\mu_{r2}=2.0$, $k_0\gamma_2=0.15$, and axial ratio *a*/*b* = 1.001 for the cylinder and $\varphi_i=180^{\circ}$. To validate the analysis and the calculated results, we computed the normalized echo pattern widths for the above chiral cylinder when it is excited by a plane wave that is transverse magnetically (TM) polarized in the axial z-direction. The results shown in Fig. 2 are in good agreement with those in [5] (circles) for an analogous chiral circular cylinder in free space, verifying the accuracy of the analysis and calculated results.

Figure 3 displays the normalized left- and right-polarized echo-width patterns for a chiral elliptic cylinder of axial ratio 2, with same the parameters as in Fig. 2 when it is embedded in an exterior chiral medium having the parameters $\varepsilon_{r1}=1.0$, $\mu_{r1}=1.0$, $k_0\gamma_1=0.15$ while excited by a LCP plane wave incident with $\varphi_i=180^{\circ}$. In this plot, the dominant left-polarized echo-width magnitude decreases gradually as the scattering angle increases from 0° to 180° while the corresponding right-polarized has an almost constant value at all scattering angles of -16 dB.

Figure 4 shows the left- and right-polarized echo-width patterns for the chiral elliptic cylinder in Fig. 2, when it is placed in a chiral medium which is similar to that in Fig. 3, but with $\varepsilon_{r1}=3.0$. When the results are compared with the ones in Fig. 3, we see that as the scattering angle increases from 0° to 180°, the reduction of the left-polarized echo-width magnitude is much higher. Also the right-polarized echo-width magnitude is much lower for all scattering angles.

Figure 5 shows is similar to Fig. 4, but with $\varepsilon_{r1}=3.0$ and $k_0\gamma_1=0.1$. We observe that as the scattering angle increases from 0° to 180°, the reduction of the left-polarized echo-width magnitude is much higher than in Figs. 3 and 4. Also the right-polarized echo-width magnitude is becoming closer to the left-polarized echo-width as the scattering angles increase. Figures 6 and 7 are similar to Fig. 5 but with $\varphi_i=45^{0}$ and $k_0\gamma_1=0.2$.

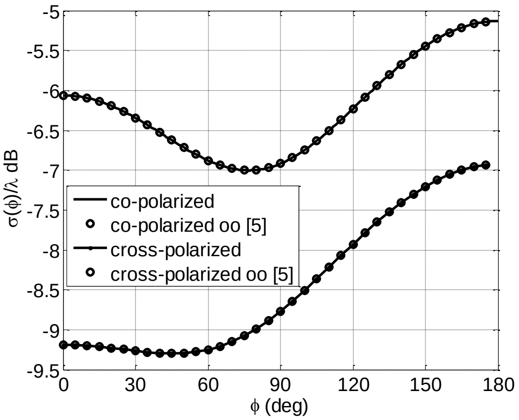

Fig. 2. Normalized co-polar and cross polar bistatic scattering widths against the scattering angle, for a chiral elliptic cylinder of axial ratio *a*/*b* =1.001, with $k_0 a = 0.16\pi$, $\varepsilon_{r2} = 4.0$, $\mu_{r2} = 2.0$, $k_0\gamma_2 = 0.15$, and located in free space, when it is excited by a TM polarized plane wave incident at $\varphi_i = 180^{\circ}$. Circles [5].

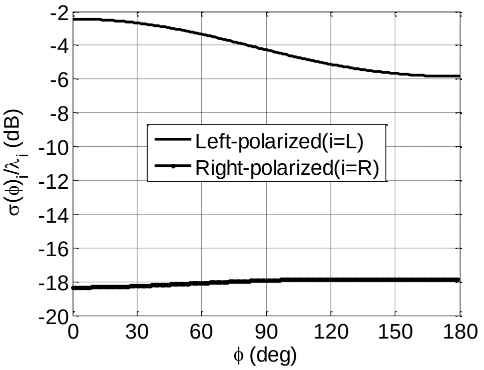

Fig. 3. Normalized left- and right-polarized bistatic scattering widths against the scattering angle for a chiral elliptic cylinder of axial ratio 2.0 and having the same parameters as those in Fig. 2, with $\varepsilon_{r1} = 1.0$, $\mu_{r1} = 1.0$, $k_0\gamma_1 = 0.15$ and $\varphi_i = 180^{\circ}$.

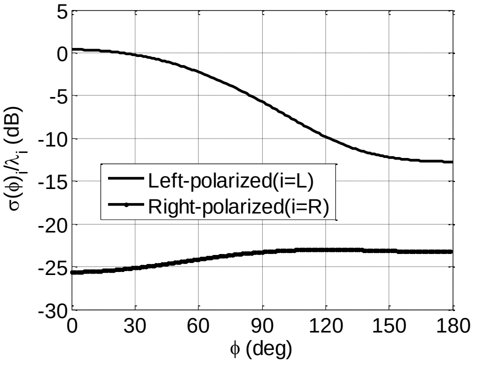

Fig. 4. Normalized left- and right-polarized bistatic scattering widths against the scattering angle for the chiral elliptic cylinder as in Fig. 3 while $\varepsilon_{r1} = 3.0$.

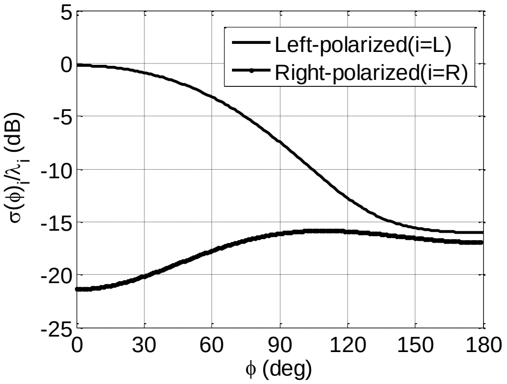

Fig. 5. Normalized left- and right-polarized bistatic scattering widths against the scattering angle for the chiral elliptic cylinder as in Fig. 4 while $\varepsilon_{r1} = 5.0$ and $k_0\gamma_1 = 0.1$.

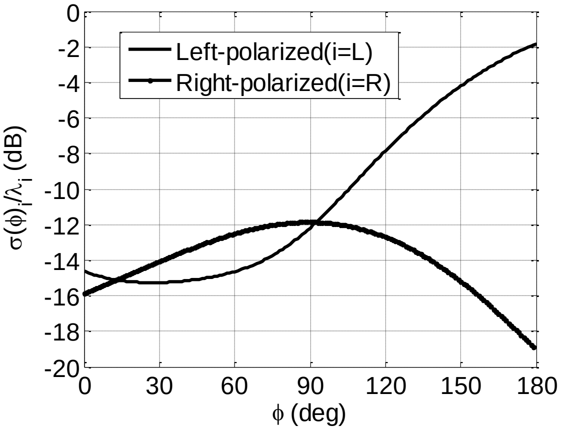

Fig. 6. Normalized left- and right-polarized bistatic scattering widths against the scattering angle for the chiral elliptic cylinder as in Fig. 5 while $\varphi_i = 45^{0}$.

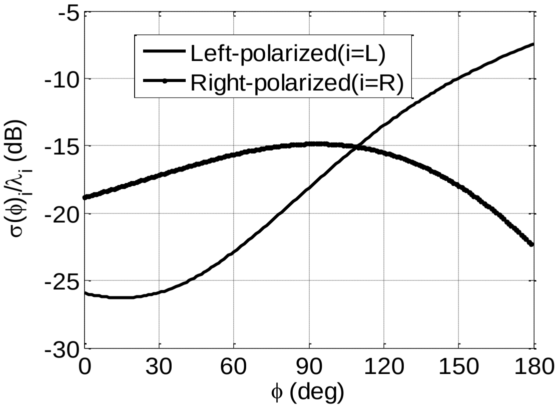

Fig. 7. Normalized left- and right-polarized bistatic scattering widths against the scattering angle for the chiral elliptic cylinder as in Fig. 5 while $k_0\gamma_1 = 0.2$.

IV. CONCLUSIONS

An analytic solution to the problem of scattering of an LCP plane wave by a chiral elliptic cylinder embedded in another infinite chiral medium is presented using the method of the separation of variables. Results have been presented as normalized bistatic for co and cross-polarized echo-width patterns for chiral elliptic cylinders of different axial ratios and chiral materials, to show the effects of these on scattering. It is seen that the presence of two different chiral materials could significantly influence the co and cross-polarized pattern widths and can be used to control the radar cross section of targets or antenna radiation pattern [8]. Finally, the solution presented in this paper is for LCP incident field while in [15] was for RCP.

ACKNOWLEDGMENT

Prof. A.-K. Hamid wishes to acknowledge the support provided by the University of Sharjah, U.A.E.

Appendix A

$$Q_{11nn} = R_{qn}^{(4)}(c_{L1}, \xi_s) N_{qn}(c_{L1}), \tag{A1}$$

$$Q_{12nm} = R_{qm}^{(4)}(c_{R1}, \xi_s) M_{qnm}(c_{L1}, c_{R1}), \tag{A2}$$

$$Q_{13nm} = -R_{qm}^{(1)}(c_{R2}, \xi_s) M_{qnm}(c_{L1}, c_{R2}), \tag{A3}$$

$$Q_{14nm} = -R_{qm}^{(1)}(c_{L2}, \xi_s) M_{qnm}(c_{L2}, c_{L1}), \tag{A4}$$

$$Q_{21nn} = R_{qn}^{(4)'}(c_{L1}, \xi_s) N_{qn}(c_{L1}), \tag{A5}$$

$$Q_{22nm} = -\frac{k_{L1}}{k_{R1}} R_{qm}^{(4)'}(c_{R1}, \xi_s) M_{qnm}(c_{L1}, c_{R1}), \tag{A6}$$

$$Q_{23nm} = -\frac{k_{L1}}{k_{R2}} R_{qm}^{(1)'}(c_{R2}, \xi_s) M_{qnm}(c_{L1}, c_{R2}), \tag{A7}$$

$$Q_{24nm} = \frac{k_{L1}}{k_{L2}} R_{qm}^{(1)'}(c_{L2}, \xi_s) M_{qnm}(c_{L2}, c_{L1}), \tag{A8}$$

$$Q_{31nn} = R_{qn}^{(4)}(c_{L1}, \xi_s) N_{qn}(c_{L1}), \tag{A9}$$

$$Q_{32nm} = -R_{qm}^{(4)}(c_{R1}, \xi_s) M_{qnm}(c_{L1}, c_{R1}), \tag{A10}$$

$$Q_{33nm} = -\frac{Z_1}{Z_2} R_{qm}^{(1)}(c_{R2}, \xi_s) M_{qnm}(c_{L1}, c_{R2}), \tag{A11}$$

$$Q_{34nm} = \frac{Z_1}{Z_2} R_{qm}^{(1)}(c_{L2}, \xi_s) M_{qnm}(c_{L2}, c_{L1}), \tag{A12}$$

$$Q_{41nn} = R_{qn}^{(4)'}(c_{L1}, \xi_s) N_{qn}(c_{L1}), \tag{A13}$$

$$Q_{42nm} = \frac{k_{L1}}{k_{R1}} R_{qm}^{(4)'}(c_{R1}, \xi_s) M_{qnm}(c_{L1}, c_{R1}), \tag{A14}$$

$$Q_{43nm} = -\frac{k_{L1} Z_1}{k_{R2} Z_2} R_{qm}^{(1)'}(c_{R2}, \xi_s) M_{qnm}(c_{L1}, c_{R2}), \tag{A15}$$

$$Q_{44nm} = -\frac{k_{L1} Z_1}{k_{L2} Z_2} R_{qm}^{(1)'}(c_{L2}, \xi_s) M_{qnm}(c_{L2}, c_{L1}), \tag{A16}$$

$$V_{1n} = -A_{qn} R_{qn}^{(1)}(c_{L1}, \xi_s) N_{qn}(c_{L1}), \tag{A17}$$

$$V_{1n} = -A_{qn} R_{qn}^{(1)'}(c_{L1}, \xi_s) N_{qn}(c_{L1}), \tag{A18}$$

$$V_2 = -A_{qn} R_{qn}^{(1)}(c_{L1}, \xi_s) N_{qn}(c_{L1}), \tag{A19}$$

$$V_3 = V_1, \tag{A20}$$

$$V_4 = V_2. \tag{A21}$$

REFERENCES

[1] N. Engheta and D. L. Jaggard, “Electromagnetic chirality and its applications,” *IEEE Antennas Propagat. Soc. Newsletter*, vol. 30, pp. 6-12, Oct. 1988.

[2] D. L. Jaggard, X. Sun, and N. Engheta, “Canonical sources and duality in chiral media,” *IEEE Trans. Antennas Propagat.*, vol. 36, pp. 1007-1013, July 1988.

[3] B. N. Khatir and A. R. Sebak, “Slot antenna on a conducting elliptic cylinder coated by nonconfocal chiral media,” *Prog. Electromag. Res. (PIER)*, vol. 93, pp. 125-143, 2009.

[4] S. Ahmed and Q. A. Naqvi, “Electromagnetic scattering from a chiral coated nihility cylinder,” *Progress in Electromag. Res. Lett.*, vol. 18, pp. 41-50, 2010.

[5] R. G. Rojas, “Integral equations for EM scattering by homo-geneous/inhomogeneous two-dimensional chiral bodies,” *IEEE Proc. Microwave Antennas Propag.*, vol. 141, pp. 385-392, 1994.

[6] M. A. Al-Kanhal and E. Arvas, “Electromagnetic scattering from a chiral cylinder of arbitrary cross section,” *IEEE Trans. Antennas Propag*., vol. 44, pp. 1041-1049, July 1996.

[7] A. Semichaevsky, A. Akyurtlu, D. Kern, D. H. Werner, and M. G. Bray, “Novel BI-FDTD approach for the analysis of chiral cylinders and spheres,” *IEEE Trans. Antennas Propagat*., vol. 54, pp. 925-932, 2006.

[8] S. Shoukat, S. Ahmed, M. Ashraf, A. Syed, and Q. Naqvi, “Scattering of electromagnetic plane wave from a chiral cylinder placed in a chiral metamaterial,” *J. Electromag. Waves Applic*., vol. 27, pp. 1127-1135, 2013.

[9] B. N. Khatir, M. Al-Kanhal, and A. Sebak, “Electromagnetic wave scattering by elliptic chiral cylinder,” *J. Electromag. Waves Applic*., vol. 20, pp. 1377-1390, 2006.

[10] A.-K. Hamid, “EM scattering by a lossy dielectric-coated nihility elliptic cylinder,” *Appl. Comp. Electromag. Soc. (ACES) Journal*, vol. 25, pp. 444-449, 2010.

[11] A.-K. Hamid, “Scattering by chiral lossy meta-material elliptic cylinders,” *Appl. Comp. Electromag. Soc. Journal*, vol. 27, pp. 603-609, 2012.

[12] I. V. Lindell, A. H. Sihvola, S. A. Tretyakov, and A. J. Viitanen, *Electromagnetic Waves in Chiral and Bi-isotropic Media*. Artech House, Boston, USA, 1994.

[13] A.-K. Hamid and F. R. Cooray, “Scattering from a chirally coated DB elliptic cylinder,” *AËU*, vol. 68,

pp. 1106-1111, 2014.

[14] A.-K. Hamid and F. R. Cooray, "Two-dimensional scattering by a homogeneous gyrotropic-type elliptic cylinder," *Advan. Electromag.*, vol. 5, pp. 106-112, Dec. 2016.

[15] A.-K. Hamid, "Scattering by a chiral elliptic cylinder placed in another infinite chiral medium," *Appl. Comp. Electromag. Soc. Conf.*, Florence, Italy, 2017.

A Magneto-Rheological Brake Excited by Permanent Magnets

Antonino Musolino [1], Marco Raugi [1], Rocco Rizzo [1], Luca Sani [1], and Efrén Diez-Jimenez [2]

[1] Department of Energy and Systems Engineering
University of Pisa, Pisa, 56122, Italy
antonino.musolino@unipi.it, marco.raugi@unipi.it, rocco.rizzo@unipi.it, luca.sani@dsea.unipi.it

[2] Mechanical Engineering Area
University of Alcalá, Alcalà de Henares, 28801, Spain
Efren.diez@uah.es

Abstract **─** In this paper an innovative brake, based on magneto-rheological fluids, is described. A system of Permanent Magnets, properly arranged in the device, has been designed to maximize the excitation field inside the fluid. The system has been analyzed by means of a 3D FEM code. The results in terms of magnetic flux density inside the fluid and the braking torque have been discussed. Furthermore, the magnetic torque necessary to perform the brake actuation has been calculated. Finally, some preliminary measurements on a prototype have been performed.

Index Terms **─** FEM, Magneto-Rheological Brake, Permanent Magnets.

I. INTRODUCTION

Magneto-Rheological Fluids (MRFs) are synthetic oil-based or water-based suspensions of magnetically polarizable micro-particles, capable of changing their rheological behavior as a function of the intensity of an external magnetic field [1]. In fact, the micro-sized ferromagnetic particles, dispersed inside the MRF, align themselves along the direction of the magnetic field, allowing a rapid and reversible transition from a liquid to a near-solid state. By removing the magnetic field, these fluids can return to their liquid state in a very short time (15-20 *ms*), being the phenomenon perfectly reversible [2]. MRF-based devices have been developed since the end of 1940s [3], when the first MRF actuator was presented. The main applications are in dampers in the automotive and aerospace industry [4]. Also, they can be found in finishing processes for optical lens, waveguides, hard disk, and so forth [5, 6].

As for magneto-rheological brakes, many solutions have been presented in past years [7-11]. The use of MRF in such devices w.r.t. conventional mechanical or electrodynamic brake, allows smooth and steady transmissible/braking torque with many applications like in space, automotive industry, robotics, industrial machines or gym/fitness equipment. Furthermore, the MRF-based brakes do not exert axial load and they can be easily controlled by tuning the magnetic field in the fluid.

Currently, most of the solutions use conventional wired electromagnets to activate the fluid. Other designs use permanent magnets (PMs) as excitation source, but very few of them have been developed till now [12-14]. There are also solutions that combines PM-coil exciter in order to control the magnetic field inside the fluid. Purely PM-based devices can be found in [15, 16]; while in [17, 18], a hybrid Electrodynamic/MRF based clutch has been described.

In the present paper, a new MRF-based brake is proposed. It uses a system of Permanent Magnets to excite the fluid. The braking torque can be controlled by rotating the PMs in the circumferential direction by an angle of 90°. The device has been analyzed by using a 3D magnetic FEM code [19]. The results in terms of magnetic flux density inside the fluid and braking torque have been discussed. Furthermore, the magnetic torque necessary to perform the brake activation has been calculated. Finally, some very preliminary measurements on a prototype have been performed.

II. THE PROPOSED BRAKE

A. The fluid characteristics

In the proposed device, the magnetorheological fluid MRF140CG has been used. It is produced by Lord Corporation, Cary NC, USA [20], and the main magnetic and mechanical characteristics are synthesized by the *B-H* curve and the *τ-H* curve (Yield/Shear stress τ vs magnetic field H), obtained by the producer.

When an external magnetic field is applied in a gap filled by the MRF, the polarizable particles align themselves along the flux lines, allowing to create particle chains that prevent the movement of the particles themselves in the fluid. Once the magnetic field is removed, the fluid come back in a liquid state.

Submitted On: July 26, 2018
Accepted On: November 4, 2018

Although many mathematical models have been developed, a very simplified equation can be used to describe the shear stress as a function of the applied magnetic field. In particular, combining the *B-H* curve and the *τ-H* curve of the fluid, the following relationship between shear stress τ and magnetic induction *B* can be used [7, 21]:

$$\tau_0(B) = 67\,B^4 - 222\,B^3 + 200\,B^2 + 17\,\mathrm{B} + 0.18. \quad (1)$$

In (1), the unit of the yield stress τ_0 is *kPa* while that of the magnetic flux density *B* is Tesla.

B. The brake characteristics

The design requirements for the brake are the following: the braking torque > 5 *Nm*; the ratio between the maximum and minimum torque > 8; maximum diameter < 100 *mm*; maximum axial length < 40 *mm*; maximum relative angular speed between the two shafts < 1500 *rpm*.

Figure 1 shows a schematic view of the proposed device with the main dimensions and materials, capable to fulfill the design requirements. It is composed of two coaxial shafts, input and output shafts of the brake, the magneto-rheological fluid inserted between the two coaxial shafts, and a third inner element carrying the permanent magnets.

The shaft number 1 is a hollowed cylindrical element made completely of ferromagnetic material.

The shaft number 2 is composed of four 90°-sections of ferromagnetic materials; in two of these sections, a certain number of non-ferromagnetic plates are inserted allowing the magnetic flux to pass through and thus, affecting the MR fluid. In the other 90º two sections, there are not non-ferromagnetic plates; therefore, any magnetic field externally applied is shielded. The number and dimensions of these non-ferromagnetic plates have been chosen by using a multi-objective optimization procedure, capable to maximize the performance of the device.

The MRF excitation system consists of four pie-shaped rare-earth NdFeB magnets, with a remanence field *Br* = 1.36 *T* and a coercivity field *Hc* = −1020 *kA/m*. They are positioned inside the two shafts, coaxially. Each of the PM occupies an angle of 45° along the circumferential direction and is magnetized along the radial direction.

As shown in Figs. 2 (a-b), the brake operates as follows: let's assume that initially the PMs are in the OFF state; the magnetic field does not pass through the fluid since the flux lines close themselves in the solid ferromagnetic sectors which act as a shunt for the flux lines just below the MRF. In this condition, the shaft number 1 rotates at a given speed and the shaft number 2 is not drag by shaft 1. Once the decision to brake the shaft number 1 has been taken, the PMs system must be rotated (by an auxiliary mechanism) along its circumferential direction (indifferently in clockwise or counter clockwise) with respect to the shaft 2. While the PMs rotate by moving away from the OFF state, the presence of non-ferromagnetic plates progressively forces the magnetic field to cross the fluid and to close its flux lines, following the path of least magnetic reluctance. The highest values of the field inside the MRF and, consequently, of the braking torque are obtained when the permanent magnets system rotates by an angle of 90°, working in the ON state.

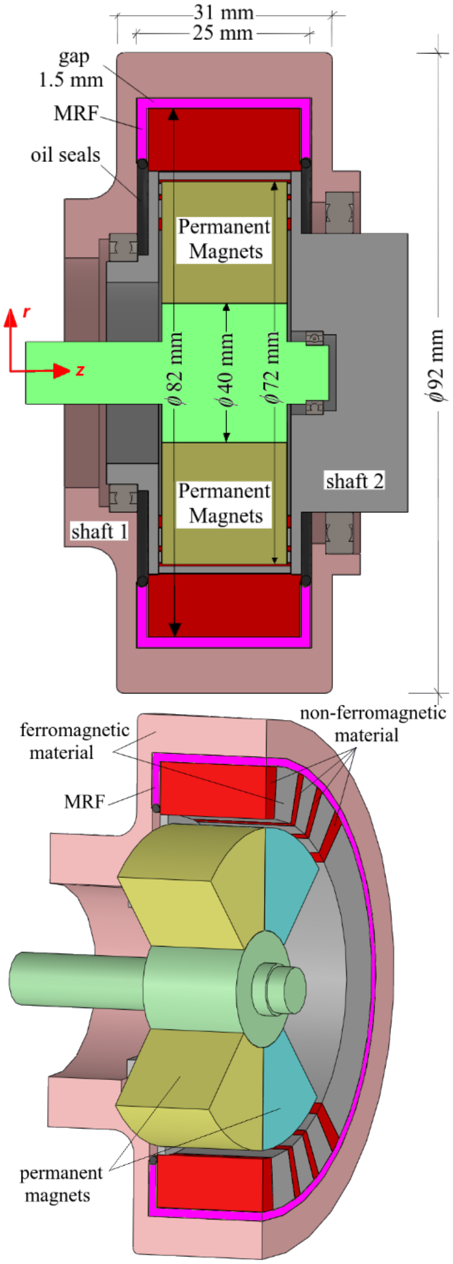

Fig. 1. The proposed brake with the main dimensions and materials.

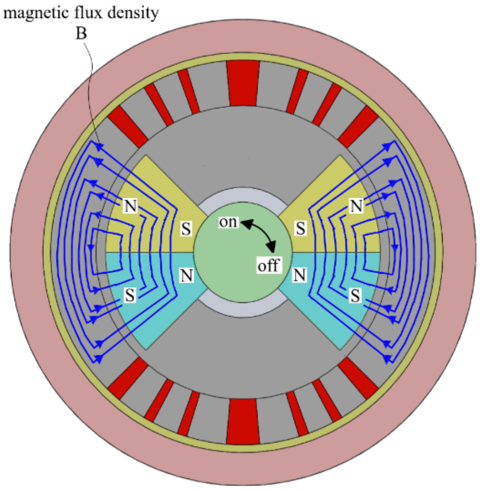

(a) OFF state

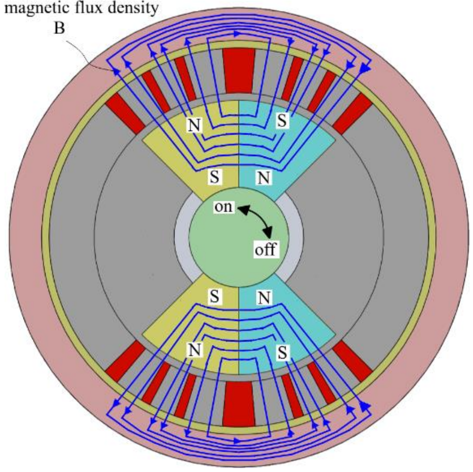

(b) ON state

Fig. 2. The operation principle of the proposed brake.

In order to actuate the brake, an auxiliary mechanism (not shown in figure) capable to produce a proper activation torque that perform the rotation of the permanent magnets from the ON to the OFF state position is used. Considering that this activation torque (see Fig. 8) is quite low, the auxiliary mechanism can be composed of a preload torsion spring, which at rest keeps the PMs in the OFF state. Then, by manually or automatically twisting the spring along its axis by a proper angle (in the range 0° to 90°), the PMs can be rotated towards the ON state, so controlling the braking torque.

C. The FE model

The device has been analyzed by using a 3D model based on a Finite Elements code [19]. The FE mesh is shown in Fig. 3, while in Table 1, the main simulation parameters and materials have been reported. The geometric dimensions of the model are shown in Fig. 1.

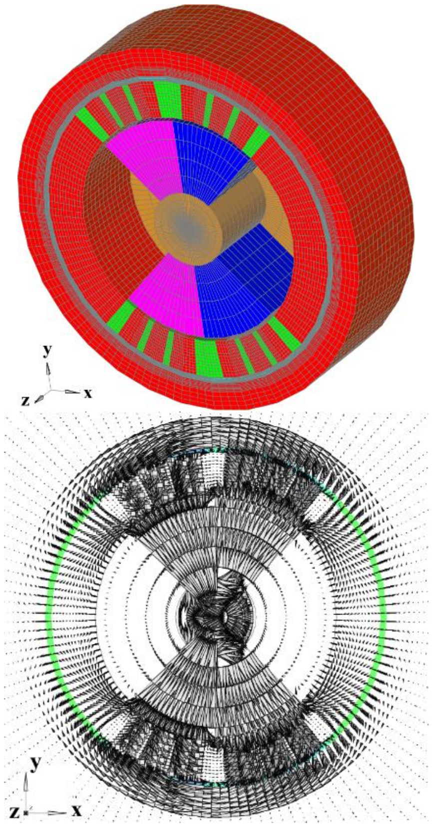

Fig. 3. The FE model and the magnetic flux density vectors in the ON state.

Table 1: Simulation parameters and data

Number of mesh elements	7×10^5
Ferromagnetic material	AISI 1018
Non-ferromagnetic material	AISI 316
Permanent Magnets: NdFeB	Br = 1.36 T; Hc = 1020 kA/m.
Magneto-rheological fluid	MRF140CG

All the simulations have been performed considering the *B-H* functions of the nonlinear materials (MRF, Permanent Magnets, ferromagnetic material).

The hysteretic behavior of these materials has been neglected, although several accurate and efficient models have been recently proposed [22-24].

As an example of simulation results, the Fig. 3 shows also the distribution of the magnetic flux density in the device when the system is in the ON state.

The performance of the device can be obtained by analyzing the magnetic flux density distribution in the MRF as produced by the permanent magnets.

Figure 4 shows the magnetic flux density on a cross-section on the x-y plane of the device, respectively when the PM system is in the OFF state (0°), in the intermediate position (45°) and in the ON state (90°).

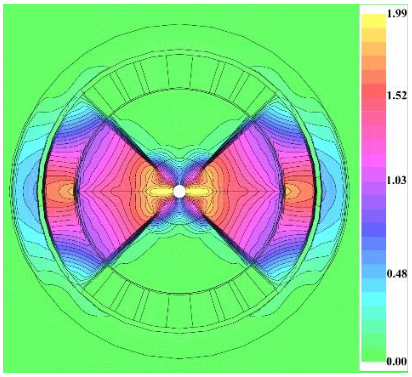

OFF state

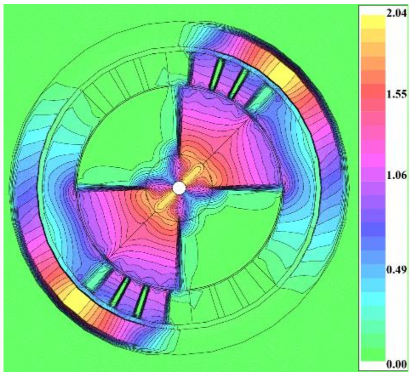

Intermediate position

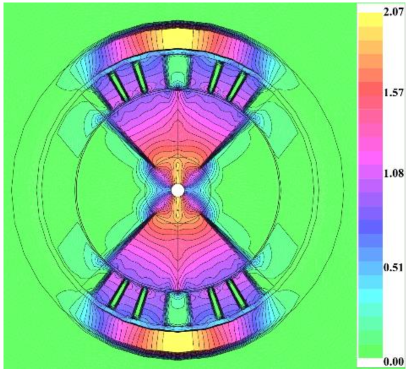

ON state

Fig. 4. The map of B (in $[T]$) on a middle cross-section of the x-y plane of the device at different conditions.

Figure 5 shows the radial component of the magnetic flux density along a circumference inside the MR fluid, in the same conditions of the previous figure.

The simulation results show that the magnetic induction in the MRF when the PMs system is in the ON state reaches up to 1 T, which is high enough to produce a high shear-stress and consequently a high level of braking torque. On the contrary, the OFF state is characterized by a very low magnetic flux density, not higher than 0.1 T and therefore low shear stress in the fluid.

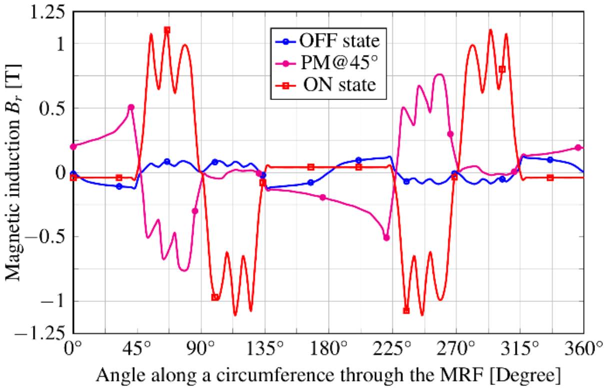

Fig. 5. The radial component of B along a circumference inside the MRF.

III. THE RESULTS

A. The braking torque

The braking torque has been calculated in a post-processing from the magnetic simulation as follows. The torque developed by a single volume element of MRF, centered at a generic r distance from the axis of the device and positioned between the two lateral surfaces of the cylindrical structure:

$$\Delta T_b = \tau_0(B)\cdot r^2\cdot\Delta\theta\cdot\Delta z. \tag{2}$$

Neglecting the edge effects along the z-direction and using the value of τ_0(B) calculated numerically from (1) in the center of the MR fluid, each cell of MR fluid produces the following contribution:

$$\Delta T_b = \tau_0(B)\cdot\left[\frac{r_{inn_{MRF}}+r_{out_{MRF}}}{2}\right]^2\cdot\Delta\theta_c\cdot l_z\,. \tag{3}$$

Then, taking into account the number of cells of the FE mesh and their azimuthal dimension, the total torque developed by the proposed brake can be approximated by a summation:

$$T_b = \sum_{n=1}^{N_c}\Delta T_b. \tag{4}$$

Using the simulation results in terms of magnetic induction and shear stress, the braking torque developed by the proposed device has been calculated by using (4). Figure 6 shows its value as a function of the position of the permanent magnets system along the circumferential direction. When the PMs are in the ON state (angular-displacement = 90°), the braking torque is about 5.5 *Nm*, while in the OFF state (angular-displacement = 0°) the torque is about 0.65 *Nm*. This latter value is mainly due to the fluid natural viscosity. Anyhow, the ratio between the maximum and minimum torque, that is between the torque in the ON and OFF state, for the proposed brake is about 8.5, a satisfactory value in this kind of device.

In the same figure, experimental data are shown. They have been obtained by using the test bench (see Fig. 7) composed of a controlled brushless motor, two elastic couplings and a torque meter. During the tests, the relative angular speed between the two shafts has been kept constant at 100 *rpm*. The braking torque has been measured respectively when the PM system was in the OFF state, in the intermediate position (45°) and in the ON state. As for the maximum relative angular speed between the two shafts, some tests have shown that the device operate quite well up to 1000 *rpm*.

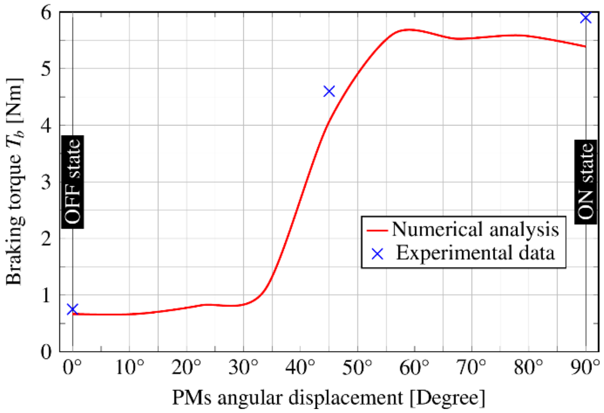

Fig. 6. The braking torque as a function of the angular displacement of the PMs.

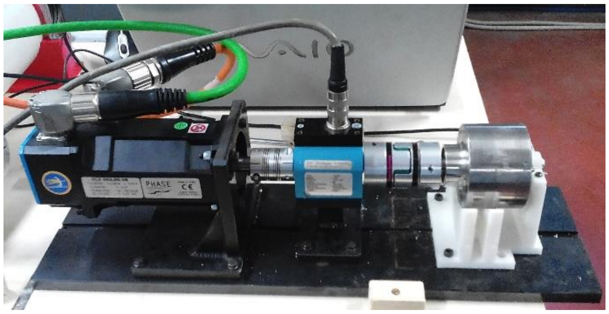

Fig. 7. The test bench.

As can be seen, the maximum deviation between the calculated torque and the measured one is about 15%. This deviation is explained because the simulation results neglect the contribution to the braking torque of the MRF that fills the gaps axially at the two bases of the cylindrical structure.

B. The brake actuation

As described in previous sections, the brake activation can be obtained by rotating the PMs system along its circumferential direction (indifferently in clockwise or counter clockwise). However, during the rotation, there is a magnetic torque that hinders the PMs motion from the OFF to the ON state and vice-versa. This activation torque is due to the natural magnetic interaction between magnets and ferromagnetic materials which constitute the shaft 2.

Figure 8 shows the activation magnetic torque value as a function of the PMs angular displacement, obtained by using the 3D FE model. As expected, the maximum value occurs when the PMs displacement is 45°, that is when the permanent magnets system is in the midway between the ON and OFF state.

An auxiliary mechanism (not shown in figure) can be exploited to move the permanent magnets from the ON to the OFF state. In this experiment a preloaded torsional spring have been used to overcome the magnetic torque and to rotate directly the PMs from OFF to ON state. By controlling more accurately the angular displacement of the PMs, using for example a stepper motor, the braking torque could be precisely modulated. Anyhow, the power required to activate/deactivate the proposed brake is a very low fraction of the braking power.

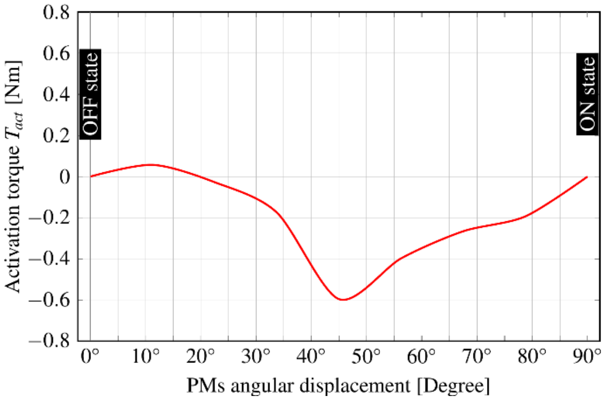

Fig. 8. The activation torque as a function of the angular position of the PMs.

VI. CONCLUSION

The authors have presented a Magneto-rheological brake excited by a system of permanent magnets. The brake is activated by rotating the PMs system along its circumferential direction (indifferently in clockwise or counter clockwise) by an angle of 90°. The proposed brake is characterized experimentally by a maximum braking torque of about 5.5 *Nm* and the ratio between the maximum and minimum torque is about 8.5, a satisfactory value in this kind of device. Finally, the results show that the actuation of the brake requires a very low power.

REFERENCES

[1] J. D. Carlson, “The promise of controllable fluids,” *Proc. of Actuator 94* (H. Borgmann and K. Lenz, Eds.), AXON Technologies Consult GmbH, pp. 266-270, 1994.

[2] W. I. Kordonsky, “Elements and devices based on magnetorheological effect,” *J. Intell. Mater. Syst. Struct.*, vol. 4, no. 1, pp. 65-69, 1993.

[3] J. Rabinow, “The magnetic fluid clutch,” *Trans-*

actions of the American Institute of Electrical Engineers, 67 (2):1308-1315, 1948.

[4] J. Gołdasz and B. Sapiński, “Insight into magneto-rheological shock absorbers,” *Springer*, New York, 2015.

[5] S. O. Lee, K. I. Jang, B. K. Min, S. J. Lee, and J. W. Seok, “A study on tribological properties of Magneto-Rheological Fluid (MRF) in polishing process,” *Proceedings of the KSPE Spring Conference*, vol. 40, pp. 20-33, 2006.

[6] A. Shorey and M. DeMarco, “Application of magneto-rheological finishing (MRF®) to the figuring of adaptive optics systems,” *Adaptive Optics: Methods, Analysis and Applications, Charlotte*, North Carolina, June 6, 2005.

[7] J. Wu, X. Jiang, J. Yao, H. Li, and Z. Li, “Design and modeling of a multi-pole and dual-gap magneto-rheological brake with individual currents,” *Advances in Mechanical Engineering*, vol. 8, pp. 1-15, 2016.

[8] Y. Shiao and Q. Nguyen, “Development of a multi-pole magnetorheological brake,” *Smart Materials and Structures*, vol. 22, no. 6, pp. 1-13, 2013.

[9] G. Yildirim and S. Genc, “Experimental study on heat transfer of the magnetorheological fluids,” *Smart Materials and Structures*, vol. 22, no. 8, pp. 1-8, 2013.

[10] H. T. Guo and W. H. Liao, “A novel multi-functional rotary actuator with magnetorheological fluid,” *Smart Materials and Structures*, vol. 21, no. 6, pp. 1-9, 2012.

[11] J. Vėžys, D. Mažeika, R. Kandrotaitė-Janutienė, E. Dragašius, A. Kilikevičius, and E. V. Korobko, “Sedimentation influence on magnetorheological brake torque moment,” *Strength Materials*, vol. 50, no. 2, pp. 357-367, 2018.

[12] G. L. Johnston, W. C. Kruckemeyer, and R. E. Longhouse, “Passive magnetorheological clutch,” *US Patent*, 5848678, 1998.

[13] T. Saito and H. Ikeda, “Development of normally closed type of magnetorheological clutch and its application to safe torque control system of human-collaborative robot,” *Journal of Intelligent Material Systems and Structures*, vol. 18, no. 12, 1181-1185, Dec. 2007.

[14] A. Wiehe and J. Maas, “Magnetorheological actuators with currentless bias torque for automotive applications,” *Journal of Intelligent Material Systems and Structures*, vol. 21, pp. 1575-1585, 2010.

[15] O. Hyun-Ung, “Characteristics of a magneto-rheological fluid isolator obtained by permanent magnet arrangement,” *Smart Mater. Struct.*, vol. 13, 2004.

[16] B. Yang, T. Chen, G. Meng, Z. Feng, J. Jiang, S. Zhang, and Q. Zhou, “Design of a safety escape device based on magnetorheological fluid and permanent magnet,” *Journal of Intelligent Material Systems and Structures*, vol. 24, pp. 49-60, 2013.

[17] H. C. Lai, R. Rizzo, and A. Musolino, “An electrodynamic/magnetorheological clutch powered by permanent magnets,” *IEEE Transactions on Magnetics*, vol. 53, no. 2, pp. 1-7, Feb. 2017.

[18] R. Rizzo, “An innovative multi-gap clutch based on magneto-rheological fluids and electrodynamic effects: magnetic design and experimental characterization,” *Smart Materials and Structures*, vol. 26, pp. 1-11, 2017.

[19] EFFE v2.00, *User Manual*, Bathwick Electrical Design Ltd., Jan. 2009.

[20] Lord Corporation Ltd., www.lord.com/products-and-solutions/magneto-rheological-(mr)/mrproducts.xml, July 2018.

[21] Q.-H. Nguyen, S.-B. Choi, and N. M. Wereley, “Optimal design magnetorheological valves via a finite element method considering control energy and a time constant,” *Smart Materials and Structures*, vol. 17, 2008.

[22] E. Cardelli, A. Faba, A. Laudani, G. M. Lozito, S. Q. Antonio, F. R. Fulginei, and A. Salvini, “Implementation of the single hysteron model in a finite-element scheme,” *IEEE Transactions on Magnetics*, 53 (11), art. no. 7912355, 2017.

[23] E. Cardelli, A. Faba, A. Laudani, M. Pompei, S. Q. Antonio, F. R. Fulginei, and A. Salvini, “A challenging hysteresis operator for the simulation of Goss-textured magnetic materials,” *Journal of Magnetism and Mag. Materials*, 432, pp. 14-23, 2017.

[24] E. Cardelli, A. Faba, A. Laudani, S. Q. Antonio, F. R. Fulginei, and A. Salvini, “A moving approach for the Vector Hysteron Model,” *Physica. B: Condensed Matter*, 486, pp. 92-96, 2016.

A New Compact Finline OMT Based on Multi-Section Transformer

Yaqing Yu, Wen Jiang, Shuai Zhang, Shuxi Gong, and Tong Cheng

National Key Laboratory of Antennas and Microwave Technology
Xidian University, Xi'an, 710071, China
yuyaqing27@163.com, jw13@vip.qq.com, zhangshuai@xidian.edu.cn, shxgong@xidian.edu.cn,
chengtong26@163.com

Abstract **─** In the millimeter wave band, the simplification of the orthomode transducer (OMT)'s structure and processing technic is placed in a more important position. The finline OMT can meet the requirement, but its size is usually not compact enough. To solve this problem, a compact finline OMT based on multi-section transformer is presented. Such OMT can enable size reduction by reasonably designing three transformers to reach the matching condition, which makes the design more flexible. As a result, the -20dB reflection bandwidth of the proposed OMT is 30.2 GHz to 49.8 GHz (49%), while the lengths of main arm's and side arm's transition for vertical polarization are $1.35\lambda_{max}$ and $0.9\lambda_{max}$ (λ_{max} denotes the maximum free space wavelength in band), respectively, which has been greatly reduced compared with the traditional ones. To verify the working performance of the design, a prototype is fabricated and measured. Finally, some assembly errors are analyzed to study its influence. The results show that the proposed OMT can be a good candidate for millimeter wave application.

Index Terms **─** Compact, finline OMT, millimeter wave application, multi-section transformer.

I. INTRODUCTION

An orthomode transducer (OMT) can separate or combine two orthogonal polarizations to double the channel capacity. In recent years, with the development of remote sensing and radio astronomy, the demands for the high operating frequency and the ultra-wideband characteristics of the receiver system are on the rise. At millimeter wave band, the physical size of the device becomes smaller, thus leading to the higher demands for machining and assembly process. To fulfill these requirements, it is necessary to expand the bandwidth of the OMT and reduce its complexity.

Generally, OMTs can be divided into planar type and waveguide type. The planar OMTs are mainly based on microstrip line structure, which have the shortcomings of large insertion loss, low power capacity and poor matching with the waveguide [1,2].

Waveguide OMTs have many merits, such as high power capacity and mechanical robustness. To achieve wideband applications, it is necessary to suppress the higher order modes, such as TE_{11} and TM_{11} modes in a square waveguide [3]. For asymmetric OMT, their fractional working bandwidth can only reach about 20%, for the higher order modes cannot be controlled effectively [4,5].

As the suppression of higher order modes is found related to the symmetry of the OMT's topology, the two-fold symmetric structure has the best effect, which separates both polarizations' power into two halves, and then can be recombined later. The representative forms are Turnstile OMT [6-9] and Bøifot OMT [9-11], featuring the advantages of broadband, high isolation, high cross-polarization discrimination, and low insertion loss. However, they all have complicated structures and usually need to be divided into three or more blocks for processing, which will introduce a lot of assembly errors in millimeter frequency range.

One-fold symmetric structure means only one of the polarizations' power will be separated and recombined, which can suppress the odd higher order modes. In general, the finline one [12-16] and the transformations of the Bøifot OMT that are based on the double ridge transition [17-20] and the reverse coupling structure [21] can be concluded as the one-folded symmetric type. The former can achieve a bandwidth of 40%-60% and will be discussed later. The latter require a height-reduced waveguide to make the higher order modes evanescent, but the transition from the double ridge to the output port will limit the OMT performance for its vertical polarization. In general, their reported working bandwidth are no more than 50%. In addition, their structures are also complicated and bulky.

In other OMTs, the quad-ridged one [22,23] also needs the absorber, and its transition needs to match the hundreds of ohms waveguide with the 50 ohms coaxial cables. Therefore, it usually needs a long transition to ensure the in-band reflection characteristic. The OMT based on the SIW [24] and the polarization-selective coupling structure [25] belong to the asymmetric type,

Submitted On: May 18, 2018
Accepted On: October 19, 2018

which both have the disadvantage of narrow bandwidth.

The proposed OMT chooses the finline form, which was first presented by Roberson [12] with the characteristics of ultra-wideband operation and simple structure. It can be manufactured with two blocks and a metal plate, so the advantage of easy fabrication makes it a good candidate for millimeter wave or terahertz application [13]. For this OMT, the main drawback is its large size, and the traditional linear or exponential double ridge transitions usually require a long transition to guarantee the matching characteristics for vertical polarization. For instance, the linear transition is used in [14] and [15], and one of them can achieve a -20dB impedance fractional bandwidth of about 52%, when its main arm's and the side arm's double ridge transition lengths are 3.2λ_{max} and 1.8λ_{max} (λ_{max} denotes the maximum free space wavelength in band), respectively. For the exponential case [13], it realizes a -15dB impedance bandwidth of 42% in the terahertz band, while the transitions' lengths are both reduced to 1.4λ_{max}. In addition, the transitions' lengths have been further reduced to 0.54λ_{max} and 0.48λ_{max} to enhance the isolation performance with the expense of narrow bandwidth [16]. Therefore, ensuring both miniaturization and high performance is still a problem for finline OMT.

In this paper, a finline OMT based on multi-section transformer is developed to solve the problem above. It works at 7mm-band (30GHz-50GHz), which is used for the detection of interstellar molecular line in radio astronomy. The multi-section transformer is widely used in waveguide matching [6], slot antenna profile reduction [26] and power divider impedance transformation [27]. However, to the best of our knowledge, the multi-section transformer has never been used to achieve the miniaturization of the finline OMT. The comparison between other OMTs and the proposed one is listed in Table 1.

The rest of the paper is arranged as follows. Section II mainly describes the theory of the multi-section transformer. The design of the multi-section transformers and OMT is put in Section III. In Section IV, a prototype is fabricated and tested to verify the proposed structure, and some error analyses are carried out. Finally, a brief summary is shown in Section V.

Table 1: The comparison between the other OMTs and the proposed one

Ref.	OMT Type	S11/dB	Bandwidth	Isolation /dB	Insertion loss /dB	Cross Pol. /dB	Size/λ_{max}^3	Complexity
[2]	Planar	<-15	41.2%		<-2	<-58		Simple
[5]	Asym.	<-22.5	12.1%	>65		<-57	1.7×2.3×0.86 (model size)	Simple
[6]	Turnstile	<-25	37%	>50	<0.2	<-50	3.4×5.2×6.8 (fabricated size)	Complex
[9]	Turnstile Bøifot	<-24 <-29	57.5% 36.6%	>40	<0.11		0.94×1.56×1.73 1.17×1.35×1.53 (model size)	Complex
[10]	Bøifot	<-28	40%	>47	<0.5	<-40		Complex
[17]	Double ridged	<-20	49.7%	>45	<0.16		4.74×4.74×5.69 (fabricated size)	Medium
[20]	Double ridged	<-20	40%	>60			2.15×1.05×4.43 (model size)	Medium
[21]	Reverse Coupling	<-20	32%	>50	<0.2	<-30		Medium
[22]	Quad-ridged	<-15	72%	>50	<3	<-55	0.8 (transition length)	Simple
[13]	Exp. finline	<-15	42%	>55	<1.7	<-57	1.4, 1.4 (transition length)	Simple
[15]	Linear finline	<-20	52%	>40		<-20	3.2, 1.8 (transition length)	Simple
This work	Stepped finline	<-20	49%	>67	<1.1	<-76	1.35, 0.9 (transition length) 2.86×3.43×4.12 (fabricated size) 0.97×3.27×2.18 (model size)	Simple

II. THEORY OF THE MULTI-SECTION TRANSFORMER

To facilitate a brief analysis of the working characteristics of the transformer, a simple model is given here. The transformer achieves the impedance matching from Z_0 to Z_L, and its fundamental circuit diagram is shown in Fig. 1. To simplify the analysis, we only discuss the case that the electrical lengths of all sections are equal [28]. The normalized complex matrix $\bar{A}$ of the transformation from Z_0 to Z_L can be written as:

$$\bar{A}=\begin{bmatrix}\bar{a}&\bar{b}\\ \bar{c}&\bar{d}\end{bmatrix}=\begin{bmatrix}\sqrt{\frac{Z_1}{Z_0}}&0\\ 0&\sqrt{\frac{Z_0}{Z_1}}\end{bmatrix}\begin{bmatrix}\cos\theta & j\sin\theta\\ -j\sin\theta&\cos\theta\end{bmatrix}\cdots$$

$$\begin{bmatrix}\sqrt{\frac{Z_N}{Z_{N-1}}}&0\\ 0&\sqrt{\frac{Z_{N-1}}{Z_N}}\end{bmatrix}\begin{bmatrix}\cos\theta & j\sin\theta\\ -j\sin\theta&\cos\theta\end{bmatrix}\begin{bmatrix}\sqrt{\frac{Z_L}{Z_N}}&0\\ 0&\sqrt{\frac{Z_N}{Z_L}}\end{bmatrix}, \quad (1)$$

where Z_1, …Z_{N-1}, Z_N, are the characteristic impedance of each section of the transformer, Z_L and Z_0 are the Port 1 and Port 2's input resistance, respectively. $\theta=\beta l$, and $\bar{a}$, $\bar{b}$, $\bar{c}$, $\bar{d}$ are the elements of the normalized complex matrix $\bar{A}$.

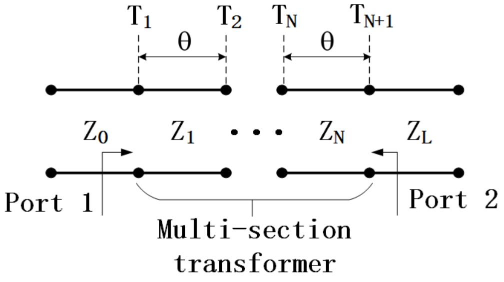

Fig. 1. Fundamental circuit diagram of multi-section impedance transformer.

Then, we can use $\bar{a}$, $\bar{b}$, $\bar{c}$, and $\bar{d}$ in (1) to express the attenuation L:

$$L=\frac{1}{|S_{21}|^2}=\frac{1}{4}\left|\bar{a}+\bar{b}+\bar{c}+\bar{d}\right|^2 . \quad (2)$$

As is known, the moduli of two complex numbers with mutual conjugation are equal:

$$\frac{1}{4}\left|\bar{a}+\bar{b}+\bar{c}+\bar{d}\right|^2=\frac{1}{4}\left|\bar{a}^*+\bar{b}^*+\bar{c}^*+\bar{d}^*\right|^2 , \quad (3)$$

where $\bar{a}*$, $\bar{b}*$, $\bar{c}*$, $\bar{d}*$ are the elements of the complex conjugate matrix $\bar{A}*$.

Because j and $\sin\theta$ always appear at the same time in (1), the elements of the complex conjugate matrix $\bar{A}*$ can be regarded as turning all sinθ to -sinθ. According to (3), it is not difficult for us to figure out that the expression of L only contains the even power of sinθ. Because $\sin^2\theta=1-\cos^2\theta$, the formula of L can be expressed as the even power of cosθ:

$$L=\sum_{i=0}^{N}A_i\cos^{2i}\theta , \quad (4)$$

where $A_i=A_i(Z_1,\ldots Z_{N-1},Z_N,Z_L),(i=0,1,2,\ldots N)$.

Since the matching condition of input port 1 is L=1, (4) can be rewritten as:

$$\sum_{i=0}^{N}A_i\cos^{2i}\theta-1=0 . \quad (5)$$

When all the coefficients satisfy certain conditions (by adjusting Z_0, Z_1, … Z_{N-1}, Z_N, Z_L), (5) can get N real roots, which is equivalent to the N zeros of its frequency response curve. By properly selecting the impedance values of each section of the transformer, it can always make full match at these frequency points, so as to realize a well-matched characteristic over a specified band. For the case that the electrical lengths of these sections are different, the corresponding proof process is given by [29].

Based on the ideas above, three transformers are designed in Section III.

III. OMT CONFIGURATION

The proposed OMT is shown in Fig. 2, including a T-type waveguide, a slotted metal plate and an absorber. The T-type waveguide is composed of a main arm and a side arm, in which three transformers are contained.

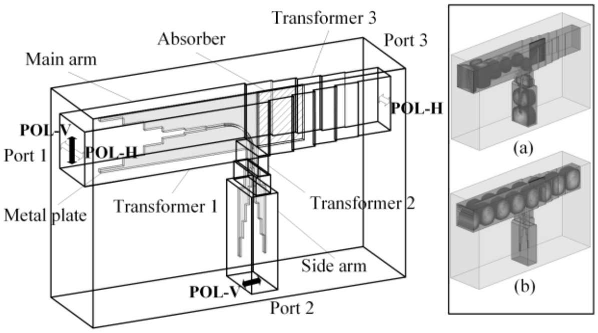

Fig. 2. General configuration of stepped double ridge structure based finline OMT. The inset describes the field distributions of the OMT at 37.5 GHz under vertical (a) and horizontal (b) polarizations.

When the vertical polarization is stimulated at the OMT's common Port 1, the field distribution is shown in the inset (a) of Fig. 2. The energy of TE_{10} mode is gradually transformed and confined to the finline gap via the main arm's transition (Transformer 1). Then the energy will be guided into the side arm by a 90-degree bend and be transferred to the port 2 by the side arm's transition (Transformer 2). When the vertical polarization is excited, the energy of TE_{01} mode travels through the metal plate virtually unperturbed by undergoing the process of separation and recombination [14]. After passing through the transformer 3, the energy will be eventually output by Port 3, which is depicted in the inset (b) of Fig. 2. In addition, to suppress the excitation of unwanted modes generated by the double ridge, an absorber is inserted [14].

It can be concluded that the OMT's matching characteristic is determined by the three transformers and the 90-degree bend. As the 90-degree bend is easily achieving low reflection by optimizing the arc slot of metal plate and the coupling window, the performances of the transformers will directly affect the overall matching characteristics of the OMT.

A. Design of the three multi-section transformers

As is known, the length of the traditional tapered double ridge transition should be long enough to achieve a good reflection coefficient characteristic. It can be explained as follows, the tapered transition in waveguide can be seen as the cascade of infinitely many small steps, and each of them will produce a reflected wave. These reflected waves are always partially cancelled at the input port, so that the total reflected wave can be maintained below a relatively small value across a wide frequency band. However, as the length of the tapered transitions increase, the size of the OMT will become excessively large.

The multi-section transformers can achieve impedance matching more effectively, which can be attributed to the fact that each section's length equals to nearly a quarter center wavelength, corresponding to $0.1875\lambda_{max}$ in the case of 50% fractional working bandwidth. Therefore, the fewer the sections are, the shorter the length will be.

In waveguide devices, since different in-band reflection characteristics can be obtained by assigning different impedance distributions to the multi-section transformers, they have an advantage of design flexibility compared to the traditional tapered one. To design these transformers, the ANSYS HFSS 15 is used, and the model of three transformers are shown in Fig. 3. Each transformer is assigned with the binomial and the Chebyshev impedance distributions, respectively, to verify different in-band responses.

Transformer 1 is a 6-section stepped double ridge waveguide with square waveguide cavity. It achieves an impedance transformation from 87 ohms to 628 ohms, which is calculated by the impedance expressions given in [30]. Transformer 2 is a 5-section double ridge waveguide with a 2-section stepped waveguide cavity, which realizes the impedance matching between 80 ohms and 314 ohms. Transformer 3 is a 4-section E-plane stepped waveguide, which transforms the impedance from 314 ohms to 628 ohms. The length of each section of these transformers is set to be a quarter wavelength of 37.5GHz. The binomial and Chebyshev impedance distributions of each transformer are given in Table 2 and Table 3, respectively.

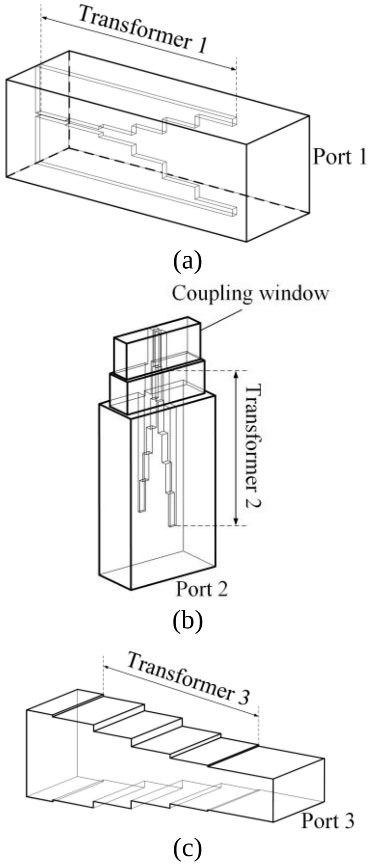

Fig. 3. The schematic of transformers: (a) transformer 1, (b) transformer 2, and (c) transformer 3.

Table 2: The binomial impedance distributions of each transformer

Transformer	1 (ohms)	2 (ohms)	3 (ohms)
1st section	89.7	84.3	328.5
2nd section	108.1	104.8	390.7
3rd section	170.4	161.3	506.5
4th section	310.3	248.3	605.4
5th section	488.9	308.7	
6th section	589.2		

Table 3: The Chebyshev impedance distributions of each transformer

Transformer	1 (ohms)	2 (ohms)	3 (ohms)
1st section	93.0	86.8	330.2
2nd section	118.2	109.9	389.9
3rd section	186.8	161.3	494.5
4th section	326.5	236.9	583.8
5th section	516.0	299.8	
6th section	582.1		

As shown in Fig. 4, the simulation result of the transformer 3 has standard responses of maximally flat and equal ripple characteristics, but the responses of other two transformers both have a little deterioration. This is mainly due to the fact that the double ridge waveguides with different ridge spacing have different cutoff frequency. It will result in the difference between the electrical length of each section and the desired quarter wavelength.

As a result, the binomial impedance distribution has the flattest reflection response, so it can be used to design the ultra-low reflection characteristic in specific frequency band. On the other hand, the Chebyshev impedance distribution has the equal ripple reflection characteristic in band, so it has the widest bandwidth under the limitation of a specified maximum standing wave, making it suitable to design for ultra-wideband applications.

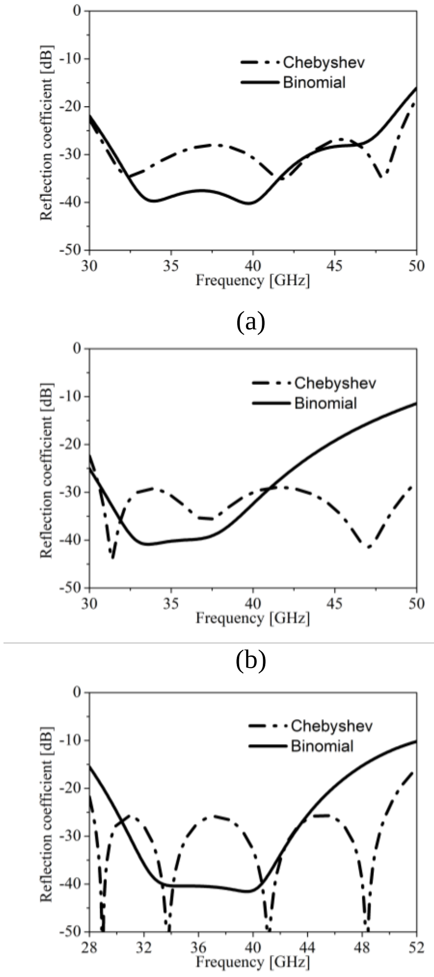

(a)

(b)

(c)

Fig. 4. The simulated reflection coefficients of each transformer: (a) transformer 1, (b) transformer 2, and (c) transformer 3.

B. Design of the OMT

To work in the 7mm-band, the size of the OMT's three ports refer to the WR-22 standard waveguide, wherein the square one is 5.69×5.69mm^2 and the rectangular one is 5.69×2.85mm^2.

As the performance of the OMT is determined by the 90-degree bend, the coupling window and the three transformers, the first two structures are designed and modeled in Fig. 5. The size of the coupling window is set to be 5×1.15×2.1mm^3.

Based on the analyses in part A, three transformers with Chebyshev impedance distribution are applied to the 7mm-band OMT design, and their in-band reflection characteristics are optimized by fine-tuning the length of each section. In particular, the 2-section waveguide cavity sizes of the transformer 2 are 5.2×1.6×1.9mm^3 and 5.69×2.85×10.1mm^3, respectively. In addition, the absorber is set in the transformer 3 to further reduce the device size, and the parameters of the transformer 3 are listed in Table 4. Other parameters can be obtained in Fig. 6.

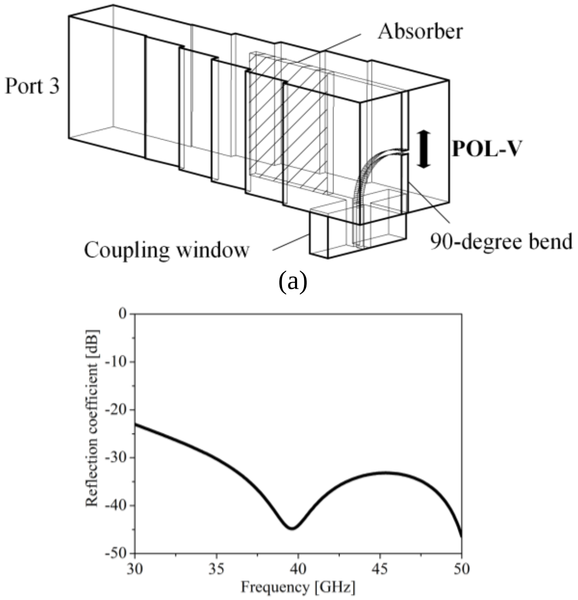

(a)

(b)

Fig. 5. Design of the 90-degree bend and the coupling window: (a) simulation model of ANSYS HFSS 15, and (b) reflection coefficient for vertical polarization.

Table 4: The specific parameters and the characteristic impedance of transformer 3

Name	Length (mm)	Width (mm)	Height (mm)
1st step	2.5	5.1	5.69
2nd step	2.5	4.4	
3rd step	2.5	3.6	
4th step	2.5	3	

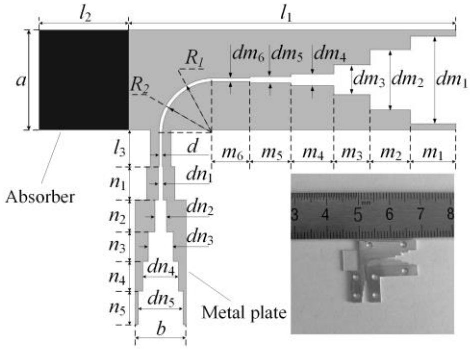

Fig. 6. The sectional view of the metal plate and the absorber. The parameters are (unit: mm): a=5.69, b=2.85, d=0.2, l_1=18.34, l_2=5, l_3=2.1, R_1=3.1, R_2=2.9, m_1=2.56, dm_1=4.99, m_2=2.26, dm_2=3.43, m_3=2.02, dm_3=1.69, m_4=2.4, dm_4=0.66, m_5=2.3, dm_5=0.34, m_6=2, dm_6=0.22, n_1=1.9, dn_1=0.28, n_2=1.8, dn_2=0.65, n_3=1.7, dn_3=1.38, n_4=1.7, dn_4=2, n_5=1.9, dn_5=2.56.

IV. MODELLING AND EXPERIMENTAL RESULTS

The electrical characteristics of the proposed finline OMT are analyzed by using full-wave simulation software ANSYS HFSS 15. To verify the simulated results, a prototype of the OMT has been fabricated, as shown in Fig. 7. In detail, the main body is split into two symmetrical aluminum blocks to manufacture with the help of CNC technique, and the slotted metal plate is fabricated by wire cut processing. Both processes have the tolerance of ±0.02mm. The absorber employs the ITO conductive glass with a surface resistance of 350±100 Ω/cm2. Finally, all parts assemble together with positioning screws and spacing slots.

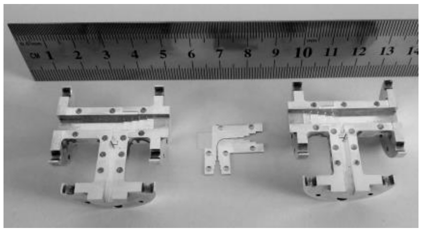

Fig. 7. The picture of the manufactured finline OMT.

The measurement system is composed of a Rohde & Schwarz ZVA 67 vector network analyzer (VNA), two coaxial cable to waveguide converters and a horn antenna used as load. In specific operations, the reflection coefficient and isolation are tested by connecting the OMT's three ports with the VNA and the horn antenna, and the insertion loss is measured with two OMTs arranged in the form of back to back. The simulated and measured results are shown in Fig. 8. Across the working band of 30.2GHz-49.8GHz, the proposed finline OMT possesses the reflection coefficient of less than -20dB, and the insertion loss of less than 1.1dB for both polarizations. Two rectangular ports' isolation is larger than 68dB, and the cross-polarization levels are less than -76dB for both polarizations.

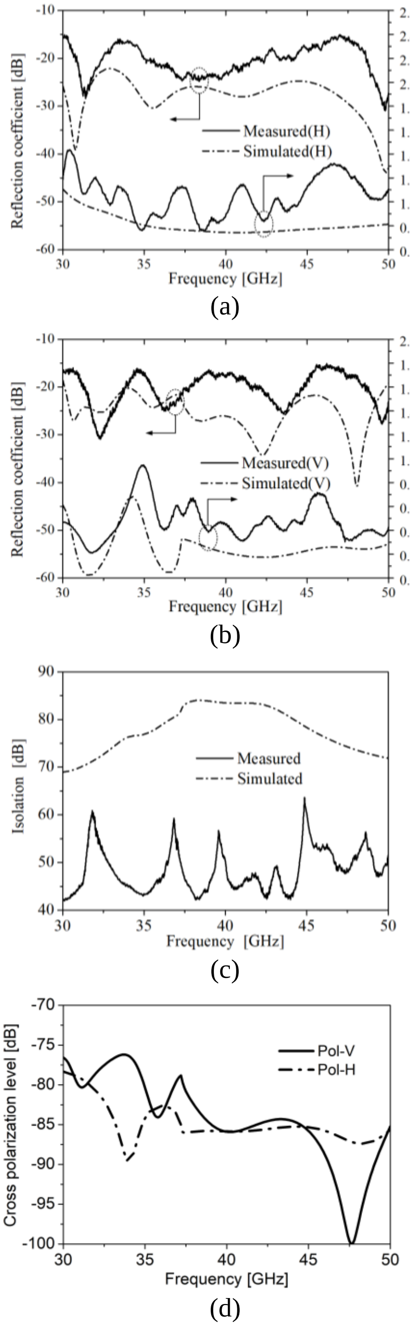

Fig. 8. The simulated and measured results of the proposed OMT: (a) reflection coefficient and insertion loss for horizontal polarization, (b) reflection coefficient and insertion loss for vertical polarization, (c) isolation of port 2 and port 3, and (d) cross-polarization level for both polarizations.

Compared with previous works, the use of multi-section transformers can make the design more compact. Specifically, the length of main arm's and side arm's transition can be reduced to $1.35\lambda_{max}$ and $0.9\lambda_{max}$, respectively.

From the results we can see that the measured ones are slightly worse than the simulated ones. Regardless of the increased reflection and insertion loss introduced by the mounting gaps of the main body, misalignment of waveguide connection interfaces and unstable electrical characteristics of the chosen absorber, the simulated results all have a close trend with the test ones except for the isolation and the reflection coefficient for horizontal polarization. For the former, it is mainly subject to the processing and assembly errors of the OMT. For the latter, the differences are additionally ascribed to the manufacturing and positioning errors of the metal plate.

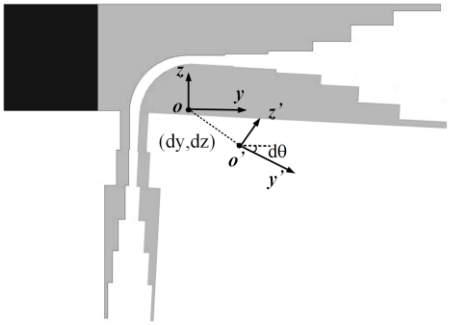

Fig. 9. The schematic of positioning errors.

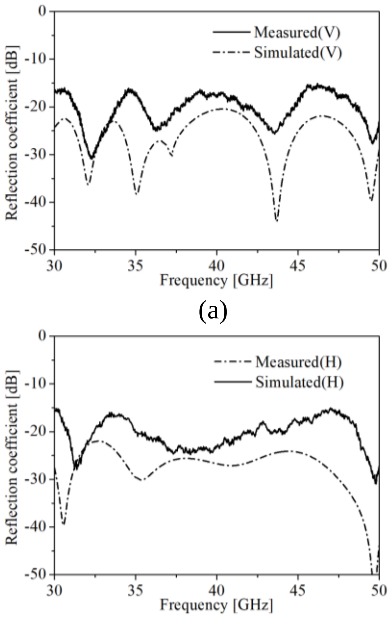

(a)

(b)

Fig. 10. Reflection coefficient of the measured results of the manufactured OMT and the simulated results of modified model for vertical polarization.

To further understand the effect of the positioning errors on the working performance, the translational error (dy,dz) and rotation error dθ of the metal plate are analyzed, as depicted in Fig. 9.

When (dy,dz)=(-0.01mm,0.04mm) and dθ=0.5deg, the simulated results of the modified model have close resonance frequency points with the measured ones for both polarizations, as shown in Fig. 10. However, due to the influence of the mounting gaps and connection reflection between the OMT and measurement system, the overall reflections will arise.

V. CONCULSION

A compact finline OMT based on multi-section transformer is proposed for operation in 30.2GHz to 49.8 GHz. Under the premise of preserving the in-band working characteristics, the design achieves the size reduction of the OMT. The proposed OMT has been tested and error analyzed. The predicted results have a good agreement with the measured ones.

ACKNOWLEDGMENT

This work was supported by National Basic Research Program of China-973 program 2015CB857100, National Natural Science Foundation of China (No. 61601350, 61401327, 61471278), the Foundation of Chinese Academy of Space Technology (CAST 2015-11).

REFERENCES

[1] R. W. Jackson, "A planar orthomode transducer," *IEEE Microwave and Wireless Components Letters*, vol. 11, (12), pp. 483-485, Dec. 2001.

[2] P. K. Grimes, O. G. King, G. Yassin, and M. E. Jones, "Compact broadband planar orthomode transducer," *Electronics Letters*, vol. 43, (21), pp. 1146-1147, Oct. 2007.

[3] J. Uher, J. Bomemann, and U. Rosenherg, *Waveguide Components for Antenna Feed Systems: Theory and CAD*. Artech House, 1993.

[4] T. J. Reck and G. Chattopadhyay, "A 600 GHz asymmetrical orthogonal mode transducer," *IEEE Microwave and Wireless Components Letters*, vol. 23, (11), pp. 569-571, Sep. 2013.

[5] M. A. Abdelaal, S. I. Shams, and A. A. Kishk, "Asymmetric compact OMT for X-band SAR applications," *IEEE Transactions on Microwave and Techniques*, vol. 66, (4), pp. 1856-1863, Apr. 2018.

[6] D. Dousset, S. Claude, and K. Wu, "A compact high-performance orthomode transducer for the Atacama large millimeter array (ALMA) band 1 (31-45GHz)," *IEEE Access*, 1, pp. 480-487, 2013.

[7] G. Virone, O. A. Peverini, M. Lumia, G. Addamo, and R. Tascone, "Platelet orthomode transducer for Q-band correlation polarimeter clusters," *IEEE Transactions on Microwave Theory and Techniques*,

vol. 62, (7), pp. 1487-1494, June 2014.

[8] J. Y. Han, S. Yoon, T. K. Lee, J. W. Lee, S. Song, and K. Oh, "Turnstile junction ortho-mode transducer for W-band radar seeker," *2016 URSI Asia-Pacific Radio Science Conference (URSI AP-RASC),* Seoul, South Korea, pp. 1796-1797, Oct. 2016.

[9] J. A. Ruiz-Cruz, J. R. Montejo-Garai, C. A. Leal-Sevillano, and J. M. Rebollar, "Orthomode transducers with folded double-symmetry junctions for broadband and compact antenna feeds," *IEEE Transactions on Antennas and Propagation*, vol. 66, (3), pp. 1160-1168, Jan. 2018.

[10] C. A. Leal-Sevillano, T. J. Reck, G. Chattopadhyay, J. A. Ruiz-Cruz, J. R. Montejo-Garai, and J. M. Rebollar, "Development of a wideband compact orthomode transducer for the 180–270 GHz band," *IEEE Transactions on Terahertz Science and Technology*, vol. 4, (5), pp. 634-636, July 2014.

[11] J. A. Ruiz-Cruz, J. R. Montejo-Garai, C. A. Leal-Sevillano, and J. M. Rebollar, "Development of folded dual-polarization dividers for broadband ortho-mode transducers," *2015 Asia-Pacific Microwave Conference (APMC)*, vol. 2, Nanjing, China, pp. 1-3, Feb. 2016.

[12] S. D. Robertson, "Recent advances in finline circuits," *IRE Transactions on Microwave Theory and Techniques*, 4, (4), pp. 263-267, 1956.

[13] C. E. Groppi, C. Y. Drouet d'Aubigny, A. W. Lichtenberger, and C. M. Lyons, "Broadband finline ortho-mode transducer for the 750-1150 GHz band," *16th International Symposium on Space Terahertz Technology*, Goteborg, Sweden, pp. 513-518, 2005.

[14] S. J. Skinner and G. L. James, "Wide-band orthomode transducers," *IEEE Transactions on Microwave and Techniques*, 39, (2), pp. 294-300, Feb. 1991.

[15] G. Chattopadhyay and J. E. Carlstrom, "Finline ortho-mode transducer for millimeter waves," *IEEE Microwave and Guided Wave Letters*, 9, (9), pp. 339-341, 1999.

[16] J. Takeuchi, A. Hirata, H. Takahashi, and N. Kukutsu, "10-Gbit/s bi-directional and 20-Gbit/s uni-directional data transmission over a 120-GHz-band wireless link using a finline ortho-mode transducer," *Microwave Conference Proceedings (APMC)*, Yokohama, Japan, pp. 195-198, 2010.

[17] G. Moorey, R. Bolton, A. Dunning, R. Gough, H. Kanoniuk, and L. Reilly, "A 77-117 GHz cryogenically cooled receiver for radio astronomy," *Proc. of the Workshop on the Applications of Radio Science*, 2006.

[18] M. A. Abdelaal, S. I. Shams, M. A. Moharram, M. Elsaadany, and A. A. Kishk, "Compact full band OMT based on dual-mode double-ridge waveguide," *IEEE Transactions on Microwave and Techniques*, pp. 1-8, Apr. 2018

[19] E. Menargues, S. Capdevila, T. Debogovic, A. Dimitriadis, J. R. Mosig, A. Skrivervik, and E. de Rijk, "Compact orthomode transducer with broadband beamforming capability," *2018 IEEE/MTT-S International Microwave Symposium – IMS*, Philadelphia, USA, Aug. 2018.

[20] G. L. Huang, S. G. Zhou, and T. Yuan, "Design of a compact wideband feed cluster with dual-polarized sum- and difference-patterns implemented via 3-D metal printing," *IEEE Transactions on Industrial Electronics*, vol. 65, (9), pp. 7353-7362, Sep. 2018.

[21] A. Navarrini and Renzo Nesti, "Symmetric reverse-coupling waveguide orthomode transducer for the 3-mm band," *IEEE Transactions on Microwave Theory and Techniques*, vol. 57, (1), Jan. 2009.

[22] A. Dunning, M. Bowen, and Yoon Chung, "Offset quad ridged ortho-mode transducer with a 3.4:1 bandwidth," *2013 Asia-Pacific Microwave Conference Proceedings (APMC)*, Seoul, South Korea, pp. 146-148, Jan. 2014.

[23] A. W. Pollak and M. E. Jones, "A compact quad-ridge orthogonal mode transducer with wide operational bandwidth," *IEEE Antennas and Wireless Propagation Letters*, vol. 17, (3), pp. 422-425, Mar. 2018.

[24] H. Y. Jin, Y. M. Huang, H. L. Jin, and K. Wu, "E-band substrate integrated waveguide orthomode transducer integrated with dual-polarized horn antenna," *IEEE Transactions on Antennas and Propagation*, vol. 66, (5), pp. 2291-2298, May 2018.

[25] A. A. Sakr, W. M. Dyab, and K. Wu, "Theory of polarization-selective coupling and its application to design of planar orthomode transducers," *IEEE Transactions on Antennas and Propagation*, vol. 66, (2), pp. 749-762, Feb. 2018.

[26] B. J. Mohammed, K. S. Bialkowski, and A. M. Abbosh, "Compact stepped slot antenna with unidirectional radiation for animal head imaging system," *2018 Australian Microwave Symposium (AMS)*, Brsibane, Australia, pp. 87-88, Apr. 2018.

[27] M. Knizek, C. Nicholl, C. Popovich, and K. A. Shamaileh, "Quad-band multi-section multi-way power divider and its miniaturization using coupled lines," *2017 IEEE International Symposium on Antennas and Propagation & USNC/URSI National Radio Science Meeting*, San Diego, CA, pp. 2253-2254, Oct. 2017.

[28] R. E. Collin, *Foundations for Microwave Engineering*. Cleveland, OH, 1973.

[29] C. Ming, "Novel design method of a multi-section transmission-line transformer using genetic algorithm techniques," *2008 International Conference on Electrical Machines and Systems*, Wuhan, China,

pp. 3793-3796, Feb. 2009.

[30] W. J. R. Hoefer and M. N. Burton, “Closed form expressions for parameters of finned and ridge waveguide,” *IEEE Transactions on Microwave and Techniques*, vol. 30, (12), pp. 2190-2194, Dec. 1982.

Yaqing Yu was born in Zhejiang province, China, in October 1990. He received the B.S. degree in Electromagnetic Field and Wireless Technology from Xidian University, Xi’an, China, in 2009. He is currently studying for a doctor’s degree in Electromagnetic Field and Microwave Technology from Xidian University. His research interests include wideband antennas, wide beam antennas and antenna feeding structures.

Wen Jiang was born in Shandong province, China, in November 1985. He received the B.S. and Ph.D. degrees from Xidian University, Xi’an, China, in 2008 and 2012, respectively. He is the Vice Director of the National Key Laboratory of Science and Technology on Antennas and Microwaves, Xidian University, where he is currently an Associate Professor. His current research interests include electromagnetic scattering and stealth technology, antenna theory and engineering, and electromagnetic measurement theory and technology.

Shuai Zhang was born in Hubei Province, China, in September 1983. He received the B.S. and Ph.D. degrees from Xidian University, Xi’an, China, in 2007 and 2012, respectively. Now, he teaches at the Electronic Engineering Institute of Xidian University, where he is an Associate Professor. His current research interests include theory and design of antennas and arrays, antenna array radiation calculation and pattern optimization, scattering calculation and electromagnetic stealth design of antennas and arrays and research on radiation and scattering calculation and control methods for large-scale array antennas.

Shuxi Gong was born in Hebei Province, China, in March 1957. He received the B.S. and M.S. degrees from Xidian University, Xi’an, China, in 1982 and 1984, respectively, and the Ph.D. degree from Xi’an Jiaotong University, Xi’an, in 1988. He was the Director of the National Key Laboratory of Science and Technology on Antennas and Microwaves, Xidian University, where he is currently a Full Professor. He has authored or coauthored over 200 refereed journal papers. He has also authored Principles of Generalized Eigenfunction Expansions in Electromagnetic Theory (Xi’an: Xidian Univ. Press, 2010), Prediction and Reduction of Antenna Radar Cross Section (Xi’an: Xidian Univ. Press, 2010), and Antennas for Mobile Communication Systems (Beijing: Electronics Industry Press, 2011). His current research interests include antenna theory and technology, prediction and control of antenna radar cross section (RCS), and RCS calculation of complex targets.

Tong Cheng was born in Hubei, China, in February 1993. He received the B.S. degree in Communication Engineering from Xidian University, Xi’an, China, in 2011. He is currently studying for a doctor’s degree in Electromagnetic Field and Microwave Technology from Xidian University. His research interests include substrate integrated waveguide antennas, circularly polarization end-fire antenna and waveguide devices.